UNIVERSITÉ PAUL CÉZANNE Aix-Marseille III

Institut Fresnel

Patrick Christian Chaumet

Habilitation à diriger les recherches
Spécialité : Physique

Modélisation électromagnétique : applications à l'imagerie optique et aux forces optiques

MM.	R. Carminati	rapporteur
	J.-M. Fournier	rapporteur
	D. Lesselier	rapporteur
Mme	F. De Fornel	
M.	H. Giovannini	

Habilitation présentée à Marseille, le 10 juillet 2007

Table des matières

Table des figures

Première partie

Curriculum Vitæ

Curriculum Vitæ

Nom patronymique : Chaumet — Prénom : Patrick
Né le 24 janvier 1971 à Paray-Le-Monial — Nationalité : Française
Situation de famille : célibataire — Email : patrick.chaumet@fresnel.fr
Tel. professionnel : 04-91-28-27-91 — Fax : 04-91-67-44-28

Formation universitaire

1998, Doctorat en physique.

Obtenu à Dijon, au laboratoire de physique de l'université de Bourgogne. Le titre de ma thèse était "Diffusion d'une Onde Electromagnétique par des Structures Arbitraires : Application à l'Emission de Lumière en STM" et a été encadré par J.-P Dufour. Le jury était constitué de :

Rapporteurs :	M. Jacques Baudon
	M. Richard Berndt
	M. Yves Borensztein
Examinateurs :	Mme Frédérique de Fornel
	M. Michel Loëte
Directeur de thèse :	M. Jean-Paul Dufour

1994, DEA interaction matière et rayonnement.

Obtenu à l'université de Dijon. Le stage avait été encadré par J.-P Dufour au laboratoire de physique de l'université de Bourgogne.

Parcours professionnel

Depuis le 01/10/2000, maître de conférence de l'université d'Aix-Marseille III.

Du 01/03/1999 au 30/09/2000, post-doctorant à l'Instituto de Ciencia de Materiales de Madrid sous la responsabilité de M. Nieto-Vesperinas.

Du 01/09/1998 au 30/02/1999, ATER à l'université de Bourgogne.

Du 01/09/1997 au 01/09/1998, demi ATER à l'université de Bourgogne.

Du 01/09/1994 au 01/09/1997, doctorant à l'université de Bourgogne (allocataire-moniteur).

Collaborations extérieures

A. Rahmani, LEOM, Ecole Centrale de Lyon.
M. Nieto-Vesperinas, ICMM CSIC, Madrid.
G. Bryant, NIST, Gaithersburg (USA).
N. Sojic, université de Bordeaux I.

Encadrements

C. Billaudeau, 2003-2004, DEA.
R. Lencrerot, 2004-2005, DEA.
F. Drsek, 2005-2008, thèse.

h-index : 11

Activités de recherche

Octobre 2000 jusqu'à ce jour en tant que Maître de conférences de l'université d'Aix-Marseille III.

• Confinement et exaltation électromagnétique pour biopuce

Ce **projet financé par une ANR** a pour but d'exploiter les effets de confinement et d'exaltation des ouvertures nanométriques mis à jour dans le projet Nanospot (ACI 2003) combiné au savoir faire de la jeune entreprise GENEWAVE (Palaiseau) sur l'exaltation de la fluorescence dans le contexte des biopuces. Outre les aspects de nanophotonique liés à la conception et à la réalisation des ouvertures, nous prenons en compte les spécificités de l'hybridation sur puce pour la définition des ouvertures (nombre, taille, espacement).

• Nano-imagerie bioanalytique

Ce **projet financé par une ANR** se propose de développer de nouveaux outils nanostructurés pour l'imagerie cellulaire et la bioanalyse hautement parallèle. Notre démarche s'articule suivant le triptyque : nanofabrication / étude des propriétés nouvelles liées à la taille nanométrique / applications bioanalytiques. La participation d'un partenaire industriel reconnu permet d'allier des objectifs fondamentaux (études sur cellules isolées, sur modèles de peaux reconstruites) à des opportunités d'applications *in vivo*. Nous proposons de réaliser un réseau de nano-cavités métalliques qui serviront comme nano-pinces optiques. Ces nano-pinces permettront ainsi de manipuler, de déplacer et d'immobiliser des populations différentes de particules modifiées par des systèmes de reconnaissance biotique (antigène-anticorps ou brins d'ADN). Les applications visées sont tournées vers l'immunodosage et les biopuces à ADN.

• Création de micro ou nano-moteurs grâce aux forces optiques

Le problème dans le cas de nano ou micro-machines est la source de puissance (moteur) permettant de les faire fonctionner. Un moteur est un système à qui on fournit de l'énergie et qui nous redonne un mouvement mécanique généralement sous la forme d'un axe en rotation. Les forces optiques, si l'objet étudié présente une dissymétrie, peuvent entraîner une rotation de celui-ci. Cet objet peut alors servir de moteur pour une machine plus

complexe. **Avec C. Billaudeau (étudiant en DEA)** nous avons développé une méthode pour calculer le couple optique.

• Imagerie optique à haute résolution

Ce projet est animé par A. Sentenac, chargé de recherche au CNRS à l'institut Fresnel, dans le cadre d'une **ACI jeunes chercheurs**. L'objectif de ce projet est de proposer une nouvelle méthode de microscopie optique, en champ lointain, permettant de restituer la forme de l'objet et sa permittivité relative, et ce avec un pouvoir de résolution supérieur à celui imposé par la limite de diffraction. Notre technique d'imagerie s'apparente à celles développées dans le domaine des micro-ondes. L'échantillon est éclairé par un faisceau laser sous différentes incidences et le champ diffracté est détecté selon différents angles d'observations. Je me suis plus particulièrement intéressé au développement des algorithmes de résolution du problème inverse afin de remonter aux caractéristiques de l'objet, et ce à trois dimensions. Afin de pouvoir pleinement appréhender le problème je suis actuellement en **CRCT (2004-2006)**. De plus c'est exactement sur ce thème que **j'ai encadré R. Lencrerot (DEA) et que j'encadre F. Drsek (début de thèse)**.

• Forces optiques, application à la nano-manipulation (pinces optiques)

Ces dernières années ont vu l'utilisation des forces optiques pour confiner et contrôler, dans les trois dimensions de l'espace, des particules avec des tailles allant de la dizaine de nanomètres à plusieurs micromètres. Nous avons montré récemment, en étroite **collaboration avec A. Rahmani (LEOM, Ecole Centrale de Lyon) et M. Nieto-Vesperinas (ICMM, Madrid)**, que ces forces optiques pouvaient servir à manipuler des objets de taille nanométrique. Ceux-ci sont déposés sur un substrat plan transparent, puis la pointe d'un microscope optique de champ proche est utilisée pour repérer pour finalement manipuler de manière sélective ces particules. Notons que la collaboration avec M. Nieto-Vesperinas fait suite à un stage post-doctoral de 1 an et demi dans son laboratoire.

• Contrôle de l'émission spontanée

Quand un environnement modifie, en un point de l'espace, la distribution spatiale et spectrale des modes électromagnétiques, il modifie aussi l'émission spontanée d'une source placée à cet endroit. Je m'intéresse à la dynamique des sources de photons dans des environnements variés tels que des cristaux photoniques. Ceci a été effectué en **collaboration avec A. Rahmani (LEOM, Ecole Centrale de Lyon)**.

• Amélioration de la convergence de la méthode des dipôles couplés

Il existe de nombreuses méthodes pour calculer la diffraction de la lumière par des objets de forme arbitraire. La méthode que j'utilise consiste à discrétiser la matière en un ensemble de petits éléments disposés sur une maille cubique. Sous l'action d'une onde incidente chacun des éléments de discrétisation va acquérir un moment dipolaire qui va dépendre de l'onde incidente et de son couplage avec tous les autres dipôles. En **collaboration avec A. Rahmani (LEOM, Lyon) et G. Bryant (NIST, Gaithersburg, USA)** nous avons proposé plusieurs possibilités pour améliorer la convergence de la méthode. La collaboration avec G. Bryant m'a amené à travailler durant **cinq semaines aux Etats-Unis (NIST, Washington) au sein de son équipe**.

• Extension de la méthode des dipôles couplés à des configurations complexes

La méthode des dipôles couplés (CDM) était limitée aux objets finis, je me suis donc intéressé à étendre la CDM aux structures périodiques et plus récemment aux structures périodiques en présence d'objets apériodiques. Ceci voit son application dans mes autres thèmes de recherche.

Mars 1999/septembre 2000, stage post-doctoral à Madrid dans le groupe dirigé par M. Nieto-Vesperinas

• Forces optiques pour des objets sur des substrats et lien optique

Lors de mon stage post-doctoral à l'université Autonoma de Madrid dans l'équipe dirigée par M. Nieto-Vesperinas, j'ai étudié les forces optiques sur des objets nano et micro-métriques. L'étude a porté essentiellement sur les forces optiques créées par des ondes évanescentes et l'influence du substrat sur lequel étaient déposées les particules. Les liens optiques entre les particules, créés par la lumière, ont aussi été étudiés.

1994/février 1999, thèse et ATER au laboratoire de physique de l'université de Bourgogne

• Emission de lumière en microscopie tunnel électronique (STM)

Mon sujet de thèse portait sur la microscopie tunnel électronique (STM). Il consistait à caractériser la nature chimique des éléments sous la pointe d'un STM à partir de l'émission de lumière de la jonction tunnel.

• Microscopie de champ proche optique

La méthode développée pour étudier l'émission de lumière en STM m'a permis aussi d'étudier le champ proche optique. Notamment la formation des images en microscopie de champ proche et la durée de vie de molécules fluorescentes.

Activités d'enseignement

Depuis octobre 2000 en qualité de Maître de Conférence de l'université d'Aix-Marseille III

J'effectue, en moyenne, chaque année 220 heures (équivalent TD) à l'IUT de Saint Jérôme dans le département Mesures Physiques excepté durant les deux années universitaires 2004/2005 et 2005/2006 du CRCT.

• Travaux dirigés en optique géométrique destinés aux étudiants de première année.
• Travaux dirigés en optique ondulatoire destinés aux étudiants de première année.
• Travaux dirigés en mécanique du point destinés aux étudiants de première année.
• Travaux dirigés en optronique destinés aux étudiants de deuxième année.
• Travaux pratiques en optique géométrique destinés aux étudiants de première année.
• Travaux pratiques en optique ondulatoire destinés aux étudiants de première année.
• Travaux pratiques en optronique destinés aux étudiants de deuxième année.

1997/1999, ATER à l'université de Dijon

• Travaux dirigés en optique géométrique destinés aux étudiants de premier cycle (DEUG B).
• Travaux pratiques en optique géométrique et ondulatoire destinés aux étudiants de premier
cycle (DEUG B et DEUG A).
• Travaux pratiques en électricité destinés aux étudiants de premier cycle (DEUG A).

1994/1997, moniteur à l'université de Dijon

• Travaux dirigés en optique géométrique destinés aux étudiants de premier cycle (DEUG B).

• Travaux pratiques en optique géométrique et ondulatoire destinés aux étudiants de premier

cycle (DEUG B et DEUG A).

• Travaux dirigés en mécanique quantique destinés aux étudiants de deuxième cycle.

Deuxième partie

Liste des publications

Articles publiés dans des revues internationales à comité de lecture

1. P. C. Chaumet, K. Belkebir et A. Sentenac,
   Numerical study of grating-assisted optical diffraction tomography
   Phys. Rev. A accepté.
2. P. C. Chaumet, B. Pouligny, R. Dimova et N. Sojic,
   Optical tweezers in interaction with an apertureless probe
   J. Appl. Phys. accepté.
3. A. Sentenac, C.-A. Guérin, P. C. Chaumet, F. Drsek, H. Giovannini, N. Bertaux et M. Holschneider,
   Influence of multiple scattering on the resolution of an imaging system : a Cramer-Rao analysis.
   Opt. Express **15**, 1340 (2007).
4. P. C. Chaumet et C. Billaudeau,
   Coupled dipole method to compute optical torque : Application to a micropropeller.
   J. Appl. Phys. **101**, 023106 (2007).
5. A. Sentenac, P. C. Chaumet, et K. Belkebir,
   Beyond the Rayleigh criterion : Grating assisted far-field optical diffraction tomography.
   Phys. Rev. Lett. **97**, 243901 (2006). **[annexe 4 page 191]**
6. P. C. Chaumet,
   Fully vectorial highly non paraxial beam close to the waist.
   J. Opt. Soc. Am. A **23**, 3197 (2006).
7. E. Popov, M. Neviere,J. Wenger, P-F. Lenne, H. Rigneault, P. C. Chaumet, N. Bonod, J. Dintinger, and T. Ebbesen,
   Field enhancement in single subwavelength apertures,
   J. Opt. Soc. Am. A. **23**, 1084 (2006). J. Opt. Soc. Am. A.
8. P. C. Chaumet, A. Rahmani, M. Nieto-Vesperinas,
   Local-field enhancement in an optical force metallic nanotrap : Application to single-molecule spectroscopy.
   App. Opt. **45**, 5185 (2006).
9. A. Rahmani et P. C. Chaumet,
   Optical Trapping near a Photonic Crystal.
   Opt. Express **14**, 6353 (2006).

10. F. Bordas, N. Louvion, S. Callard, P. C. Chaumet, and A. Rahmani,
Coupled dipole method for radiation dynamics in finite photonic crystal structures.
Phys. Rev. E. **73**, 056601 (2006).

11. P. C. Chaumet, K. Belkebir, and R. Lencrerot,
Three-dimensional optical imaging in layered media,
Opt. Exp. **14**, 3415 (2006).

12. K. Belkebir, P. C. Chaumet, A. Sentenac,
Influence of multiple scattering on three-dimensional imaging with optical diffraction tomography.
J. Opt. Soc. Am. A. **23**, 586 (2006). [**annexe 4 page 181**]

13. P. C. Chaumet, A. Sentenac,
Numerical simulation of the electromagnetic field scattered by defects in a double-periodic structure.
Phys. Rev. B **72**, 205437-8 (2005). [**annexe 4 page 97**]

14. P. C. Chaumet, A. Rahmani, A. Sentenac, and G. W. Bryant,
Efficient computation of optical forces with the coupled dipole method.
Phys. Rev. E **72**, 046708-6 (2005).

15. K. Belkebir, P. C. Chaumet, A. Sentenac,
Superresolution in total-internal reflection tomography.
J. Opt. Soc. Am. A. **22**, 1889-1897 (2005). [**annexe 4 page 172**]

16. E. Popov, N. Bonod, M. Nevière, H. Rigneault, P.-F. Lenne, and P. C. Chaumet,
Surface plasmon excitation on a single subwavelength hole in a metallic sheet.
Appl. opt. **44**, 2332-2337 (2005).

17. P. C. Chaumet, A. Rahmani, and M. Nieto-Vesperinas,
Photonic force spectroscopy on metallic and absorbing nanoparticles.
Phys. Rev. B **71**, 045425-7 (2005). [**annexe 4 page 155**]

18. P. C. Chaumet, K. Belkebir, A. Sentenac,
Superresolution of three-dimensional optical imaging by use of evanescent waves.
Opt. Lett. **29**, 2740-2742 (2004). [**annexe 4 page 169**]

19. P. C. Chaumet, A. Sentenac, and A. Rahmani,
Coupled dipole method for scatterers with large permittivity.
Phys. Rev. E **70**, 036606-6 (2004). [**annexe 4 page 86**]

20. P. C. Chaumet, K. Belkebir, and A. Sentenac,
Three-dimensional sub-wavelength optical imaging using the coupled dipole method.
Phys. Rev. B **69**, 245405-7 (2004). [**annexe 4 page 162**]

21. A. Rahmani, P. C. Chaumet, and G. W. Bryant,
On the Importance of Local-Field Corrections for Polarizable Particles on a Finite Lattice : Application to the Discrete Dipole Approximation.
Astrophysical J. **607**, 873-878 (2004). [**annexe 4 page 105**]

22. M. Nieto-Vesperinas, P. C. Chaumet, and A. Rahmani,
Near-field photonic forces.
Phil. Trans. Roy. Soc. Lond. A **362**, 719-737 (2004).

23. P. C. Chaumet,
Comment on "Trapping force, force constant, and potential depths for dielectric spheres in the presence of spherical aberrations".
Appl. Opt. **43**, 1825-1826 (2004).

24. P. C. Chaumet, A. Rahmani, and G. W. Bryant,
Generalization of the coupled dipole method to periodic structure.
Phys. Rev. B **67**, 165404-5 (2003). [**annexe 4 page 92**]

25. A. Rahmani, P. C. Chaumet, and G. W. Bryant,
Coupled dipole method with an exact long-wavelength limit and improved accuracy at finite frequencies.
Opt. Lett. **27**, 2118-2120 (2002). [**annexe 4 page 111**]

26. P. C. Chaumet, A. Rahmani, and M. Nieto-Vesperinas,
Selective nanomanipulation using optical forces.
Phys. Rev. B **66**, 195405-11 (2002). [**annexe 4 page 144**]

27. P. C. Chaumet, A. Rahmani, and M. Nieto-Vesperinas,
Optical trapping and manipulation of nano-object with an apertureless probe.
Phys. Rev. Lett. **88**, 123601-4 (2002). [**annexe 4 page 140**]

28. A. Rahmani, P. C. Chaumet, and G. W. Bryant,
Local-field correction for an interstitial impurity in a crystal.
Opt. Lett. **27**, 430-432 (2002). [**annexe 4 page 206**]

29. P. C. Chaumet, and M. Nieto-Vesperinas,
Optical binding of particles with or without the presence of a flat dielectric surface.
Phys. Rev. B **64**, 035422-7 (2001). [**annexe 4 page 133**]

30. A. Rahmani, P. C. Chaumet, et F. de Fornel,
Enrironment-induced modification of spontaneous emission : Single-molecule near-field probe.
Phys. Rev A **63**, 023819-11 (2001). [**annexe 4 page 195**]

31. P. C. Chaumet, and M. Nieto-Vesperinas,
Electromagnetic force on a metallic particle in the presence of a dielectric surface.
Phys. Rev. B **62**, 11185-11191 (2000). [**annexe 4 page 126**]

32. P. C. Chaumet, and M. Nieto-Vesperinas,
Time-averaged total force on a dipolar sphere in an electromagnetic field.
Opt. Lett. **25**, 1065-1067 (2000). [**annexe 4 page 114**]

33. P. C. Chaumet, and M. Nieto-Vesperinas,
Coupled dipole method determination of the electromagnetic force on a particle over a flat dielectric substrate.
Phys. Rev. B **61**, 14119-14127 (2000). [**annexe 4 page 117**]

34. P. C. Chaumet, and A. Rahmani,
Comment on "Physical picture for light emission in scanning tunneling microscopy".
Phys. Rev. Lett. **84**, 3498-3401 (2000).

35. P. C. Chaumet, A. Rahmani, F. de Fornel, and J.-P. Dufour,
Evanescent light scattering : The validity of the dipole approximation.
Phys. Rev. B **58**, 2310-2315 (1998).

36. P. C. Chaumet, and J.-P. Dufour,
Electric potential and field between two different spheres.
J. of Electrostatics **43**, 145-159 (1998).

37. A. Rahmani, P. C. Chaumet, F. de Fornel, and C. Girard,
Field propagator of a dressed junction : Fluorescence lifetime calculations in a confined geometry.
Phys. Rev A **56**, 3245-3254 (1997).

Proceeding et Conférences avec publication des actes

1. A. Sentenac, P. C. Chaumet et K. Belkebir, Grating-assisted optical diffraction tomography with near-field resolution. Focus On Microscopy (FOM 2007) avril 2007 Valencia (Espagne).
2. A. Sentenac, K. Belkebir et P. C. Chaumet : Reconstruction procedures in structured illumination fluorescent microscopy. Focus On Microscopy (FOM 2007) avril 2007 Valencia (Espagne).
3. H. Giovannini, D. Konan, A. Sentenac, F. Drsek, P. C Chaumet, K. Belkebir, V. Lauer, et F Maffezzini : Far-field reflection microscope using optical diffraction tomography-application to profilometry. Focus On Microscopy (FOM 2007) avril 2007 Valencia (Espagne).
4. P. C. Chaumet, K. Belkebir, F. Drsek, H. Giovannini, A. Sentenac : Nanoscopy with Grating-Assisted Optical Diffraction Tomography. Annual Review of Progress in Applied Computational Electromagnetics, mars 2007 Verona (Italie).
5. F. Drsek, H. Giovannini, P. Chaumet, K. Belkebir, A. Sentenac : Optical diffraction tomography in reflection. PSIP 2007 - Physics in Signal and Image Processing - Mulhouse 31 jan.-2 fev. 2007.
6. A. Sentenac, C.-A. Guérin, P. C. Chaumet, F. Drsek, N. Bertaux, H. Giovannini, M. Holschneider : Influence of multiple scattering on the resolution of an imaging system, a Cramér-Rao analysis. PSIP 2007 - Physics in Signal and Image Processing - Mulhouse 31 jan.-2 fev. 2007.
7. A. Sentenac, P. C. Chaumet, K. Belkebir :Grating-assisted optical diffraction tomography with nearfield resolution. The 88 th Eastern Forum of Science and Technology Challenges and Opportunities in Nano-Optics Jan 5-9, 2007, Fudan University, Shanghai, China.
8. A. Sentenac, P. C. Chaumet, K. Belkebir : Grating-assisted optical diffraction tomography with nearfield resolution, EOS Annual Meeting 2006 : Paris, France, 16-19 October 2006.
9. P. C. Chaumet,K. Belkebir, A. Sentenac : High resolution three-dimensional imaging with optical diffraction tomography. Mediterranean Microwave Symposium (MMS), Genova, Italy, 19-21 september 2006.
10. A. Sentenac, K. Belkebir, P. C. Chaumet : Inversion techniques in structured illumination fluorescent microscopy. International Symposium - Optical Analysis of Biomolecular Machines, Berlin, Germany, 13-16 july 2006.

11. J.-M. Geffrin, C. Eyraud, P. Sabouroux, P. C. Chaumet, H. Tortel, and H. Giovannini : Validation of 3D Scattering Measurements, IEEE AP-S International Symposium and USNC/URSI National Radio Science Meeting, 9-14 July 2006.
12. K. Belkebir, P. C. Chaumet, and A. Sentenac : Optical imaging of sub-wavelength objects, 2005 IEEE AP-S International Symposium and USNC/URSI National Radio Science Meeting, 3-8 July 2005.
13. P. C. Chaumet, K. Belkebir, and A. Sentenac : High resolution three-dimensional imaging with optical diffraction tomography, Focus on Microscopy 2005, Friedrich Schiller University Jena, Germany, 20-23 mars 2005.
14. K. Belkebir, P. C. Chaumet, A. Sentenac : Three-dimensional sub-wavelength optical imaging using the Coupled Dipole Method, Mediterranean Microwave Symposium (MMS), Marseille, 1-3 juin 2004.
15. P. C. Chaumet, K. Belkebir, and A. Sentenac : High resolution imaging with optical diffraction tomography, role of the evanescent waves, PIERS, Pisa, Italy, 28-31 march 2004.
16. P. C. Chaumet, K. Belkebir, and A. Sentenac : Sub-wavelength imaging with diffraction tomography, EOS Topical Meeting - Advanced Imaging Techniques, Delft, The Netherlands, 20-23 October 2003.
17. A. Rahmani, P. C. Chaumet, and G. W. Bryant : Modeling Nano-optics : towards a more physical formulation of the coupled dipole method, CLEO/QELS Long Beach, USA, May 2002.
18. A. Rahmani, P. C. Chaumet, and G. W. Bryant : Local-field correction for a nanosource in a crystal, CLEO/QELS Long Beach, USA, May 2002.
19. M. Nieto-Vesperinas, J. Ricardo Arias-Gonzales, P. C. Chaumet, and M. Lester, Nanoparticles on surfaces : resonances and optical forces, Trends in Nanotechnology - TNT Toledo 16-20 October 2000.
20. J. Ricardo Arias-Gonzales, P. C. Chaumet, and M. Nieto-Vesperinas, *Nanoparticles on surfaces : Resonance and optical forces.* International school of physics "Enrico Fermi", 27 June-7 July 2000.
21. A. Rahmani, P. C. Chaumet, and F. de Fornel : Modification of spontaneous emission : Single-molecule near-field probe, NFO6 Twente, Netherland, August 2000.
22. P. C. Chaumet and A. Rahmani : Limite d'une description dipolaire pour des objets métalliques, Congrès National de la S.F.P., Paris, France, 7-11 July 1997.
23. A. Rahmani and P. C. Chaumet : Fluorescence en optique de champ proche, Congrès National de la S.F.P., Paris, France 7-11 July 1997.
24. P. C. Chaumet : Photoémission en STM, Journées Franco-Algériennes sur la Matière Condensée, Dijon, France, 9-12 septembre 1996.
25. P. C. Chaumet and J.-P. Dufour, and F. de Fornel : Photoémission inverse en microscopie tunnel électronique, Congrès National de la S.F.P., Marseille, France, 4-8 Septembre 1995.

Troisième partie

Résumé de mes activités d'enseignement

Résumé de mes activités d'enseignement

Généralités

Je suis maître de conférence à l'université d'Aix-Marseille III depuis le 1er octobre 2000. J'enseigne au département mesures physiques de l'institut universitaire de technologie (IUT) de Marseille. Le département mesures physiques de l'IUT a l'avantage d'être une formation pluridisciplinaire, très appréciée dans les secteurs les plus divers. Ceci permet aux étudiants d'exercer directement leurs compétences tant dans l'encadrement technique industriel (grandes entreprises, PME, PMI), que dans des secteurs plus spécialisés tels le médical ou le paramédical, les bureaux d'études, les laboratoires de recherche ou dans certaines professions technico-commerciales.

Après l'IUT mesures physiques de très nombreuses poursuites d'études sont accessibles à la majorité des étudiants : écoles d'ingénieurs (ENSI, INSA, réseaux EIFFEL et ARCHIMÈDE ...), licences classiques et technologiques, IUP/Masters, ... sans oublier les diplômes à l'étranger (Bachelor of Sciences par exemple...).

Horaires

Années 2000 à 2004 :

Durant ces trois années scolaires, j'ai effectué en moyenne 220 heures (équivalent TD).

Années 2004 à 2006 :

Pour les années scolaires 2004/2005 et 2005/2006 j'ai obtenu un congé pour recherche et conversion thématique (CRCT) avec un service d'enseignement réduit à 96 heures équivalent TD.

Enseignement réalisé

L'enseignement au département mesures physiques de l'IUT se fait aussi bien en travaux pratiques qu'en travaux dirigés.

• *Travaux dirigés et pratiques en optique géométrique destinés aux étudiants de première année :*

-Etude des lois de la réflexion et de la réfraction sur une interface séparant deux milieux d'indices différents.

-Dioptres sphériques et lentilles minces (convergents et divergents) : relations de conjugaison et application aux instruments d'optique (télescope, microscope, appareil photographique,. . .). Notions d'objet et d'image.

-Miroir convexe, concave, et plan.

-Mise en évidence des aberrations chromatiques et géométriques (sphéricité, coma, astigmatisme, courbures de champ, distorsions).

• *Travaux dirigés et pratiques en optique ondulatoire destinés aux étudiants de première année :*

-Concept d'onde électromagnétique, notation complexe.

-Etude de la diffraction en champ lointain : par une fente, un trou rectangulaire et circulaire.

-Notions d'interférométrie : Interféromètre de Fizeau, de Michelson.

• *Travaux dirigés en mécanique du point destinés aux étudiants de première année :*

-Définition de la vitesse et de l'accélération moyenne et instantanée.

-Deuxième loi de Newton.

-Changement de repère en translation et rotation (accélération de corriolis).

-Conservation de la quantité de mouvement (choc élastique et inélastique).

-Couple, moment cinétique, moment d'inertie, conservation du moment cinétique.

• *Travaux dirigés et pratiques en optronique destinés aux étudiants de deuxième année :*

-Polarisation de la lumière, coefficient de Fresnel, angle de Brewster.

-Fibres optiques.

-Récepteurs (photodiodes).

Co-responsable des stages

Les étudiants à la fin de leur formation de deux ans, se doivent de finir par un stage en entreprise de 11 semaines. Depuis 2006 je suis co-responsable de l'organisation des stages avec M. Brutin.

Visites de stage

Lors du stage en entreprise effectué par les élèves, chaque professeur, afin de contrôler l'insertion et le sérieux de l'élève va le voir au sein de l'entreprise.

En moyenne je vois chaque année trois ou quatre élèves pendant leur stage.

Quatrième partie

Résumé de mes activités de recherche et d'encadrement

Introduction générale

C'est pas parce qu'on a rien à dire qu'il faut fermer sa gueule.
M. Audiard

L'optique est la branche de la physique qui étudie tout ce qui est en rapport avec la lumière au sens large du terme, *i.e.*, quelle que soit la longueur d'onde considérée. Il y a cinquante ans, l'optique était considérée comme une science achevée grâce aux équations de Maxwell, qui constituent les postulats de base de l'électromagnétisme avec l'expression de la force électromagnétique de Lorentz, les travaux de M. Planck et A. Einstein, qui introduisent le concept de photon, et Louis de Broglie en 1924, qui réussit à concilier la dualité onde-corpuscule. Or, depuis la dernière guerre mondiale, avec l'avènement du laser nous assistons à un bouleversement de l'optique. Le laser nous a ouvert notamment des domaines de l'optique jusqu'alors inconnus tels que la microscopie de champ proche optique, la spectroscopie à haute résolution, l'optique intégrée, l'optique non linéaire, pour ne citer que quelques exemples.

Cette partie présente mes activités de recherche qui se situent toutes dans le domaine de l'optique. Elles ont été réalisées d'une part lors de mon stage post-doctoral à Madrid à l'Instituto de Ciencia de Materiales de Madrid, où j'ai alors travaillé au département de la matière condensée au sein du groupe de M. Nieto-Vesperinas pour la période 1999-2000, puis d'autre part, depuis que je suis à l'Institut Fresnel de Marseille (2000-2007) en tant que maître de conférence au sein des équipes SEMO (Sondage ElectroMagnétique et Optique) et CLARTE (Contrôle de la Lumière et Analyse du Rayonnement : Traitement Electromagnétique).

Ma recherche couvre *a priori* des domaines assez variés de l'optique, tels que la fluorescence, le sondage électromagnétique, et les forces optiques, mais ils ont deux dénominateurs communs. Le premier et le plus évident, est bien sûr le concept d'onde évanescente, mis en évidence par Newton,[i] qui est de première importance dans les études que j'ai réalisées. Le deuxième est la méthode employée pour résoudre les différents problèmes posés.

Le premier chapitre est consacré à la méthode que j'utilise pour calculer la diffusion d'une onde électromagnétique par des objets de forme et de permittivité relative arbitraires. Cette méthode, dite méthode des dipôles couplés (CDM), est utilisée aussi bien pour étudier la fluorescence, que les forces optiques ou réaliser du sondage électromagné-

[i] Soit un prisme éclairé avec un angle d'incidence supérieur à l'angle limite à la réflexion totale. En posant une lentille sphérique sur la face du prisme on s'aperçoit alors qu'une partie de la lumière est transmise à travers la lentille dans le second milieu.

tique. Je vais donc expliciter les différents développements que je dus apporter à la CDM pour pouvoir l'appliquer aux configurations souhaitées.

Le second chapitre aborde les forces optiques. Après une courte introduction pour poser les principes et l'utilité des forces optiques dans la physique moderne, je vais expliciter les différents travaux que j'ai effectués sur le sujet. Je vais notamment me focaliser sur le résultat majeur qui est la nano-manipulation, *i.e.*, comment repérer puis déplacer des objets de taille nanométrique déposés sur un substrat plan.

Le troisième chapitre est dédié au sondage électromagnétique. Cela consiste à partir du seul champ diffracté par un objet (ou des objets) à pouvoir le (les) localiser et si possible le (les) caractériser (forme, permittivité relative,...). Ce travail réalisé au sein de l'équipe SEMO a pour but de fabriquer un microscope avec une résolution très fortement inférieure au critère de Rayleigh.

Le quatrième chapitre quant à lui est consacré au phénomène de la fluorescence, c'est à dire la durée de vie d'un atome (ou d'une molécule) dans son état excité en fonction de l'environnement dans lequel il est situé.

Quelques notes sur la rédaction

- Le cadre dans lequel a été effectué un travail donné est à chaque fois précisé : collaboration nationale ou internationale, localisation des différentes personnes, et le ou les laboratoires impliqués.
- Avant d'aborder les quatre chapitres consacrés à ma recherche, il faut souligner qu'ils s'adressent à un public relativement large, et donc que chaque paragraphe présente une idée ayant amené à une, ou plusieurs publications, en évitant au maximum les équations absconses. J'ai essayé d'exposer le travail effectué et la physique sous-jacente sans qu'il soit nécessaire d'aller regarder les publications liées au travail expliqué. Néanmoins, les lecteurs intéressés par les détails abstrus, et les grandes équations alambiquées pourront se reporter aux annexes.
- Les références bibliographiques associées à chaque chapitre concernent mes articles et les articles les plus fondateurs sur le sujet. Pour avoir une bibliographie plus complète il faut se reporter aux annexes.
- A noter que les chapitres ne sont pas rédigés à la première personne du singulier, mais à la première personne du pluriel. Ceci est dû au fait que le travail de recherche que j'ai effectué n'a pas été réalisé seul, comme l'attestent les auteurs de ma liste de publication.

Chapitre 1

Amélioration, et généralisation à des structures complexes, de la méthode des dipôles couplés

Ceux qui ne savent rien en savent toujours autant
que ceux qui n'en savent pas plus qu'eux.
Pierre Dac

Sommaire

1.1 Introduction

Il existe de nombreuses méthodes permettant d'étudier la diffraction d'une onde électromagnétique par un objet de forme et de permittivité relative arbitraires. Nous n'allons par faire ici une liste exhaustive de ces méthodes, mais le lecteur intéressé peut se reporter à l'article de F. M. Kahnert qui détaille les forces et les faiblesses des méthodes les plus usuelles.[1]

La méthode que nous utilisons s'appelle la méthode des dipôles couplés (CDM). Cette méthode, dite volumique car le champ diffracté est obtenu à partir d'une intégrale dont le support est le volume de l'objet considéré, a été introduite par E. M. Purcell et C. R. Pennypacker en 1973 pour étudier la diffusion de la lumière par des grains dans le milieu interstellaire.[2] La CDM a été par la suite étendue à des objets en présence d'un substrat plan ou dans un système multicouche, voir par exemple Ref. [3]. Nous nous sommes attachés ces dernières années, à d'une part étendre la CDM à des géométries plus complexes (réseaux avec ou sans défaut), et d'autre part à augmenter sa précision. Ces améliorations

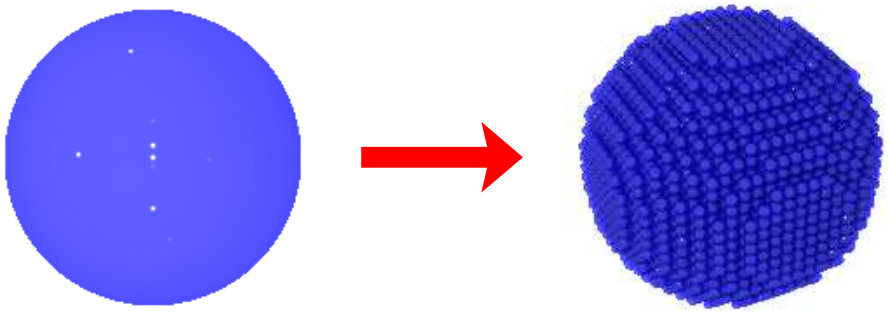

Fig. 1.1 : *Principe de la CDM : l'objet à étudier (à gauche) est discrétisé en un ensemble de petits dipôles (à droite).*

confèrent à ce chapitre un côté un peu technique, mais elles voient leurs applications dans les chapitres suivants. Mais avant d'étudier plus en détails les dernières avancées de la CDM, rappelons d'abord son principe.

1.2 Le principe de la méthode des dipôles couplés

Soit un objet de forme et de permittivité relative arbitraires dans un espace homogène, que nous supposerons ici être le vide. Cet objet est soumis à une onde électromagnétique incidente de longueur d'onde λ ($k_0 = 2\pi/\lambda$). Le principe de la CDM consiste à représenter l'objet en un ensemble de N petits cubes d'arête a [par petits, nous entendons plus petits que la longueur d'onde dans l'objet : $a \ll \lambda/\sqrt{\varepsilon}$ (Fig. 1.1)]. Chacun des petits cubes sous l'action de l'onde incidente va se polariser, et donc acquérir un moment dipolaire, dont la valeur va dépendre du champ incident et de son interaction avec ses voisins. Le champ local à la position d'un dipôle localisé en $\boldsymbol{r}_i$, $\boldsymbol{E}(\boldsymbol{r}_i)$, est, en l'absence de lui-même, la somme de l'onde incidente et du champ rayonné par les $N-1$ autres dipôles :

$$\boldsymbol{E}(\boldsymbol{r}_i) = \boldsymbol{E}_0(\boldsymbol{r}_i) + \sum_{j=1, i\neq j}^{N} \boldsymbol{T}(\boldsymbol{r}_i, \boldsymbol{r}_j)\alpha(\boldsymbol{r}_j)\boldsymbol{E}(\boldsymbol{r}_j). \tag{1.1}$$

$\boldsymbol{E}_0$ est le champ incident, $\boldsymbol{T}$ la susceptibilité linéaire du champ en espace homogène, [i–ii–4] et α la polarisabilité de chaque élément de discrétisation obtenue à partir de la relation de Claussius-Mossotti. Notons que la polarisabilité α, pour respecter le théorème optique, se doit de contenir un terme dit de réaction de rayonnement.[5,6] L'Eq. (1.1) est vraie pour $i = 1, \cdots, N$, et représente donc un système de $3N$ équations linéaires à résoudre, les champs locaux, $\boldsymbol{E}(\boldsymbol{r}_i)$, étant les inconnus. Une fois le système d'équations linéaires résolu, le champ diffusé par l'objet à une position $\boldsymbol{r}$ arbitraire, est obtenu en faisant la somme de tous les champs rayonnés par chacun des dipôles :

$$\boldsymbol{E}(\boldsymbol{r}) = \sum_{j=1}^{N} \boldsymbol{T}(\boldsymbol{r}, \boldsymbol{r}_j)\alpha(\boldsymbol{r}_j)\boldsymbol{E}(\boldsymbol{r}_j). \tag{1.2}$$

[i] $\boldsymbol{T}(\boldsymbol{r}_i, \boldsymbol{r}_j) = e^{ik_0 r}\left[\left(3\frac{\boldsymbol{r}\otimes\boldsymbol{r}}{r^2} - \boldsymbol{I}\right)\left(\frac{1}{r^3} - \frac{ik_0}{r^2}\right) + \left(\boldsymbol{I} - \frac{\boldsymbol{r}\otimes\boldsymbol{r}}{r^2}\right)\frac{k_0^2}{r}\right]$ avec $\boldsymbol{I}$ la matrice unité et $\boldsymbol{r} = \boldsymbol{r}_i - \boldsymbol{r}_j$.
[ii] Notons qu'entre $\boldsymbol{T}$ et la fonction de Green il y a un facteur multiplicatif $(-k_0^2)$.

Quand l'objet est en présence d'un substrat plan, ou dans un multicouche, il suffit de remplacer $\boldsymbol{T}$, par la susceptibilité linéaire du champ du système de référence.

Nous venons de présenter la CDM telle que l'ont présentée E. M. Purcell and C. R. Pennypacker.[2] Notons qu'une autre méthode très proche de la CDM existe. Cette méthode, dite méthode des moments, part de l'équation intégrale de Lippman Schwinger, est, moyennant quelques hypothèses, strictement identique à la CDM. La démonstration de l'équivallence entre ces deux méthodes étant un peu technique, elle est explicitée dans l'annexe 1 page 73.

Les avantages de la CDM sont qu'elle est applicable à des objets de forme arbitraire, inhomogène (chose difficilement réalisable dans le cas de méthode surfacique), et anisotrope (la polarisabilité associée aux éléments de discrétisation devient alors tensorielle). La condition d'onde sortante est automatiquement satisfaite à travers la susceptibilité linéaire du champ. Notons enfin, que seul l'objet est discrétisé, contrairement aux méthodes de différences finies et éléments finis.[1]

L'inconvénient majeur de la CDM consiste en une croissance rapide du temps de calcul avec l'augmentation du nombre d'éléments de discrétisation, *i.e.*, l'augmentation de la taille du système d'équations linéaires à résoudre. Il existe des moyens pour accélérer la résolution d'un système d'équations linéaires de très grande taille, telle que la méthode des gradients conjugués, mais malgré tout, des valeurs de $N > 10^6$ en espace homogène sont difficiles à traiter.

1.3 Diffraction par une structure bi-périodique avec et sans la présence d'un défaut

1.3.1 Diffraction par une structure bi-périodique

La CDM, étant une méthode volumique, ne peut s'appliquer *a priori*, que dans le cas de structure de taille finie. En fait, nous avons montré récemment, que si l'objet est une structure bi-périodique sur un substrat plan (ou en espace homogène), il est quand même possible d'utiliser la CDM si l'éclairement est réalisé avec une onde plane. Dans ce cas, le champ en tout point de l'espace est quasi périodique :

$$\boldsymbol{E}(\boldsymbol{r} + m\boldsymbol{u} + m'\boldsymbol{v}) = \boldsymbol{E}(\boldsymbol{r}) e^{i\boldsymbol{k}_{0\parallel}\cdot(m\boldsymbol{u}+m'\boldsymbol{v})}, \tag{1.3}$$

avec $(m, m') \in \mathbb{Z}^2$, $\boldsymbol{k}_{0\parallel}$ la composante du vecteur d'onde du champ incident ($\boldsymbol{k}_0$) parallèle au substrat, et $\boldsymbol{u}$, $\boldsymbol{v}$ les vecteurs de base générant la structure bi-périodique. La conséquence de l'Eq. (1.3) est que le champ local, à chaque position de discrétisation de l'ensemble de la structure, est aussi quasi-périodique, et donc le nombre d'inconnues se réduit au nombre d'éléments servant à discrétiser le motif décrivant le réseau bi-périodique. La susceptibilité linéaire du champ est quant à elle modifiée pour tenir compte de la périodicité de la structure, mais elle reste simple à calculer, voir annexe 4 page 92.[8] La CDM périodisée est illustrée avec la Fig. 1.2(b) qui montre la carte de champ proche obtenue avec le réseau décrit Fig. 1.2(a).

<u>Cadre de ce travail</u> : Ce travail est le fruit d'une collaboration internationale entre A. Rahmani (alors au National Institute of Standards and Technology (NIST), USA), et G. W. Bryant (NIST, USA). Ce travail fait suite à ma visite de cinq semaines au NIST dans l'équipe "Quantum Processes and Metrology" dirigée par G. W. Bryant.

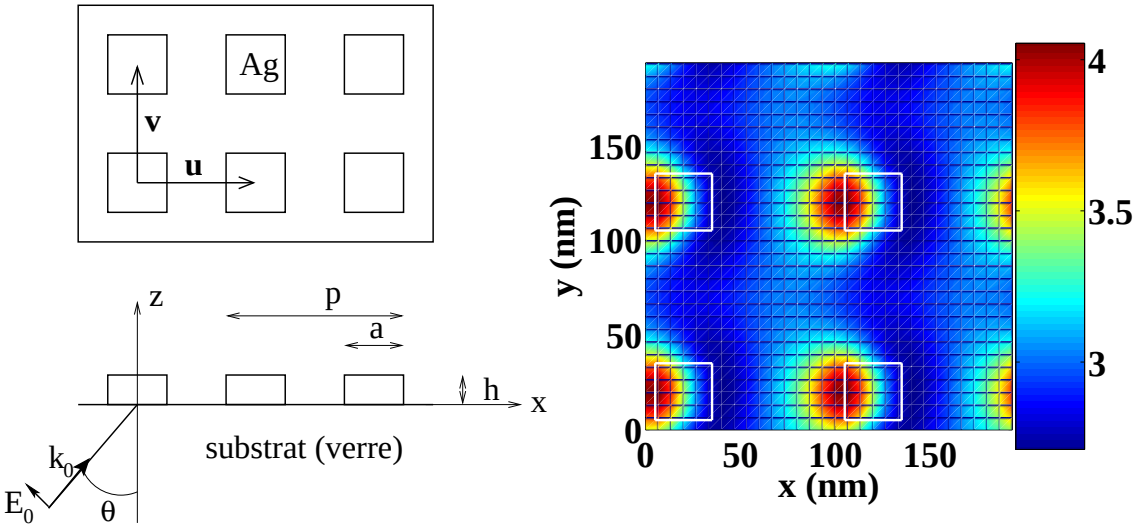

Fig. 1.2 : *(a) Schéma de la configuration : plots d'argent de largeur $a = 30$ nm et de hauteur $h = 10$ nm, disposés sur une maille carrée de période $p = 100$ nm sur un substrat de verre. $\theta = 50°$ est l'angle d'incidence, $\lambda = 600$ nm, et le champ est polarisé TM. (b) Module du champ à 20 nm au-dessus du substrat de verre. Les carrés blancs représentent la position des pavés d'argent.*

1.3.2 Diffraction par une structure bi-périodique en présence de défauts

S'il existe de nombreuses méthodes permettant de traiter une structure bi-périodique, voir par exemple Ref. [9], il est par contre plus délicat de calculer la diffraction par une structure bi-périodique en présence d'un ou plusieurs défauts. Nous avons étendu la CDM à ce type de configuration. Le principe en soi est simple : rappelons que la CDM est entièrement basée sur la discrétisation de l'objet diffractant d'une part (dans le cas présent un défaut dans la structure bi-périodique), la susceptibilité linéaire du champ du système de référence d'autre part (ici la structure bi-périodique sur le substrat plan), et pour finir le champ incident dans ce même système de référence. Celui-ci est obtenu facilement grâce au travail présenté § 1.3.1, et la susceptibilité linéaire du champ du réseau plus le substrat est quant à elle obtenue en la décomposant en une série de Fourier. [iii – 10] Il est alors aisé à partir des Eqs. (1.1) et (1.2), en remplaçant $\boldsymbol{E}_0$ et $\boldsymbol{T}$ de l'espace homogène par ceux du réseau bi-périodique, de calculer le champ diffracté par le défaut, voir annexe 4 page 97. [10] La Fig. 1.3 présente quelques configurations étudiées. A noter qu'avec cette méthode, nous pouvons aussi bien rajouter un ou plusieurs défauts, que créer une lacune dans la structure bi-périodique.

<u>Cadre de ce travail</u> : Ce travail a été réalisé au sein de l'Institut Fresnel en collaboration avec A. Sentenac.

1.4 Augmentation de la précision de la CDM

La précision du résultat de la CDM est directement reliée à la taille des éléments de discrétisation. Plus celle-ci est petite, plus la CDM gagne en précision. Malheureusement, pour un objet donné, diminuer la taille de la discrétisation, revient à augmenter la valeur

[iii] Joseph Fourier (1768-1830) : mathématicien et physicien français

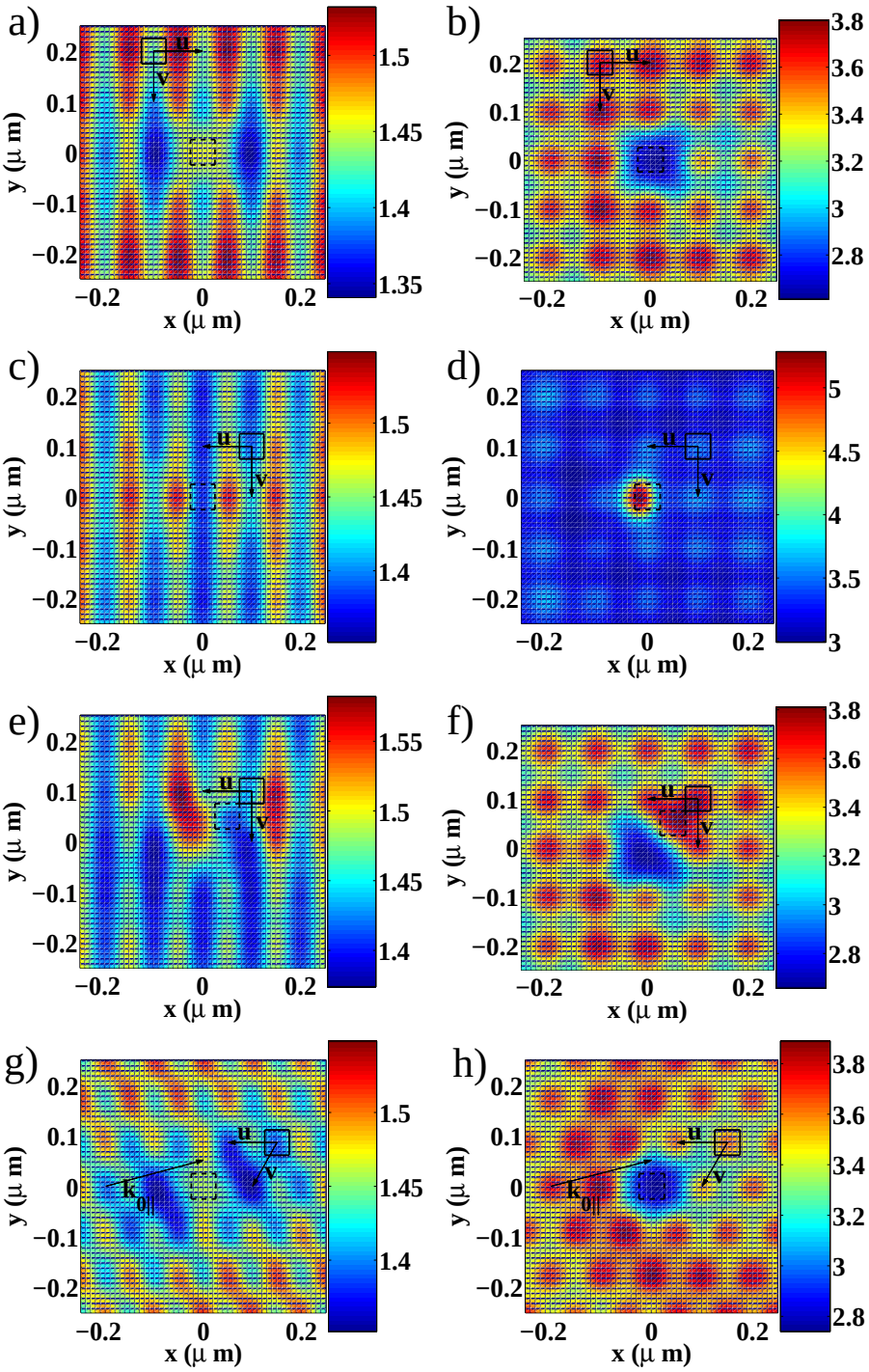

Fig. 1.3 : *Images de champ proche obtenues à $z = 100$ nm, $\lambda = 600$ nm, pour une structure bi-périodique en présence d'un défaut. La structure bi-périodique est constituée de pavés de silicium tels que $a = 50$ nm (notation de la Fig. 1.2). Pour les six premières images $\boldsymbol{k}_{0\|}$ est parallèle à l'axe x avec $\boldsymbol{u} = (100, 0)$ nm et $\boldsymbol{v} = (0, 100)$ nm. Pour les deux dernières images [(g) et (h)], $\boldsymbol{k}_{0\|}$ est comme montré sur les figures avec $\boldsymbol{u} = (100, 0)$ nm et $\boldsymbol{v} = (50, 86)$ nm. Sur chaque figure le carré en trait plein représente le motif du réseau et $\boldsymbol{u}$, $\boldsymbol{v}$ les vecteurs de base de celui-ci. (a), (c) (e) et (g) sont obtenus pour $\theta = 0°$. (b), (d), (f) et (h) sont obtenus pour $\theta = 50°$. (a), (b), (g) et (h) le carré en pointillé représente la lacune dans la structure bi-périodique. (c) et (d) le défaut est un pavé en argent de même taille que ceux de silicium. (e) et (f) le carré en pointillé est un cube de silicium qui a été déplacé.*

de N. Comme dit au § 1.2, quand N devient grand il est numériquement difficile de résoudre le système d'équations linéaires représenté par l'Eq. (1.1). Il est donc intéressant d'augmenter la précision de la CDM à N fixé.

1.4.1 Correction de champ local

La CDM a pour principe de discrétiser l'objet à étudier en un ensemble de petits cubes, et à chacun de ces petits cubes est associée une polarisabilité. Différentes expressions de la polarisabilité pour les petits cubes constituant l'objet ont été établies, mais toutes sont basées sur la relation de Claussius-Mossotti.[11] Rappelons que la relation de Claussius-Mossotti est établie pour une sphère en espace homogène dans un champ statique uniforme.[12] En isolant un des éléments de discrétisation, il est clair que d'une part celui-ci n'est pas dans un espace homogène et que d'autre part le champ local qui s'applique à celui-ci n'est pas homogène, étant la somme du champ incident et du champ rayonné par tous les autres dipôles. L'idée est donc de tenir compte de l'environnement pour modifier la polarisabilité de chaque élément de discrétisation, et donc introduire une polarisabilité effective.[13,14]

Soit une sphère dans un champ statique : ce problème peut être résolu exactement, et le champ macroscopique à l'intérieur de celle-ci est donc parfaitement défini. Si nous discrétisons cette sphère avec la CDM, nous pouvons calculer le champ macroscopique à la position de chaque élément de discrétisation. En égalant le champ macroscopique calculé rigoureusement et celui obtenu *via* la CDM, nous pouvons en déduire une polarisabilité effective pour chacun des éléments de la discrétisation. Ensuite, pour tenir compte du fait que notre objet est éclairé par une onde électromagnétique en $e^{-i\omega t}$ il suffit de rajouter la réaction de rayonnement à cette nouvelle polarisabilité (voir annexe 4 page 105 et page 111).[13,14]

L'inconvénient de cette méthode est qu'il faut obtenir rigoureusement le champ macroscopique pour un objet soumis à un champ électrostatique uniforme. Ceci n'est possible analytiquement que dans le cas où le facteur de champ local est constant dans l'objet, *i.e.*, pour des ellipsoïdes (la sphère étant un cas particulier) et des slabs. Figure 1.4 présente le cas du slab possédant une forte permittivité relative. Le calcul exact est en trait discontinu, le calcul avec la CDM usuelle avec les symboles carrés (old CDM), et la CDM avec la polarisabilité effective avec les symboles triangles (new CDM) : il est clair que non seulement cette nouvelle méthode augmente la précision de la CDM de manière conséquente, mais en plus elle fait disparaître les oscillations du champ à l'intérieur du slab.

<u>Cadre de ce travail</u> : Ce travail a été réalisé en collaboration avec A. Rahmani et G. W. Bryant (NIST) lors de ma visite de 5 semaines au NIST.

1.4.2 Intégration de la susceptibilité linéaire du champ

La méthode présentée § 1.4.1 est astreinte à des géométries particulières de l'objet. Dans ce paragraphe nous établissons un autre moyen d'augmenter la précision de la CDM, mais sans contrainte quant à la forme de l'objet.

En fait la CDM telle que nous l'avons présentée § 1.2 fait appel à deux approximations. La première consiste à supposer le champ uniforme sur une maille de discrétisation (l'utilité de cette approximation est détaillée dans l'annexe 1 page 73) . Cette approximation si la maille est très petite vis-à-vis de la longueur d'onde dans le milieu considéré est parfaitement licite. La deuxième approximation est de supposer la susceptibilité linéaire

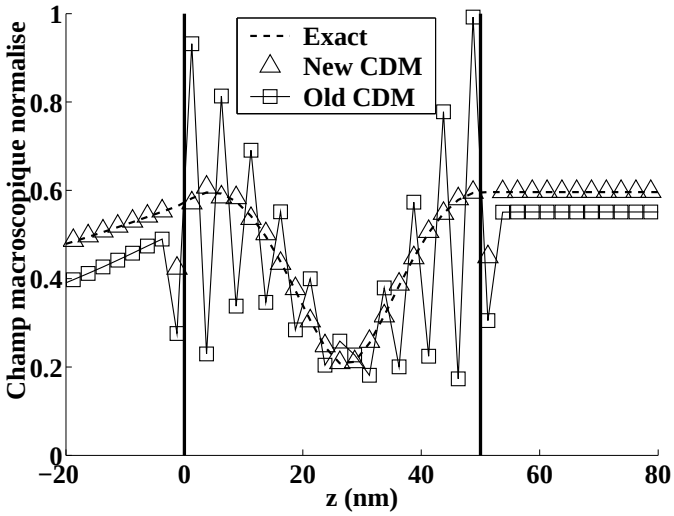

Fig. 1.4 : *Module du champ à l'extérieur et à l'intérieur d'un slab. Le slab est défini par* $0 \leq z \leq 50$ *nm délimité par les lignes verticales. L'onde plane incidente (*λ*=400 nm) arrive de la gauche avec un angle de* θ*=50° polarisée en TM. La permittivité relative du slab est :* ϵ*=20.*

du champ uniforme sur une maille, *i.e.*, $\boldsymbol{T}(\boldsymbol{r}_i, \boldsymbol{r}) = \boldsymbol{T}(\boldsymbol{r}_i, \boldsymbol{r}_j)$ quelle que soit la position $\boldsymbol{r}$ appartenant à la maille j (Ceci permet de ne pas calculer l'intégration de la susceptibilité linéaire du champ sur la maille, voir annexe 1 page 73). Si nous prenons deux mailles contiguës et petites, il est clair que la décroissance en $1/r^3$ de la susceptibilité linéaire du champ, ne permet plus de supposer celle-ci uniforme. Pour tenir compte de cette variation il suffit d'intégrer la susceptibilité linéaire du champ sur la maille : $\int_{V_j} \boldsymbol{T}(\boldsymbol{r}_i, \boldsymbol{r})\mathrm{d}\boldsymbol{r}$. Cette modification permet d'améliorer la convergence de la CDM surtout quand la permittivité relative de l'objet est très forte (annexe 4 page 86).[7]

Cadre de ce travail : Ce travail a été réalisé en collaboration avec A. Rahmani (Lyon) et A. Sentenac. Ce travail montre la parfaite équivalence entre la CDM et la méthode des moments.

1.5 Conclusion

Ce chapitre consacré à la CDM donne les récents avancements que nous avons réalisés en ce qui concerne la CDM : d'une part des avancées réalisées au niveau de la précision de la CDM (à travers la correction de facteur de champ local cf § 1.4.1, ou l'intégration de la susceptibilité linéaire du champ sur une maille cf § 1.4.2), et d'autre part au niveau des géométries que celle-ci peut désormais traiter : réseau bi-périodique (cf § 1.3.1), et défaut en présence d'un réseau bi-périodique (cf § 1.3.2).

Chapitre 2

Forces dues à la lumière : forces optiques

The Force will be with you, always.
Obi-Wan Kenobi "Star War"

Sommaire

2.1 Introduction

L'action de la lumière sur la matière est connue depuis fort longtemps. En effet en 1616, Johannes Kepler, [i] observant le mouvement d'une comète constate alors que les cristaux de glace et les poussières constituant la queue sont repoussés dans la direction opposée à celle du soleil, ceci l'amenant à supposer que la lumière solaire exerçait sur ces particules une poussée, qui sera appelée plus tard pression de radiation.[ii] Mais cette force due à la lumière est très faible, et il a fallu attendre l'avènement des lasers, pour que dans les années 70, Arthur Ashkin montre que la lumière pouvait déplacer des particules de taille micrométrique, voire même des atomes.[15,16]

A partir des articles fondateurs de Arthur Ashkin, se sont développées des techniques de piégeage optique et de manipulation de petites particules neutres par des lasers. Les applications biologiques de ces techniques sont nombreuses : fabrication de pinces optiques

[i] Johannes Kepler (1571-1630) : astronome et physicien allemand

[ii] En toute rigueur une comète a une queue ionique de couleur bleue pâle, et une queue de poussière de couleur blanche. C'est bien sûr la queue de poussière qui subit la pression de radiation. Ce processus étant relativement lent, l'éjection est aussi affectée par le mouvement de la comète et la queue s'en trouve courbée. La queue ionique, quant à elle, est constituée d'atomes ionisés lors du dégazage de la comète. Sa trajectoire rectiligne (direction opposée au Soleil) est due à l'interaction des ions avec le vent solaire.

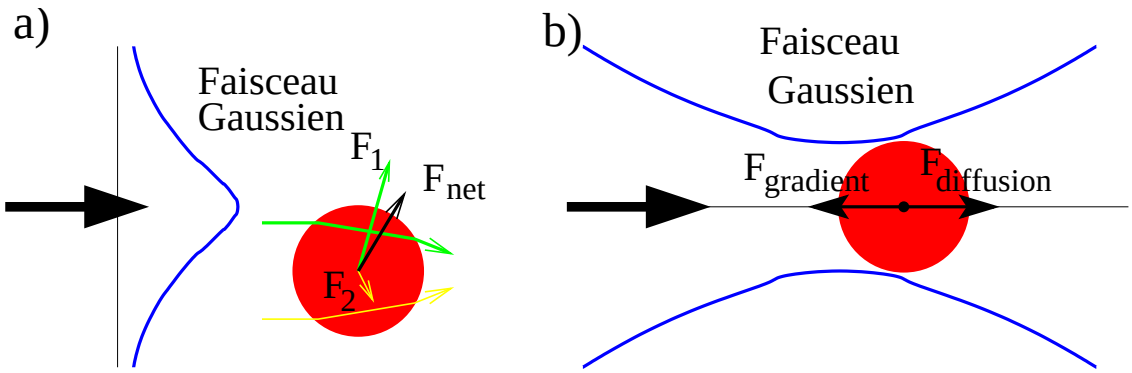

Fig. 2.1 : *(a) Force subie par une sphère diélectrique dans un faisceau gaussien quand elle est située hors axe. (b) Piégeage optique d'une sphère diélectrique située sur l'axe d'un faisceau gaussien.*

pour manipuler des virus au sein d'une cellule *in vitro*, mesure des propriétés mécaniques des différentes parties constituant la cellule,[17,18]...

Le principe de base des forces optiques est représenté Fig. 2.1 où une sphère diélectrique est immergée dans un liquide tel que l'indice de la sphère est plus fort que l'indice du liquide. Considérons une paire de rayons arrivant sur la sphère [Fig. 2.1(a)] et négligeons en première approximation les réflexions de ces rayons sur les interfaces. Par conservation de la quantité de mouvement, le rayon du haut dévié vers le bas donne une force F_1 dirigée vers le haut, et le rayon du bas dévié vers le haut une force F_2 dirigée vers le bas. Le rayon lumineux du haut étant plus intense que celui du bas, la force totale F_{net} s'exerçant sur la sphère, la pousse vers le centre du faisceau gaussien.[iii] En additionnant tous ces rayons par paires sur toute la surface de la sphère exposée au faisceau gaussien, nous obtenons une force qui peut se décomposer en deux parties : une composante qui pousse la sphère vers l'axe du faisceau gaussien, dite force due au gradient du champ, et une autre composante qui pousse la sphère dans l'axe du faisceau gaussien, dite force de diffusion (pression de radiation). La Fig. 2.1(b) montre alors comment il est possible de faire un piège optique à partir d'un faisceau gaussien. Il suffit que la force due au gradient du champ (qui attire la sphère dans la zone la plus étroite du faisceau) et la force de diffusion (qui pousse la sphère loin du waist) s'équilibrent.

Mais les théories qui existaient pour calculer les forces optiques, il y a une dizaine d'années, n'étaient pas nombreuses et c'est pourquoi nous nous sommes intéressés à ce domaine. En effet, il existait des modèles basés sur l'approximation dipolaire ou l'approximation géométrique (tel que nous l'avons montré au paragraphe ci-dessus) mais très peu sur une résolution rigoureuse des équations de Maxwell. Nous nous sommes donc intéressés au cas où la taille de la particule est dans le domaine résonnant, *i.e.*, la taille de la particule est de l'ordre de grandeur de la longueur d'onde d'illumination, configuration dans laquelle la CDM est parfaitement adaptée.

2.2 Calcul des forces optiques avec la CDM

Soit un objet en espace homogène soumis à un champ électromagnétique incident. La CDM discrétise l'objet à étudier en un ensemble de petits cubes, assimilables à des dipôles ponctuels sous l'action du champ incident. A partir de l'expression de la force de Lorentz,

[iii] Johann Carl Friedrich Gauss (1777-1855) : mathématicien allemand.

il est alors aisé de connaître la force $\boldsymbol{F}$ exercée par un champ électromagnétique $(\boldsymbol{E}, \boldsymbol{B})$ sur un des dipôles $\boldsymbol{p}$ formant l'objet :

$$\boldsymbol{F} = (\boldsymbol{p}.\nabla)\boldsymbol{E} + \frac{1}{c}\boldsymbol{p} \times \boldsymbol{B}. \tag{2.1}$$

L'Eq. (2.1) fait intervenir le champ électrique local et magnétique local. En utilisant la relation de Maxwell-Ampère, $\boldsymbol{B} = \frac{c}{i\omega}\nabla \times \boldsymbol{E}$, la force à laquelle est soumis le dipôle peut s'exprimer uniquement en fonction du champ électrique et de sa dérivée (annexe 4 page 114).[19] Le champ électrique à la position de chaque dipôle se calcule grâce à l'Eq. (1.1), et sa dérivée est obtenue en dérivant l'Eq. (1.1), moyennant quelques précautions.[20] Il est alors facile de calculer la force sur chaque dipôle et par conséquent la force totale à laquelle est soumis l'objet. Mais dans le domaine des fréquences correspondant au domaine du visible, $\nu \approx 10^{14}$ Hz, il convient d'effectuer la moyenne temporelle de la force. A noter que pour un calcul correct des forces optiques avec la CDM, il est d'une importance vitale de prendre en compte la réaction de rayonnement afin de respecter le théorème optique.[19] Notons que les résultats obtenus au chapitre 1, § 1.4.1 et § 1.4.2, peuvent s'appliquer ce qui augmente alors la précision sur le calcul des forces optiques.[20]

Nantis du formalisme nécessaire pour le calcul des forces optiques, nous désirions alors faire de la nanomanipulation, mais auparavant il nous fallait connaître parfaitement l'effet de l'interaction de l'objet à manipuler avec le substrat sur lequel il était déposé, ainsi que les interactions dans le cas d'objets multiples.

<u>Cadre de ce travail</u> : Le travail sur les forces optiques a débuté lors de mon stage post-doctoral dans l'équipe de M. Nieto-Vesperinas à l'Instituto de Ciencia de Materiales de Madrid (mars 1999) et continue jusqu'à ce jour au sein de l'institut Fresnel.

2.3 Forces optiques exercées sur une sphère en interaction avec un substrat plan

Dans le cas d'un objet posé sur une surface plane, la diffusion multiple entre celui-ci et le substrat doit être prise en compte. Ceci est facile à réaliser avec la CDM à travers la susceptibilité linéaire du champ associée à la surface. Le cas de sphères diélectriques et métalliques posées sur un substrat plan dans les cas d'un éclairement propagatif ou évanescent a donc été étudié (annexe 4 page 117 et page 126). Principalement notons que :

- dans le cas de sphères de petite taille vis-à-vis de la longueur d'onde, l'interaction de la sphère avec elle même, *via* le substrat, donne toujours une force attirant celle-ci contre le substrat, et ce quelle que soit la nature de l'éclairement et de la particule.[21,22]
- il est habituellement dit que lorsqu'un objet est dans un faisceau gaussien les forces optiques l'attirent vers les zones où l'intensité est la plus forte. En fait ceci n'est vrai que si l'objet est diélectrique. Dans le cas d'une sphère métallique cette assertion n'est pas toujours vérifiée. Par exemple dans le cas d'une sphère d'argent, en choisissant bien la longueur d'onde d'illumination, les forces optiques peuvent attirer la sphère vers les zones de plus faible intensité. Nous avons étudié cet effet et l'influence du substrat dans ce cas là.

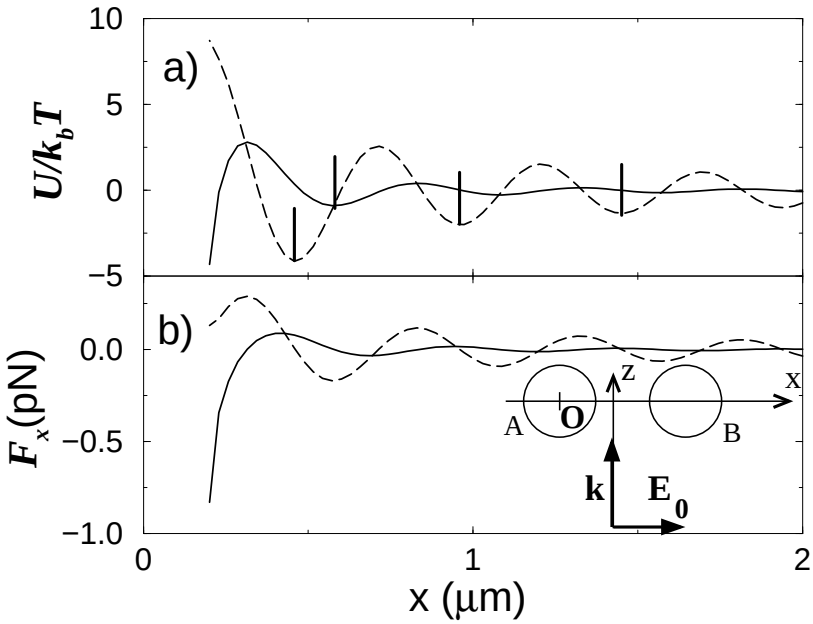

Fig. 2.2 : *Les traits pleins correspondent à la polarisation suivant x, et les traits pointillés à la polarisation perpendiculaire à x. (a) Potentiel de piégeage sur la sphère B normalisé à k_bT en fonction de la distance entre les deux sphères. La hauteur des barres représente $3k_bT$: si le puits de potentiel est supérieur à cette valeur alors le piégeage est considéré comme stable. (b) Force suivant x exercée sur la sphère B.*

<u>Cadre de ce travail</u> : L'étude des forces optiques s'exerçant sur un objet en interaction avec un substrat a entièrement été réalisée à Madrid avec M. Nieto-Vesperinas.

2.4 Lien optique entre deux sphères

Quand il y a plusieurs objets dans un même piège optique, il y a une interaction entre ceux-ci. On peut se demander si le couplage électromagnétique entre ces particules ne pourrait pas produire un nouvel état de la matière, c'est-à-dire, une disposition particulière des objets étudiés qui serait ordonnée par ces interactions. En 1989, Burns *et al.* ont montré expérimentalement que quand deux sphères étaient dans le point de focalisation de deux lentilles cylindriques, la distance entre les deux sphères prenait des valeurs particulières.[23,24] Nous nous sommes penchés sur ce problème en étudiant l'interaction entre deux sphères éclairées par une onde plane, quand les sphères sont en espace homogène ou disposées sur un substrat plan.[25] Nous détaillons ici le résultat le plus marquant, obtenu pour deux sphères en verre d'un rayon de 100 nm, immergées dans de l'eau, éclairées comme décrit par la vignette de la Fig. 2.2(b). L'intensité du laser est de 0.2 W/μm^2 avec $\lambda = 632.8$ nm dans le vide. Figure 2.2(a) montre le potentiel de piégeage suivant l'axe x, normalisé par rapport à k_bT (T est la température de l'eau et k_b la constante de Boltzmann[iv]) pour la sphère B tandis que la Fig. 2.2(b) trace la force s'exerçant sur cette même sphère. Notons que les puits de potentiel sont espacés d'une longueur d'onde, en parfait accord avec les expériences[23] et ce quelle que soit la polarisation du faisceau incident. Ce résultat peut se comprendre intuitivement en assimilant les sphères à des dipôles : quand

[iv] Ludwig Eduard Boltzmann (1844-1906) : physicien autrichien.

le dipôle associé à la sphère B (induit par le champ incident en première approximation) est en phase (respectivement en opposition de phase) avec le champ rayonné par le dipôle associé à la sphère A, alors la sphère B est attirée (respectivement repoussée) par la sphère A [Fig. 2.2(a)]. Ce qui donne des positions d'équilibre espacées chacune d'une longueur d'onde pour les deux polarisations. Les puits de potentiels supérieurs à $3k_bT$ [barres verticales sur la Fig. 2.2(a)] dans le cas de la polarisation perpendiculaire à x, nous donne 2 ou 3 positions d'équilibre stable où le mouvement brownien[v] ne devrait pas perturber le piégeage optique. Dans le cas de l'autre polarisation (champ électrique suivant l'axe x), il conviendrait d'augmenter l'intensité du faisceau incident pour que les positions d'équilibre stable ne soient pas perturbées par le mouvement brownien. Cette différence d'amplitude entre les deux polarisations vient du fait (toujours en associant un dipôle à chacune des sphères) qu'un dipôle rayonne un champ d'intensité maximum perpendiculairement à son orientation. Notons que quand les sphères sont en contact, le comportement est par contre différent suivant la polarisation : quand le champ est polarisé suivant x les deux sphères s'attirent (car le dipôle associé à la sphère B est en phase avec le champ créé en B par le dipôle associé à la sphère en A) et quand le champ est polarisé perpendiculairement à x les deux sphères se repoussent (car le dipôle associé à la sphère B est en opposition de phase avec le champ créé en B par le dipôle associé à la sphère en A). Pour plus de détails voir annexe 4 page 133.[25]

<u>Cadre de ce travail</u> : L'étude des liens optiques entre deux sphères en interaction a commencé à Madrid avec M. Nieto-Vesperinas et a été terminé lors de mon installation à Marseille.

2.5 Pinces optiques : nano-manipulation

Les pinces optiques sont habituellement utilisées pour la manipulation d'objets biologiques[17] ou des sphères de forte taille (plusieurs dizaines de longueurs d'onde en diamètre).[26] Nous nous sommes plus particulièrement intéressés à la manipulation d'objets de taille nanométrique. Un premier article en 1997 montrait une telle possibilité en utilisant une pointe en or éclairée par une onde plane.[27] L'exaltation du champ électromagnétique à l'apex de la pointe formait alors un piège très localisé. Mais le principal inconvénient de ce piège était de travailler dans l'eau, et il n'y avait alors pas de possibilité de sélectionner les particules à piéger, celles-ci étant fortement soumises au mouvement brownien : il fallait donc attendre qu'une particule tombe dans le piège.

Pour éviter le problème dû au mouvement brownien nous avons décidé de placer les particules dans l'air, celles-ci étant déposées sur un substrat plan (Fig. 2.3). Pour localiser celles-ci nous avons choisi d'utiliser un microscope de champ proche optique sans ouverture.[28] Ce microscope est constitué d'une pointe métallique (souvent en tungstène) balayant la surface, sur laquelle les objets à étudier sont posés.[vi] Dans la configuration choisie le substrat est éclairé par en dessous en réflexion totale avec deux ondes contrapropagatives non cohérentes. Le flux lumineux alors diffusé par la pointe lors de son balayage est collecté,[vii] et nous obtenons une image optique de l'échantillon, ce qui permet

[v] Robert Brown (1773-1858) : botaniste britannique

[vi] Pour être plus précis, la pointe oscille perpendiculairement à la surface avec une amplitude d'oscillation d'environ 100 nm, et une fréquence de quelques kilohertz. L'amplitude d'oscillation est maintenue constante par un système d'asservissement, ce qui nous donne accès à la topographie de l'échantillon.

[vii] La lumière diffusée par la pointe est collectée par un objectif de microscope et dirigée vers un photomultiplicateur. Une détection synchrone démodule le signal à la fréquence de vibration de la pointe, et permet d'extraire le signal de champ proche du fond continu de champ lointain.

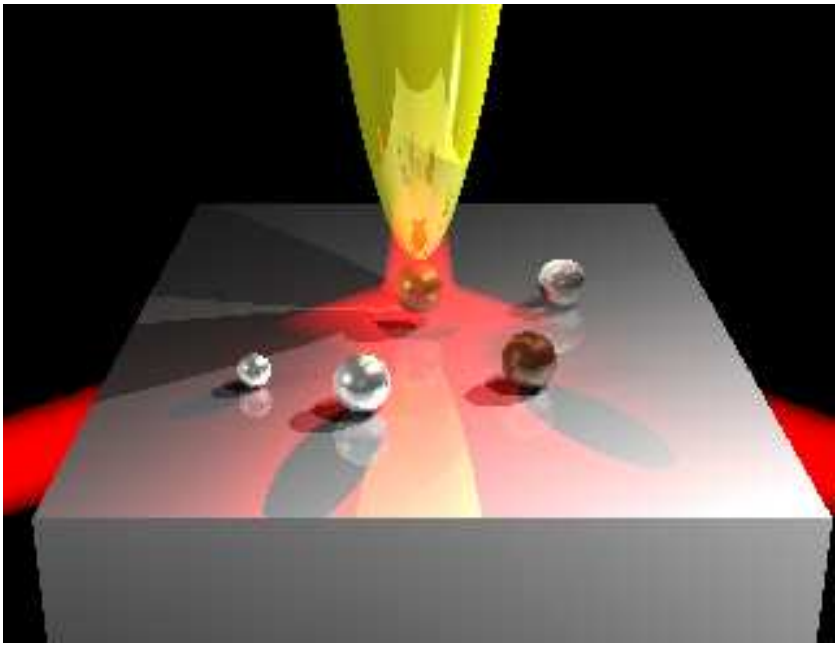

Fig. 2.3 : *Plusieurs nano-particules de natures différentes sont déposées sur un substrat plan en verre. La pointe au-dessus de la surface balaye celle-ci afin d'obtenir une image optique de l'échantillon étudié, ce qui permet de localiser et caractériser les différentes particules en présence.*

donc de localiser les particules de différentes natures déposées sur le substrat (voir annexe 4 page 140).[29]

Figure 2.4 montre l'évolution de la force optique quand la pointe métallique du microscope approche une sphère de taille nanométrique $a = 10$ nm déposée sur un substrat de verre. En mode TE la sphère n'est pas du tout attirée par la pointe [Fig. 2.4(b)], alors qu'en mode TM quand la pointe est suffisamment proche de la sphère ($z < 25$ nm), l'exaltation du champ électromagnétique à l'extrémité de la pointe, crée une force positive qui va attirer et soulever la sphère : Fig. 2.4(a) et sa vignette.

La procédure pour manipuler des nano-particules est la suivante :

- le faisceau incident est polarisé en mode TE et la pointe balaye le substrat pour faire une image optique de l'échantillon, afin de localiser et sélectionner la particule souhaitée.
- la pointe est amenée au-dessus de la particule sélectionnée, et le faisceau incident est polarisé en mode TM. La pointe s'approche alors de la particule pour la capturer.
- la pointe soulève la particule et peut la déplacer à sa nouvelle position.
- en repassant en polarisation TE la particule est de nouveau posée sur le substrat.

Le grand avantage de cette procédure par rapport à la proposition de Novotny *et al.* [27] est la possibilité de pouvoir choisir la particule à piéger, et de la déplacer à l'endroit désiré. Notons que les particules à manipuler peuvent être aussi bien diélectriques[30] que métalliques,[31] comme montré annexe 4 page 144 et page 155. Si la sphère en verre est remplacée par une sphère de même taille mais en or, avec un éclairement correspondant à la résonance plasmon de celle-ci, la force exercée par la pointe sur la particule quand elles sont en contact est alors proche de 200 pN, soit 50 fois plus qu'avec une particule en verre.

A noter que la configuration étudiée pour manipuler de petites particules, peut aussi être utilisée pour contrôler l'exaltation (en amplitude et en fréquence) du champ électromagnétique autour de la particule. En effet en jouant sur la nature de la pointe, de la

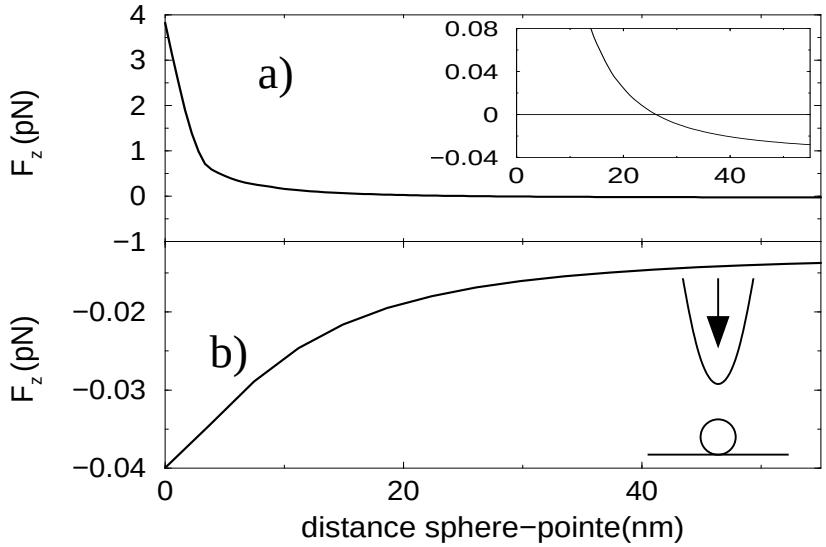

Fig. 2.4 : *Force optique s'exerçant sur une sphère en verre en fonction de la distance pointe-sphère : L'irradiance du faisceau incident est de 0.05 $W/\mu m^2$ avec un angle d'incidence de $\theta = 43° > \theta_c = 41.8°$ et $\lambda = 500$ nm. La pointe est en tungstène avec un rayon de courbure à son apex de 10 nm. (a) Polarisation TM. (b) Polarisation TE.*

sphère métallique sélectionnée, et de la distance pointe sphère, l'exaltation du mode de plasmon de la cavité ainsi créée peut être contrôlée. Cette possibilité voit une application immédiate dans la spectroscopie SERS (Surface Enhanced Raman Spectroscopy) qui fournit une analyse détaillée de la structure chimique d'un objet (dans notre cas une molécule placée entre la pointe et la particule [viii]).[32]

<u>Cadre de ce travail</u> : L'étude de la nano-manipulation a été réalisée à Marseille en collaboration avec M. Nieto-Vesperinas et A. Rahmani.

2.6 Piégeage avec un cristal photonique

Nous avons montré très récemment que le confinement de la lumière induit par un cristal photonique pouvait être exploité pour piéger des particules nanométriques. La configuration que nous avons étudiée correspond au cristal photonique présenté Fig. 4.3 mais dans le cadre d'une cavité H1 (un trou cylindrique est enlevé à la structure périodique). La présence de cette cavité crée une très forte exaltation du champ électromagnétique et par conséquence de forts gradients de l'intensité du champ. Ces forts gradients permettent alors d'avoir un potentiel de piégeage proche de la cavité avec une profondeur suffisante pour que le mouvement brownien ne sorte pas la particule du piège.[33]

[viii] La section efficace de diffusion Raman d'une molécule est souvent faible, et son signal ne peut être détecté sans utiliser un processus d'exaltation efficace de la diffusion. Dans notre cas c'est le mode de cavité qui crée une exaltation du champ.

Cadre de ce travail : L'étude du piégeage de nanoparticules au voisinage d'un cristal photonique a été réalisé en collaboration avec A. Rahmani.

2.7 Pièges multiples

Une des branches des forces optiques prenant de l'importance ces dernières années est celle des pièges multiples : il s'agit de piéger plusieurs dizaines de particules en même temps. Les premiers à avoir abordé la notion de piège multiple sont Dholakia *et al.* [34] mais les particules piégées sont de taille largement plus grande que la longueur d'onde. Il serait intéressant de piéger plusieurs milliers de petites particules métalliques.

Pour ce faire, un projet financé par une ANR a vu le jour fin 2005. Il a pour but de développer de nouveaux outils nanostructurés pour l'imagerie cellulaire et la bioanalyse hautement parallèle. Notre démarche s'articule suivant le triptyque : nanofabrication / étude des propriétés nouvelles liées à la taille nanométrique / applications bioanalytiques. Dans un premier temps, l'objectif est de réaliser l'imagerie en champ proche optique en utilisant un microréseau constitué de 3000 nanosondes.[35] Etant donné la taille caractéristique des cellules biologiques visées, cette approche permettra de sonder simultanément deux échelles (composants sub-cellulaires et intercellulaires) et de corréler les informations spectroscopiques ainsi collectées. La participation d'un partenaire industriel reconnu permet d'allier des objectifs fondamentaux (études sur cellules isolées, sur modèles de peaux reconstruites) à des opportunités d'applications *in vivo*. Dans un second temps, nous proposons de réaliser un réseau de nano-cavités métalliques qui serviront comme nano-pinces optiques. Ces nano-pinces permettront ainsi de manipuler, de déplacer et d'immobiliser des populations différentes de particules modifiées par des systèmes de reconnaissance biotique (antigène-anticorps ou brins d'ADN). L'étape de détection aura lieu par voie optique ou par voie électrochimique dans l'environnement confiné de la nano-cavité ; ce confinement induisant une exaltation du signal. Les applications visées sont tournées vers l'immunodosage et les biopuces à ADN.[ix] L'intérêt de cette approche est de réaliser un nano-système analytique complètement intégré permettant l'immobilisation sélective et la détection hautement parallèle, à l'échelle nanométrique, de biomolécules.

Mon travail sur ce projet consiste à étudier la possibilité de piéger des particules nanométriques avec une pointe sans ouverture (métallique) ou avec ouverture et surtout comment amener ces particules au voisinage de ces nano-pièges.

Cadre de ce travail Ce projet fait donc l'objet d'un financement ANR ayant pour titre "NANO-IMAGERIE BIOANALYTIQUE". Ce projet ANR lancé par N. Sojic (LACReM, Bordeaux) fait intervenir différents laboratoires tels que le LPCM (Talence), DRFMC-CEA (Grenoble), CRPP (Pessac), l'université de Southampton, le Max Planck Institut, ainsi qu'un partenaire industriel (l'Oreal[x]).

[ix] Une biopuce est un petit outil d'analyse et de diagnostic d'environ 1 cm^2. Elle se présente sous la forme d'un support en verre ou en silicium sur lequel sont fixés des protéines ou des milliers de fragments d' ADN ou d' ARN. Une biopuce permet d'identifier en un temps record un grand nombre de gènes (puces à ADN ou à ARN) et de protéines (puces à protéines) ou d'en étudier le fonctionnement.

[x] Parce que je le vaux bien !

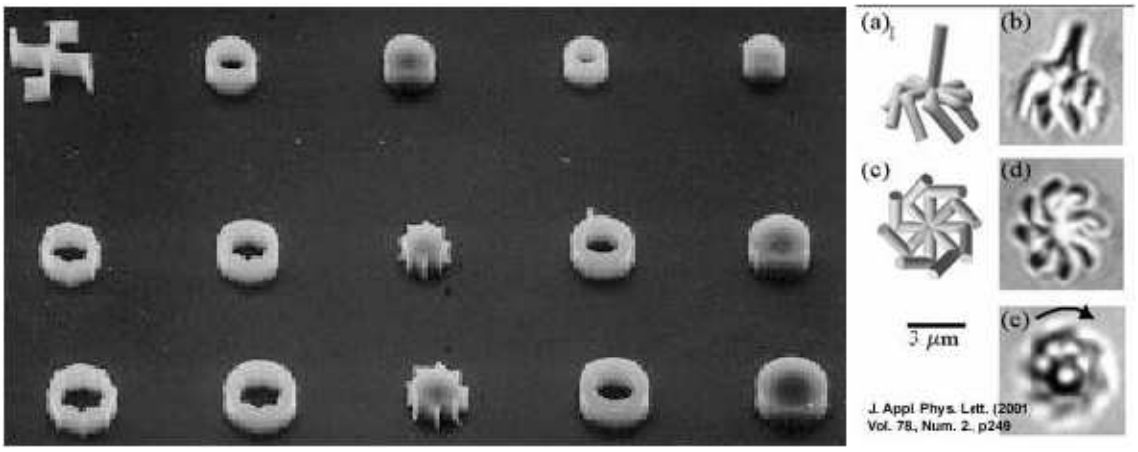

Fig. 2.5 : *Exemples de micro-moteurs.*[36]

2.8 Micro-moteurs : couples optiques

Ces dernières décennies ont vu le champ d'application des micro-systèmes, et même des nano-systèmes, devenir de plus en plus étendu. C'est ainsi que ces dix dernières années nous avons vu apparaître des micro-moteurs dont la source de puissance était un faisceau laser : la rotation est engendrée par les forces induites par la lumière (voir Fig. 2.5). Pour l'instant, les études sont essentiellement expérimentales et portent surtout sur des moteurs qui ont une taille de l'ordre de quelques microns,[37] domaine où l'optique géométrique peut s'appliquer.[38] Mais l'étude de la rotation d'objets nanométriques commence à prendre de l'ampleur, et les applications dans ce cas peuvent être diverses, tels que les nanomoteurs, ou l'étude de la viscosité et de l'élasticité d'un fluide.[39]

A partir des travaux réalisés par Draine[40] nous avons récemment établi les expressions rigoureuses pour obtenir le couple optique à partir de la CDM. Nantis de ces expressions nous avons calculé le couple exercé sur un objet ayant une forme s'apparentant à celle d'une aile d'avion.[41] Nous en sommes au début de l'étude sur les couples optiques, mais les perspectives sont nombreuses et il serait intéressant d'étudier les couples optiques avec soit des faisceaux de structure plus complexe, tels que des faisceaux de bessel, gaussien fortement focalisé, ou avec des matériaux possédant une forte anisotropie ou des propriétés rotatoires.

<u>Cadre de ce travail</u> : La mise en place de la théorie et le début de l'étude sur le couple optique ont été effectués lors du stage de DEA de C. Billaudeau.

2.9 Conclusion

Cela fait maintenant plusieurs années que je consacre une partie de mes activités de recherche aux forces optiques. Nous avons étudié les forces optiques exercées sur des particules en présence d'un substrat et notamment la possibilité de nano manipulations sélectives de celles-ci.

Chapitre 3

Sondage électromagnétique

La théorie, c'est quand on sait tout et que rien ne fonctionne.
La pratique, c'est quand tout fonctionne et que personne ne sait pourquoi.
Ici, nous avons réuni théorie et pratique :
Rien ne fonctionne... et personne ne sait pourquoi !
A. Einstein

Sommaire

3.1 Introduction

3.1.1 Généralités

Le chapitre 1 a été consacré à la diffusion d'une onde électromagnétique par un objet de permittivité relative et de forme arbitraires. C'est ce que nous définissons comme étant le problème direct, *i.e.*, l'objet étant connu, il faut calculer en un ou plusieurs points d'observations donnés, le champ diffracté. Il est alors possible de définir le problème inverse : connaissant le champ diffracté en différents points d'observations, il s'agit de "trouver l'objet" qui a créé ce champ diffracté. Le terme "trouver l'objet" est mis entre guillemets, car il peut avoir différentes significations suivant la problématique posée :

- détection : repérer le nombre de diffuseurs.
- localisation : connaître la position des diffuseurs.

– contour : déterminer la forme des objets inconnus.
– caractérisation : accéder à la forme et à la permittivité relative des diffuseurs.

Le problème inverse tel que nous l'avons défini correspond donc au sondage de la matière par des ondes électromagnétiques. Il existe de nombreux domaines d'application du sondage électromagnétique (recherche de mines antipersonnelles, détection de barres d'acier dans le béton,...), mais nous allons plus particulièrement nous focaliser sur l'une d'entre elle, qui est la microscopie optique à haute résolution.

3.1.2 Quelques mots sur la résolution

Avant d'aborder la microscopie optique à haute résolution, nous devons d'abord définir dans le domaine de la microscopie optique classique [i] ce qu'on entend par le terme de résolution (la résolution étant le pouvoir séparateur de l'instrument d'optique considéré). La définition la plus commune de la résolution se fait à travers le critère de Rayleigh : [ii−iii] la résolution d'un instrument c'est l'écart angulaire minimal entre deux objets lumineux ponctuels incohérents, pour que l'observateur puisse les distinguer l'un de l'autre avec l'instrument considéré :[iv]

$$\Delta\theta = 1.22\frac{\lambda}{a}, \tag{3.1}$$

où λ est la longueur d'onde utilisée et a est le diamètre instrumental. L'Eq.(3.1), dans le cas d'un microscope travaillant dans l'air, donne :

$$d = \frac{1.22\lambda}{2\sin\alpha} \Rightarrow d_{\text{minimum}} = 0.61\lambda, \tag{3.2}$$

où d est la plus petite distance pour laquelle deux objets peuvent être séparés, et α l'angle de collection de la lentille objectif. Au mieux $\alpha = \pi/2$, soit un pouvoir de séparation de 0.61λ. Dans le domaine du visible pour des microscopes optiques en transmission la résolution est donc typiquement de 300 nm. Notons que dans le cadre d'un microscope en champ proche optique, type PSTM par exemple,[42] il est de coutume de dire que son pouvoir de résolution est largement inférieur au critère de Rayleigh, vu que des objets séparés de quelques dizaines de nanomètres sont discernables. Mais nous étudions alors des objets qui n'ont plus un caractère ponctuel, et qui de plus sont fortement couplés de par la distance qui les sépare. Il est alors difficile dans ces conditions de définir un critère de résolution, celle-ci variant suivant la diffusion multiple entre les objets.[43]

3.1.3 La microscopie optique à haute résolution

Les progrès rapides de la science sur les structures de taille nanométrique, dans le domaine de la biologie, des matériaux, de la microélectronique, ont provoqué un intérêt croissant pour les techniques d'imagerie à haut pouvoir de résolution. La microscopie électronique, la microscopie à force atomique produisent des images dont la résolution est inférieure à une dizaine de nanomètres. Cependant, ce sont des techniques coûteuses,

[i] Notons que l'invention du microscope optique remonte à 1595. Le hollandais Zacharias Janssen profite de ses compétences de fabriquant de lentilles pour inventer un système optique qui va bouleverser la biologie : le microscope. Il est alors équipé de deux lentilles convexes dans un ensemble de tubes coulissants. Grâce aux modifications apportées par Antoine van Leeuwenhoek et Robert Hooke, le microscope permettra notamment à ce dernier d'aboutir à la découverte de la cellule en 1665.

[ii] John William Strutt Lord Rayleigh (1842-1919).

[iii] Le critère de Rayleigh n'est pas l'unique critère existant, voir annexe 2.

[iv] Cela correspond au moment où le maximum de la tache de diffraction de la première source coïncide au premier minimum de la tache de diffraction pour la seconde source, pour plus de précision voir annexe 2.

difficiles à mettre en œuvre et elles ne permettent pas de faire, sans intrusion, une cartographie tridimensionnelle de l'objet. Or, de plus en plus, les nano-structures manufacturées deviennent complexes selon les trois dimensions de l'espace. Le besoin en techniques d'imagerie tridimensionnelle non intrusives ayant un pouvoir de résolution inférieur à une centaine de nanomètres est donc patent, pour la caractérisation et le contrôle de ces nouveaux composants, mais aussi, de manière générale, pour l'analyse des structures internes d'objets semi-transparents. Les microscopes optiques traditionnels n'atteignent pas ce niveau de résolution et ne permettent pas de restituer la carte de permittivité relative de l'objet en trois dimensions.

La technique d'imagerie que nous sommes en train de développer s'apparente à de la tomographie par diffraction : l'échantillon étudié est éclairé par un faisceau laser sous différentes incidences successives, et le champ diffracté est alors mesuré en différents points d'observations, c'est-à-dire qu'il nous faut mesurer le module **et** la phase du champ diffracté. Notons que si la mesure de la phase du champ diffracté dans le domaine des micro-ondes est chose facile à réaliser, dans le domaine du visible les fréquences sont telles ($\approx 10^{14}$ Hz) qu'un montage interférométrique est nécessaire pour l'obtention de la phase. Contrairement à un microscope conventionnel, où l'image de l'objet est construite analogiquement par l'action des lentilles sur le champ diffracté, nous utilisons des algorithmes de résolution du problème inverse afin de remonter à la carte de permittivité relative de l'objet.

Cadre de ce travail : Ce chapitre, entièrement dédié aux méthodes d'inversions tridimensionnelles, est le fruit d'une collaboration avec K. Belkebir et A. Sentenac. Ce projet, initié par A. Sentenac, est financé par une ACI jeune chercheur sur le thème de la microscopie optique à haute résolution. Ma forte implication sur ce projet a motivé d'une part ma demande de CRCT pour les années 2004-2006, et d'autre part, mon intégration dans l'équipe SEMO en 2007. En 2004 j'ai encadré R. Lencrerot en DEA sur le sondage électromagnétique, et c'est sur le thème de la microscopie à haute résolution que je coencadre actuellement la thèse de F. Drsek avec H. Giovannini et A. Sentenac ; A. Sentenac et moi-même nous focalisant plus sur l'aspect théorique et H. Giovannini plus sur le côté expérimental.

3.2 Formulation du problème

L'objet étudié (en espace homogène, sur un substrat ou dans une configuration plus compliquée) est éclairé successivement par L différentes ondes planes. Pour chacune de ces ondes planes incidentes le champ diffracté, $\boldsymbol{f}_l$, est mesuré en amplitude et en phase sur une surface Γ comprenant M points d'observations (Fig. 3.1). Ce champ mesuré expérimentalement, qui dans notre cas est simulé théoriquement, s'écrit très simplement à partir des Eqs. (1.1)-(1.2) :

$$\boldsymbol{E}_l = \boldsymbol{E}_{0,l} + \boldsymbol{A}\boldsymbol{p}_l \tag{3.3}$$

$$\boldsymbol{f}_l = \boldsymbol{B}\boldsymbol{p}_l, \tag{3.4}$$

avec $l = 1, \cdots, L$, $\boldsymbol{A}$ la matrice contenant toutes les susceptibilités linéaires du champ permettant d'accéder au champ dans l'objet, et $\boldsymbol{B}$ la matrice permettant de calculer le champ diffusé par l'objet. A partir du champ diffracté pour chaque angle d'incidence, il

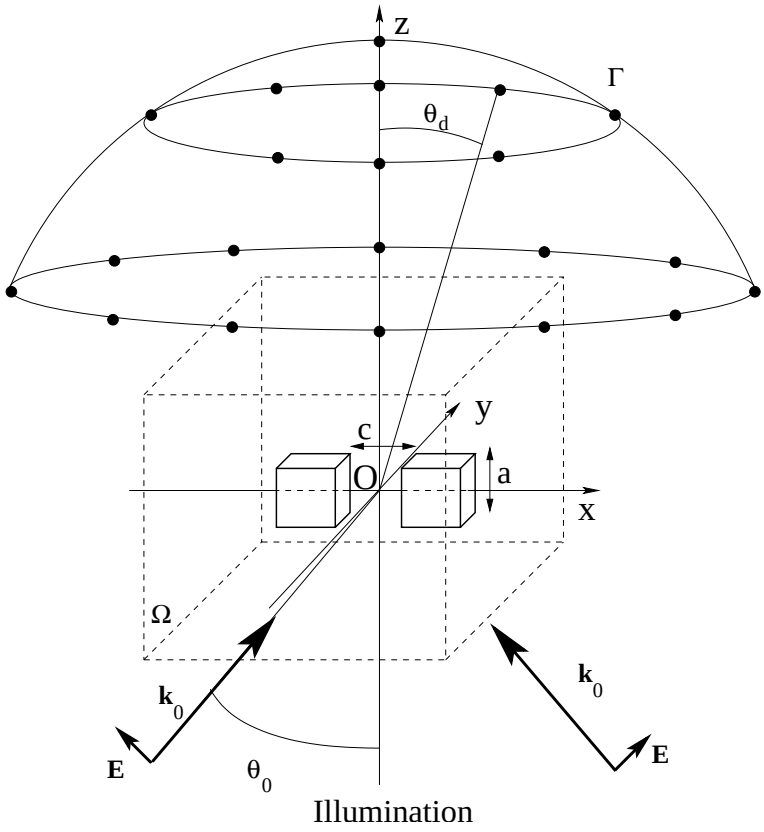

Fig. 3.1 : *L'objet ou les objets (deux cubes sur le schéma proposé) sont éclairés avec L différents angles d'incidence et le champ électromagnétique (module+phase) est mesuré sur la surface* Γ *en M points d'observations. En pointillé est défini le domaine d'investigation* Ω *dans lequel l'objet est supposé être.*

nous faut donc retrouver les caractéristiques de l'objet. Pour ce faire nous définissons un domaine Ω, que nous appellerons domaine d'investigation, dans lequel nous savons que l'objet est situé (Fig. 3.1). La méthode que nous suivons est alors une démarche itérative. A partir d'une estimation initiale, située dans Ω, nous allons "changer l'objet" pas à pas, de façon à ce que le champ diffracté par celui-ci ressemble de plus en plus à celui mesuré. Pour ce faire nous définissons une fonction coût qui est la différence entre le champ diffracté par l'objet estimé, $\boldsymbol{f}_l^e$, et le champ effectivement mesuré $\boldsymbol{f}_l$:

$$\mathcal{F} = \sum_{l=1}^{L} |\boldsymbol{f}_l^e - \boldsymbol{f}_l|^2. \tag{3.5}$$

La minimisation de cette fonction coût peut se faire par différentes techniques. Pour plus de détails sur les principales méthodes de minimisations, voir Ref. 44 où ces méthodes sont confrontées à des données expérimentales dans le domaine des micro-ondes. Notons que dans le cadre de ce tapuscrit l'éclairement se fera toujours dans la direction des z positifs (exception faite du § 3.5.2) où θ_0 est l'angle formé par $\boldsymbol{k}_0$ (vecteur d'onde du champ incident) et l'axe z, et la mesure du champ diffracté toujours au-dessus de l'objet où θ_d est l'angle formé par $\boldsymbol{k}_d$ (vecteur d'onde du champ diffracté) et l'axe z. Ceci correspond donc typiquement à la configuration utilisée par un microscope optique en transmission.

Quelques mots sur la sphère d'Ewald[v]

Dans le cas où le diffuseur est petit vis-à-vis de la longueur d'onde, par exemple une sphère de diamètre $\lambda/10$, le champ diffusé par celle-ci peut s'écrire, en utilisant l'Eq. (3.4) et les propriétés de la susceptibilité linéaire du champ, comme :

$$\boldsymbol{f}_l(\boldsymbol{r}) \propto \frac{e^{ik_d r}}{r} \boldsymbol{E}_0^{\perp} \tilde{\chi}(\boldsymbol{k}_d - \boldsymbol{k}_0). \tag{3.6}$$

Le champ diffracté par l'objet au point d'observation $\boldsymbol{r}$ est donc proportionnel à la transformée de Fourier de la susceptibilité linéaire χ prise en $\boldsymbol{k}_d - \boldsymbol{k}_0$, $\boldsymbol{E}_0^{\perp}$ étant la composante du champ incident perpendiculaire à la direction d'observation. En faisant varier la direction du champ incident et la position d'observation, il est donc possible d'accéder à un certain domaine spectral de $\tilde{\chi}$. Par exemple, dans la configuration d'un microscope optique en transmission, quand l'angle d'incidence est tel que $\theta_0 \in [-90°; 90°]$ nous obtenons $k_{0,x} \in [-k_0; k_0]$ et $k_{0,z} \in [0; k_0]$. Quant au champ diffracté, si les points d'observations sont tels que $\theta_d \in [-90°; 90°]$ nous obtenons $k_{d,x} \in [-k_0; k_0]$ et $k_{d,z} \in [0; k_0]$. Le support spectral accessible pour $\tilde{\chi}$ est alors de $[-2k_0; 2k_0]$ suivant la direction transversale et de $[-k_0; k_0]$ dans la direction longitudinale.[vi] Normalement avec un tel domaine de fréquence la résolution transverse est de 0.3λ, mais il convient de tempérer ce résultat. En effet, avoir accès à un large domaine spectral n'assure en rien l'existence des hautes fréquences, ou de leurs signatures plus élevées par rapport au bruit. Par exemple, pour un objet dipolaire déposé sur un substrat plan, il est toujours possible de mettre un point d'observation à $\theta_d \approx 90°$, mais il n'y aura pas de champ diffracté...

3.3 Approche qualitative rapide

La méthode initialement développée est basée sur une minimisation rapide de la fonction coût $\mathcal{F}$. Dans ce cas la minimisation de la fonction coût se fait sur les dipôles, $\boldsymbol{p}_l$. Quand les dipôles sont obtenus, en utilisant l'Eq. (3.3), le champ à l'intérieur de l'objet est calculé, pour finalement en déduire la permittivité relative (annexe 4 page 162).[45] Comme la minimisation se fait sur les moments dipolaires, et non sur la polarisabilité, cette méthode ne permet que de la localisation. Néanmoins elle présente l'avantage d'être très rapide (typiquement quelques minutes) ce qui peut être utile en biologie où un résultat immédiat est parfois souhaité.

Etudions par exemple le cas où différents objets (absorbants ou non) sont immergés au sein d'un système multicouche. La Fig. 3.2(c) indique les données optogéométriques du problème, tandis que les Figs. 3.2(a) et 3.2(b) montrent la reconstruction pour la partie réelle et la partie imaginaire de la permittivité relative, respectivement. Figures 3.2(a) et 3.2(b) localisent clairement la position des différents diffuseurs et montrent si ceux-ci sont absorbants ou non.[46] A noter que la méthode développée dans ce paragraphe peut être fortement améliorée avec de l'information *a priori*, par exemple en connaissant la permittivité relative des objets inconnus.[45]

3.4 Caractérisation de un ou de plusieurs objets inconnus

Dans le cas où nous désirons trouver la forme **et** la permittivité relative de un ou de plusieurs objets inconnus, plusieurs méthodes non linéaires, évitant donc l'approximation

[v] Paul Peter Ewald (1888-1985) : physicien allemand.

[vi] Si l'incident et la position d'observation tournent tout autour de l'objet alors le domaine spectral accessible est de $[-2k_0; 2k_0]$ dans toutes les directions de l'espace.

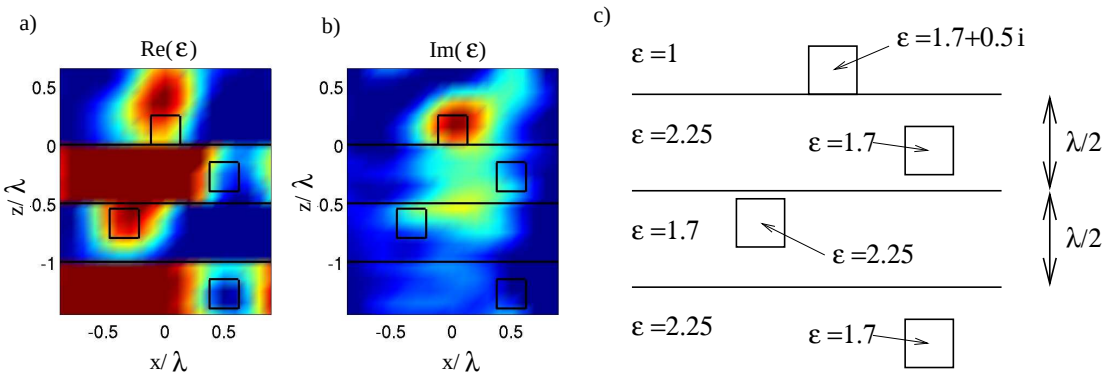

Fig. 3.2 : *(c) Schéma de la configuration étudiée : la taille du domaine d'investigation est de $2\lambda \times 2\lambda \times 2.2\lambda$, les objets sont des cubes de côté $\lambda/4$ éclairés par 16 ondes planes se propageant dans la direction des z positifs avec $\theta_0 \in [-80°, 80°]$. Le champ électromagnétique est mesuré au-dessus de la surface avec $\theta_d \in [-80°, 80°]$. (a) Reconstruction de la partie réelle de la permittivité relative. (b) Reconstruction de la partie imaginaire de la permittivité relative.*

de Born, [vii−viii] existent, tels que le gradient conjugué, le gradient modifié et des méthodes hybrides.[47–49] La méthode que nous avons choisie est une méthode des gradients conjugués où la variable de minimisation est la polarisabibilité (donc la permittivité relative à travers la relation de Claussius-Mossotti). Dans ce cas, à chaque itération la polarisabilité de chaque élément de discrétisation est mise à jour. Pour plus de détails sur cette méthode des gradients conjugués le lecteur peut se repporter à l'annexe 3. Notons que l'inconvénient principale de cette méthode est qu'à chaque itération, il nous faut recalculer le champ auto-cohérent dans le domaine d'investigation Ω, et donc résoudre le système d'équations linéaires représenté par l'Eq. (3.3). Le nombre d'itérations étant important, la résolution de l'Eq. (3.3) prend un temps considérable et l'inversion demande alors plusieurs heures. Nous donnons ci-dessous les résultats les plus marquants obtenus par cette méthode.

3.4.1 Objets en espace homogène

Soit deux objets de côté $\lambda/4$ séparés par une distance $c = \lambda/7$ suivant l'axe x, de permittivité relative $\varepsilon = 2.25$ éclairés par 16 ondes planes tel que $\theta_0 \in [-80°, 80°]$. Le champ est mesuré en 65 points sur une calotte sphérique disposée au-dessus de l'objet tel que $\theta_d \in [-80°, 80°]$. Figure 3.3 présente la reconstruction obtenue après convergence. Il est clair que la permittivité relative est bien retrouvée et que les deux objets sont parfaitement séparés alors qu'une distance de seulement $\lambda/7$ les sépare, ce qui correspond à une distance centre à centre d'environ 0.4λ. Notons que le domaine des fréquences spectrales auquel nous avons accès, avec l'illumination choisie, est de $[-2k_0; 2k_0]$ dans la direction x.

[vii] L'approximation de Born consiste à supposer que le champ dans l'objet correspond au champ incident : l'Eq. (3.3) s'écrit alors : $\boldsymbol{E}_l = \boldsymbol{E}_{0,l}$.

[viii] Max Born (1882-1970) : physicien allemand, puis britannique.

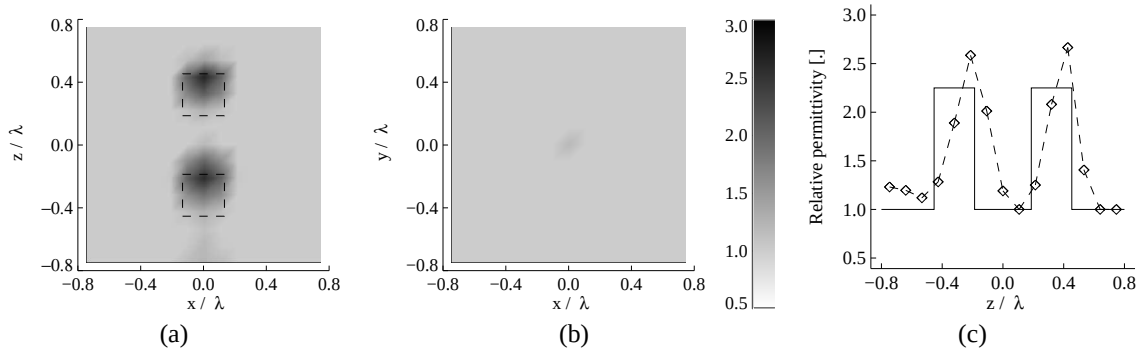

Fig. 3.4 : *Cubes de côté $\lambda/4$ espacés de $\lambda/3$ disposés suivant l'axe z. (a) Carte de la permittivité relative dans le plan (x, z). (b) Carte de la permittivité relative dans le plan (x, y). (c) Coupe de la permittivité relative selon z à $x = y = 0$. En trait plein le profil réel de la permittivité relative.*

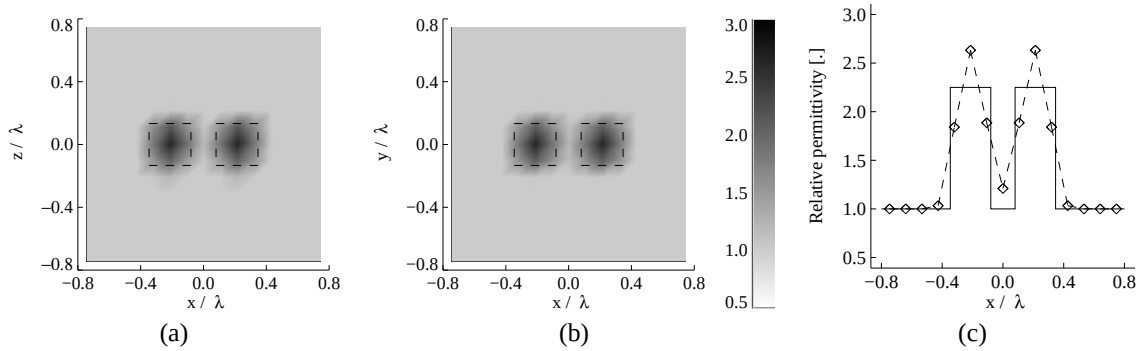

Fig. 3.3 : *Cubes de côté $\lambda/4$ espacés d'une distance $c = \lambda/7$ disposés suivant l'axe x. (a) Carte de la permittivité relative dans le plan (x, z). (b) Carte de la permittivité relative dans le plan (x, y). (c) Coupe de la permittivité relative selon x à $z = y = 0$. En trait plein le profil réel de la permittivité relative.*

Les deux objets sont toujours éclairés de la même façon mais ils sont cette fois ci alignés suivant l'axe z avec une distance $c = \lambda/3$, ce qui correspond à une distance centre à centre d'environ 0.6λ. Figure 3.4 montre une bonne séparation des objets, mais la résolution est moindre suivant la direction z que suivant la direction x. Ceci s'explique facilement à partir de l'éclairement choisi, qui donne un domaine de fréquences spectrales de seulement $[-k_0; k_0]$ pour la direction z, soit deux fois moindre que suivant la direction x.

3.4.2 Objets déposés sur un substrat plan

Dans le cadre de l'ACI jeune chercheur "microscopie à haute résolution" nous nous intéressons plus particulièrement à des objets déposés sur une surface. En éclairant par des ondes évanescentes, *i.e.*, $\theta_{\text{inc}} > \theta_c$, où θ_c est l'angle limite à la réflexion totale, nous avons alors accès à de plus hautes fréquences spatiales. En regardant plus particulièrement la sphère d'Ewald, et en supposant que l'éclairement se fait uniquement en réflexion interne et que les points d'observation sont au-dessus du substrat, la projection des vecteurs d'onde suivant l'axe x montre que le domaine spectral maximum est maintenant de $[-(n+1)k_0; (n+1)k_0]$, avec n l'indice optique de la surface. Avec $n = 1.5$ le domaine spectral est augmenté de 25% par rapport à la même configuration dans l'espace homo-

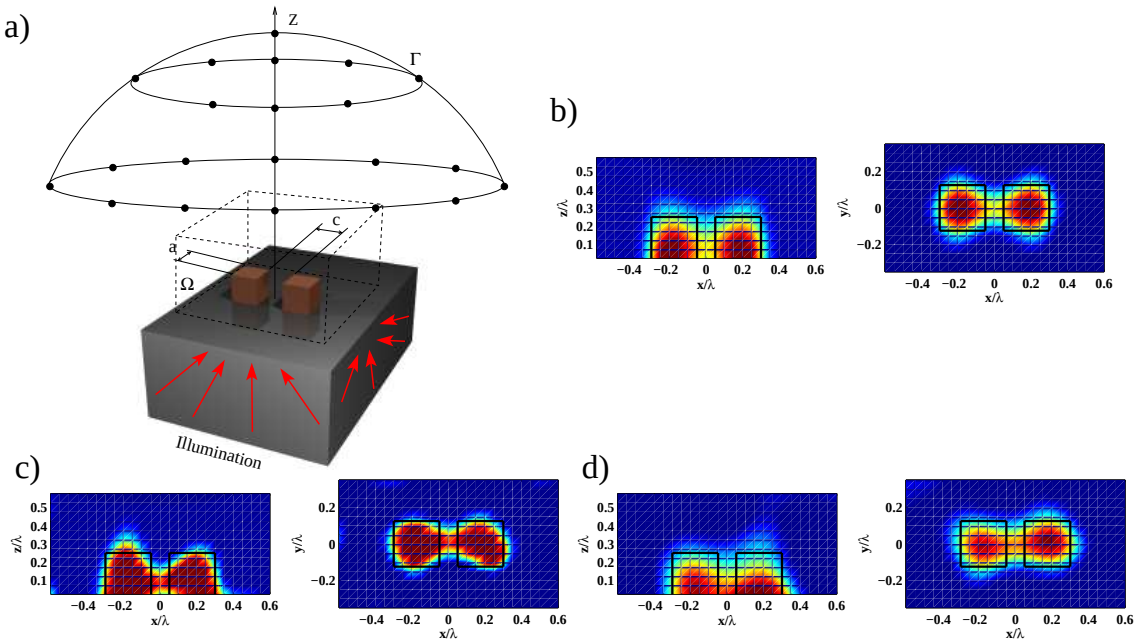

Fig. 3.5 : *(a) Schéma de la configuration utilisée. (b), (c), et (d) Carte de la permittivité relative dans le plan (x, y) à $z = \lambda/40$ et dans le plan (x, z) à $y = 0$. (b) Seules les ondes évanescentes sont utilisées : $\theta_0 \in [-80°, -43°] \cup [80°, 43°]$. (c) Seules les ondes évanescentes sont utilisées mais le champ diffracté est bruité. (d) Ondes propagatives + évanescentes ($\theta_0 \in [-80°, 80°]$) avec le champ diffracté bruité.*

gène. Mais attention, avoir un domaine spectral plus large, ne signifie par forcément avoir une meilleure résolution, car il faut encore avoir de la lumière diffractée pour les angles correspondants aux hautes fréquences.

La configuration étudiée est décrite Fig. 3.5(a). Les reconstructions présentées dans la Fig. 3.5(b) montrent que quand seules les ondes évanescentes sont utilisées la séparation des deux cubes est parfaitement accomplie. Mais si nous bruitons le champ diffracté [ix] $\boldsymbol{f}_l$ pour se rapprocher d'avantage de l'expérience la Fig. 3.5(c) montre que la reconstruction est très sensible au bruit : phénomène bien connu de la sensibilité au bruit des hautes fréquences spatiales. Pour éviter ce problème il convient de stabiliser la procédure d'inversion en introduisant des fréquences plus basses, *i.e.*, des ondes propagatives dans l'éclairement. Dans ce cas nous avons $\theta_0 \in [-80°, 80°]$ et la résolution est celle donnée par les ondes évanescentes, et la robustesse au bruit est due aux ondes propagatives [Fig. 3.5(d)]. Pour plus de précision sur l'influence du bruit, ou sur l'influence du substrat dans la reconstruction, voir annexe 4 page 169 et page 172.[50,51]

3.4.3 Objets au-dessus d'un réseau

Afin d'améliorer la résolution latérale, il faut que la composante parallèle à la surface du vecteur d'onde incident soit la plus grande possible. L'idée est donc d'utiliser, non pas un substrat qui a forcément un indice limité ($n = 2.4$ au maximum dans le domaine du visible), mais un réseau pour éclairer les objets [Fig. 3.6(a)].[52] Le champ diffracté par un

[ix] Pour plus de précision sur la méthode utilisée pour bruiter le champ diffracté, voir Ref. 51.

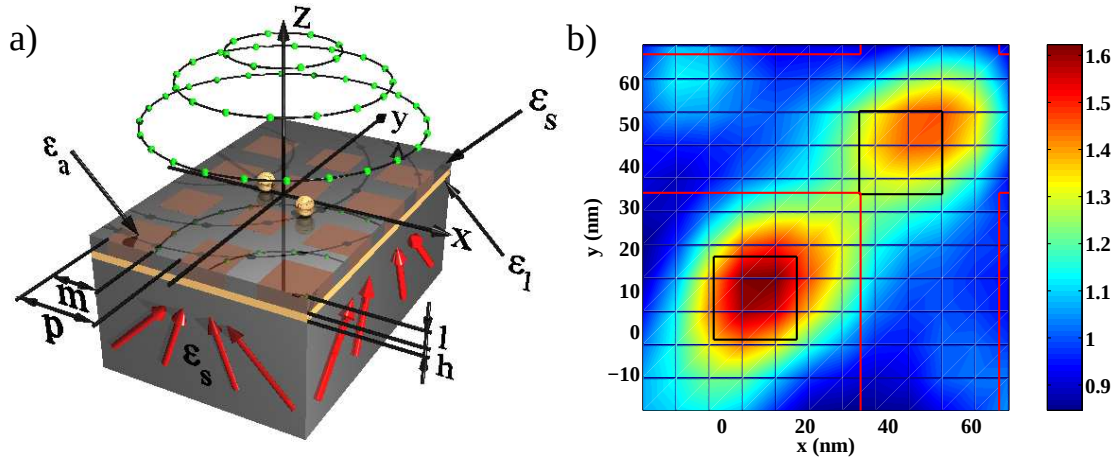

Fig. 3.6 : *(a) Deux objets dipolaires (cubes de 20 nm de côté et de permittivité relative 2.25) sont déposés sur un réseau caractérisé par $p = 100$ nm, $m = 66.7$ nm, $l = 6.66$ nm, $h = 6.75$ nm, $\varepsilon_s = 2.25$, $\varepsilon_a = 4.41$, $\varepsilon_l = -8.4537 + 0.6984i$ (argent). Le réseau est éclairé par 8 ondes planes polarisées TM tel que $\theta_0 = 80°$ et $\lambda = 500$ nm dans le vide. Le champ diffracté est mesuré sur 80 points d'observations tel que montré sur la figure. (b) Carte de permittivité relative reconstruite dans le plan (x, y) à une altitude de 12 nm par rapport au substrat nanostucturé. Le champ diffracté a été corrompu avec 10% de bruit. Les carrés noirs représentent la vraie position des cubes et en rouge les motifs du réseau.*

réseau éclairé en incidence normale (à une dimension) s'écrit :

$$E(x,z) = \sum_{j=-\infty}^{\infty} A_j e^{i\frac{2\pi}{p}jx} e^{i\gamma z}, \tag{3.7}$$

avec $\gamma = \sqrt{k_0^2 - \left(\frac{2\pi}{p}j\right)^2}$. Si seul l'ordre 1 est non nul ($A_1 \neq 0$ et $A_j = 0$ pour $j \neq 1$) alors la composante du vecteur d'onde incident suivant x est égale à $\frac{2\pi}{p}$. Avec $p = \lambda/5$, soit dans les 100 nm pour $\lambda = 500$ nm, nous obtenons $k_x = 5k_0$. Le rayon de la sphère d'Ewald est alors augmenté et de par ce fait, la résolution latérale s'accroît. A noter que le champ au-dessus du réseau est alors fortement évanescent ce qui n'est pas un problème car les objets étudiés sont très petits vis-à-vis de la longueur d'onde, et ne sont donc pas très hauts.

La géométrie que nous avons choisie pour étudier la résolution de notre configuration est représentée Fig. 3.6(a) : deux dipôles sont disposés sur un substrat constitué d'une faible couche d'argent déposée sur un substrat de verre (n =1.5) sur laquelle est disposé un réseau formé par une couche de verre (n =1.5) avec des plots d'indice n =2.1. En optimisant les différents paramètres (angle d'incidence, indices optiques, taille des pavés, épaisseurs) le champ incident au-dessus du réseau n'est plus constitué que des ordres (0,0) et (1,0). Les très hautes fréquences spatiales contenues dans le champ incident permettent de distinguer les deux dipôles séparés de seulement 50 nm, soit $\lambda/10$ [Fig. 3.6(b)]. Notons que pour effectuer le problème direct il convient de calculer le champ diffracté par des objets en présence d'un réseau. Pour ce faire nous utilisons les outils développés § 1.3.1, et § 1.3.2 pour le calcul du champ diffracté. Pour le problème inverse nous appliquons les procédures d'inversion développées dans ce chapitre, mais il serait très long en temps de calcul dans l'inversion de prendre en compte le réseau : en effet cela demanderait à chaque itération de résoudre l'Eq. (3.3). Comme dans ce cas les objets sont très petits vis-à-vis de la longueur d'onde, l'inversion est réalisée avec l'approximation de Born.

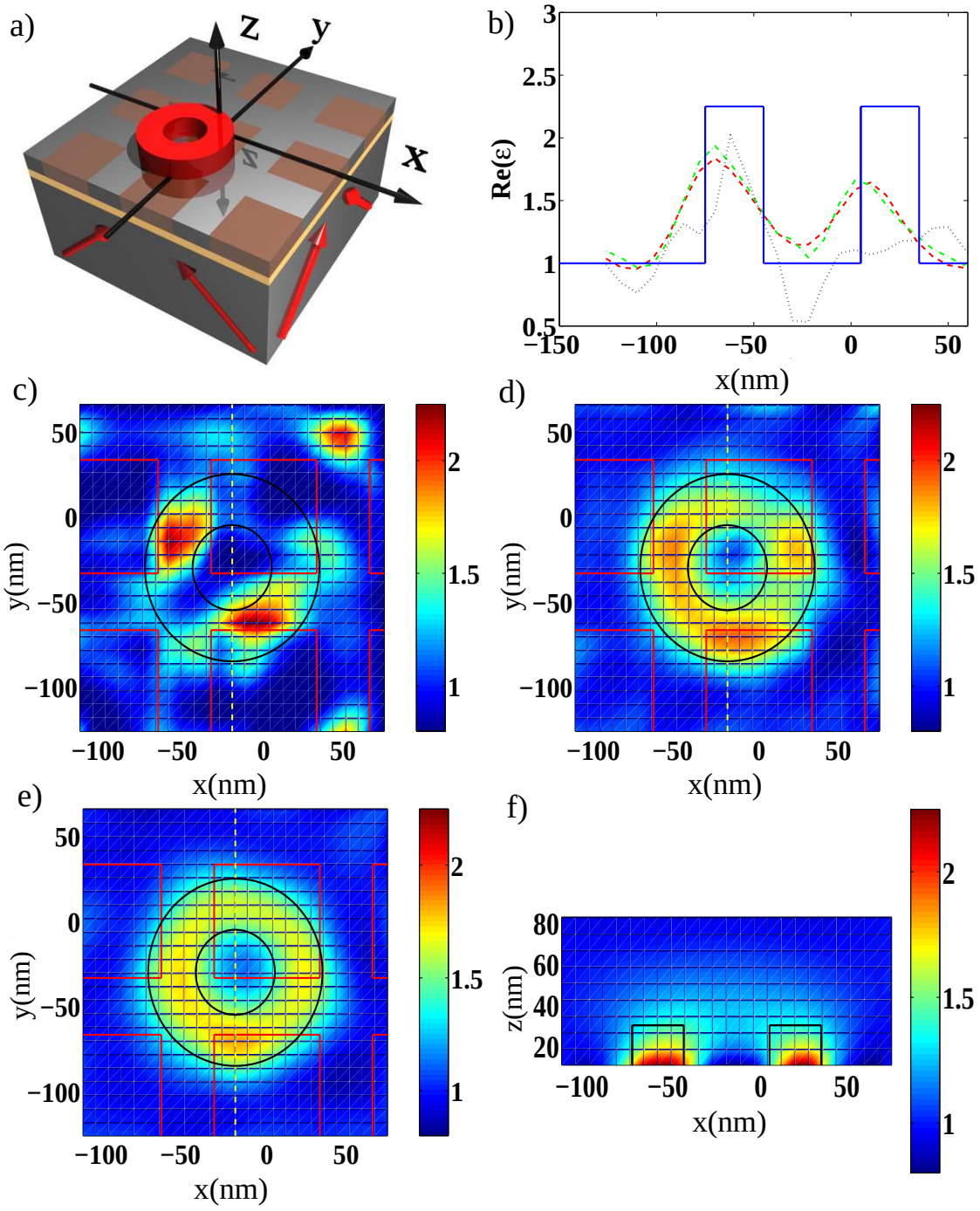

Fig. 3.7 : *(a) Configuration étudiée. (b) Coupes réalisées pour différentes approximations dans la méthode d'inversion. En bleu le profil réel de la permittivité relative. (c), (d) et (e) Carte de permittivité relative dans le plan (x, y) à 12 nm au-dessus de la surface : (c) inversion en utilisant l'approximation de Born. (d) inversion en supposant l'objet en espace homogène. (e) inversion en supposant l'objet sur un substrat plan. (f) Carte de permittivité relative dans le plan (x, z). L'inversion est effectuée en supposant l'objet sur un substrat plan.*

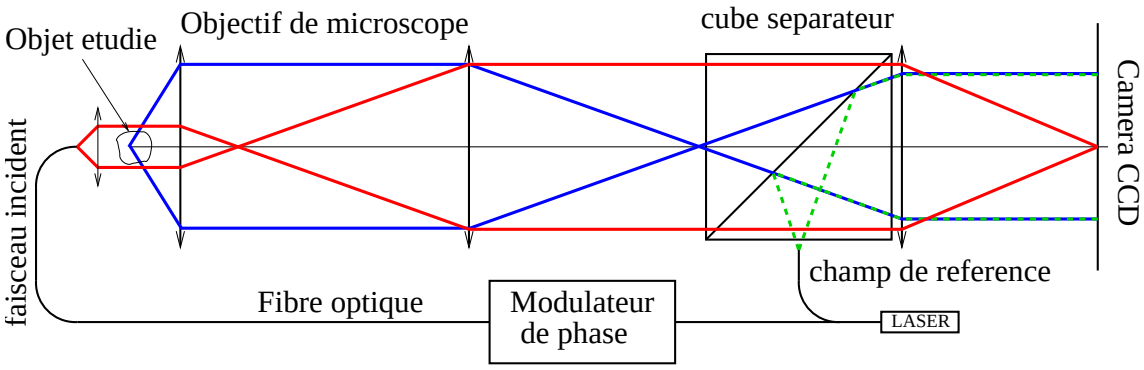

Fig. 3.8 : *Configuration expérimentale pour mesurer le champ diffracté en module et phase dans le cas de la transmission. En rouge le champ incident qui éclaire l'objet, en bleu le champ diffracté par l'objet et en vert le champ de référence qui vient interférer avec le champ incident (sur un pixel de la caméra) et le champ diffracté par l'objet.*

Le prochain objet étudié est un tore à section carrée qui a pour diamètre extérieur 110 nm et diamètre intérieur 55 nm et une permittivité relative de 2.25 [Fig. 3.7(a)]. Cet objet a été choisi car, au vu de sa taille, il est évident que la variation du champ incident sur le support de l'objet est importante. De plus le trou à l'intérieur est suffisamment petit ($\approx \lambda/10$) pour que celui-ci soit invisible à un microscope optique classique. Pour effectuer l'inversion plusieurs niveaux d'approximation ont été étudiés, toujours pour éviter de résoudre exactement l'Eq. (3.3). Pour la Fig. 3.7(c) l'inversion a été faite en utilisant l'approximation de Born, Fig. 3.7(d) en supposant l'objet en espace homogène, et quant à la Fig. 3.7(e) en prenant le substrat en compte mais le réseau est simulé par une couche homogène. La Fig. 3.7(b) rassemble les profils obtenus avec les différentes approximations. Il est clair que l'approximation de Born donne un résultat qui ne représente pas l'objet réel, ce qui était attendu du fait de la taille de l'objet [Fig. 3.7(c)]. Par contre le fait de négliger la présence du substrat dans les algorithmes de reconstruction permet quand même d'avoir une très bonne estimation de la permittivité relative de l'objet [Fig. 3.7(d)] et prendre en compte le substrat permet juste d'avoir un objet reconstruit un peu plus homogène comme montré Figs. 3.7(e) et 3.7(f). A noter que la Fig. 3.7(f) montre que le trou du tore se voit moins bien au fur et à mesure que l'observation s'éloigne du substrat nanostructuré. Ceci n'est pas surprenant vu que la résolution est directement reliée aux ondes évanescentes, qui décroissent très vite quand on s'éloigne du substrat.

Beaucoup de travail reste à faire sur ce sujet notamment une étude de l'influence du bruit sur la mesure du champ diffracté, mais aussi l'influence des défauts de construction du réseau (plots manquants ou mal placés, période mal connue), car il est évident que tout est conditionné par la connaissance du champ incident au-dessus du réseau nano structuré.

3.5 Réalisation expérimentale

3.5.1 Dispositif expérimental

Comme précisé § 3.1.3 la partie expérimentale est effectuée par F. Drsek que je coencadre avec H. Giovannini et A. Sentenac. La mesure de la phase est réalisée par un dispositif semblable à celui inventé par V. Lauer,[53] mais permettant de travailler en transmission (Fig. 3.8) et en réflexion.

L'objet étudié est éclairé par un faisceau laser (en rouge sur la Fig. 3.8) dont l'incidence peut varier (le système contrôlant l'incidence n'est pas représenté sur la Fig. 3.8). Le champ

diffracté par l'objet (en bleu sur la Fig. 3.8) est dirigé, *via* un système de lentilles, sur une caméra CCD. La valeur du module du champ diffracté se déduit directement de la mesure de l'intensité sur la caméra CCD.

La mesure de la phase quant à elle est plus délicate, surtout dans le domaine du visible, et demande de passer par un système de mesure basé sur les interférences. Dans le cas de la Fig. 3.8, l'hypothèse doit être faite que le champ incident, après traversée des lentilles, se focalise en un point de la caméra CCD, et est peu perturbé par le champ diffracté par l'objet. Cette approximation est parfaitement légitime vu que nous voulons étudier des particules de tailles nanométriques. Nous superposons au champ diffracté par l'objet un champ (rayon vert sur la Fig. 3.8) de référence issu de la même source que le champ incident : les deux ondes sont isochrones. Nantis de cette hypothèse, la mesure de l'intensité résultant de l'interférence entre, d'une part, le champ de référence et le champ incident **et** d'autre part, entre ce même champ de référence et le champ diffracté par l'objet, permet *via* un modulateur de phase, de remonter à la phase du champ diffracté par l'objet par rapport au champ incident. En fait le schéma est un peu plus compliqué que ce qui est représenté Fig. 3.8, d'une part pour permettre la mesure dans le cas de la réflexion et d'autre part pour pouvoir faire varier l'angle d'incidence.

3.5.2 Les premiers résultats

Pour les premières expériences, nous avons choisi d'étudier un échantillon constitué d'une surface plane réfléchissante dans laquelle trois pistes ont été gravées. Le dispositif expérimental est donc utilisé en réflexion. Figure 3.9(a) montre l'enregistrement sur la caméra CCD du module du champ diffracté par l'objet dans le cas de l'incidence normale. Ensuite quatre enregistrements sont effectués avec une incidence de $\theta = 25°$ (θ est l'angle entre la normale à la surface et le faisceau incident) mais avec différents ϕ [$\phi = 0°$, $\phi = 90°$, $\phi = 180°$ et $\phi = 270°$, respectivement Figs. 3.9(f), 3.9(c), 3.9(d) et 3.9(e)]. Ces quatre enregistrements, ayant un éclairement différent, permettent d'accéder à des fréquences spatiales différentes. En sommant ces quatre images (en faisant attention d'ajuster les phases de manière adéquate), une nouvelle image du champ diffracté est formée [Fig. 3.9(b)], avec une plage de fréquences spatiales plus large qu'avec une seule incidence (le cercle noir étant bien plus grand que chacun des cercles blancs pris séparément).

Moyennant quelques approximations, la phase de la transformée de Fourier du champ diffracté est reliée au profil de l'échantillon. [x] Figure 3.10(a) montre la reconstruction de l'objet dans le cas ou huit incidences sont utilisées : l'objet est formé de trois pistes verticales qui apparaissent dans un cercle correspondant au diaphragme placé avant le cube séparateur. Figures 3.10(b) et 3.10(c) montrent les coupes obtenues suivant les axes x et y, à partir d'une seule incidence (courbes rouges : -.) , quatre incidences (courbes bleues : - -) et huit incidences (courbes noires : -).

L'observation au microscope à force atomique de notre objet donne une profondeur de 120 nm pour les pistes avec une largeur de 5 μm. Quel que soit le nombre d'incidences utilisées pour la reconstruction, nous obtenons bien une profondeur de 120 nm avec une largeur entre 5 et 6 μm, ce qui nous permet de dire que nous faisons du quantitatif. Mais il est clair que l'augmentation de la plage de fréquences spatiales du champ diffracté, en augmentant le nombre des incidences, permet de renforcer la qualité de la reconstruction. Cette première réalisation expérimentale est très encourageante, et il serait intéressant

[x] $\phi(x,y) = 2k_0 \cos\theta h(x,y)$ avec $\phi(x,y)$ la phase de la transformée de Fourier du champ diffracté, $h(x,y)$ le profil de l'échantillon et θ l'angle d'incidence des différents éclairements.

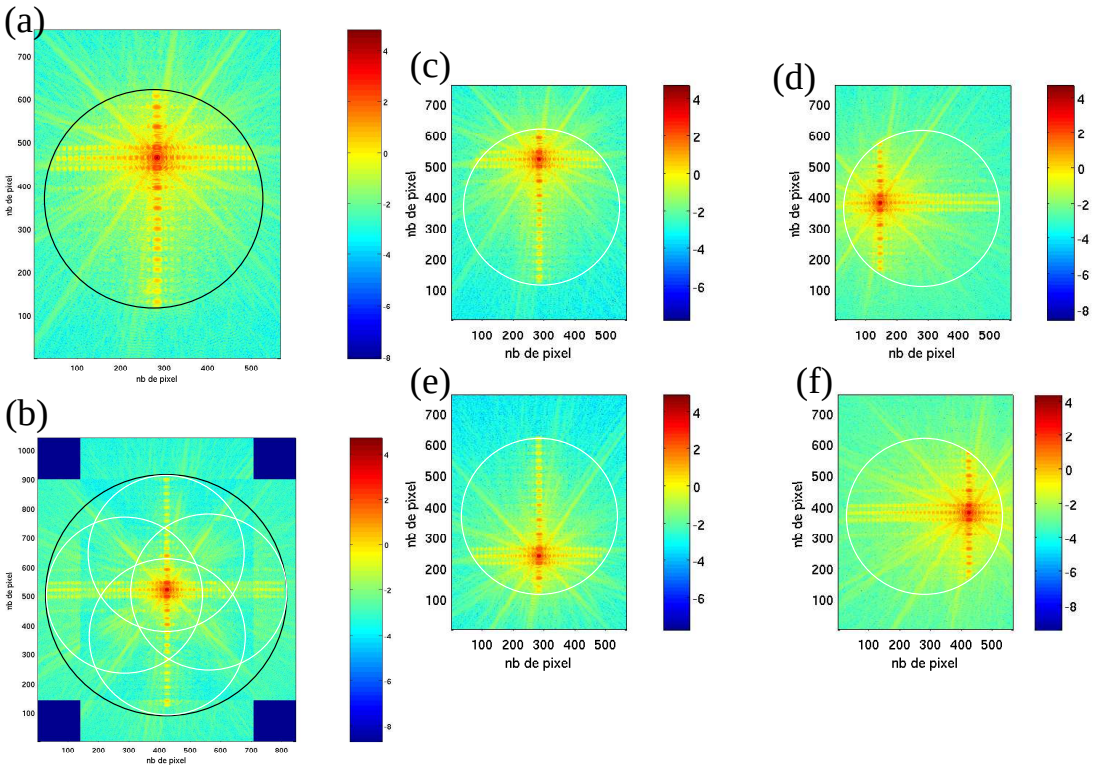

Fig. 3.9 : *Module du champ diffracté enregistré sur la caméra CCD. Le maximum d'intensité correspondant au faisceau incident (spéculaire). Les cercles montrent la plage de fréquences spatiales accessibles à travers la mesure du champ diffracté. (a) Champ diffracté en incidence normale. (b) Somme de (f), (c), (d) et (e) chacune étant enregistrée avec une incidence de* $\theta = 25°$ *avec* $\phi = 0°$, $\phi = 90°$, $\phi = 180°$ *et* $\phi = 270°$ *respectivement.*

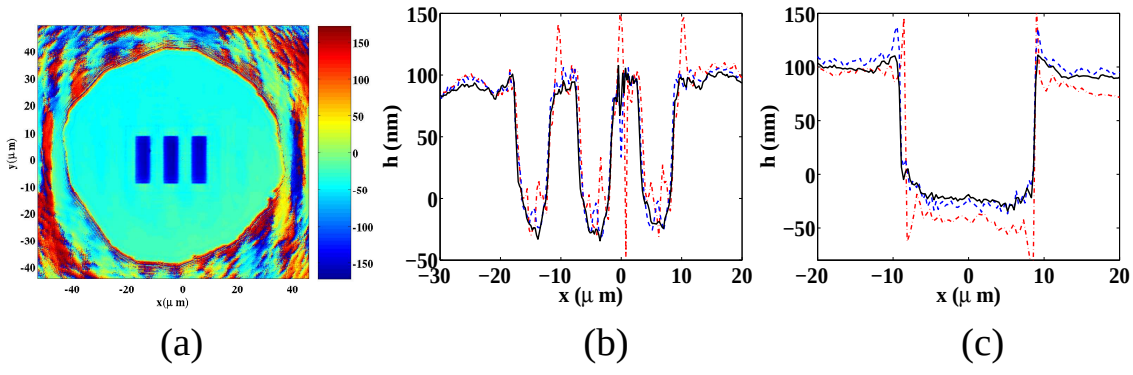

Fig. 3.10 : *(a) Reconstruction de l'objet obtenue avec 8 incidences. La palette de couleur à droite de la figure exprime la hauteur en nm. (b) Coupe en* $y = 0$. *(c) Coupe verticale sur le troisième objet : une incidence : courbes rouges (-.) ; quatre incidences : courbes bleues (- -) ; huit incidences :courbes noires : (-).*

d'effectuer la reconstruction de l'objet avec des méthodes plus précises, par exemple avec l'approximation de Kirchoff. [xi]

3.6 Conclusion

Dans ce chapitre dédié au sondage électromagnétique, nous avons évité au maximum les équations et juste donné le principe de base de la reconstruction des cartes de permittivité relative. En effet les différents algorithmes d'inversion sont assez complexes et difficilement compréhensibles par le profane. Nous nous sommes donc focalisés sur les résultats obtenus et sur notre démarche pour aboutir à un microscope optique à haute résolution, qui est la finalité de notre étude. Mais comme le montrent les § 3.4.3 et § 3.5, il reste encore du travail à réaliser, aussi bien théorique qu'expérimental, pour atteindre les objectifs que nous nous sommes fixés.

A noter que l'étude commencée sur le réseau afin d'obtenir une sphère d'Ewald de plus grand rayon, peut aussi s'appliquer dans le cas de microscopes à fluorescence. [54]

[xi] Gustav Robert Kirchoff (1824-1887) : physicien allemand.

Chapitre 4

Etude de la fluorescence en espace confiné

In fact, the mere act of opening the box will determine the state of the cat, although in this case there were three determinate states the cat could be in : these being Alive, Dead, and Bloody Furious.

Schrodinger's Moggy explained (Terry Pratchett, Lords and Ladies).

Sommaire

4.1 Introduction

Ce chapitre est consacré à la durée de vie et du rayonnement d'une molécule fluorescente dans un environnement plus ou moins complexe. Mais avant de détailler le travail réalisé dans ce domaine de recherche, voyons déjà la fluorescence d'une molécule en espace homogène : une molécule fluorescente (ou atome, ion, boîte quantique) recevant une radiation va absorber celle-ci, et passer à un niveau excité. Après une relaxation partielle, avec par exemple perte de chaleur par échange avec le milieu ambiant, la molécule va retourner à l'état fondamental par une émission lumineuse. En raison de la perte énergétique lors de la relaxation partielle, le spectre de fluorescence est décalé vers le rouge, par rapport à la fréquence de l'onde incidente,[i] voir Fig. 4.1.

En fait, l'explication de l'émission spontanée d'un photon par une molécule fluorescente est purement quantique : l'émission spontanée résulte du couplage de la molécule aux modes électromagnétiques. Quand un environnement modifie, en un point de l'espace, la distribution spatiale et spectrale des modes électromagnétiques, il modifie alors la façon dont la molécule se couple au champ électromagnétique, et de par ce fait son émission spontanée, voir par exemple les expériences fondatrices de Selényi, puis Drexhage.[55,56]

[i] A propos de la fluorescence on parle parfois de "lumière froide".

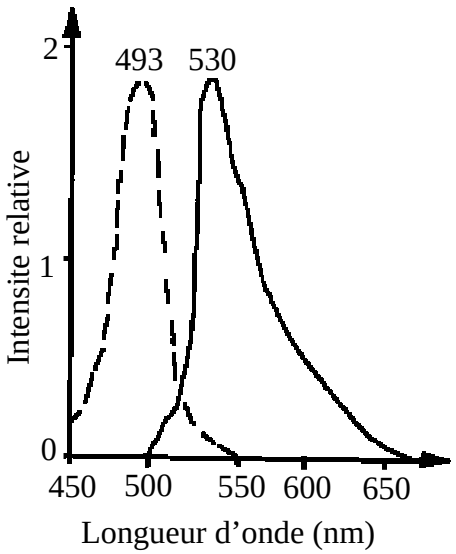

Fig. 4.1 : *Molécule fluorescente émettant dans le domaine du visible. En pointillé le spectre de la source excitatrice, et en trait plein le spectre rayonné par le source.*

L'intérêt pour l'émission spontanée grandit d'année en année de par la multiplication des applications de celle-ci : création d'un laser sans seuil, source à un photon (très utile pour la cryptographie[57]), source de lumière localisée, sonde locale,[58] ... Il convient donc de pouvoir calculer le taux d'émission spontanée[ii] dans des environnements complexes. Mais il est très délicat dans des géométries non canoniques de calculer celui-ci avec le formalisme quantique. Néanmoins, il est possible de montrer que le taux d'émission spontanée est directement relié à la susceptibilité linéaire du champ électrique, qui elle peut se calculer par une approche classique. [iii] Le calcul de la durée de vie d'une molécule fluorescente peut donc se faire par la CDM, mais au lieu de calculer le champ électrique diffusé par l'objet étudié, c'est la susceptibilité linéaire du champ qui est calculée.[59]

4.2 Utilisation d'une molécule fluorescente comme sonde locale

Depuis les travaux fondateurs de Courjon,[60] les microscopes optiques de champ proche se sont développés de manière très importante. Ces microscopes utilisent une sonde de petite dimension (typiquement une fibre optique amincie à son extrémité ayant un rayon de courbure au minimum de 50 nm, ou une pointe métallique d'un rayon de courbure de 10 nm dans le cas de microscope apertureless) qui balaye la surface pour capter ou diffuser les ondes évanescentes.[61,62] La limite de résolution de ces microscopes est principalement due à la taille finie de la pointe, qui donne une image convoluée de la topographie de la surface avec celle-ci. La grande sensibilité d'une molécule fluorescente à son environnement proche, et son caractère ponctuel, en fait donc une candidate idéale comme sonde locale de champ proche optique.[63] Figure 4.2 représente le taux d'émission spontanée d'une molécule quand celle-ci balaye une surface sur laquelle sont présents des objets. Quand le

[ii] Le taux d'émission spontanée est l'inverse de la durée de vie.

[iii] Le taux d'émission spontanée est relié à la partie imaginaire de la susceptibilité linéaire du champ.

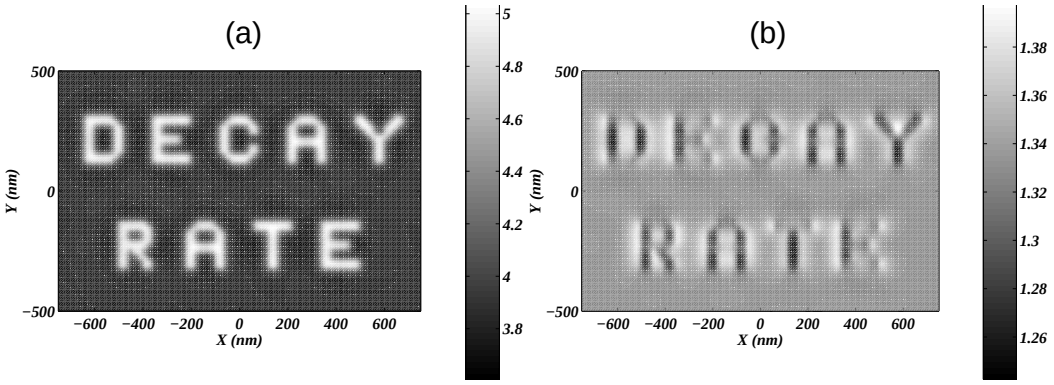

Fig. 4.2 : *La molécule fluorescente est attachée à une pointe formée d'un matériau diélectrique. Celle-ci balaye la surface (en verre), où l'objet à étudier est déposé, à une hauteur constante de 40 nm. La molécule rayonne à $\lambda = 488$ nm, et le taux d'émission spontanée en fonction de la position de la molécule est représenté. (a) Le moment dipolaire associé à la transition est selon l'axe z. (b) Le moment dipolaire associé à la transition est selon l'axe x.*

moment dipolaire associé à la transition est orienté selon l'axe z [Fig. 4.2(a)] les objets sur le substrat plan sont parfaitement reconnus. Ceci nous donne donc un microscope avec une résolution latérale en dessous de 20 nm (annexe 4 page 195). Dans le cas où le moment dipolaire associé à la transition est orienté selon l'axe x [Fig. 4.2(b)] il est plus délicat de reconnaître les objets.

Cadre de ce travail : Ce travail est le fruit d'une collaboration entre A. Rahmani alors au NIST, et F. de Fornel à Dijon (équipe champ proche optique).

4.3 Impureté interstitielle dans un cristal

L'influence de l'environnement sur les propriétés électrodynamiques d'une nano source est un point important de l'optique moderne. Il est donc essentiel de connaître la correction de champ local d'une impureté interstitielle. Dans le cas d'un cristal possédant une symétrie cubique celle-ci peut être calculée avec la CDM. Le calcul est assez complexe, et le lecteur intéressé peut se référer à l'annexe 4 page 206.[64]

Cadre de ce travail : Ce travail a été réalisé lors de ma visite de 5 semaines au NIST (USA) dans le laboratoire de G. W. Bryant en collaboration avec A. Rahmani et G. W. Bryant.

4.4 Rayonnement d'une molécule fluorescente

4.4.1 Source fluorescente dans un cristal photonique

Dans ce paragraphe nous nous intéressons à la dynamique d'une source de photons (par exemple un "quantum dot") située dans un cristal photonique, ou plus précisément du contrôle de cette dynamique en façonnant le paysage électromagnétique environnant la

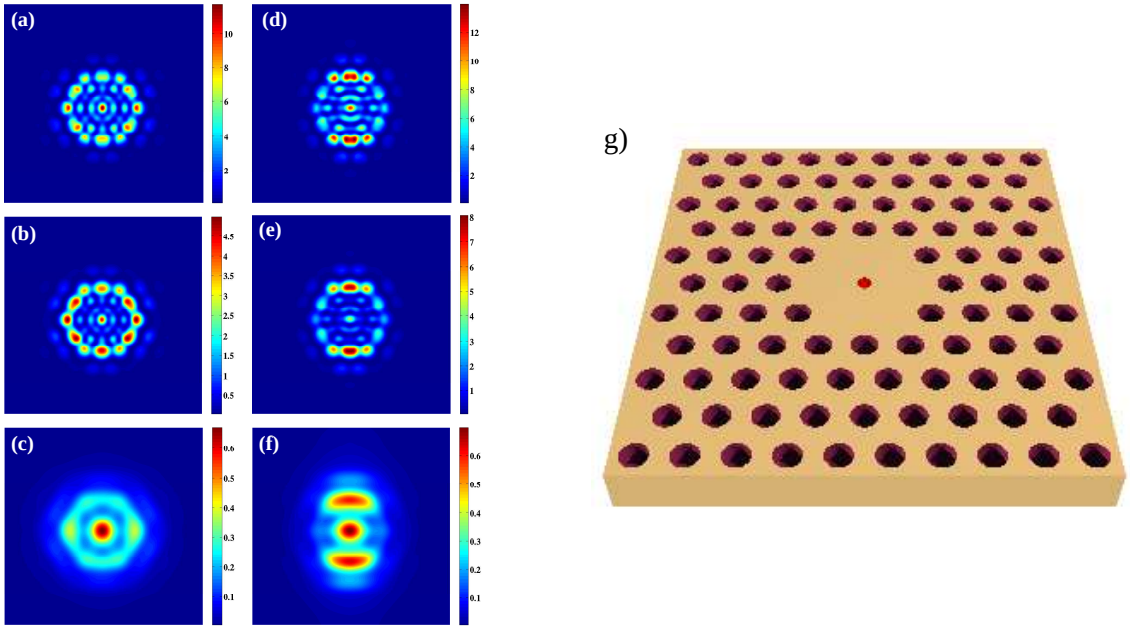

Fig. 4.3 : *(g) Schéma d'une micro cavité H2. L'épaisseur du slab est de 250 nm avec un indice de 3.17. La période du réseau est de 535 nm, avec un diamètre pour les cylindres de 178 nm. Le point rouge représente la position de la source. (a)-(f) Module du champ électrique (en unité arbitraire) au-dessus de la cavité pour une longueur d'onde d'émission de* $\lambda = 1405$ *nm pour les figures (a)-(c) et* $\lambda = 1410$ *nm pour les figures (d)-(f). Le résultat a été moyenné sur toutes les orientations du dipôle dans le plan* (x, y)*. Les cartes de champ sont calculées pour différentes hauteurs z : (a) et (d) : z=50 nm ; (b) et (e) : z=100 nm ; (c) et (f) : z=500 nm*

source. Figure 4.3(g) montre la structure que nous avons choisie d'étudier (cavité H2[iv]). La CDM permet alors de calculer les cartes de champ proche et de champ lointain au-dessus de la cavité H2 pour différentes positions de la source dans la cavité H2.[66]

Les cartes de champ proche présentées ont été retrouvées expérimentalement[67] et montrent que la CDM nous permet d'étudier la dynamique d'une source, *i.e.*, sa durée de vie en même temps que son rayonnement champ proche et champ lointain.[66]

Cadre de ce travail : Ce projet est mené essentiellement à l'école centrale de Lyon au LEOM (financé par une ACI jeune chercheur) et ma participation avec A. Rahmani porte sur l'utilisation de la CDM pour simuler les cartes de champ proche optique obtenues expérimentalement.

4.4.2 Molécule fluorescente dans une ouverture nanométrique

Ce projet vise à atteindre, dans un contexte industriel, la détection par marquage fluorescent de multiples molécules uniques, sur format puce à ADN, en détection hautement parallèle. Il exploite les effets de confinement et d'exaltation des ouvertures nanométriques.[68] Pour ce faire il convient de bien connaître la diffraction par une ouverture nanométrique[69] telle que représentée Fig. 4.4(a) puis d'accéder au diagramme de rayonnement d'une molécule située dans ce trou. Pour avoir un diagramme de rayonnement

[iv] Pour plus de précision sur les cristaux photoniques voir Ref. 65.

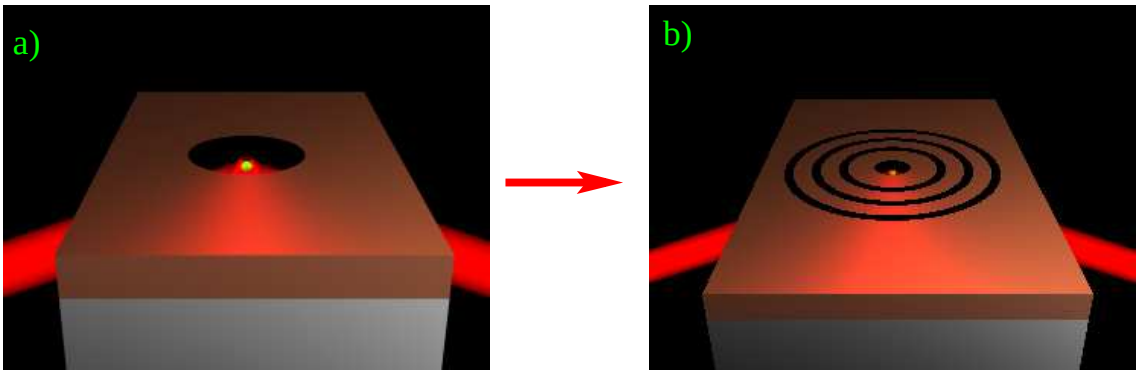

Fig. 4.4 : *(a) Une couche métallique percée d'un trou est déposée sur un substrat de verre. Un laser excite une molécule fluorescente placée dans le trou et la puissance rayonnée par celle-ci est alors mesurée. (b) Une structure plus compliquée peut être ajoutée afin que la lumière rayonnée par la source soit plus focalisée.*

très focalisé il est alors possible d'adjoindre au trou une structure plus compliquée comme montrée Fig. 4.4(b).

<u>Cadre de ce travail</u> : Ce projet financé par une ANR est initié par H. Rigneault de l'institut Fresnel. L'exploitation des effets de confinement et d'exaltation des ouvertures nanométriques mis à jour dans le projet Nanospot (ACI 2003) est combinée au savoir-faire de la jeune entreprise GENEWAVE (Palaiseau) sur l'exaltation de la fluorescence, dans le contexte des biopuces. Outre les aspects de nanophotonique liés à la conception et réalisation des ouvertures, nous prenons en compte les spécificités de l'hybridation sur puce pour la définition des ouvertures (nombre, taille, espacement).

4.5 Conclusion

A l'origine la fluorescence n'était pas un de mes principaux axes de recherche, mais une collaboration étroite avec A. Rahmani m'a initié à ce sujet. Maintenant, comme le montrent les § 4.4.1 et § 4.4.2 cette thématique à travers différentes collaborations tend à prendre de l'ampleur.

De plus les résultats obtenus § 4.4.1 permettent de faire un lien entre la fluorescence et le piégeage optique présenté chapitre 2. En effet les cavités H2 ou H1 présentant un fort facteur de qualité créent donc une forte exaltation locale du champ électrique, ce qui permettrait alors de piéger une ou des particules.

Conclusion générale et perspectives

- Oui ce sera la fin du spectacle, le cri de la spontanéité. Tu diras ce qui te passera par la tête.
- Mais il y a des fois où il n'y passe rien !
Uderzo et Goscinny, "Astérix et le chaudron"

Dans ce présent tapuscript j'ai donc présenté les travaux réalisés depuis l'obtention de mon doctorat. Comme souligné dans l'introduction, le dénominateur commun de mes travaux de recherche est la méthode des dipôles couplés que nous avons améliorée au fil du temps, soit en gagnant en précision (convergence plus rapide), soit en permettant d'étudier des géométries plus complexes. Dans tous les cas ces améliorations trouvent leurs applications dans les domaines que j'ai étudiés, fluorescence, forces optiques, et sondage électromagnétique. Les perspectives à long terme concernent mes deux principaux axes de recherche, *i.e.*, les forces optiques et le sondage électromagnétique.

• En ce qui concerne les forces optiques, plusieurs pistes s'ouvrent au vu des compétences et des moyens de développement acquis au cours de ces dernières années. Toutes les études que j'ai réalisées jusqu'à ce jour ont été faites dans le cas du régime harmonique. Plus précisément, dans la littérature à ma connaissance un seul article étudie la force s'exerçant sur un atome lorsque celui-ci est soumis à une impulsion lumineuse et ce en négligeant la pression de radiation.[70] Il serait dont intéressant de regarder la force optique exercée sur un objet (ou des objets pour voir la conséquence de la diffusion multiple) dans le cas d'une impulsion et ce sans approximation. Ceci permettrait notamment d'étudier la force d'Abraham et de décrire une expérience permettant de mettre celle-ci en évidence.[71,72] Pour un dipôle ce terme est directement relié à la dérivée par rapport au temps du vecteur de Poynting (qui, dans le cas du régime harmonique, a une moyenne temporelle nulle) : le cas extrêmement simple du dipôle en régime impulsionnel devra donc être étudié en premier de par son côté didactique et permettra de voir l'importance de ce nouveau terme par rapport aux termes plus connus que sont la pression de radiation et la force due au gradient du champ. Pour ce faire il convient de passer la méthode des dipôles couplés en régime temporel. Ceci paraît délicat à réaliser car la CDM est *a priori* purement

basée sur le régime harmonique (contrairement à des méthodes comme la FDTD, éléments finis qui discrétisent dès le départ le temps et l'espace), mais à l'aide de transformées de Fourier (ou de Laplace) il est possible de palier à cet inconvénient.

Une autre voie à étudier concerne le couple optique. En effet la force optique peut engendrer un couple optique pour peu que l'objet et/ou l'éclairement soient bien choisis. Les premières études réalisées ont consisté à analyser l'effet de la géométrie d'un objet sur le couple optique. Bien sûr il existe une infinité de possibilité sur la forme d'un objet, mais j'ai encore peu regardé l'influence du faisceau éclairant l'objet (faisceau gaussien, faisceau de Bessel,...). De plus l'effet d'une permittivité relative anisotrope, et/ou présentant des propriétés rotatoires pourrait renforcer le couple optique. Il serait donc intéressant de regarder l'influence de ces différents paramètres dans le but d'optimiser des micro-moteurs par exemple.

De plus le projet ANR sur la nano imagerie bioanalytique ouvre la voie à la notion de piège multiple. Cette voie de recherche est en train de prendre de l'importance au sein de la communauté mondiale, mais avec des objets piégés de plusieurs micromètres. Dans notre cas cela concernera plutôt des objets (particules d'or par exemple) de quelques dizaines de nanomètres piégés *via* un réseau de fibres optiques. Pour ce faire, il conviendra de simuler le piégeage optique d'une particule proche ou contre l'apex d'une pointe, avec et sans ouverture. La difficulté dans cette configuration consiste à amener la particule dans un piège optique de dimension sub longueur d'onde à un endroit bien précis, en effet le mouvement brownien pour de petites particules est très dérangeant. Une possibilité consiste à mettre beaucoup de particules et d'attendre qu'une particule daigne tomber dans le piège, mais cette méthode n'est pas très sélective. Une autre possibilité, sous étude actuellement, est d'abord de piéger la particule par un faisceau gaussien (piégeage parfaitement maîtrisé de nos jours), et d'utiliser ce piège optique intermédiaire pour amener la particule proche de l'extrémité de la pointe. Cette étude nous permettra alors de donner aux expérimentateurs les caractéristiques des faisceaux lasers à utiliser pour le premier piégeage (suivant la nature et la taille de la particule) et la procédure à suivre pour aboutir au piège final, sub-longueur d'onde, souhaité.

• Pour le sondage électromagnétique, il convient de développer aussi bien le côté expérimental que théorique, les deux étant intimement liés au sein de l'équipe SEMO.

Pour la partie expérimentale, à court terme plusieurs travaux s'offrent à nous. En premier lieu il convient d'affiner le montage expérimental proposé Fig. 3.8 : la manipulation est en cours d'automatisation afin de permettre l'enregistrement avec un nombre d'incident important, mais pour l'instant seul le montage en réflexion est utilisé dans le cas d'objets réfléchissants évidemment. Pour l'instant, comme dit § 3.5.2, nous avons uniquement utilisé des algorithmes basés sur l'approximation de Fraunhofer (de simples transformées de Fourier du champ diffracté permettant de relier la phase au profil de l'échantillon) pour retrouver le profil des échantillons, mais si les angles d'incidence deviennent grands (supérieurs à 25°) il convient d'envisager des algorithmes autres, basés par exemple, sur la résolution rigoureuse de la diffraction par une surface parfaitement conductrice (méthode surfacique). De telles surfaces peuvent bien sûr être observées par d'autres techniques (microscope électronique, scanning tunneling microscope, atomic force microscope), c'est pourquoi nous envisagerons très rapidement par exemple des objets en verre sur des surfaces métalliques. Dans ce cas retrouver la forme des objets en verre et quantifier leurs indices est un défi que seul notre processus expérimental, avec des algorithmes d'inversion évolués, peut relever.

A moyen terme il serait particulièrement intéressant de passer la manipulation dans le cas de l'éclairement en transmission pour étudier des objets transparents (enterrés ou non) afin de confronter les algorithmes d'inversion présentés Chap. 3 à la réalité. Cette première étape validée il sera alors possible de passer à la microscopie à très haute résolution. Pour ce faire il sera très important d'optimiser et de réaliser un réseau bi-périodique, comme décrit § 3.4.3. Ceci nécessitera une collaboration avec des laboratoires possédant un grand savoir-faire quant à la réalisation de tels objets, par exemple le groupe d'Optique des nanoStructures Semi-conductrices du Laboratoire de Photonique et de Nanostructures. A noter qu'en théorie il reste encore un travail important à faire, car nous n'avons pas encore étudié de façon sérieuse les effets sur la reconstruction des bruits de mesure et plus particulièrement de l'influence de défauts dans le réseau (plots manquants, déplacés, plus gros ou plus petits que prévu, ...) et de la méconnaissance de la phase à l'origine. Ce dernier point est le plus délicat et demandera sûrement une optimisation de la position du réseau en même temps que la minimisation de la fonction coût qui permet de trouver la carte de permittivité relative.

Notons que l'utilisation d'un réseau comme substrat nanostructuré pour parvenir à la très haute résolution en microscopie en champ lointain peut aussi s'appliquer en microscopie de fluorescence.

Une autre façon de mettre les algorithmes que nous avons développés à l'épreuve de l'expérience, est d'utiliser la chambre anéchoïque mise à disposition de l'équipe SEMO. Cette chambre anéchoïque permet, dans le domaine des micro-ondes, des mesures du champ diffracté, amplitude plus phase, pour des objets tridimensionnels. Il serait donc intéressant de retrouver expérimentalement les résultats présentés § 3.4.1 sur les objets en espace homogène. Pour l'instant nous en sommes au début de l'étude et nous avons commencé une comparaison entre le champ diffracté expérimental et théorique, puis réalisé nos premières inversions sur des objets simples (cubes, sphères). L'excellent accord obtenu entre les champs diffractés calculés théoriquement et ceux mesurés expérimentalement était encourageant (cet accord entre les champs expérimentaux et théoriques est essentiellement dû à un travail important des expérimentateurs qui ont diminué le bruit de mesure de manière drastique) et nous a permis de lancer des inversions pour deux sphères jointives et deux cubes identiques. Là encore, les résultats sont très bons et nous permettent d'envisager des inversions avec de multiples objets de forme non canonique.

Plus généralement, en ce qui concerne la partie théorique, le sondage électromagnétique tridimensionnel en est encore à ses balbutiements dans l'équipe SEMO (nous n'avons pour l'instant que regarder des méthodes d'inversion basées sur un simple gradient conjugué), par contre le cas bidimensionnel est parfaitement maîtrisé, avec une panoplie d'algorithmes très évolués (méthode du gradient modifié, méthode hybride, ...). En première étape, il serait donc souhaitable de passer à ces méthodes hautement performantes dans le cadre de la CDM de façon à gagner en précision et surtout en rapidité. En effet la méthode pour l'instant utilisée nécessite un grand nombre d'itérations pour aboutir à la convergence, ce qui demande alors un temps de calcul non négligeable (plusieurs heures) : il serait donc souhaitable de diminuer le temps de calcul. Par la suite le champ d'étude s'élargirait alors à des configurations plus complexes ; notamment utiliser des impulsions lumineuses plutôt qu'un régime harmonique. Le caractère multifréquence du régime temporel, donne avec les fréquences basses une bonne résistance au bruit, et avec les hautes fréquences une bonne résolution.[73] Pour ce faire il convient bien sûr de passer la CDM en régime temporel ce qui rejoint en partie l'étude sur les forces optiques dans le régime temporel. Par la suite, la méthode de la décomposition de l'opérateur de retournement temporel pourrait être

appliquée afin d'obtenir une meilleure reconstruction dans le cadre d'objets en présence de bruit de structure. A noter que dans ce cas là encore, la chambre anéchoïque permet de faire des mesures expérimentales dans le domaine des micro-ondes et donc une confrontation entre la théorie et l'expérience est envisageable.

Bien sûr les perspectives décrites ci-dessus ne constituent que la partie émergée de l'iceberg, *i.e.*, la partie ludique. En effet, il sera indispensable pour parvenir aux objectifs fixés de réaliser des innovations et du développement relatifs à la CDM et aux méthodes d'inversion.

Bibliographie

La bibliographie se fait après
et non avant d'aborder un sujet de recherche.
Jean Perrin

Bibliographie liée au chapitre 1 : Amélioration, et généralisation à des structures complexes, de la méthode des dipôles couplés

[1] F. M. Kahnert, J. Quant. Spect. Rad. Trans. **79-80**, 775 (2003).

[2] E. M. Purcell and C. R. Pennypacker, Astrophys. J. **186**, 705 (1973).

[3] A. Rahmani, P. C.Chaumet, F. de Fornel, and C. Girard, Phys. Rev A **56**, 3245 (1997).

[4] J. D. Jackson, *Classical Electrodynamics*, Wiley 2ème ed. 1975.

[5] B. T. Draine, Astrophys. J. **333**, 848 (1988).

[6] P. C. Chaumet, Appl. Opt. **43**, 1825 (2004).

[7] {**Annexe page 86**} P. C. Chaumet, A. Sentenac, and A. Rahmani, Phys. Rev. E **70**, 036606 (2004).

[8] {**Annexe page 92**} P. C. Chaumet, A. Rahmani, and G. W. Bryant, Phys. Rev. B **67**, 165404 (2003).

[9] E. Popov, M. Nevière, B. Gralak, et G. Tayeb, J. Opt. Soc. Am. A **19**, 33 (2002).

[10] {**Annexe page 97**} P. C. Chaumet, A. Sentenac, Phys. Rev. B **72**, 205437 (2005).

[11] B. T. Draine, et J. Goodman, Astrophys. J. **405**, 685 (1993).

[12] J. A. Stratton, *Electromagnetic theory*, McGraw-Hill, New-York, (1941).

[13] {**Annexe page 105**} A. Rahmani, P. C. Chaumet, and G. W. Bryant, Astrophysical J. **607**, 873 (2004).

[14] {**Annexe page 111**} A. Rahmani, P. C. Chaumet, et G. W. Bryant, Opt. Lett. **27**, 2118 (2002).

Bibliographie liée au chapitre 2 : Forces dues à la lumière : forces optiques

[15] A. Ashkin, Phys, Rev. Lett. **24** 156 (1970).

[16] A. Ashkin, Phys. Rev. Lett. **25** 1321 (1970).

[17] A. Ashkin, et J. M. Dziedzic, Science **235**, 1517 (1987).

[18] A. Ashkin, et J. M. Dziedzic, Proc. Natl. Acad. Sci. USA Cell Biology **86**, 7914 (1989).

[19] {**Annexe page 114**} P. C. Chaumet, et M. Nieto-Vesperinas, Opt. Lett. **25**, 1065-1067 (2000).

[20] P. C. Chaumet, A. Rahmani, A. Sentenac, et G. W. Bryant, Phys. Rev. E **72**, 046708 (2005).

[21] {**Annexe page 117**} P. C. Chaumet, et M. Nieto-Vesperinas, Phys. Rev. B **61**, 14119 (2000).

[22] {**Annexe page 126**} P. C. Chaumet, et M. Nieto-Vesperinas, Phys. Rev. B **62**, 11185 (2000)

[23] M. Burns, J.-M. Fournier, et J. Golovchenko, Phys. Rev. Lett. **63**, 1233 (1989).

[24] M. Burns, J.-M. Fournier, et J. A. Golovchenko, Science **249**, 749-754 (1990).

[25] {**Annexe page 133**} P. C. Chaumet, et M. Nieto-Vesperinas, Phys. Rev. B **64**, 035422-7 (2001).

[26] R. Holmlin, M. Schiavoni, C. Chen, S. Smith, M. Prentiss, and G. Whitesides, Angew. Chem. Int. Ed. **39**, 3503, (2000)

[27] L. Novotny, R. X. Bian, and X. Sunney Xie, Phys. Rev. Lett. **79** 645 (1997).

[28] G. A. Wurtz, N. M. Dimitrijevic, et G. Wiederrecht, Jpn. J. Appl. Phys. **41** L351 (2002).

[29] {**Annexe page 140**} P. C. Chaumet, A. Rahmani, et M. Nieto-Vesperinas, Phys. Rev. Lett. **88**, 123601 (2002).

[30] {**Annexe page 144**} P. C. Chaumet, A. Rahmani, et M. Nieto-Vesperinas, Phys. Rev. B **66**, 195405 (2002).

[31] {**Annexe page 155**} P. C. Chaumet, A. Rahmani, et M. Nieto-Vesperinas, Phys. Rev. B **71**, 045425 (2005).

[32] P.C. Chaumet, A. Rahmani, et M. Nieto-Vesperinas, App. Opt. **45**, 5185 (2006).

[33] A. Rahmani et P.C. Chaumet, Opt. Express **14**, 6353 (2006).

[34] V. Garcès-Chàvez, D. McGloin, H. Melville, W. Sibbet, et K. Dholakia, Nature, **419** 145 (2002).

[35] A. Chovin, P. Garrigue, I. Manek-Hönninger, N. Sojic Nano Letters **4**, 1965 (2004).

[36] P. Galajda et P. Ormos, Appl. Phys. Lett. **78**, 249 (2001).

[37] E. Higurashi, H. Ukita, H. Tanaka, and O. Ohguchi, Appl. Phys. Lett. **64**, 2209 (1994).

[38] R. C. Gauthier, Appl. Phys. Lett. **67**, 2269 (1995).

[39] A. I. Bishop, T. A. Nieminen, N. R. Heckenberg, and H. Rubinsztein-Dunlop, Phys. Rev. A **68**, 033802 (2003).

[40] B. T. Draine, and J. C. Weingartner, Astrophys. J. **470**, 551 (1996).

[41] P. C.chaumet et C. Billaudeau, J. Appl. Phys. **101**, 023106 (2007)

Bibliographie liée au chapitre 3 : Sondage électromagnétique

[42] F. de Fornel, *Evanescent Waves*, Springer series in Optical Sciences, vol. 73 (Springer Verlag, Berlin, 2001).

[43] A. Sentenac, C.-A. Guérin, P. C. Chaumet, F. Drsek, H. Giovannini, N. Bertaux et M. Holschneider, Opt. Express. **15**, 1340 (2007).

[44] Inverse problem, **21**, pages S1-S178, Eds. K. Belkebir, et M. Saillard (2005).

[45] {**Annexe page 162**} P. C. Chaumet, K. Belkebir, et A. Sentenac, Phys. Rev. B **69**, 245405 (2004).

[46] P. C. Chaumet, K. Belkebir, et R. Lencrerot, Opt. Exp. **14**, 3415 (2006).

[47] A. G. Tijhuis, K. Belkebir, A. C. S. Litman, et B. P. Hon, IEEE Trans. Geosci. Remote Sens. **39**, 1316 (2001).

[48] R. E. Kleinman et A. G. Tijhuis, J. Comput. Appl. Math. **42**, 17 (1992).

[49] K. Belkebir et A. G. Tijhius, Inverse Probl. **17**, 1671 (2001).

[50] {**Annexe page 169**} P. C. Chaumet, K. Belkebir, A. Sentenac, Opt. Lett. **29**, 2740 (2004).

[51] {**Annexe page 172**} K. Belkebir, P. C. Chaumet, A. Sentenac, J. Opt. Soc. Am. A. **22**, 1889 (2005).

[52] {**Annexe page 191**} A. Sentenac, P. C. Chaumet, et K. Belkebir, Phys. Rev. Lett. **97**, 243901 (2006).

[53] V. Lauer, J. Microsc. **205**, 165 (2002).

[54] J. T. Frohn, H. F. Knapp, et A. Stemmer, PNAS **97**, 7232 (2000).

Bibliographie liée au chapitre 4 : Etude de la fluorescence en espace confiné

[55] P. Selényi, Phys. Rev. **56**, 477 (1939).

[56] K. H. Drexhage, J. Lumin. **1,2**, 693 (1970).

[57] A. Beveratos, R. Brouri, T. Gacoin, A. Villing, J.-P. Poizat, et P. Grangier, Phys. Rev. Lett. **89**, 187901 (2002).

[58] J. Michaelis, C. Hettich, J. Mlynek et V. Sandoghdar, Nature **405**, 325 (2000).

[59] A. Rahmani, Ph.D. thesis, Université de Bourgogne, France (1998).

[60] D. Courjon, K. Sarayeddine, M. Spajer, Opt. Comm. **71**, 23 (1989).

[61] F. de Fornel, *Evanescent Waves*, Springer series in Optical Sciences, vol. 73 (Springer Verlag, Berlin, 2001).

[62] J.-J. Greffet, R. Carminati, Progress in surface science **56** 133 (1997).

[63] {**Annexe page 195**} A. Rahmani, P. C. Chaumet, et F. de Fornel, Phys. Rev A **63**, 023819-11 (2001).

[64] {**Annexe page 206**} A. Rahmani, P. C. Chaumet, et G. W. Bryant, Opt. Lett. **27**, 430 (2002).

[65] J.-M. Lourtioz, H. Benisty, V. Berger, J.-M. Gérard, D. Maystre et A. Tchelnokov, *Les cristaux photoniques, ou la lumière en cage*, par Ed. Hermès Science Publications (Collection technique et scientifique des télécommunications), 2003.

[66] F. Bordas, N. Louvion, S. Callard, P. C. Chaumet, et A. Rahmani, Phys. Rev. E. **73**, 056601 (2006).

[67] N. Louvion, D. Gérard, J. Mouette, F. de Fornel, C. Seassal, X. Letartre, A. Rahmani, et S. Callard, Phys. Rev. Lett. **94**, 113907 (2005).

[68] H. Rigneault, J. Capoulade, J. Dintinger, J. Wenger, N. Bonod, E. Popov, T. W. Ebbesen, et P.-F. Lenne, Phys. Rev. Lett. **95**, 117401 (2005).

[69] E. Popov, N. Bonod, M. Nevière, H. Rigneault, P.-F. Lenne, et P.C. Chaumet, Appl. opt. **44**, 2332 (2005).

Bibliographie liée à la conclusion et à l'annexe 2

[70] J. P. Gordon, Phys. Rev. A **8**, 14 (1975).

[71] S. Antoci and L. Mihich, Eur. Phys. J. D **3**, 205-210 (1998).

[72] S. Antoci and L. Mihich, arXiv :physics/9808002 (1998).

[73] A. Dubois, J.-M. Geffrin, K. Belkebir et M. Saillard, Appl. Phys. Lett. **88**, 164104,(2006).

[74] S. Grill, et E. H. K. Stelzer, J. Opt. Soc. Am. A **16**, 2658 (1999).

[75] M. Shahram, et P. Milanfar, IEEE Trans. Image Proc. **13**, 677 (2004).

[76] J.-M. Vigoureux, Annales de la Fondation Louis de Broglie, **28**, 525 (2003).

Cinquième partie

Annexes

Chapitre 1

Equivalence entre la CDM et la méthode des moments

Une chose ne peut jamais être identique qu'avec elle-même,
jamais avec une autre.
Ainsi deux choses peuvent-elles certes être équivalentes,
mais jamais identiques.
Ulrich Wickert

Sommaire

1.1 Les équations de Maxwell et *tutti quanti*

Dans ce chapitre nous allons montrer que la méthode des moments, moyennant quelques hypothèses, est équivalente à la CDM telle que l'ont introduite E. M. Purcell et C. R. Pennypacker en 1973.[2] Pour ce faire nous allons commencer par le commencement, *i.e.* les équations de Maxwell en espace homogène : [i]

$$\boldsymbol{\nabla} \times \boldsymbol{E} = -\frac{1}{c}\frac{\partial}{\partial t}(\boldsymbol{H} + 4\pi\boldsymbol{M}) \quad \text{(A 1.1a)}$$

$$\boldsymbol{\nabla}.(\boldsymbol{H} + 4\pi\boldsymbol{M}) = 0 \quad \text{(A 1.1b)}$$

$$\boldsymbol{\nabla} \times \boldsymbol{H} = \frac{1}{c}\frac{\partial}{\partial t}(\boldsymbol{D} + 4\pi\boldsymbol{P}) \quad \text{(A 1.1c)}$$

$$\boldsymbol{\nabla}.(\boldsymbol{D} + 4\pi\boldsymbol{P}) = 0, \quad \text{(A 1.1d)}$$

avec $\boldsymbol{P}$ la polarisation électrique et $\boldsymbol{M}$ l'aimantation magnétique. En combinant ces quatre équations nous pouvons écrire :

$$(\boldsymbol{\nabla}^2 + k_0^2)\boldsymbol{E} = -4\pi[k_0^2\boldsymbol{P} + \boldsymbol{\nabla}(\boldsymbol{\nabla}.\boldsymbol{P})] - 4\pi i k_0 \boldsymbol{\nabla} \times \boldsymbol{M} \quad \text{(A 1.2a)}$$

$$(\boldsymbol{\nabla}^2 + k_0^2)\boldsymbol{H} = -4\pi[k_0^2\boldsymbol{M} + \boldsymbol{\nabla}(\boldsymbol{\nabla}.\boldsymbol{M})] + 4\pi i k_0 \boldsymbol{\nabla} \times \boldsymbol{P}. \quad \text{(A 1.2b)}$$

[i] Il n'aura pas échappé au lecteur averti que je travaille en CGS, d'où les 4π qui traînent un peu partout !

Pour le cas qui nous intéresse dans l'immédiat le terme de source se résume à un unique dipôle électrique placé en $\boldsymbol{r}_0$, soit :

$$\boldsymbol{P}(\boldsymbol{r}) = \boldsymbol{p}\delta(\boldsymbol{r}-\boldsymbol{r}_0) \tag{A 1.3}$$

$$\boldsymbol{M}(\boldsymbol{r}) = 0. \tag{A 1.4}$$

Le milieu choisi étant non magnétique, seule la solution de l'Eq. (A 1.2a) nous intéresse, et celle-ci peut s'écrire, en tout point $\boldsymbol{r}$ différent de $\boldsymbol{r}_0$, sous la forme suivante :

$$\boldsymbol{E}(\boldsymbol{r}) = [k_0^2\boldsymbol{p} + \boldsymbol{\nabla}(\boldsymbol{\nabla}.\boldsymbol{p})]\frac{e^{ik_0|\boldsymbol{r}-\boldsymbol{r}_0|}}{|\boldsymbol{r}-\boldsymbol{r}_0|} = \boldsymbol{T}(\boldsymbol{r},\boldsymbol{r}_0)\boldsymbol{p}. \tag{A 1.5}$$

$\boldsymbol{T}(\boldsymbol{r},\boldsymbol{r}_0)$ est le tenseur de susceptibilité linéaire du champ [ii] et s'écrit :

$$\begin{aligned}\boldsymbol{T}(\boldsymbol{r},\boldsymbol{r}_0) = {} & e^{ik_0|\boldsymbol{r}-\boldsymbol{r}_0|} \\ & \times \left[(3\widehat{\boldsymbol{r}}.\widehat{\boldsymbol{r}} - \boldsymbol{I})\left(\frac{1}{|\boldsymbol{r}-\boldsymbol{r}_0|^3} - \frac{ik_0}{|\boldsymbol{r}-\boldsymbol{r}_0|^2}\right) + (\boldsymbol{I} - \widehat{\boldsymbol{r}}.\widehat{\boldsymbol{r}})\frac{k_0^2}{|\boldsymbol{r}-\boldsymbol{r}_0|}\right],\end{aligned} \tag{A 1.6}$$

avec $\widehat{\boldsymbol{r}} = (\boldsymbol{r}-\boldsymbol{r}_0).(\boldsymbol{r}-\boldsymbol{r}_0)^t/|\boldsymbol{r}-\boldsymbol{r}_0|^2$, t symbole de la transposition, $\boldsymbol{I}$ tenseur identité et k_0 le nombre d'onde dans l'espace homogène. La dépendance en $1/|\boldsymbol{r}-\boldsymbol{r}_0|$ correspond au rayonnement d'un dipôle électrique en champ lointain, tandis que le terme en $1/|\boldsymbol{r}-\boldsymbol{r}_0|^3$ correspond au champ électrique créé par un dipôle électrique dans le régime électrostatique.

1.2 La méthode des moments

Un objet (non magnétique) dans l'espace homogène, de permittivité relative ε_0, est soumis à une onde incidente $\boldsymbol{E}_0(\boldsymbol{r})$. Le champ en tout point $\boldsymbol{r}$ peut alors se calculer à partir de l'équation volumique intégrale suivante :

$$\boldsymbol{E}(\boldsymbol{r}) = \boldsymbol{E}_0(\boldsymbol{r}) + \int \boldsymbol{T}(\boldsymbol{r},\boldsymbol{r}')\boldsymbol{P}(\boldsymbol{r}')\mathrm{d}\boldsymbol{r}', \tag{A 1.7}$$

où $\boldsymbol{E}_0(\boldsymbol{r})$ est solution de l'Eq. (A 1.2a) homogène (cela correspond au champ électrique qu'il y aurait dans tout l'espace en l'absence de l'objet) et $\int \boldsymbol{T}(\boldsymbol{r},\boldsymbol{r}')\boldsymbol{P}(\boldsymbol{r}')\mathrm{d}\boldsymbol{r}'$ est une solution particulière de l'Eq. (A 1.2a) (l'intégration se fait *a priori* sur tout l'espace). En utilisant le lien entre le champ et la polarisation [$\boldsymbol{P}(\boldsymbol{r}') = \chi(\boldsymbol{r}')\boldsymbol{E}(\boldsymbol{r}') = \frac{\varepsilon(\boldsymbol{r}')-\varepsilon_0}{4\pi}\boldsymbol{E}(\boldsymbol{r}')$] nous obtenons la fameuse équation de Lippmann-Schwinger :

$$\boldsymbol{E}(\boldsymbol{r}) = \boldsymbol{E}_0(\boldsymbol{r}) + \int \boldsymbol{T}(\boldsymbol{r},\boldsymbol{r}')\frac{\varepsilon(\boldsymbol{r}')-\varepsilon_0}{4\pi}\boldsymbol{E}(\boldsymbol{r}')\mathrm{d}\boldsymbol{r}', \tag{A 1.8}$$

avec $\varepsilon(\boldsymbol{r}')$ la permittivité relative de l'objet. Cette équation est auto-cohérente car elle fait apparaître le champ recherché dans le membre de gauche et de droite à travers l'intégration. A noter que l'intégration ne s'effectue que sur le support de l'objet, la susceptibilité étant nulle en dehors de celui-ci. L'Eq. (A 1.8) peut être vue comme une généralisation du principe de Huygens-Fresnel, car le champ en tout point $\boldsymbol{r}$ est la somme des champs rayonnés par tous les dipôles constituant l'objet. C'est l'Eq. (A 1.8) qui constitue la base de la méthode des moments. La première étape consiste à connaître le champ macroscopique à l'intérieur de l'objet que nous noterons $\boldsymbol{E}_m$. Pour ce faire, l'objet est par exemple découpé

[ii] A noter que $\frac{e^{ik_0|\boldsymbol{r}-\boldsymbol{r}_0|}}{|\boldsymbol{r}-\boldsymbol{r}_0|}$ est la fonction de Green de l'espace homogène.

en N petits cubes de coté d ("petit" signifiant plus petit que la longueur d'onde dans l'objet étudié), ce qui permet d'écrire le champ au centre de la maille cubique i comme :

$$\boldsymbol{E}_m(\boldsymbol{r}_i) = \boldsymbol{E}_0(\boldsymbol{r}_i) + \sum_{j=1}^{N} \int_{V_j} \boldsymbol{T}(\boldsymbol{r}_i, \boldsymbol{r}') \frac{\varepsilon(\boldsymbol{r}') - \varepsilon_0}{4\pi} \boldsymbol{E}_m(\boldsymbol{r}') \mathrm{d}\boldsymbol{r}', \tag{A 1.9}$$

où $\boldsymbol{r}_i$ repère la position du centre du cube i et $\int_{V_j}$ signifie que l'intégration est effectuée sur le volume de la maille j. Si la discrétisation de l'objet est suffisamment fine alors la permittivité relative sur chacun des petits cubes peut être supposée comme uniforme ainsi que le champ électrique ce qui permet d'écrire :

$$\boldsymbol{E}_m(\boldsymbol{r}_i) = \boldsymbol{E}_0(\boldsymbol{r}_i) + \sum_{j=1}^{N} \left[\int_{V_j} \boldsymbol{T}(\boldsymbol{r}_i, \boldsymbol{r}') \mathrm{d}\boldsymbol{r}' \right] \frac{\varepsilon(\boldsymbol{r}_j) - \varepsilon_0}{4\pi} \boldsymbol{E}_m(\boldsymbol{r}_j). \tag{A 1.10}$$

En écrivant l'Eq. (A 1.10) pour $i = 1, \cdots, N$ nous obtenons un système d'équations linéaires à résoudre. Ceci constitue la méthode des moments. Ensuite pour accéder au champ diffusé par l'objet en une position $\boldsymbol{r}$ en dehors de l'objet, il suffit de reprendre l'Eq. (A 1.10) :

$$\boldsymbol{E}(\boldsymbol{r}) = \boldsymbol{E}_0(\boldsymbol{r}) + \sum_{j=1}^{N} \left[\int_{V_j} \boldsymbol{T}(\boldsymbol{r}, \boldsymbol{r}') \mathrm{d}\boldsymbol{r}' \right] \frac{\varepsilon(\boldsymbol{r}_j) - \varepsilon_0}{4\pi} \boldsymbol{E}_m(\boldsymbol{r}_j). \tag{A 1.11}$$

1.3 Comment retrouver la CDM à partir de la méthode des moments

Pour retrouver la CDM il convient de faire l'hypothèse que le tenseur de susceptibilité linéaire du champ est constant sur une maille j pour $i \neq j$. Pour simplifier, faisons aussi l'hypothèse que quand $i = j$, nous avons $\boldsymbol{T}(\boldsymbol{r}_i, \boldsymbol{r}') = -\frac{4\pi}{3\varepsilon_0} \boldsymbol{I} \delta(\boldsymbol{r}' - \boldsymbol{r}_i)$. [iii] Il faut bien noter que cette hypothèse n'est en rien obligatoire pour retrouver la CDM, mais cela facilitera les expressions dans le cadre de cette annexe. Les lecteurs qui désirent plus de précisions quant aux calculs rigoureux de l'intégration du tenseur sur la maille qui contient le terme source, peuvent se reporter à l'annexe 4 page 86. Nanti de ces hypothèses l'Eq. (A 1.10) se réduit à :

$$\begin{aligned} \boldsymbol{E}_m(\boldsymbol{r}_i) = \boldsymbol{E}_0(\boldsymbol{r}_i) \\ + \sum_{j=1, i \neq j}^{N} \boldsymbol{T}(\boldsymbol{r}_i, \boldsymbol{r}_j) \frac{\varepsilon(\boldsymbol{r}_j) - \varepsilon_0}{4\pi} d^3 \boldsymbol{E}_m(\boldsymbol{r}_j) - \frac{\varepsilon(\boldsymbol{r}_i) - \varepsilon_0}{3\varepsilon_0} \boldsymbol{E}_m(\boldsymbol{r}_i). \end{aligned} \tag{A 1.12}$$

[iii] L'expression du terme de contact dépend de la forme prise pour la discrétisation : la CDM utilise la plupart du temps une discrétisation cubique avec une collocation au centre. Pour plus de précision, voir la note de bas de page iv, page suivante.

En réunissant dans le membre de gauche le champ macroscopique estimé en $\boldsymbol{r}_i$ et en posant [iv] que $\boldsymbol{E}(\boldsymbol{r}_i) = \boldsymbol{E}_m(\boldsymbol{r}_i)\dfrac{\varepsilon(\boldsymbol{r}_i)+2\varepsilon_0}{3\varepsilon_0}$ l'expression finale est :

$$\boldsymbol{E}(\boldsymbol{r}_i) = \boldsymbol{E}_0(\boldsymbol{r}_i) + \sum_{j=1, i\neq j}^{N} \boldsymbol{T}(\boldsymbol{r}_i, \boldsymbol{r}_j)\frac{\varepsilon(\boldsymbol{r}_j)-\varepsilon_0}{\varepsilon(\boldsymbol{r}_j)+2\varepsilon_0}\frac{3d^3\varepsilon_0}{4\pi}\boldsymbol{E}(\boldsymbol{r}_j), \qquad \text{(A 1.13)}$$

où $\boldsymbol{E}(\boldsymbol{r}_i)$ est le champ local à la position $\boldsymbol{r}_i$ et correspond au champ rayonné en $\boldsymbol{r}_i$ par les $N-1$ autres dipôles, en l'absence de la maille i. Il est clair que cette expression est strictement équivalente à l'Eq. (1.1) de la page 26 où α était l'expression de la polarisabilité de Claussius-Mossotti.[v] L'Eq. (A 1.13) s'écrit pour $i = 1, \cdots, N$ et reste à résoudre un système d'équations linéaires. Notons que plus l'objet est grand, ou plus la permittivité relative de l'objet est grande, plus le nombre d'éléments nécessaires pour discrétiser l'objet deviendra important. Dans ce cas pour résoudre un grand système d'équations linéaires nous utilisons une méthode de résolution itérative. Une fois les champs $\boldsymbol{E}_m(\boldsymbol{r}_i)$ obtenus pour tout $i = 1, \cdots, N$, le champ diffusé par l'objet s'obtient de manière équivalente à l'Eq. (A 1.11) :

$$\boldsymbol{E}(\boldsymbol{r}) = \boldsymbol{E}_0(\boldsymbol{r}) + \sum_{j=1}^{N} \boldsymbol{T}(\boldsymbol{r}, \boldsymbol{r}_j)\frac{\varepsilon(\boldsymbol{r}_j)-\varepsilon_0}{\varepsilon(\boldsymbol{r}_j)+2\varepsilon_0}\frac{3d^3\varepsilon_0}{4\pi}\boldsymbol{E}(\boldsymbol{r}_j), \qquad \text{(A 1.14)}$$

L'expression $\frac{\varepsilon(\boldsymbol{r}_j)-\varepsilon_0}{\varepsilon(\boldsymbol{r}_j)+2\varepsilon_0}\frac{3d^3\varepsilon_0}{4\pi}\boldsymbol{E}(\boldsymbol{r}_j)$ correspond au dipôle induit à la maille j, et le champ diffusé par l'objet est donc la somme de tous les champs diffusés par les dipôles constituant l'objet.

[iv] La relation entre le champ local et le champ macroscopique peut se retrouver à partir d'un simple raisonnement en électrostatique : une sphère plongée dans un champ électrique uniforme $\boldsymbol{E}_0$ se polarise. Ces charges de polarisation créent un champ dépolarisant, $-\frac{\boldsymbol{P}}{3\varepsilon_0}$. Le champ électrique macroscopique à l'intérieur de la sphère, $\boldsymbol{E}_m$, est la somme du champ incident et du champ dépolarisant : $\boldsymbol{E}_m = \boldsymbol{E}_0 - \frac{\boldsymbol{P}}{3\varepsilon_0} = \boldsymbol{E}_0 - \frac{\varepsilon-\varepsilon_0}{3\varepsilon_0}\boldsymbol{E}_m$. La relation entre le champ appliqué et le champ macroscopique s'écrit alors : $\boldsymbol{E}_0 = \boldsymbol{E}_m\frac{\varepsilon+2\varepsilon_0}{3\varepsilon_0}$. A noter que le champ dépolarisant est uniforme dans la sphère, et que dans le cas d'un cube il a exactement la même valeur que celui de la sphère uniquement en son centre. C'est pourquoi avec le maillage cubique de notre objet et la collocation au centre de la maille, le facteur de dépolarisation reste le même que celui d'une sphère.

[v] Une intégration plus précise du tenseur faisant apparaître la réaction de rayonnement dans l'expression de la polarisabilité.[7]

Chapitre 2

Remarques sur la résolution

Il faut tenir à une résolution parce qu'elle est bonne,
et non parce qu'on l'a prise.
La Rochefoucauld

Sommaire

2.1 Diffraction par un trou circulaire : tache d'Airy

L'image d'un objet ponctuel, donnée par un instrument d'optique n'est pas ponctuelle. Le phénomène de diffraction, dû à la nature ondulatoire de la lumière, implique la formation d'un disque (disque d'Airy [i] ou tache de diffraction) entouré d'anneaux concentriques. En fait, l'intensité lumineuse d'une source ponctuelle sur un écran d'observation donné, satisfait la relation récurrente suivante :

$$I(\alpha) \propto \left(2\frac{J_1(\pi\alpha d/\lambda)}{\pi\alpha d/\lambda}\right)^2, \qquad \text{(A 2.1)}$$

avec J_1 la fonction de Bessel de première espèce, λ la longueur d'onde de la source, d le diamètre instrumental, et α l'angle entre la direction d'observation et la direction centrale, *i.e.* l'axe optique du système. Cette fonction présente un maximum à $\alpha = 0$ et pour des α grands oscille comme $(\sin x/x)^2$ avec $x = \pi\alpha d/\lambda$. La fonction J_1 présente donc des minima, et le premier minimum de J_1 est obtenu pour $x = 3.83$.

2.2 Critère de Rayleigh

La diffraction est le phénomène limitant le pouvoir de résolution de l'instrument. Il est évident que quand deux sources de même intensité, incohérentes, sont très proches l'une de l'autre, alors la mesure de l'intensité totale (qui dans ce cas est la somme de l'intensité de chacune des ondes, car celles-ci sont incohérentes) ne permet pas forcément de les séparer.

[i] Sir George Biddell Airy, astronome anglais (1801-1892).

Le critère de Rayleigh consiste à dire que les deux sources sont séparables si le minimum de la tache d'Airy d'une source correspond au maximum de la tache d'Airy de l'autre source, ce qui implique que $\alpha = 1.22\lambda/d$. Dans le cas d'une longueur d'onde dans le vert, en exprimant le diamètre instrumental en millimètres et α en secondes d'arc, nous obtenons $\alpha = 140/d$. Figure A 2.1 présente l'intensité totale (+), résultant de la superposition des intensités de chacune des sources en fonction de x.

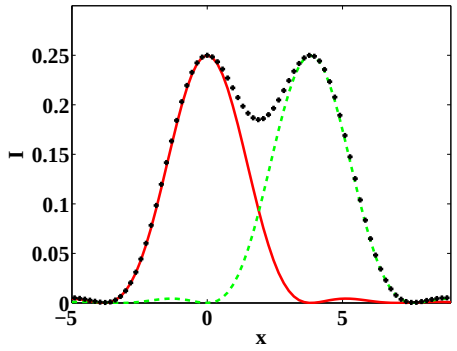

Fig. A 2.1 : *Intensité totale (+) en fonction de x pour deux sources de même intensité, incohérentes et ponctuelles.*

2.3 Critère de Dawes

Le critère de Dawes [ii] a quant à lui été déterminé par Dawes empiriquement, en observant des systèmes d'étoiles binaires ayant une magnitude de 6. Notons que ce critère est utilisé couramment en astronomie, photographie, mais plus rarement en microscopie. L'écart angulaire minimum pour séparer deux étoiles est $\alpha = 115/d$ avec les mêmes conventions qu'au § 2.2 (Fig. 2.2).

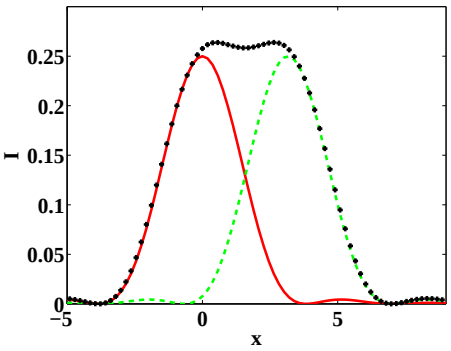

Fig. A 2.2 : *Même légende que Fig. A 2.1.*

Il est clair que le minimum entre les deux pics est plus faible avec ce critère qu'avec le critère de Rayleigh.

2.4 Critère de Sparrow

Sparrow a pour sa part défini son critère dans le domaine de l'astronomie, mais il est quelquefois utilisé en microscopie. D'après Sparrow il est encore possible de séparer deux objets pour peu que l'intensité totale, résultant de la superposition des deux intensités, présente un plat sur le sommet, ou pour être plus précis que la dérivée seconde de l'intensité totale s'annule (Fig. A 2.3). Dans ce cas l'écart angulaire minimum pour séparer deux étoiles est $\alpha = 108/d$. Le critère de Sparrow, des trois critères utilisés en astronomie, est le moins exigeant.

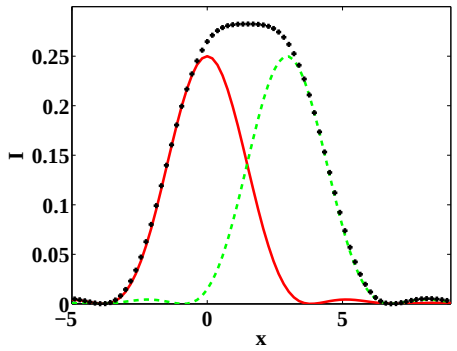

Fig. A 2.3 : *Même légende que Fig. A 2.1.*

[ii] William Rutter Dawes, astronome britannique (1799-1868).

2.5 Critère d'Abbe

Une autre manière de définir la résolution a été établie par Abbe en 1873. [iii] Celui-ci établit son raisonnement en assimilant l'objet à un fin réseau de période d éclairé par une source monochromatique de longueur d'onde λ. Pour caractériser le réseau il faut qu'au moins l'ordre 1 ou -1 soit propagatif, et ceci s'obtient si $d \geq \lambda/2$. Abbe en déduisit que deux objets séparés de moins de $\lambda/2$, ne pouvaient être distingués, ce qui rejoint le critère de Rayleigh, cf § 3.1.2.

2.6 Conclusion

Dans cette annexe nous avons présenté quelques critères de résolution, mais la liste n'est pas exhaustive (critère de Houston où la résolution est définie par rapport à la largeur à mi-hauteur du pic central [$\alpha = 117/d$], critère de Schuster qui stipule que deux points objets sont séparés s'il n'y a aucun recouvrement des lobes centraux de leurs taches de diffraction [$\alpha = 280/d$], ...). A noter, au vu de tous les critères que nous avons rappelés, que la définition de la résolution peut sembler un peu arbitraire. Pour avoir une définition plus physique, le principe d'incertitude de Heisenberg [iv] est une possibilité et il permet alors d'établir, hors approximation paraxiale, la résolution latérale et longitudinale.[74]

Mais toutes les définitions des critères présentés en cette annexe se font toujours en l'absence de bruit de mesure. Dans ce cas nous connaissons exactement le champ électromagnétique (module + phase) diffracté par l'objet sur une surface donnée, et l'objet peut être alors entièrement caractérisé, ce qui implique une résolution infinie. Ceci n'est bien sûr pas possible, car toute mesure est nécessairement entachée de bruit, et il est évident que la résolution va dépendre très fortement de celui-ci. Dans ce cas une analyse statistique de la résolution du système doit être envisagée, *via* par exemple la borne de Cramer-Rao.[75] C'est l'approche que nous avons étudiée récemment, ce que nous a permis en plus d'appréhender l'influence de la diffusion multiple sur la résolution.[43]

A noter que si pour de nombreux physiciens cette barrière de $\lambda/2$ paraissait infranchissable, Abbe quant à lui n'a jamais considéré que son critère était une limite infranchissable, et écrivait ainsi en 1876 : "*Il se peut que dans l'avenir, l'esprit humain découvre des processus et des forces permettant de franchir ce mur qui nous paraît actuellement infranchissable. Je pense personnellement que cela se fera. Mais en même temps, je crois que quel qu'il soit, l'outil qui nous permettra d'étudier l'infiniment petit de manière plus efficace que notre microscope actuel, n'aura en commun avec lui que le nom.*"[76]

[iii] Ernst Abbe, physicien opticien allemand (1840-1905).
[iv] Werner Karl Heisenberg, Physicien allemand (1901-1976).

Minimisation de la fonction coût par la méthode des gradients conjugués

Il n'y a que le premier pas qui coûte.
Marie du Deffand

Sommaire

3.1 Formulation du problème

Comme décrit au chapitre 3, § 3.2 et § 3.4, dans la configuration que nous étudions, le problème inverse se résume à trouver la distribution de permittivité relative (dans un domaine d'investigation donné) qui minimise la fonction coût suivante :[i]

$$\mathcal{F} = \frac{\sum_{l=1}^{L} ||\boldsymbol{f}_l^e - \boldsymbol{f}_l||^2}{\sum_{l=1}^{L} ||\boldsymbol{f}_l^e||^2} = W \sum_{l=1}^{L} ||\boldsymbol{f}_l^e - \boldsymbol{f}_l||^2. \qquad \text{(A 3.1)}$$

$||.||$ est une norme L^2 effectuée sur les M points d'observation. $\boldsymbol{f}_l^e$ est le champ mesuré expérimentalement pour l'incidence l à tous les points d'observation, et $\boldsymbol{f}_l$ le champ diffracté calculé pour une distribution de permittivité relative donnée dans le domaine d'investigation pour une incidence l. $\boldsymbol{f}_l$ se calcule à partir des deux relations suivantes :

$$\boldsymbol{f}_l = \boldsymbol{B}\alpha\boldsymbol{E}_l \qquad \text{(A 3.2)}$$

$$\boldsymbol{E}_l = \boldsymbol{E}_{0,l} + \boldsymbol{A}\alpha\boldsymbol{E}_l. \qquad \text{(A 3.3)}$$

L'Eq. (A 3.3) permet de connaître le champ dans le domaine d'investigation pour une distribution donnée de permittivité relative (α étant relié à la permittivité relative par la

[i] Nous avons ajouté à l'Eq. (A 3.1) un facteur de normalisation par rapport à l'Eq. (3.5) du chapitre 3, mais cela ne change rien au problème posé.

relation de Claussius-Mossotti) et l'Eq. (A 3.2) d'en calculer le champ diffracté. $\boldsymbol{A}$ et $\boldsymbol{B}$ sont des matrices définies au chapitre 3 § 3.2.

3.2 La méthode des gradients conjugués

Nous désirons donc minimiser la fonction coût $\mathcal{F}$ par rapport au paramètre d'intérêt qu'est la polarisabilité. Pour ce faire le domaine d'investigation est discrétisé en N petits cubes, puis nous allons construire une suite satisfaisant la relation suivante :

$$\alpha_n = \alpha_{n-1} + a_n d_n, \tag{A 3.4}$$

où la polarisabilité à l'étape n est déduite de la polarisabilité à l'étape $n-1$ plus une correction. Cette correction est constituée de deux termes : un scalaire a_n et une direction de descente d_n. A noter que cette suite est définie pour tout point de discrétisation du domaine d'investigation (α_n et d_n sont donc de dimension N), mais que le paramètre a_n est global.

Définissons l'erreur résiduelle $\boldsymbol{h}_{l,n}$ comme l'écart entre le champ diffracté expérimentalement et le champ diffracté par la distribution de polarisabilité obtenue à l'étape n et ce pour l'incidence l :

$$\boldsymbol{h}_{l,n} = \boldsymbol{f}_l^e - \boldsymbol{B}\alpha_n \boldsymbol{E}_{l,n}, \tag{A 3.5}$$

la fonction coût s'écrivant alors à l'étape n comme :

$$\mathcal{F}_n = W \sum_{l=1}^{L} ||\boldsymbol{h}_{l,n}||^2. \tag{A 3.6}$$

En utilisant l'expression donnée par l'Eq. (A 3.4) et la définition de la fonction coût Eq. (A 3.6), celle-ci peut se réécrire comme une fonction de a_n :

$$\mathcal{F}_n(a_n) = W \sum_{l=1}^{L} \left(||\boldsymbol{h}_{l,n-1}||^2 + |a_n|^2 ||\boldsymbol{B} d_n \boldsymbol{E}_{l,n-1}||^2 - 2a_n \mathrm{Re}\left\langle \boldsymbol{h}_{l,n-1} | \boldsymbol{B} d_b \boldsymbol{E}_{l,n-1} \right\rangle \right), \tag{A 3.7}$$

où $\langle . \rangle$ défini un produit scalaire sur le domaine des points d'observation. Le paramètre a_n est choisi de telle façon qu'il minimise la fonction coût, *i.e.* l'Eq. (A 3.7). La fonction coût étant dans ce cas un polynôme de degré deux en a_n, le minimum est unique et s'obtient pour :

$$a_n = \frac{\sum_{l=1}^{L} \langle \boldsymbol{B} d_b \boldsymbol{E}_{l,n-1} | \boldsymbol{h}_{l,n-1} \rangle}{\sum_{l=1}^{L} ||\boldsymbol{B} d_n \boldsymbol{E}_{l,n-1}||^2}. \tag{A 3.8}$$

Pour la direction de descente il existe plusieurs possibilités, la plus simple étant le gradient de la fonction coût par rapport au paramètre d'intérêt (le gradient correspondant à la direction pour laquelle la dérivée directionnelle est maximale), mais ce choix peut parfois se révéler inefficace (par exemple quand les iso-paramètres forment des vallées étroites). Pour remédier à ce problème nous avons choisi la méthode de gradient conjugué de type Polak et Ribière qui combine le gradient considéré et la direction de descente précédente :

$$d_n = g_n + \gamma_n d_{n-1}. \tag{A 3.9}$$

g_n, comme dit précédemment, est le gradient de la fonction coût par rapport à la polarisabilité, en supposant que le champ interne du domaine d'investigation ne change pas. Nous allons donc commencer par calculer la dérivée de $\mathcal{F}$ par rapport à la polarisabilité dans la direction u :

$$\nabla_\alpha \mathcal{F} = \lim_{t\to 0} \frac{\mathcal{F}(\alpha + tu) - \mathcal{F}(\alpha)}{t} \tag{A 3.10}$$

$$= \lim_{t\to 0} \frac{W}{t} \sum_{l=1}^{L} \left[\langle \boldsymbol{h}_l | \boldsymbol{h}_l \rangle - \langle \boldsymbol{h}_l - \boldsymbol{B}tu\boldsymbol{E} | \boldsymbol{h}_l - \boldsymbol{B}tu\boldsymbol{E} \rangle\right] \tag{A 3.11}$$

$$= \lim_{t\to 0} \sum_{l=1}^{L} \frac{W}{t} \left[t \langle \boldsymbol{h}_l | \boldsymbol{B}u\boldsymbol{E} \rangle + t \langle \boldsymbol{B}u\boldsymbol{E} | \boldsymbol{h}_l \rangle + O(t^2)\right] \tag{A 3.12}$$

$$= 2W \sum_{l=1}^{L} \mathrm{Re}[\langle \boldsymbol{h}_l | \boldsymbol{B}u\boldsymbol{E} \rangle] \tag{A 3.13}$$

$$= 2W \sum_{l=1}^{L} \mathrm{Re}\left[\left\langle \boldsymbol{E}^* \boldsymbol{B}^\dagger \boldsymbol{h}_l | u \right\rangle\right]. \tag{A 3.14}$$

Nous cherchons alors la valeur de u qui maximise la dérivée de la fonction coût, ce qui à l'étape n nous donne comme gradient g_n :

$$g_n = -W \sum_{l=1}^{L} \boldsymbol{E}^*_{l,n-1} \boldsymbol{B}^\dagger \boldsymbol{h}_{l,n-1}. \tag{A 3.15}$$

$\boldsymbol{B}^\dagger$ est l'adjoint de $\boldsymbol{B}$ soit dans notre cas la matrice transposée conjuguée de $\boldsymbol{B}$. Le coefficient scalaire γ_n est quant à lui défini par la relation suivante :

$$\gamma_n = \frac{\langle g_n | g_n - g_{n-1} \rangle}{||g_{n-1}||^2}. \tag{A 3.16}$$

Pour compléter la procédure d'inversion donnée dans le chapitre de cette annexe, il convient encore de définir l'étape $n = 0$. La polarisabilité initiale, α_0, est donnée par une rétropropagation, [ii] avec $\gamma_0 = 0$ ce qui donne une direction de descente égale au gradient comme point de départ.

[ii] Pour plus de détails sur cette procédure le lecteur intéressé peut se reporter à l'annexe 4 page 181.

Chapitre 4

Publications incluses dans le tapuscript

Publish or perish

Vox populi !

Sommaire

PHYSICAL REVIEW E **70**, 036606 (2004)

Coupled dipole method for scatterers with large permittivity

Patrick C. Chaumet
Institut Fresnel (UMR 6133), Universitié d'Aix-Marseille III, Av. Escadrille Normandie-Niemen, F-13397 Marseille Cedex 20, France

Anne Sentenac
Institut Fresnel (UMR 6133), Université d'Aix-Marseille III, Av. Escadrille Normandie-Niemen, F-13397 Marseille Cedex 20, France

Adel Rahmani
Laboratoire d'Electronique, Optoélectronique et Microsystèmes, UMR CNRS 5512, Ecole Centrale de Lyon 36, avenue Guy de Collongue, F-69134 Ecully Cedex, France
(Received 31 March 2004; published 17 September 2004)

In the coupled dipole method, a three-dimensional scattering object is discretized over a lattice into a set of polarizable units that are coupled self-consistently. Starting from the volume integral equation for the field, we show that performing the integration of the free-space field susceptibility tensor over the lattice cell dramatically improves the accuracy of the method when the permittivity of the object is large. This integration, done without any approximation, allows us to define a prescription for the polarizability used in the coupled dipole method. Our derivation is not restricted to any particular shape of the scatterer or to a cubic discretization lattice.

DOI: 10.1103/PhysRevE.70.036606 PACS number(s): 42.25.Fx, 42.25.Bs, 41.20.−q

I. INTRODUCTION

The scattering of an electromagnetic wave by an arbitrary, three-dimensional scatterer is a complex problem of central importance in optics and photonics. Aside from a few particular systems, the interaction of electromagnetic waves with an arbitrary object eludes an analytical representation and numerical methods are needed. Many such methods have been developed and we refer the reader to the detailed review by Kahnert [1] where the strengths and weaknesses of each method are discussed.

In this article we consider one such three-dimensional scattering approach called the coupled dipole method (CDM). This method was introduced by Purcell and Pennypacker [2] to study the scattering of light by interstellar grains with arbitrary shapes. It has been used to compute cross sections [3], optical forces [4–6], near-field light scattering [7], and spontaneous emission [8]. The theoretical foundation of the CDM relies on the fact that when an object interacts with an electromagnetic field it develops a polarization. If one considers a small enough volume inside the object, the induced polarization is uniform within this volume, and hence that small region can be represented by an electric dipole with the appropriate polarizability. Therefore, any object can be discretized as a collection of dipolar subunits. In this article we show that accounting for finite size effects for the subunits significantly improves the description of light scattering by arbitrary objects. Our formulation of the CDM is obtained through the integration of the field susceptibility tensor over the volume associated with the dipole, hence defining a different form for the polarizability. The formulation of the CDM derived here improves the accuracy of the method when dealing with scatterers with large permittivities, a situation where the conventional CDM performs poorly.

In Sec. II we describe our formulation of the CDM. In Sec. III we test the accuracy of this formulation of the polarizability and compare it to previous prescriptions. Finally, in Sec. IV we present our conclusions. The details of the computation of the integrated field susceptibility tensor are given in the Appendix.

II. THEORY

Let $\mathbf{E}^0(\omega)$ be the electric field associated with an electromagnetic wave impinging on an arbitrary object (for the sake of simplicity we will assume that the object is nonmagnetic). The incident field induces a polarization inside the object. The self-consistent electric field inside the object reads

$$\mathbf{E}(\mathbf{r},\omega) = \mathbf{E}^0(\mathbf{r},\omega) + \int_V \overleftrightarrow{\mathbf{G}}(\mathbf{r},\mathbf{r}',\omega)\chi(\mathbf{r}',\omega)\mathbf{E}(\mathbf{r}',\omega)d\mathbf{r}', \qquad (1)$$

where the integration is performed over the volume of the object. $\mathbf{E}(\mathbf{r}',\omega)$ is the macroscopic field inside the object, $\chi(\mathbf{r}',\omega)$ is the linear susceptibility of the object which we will suppose to be homogeneous, i.e.,

$$\chi(\mathbf{r}',\omega) = \chi(\omega) = \frac{\varepsilon(\omega)-1}{4\pi}, \qquad (2)$$

where $\varepsilon(\omega)$ is the relative permittivity of the object, and $\overleftrightarrow{\mathbf{G}}(\mathbf{r},\mathbf{r}',\omega)$ is the free-space electric field susceptibility tensor, which can be written as [9]

$$\overleftrightarrow{\mathbf{G}}(\mathbf{r},\mathbf{r}',\omega) = e^{(ik_0R)}\left[\left(3\frac{\mathbf{R}\otimes\mathbf{R}}{R^2}-\overleftrightarrow{\mathbf{I}}\right)\left(\frac{1}{R^3}-\frac{ik_0}{R^2}\right) + \left(\overleftrightarrow{\mathbf{I}}-\frac{\mathbf{R}\otimes\mathbf{R}}{R^2}\right)\frac{k_0^2}{R}\right] - \frac{4\pi}{3}\overleftrightarrow{\mathbf{I}}\delta(\mathbf{R}), \qquad (3)$$

with $\mathbf{R}=\mathbf{r}-\mathbf{r}'$, k_0 the modulus of the wave vector in vacuum, and $\overleftrightarrow{\mathbf{I}}$ the unit tensor. To solve Eq. (1) numerically we dis-

cretize the object into a set of N subunits arranged on a cubic lattice (for simplicity, but our approach holds for any arbitrary orthogonal lattice); hence Eq. (1) becomes

$$\mathbf{E}(\mathbf{r},\omega) = \mathbf{E}^0(\mathbf{r},\omega) + \sum_{j=1}^{N} \int_{V_j} \overleftrightarrow{\mathbf{G}}(\mathbf{r},\mathbf{r}',\omega)\chi(\omega)\mathbf{E}(\mathbf{r}',\omega)d\mathbf{r}'. \quad (4)$$

To solve Eq. (1) numerically we need to make some approximations. The first one is usually to assume that the electromagnetic field is uniform over one subunit, which is a good approximation if the subunit is smaller than the wavelength inside the object. Then Eq. (4) can be written as

$$\mathbf{E}(\mathbf{r}_i,\omega) = \mathbf{E}^0(\mathbf{r}_i,\omega) + \sum_{j=1}^{N} \left(\int_{V_j} \overleftrightarrow{\mathbf{G}}(\mathbf{r}_i,\mathbf{r}',\omega)d\mathbf{r}' \right) \chi(\omega)\mathbf{E}(\mathbf{r}_j,\omega). \quad (5)$$

Equation (5) is the starting point of our method. In the original form of the CDM, another approximation is made: the field susceptibility tensor is taken to be constant over any subunit. This entails that

$$\mathbf{E}(\mathbf{r}_i,\omega) = \mathbf{E}^0(\mathbf{r}_i,\omega) + \sum_{j=1,j\neq i}^{N} \overleftrightarrow{\mathbf{G}}(\mathbf{r}_i,\mathbf{r}_j,\omega)\chi(\omega)\mathbf{E}(\mathbf{r}_j,\omega) - \frac{\varepsilon(\omega)-1}{3}\mathbf{E}(\mathbf{r}_i,\omega). \quad (6)$$

If we factorize the terms corresponding to the index i, we get

$$\mathbf{E}^l(\mathbf{r}_i,\omega) = \mathbf{E}^0(\mathbf{r}_i,\omega) + \sum_{j=1,j\neq i}^{N} \overleftrightarrow{\mathbf{G}}(\mathbf{r}_i,\mathbf{r}_j,\omega)\alpha_j^0(\omega)\mathbf{E}^l(\mathbf{r}_j,\omega) \quad (7)$$

with

$$\alpha_j^0(\omega) = \frac{3}{4\pi}\frac{\varepsilon(\omega)-1}{\varepsilon(\omega)+2}V_j. \quad (8)$$

Equation (8) is the Clausius-Mossotti relation for the polarizability of the cubic subunit j and $\mathbf{E}^l=[(\varepsilon+2)/3]\mathbf{E}$ is the local field expressed in terms of the macroscopic field. Equation (7) is the original form of the CDM introduced by Purcell and Pennypacker [2]. The problem with this formulation is that if one computes the cross section using Eq. (8) one gets an incorrect result. This is due to the fact that the optical theorem is not satisfied. A radiation reaction term must be introduced in the expression of the polarizability to satisfy the optical theorem [3,10]:

$$\alpha_j(\omega) = \alpha_j^0(\omega)/[1-(2/3)ik_0\alpha_j^0(\omega)]. \quad (9)$$

The importance of including the radiation reaction term in the polarizability is also discussed in detail in Refs. [5,11] Several ideas have been put forward to improve the accuracy of the CDM [12–15]. These approaches have in common that they all start from the Clausius-Mossotti relation and simply add a finite-frequency correction. They also suppose that the field susceptibility tensor is constant over any given subunit. Recently, it was pointed out that the Clausius-Mossotti relation may not hold for every subunit; rather, for each subunit the polarizability should be related to its local environment [16,17]. However, so far this approach has been restricted to special geometries.

In this paper we propose a formulation of the scattering process that accounts for the geometry of the scatterer without being restricted to a particular set of shapes. Going back to Eq. (5), instead of the usual approach described previously, we compute the volume integration of the free-space susceptibility numerically. Equation (5) thus becomes

$$\mathbf{E}(\mathbf{r}_i,\omega) = \mathbf{E}^0(\mathbf{r}_i,\omega) + \sum_{j=1,j\neq i}^{N} \left(\int_{V_j} \overleftrightarrow{\mathbf{G}}(\mathbf{r}_i,\mathbf{r}',\omega)d\mathbf{r}' \right) \chi(\omega)\mathbf{E}(\mathbf{r}_j,\omega) + \left(\int_{V_i} \overleftrightarrow{\mathbf{G}}(\mathbf{r}_i,\mathbf{r}',\omega)d\mathbf{r}' \right) \chi(\omega)\mathbf{E}(\mathbf{r}_i,\omega). \quad (10)$$

The integrated tensor is defined as $\overleftrightarrow{\mathbf{G}}^{\text{int}}(\mathbf{r}_i,\mathbf{r}_j,\omega) = \int_{V_j} \overleftrightarrow{\mathbf{G}}(\mathbf{r}_i,\mathbf{r}',\omega)d\mathbf{r}'$. We have isolated the diagonal term ($i=j$) as, whereas the case $i\neq j$ is easy to perform numerically, the diagonal term needs particular attention. To compute the last term of Eq. (10), $\overleftrightarrow{\mathbf{G}}^{\text{int}}(\mathbf{r}_i,\mathbf{r}_i,\omega)$, a Weyl expansion of the tensor is performed. After a tedious derivation we can write this term as

$$\overleftrightarrow{\mathbf{G}}^{\text{int}}(\mathbf{r}_i,\mathbf{r}_i,\omega) = \frac{16}{\pi}\overleftrightarrow{\mathbf{I}}\left\{ \int_{w_0=0}^{k_0} \frac{-k_0^2(1-e^{iw_0\Delta/2}) - w_0^2 e^{iw_0\Delta/2}}{w_0} \left[\int_{\theta=0}^{\pi/2} \frac{\sin(k_p\cos\theta\Delta/2)\sin(k_p\sin\theta\Delta/2)}{k_p^2\cos\theta\sin\theta} d\theta \right] dw_0 + \int_{\beta=0}^{\infty} \frac{k_0^2-(k_0^2+\beta^2)e^{-\beta\Delta/2}}{\beta} \left[\int_{\theta=0}^{\pi/2} \frac{\sin(k_e\cos\theta\Delta/2)\sin(k_e\sin\theta\Delta/2)}{k_e^2\cos\theta\sin\theta} d\theta \right] d\beta \right\}, \quad (11)$$

with $k_p=\sqrt{k_0^2-w_0^2}$, $k_e=\sqrt{k_0^2+\beta^2}$, and Δ the lattice spacing. Equation (11) does not contain any approximations. To our knowledge this is the first time that $\overleftrightarrow{\mathbf{G}}^{\text{int}}(\mathbf{r}_i,\mathbf{r}_i,\omega)$ has been expressed in an exact form which can be computed numerically in an efficient way. Further details on the derivation of Eq. (11) are given in the Appendix.

When Δ tends toward 0, we find that $\lim_{\Delta\to 0}\overleftrightarrow{\mathbf{G}}^{\text{int}}(\mathbf{r}_i,\mathbf{r}_i,\omega) = -(4\pi/3)\overleftrightarrow{\mathbf{I}}$ which is the depolarization

factor computed at the center of a cube as given by Yaghjian [18]. After some work, Eq. (10) can be written in the form introduced by Purcell and Pennypacker [2]:

$$\mathbf{E}^l(\mathbf{r}_i,\omega)=\mathbf{E}^0(\mathbf{r}_i,\omega)+\sum_{j=1,j\neq i}^{N}\frac{\overleftrightarrow{\mathbf{G}}^{\mathrm{int}}(\mathbf{r}_i,\mathbf{r}_j,\omega)}{V_j}\alpha_j(\omega)\mathbf{E}^l(\mathbf{r}_j,\omega), \quad (12)$$

where the local field is defined by

$$\mathbf{E}^l(\mathbf{r}_i,\omega)=\left(\overleftrightarrow{\mathbf{I}}-\overleftrightarrow{\mathbf{G}}^{\mathrm{int}}(\mathbf{r}_i,\mathbf{r}_i,\omega)\frac{\varepsilon(\omega)-1}{4\pi}\right)\mathbf{E}(\mathbf{r}_i,\omega). \quad (13)$$

Notice that when $\overleftrightarrow{\mathbf{G}}^{\mathrm{int}}(\mathbf{r}_i,\mathbf{r}_i,\omega)$ reduces to $(-4\pi/3)\overleftrightarrow{\mathbf{I}}$ we recover the definition of the local field that we derived previously. The polarizability of the subunit j is now expressed as

$$\alpha_j(\omega)=\alpha_j^0(\omega)\left(1-\frac{G^{\mathrm{int}}(\mathbf{r}_j,\mathbf{r}_j,\omega)+4\pi/3}{V_j}\alpha_j^0(\omega)\right)^{-1}. \quad (14)$$

In the present study the subunit has a cubic shape and the medium is isotropic; hence the polarizability is a scalar. In Eq. (12), the quantity $\alpha_j(\omega)\mathbf{E}^l(\mathbf{r}_j,\omega)=\mathbf{p}(\mathbf{r}_j,\omega)$ is the dipole moment of subunit j induced by the incident field and the field scattered by all other subunits. Working with the local field is very convenient if one wants to evaluate the optical forces [5,6]. Yet there exist other approaches, such as the method of moments (MOM), that use the macroscopic field instead. In most three-dimensional implementations, the MOM simply amounts to solving Eq. (6), which is formally equivalent to the CDM [12,19] Eq. (7). However, only in the special case of two-dimensional objects in a stratified medium, has the integration of the field susceptibility tensor over the subunits been proposed [20].

If we perform a Taylor expansion of the imaginary part of $G^{\mathrm{int}}(\mathbf{r}_i,\mathbf{r}_i,\omega)$ with respect to $k_0\Delta$, we obtain $\mathrm{Im}[G^{\mathrm{int}}(\mathbf{r}_i,\mathbf{r}_i,\omega)/V_i]\approx(2/3)k_0^3$. Hence the radiation reaction term that is usually added to the Clausius-Mossotti polarizability appears naturally in our formulation. This radiation reaction term represents the damping of the dipole by its self-field. As the dipole oscillates, it generates an electric field $\mathbf{E}_{RR}$ at its location. The part of the electric field that is in quadrature with the dipole oscillations performs work on the dipole which dampens its oscillations. For a point dipole we have $\mathbf{E}_{RR}=i(2/3)k_0^3\mathbf{p}$ [9]. In our case, due to the finite size of the subunit, the radiation reaction field is directly connected to the integration of the imaginary part of the free-space field susceptibility: $\mathbf{E}_{RR}=i\mathrm{Im}[\overleftrightarrow{\mathbf{G}}^{\mathrm{int}}(\mathbf{r}_i,\mathbf{r}_i,\omega)/V_i]\mathbf{p}$.

We have performed the quadrature over a cubic subunit, but the quadrature can be done over a parallelepiped (see the Appendix). In that case $\overleftrightarrow{\mathbf{G}}^{\mathrm{int}}(\mathbf{r}_i,\mathbf{r}_i,\omega)$ would always be a diagonal tensor but the elements of the diagonal can be different [see Eq. (A8) of the Appendix]. Such a lattice geometry would, for instance, be useful to study the scattering of light by an object with significantly different extensions in the three directions of space.

III. RESULTS

To test the accuracy resulting from the integration of the tensor we study the scattering of light by a homogeneous sphere, as an analytic solution is known in the form of a Mie series, but we emphasize that the method presented here does not depend on the shape of the scatterer. We will compare our results to the extinction, absorption, and scattering efficiencies computed after using the Mie solution. The computation of the cross sections with the CDM is performed using Eq. (3.01) of Ref. [3] for the extinction, and Eq. (3.06) of Ref. [3] for the absorption, i.e.,

$$C_{\mathrm{ext}}=\frac{4\pi k_0}{|\mathbf{E}^0|^2}\sum_{j=1}^{N}\mathrm{Im}[\mathbf{E}^0(\mathbf{r}_j,\omega)\cdot\mathbf{p}^*(\mathbf{r}_j,\omega)], \quad (15)$$

$$C_{\mathrm{abs}}=\frac{4\pi k_0}{|\mathbf{E}^0|^2}\sum_{j=1}^{N}|\mathbf{p}(\mathbf{r}_j,\omega)|^2\left[\mathrm{Im}\left(\frac{1}{\alpha_j(\omega)}\right)-\frac{2}{3}k_0^3\right]. \quad (16)$$

The scattering cross section is obtained as the difference between the extinction and absorption cross sections [3]. If we use the polarizability defined by Eq. (14), Eq. (15) is always used for obtaining the extinction cross section, but the absorption cross section is now computed as

$$C_{\mathrm{abs}}=\frac{4\pi k_0}{|E_0|^2}\sum_{j=1}^{N}|\mathbf{E}^l(\mathbf{r}_j,\omega)|^2\{\mathrm{Im}[\alpha_j(\omega)]-\mathrm{Im}[G^{\mathrm{int}}(\mathbf{r}_j,\mathbf{r}_j,\omega)]|\alpha_j(\omega)|^2\}, \quad (17)$$

where $\mathrm{Im}[G^{\mathrm{int}}(\mathbf{r}_j,\mathbf{r}_j,\omega)]$ represents the energy lost by a radiating dipole. We will compare the present formulation (IT for integrated tensor) of the polarizability to other known prescriptions. We will consider the usual CDM with radiation reaction (RR) correction [Eq. (9)], the lattice dispersion relation (LDR) [15], and the polarizability defined by Lakhtakia (LAK) [12]. Lakhtakia defines the polarizability by integrating the field susceptibility over a spherical region of the same volume as the cubic subunit [19]. In that case the polarizability is analytical. To check the validity of the approximation done by Lakhtakia, we will compute the cross sections with Eq. (14) for the definition of the polarizability, i.e., by integrating only the diagonal elements of the tensor (IDT).

The sphere is discretized into $N=2320$ subunits. We present in Figs. 1 and 2 the relative error in percent between Mie and the different method used versus $|n|k_0\Delta$, where n is the refractive index of the object: $n=\sqrt{\varepsilon}$ ($|n|k_0\Delta$ large corresponds to a large value of Δ).

In Fig. 1 we have taken $\varepsilon=2.25+i$. We first observe that the integration of the diagonal term only (IDT) leads to a result very close to that obtained with the polarizability of Lakhtakia. Thus, the approximation made by Lakhtakia by replacing the cube by a sphere is valid. Then, we notice that the integration of the field susceptibility tensor for all terms (IT) yields an overall slightly more accurate cross section.

In Fig. 2 we perform the same calculation but for a large relative permittivity: $\varepsilon=10+10i$. The IDT result is still close to the one given by the Lakhtakia method. We see that the IT method is better for all the cross sections from small values of $|n|k_0\Delta$ until $|n|k_0\Delta\approx0.3$. The fact that the IT method is better for small $|n|k_0\Delta$ is always true irrespective of the value of the relative permittivity (in Fig. 1 due to the small

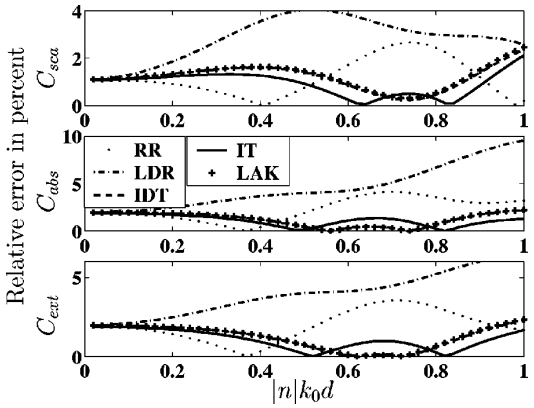

FIG. 1. Scattering properties of a pseudosphere with $N=2320$ and $\varepsilon=n^2=2.25+i$. Relative error (in percent) for the extinction, absorption, and scattering cross sections between different methods and the exact Mie result. The relative error is plotted versus the normalized lattice spacing $|n|k_0\Delta$, where k_0 is the free-space wave vector of the incident light. Dotted line, radiation reaction correction (RR); dash-dotted line, lattice dispersion relation (LDR); dashed line, polarizability is defined by integrating only the diagonal element of the tensor (IDT); solid line, computation is done by integrating all the elements of the field susceptibilities tensor (IT). The curves with the symbol + pertain to calculations using the polarizability defined by Lakhtakia.

value of the relative permittivity this is true only until $|n|k_0\Delta=0.1$). When the size of the subunit is very small compared to the wavelength, the field susceptibility tensor $\overleftrightarrow{\mathbf{G}}(\mathbf{r}_j,\mathbf{r}_j,\omega)$ for $\mathbf{r}_j$ in the vicinity of $\mathbf{r}_i$ varies as $1/|\mathbf{r}_j-\mathbf{r}_i|^3$; hence the approximation of a uniform field susceptibility tensor over the subunit does not hold. Therefore, the integration of $\overleftrightarrow{\mathbf{G}}(\mathbf{r}_j,\mathbf{r}_j,\omega)$ allows us to go beyond this approximation. For any given value of $|n|k_0\Delta$, different relative permittivities correspond to different sizes of the subunit, the size decreasing when the relative permittivity increases. This is the reason why the difference between the IT and the other results is more visible in Fig. 2 where the relative permittivity is larger.

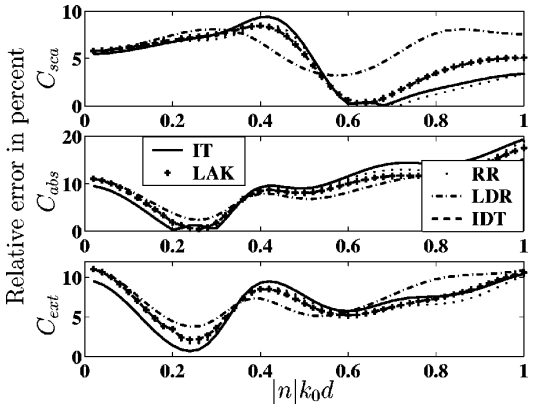

FIG. 2. Same as Fig. 1 but for $\varepsilon=n^2=10+10i$.

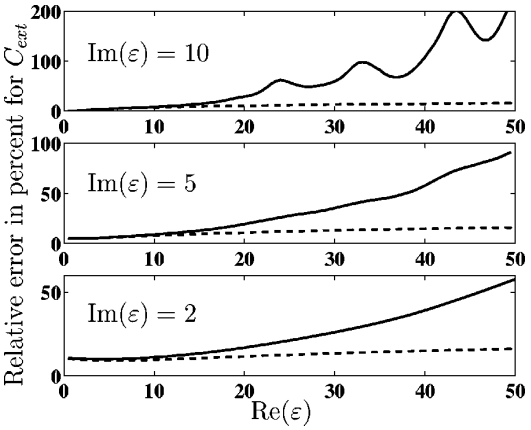

FIG. 3. Relative error (in percent) for the extinction cross section for $|n|k_0\Delta=0.02$ versus $\mathrm{Re}(\varepsilon)$ for three different values of $\mathrm{Im}(\varepsilon)$. Solid line, radiation reaction correction (RR); dashed line, computation done by integrating all the elements of the field susceptibility tensor (IT).

To be more general, Fig. 3 presents the error on the extinction cross section for a given $|n|k_0\Delta=0.02$, versus the real part of the relative permittivity for three different imaginary part of the relative permittivity: $\mathrm{Im}(\varepsilon)=2$, 5, and 10. We compare the IT result to the standard calculation accounting only for the radiation reaction term (RR). Note that all the other prescriptions of the polarizability are equivalent to RR for this small value of $|n|k_0\Delta$. Figure 3 shows clearly that the IT method leads to a better estimate of the cross section. This is particularly true when the polarizability has a small imaginary part (2) and a large real part (50). In that case the relative error is about 200% for RR whereas the IT calculation gives a relative error below 15%. We can even see some oscillations in the RR method due to morphological resonances, which are usually hard to describe with the CDM when the imaginary part of the permittivity is small. These oscillations are not present in the IT calculation, which demonstrates the robustness of our present prescription for the polarizability. In fact, irrespective of $\mathrm{Im}(\varepsilon)$, the IT method gives the same relative error for $\mathrm{Re}(\varepsilon)=50$, less than 15%. Notice that for the sake of computation time we use a small number N of subunits; however, increasing N would decrease the relative error.

IV. CONCLUSION

In conclusion we have derived a prescription for the polarizability in which the interaction of each subunit with itself is treated by accounting for its finite volume, through the integration of the full field susceptibility tensor over the subunit. This integration is performed without any approximation. In doing this we validate the approximations used by Lakhtakia in his derivation of a polarizability with finite-size effects. Our derivation is, however, more general and can be applied to a formulation of the coupled dipole method with a noncubic orthogonal lattice. It should be possible to extend our approach to a case where the subunits have arbitrary

shapes; however, in such a case the polarizability tensor may not be diagonal. We showed that integrating the full field susceptibility tensor increases the accuracy of the CDM when the size of the subunit is small compared to the wavelength in the medium. These results are particularly dramatic when the relative permittivity becomes large, a situation where the conventional formulation of the CDM performs very poorly. Finally, we emphasize that the approach presented here is not restricted to any particular geometry of the scatterer.

ACKNOWLEDGMENT

A.R. thanks the Ecole Centrale de Lyon BQR program for funding.

APPENDIX: COMPUTATION OF THE DIAGONAL TERM OF THE FREE-SPACE FIELD SUSCEPTIBILITY

A Weyl expansion of the tensor $\overleftrightarrow{\mathbf{G}}$ yields [21]

$$\overleftrightarrow{\mathbf{G}}(\mathbf{r}_i,\mathbf{r}',\omega)=\frac{i}{2\pi}\left[\int_{\mathbf{k}}\frac{dk_xdk_y}{w_0}\overleftrightarrow{\mathbf{M}}\times e^{\{i[k_x(x_i-x')+k_y(y_i-y')+iw_0|z_i-z'|]\}}\right]-4\pi\delta(\mathbf{r}_i-\mathbf{r}') \tag{A1}$$

with

$$\overleftrightarrow{\mathbf{M}}=\begin{pmatrix}k_0^2-k_x^2 & -k_xk_y & -\gamma w_0k_x\\ k_xk_y & k_0^2-k_y^2 & -\gamma w_0k_y\\ -\gamma w_0k_x & -\gamma w_0k_y & k^2\end{pmatrix}, \tag{A2}$$

where $\gamma=\mathrm{sgn}(z_i-z')$, $w_0=\sqrt{k_0^2-k^2}$, and $k^2=k_x^2+k_y^2$. Using Eq. (A1), the integrated tensor over a subunit is defined as

$$\overleftrightarrow{\mathbf{G}}^{\mathrm{int}}(\mathbf{r}_i,\mathbf{r}_i,\omega)=\left[\int_{V_i}d^3\mathbf{r}'\frac{i}{2\pi}\int_{\mathbf{k}}\frac{dk_xdk_y}{w_0}\overleftrightarrow{\mathbf{M}}\times e^{\{i[k_x(x_i-x')+k_y(y_i-y')+iw_0|z_i-z'|]\}}\right]-4\pi \tag{A3}$$

$$=\frac{i}{2\pi}\left[\int_{\mathbf{k}}\frac{dk_xdk_y}{w_0}\overleftrightarrow{\mathbf{M}}\int_{V_i}d^3\mathbf{r}'\times e^{\{i[k_x(x_i-x')+k_y(y_i-y')+iw_0|z_i-z'|]\}}\right]-4\pi.$$

It is easy to perform the integration over the spatial coordinates using Δ as the spacing lattice of the subunit ($V_i=\Delta^3$). Incidentally, one can note that the nondiagonal terms of the integrated tensor vanish, and that the components xx, yy, and zz are physically identical. Hence, with $M_{zz}=k^2$, we obtain

$$G_{zz}^{\mathrm{int}}(\mathbf{r}_i,\mathbf{r}_i,\omega)=\frac{4}{\pi}\left[\int_{\mathbf{k}}dk_xdk_y\frac{\sin(k_x\Delta/2)\sin(k_y\Delta/2)}{k_xk_y}\times\frac{k^2}{w_0^2}(-1+e^{iw_0\Delta/2})\right]-4\pi. \tag{A4}$$

The problem in computing this integral numerically is that the integral converges very slowly, as the integrand varies as $1/k$ when k_x,k_y tend to infinity. To solve this problem of convergence we use the following relation:

$$I=-\frac{4}{\pi}\int_{\mathbf{k}}dk_xdk_y\frac{\sin(k_x\Delta/2)\sin(k_y\Delta/2)}{k_xk_y}=-4\pi. \tag{A5}$$

Now if we move to polar coordinates ($dk_xdk_y=kdkd\theta$), we have

$$G_{zz}^{\mathrm{int}}(\mathbf{r}_i,\mathbf{r}_i,\omega)=\frac{4}{\pi}\int_{k=0}^{\infty}\int_{\theta=0}^{2\pi}\frac{kdkd\theta}{w_0^2}(-k_0^2+k^2e^{iw_0\Delta/2})\times\frac{\sin(k\cos\theta\Delta/2)\sin(k\sin\theta\Delta/2)}{k^2\cos\theta\sin\theta}. \tag{A6}$$

This new integrand converges as $1/k^3$ when k tends to infinity; hence a fast convergence is obtained. However, when $k=k_0$ we have $w_0=0$ and the integrand is not defined. This value corresponds to the transition from propagating to evanescent modes ($k>k_0$). We change the variable of integration to w_0 and use $kdk=-w_0dw_0$. Using parity considerations we finally get

$$G_{zz}^{\mathrm{int}}(\mathbf{r}_i,\mathbf{r}_i,\omega)=\frac{16}{\pi}\left(\int_{w_0=k_0}^{0}+\int_{w_0=0}^{i\infty}\right)\times\left[\int_{\theta=0}^{\pi/2}d\theta\frac{\sin(k\cos\theta\Delta/2)\sin(k\sin\theta\Delta/2)}{k^2\cos\theta\sin\theta}\right]\times\frac{k_0^2-k^2e^{iw_0\Delta/2}}{w_0}dw_0. \tag{A7}$$

Equation (A7) is the sum of two integrals. The first one is the integration over the propagating mode ($w_0=0,\ldots,k_0$) and the second one that over the evanescent mode ($w_0=0,\ldots,i\infty$). Therefore Eq. (A7) is defined irrespective of the values of w_0, k, and θ. With a little algebra, Eq. (A7) can be written as Eq. (11) where for the sake of clarity we have separated the two integrals.

If the subunit is not a cube but a parallelepiped ($\Delta_x\times\Delta_y\times\Delta_z$), a similar derivation yields

$$G_{zz}^{\mathrm{int}}(\mathbf{r}_i,\mathbf{r}_i,\omega)=\frac{16}{\pi}\left(\int_{w_0=k_0}^{0}+\int_{w_0=0}^{i\infty}\right)\times\left[\int_{\theta=0}^{\pi/2}d\theta\frac{\sin(k\cos\theta\Delta_x/2)\sin(k\sin\theta\Delta_y/2)}{k^2\cos\theta\sin\theta}\right]\times\frac{k_0^2-k^2e^{iw_0\Delta_z/2}}{w_0}dw_0, \tag{A8}$$

where $G_{xx}^{\mathrm{int}}(\mathbf{r}_i,\mathbf{r}_i,\omega)$ and $G_{yy}^{\mathrm{int}}(\mathbf{r}_i,\mathbf{r}_i,\omega)$ are obtained by permutation of the indices x,y,z.

[1] F. M. Kahnert, J. Quant. Spectrosc. Radiat. Transf. **79-80**, 775 (2003)
[2] E. M. Purcell and C. R. Pennypacker, Astrophys. J. **186**, 705 (1973)
[3] B. T. Draine, Astrophys. J. **333**, 848 (1988).
[4] B. T. Draine and J. C. Weingartner, Astrophys. J. **470**, 551 (1996).
[5] P. C. Chaumet and M. Nieto-Vesperinas, Opt. Lett. **25**, 1065 (2000).
[6] P. C. Chaumet and M. Nieto-Vesperinas, Phys. Rev. B **61**, 14119 (2000).
[7] A. Liu, A. Rahmani, G. W. Bryant, L. Richter, and S. Stranick, J. Opt. Soc. Am. A **18**, 704 (2001).
[8] A. Rahmani, P. C. Chaumet, and F. de Fornel, Phys. Rev. A **63**, 023819 (2001).
[9] J. D. Jackson, *Classical Electrodynamics*, 2nd ed. (John Wiley, New York, 1975).
[10] A. Wokaun, J. P. Gordon, and P. F. Liao, Phys. Rev. Lett. **48**, 957 (1982).
[11] P. C. Chaumet, Appl. Opt. **43**, 1825 (2004).
[12] A. Lakhtakia, Int. J. Mod. Phys. C **3**, 583 (1992).
[13] K. Klumme and J. Rahola, Astrophys. J. **425**, 653 (1994).
[14] C. E. Dungey and C. F. Bohren, J. Opt. Soc. Am. A **8**, 81 (1991).
[15] B. T. Draine and J. Goodman, Astrophys. J. **405**, 685 (1993).
[16] A. Rahmani, P. C. Chaumet, and G. W. Bryant, Opt. Lett. **27**, 2118 (2002).
[17] A. Rahmani, P. C. Chaumet, and G. W. Bryant, Astrophys. J. **607**, 873 (2004)
[18] A. D. Yaghjian, Proc. IEEE **68**, 248 (1980).
[19] A. Lakhtakia and G. Mulholland, J. Res. Natl. Inst. Stand. Technol. **98**, 699 (1993).
[20] F. Pincemin, A. Sentenac, and J.- J. Greffet, J. Opt. Soc. Am. A **11**, 1117 (1994).
[21] G. S. Agarwal, Phys. Rev. A **11**, 230 (1975).

PHYSICAL REVIEW B **67**, 165404 (2003)

Generalization of the coupled dipole method to periodic structures

Patrick C. Chaumet*
Institut Fresnel (Unité Mixte de Recherche 6133), Faculté des Sciences et Techniques de St Jérôme, Avenue Escadrille Normandie-Niemen, F-13397 Marseille cedex 20, France

Adel Rahmani
Laboratoire d'Electronique, Optoélectronique et Microsystèmes, UMR CNRS ECL 5512, 36 avenue Guy de Collongue, F-69134 Ecully, France

Garnett W. Bryant
Atomic Physics Division, National Institute of Standards and Technology, Gaithersburg, Maryland 20899-8423
(Received 27 November 2002; published 2 April 2003)

We present a generalization of the coupled dipole method to the scattering of light by arbitrary periodic structures. This formulation of the coupled dipole method relies on the same direct-space discretization scheme that is widely used to study the scattering of light by finite objects. Therefore, all the knowledge acquired previously for finite systems can be transposed to the study of periodic structures.

DOI: 10.1103/PhysRevB.67.165404 PACS number(s): 78.67.−n, 42.25.Fx, 42.79.Dj

I. INTRODUCTION

In its original form, the coupled dipole method (CDM) was developed for the study, in free space, of the scattering of light by an object with finite dimensions.[1,2] The method was subsequently extended to deal with objects near a substrate[3,4] or inside a multilayer system.[5] The principle of the method is always the same: the object is represented by a cubic array of N polarizable subunits, each with a size small enough compared to the spatial variations of the electromagnetic field for the dipole approximation to apply. If the CDM could be extended to deal with local scatterers near periodic structures, the CDM could then also be used, for example, to study light scattering by objects near surface gratings or by defects or cavities in photonic crystals. The first step toward such an extension is to develop a form of the CDM capable of describing periodic structures efficiently. In this paper, we present a generalization of the CDM to arbitrary periodic structures.

II. SELF-CONSISTENT FIELD FOR A PERIODIC STRUCTURE

We consider a plane substrate occupying the region $z \leqslant 0$. For a single object on the substrate, the self-consistent field at the ith subunit at location $\mathbf{r}_i$ is given by

$$\mathbf{E}(\mathbf{r}_i,\omega)=\mathbf{E}_0(\mathbf{r}_i,\omega)+\sum_{j=1}^{N}[\mathbf{S}(\mathbf{r}_i,\mathbf{r}_j,\omega)+\mathbf{F}(\mathbf{r}_i,\mathbf{r}_j,\omega)]\alpha_j(\omega)\mathbf{E}(\mathbf{r}_j,\omega), \quad (1)$$

where $\mathbf{E}_0(\mathbf{r}_i,\omega)$ is the (initial) field at $\mathbf{r}_i$ in the absence of the scattering object. Note that none of the subunits lies in the plane $z=0$. The tensors $\mathbf{F}$ and $\mathbf{S}$ are the field susceptibilities (linear responses) associated with the free space[6] and the substrate.[7] Note that the diagonal term of the free-space susceptibility $\mathbf{F}(\mathbf{r}_i,\mathbf{r}_i,\omega)$is excluded from the sum in Eq. (1) because this term is automatically taken into account in the dynamic polarizability $\alpha_i(\omega)$ (see, for instance, Ref. 8). The dynamic polarizability accounts for radiation reaction as well.[2,9] The self-consistent field $\mathbf{E}(\mathbf{r}_i,\omega)$ is found by solving the symmetric linear system formed by writing Eq. (1) for $i=1,\ldots,N$. The total field at position $\mathbf{r}$ is computed as

$$\mathbf{E}(\mathbf{r},\omega)=\mathbf{E}_0(\mathbf{r},\omega)+\sum_{j=1}^{N}[\mathbf{S}(\mathbf{r},\mathbf{r}_j,\omega)+\mathbf{F}(\mathbf{r},\mathbf{r}_j,\omega)]\alpha_j(\omega)\mathbf{E}(\mathbf{r}_j,\omega). \quad (2)$$

This conventional form of the CDM is well adapted to deal with localized objects. If, instead of a single object, one wants to study a periodic structure created by the repetition of the object over a lattice located above the substrate, Eq. (1) becomes

$$\mathbf{E}(\mathbf{r}_i,\omega)=\mathbf{E}_0(\mathbf{r}_i,\omega)+\sum_{j=1}^{N}\sum_{m,n=-\infty}^{\infty}[\mathbf{S}(\mathbf{r}_i,\overline{\mathbf{r}}_j+m\mathbf{u}+n\mathbf{v},\omega)+\mathbf{F}(\mathbf{r}_i,\overline{\mathbf{r}}_j+m\mathbf{u}+n\mathbf{v},\omega)]\alpha_j(\omega)\times\mathbf{E}(\overline{\mathbf{r}}_j+m\mathbf{u}+n\mathbf{v},\omega). \quad (3)$$

The vectors $\mathbf{u}$ and $\mathbf{v}$ are the basis vectors of the lattice (Fig. 1). The index i runs over all the subunits of the structure. $\mathbf{r}_i$ is the position of subunit i. The sum over j is restricted to the N subunits of a single object with position $\overline{\mathbf{r}}_j$ inside the object. The number of subunits is now infinite, and therefore so is the size of the linear system to be solved. One solution would be to truncate the infinite sum and solve the system for a large but finite number of objects, but this is impractical because the sums over the lattice converge very slowly. This problem can be circumvented by using a plane-wave decomposition of the incident field. In the case of plane-wave (propagating or evanescent) illumination, the field above the surface can be written as (we note by $\mathbf{k}_{0\|}$ the projection of vector $\mathbf{k}_0$ on a plane parallel to the surface)

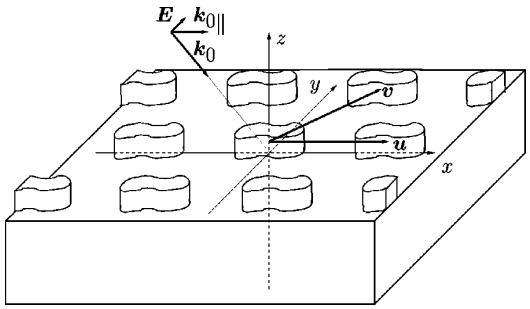

FIG. 1. Example of a periodic structure created by the repetition of an object over a lattice parallel to a substrate.

$$\mathbf{E}_0(\overline{\mathbf{r}_i}+m\mathbf{u}+n\mathbf{v},\omega)=\mathbf{E}_0(\overline{\mathbf{r}_i},\omega)\exp[i\mathbf{k}_{0\parallel}\cdot(m\mathbf{u}+n\mathbf{v})], \quad (4)$$

where $\mathbf{k}_0$ is the wave vector in free space. Because of the periodicity of the system and the translational invariance of the field susceptibilities, the self-consistent field satisfies the same relation as the incident field [Eq. (4)], and at any subunit Eq. (3) can be written as

$$\mathbf{E}(\mathbf{r}_i,\omega)=\mathbf{E}_0(\mathbf{r}_i,\omega)+\sum_{j=1}^{N}\left(\sum_{m,n=-\infty}^{\infty}[\mathbf{S}(\mathbf{r}_i,\overline{\mathbf{r}_j}+m\mathbf{u}+n\mathbf{v},\omega)+\mathbf{F}(\mathbf{r}_i,\overline{\mathbf{r}_j}+m\mathbf{u}+n\mathbf{v},\omega)]\times\exp[i\mathbf{k}_{0\parallel}\cdot(m\mathbf{u}+n\mathbf{v})]\right)\alpha_j(\omega)\mathbf{E}(\overline{\mathbf{r}_j},\omega). \quad (5)$$

The self-consistent field on the right-hand side of Eq. (5) is independent of (m,n) and can be taken out of the infinite sum. Hence, the sum over subunits in Eq. (5) only involves $j=1,\ldots,N$, that is, the number of subunits in a unit cell, which we choose to be the cell for which $m=n=0$. Moreover, because of the translational symmetry of the self-consistent field, we only need to find $\mathbf{E}$ in one cell. Once the self-consistent field is found in the central cell, the field in any other cell is obtained by multiplying by the appropriate phase factor. Thus we only have to solve a linear system of the same size as the one describing a single object. The major issue in solving Eq. (5) is to compute efficiently the infinite, slowly convergent sums without performing a truncation of the sums. This is possible owing to the translational invariance of the field susceptibilities in a plane parallel to the surface. The dependence on $(\overline{\mathbf{r}_i},\overline{\mathbf{r}_j},\omega)$ can be written as $(\boldsymbol{\rho}_{ij},z_i,z_j,\omega)$ with $\boldsymbol{\rho}_{ij}=(\overline{\mathbf{r}_i}-\overline{\mathbf{r}_j})_\parallel$. Hence, the infinite sums of Eq. (5) become

$$\begin{aligned}K&=\sum_{m,n=-\infty}^{\infty}[\mathbf{S}(\overline{\mathbf{r}_i},\overline{\mathbf{r}_j}+m\mathbf{u}+n\mathbf{v},\omega)+\mathbf{F}(\overline{\mathbf{r}_i},\overline{\mathbf{r}_j}+m\mathbf{u}+n\mathbf{v},\omega)]\\&\quad\times\exp[i\mathbf{k}_{0\parallel}\cdot(m\mathbf{u}+n\mathbf{v})]\\&=\int d\mathbf{r}_\parallel\sum_{m,n=-\infty}^{\infty}\delta(\mathbf{r}_\parallel-m\mathbf{u}-n\mathbf{v})\exp(i\mathbf{k}_{0\parallel}\cdot\mathbf{r}_\parallel)\\&\quad\times[\mathbf{S}(\boldsymbol{\rho}_{ij}-\mathbf{r}_\parallel,z_i,z_j,\omega)+\mathbf{F}(\boldsymbol{\rho}_{ij}-\mathbf{r}_\parallel,z_i,z_j,\omega)]. \quad (6)\end{aligned}$$

We define the two-dimensional Fourier transform as $\mathcal{F}[b(\mathbf{r}_\parallel)]=\int d\mathbf{r}_\parallel b(\mathbf{r}_\parallel)\exp(-i\mathbf{r}_\parallel\cdot\mathbf{h}_\parallel)$, and its inverse as $\mathcal{F}^{-1}[B(\mathbf{h}_\parallel)]=[1/(2\pi)^2]\int d\mathbf{h}_\parallel B(\mathbf{h}_\parallel)\exp(i\mathbf{r}_\parallel\cdot\mathbf{h}_\parallel)$. Using the Parseval-Plancherel theorem, Eq. (6) becomes

$$\begin{aligned}K&=\frac{1}{(2\pi)^2}\int d\mathbf{h}_\parallel M\sum_{m,n=-\infty}^{\infty}\delta(\mathbf{h}_\parallel-m\mathbf{u}'-n\mathbf{v}'+\mathbf{k}_{0\parallel})\\&\quad\times\mathcal{F}[\mathbf{S}(\boldsymbol{\rho}_{ij}-\mathbf{r}_\parallel,z_i,z_j,\omega)+\mathbf{F}(\boldsymbol{\rho}_{ij}-\mathbf{r}_\parallel,z_i,z_j,\omega)], \quad (7)\end{aligned}$$

where

$$\mathbf{u}'=2\pi(v_y\hat{\mathbf{x}}-v_x\hat{\mathbf{y}})/(u_xv_y-v_xu_y)$$

and

$$\mathbf{v}'=2\pi(-u_y\hat{\mathbf{x}}+u_x\hat{\mathbf{y}})/(u_xv_y-v_xu_y)$$

are the basis vectors of the reciprocal lattice, and $M=(2\pi)^2/(u_xv_y-v_xu_y)$. $\hat{\mathbf{x}}$ and $\hat{\mathbf{y}}$ are the basis vectors of the coordinate system. Using the angular spectrum representations $\mathbf{W}$ and $\mathbf{G}$ of tensors $\mathbf{S}$ and $\mathbf{F}$, Eq. (7) becomes[6,7]

$$\begin{aligned}K&=\frac{i}{2\pi}M\sum_{m,n=-\infty}^{\infty}\exp[i(m\mathbf{u}'+n\mathbf{v}'+\mathbf{k}_{0\parallel})\cdot\boldsymbol{\rho}_{ij}]\\&\quad\times\{\mathbf{W}(m\mathbf{u}'+n\mathbf{v}'+\mathbf{k}_{0\parallel},\mathbf{k}_0)\exp[iw_0(z_i+z_j)]\\&\quad+\mathbf{G}(m\mathbf{u}'+n\mathbf{v}'+\mathbf{k}_{0\parallel},\mathbf{k}_0)\exp[iw_0|z_i-z_j|]\}, \quad (8)\end{aligned}$$

with

$$\mathbf{G}(\mathbf{k}_\parallel,\mathbf{k}_0)=\begin{pmatrix}\frac{k_0^2-k_x^2}{w_0} & -\frac{k_xk_y}{w_0} & -\gamma k_x\\ -\frac{k_xk_y}{w_0} & \frac{k_0^2-k_y^2}{w_0} & -\gamma k_y\\ -\gamma k_x & -\gamma k_y & \frac{k_\parallel^2}{w_0}\end{pmatrix}, \quad (9)$$

and

$$\mathbf{W}(\mathbf{k}_\parallel,\mathbf{k}_0)=\begin{pmatrix}\frac{k_x^2w_0\Delta_p}{k_\parallel^2}-\frac{k_y^2k_0^2\Delta_s}{k_\parallel^2w_0} & \frac{k_xk_y}{w_0k_\parallel^2}(w_0^2\Delta_p+k_0^2\Delta_s) & k_x\Delta_p\\ \frac{k_xk_y}{w_0k_\parallel^2}(w_0^2\Delta_p+k_0^2\Delta_s) & \frac{k_y^2w_0\Delta_p}{k_\parallel^2}-\frac{k_x^2k_0^2\Delta_s}{k_\parallel^2w_0} & k_y\Delta_p\\ -k_x\Delta_p & -k_y\Delta_p & -\frac{\Delta_pk_\parallel^2}{w_0}\end{pmatrix}, \quad (10)$$

where $\gamma=\mathrm{sgn}(z_i-z_j)$, $\mathbf{k}_\parallel=m\mathbf{u}'+n\mathbf{v}'+\mathbf{k}_{0\parallel}=k_x\hat{\mathbf{x}}+k_y\hat{\mathbf{y}}$, and w_0 is the component along z of the wave vector $\mathbf{k}_0$, i.e., $w_0=(k_0^2-k_x^2-k_y^2)^{1/2}$. Δ_p and Δ_s are the Fresnel reflection coefficients for the substrate. Sums involving different susceptibility tensors (free space or surface) will have a different behavior, due to the different arguments of the exponential terms (z_i+z_j and $|z_i-z_j|$). They will be computed separately.

For the surface term, the convergence of the sum is ensured by the exponential term. As m and n increase, the magnitude of $\mathbf{k}_\parallel$ increases and the nature of the plane wave changes from propagating to evanescent. Because z_i+z_j never vanishes, and because the subunits are never exactly on the surface, this exponential term is always present and ensures the rapid convergence of the sum. Hence, the periodic field susceptibility associated to the surface is computed in the reciprocal space.

For the free-space part, the argument of the exponential term is $|z_i-z_j|$ and the rapid convergence of the sums is not as trivial. We use the method introduced to derive the Green function of a two-dimensional (2D) square grating.[10] We consider two cases. The first case pertains to the interaction between elements from different ''layers'' of the lattice, and corresponds to the case $z_i\neq z_j$. This case is similar to the surface case where the rapid convergence of the sum is ensured by the exponential term. Accordingly, this sum is also computed in the reciprocal space.

In the second case $z_i=z_j$ and the exponential term disappears making the convergence of the sum in the reciprocal space slow. Therefore, another strategy is needed to compute this term efficiently. We cast the free-space part of the infinite sum in two different forms. Let $\mathbf{a}(\mathbf{r}_\parallel,z_i-z_j)$ be the sum expressed in direct space [the **F** terms in Eq. (6)], and let $\mathbf{A}(\mathbf{k}_\parallel,z_i-z_j)$ be the sum in reciprocal space [the **G** terms in Eq. (8)]. Note that these two sums represented the same quantity (sum of free-space terms) expressed in two forms, one in direct space and the other in reciprocal space. By combining these two forms we can improve the convergence of the sum in the case $z_i=z_j$. When $z_i=z_j$, we write the sum as

$$\mathbf{a}(\mathbf{r}_\parallel,0)=\mathbf{A}(\mathbf{k}_\parallel,h)+[\mathbf{a}(\mathbf{r}_\parallel,0)-\mathbf{a}(\mathbf{r}_\parallel,h)], \tag{11}$$

where h is an offset parameter. We emphasize that $\mathbf{A}(\mathbf{k}_\parallel,h)$ and $\mathbf{a}(\mathbf{r}_\parallel,h)$ represent the same sum expressed in reciprocal and direct space, respectively. The auxiliary sum in the reciprocal space $[\mathbf{A}(\mathbf{k}_\parallel,h)]$ can be computed efficiently owing to the presence of an exponentially decreasing term. The difference of direct-space sums $\mathbf{a}(\mathbf{r}_\parallel,0)-\mathbf{a}(\mathbf{r}_\parallel,h)$ goes as $1/r_\parallel^2$ and can also be computed efficiently. With Eq. (11) we can ensure a rapid convergence of the sums in a discretization plane despite the absence of an exponentially decreasing term in the original sum.

To improve further on the convergence of the sums (both the sums in direct space and reciprocal space for the field susceptibility of free space and the surface), we use Shanks' transformation.[11] The principle is the following: consider the sum $S=\Sigma_{i=1}^{\infty}a_i$. Let us define the partial sum $S_n=\Sigma_{i=1}^{n}a_i$ and a new sequence $e_{s+1}(S_n)$ such that

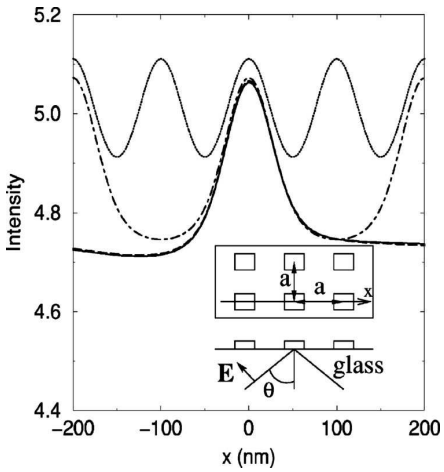

FIG. 2. Intensity of the electric field above a dielectric substrate in the direction of the x axis with a 2D grating of parallelepipeds. The inset shows the geometry used. The solid line is for an isolated parallelepiped. The other curves are obtained for the 2D grating with $a=100$ nm (dotted line), $a=200$ nm (dot dashed line), $a=1000$ nm (dashed line).

$$e_{s+1}(S_n)=e_{s-1}(S_{n+1})+\frac{1}{e_s(S_{n+1})-e_s(S_n)} \tag{12}$$

for $s=1,\ldots,n-1$ with

$$e_0(S_n)=S_n, \quad \text{and} \quad e_1(S_n)=\frac{1}{e_0(S_{n+1})-e_0(S_n)}. \tag{13}$$

The new sequence formed by the even-order terms $e_{2p}(S_n)$ converges toward S faster than the original sum $S=\Sigma_{i=1}^{\infty}a_i$.

Because we are dealing with double sums (over m and n), one way to evaluate the double sums would be to apply successively Shanks' accelerator to the inner (n) and outer (m) sums (as suggested in Ref. 12). The problem with this approach is that in our case, the convergence of the inner sum (over n) can be very slow for high values of m (outer sum). A better solution consists in defining one element l of the Shanks series as the sum over $m=-l,l$ for $n=-l,\ldots,l$ and $n=-l,l$ for $m=-l+1,\ldots,l-1$. This strategy gets rid of the inner/outer sum problem and results in a faster convergence and an easier implementation of the Shanks' algorithm.

Note that there is another way of computing efficiently the free-space term. As we did earlier, when we introduced a parameter h, it is possible to split the infinite sum (**F**) terms in Eq. (6) in two parts; one in the direct space and one in the reciprocal space, where these two sums converge quickly owing to a damping function.[13,14] The convergence is the best when $h=\sqrt{\pi/(u_x v_y-v_x u_y)}$. Poppe *et al.* introduced this method to study the optical response of an atomic monolayer; the period of the structure was therefore very small compared to the wavelength.

Once the periodic susceptibility tensors are known, we solve the linear system of Eq. (5) to find the self-consistent

TABLE I. Computation time in seconds for the coefficients of the linear system [Eq. (6)] used to solve Eq. (5). N is the number of subunits. CDM is the time for the classical CDM for one parallelepiped. CDM_1 is the time for the periodic CDM when the free-space contribution is computed with Eq. (8), and CDM_2 is the time for the periodic CDM when the free-space contribution is computed with Ref. 13. The infinite sums of the series are stopped when the relative error is less than 10^{-3} (10^{-6}).

	N	32	256	500	1372
	CDM	2	18	39	137
$a=$	CDM_1	0.3 (2)	4 (17)	10 (34)	43 (116)
100 nm	CDM_2	0.2 (0.4)	2.7 (5.5)	7 (13)	29 (54)
$a=$	CDM_1	0.7 (2)	12 (30)	30 (75)	119 (300)
200 nm	CDM_2	0.4 (1)	7 (16)	18 (40)	72 (158)
$a=$	CDM_1	5.7 (16)	96 (281)	246 (684)	949 (4020)
1 μm	CDM_2	5.6 (16)	96 (276)	233 (674)	900 (2460)

field at each site. Once the field at all subunits is known, the scattered field at any position $\mathbf{r}$, above, below, or inside the periodic structures is readily computed through Eq. (5) with the exchange $\mathbf{r}\leftrightarrow\mathbf{r}_i$. Notice that the new linear system is no longer symmetric. This is due to the fact that the elements of the system depend on the incident plane wave via the exponential term in Eq. (5).

III. EXAMPLE: SCATTERING BY A PERIODIC STRUCTURE LYING ON A SUBSTRATE

To illustrate the method we consider the case of a dielectric substrate (the relative permittivity is 2.25) on which lies a 2D grating of parallelepipeds with the same permittivity. The structure is illuminated in TM polarization from the substrate side by total internal reflection at an angle of incidence $\theta=45°$; then

$$\mathbf{k}_{0\|}=\left(\frac{2\pi}{\lambda}\sin\theta\sqrt{2.25},0\right).$$

The wavelength in vacuum is $\lambda=632.8$ nm, and the basis vectors of the lattice $\mathbf{u}=(a,0)$, $\mathbf{v}=(0,a)$. The parallelepipeds have a square base of 40×40 nm^2, and a height of 20 nm (see inset in Fig. 2). In Fig. 2, we present the intensity of the electric field, normalized to the incident field, along the x axis, 60 nm above the dielectric substrate for different value of a. The curves are obtained for $N=256$, hence the size of the subunit is $5\times5\times5$ nm^3 (but convergence is already achieved for $N=32$). Notice that the solid line is for an isolated parallelepiped on the substrate, i.e., the electric field is computed with the conventional CDM.[4] When a is small, the computed curves for the electric field are notably different from the single object case. This denotes a strong coupling between parallelepipeds. Conversely, for large a ($a=1000$ nm), the curve is very similar to the curve for an isolated parallelepiped.

Table I presents the computation time for the coefficients of the linear system [Eq. (6)] used to solve Eq. (5), for different values of N, and three values of a. The factor h has an important influence on the computation time, therefore we have chosen the optimal value of h for each case. As a reference, we use the conventional CDM to compute the field for a single parallelepiped.[15]

Table I shows three computation times: CDM is the time for the classical CDM for one parallelepiped. CDM_1 is the time for the periodic CDM when the free-space contribution is computed with Eq. (8), and CDM_2 is the time for the periodic CDM when the free-space contribution is computed with Ref. 13. CDM_2 is faster than CDM_1 for small periods. For $a=1$ μm, the computation times are similar. For larger periods, CDM_2 fails to converge to the reference result because the method of Ref. 13 used to compute the free-space term does not work well for large a. We note that the computation time increases with a. This is mainly due to the surface term. The convergence of the series depends on the term $\exp[iw_0(z_i+z_j)]$. In our case the moduli of the vectors of the reciprocal basis are $|\mathbf{u}'|=|\mathbf{v}'|=2\pi/a$. Hence when a decreases, the modulus of the vector basis increases, w_0 becomes imaginary for smaller values of (m,n), and the exponential term produces a stronger damping. Obviously, when N increases, the computation time increases due to the increased number of subunits involved. But there is another effect of the surface term. As the size of the subunit becomes smaller (N increases), there are more subunits close to the substrate with a small value of z_i+z_j and a slower exponential decay. When we compare the classical CDM to the periodic CDM, we see that for a smaller than 200 nm the computation time of the periodic CDM is shorter. When the size of the period becomes larger than the wavelength used, the convergence becomes slower.

IV. CONCLUSION

In conclusion we have generalized the coupled dipole method (CDM) to periodic structures. We have discussed explicitly the case of a three-dimensional structure, periodic in two directions, placed on a substrate. However, the principle of the approach described here applies to a broad range of configurations with one-, two-, or three-dimensional structures. The main advantage of this formulation is that it relies on the same straightforward, direct-space discretization scheme that is used for a single localized object. Therefore, all the knowledge acquired previously in CDM modeling of finite systems can be transposed to the study of periodic structures.[16] Optical anisotropy, for instance, can be included by taking the appropriate permittivity tensor. Also, as shown here, the symmetry of the periodic lattice can be arbitrary. Here, we have considered the case of plane-wave illumination. In the case of arbitrary illumination, each spectral component of the incident field must be treated individually. An interesting extension of the present work would be to merge the periodic CDM and the conventional CDM into a single approach to light scattering. This would be particularly useful in dealing with localized defects in periodic structures or the interaction between a near-field probe (microscope tip, fluorescing particle, . . .) and a periodic system. The periodic generalization of the coupled dipole method can also be used to draw a better physical picture of the local-field corrections that appear during the multiple scattering of light by a discrete set of scatterers.[17]

*Email address: pchaumet@loe.u-3mrs.fr

[1] E.M. Purcell and C.R. Pennypacker, Astrophys. J. **186**, 705 (1973).
[2] B.T. Draine, Astrophys. J. **333**, 848 (1988); B.T. Draine and J. Goodman, *ibid.* **405**, 685 (1993); B.T. Draine and P.J. Flatau, J. Opt. Soc. Am. A **11**, 1491 (1994) and references therein.
[3] R. Schmehl, B.M. Nebeker, and E.D. Hirleman, J. Opt. Soc. Am. A **14**, 3026 (1997).
[4] P.C. Chaumet and M. Nieto-Vesperinas, Phys. Rev. B **61**, 14 119 (2000); **62**, 11 185 (2000); **64**, 035422 (2001).
[5] A. Rahmani, P.C. Chaumet, and F. de Fornel, Phys. Rev. A **63**, 023819 (2001).
[6] A. Rahmani and G.W. Bryant, Opt. Lett. **25**, 433 (2000).
[7] G.S. Agarwal, Phys. Rev. A **11**, 230 (1975); **12**, 1475 (1975).
[8] A. Lakhtakia, Int. J. Mod. Phys. C **3**, 583 (1992).
[9] P.C. Chaumet and M. Nieto-Vesperinas, Opt. Lett. **25**, 1065 (2000).
[10] R.E. Jorgenson and R. Mittra, IEEE Trans. Antennas Propag. **38**, 633 (1990).
[11] D. Shanks, J. Math. Phys. **34**, 1 (1955).
[12] S. Singh and R. Singh, IEEE Trans. Med. Imaging **39**, 1226 (1991).
[13] G.P.M. Poppe, C.M.J. Wijers, and A. van Silfhout, Phys. Rev. B **44**, 7917 (1991).
[14] Note that there are typographical errors in Ref. 13. In Eq. (A15), the argument of the exponential term of the first sum should have a plus sign. In Eq. (A19), the argument of the erfc function should have a minus sign.
[15] We use a 750-MHz monoprocessor PC.
[16] L. Salomon, F.D. Grillot, A.V. Zayats, and F. de Fornel, Phys. Rev. Lett. **86**, 1110 (2001); L. Martín-Moreno, F.J. García-Vidal, H.J. Lezec, K.M. Pellerin, T. Thio, J.B. Pendry, and T.W. Ebbesen, *ibid.* **86**, 1114 (2001).
[17] A. Rahmani and G.W. Bryant, Phys. Rev. A **65**, 033817 (2002); A. Rahmani, P.C. Chaumet, and G.W. Bryant, Opt. Lett. **27**, 430 (2002).

PHYSICAL REVIEW B **72**, 205437 (2005)

Numerical simulations of the electromagnetic field scattered by defects in a double-periodic structure

Patrick C. Chaumet and Anne Sentenac
Institut Fresnel (UMR 6133), Université Paul Cézanne, Avenue Escadrille Normandie-Niemen, F-13397 Marseille cedex 20, France
(Received 21 June 2005; revised manuscript received 29 September 2005; published 23 November 2005)

We have developed a rigorous numerical method that permits the simulation of the electromagnetic field scattered by an aperiodic object in presence of a double-periodic structure (grating). Our volume integral formulation, which is an extension of the classic coupled dipole method, is versatile and can address inhomogeneous objects and gratings of any shape. The electromagnetic field is calculated both in the near-field and far-field region. In this latter case we propose an efficient technique based on the reciprocity theorem.

DOI: 10.1103/PhysRevB.72.205437 PACS number(s): 42.25.Fx, 41.20.−q, 02.70.Dh

I. INTRODUCTION

Development of numerical tools that simulate the electromagnetic field inside complex structures is crucial for the understanding of physical phenomena and the design of new components. The study of the interaction between the electromagnetic field and an object placed in the vicinity of a planar periodic structure has many applications. For example, it permits one to evaluate the field enhancement inside microcavities in photonic crystal slabs, to calculate the scattering by grating defects, or to simulate the radiation pattern of sources in a structured planar waveguide.[1]

Several numerical techniques have been proposed to solve the Maxwell equations without any approximation except that necessary for the numerical implementation. Among these are the finite difference time domain method (FDTD), the finite element method (FEM), the multiple multipole method (MMP), the volume integral equation [such as the coupled dipole method (CDM) or method of moment (MoM)], the surface integral equation.[2] However, despite the progress of the computing capabilities, these techniques are usually adapted to specific configurations to limit the calculation cost. Hence the evaluation of the field scattered by a bounded three-dimensional object immersed in an homogeneous space will not be addressed in the same way as that of the field scattered by an infinite periodic structure (or grating).[3]

In our configuration, the structure is an aperiodic object (defect) in the presence of a double-periodic structure (grating), hence it is neither periodic nor bounded and few simulation tools are adapted to this problem. If one assumes that the defect is duplicated periodically (with a period much larger than that of the grating), codes adapted to periodic structures, such as the differential or coupled-wave methods,[4] can be used. This supercell technique gives an accurate result if the defect period is large enough so that the coupling between adjacent objects can be neglected. In general this leads to a large number of unknowns in the Fourier field representation and a very high computation cost. FDTD techniques with periodic boundary conditions can also be proposed.[5] In this case, the discretized domain must be large enough so that the influence of the defect at the edges is negligible.[6,7]

In this paper we propose an efficient method that simulates the field scattered by a defect in a two-dimensional periodic structure without invoking the supercell technique. Our approach is an extension of the coupled dipole method or equivalently the method of moment.[8] One first calculates the field susceptibility tensor of the grating which gives the field scattered by a dipole in the presence of the double-periodic structure. In this work, the tensor is obtained through a volume integral formulation which can address inhomogeneous gratings of any shapes. Then, the aperiodic object is considered as a collection of dipoles whose exciting field is obtained by solving a self-consistent linear system involving the field susceptibility tensor of the grating. Last, when the local field inside the aperiodic object is known, the scattered field is evaluated in the near-field and far-field regions. Since the CDM is a volume integral equation method, it can address any arbitrary shaped, inhomogeneous, anisotropic defect and periodic structure. Another important advantage of this technique is that its numerical cost lies essentially in the calculation of the field susceptibility tensor. Once the latter is evaluated and memorized, one can easily study the scattering by various objects (for example, different kinds of microcavities). The additional numerical effort will be the same as that obtained if the objects were in a homogeneous medium.

Our paper is organized as follows: In Sec. II A the principles of the coupled dipole method are developed. The calculation of the field susceptibility tensor of the double-periodic structure is given in Sec. II B, and the field scattered in far field is investigated in Sec. II C. In Sec. II D we show how this method can be used to calculate the scattering by a lacuna of the grating. Section III is devoted to some numerical results and comparisons with other techniques, and we draw our conclusion in Sec. IV.

II. COMPUTATION OF THE DIFFRACTED FIELD BY A DEFECT IN A PERIODIC STRUCTURE

A. Formalism of the problem

In its original form, the coupled dipole method (CDM) was developed to study the free-space scattering of light by an object with finite dimensions.[9,10] The method was subse-

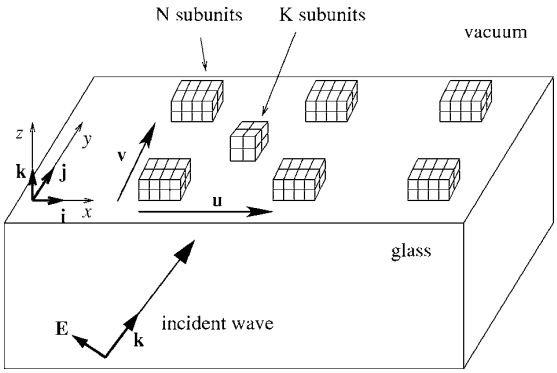

FIG. 1. Geometry of the system: double-periodic structure with basis vector **u** and **v**. The base cell of the periodic structure is discretized in *N* subunits. In this periodic structure a defect is introduced, and is discretized in *K* subunits. The double-periodic structure and the defect are above a flat substrate.

quently extended to deal with objects near a substrate[11,12] or inside a multilayer system.[13] Recently the CDM has been extended to planar periodic structures or gratings.[3] Now we consider the scattering by an aperiodic object deposited on a grating (Fig. 1). More precisely, in our configuration, a planar homogeneous substrate occupies the region $z \leqslant 0$ and the grating and object occupy the region $z > 0$. The grating is made of a motif (or base cell) that is duplicated periodically on the substrate. The whole structure is illuminated by a plane wave which comes either from the substrate or the superstrate. In the coupled dipole method, the objects are represented by a cubic array of polarizable subunits, each with a size small enough compared to the spatial variations of the electromagnetic field for the dipole approximation to apply. Hence, in our configuration, the local electric field at the ith subunit at location $\mathbf{r}_i$ is given by the self-consistent equation,

$$\mathbf{E}(\mathbf{r}_i) = \mathbf{E}^0(\mathbf{r}_i) + \sum_{j=1}^{N} \sum_{m,n=-\infty}^{\infty} [\mathbf{H}(\mathbf{r}_i, \bar{\mathbf{r}}_j + m\mathbf{u} + n\mathbf{v}) + \mathbf{F}(\mathbf{r}_i, \bar{\mathbf{r}}_j + m\mathbf{u} + n\mathbf{v})] \alpha_{\mathrm{p}}(\bar{\mathbf{r}}_j) \mathbf{E}(\bar{\mathbf{r}}_j + m\mathbf{u} + n\mathbf{v}) + \sum_{k=1}^{K} [\mathbf{H}(\mathbf{r}_i, \mathbf{r}_k) + \mathbf{F}(\mathbf{r}_i, \mathbf{r}_k)] \alpha_{\mathrm{d}}(\mathbf{r}_k) \mathbf{E}(\mathbf{r}_k), \quad (1)$$

where $\Sigma_{m,n=-\infty}^{\infty}$ means that we perform a double sum, i.e., $\Sigma_{m=-\infty}^{\infty} \Sigma_{n=-\infty}^{\infty}$. The index i runs over all the subunits of the structure (grating and defect). **F** is the free-space field susceptibility[14] and **H** represents the field susceptibility associated with the surface.[13] The aperiodic object (or defect) is discretized into K subunits located at $\mathbf{r}_k$ with $k = 1, \ldots, K$ and polarizability $\alpha_{\mathrm{d}}(\mathbf{r}_k)$. The elementary motif of the grating (restricted to one period) is discretized into N subunits placed at $\bar{\mathbf{r}}_j$ with $j = 1, \ldots, N$ and polarizability $\alpha_{\mathrm{p}}(\bar{\mathbf{r}}_j)$. The whole grating is described by an infinite set of dipoles, placed at $\bar{\mathbf{r}}_j + m\mathbf{u} + n\mathbf{v}$ with $(m,n) \in \mathbb{Z}^2$. $(\mathbf{u}, \mathbf{v})$ is the period of the grating with $\mathbf{u} = u_x\mathbf{i} + u_y\mathbf{j}$ and $\mathbf{v} = v_x\mathbf{i} + v_y\mathbf{j}$. The expression of the polarizability of each subunit is given by

$$\alpha_{\mathrm{d,p}}(\mathbf{r}_i) = \alpha^0_{\mathrm{d,p}}(\mathbf{r}_i) / [1 - (2/3) i k_0^3 \alpha^0_{\mathrm{d,p}}(\mathbf{r}_i)], \quad (2)$$

where the lower index d, p denotes the polarizability associated with the defect or the period respectively. k_0 is the modulus of the wave vector of the electromagnetic field in vacuum, and $\alpha^0_{\mathrm{d,p}}(\mathbf{r}_i)$ satisfies the Clausius-Mossotti relation :

$$\alpha^0_{\mathrm{d,p}}(\mathbf{r}_i) = \frac{3 d^3_{\mathrm{d,p}}}{4\pi} \frac{\varepsilon_{\mathrm{d,p}}(\mathbf{r}_i) - 1}{\varepsilon_{\mathrm{d,p}}(\mathbf{r}_i) + 2}. \quad (3)$$

In Eq. (3) $d_{\mathrm{d,p}}$ is the spacing of the object discretization (defect or grating) and $\varepsilon_{\mathrm{d,p}}(\mathbf{r}_i)$ stands for its relative permittivity. The term $(2/3) i k_0^3 \alpha^0_{\mathrm{d,p}}(\mathbf{r}_i)$ in Eq. (2) is related to the radiative reaction term and is essential to satisfy the optical theorem.[15,16] Note that the the contact term $\mathbf{F}(\mathbf{r}_i, \mathbf{r}_i)$ in Eq. (1) is equal to zero inasmuch as we are dealing with the local electric field.[8] In Eq. (1), due to the grating, the number of subunits is infinite, and therefore so is the size of the linear system to be solved. One solution would be to truncate the infinite sum, and solve the system for a large but finite number of objects, but this is impractical because the sums over the lattice converge very slowly.

This problem can be circumvented by taking the substrate and the grating as the reference system of the problem. To this aim, one introduces the field susceptibility tensor of the double periodic structure **G**, such that $\mathbf{G}(\mathbf{r}, \mathbf{r}')\mathbf{p}(\mathbf{r}')$ is the electric field at $\mathbf{r}$ radiated by a dipole $\mathbf{p}(\mathbf{r}')$ placed at $\mathbf{r}'$ in presence of the grating. With this tool, one can calculate the local field inside the aperiodic object through a self-consistent integral equation. Namely, the local field is the sum of the field that would exist in absence of the defect $\mathbf{E}_{\mathrm{per}}(\mathbf{r})$ (this field can be obtained with any classic grating method; in Appendix A and B we provide a means to calculate it with the CDM formalism), plus the field radiated *in the presence of the grating* by the K dipoles forming the aperiodic object. The self-consistent equation giving the local field inside the aperiodic object reads

$$\mathbf{E}(\mathbf{r}_i) = \mathbf{E}_{\mathrm{per}}(\mathbf{r}_i) + \sum_{k=1}^{K} \mathbf{G}(\mathbf{r}_i, \mathbf{r}_k) \alpha_{\mathrm{d}}(\mathbf{r}_k) \mathbf{E}(\mathbf{r}_k). \quad (4)$$

Equation (4) is a linear system to solve whose size is $3K \times 3K$. Once the local field $\mathbf{E}(\mathbf{r}_i)$ is known at each $\mathbf{r}_i$, for $i = 1, \ldots, K$ the electric field can be computed everywhere outside the aperiodic object through the equation

$$\mathbf{E}(\mathbf{r}) = \mathbf{E}_{\mathrm{per}}(\mathbf{r}) + \sum_{k=1}^{K} \mathbf{G}(\mathbf{r}, \mathbf{r}_k) \alpha_{\mathrm{d}}(\mathbf{r}_k) \mathbf{E}(\mathbf{r}_k). \quad (5)$$

From Eqs. (4) and (5), it appears that the main difficulty of the CDM is to calculate the field susceptibility tensor of the periodic structure.

B. Field susceptibility tensor of a double-periodic structure

Very few techniques have been proposed to calculate the field susceptibility tensor of a periodic structure. In Ref. 1 one calculates the field scattered by a dipole placed in a grating with an *S*-matrix approach and the use of the Fourier modal method. This method is efficient when the field inside

the periodic structure can be represented adequately by a small number of Fourier coefficients, i.e., when the period of the grating is small. In this paper, we use a volume integral approach which is efficient when the grating motif can be described by a small number of dipoles, regardless of the period. The field susceptibility tensor $\mathbf{G}(\mathbf{r},\mathbf{r}')$ which gives the field in $\mathbf{r}$ radiated by a dipole placed in $\mathbf{r}'$ in presence of the grating is written as the sum of the field radiated by the dipole in presence of the substrate alone with the field radiated by the infinite number of subunits periodically placed on the substrate and constituting the grating:

$$\mathbf{G}(\mathbf{r},\mathbf{r}') = \mathbf{S}(\mathbf{r},\mathbf{r}') + \sum_{j=1}^{N} \sum_{m,n=-\infty}^{\infty} \mathbf{S}(\mathbf{r},\bar{\mathbf{r}}_j + m\mathbf{u} + n\mathbf{v}) \times \alpha_p(\bar{\mathbf{r}}_j)\mathbf{G}(\bar{\mathbf{r}}_j + m\mathbf{u} + n\mathbf{v},\mathbf{r}'), \quad (6)$$

with $\mathbf{S}(\mathbf{r},\mathbf{r}')=\mathbf{F}(\mathbf{r},\mathbf{r}')+\mathbf{H}(\mathbf{r},\mathbf{r}')$ and $(\mathbf{u},\mathbf{v})$ are the basis vectors of the grating. It is worth noting here that one could replace the field susceptibility tensor of the surface by the field susceptibility tensor of a multilayer. It amounts to changing the Fresnel reflection and transmission coefficients present in the expression of $\mathbf{H}$ by that of the multilayer. In the same way, we can remove the substrate with $\mathbf{H}=0$.

To compute $\mathbf{G}(\mathbf{r},\mathbf{r}')$ we define a new tensor as

$$\mathbf{G}_{per}(\mathbf{r},\mathbf{r}',\mathbf{k}_\parallel) := \sum_{p,q=-\infty}^{\infty} \mathbf{G}(\mathbf{r}+p\mathbf{u}+q\mathbf{v},\mathbf{r}') \times \exp[i\mathbf{k}_\parallel . (p\mathbf{u}+q\mathbf{v})], \quad (7)$$

where the tensor $\mathbf{G}_{per}$ is pseudoperiodic with $\mathbf{G}_{per}(\mathbf{r}+m\mathbf{u}+n\mathbf{v},\mathbf{r}',\mathbf{k}_\parallel)=\mathbf{G}_{per}(\mathbf{r},\mathbf{r}',\mathbf{k}_\parallel)\exp[-i\mathbf{k}_\parallel.(m\mathbf{u}+n\mathbf{v})]$. Similarly, we introduce a pseudoperiodic tensor associated with the surface:

$$\mathbf{S}_{per}(\mathbf{r},\mathbf{r}',\mathbf{k}_\parallel) := \sum_{p,q=-\infty}^{\infty} \mathbf{S}(\mathbf{r}+p\mathbf{u}+q\mathbf{v},\mathbf{r}') \times \exp[i\mathbf{k}_\parallel . (p\mathbf{u}+q\mathbf{v})]. \quad (8)$$

Notice that this new tensor $\mathbf{S}_{per}$, as detailed in Refs. 3,17, can be computed very efficiently. Due to the translational invariance of the substrate $\mathbf{S}_{per}$ has some properties, notably we have $\mathbf{S}_{per}(\mathbf{r}+p\mathbf{u}+q\mathbf{v},\mathbf{r}',\mathbf{k}_\parallel)=\mathbf{S}_{per}(\mathbf{r},-p\mathbf{u}-q\mathbf{v}+\mathbf{r}',\mathbf{k}_\parallel)=\mathbf{S}_{per}(\mathbf{r},\mathbf{r}',\mathbf{k}_\parallel)\exp[-i\mathbf{k}_\parallel.(p\mathbf{u}+q\mathbf{v})]$.

Introducing Eq. (6) in Eq. (7) and using the definition of Eq. (8) and the property of $\mathbf{S}_{per}$, Eq. (7) can be written as

$$\mathbf{G}_{per}(\mathbf{r},\mathbf{r}',\mathbf{k}_\parallel) = \mathbf{S}_{per}(\mathbf{r},\mathbf{r}',\mathbf{k}_\parallel) + \sum_{j=1}^{N} \mathbf{S}_{per}(\mathbf{r},\bar{\mathbf{r}}_j,\mathbf{k}_\parallel) \times \alpha_p(\bar{\mathbf{r}}_j)\mathbf{G}_{per}(\bar{\mathbf{r}}_j,\mathbf{r}',\mathbf{k}_\parallel). \quad (9)$$

To obtain $\mathbf{G}_{per}(\mathbf{r},\mathbf{r}',\mathbf{k}_\parallel)$ from Eq. (9), one needs to compute $\mathbf{G}_{per}(\bar{\mathbf{r}}_j,\mathbf{r}',\mathbf{k}_\parallel)$ which is the solution of the following self-consistent equation:

$$\mathbf{G}_{per}(\bar{\mathbf{r}}_k,\mathbf{r}',\mathbf{k}_\parallel) = \mathbf{S}_{per}(\bar{\mathbf{r}}_k,\mathbf{r}',\mathbf{k}_\parallel) + \sum_{j=1}^{N} \mathbf{S}_{per}(\bar{\mathbf{r}}_k,\bar{\mathbf{r}}_j,\mathbf{k}_\parallel) \times \alpha_p(\bar{\mathbf{r}}_j)\mathbf{G}_{per}(\bar{\mathbf{r}}_j,\mathbf{r}',\mathbf{k}_\parallel). \quad (10)$$

Equation (10) is a linear system of equation of size $3N \times 3N$ where $\mathbf{G}_{per}(\bar{\mathbf{r}}_k,\mathbf{r}',\mathbf{k}_\parallel)$ are the unknowns. Once this system is solved, $\mathbf{G}_{per}(\mathbf{r},\mathbf{r}',\mathbf{k}_\parallel)$ can be obtained for any position $\mathbf{r}$ and $\mathbf{r}'$.

Now, the pseudoperiodic $\mathbf{G}_{per}(\mathbf{r},\mathbf{r}',\mathbf{k}_\parallel)$ [Eq. (7)] can be cast into a Fourier series whose elements are given by the following integral:

$$\mathbf{G}(\mathbf{r},\mathbf{r}'+m\mathbf{u}+n\mathbf{v}) = \frac{1}{S}\int\int_S \mathbf{G}_{per}(\mathbf{r},\mathbf{r}',\mathbf{k}_\parallel) \times \exp[-i\mathbf{k}_\parallel . (m\mathbf{u}+n\mathbf{v})]d\mathbf{k}_\parallel \quad (11)$$

where $\int\int_S$ means that the integration is performed over the first Brillouin zone of the grating, defined by the two following vectors:

$$\mathbf{U} = 2\pi(v_y\mathbf{i} - v_x\mathbf{j})/(u_xv_y - v_xu_y), \quad (12)$$

$$\mathbf{V} = 2\pi(-u_y\mathbf{i} + u_x\mathbf{j})/(u_xv_y - v_xu_y), \quad (13)$$

and $S=|\mathbf{U}\times\mathbf{V}|$. Hence taking $(m,n)=(0,0)$ Eq. (11) leads to the following expression for the field tensor susceptibility of the double periodic structure:

$$\mathbf{G}(\mathbf{r},\mathbf{r}') = \frac{1}{S}\int\int_S \mathbf{G}_{per}(\mathbf{r},\mathbf{r}',\mathbf{k}_\parallel)d\mathbf{k}_\parallel. \quad (14)$$

The tensor $\mathbf{G}$ is then obtained through Eq. (14) which is discretized for numerical purposes as

$$\mathbf{G}(\mathbf{r},\mathbf{r}') \approx \frac{1}{MM'}\sum_{l=0}^{M-1}\sum_{l'=0}^{M'-1} \mathbf{G}_{per}\left(\mathbf{r},\mathbf{r}',\frac{l}{M}\mathbf{U}+\frac{l'}{M'}\mathbf{V}\right), \quad (15)$$

with (M,M') a natural positive number. Note that this discretization has a physical meaning. Indeed, the field susceptibility tensor obtained with Eq. (15) is doubly periodical with periods equal to $M\mathbf{u}$ and $M'\mathbf{v}$. In the other term, it gives the field in $\mathbf{r}$ radiated by an infinite set of dipoles placed at $\mathbf{r}'+lM\mathbf{u}+l'M'\mathbf{v}$ where $(l,l')\in\mathbb{Z}^2$. The larger (M,M') the better the approximation for the tensor. Hence we are faced with the same problem of convergence as that encountered in a supercell method.[6] At this point, it is worth stressing that the field radiated by a dipole in the presence of a grating is the sum of the field radiated by the dipole in the presence of the bare substrate (given by $\mathbf{S}$) plus the field radiated by each subunits forming the grating. To minimize the influence of the field radiated by the discretization-induced dipoles we calculate the field susceptibility tensor by injecting Eq. (9) in Eq. (14), while using Eq. (8). We obtain

$$\mathbf{G}(\mathbf{r},\mathbf{r}') = \mathbf{S}(\mathbf{r},\mathbf{r}') + \frac{1}{S}\int\int_S \sum_{j=1}^{N} [\mathbf{S}_{per}(\mathbf{r},\bar{\mathbf{r}}_j,\mathbf{k}_\parallel) \times \alpha_p(\bar{\mathbf{r}}_j)\mathbf{G}_{per}(\bar{\mathbf{r}}_j,\mathbf{r}',\mathbf{k}_\parallel)]d\mathbf{k}_\parallel, \quad (16)$$

$$\approx \mathbf{S}(\mathbf{r},\mathbf{r}') + \frac{1}{MM'}\sum_{l=0}^{M-1}\sum_{l'=0}^{M'-1}\sum_{j=1}^{N}\left[\mathbf{S}_{\mathrm{per}}\left(\mathbf{r},\bar{\mathbf{r}}_j,\frac{l}{M}\mathbf{U}+\frac{l'}{M'}\mathbf{V}\right)\right.$$
$$\left.\times\,\alpha_{\mathrm{p}}(\bar{\mathbf{r}}_j)\mathbf{G}_{\mathrm{per}}\left(\bar{\mathbf{r}}_j,\mathbf{r}',\frac{l}{M}\mathbf{U}+\frac{l'}{M'}\mathbf{V}\right)\right], \quad (17)$$

where $\mathbf{G}_{\mathrm{per}}(\bar{\mathbf{r}}_j,\mathbf{r}',\mathbf{k}_{\|})$ is obtained from Eq. (10). With this formulation, the calculation of $\mathbf{S}$ is independent of the discretization due to the numerical procedure. Hence, at the observation point, the field radiated by the dipole via the bare substrate is accurately accounted for. The unwanted contribution of the discretization-induced dipoles located at $\mathbf{r}'+lM\mathbf{u}+l'M'\mathbf{v}$ is solely felt through multiple scattering with the subunits of the grating. It is worth noting that the field radiated in $\mathbf{r}$ by the discretization-induced dipoles will be significantly smaller than that radiated by the "real" dipole placed at $\mathbf{r}'$ if $|\mathbf{r}-\mathbf{r}'|\ll\min(|\mathbf{r}-\mathbf{r}'-M\mathbf{u}|,|\mathbf{r}-\mathbf{r}'-M'\mathbf{v}|)$.

C. Evaluation of the field in the far-field zone

The method presented in Sec. II B to calculate the field susceptibility tensor is not efficient if the position of observation $\mathbf{r}$ is located in the far-field zone. Indeed, to minimize the contribution of the discretization-induced dipoles, Eq. (17), one should have $|\mathbf{r}|\ll\min(|M\mathbf{u}|,|M'\mathbf{v}|)$, which is impossible when $|\mathbf{r}|$ is very large compared to the wavelength. In this case, it is much simpler and efficient to use the reciprocity theorem to calculate the tensor. The latter states that, whatever the configuration under study (and, in particular, in presence of the grating) the field $\mathbf{E}'(\mathbf{r}_k)$ created by a dipole $\mathbf{p}'$ placed at $\mathbf{r}$ is related to the field $\mathbf{E}(\mathbf{r})$ created by a dipole $\mathbf{p}$ placed at $\mathbf{r}_k$ through the relation[18]

$$\mathbf{p}(\mathbf{r}_k)\cdot\mathbf{E}'(\mathbf{r}_k) = \mathbf{p}'(\mathbf{r})\cdot\mathbf{E}_k(\mathbf{r}). \quad (18)$$

Now, the field scattered by the dipole $\mathbf{p}'$ placed at $\mathbf{r}$ in far field and impinging on the defect embedded in the grating can be written as

$$\mathbf{E}^0(\mathbf{r}_k) = \mathbf{p}'_{\perp}(\mathbf{r})\frac{e^{ik_0|\mathbf{r}-\mathbf{r}_k|}}{|\mathbf{r}-\mathbf{r}_k|} \approx \mathbf{p}'_{\perp}(\mathbf{r})\frac{e^{ik_0|\mathbf{r}|}}{|\mathbf{r}|}e^{-i\mathbf{k}_0\cdot\mathbf{r}_k}, \quad (19)$$

where $\mathbf{p}'_{\perp}(\mathbf{r})$ means that we take only the component of the dipole moment perpendicular to the vector $\mathbf{r}$ and $\mathbf{k}_0=k_0\mathbf{r}/r$. Hence $\mathbf{E}^0$ can be assimilated to an incident plane wave with magnitude $e^{ik_0|\mathbf{r}|}/|\mathbf{r}|$. To compute the field $\mathbf{E}'(\mathbf{r}_k)$ we use Eqs. (5) and (A1) where the incident field $\mathbf{E}^0$ is replaced by the expression given by Eq. (19). Once $\mathbf{E}'(\mathbf{r}_k)$ is evaluated for the two fundamental polarizations it is easy to compute $\mathbf{E}_k(\mathbf{r})$ from Eq. (18). Finally, to obtain the field diffracted by the object in the presence of the grating in far field, we add the field contribution of each dipole forming the object as

$$\mathbf{E}(\mathbf{r}) = \mathbf{E}_{\mathrm{per}}(\mathbf{r}) + \sum_{k=1}^{K}\mathbf{E}_k(\mathbf{r}). \quad (20)$$

D. Particular case where the defect is a lacuna in the double-periodic structure

The method that we have presented can be used to create a lacuna in the double-periodic structure. In this case, the aperiodic object must have exactly the same discretization as that of the grating motif and the same polarizability with opposite sign: $\alpha_{\mathrm{d}}(\bar{\mathbf{r}}'_j)=-\alpha_{\mathrm{p}}(\bar{\mathbf{r}}_j+m\mathbf{u}+m'\mathbf{v})$ for $j=1,\ldots,N$ [it is obvious from Eq. (1) that the resulting structure will be a grating with a missing motif]. For example, the field scattered by a grating whose central motif has been suppressed, i.e., $(m,n)=(0,0)$ which implies $\bar{\mathbf{r}}'_j=\bar{\mathbf{r}}_j$, is given by

$$\mathbf{E}(\mathbf{r}) = \mathbf{E}_{\mathrm{per}}(\mathbf{r}) + \sum_{k=1}^{N}\mathbf{G}(\mathbf{r},\bar{\mathbf{r}}_k)\alpha_{\mathrm{d}}(\bar{\mathbf{r}}_k)\mathbf{E}(\bar{\mathbf{r}}_k), \quad (21)$$

$$\mathbf{E}(\bar{\mathbf{r}}_k) = \mathbf{E}_{\mathrm{per}}(\bar{\mathbf{r}}_k) + \sum_{l=1}^{N}\mathbf{G}(\bar{\mathbf{r}}_k,\bar{\mathbf{r}}_l)\alpha_{\mathrm{d}}(\bar{\mathbf{r}}_l)\mathbf{E}(\bar{\mathbf{r}}_l), \quad (22)$$

where $\mathbf{E}_{\mathrm{per}}(\bar{\mathbf{r}}_k)$ is obtained with Eq. (A1) and the field susceptibility tensor of the grating $\mathbf{G}$ is given by Eq. (17). In Eq. (21) the sum over k represents the field scattered by the defect with the negative polarizability, i.e., the difference between the field scattered by the periodic structure minus the field scattered by the structure with the lacuna. Obviously, with the same technique, it is also possible to displace or to change the nature of one base cell of the grating.

III. NUMERICAL RESULTS

In this section, we present some numerical results and we check the convergence of our method. We consider a double-periodic structure made of silicon cubes of width a deposited along a square lattice of period $\mathbf{u}=(p,0)$ and $\mathbf{v}=(0,p)$ on a glass substrate. The aperiodic object is a cube of silver with the same width a, placed at the center of the square cell [see Figs. 2(a) and 2(b)]. The substrate is illuminated from the substrate, with a TM polarized plane wave with angle of incidence θ [see Figs. 2(b)], and the magnitude of the incident field is set to 1. The angle of incidence can be chosen so as to illuminate the grating in total internal reflection. In the first example, we have taken $a=50$ nm, $p=200$ nm, and $\lambda=600$ nm. The relative permittivity of the material are taken from Palik's handbook.[19] Figures 2(c) and 2(d) show the modulus of the electromagnetic field calculated at an altitude $h=100$ nm for an angle of incidence $\theta=0°$ and $\theta=50°$, respectively. These figures show clearly the coupling between the silver defect and the neighboring silicon cubes and the limits of its influence. Within a few periods away from the defect, the field is not affected by its presence. In this example, the calculation has been done for $M=M'=11$, and one can wonder if the convergence is obtained. In the next example we study the influence of the number of modes (M,M') on the accuracy of the results. In Figs. 3(a) and 3(b), we plot the near field along the dotted line shown in Figs. 2(a) and 2(b) ($z=h=100$ nm, $y=p/2=100$ nm) for different values of M and M'. Note that this line overhangs the defect. It is the place where the field is the most affected by the presence of the object. It is observed that, when the observation point is just above the defect, the calculation with $M=M'=3$ is very close to that obtained with $M=M'=5$ and $M=M'=11$ (the convergence rate is quick). On the other hand, if the observation point moves away from the defect,

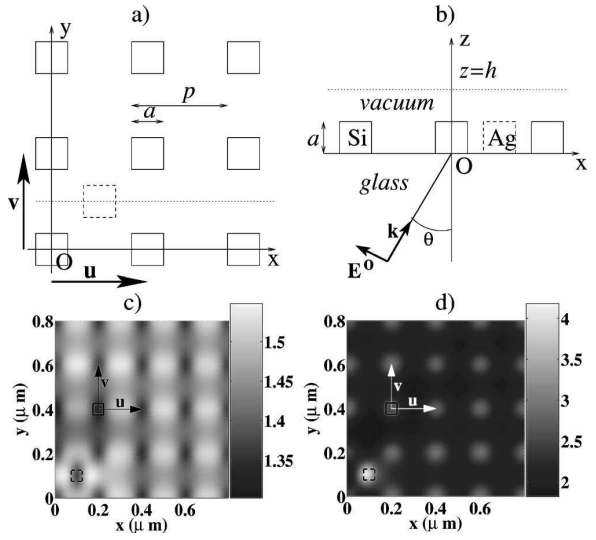

FIG. 2. (a) and (b) top view and side view of the geometry of the system: the double-periodic structure is formed by pads in silicon with size a^3, and a square periods p. The defect is a silver pad with the same size (a^3), and the wavelength of the TM polarized illumination is $\lambda=600$ nm. (c) Near field intensity for $a=50$ nm, $p=200$ nm, $h=100$ nm, and $\theta=0^\circ$. (d) Near-field intensity for $a=50$ nm, $p=200$ nm, $h=100$ nm, and $\theta=50^\circ$.

the value obtained for $M=M'=3$ departs from that given with $M=M'=5$ and $M=M'=11$. This result is in agreement with the previous discussion on the influence of the "parasite dipoles" which increases when the observation point is far from the object. Note that, as expected, in the converged cases, as the point of observation moves away from the defect, the intensity comes closer to that obtained for the grating without the defect.

If the observation point is in far field [Figs. 3(c) and 3(d)] the sensibility to the number of modes M and M' is very small due to the accurate evaluation of the far field with the reciprocity theorem. In this case, the mode numbers influences solely the calculation of the field inside the defect and the convergence of this near-field calculation is obtained with a relatively small number of modes. For comparison purpose, we also plot in the solid line the field scattered by the defect alone on the substrate. In this example, we observe that the grating does not modify the field scattered by the defect in far field. This means that the coupling between the defect (silver pad) and the silicon pads of the grating is weak. In Fig. 4 the same study is conducted for a smaller period of the grating, $p=100$ nm, so that a stronger coupling is expected. The same observations as that done for the previous Figs. 3(a) and 3(b) can be done for Figs. 4(a) and 4(b) except that the convergence is obtained for a significantly higher number of modes $M=M'=21$. This was to be expected since the period of the grating is smaller. In the far-field case, Figs. 4(c) and 4(d), we observe that the field scattered by the defect in the presence of the grating differs strongly from that scattered by the defect alone on the substrate; this implies a strong coupling between the defect and the grating. Note that, contrary to the near-field calculation, the convergence is

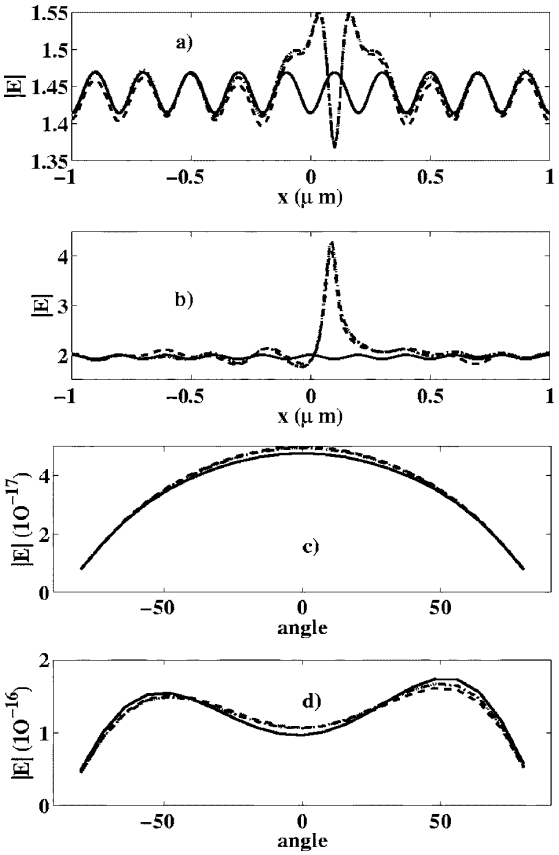

FIG. 3. We present the modulus of the field in the near-field [(a) and (b)] and in the far-field zone [(c) and (d)]. Computations done with $M=M'=3$ are in the dashed line, for $M=M'=5$ in the dot-dashed line, and for $M=M'=11$ in the dotted line. (a) and (b) modulus of the field in the near-field zone: $z=h=100$ nm, and $y=p/2=100$ nm. In plain line the field obtained without the defect (a) $\theta=0^\circ$. (b) $\theta=50^\circ$. (c) and (d) modulus of the field in the far-field zone $y=0$ and $x^2+z^2=1$ m, and in the solid line the field scattered by the defect without the double-periodic structure (c) $\theta=0^\circ$. (d) $\theta=50^\circ$.

almost reached for $M=M'=3$. The evaluation of the far-field amplitude does not necessitate an accurate calculation of the near field. Indeed, the propagation in vacuum is a low-pass filter, so that the high-frequency components of the near field (that are the most difficult to calculate accurately) are suppressed. Hence very few modes are necessary to evaluate the far-field scattered by the defect.

In Fig. 5, we study the number of duplicated motifs that are necessary to simulate the presence of an infinite grating and we compare the results to that of our method. The structure under study is the same as that of Fig. 4 and it is illuminated under normal incidence and in total internal reflection configuration $\theta=50^\circ$. We use the classic CDM[12] to simulate the field scattered by an object consisting in a silver cube surrounded by a finite number of silicon cubes, i.e., we truncate the sums in Eq. (1): $\Sigma_{m,n=-\infty}^{\infty} \approx \Sigma_{m,n=-M_{\max}}^{M_{\max}}$. Note that the linear system that has to be solved in this case is quite

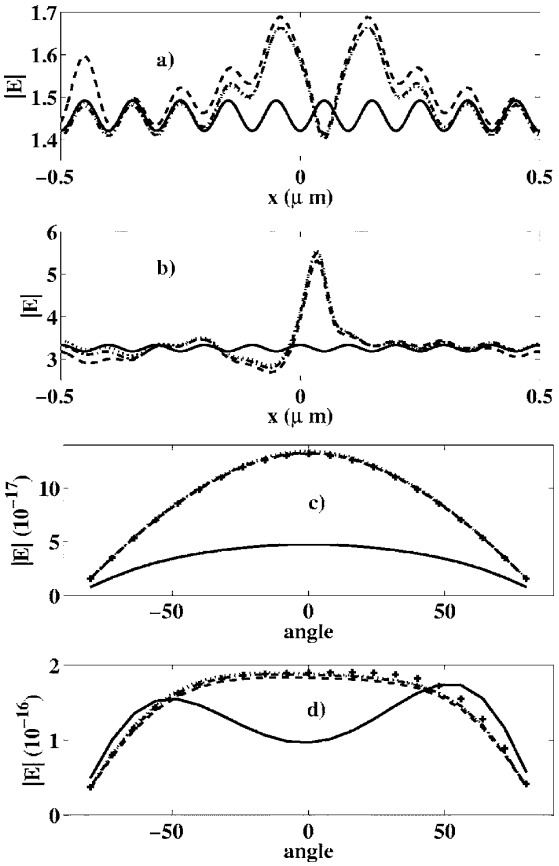

FIG. 4. We present the modulus of the field in the near-field [(a) and (b)] and in the far-field zone [(c) and (d)]. Computations done with $M=M'=3$ are indicated with crosses [not represented in (a) and (b)], for $M=M'=5$ in the dashed line, for $M=M'=11$ in the dot-dashed line, and $M=M'=21$ in the dotted line. (a) and (b) modulus of the field in near field zone: $z=h=100$ nm, and $y=p/2=50$ nm. In the solid line the field obtained without the defect. (a) $\theta=0^\circ$. (b) $\theta=50^\circ$. (c) and (d) modulus of the field in the far-field zone $y=0$ and $x^2+z^2=1$ m, and in the solid line the field scattered by the defect without the double-periodic structure (c) $\theta=0^\circ$. (d) $\theta=50^\circ$.

large (for example, 1600 base cells for $M_{\max}=20$). In Fig. 5 we compare the near field above the defect, in the presence of the infinite grating and for various truncated gratings. The number of periods, $M_{\max}$, is successively equal to 0 (object alone, dotted line), $M_{\max}=5$ (dashed line), and $M_{\max}=20$ (solid line). The field scattered by the defect in the presence of the infinite structure is represented by the bold line. For the angle of incidence $\theta=50^\circ$, Fig. 4, we observe that more than $M_{\max}=20$ is necessary to reproduce the influence of the infinite grating. Under normal incidence, the convergence is reached more easily but still, five periods are not enough to give a good estimation of the field. This numerical test permits the validation of our method and it shows the difficulty of replacing the infinite grating by a truncated one. Note that the time of computation with the classic CDM and the truncated grating with $M_{\max}=20$ is 25 times larger than that of our technique.

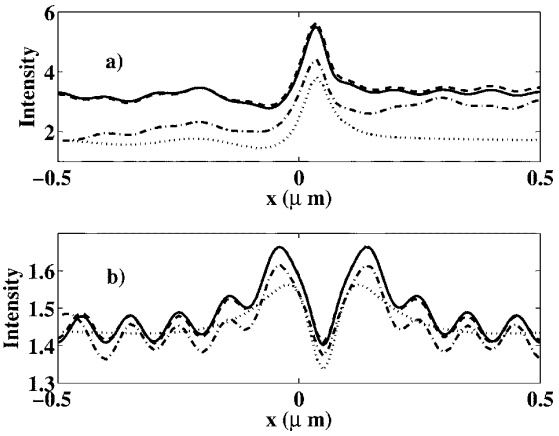

FIG. 5. The configuration used for these curves is the same as the one used in Fig. 4. In the solid line the computation is done as in Fig. 4 with $M=M'=11$. The other curves are obtained by truncating the infinite sum in Eq. (1). The curve in the dotted line is obtained for the object alone ($M_{\max}=0$), in the dot-dashed line with $M_{\max}=5$, and in the dashed line with $M_{\max}=20$ ($M_{\max}$ is defined in the text). (a) $\theta=50^\circ$. (b) $\theta=0^\circ$.

In Fig. 6 we give different examples of the wide possibilities of our method. We keep the same grating as that of Fig. 2 with $p=100$ nm and we change the nature of the defect. All the calculations are performed with $M=M'=11$ since Fig. 4 has shown that convergence had been reached in this case. In Figs. 6(a) and 6(b) we remove a silicon cube [we create a lacuna with an aperiodic object with negative polarizability, opposite to that of the grating, $\alpha_d(\bar{\mathbf{r}}_j)=-\alpha_{Si}(\bar{\mathbf{r}}_j)$]. In Figs. 6(c) and 6(d) the silicon cube at the center of the image is replaced by a silver cube $\alpha_d(\bar{\mathbf{r}}_j)=-\alpha_{Si}(\bar{\mathbf{r}}_j)+\alpha_{Ag}(\bar{\mathbf{r}}_j)$. In Figs. 6(e) and 6(f) the silicon cube at the center of the image is moved at the position $(p/2)\mathbf{u}+(p/2)\mathbf{v}$; the method consists in that case to first cancel one silicon cube by creating a lacuna then adding a cube in silicon at the new position. Note that all these different examples are easily computed once the field susceptibility tensor of the grating is known. When the illumination is normal to the substrate in Figs. 6(a), 6(c), and 6(e), the incident electric field is directed along the x axis. Assuming that the field direction in the structure is close to that of the transmitted incident field, one can explain the pattern of the near-field intensity by invoking the continuity of the field displacement $\mathbf{D}=\varepsilon\mathbf{E}$ along the x axis, (where ε is either the permittivity of vacuum or that of silicon), and the continuity of $\mathbf{E}$ along the y axis. As expected, the field minimum is found inside the silicon pads, and, by continuity, this low field is retrieved along lines oriented along the y axis. The minimum of intensity above the silicon pads neighboring the lacuna on the left and right can also be explained by invoking the continuity of the field displacement. In Fig. 6(c), the central silicon pad has been replaced by a silver pad. The resulting map of intensity is close to that of the unperturbed grating. Indeed, at this wavelength the permittivity of silver is close to that of silicon in

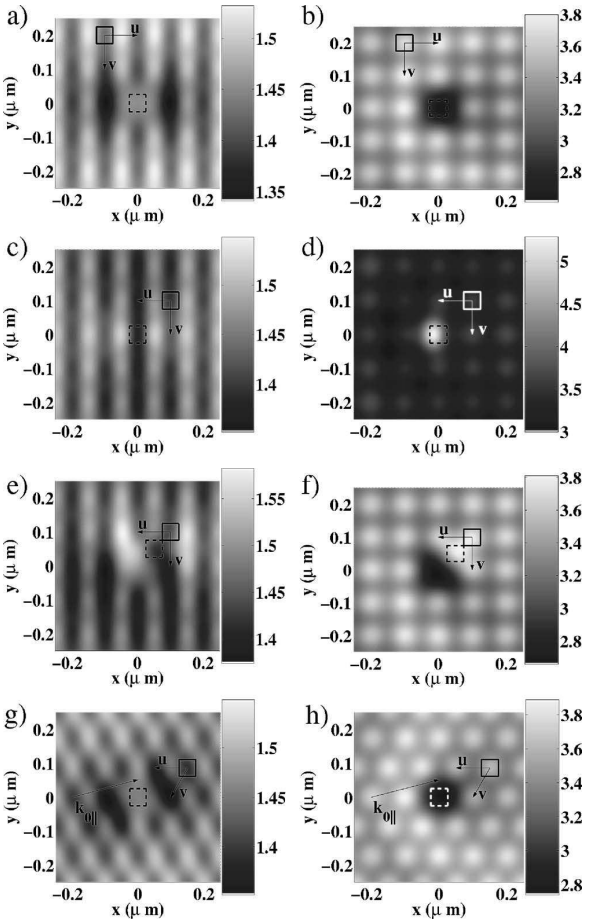

FIG. 6. Near-field images obtained from a double-periodic structure as described in Fig. 2 with $p=100$ nm, $a=50$ nm, $\mathbf{k}_{0\|}$ along the x axis for the first six images, and with $\mathbf{u}=(100,0)$ nm, $\mathbf{v}=(50,86)$ nm, $\mathbf{k}_{0\|}$ as showed in the figure for images (g) and (h). The square in the solid line represents the base cell and $\mathbf{u}$ and $\mathbf{v}$ represent the basis vector of the double-periodic structure. We have taken $h=100$ nm, and $\lambda=600$ nm, and the pads are in silicon. (a), (c), (e), and (g) are obtained for $\theta=0°$. (b), (d), (f), and (h) are obtained for $\theta=50°$. (a), (b), (g), and (h) the square in dashed line represents a lacuna in the double-periodic structure. (c) and (d) the square in the dashed line is in silver. (e) and (f) the square in dashed line is a pad of silicon that has been displaced in the double-periodic structure.

absolute value ($\varepsilon_{Ag}=-13+0.9i$ instead of $\varepsilon_{Si}=15+0.2i$). Hence one expects the intensity inside the silver pad to be similar to that existing in a silicon pad. As a consequence, the intensity map is not strongly modified by the presence of this defect in the grating. In Figs. 6(b), 6(d), and 6(f), the incident angle is $\theta=50°$, hence the transmitted incident field is mostly directed along the z axis and it decays exponentially quicker in air than in silicon. This might explain why the field above the lacuna is smaller than the field above the silicon pads in all these plots. The enhancement of the field above the silver pad can be due to the fact that the polarizability of the silver pad is bigger than that of the silicon pad, so that the radiated field by the defect is stronger than that radiated by a base cell of the grating. In Figs. 6(g) and 6(h), we have changed the grating and taken a triangular lattice [$\mathbf{u}=(100,0)$ nm and $\mathbf{v}=(50,86)$ nm]. The defect consists in a lacuna at the origin. The illumination is chosen so that there is an angle of 10° between the x axis and $\mathbf{k}_{0\|}$. To explain the main features of the intensity map, the same comment as that given for Figs. 6(a) and 6(b) holds also in this case.

IV. CONCLUSION

We have proposed a rigorous numerical technique based on the principles of the coupled dipole method, that permits the simulation of the field scattered by an object embedded in a planar periodic structure. We have presented an efficient means to calculate the field radiated by a dipole in the presence of a grating both in near and far field and studied carefully the convergence of the technique. The advantage of our method is that it addresses any kind of inhomogeneous objects and gratings (in particular the object can be a lacuna). Moreover, in this paper, the periodic structure was deposited on flat homogeneous substrate, but the latter could easily be replaced by a multilayer (that supports guided waves, for example). Once the field susceptibility tensor of the grating is known, the computation cost of the method depends solely on the size of the object compared to the wavelength. It is thus possible to study rapidly many kinds of defects. This method should be very useful for designing optical planar components using cavities in slices of two-dimensional photonic crystal.[20,21]

APPENDIX A: FIELD DIFFRACTED BY THE GRATING IN ABSENCE OF THE DEFECT

Once the field susceptibility tensor of the double-periodic structure is known for any pair of points $(\mathbf{r},\mathbf{r}')$, the field can be evaluated at any position $\mathbf{r}$ by solving the linear system Eq. (4) and using Eq. (5). The last step is then to evaluate the field that would exist in the absence of the defect, $\mathbf{E}_{per}$. The incident beam being a plane wave, $\mathbf{E}_{per}$ can be obtained by any grating methods.[3] With our formulation $\mathbf{E}_{per}$ is simply given through

$$\mathbf{E}_{per}(\bar{\mathbf{r}}_j)=\mathbf{E}^0(\bar{\mathbf{r}}_j)+\sum_{l=1}^{N}\mathbf{S}_{per}(\bar{\mathbf{r}}_j,\bar{\mathbf{r}}_l,\mathbf{k}_{0\|})\alpha_p(\bar{\mathbf{r}}_l)\mathbf{E}_{per}(\bar{\mathbf{r}}_l), \tag{A1}$$

with $j=1,\ldots,N$. To obtain Eq. (A1) we have used the fact that the substrate is illuminated by a plane wave whose wave vector $\mathbf{k}_0$, projected onto the $(\mathbf{u},\mathbf{v})$ plane is $\mathbf{k}_{0\|}$ so that

$$\mathbf{E}^0(\bar{\mathbf{r}}_i+m\mathbf{u}+n\mathbf{v})=\mathbf{E}^0(\bar{\mathbf{r}}_i)\exp[i\mathbf{k}_{0\|}.(m\mathbf{u}+n\mathbf{v})]. \tag{A2}$$

The linear system (of size $3N\times 3N$) represented by Eq. (A1) is easy to solve, and then the electric field due to the double-periodic structure can be computed at any arbitrary position $\mathbf{r}$:

$$\mathbf{E}_{\mathrm{per}}(\mathbf{r}) = \mathbf{E}^0(\mathbf{r}) + \sum_{j=1}^{N} \mathbf{S}_{\mathrm{per}}(\mathbf{r}, \overline{\mathbf{r}}_j, \mathbf{k}_{0\|}) \alpha_{\mathrm{p}}(\overline{\mathbf{r}}_j) \mathbf{E}_{\mathrm{per}}(\overline{\mathbf{r}}_j). \quad \text{(A3)}$$

More details on the numerical evaluation of $\mathbf{E}_{\mathrm{per}}$ can be found in Ref. 3.

APPENDIX B: EFFICIENT COMPUTATION OF THE MAP OF $\mathbf{E}_{\mathrm{per}}(\mathbf{r})$

In this appendix we propose an efficient way to compute $\mathbf{E}_{\mathrm{per}}(\mathbf{r})$ for many positions above the grating with the coupled dipole method. This technique can be useful to obtain the map of the field at different altitudes (for near-field microscopy experiments, for example). Using the previous appendix, we calculate the field on the surface of the base cell at a constant altitude z above the grating. Bearing in mind the pseudoperiodicity of the field, we cast the latter into a Fourier series,

$$\mathbf{E}_{\mathrm{per}}(\mathbf{r}_\|, z) = e^{i\mathbf{k}_{0\|}\cdot\mathbf{r}_\|} \sum_{m,n=-\infty}^{\infty} \boldsymbol{\mathcal{E}}_{m,n}(\mathbf{k}_{0\|}, z) e^{i(m\mathbf{U}+n\mathbf{V})\cdot\mathbf{r}_\|}, \quad \text{(B1)}$$

with

$$\boldsymbol{\mathcal{E}}_{m,n}(\mathbf{k}_{0\|}, z) = \frac{1}{|\mathbf{u}\times\mathbf{v}|} \int\int_{\mathrm{Cell}} \mathbf{E}_{\mathrm{per}}(\mathbf{r}_\|, z) e^{-i(\mathbf{k}_{0\|}+m\mathbf{U}+n\mathbf{V})\cdot\mathbf{r}_\|} d\mathbf{r}_\|. \quad \text{(B2)}$$

Once the modes $\boldsymbol{\mathcal{E}}_{m,n}(\mathbf{k}_{0\|}, z)$ are known, one obtains the field above the double-periodic structure at any altitude z' above the grating with

$$\mathbf{E}_{\mathrm{per}}(\mathbf{r}_\|, z') = e^{i\mathbf{k}_{0\|}\cdot\mathbf{r}_\|} \sum_{m,n=-\infty}^{\infty} \boldsymbol{\mathcal{E}}_{m,n}(\mathbf{k}_{0\|}, z) e^{[i(m\mathbf{U}+n\mathbf{V})\cdot\mathbf{r}_\| + \gamma_{m,n}(z'-z)]}, \quad \text{(B3)}$$

with $\gamma_{m,n} = [k_0^2 - |\mathbf{k}_{0\|} + m\mathbf{U} + n\mathbf{V}|^2]^{1/2}$.

[1] H. Rigneault, F. Lemarchand, and A. Sentenac, J. Opt. Soc. Am. A **17**, 1048 (2000).

[2] F. M. Kahnert, J. Quant. Spectrosc. Radiat. Transf. **79-80**, 775 (2003).

[3] P. C. Chaumet, A. Rahmani, and G. W. Bryant, Phys. Rev. B **67**, 165404 (2003).

[4] E. Popov, M. Nevière, B. Gralak, and G. Tayeb, J. Opt. Soc. Am. A **19**, 33 (2002), and references therein.

[5] C. T. Chan, Q. L. Yu, and K. M. Ho, Phys. Rev. B **51**, 16635 (1995).

[6] R. D. Meade, A. M. Rappe, K. D. Brommer, J. D. Joannopoulos, and O. L. Alherhand, Phys. Rev. B **48**, 8434 (1993); **55**, 15942 (1993).

[7] M. Okano, A. Chutinan, and S. Noda, Phys. Rev. B **66**, 165211 (2002).

[8] P. C. Chaumet, A. Sentenac, and A. Rahmani, Phys. Rev. E **70**, 036606 (2004).

[9] E. M. Purcell and C. R. Pennypacker, Astrophys. J. **186**, 705 (1973).

[10] B. T. Draine, Astrophys. J. **333**, 848 (1988); B. T. Draine and J. Goodman, *ibid.* **405**, 685 (1993), and references therein.

[11] R. Schmehl, B. M. Nebeker, and E. D. Hirleman, J. Opt. Soc. Am. A **14**, 3026 (1997).

[12] P. C. Chaumet and M. Nieto-Vesperinas, Phys. Rev. B **61**, 14119 (2000); **62**, 11185 (2000); **64**, 035422 (2001).

[13] A. Rahmani, P. C. Chaumet, and F. de Fornel, Phys. Rev. A **63**, 023819 (2001).

[14] J. D. Jackson, *Classical Electrodynamics*, 2nd ed. (John Wiley, New York, 1975), p. 395.

[15] P. C. Chaumet and M. Nieto-Vesperinas, Opt. Lett. **25**, 1065 (2000).

[16] P. C. Chaumet, Appl. Opt. **43**, 1825 (2004).

[17] G. P. M. Poppe, C. M. J. Wijers, and A. van Silfhout, Phys. Rev. B **44**, 7917 (1991).

[18] S. Seely and A. D. Poularikas, *Electromagnetics Classical and Modern Theory and Applications*, (Marcel Dekker, New York, 1979).

[19] *Handbook of Optical Constants of Solids*, edited by E. D. Palik (Academic Press, New York, 1985).

[20] C. Sauvan, P. Lalanne, and J. P. Hugonin, Phys. Rev. B **71**, 165118 (2005).

[21] N. Louvion, D. Gérard, J. Mouette, F. de Fornel, C. Seassal, X. Letartre, A. Rahmani, and S. Callard, Phys. Rev. Lett. **94**, 113907 (2005).

The Astrophysical Journal, 607:873–878, 2004 June 1

ON THE IMPORTANCE OF LOCAL-FIELD CORRECTIONS FOR POLARIZABLE PARTICLES ON A FINITE LATTICE: APPLICATION TO THE DISCRETE DIPOLE APPROXIMATION

Adel Rahmani
Laboratoire d'Electronique, Optoélectronique et Microsystèmes-UMR CNRS-ECL 5512 36, Avenue Guy de Collongue, F-69134 Ecully, France; adel.rahmani@ec-lyon.fr

Patrick C. Chaumet
Institut Fresnel (UMR 6133), Faculté des Sciences et Techniques de St Jérôme, Avenue Escadrille Normandie-Niemen, F-13397 Marseille Cedex 20, France; pchaumet@loe.u-3mrs.fr

and

Garnett W. Bryant
Atomic Physics Division, National Institute of Standards and Technology, Gaithersburg, MD 20899-8423; garnett.bryant@nist.gov
Received 2003 November 27; accepted 2004 February 16

ABSTRACT

We investigate the influence of local-field effects on the electromagnetic response of a collection of dipoles. We derive the local-field corrected static polarizability for a collection of dipoles in the case of a scatterer with uniform depolarization. We then use this correction within the discrete dipole approximation to study the scattering of an electromagnetic wave by a spherical particle. The local-field correction leads to a new formulation of the discrete dipole approximation that is exact in the long-wavelength limit and more accurate at finite frequencies. We also discuss the feasibility of a generalization of the local-field correction to arbitrary scatterers.

Subject headings: dust, extinction — scattering

1. INTRODUCTION

The scattering of electromagnetic waves by irregular objects can be addressed from many viewpoints. For simple or special configurations, analytical solutions can be found. However, in the majority of cases the scattering problem is not amenable to an analytic solution and numerical methods must be used. Many computational approaches exist, relying on different strategies (Mishchenko et al. 2000; Kahnert 2003). Among these methods one finds volume integral methods, of which the discrete dipole approximation (DDA) is a discretized version. The DDA was introduced by Purcell & Pennypacker (1973) to study the scattering of light by interstellar dust grains with arbitrary shapes. Dust grains can alter the electromagnetic signature of stars and galaxies, some wavelengths being attenuated or, conversely, strengthened by the scattering process (Draine 2003). An accurate description of the scattering of light by arbitrary dust grains is therefore an essential part of the astrophysics of the interstellar medium. The theoretical foundation of the DDA stems from a simple observation. When an object interacts with an electromagnetic field, it develops a polarization. If one considers a small enough volume inside the object, the induced polarization will be uniform within this volume and hence that small region can be represented by an electric dipole. Accordingly, in the DDA the scatterer is discretized over a cubic lattice and its electromagnetic properties are described by those of a collection of coupled electric dipoles. Therefore, the central quantity in the DDA is the electric polarizability associated with the dipoles (polarizable regions forming the scatterer).

The original formulation of the DDA (Purcell & Pennypacker 1973) used the Clausius-Mossotti (CM) polarizability. However, the CM polarizability is only exact in the long-wavelength (static) regime, and for an isolated dipole in free-space (or a dipole in an infinite lattice). Consequently, problems such as the violation of the optical theorem arise when the DDA is used at finite frequencies, a critical issue for the calculation of absorption cross sections or optical forces and torques (Draine & Weingartner 1996; Chaumet & Nieto-Vesperinas 2000; Chaumet et al. 2002). Subsequent formulations of the DDA improved on the CM polarizability by accounting for retardation and propagation effects (Draine & Flatau 1994 and references therein). For instance, Draine (1988) introduced a radiation-reaction correction to the CM polarizability, thereby ensuring that the optical theorem is satisfied (i.e., the total electromagnetic energy is conserved). Later, Draine & Goodman (1993) introduced the lattice dispersion relation (LDR) correction to derive a polarizability such that the lattice would reproduce the propagation properties of a continuum. Other forms of the polarizability were also proposed in order to improve the performance of the DDA at finite frequencies (Dungey & Bohren 1991; Lakhtakia 1992). A point worth emphasizing is that although several prescriptions exist for the polarizability, *they all reduce to the Clausius-Mossotti expression in the long-wavelength (static) limit*. In other words, it has been widely accepted that the CM polarizability was the correct starting point and that any improvement of the DDA in describing electromagnetic scattering has to come from an improvement of how dynamic (i.e., finite frequency) effects are accounted for.

However, in his study of light scattering by spherical particles Draine (1988) pointed out some discrepancies between the DDA and the exact Mie calculation in the long-wavelength limit. These discrepancies are most noticeable for large values of $|n-1|$ (n being the complex refractive index of the sphere), and are not due to a mere convergence issue since increasing the number of dipoles does not solve the problem. In the long-wavelength regime radiative corrections are irrelevant; therefore, the problem pointed out by Draine suggests that the conventional form of the DDA overlooks some fundamental issues that exist in the long-wavelength regime.

While this long-wavelength anomaly may hinder high-precision scattering calculations at any wavelength (the

finer the discretization, the closer to the long-wavelength limit), it will have particularly dramatic consequences in the infrared (IR) part of the electromagnetic spectrum ($1\ \mu\text{m} <$ wavelength $< 300\ \mu$m). Indeed, consider the scattering of electromagnetic radiation by interstellar dust particles. In the IR region, two effects will contribute to the dramatic increase of the long-wavelength anomaly. First, for a given size of the scatterer as the wavelength gets larger one moves deeper into the long-wavelength regime. The second effect results from the large refractive index (and the usually concomitant large absorption) that most materials exhibit as the wavelength increases, which demands a fine discretization in the DDA and hence ensures again that the long-wavelength regime will be attained. These two effects can drastically reduce the accuracy of the DDA, putting the method in a delicate situation. A coarse discretization will fail at describing accurately the scattering properties of the particle. But on the other hand, a fine discretization will hit the long-wavelength anomaly. The only way to overcome this problem is by understanding the physics of the scattering of electromagnetic waves by a collection of dipoles in the long-wavelength regime.

In this paper, we address the problem of the static polarizability for a dipole in a finite lattice, by deriving an expression of the polarizability that takes into account the particular environment of each dipole. Because the correction is made on the static polarizability, the usual radiative corrections, such as the LDR, still apply. We illustrate the relevance of local-field corrections by computing the scattering properties of a spherical particle and comparing them to the exact Mie results. We also discuss the possibility of extending this approach to arbitrary scatterers.

2. DERIVATION OF A STATIC POLARIZABILITY THAT ACCOUNTS FOR LOCAL-FIELD EFFECTS

The idea behind our derivation is quite simple. When a static electric field is applied to a collection of small polarizable particles, each particle will develop an induced dipole moment that will depend on the applied field but also on the field resulting from all other induced dipoles. This local-field effect will be responsible for all particle not having an identical polarization, which in other terms means that not all particles will have the same effective polarizability. The simplest way to see this is to consider a slab of matter discretized over a cubic lattice with infinite extension along directions x and y, and a finite thickness, larger than a few layers, along z. From symmetry considerations, a dipole near the center of the slab should have equal polarizabilities along directions x, y, and z. On the other hand, for a dipole at the surface of the slab one should expect that the response (polarizability) to an applied field within the xy plane will differ from the response to a field applied along z. We now express this idea in a more formal way. For the sake of clarity we reproduce here the derivation of the static polarizability as described in Rahmani et al. (2002). However, we will make an essential distinction between two classes of scattering objects that was not made in Rahmani et al. (2002). The first class, with uniform depolarization (response of the material due to polarization charges when an electric field is applied), is discussed in the next section. The second class, with nonuniform depolarization, will be discussed in § 3.2.

2.1. *Class A: Objects with Uniform Depolarization*

From a mathematical viewpoint, the first class of objects comprises shapes for which the depolarization tensor is uniform over the volume of the object. The depolarization tensor $\mathbf{L}$ can be viewed as a geometrical factor whose value is determined by the shape of the object (Yaghjian 1980). From a physical viewpoint, these are objects that respond to a uniform static electric field by exhibiting a uniform electric polarization (not necessarily parallel to the initial field). This class includes objects such as slabs, infinite cylinders, spheres, and spheroids. Consider a class A homogeneous scatterer with permittivity ϵ (assumed to be scalar for simplicity), whose electromagnetic properties are approximated by a set of N electric dipoles with electric polarizability α_i ($i = 1, N$), arranged on a cubic lattice with spacing d. The self-consistent local field at subunit i is

$$\boldsymbol{E}_i^{\rm loc}(\omega) = \boldsymbol{E}_i^0(\omega) + \sum_{j\neq i} \mathbf{F}_{ij}(\omega)\alpha_j(\omega)\boldsymbol{E}_j^{\rm loc}(\omega). \tag{1}$$

$\boldsymbol{E}_i^0(\omega)$ is the incident field at subunit i, $\mathbf{F}(\omega)$ is the free-space field susceptibility (Green tensor), and ω is the angular frequency of the electromagnetic wave. The sum over j runs over all the subunits forming the scatterer. Note that the term $j = i$ is not included in the sum; this term is automatically dealt with by accounting for the finite volume of the dipoles.

We make the electrostatic approximation ($\omega = 0$; the angular frequency will be omitted in the equations henceforth) and consider a uniform applied field $\boldsymbol{E}^0$. In the case where the macroscopic field $\boldsymbol{E}^m$ is uniform over the lattice, it can be related to the applied field through the (uniform) depolarization tensor $\boldsymbol{L}$ such that

$$\left(1 + \frac{\epsilon - 1}{4\pi}\mathbf{L}\right)\boldsymbol{E}^m = \boldsymbol{E}^0, \tag{2}$$

where 1 is the identity tensor. Once the macroscopic field is introduced in equation (1) we obtain

$$\boldsymbol{E}_i^{\rm loc} = \left(1 + \frac{\epsilon - 1}{4\pi}\mathbf{L}\right)\boldsymbol{E}^m + \sum_{j\neq i} \mathbf{F}_{ij}\alpha_j\boldsymbol{E}_j^{\rm loc}. \tag{3}$$

By definition, the local-field tensor $\mathbf{\Lambda}_i$ satisfies

$$\boldsymbol{E}_i^{\rm loc} = \mathbf{\Lambda}_i\boldsymbol{E}^m. \tag{4}$$

Using the fact that the (uniform) polarization can be written as

$$\boldsymbol{P} = \frac{\alpha_i}{d^3}\boldsymbol{E}_i^{\rm loc} = \frac{\epsilon - 1}{4\pi}\boldsymbol{E}^m = \frac{\epsilon - 1}{4\pi}\mathbf{\Lambda}_i^{-1}\boldsymbol{E}_i^{\rm loc}, \tag{5}$$

we can express the polarizability in terms of the local-field tensor:

$$\alpha_i = \frac{\epsilon - 1}{4\pi}\mathbf{\Lambda}_i^{-1}d^3. \tag{6}$$

The local-field tensor is derived by using equations (4)–(6) to express the local field in terms of the macroscopic field in equation (3), leading to

$$\mathbf{\Lambda}_i = 1 + \frac{\epsilon - 1}{4\pi}\mathbf{L} + \sum_{j\neq i}\mathbf{F}_{ij}\frac{\epsilon - 1}{4\pi}d^3. \tag{7}$$

The local-field corrected static polarizability (LFCSP) of equation (6) reduces to the CM expression only for a single,

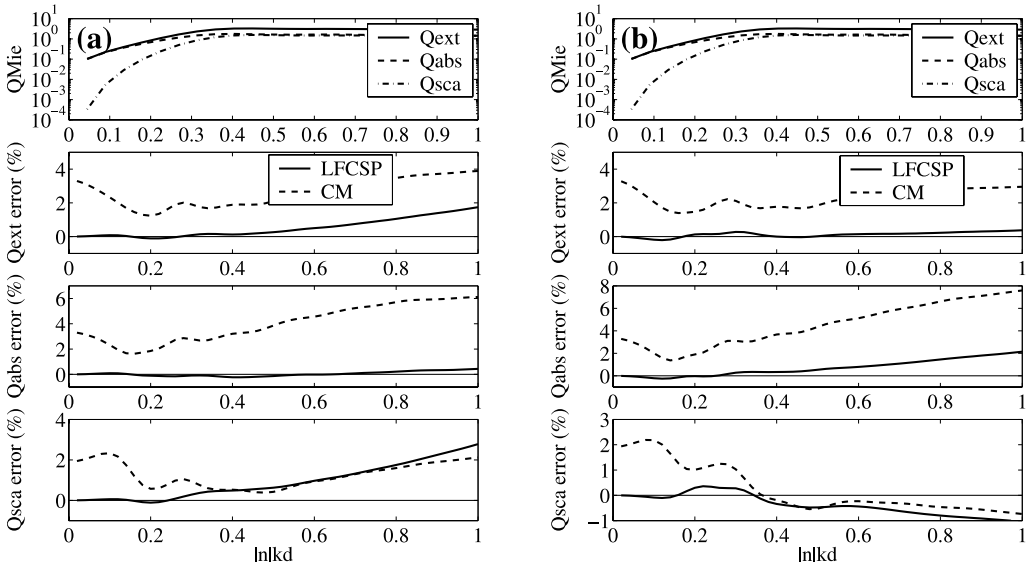

FIG. 1.—Scattering properties of a pseudosphere with $N = 17904$ and $\epsilon = n^2 = 5 + 5i$. The incident wave vector is along direction [1 1 1] of the lattice. The electric field is polarized along direction $[2\ \bar{1}\ \bar{1}]$ of the lattice. From top to bottom the figure shows extinction, absorption, and scattering efficiencies ($Q_{\rm ext}$, $Q_{\rm abs}$, and $Q_{\rm sca}$; *top panel*) as given by Mie as a function of the normalized lattice spacing $|n|kd$, where k is the free-space wave vector of the incident light; and the relative error in the DDA computed values of the extinction, absorption, and scattering efficiencies (*lower three panels*). The static polarizability (*dashed lines*) is defined according to the Clausisu-Mossotti relation. The static polarizability (*solid lines*) is defined according to eq. (6). A dynamic correction is applied to both forms of the static polarizability. (*a*) Lattice dispersion relation (LDR); (*b*) radiation reaction.

isolated dipole in free space, or a dipole in an infinite lattice (for any practical purpose, a dipole more than a few lattice sites away from any interface can in general be considered as immersed in an infinite lattice).

We emphasize that our correction affects the static polarizability, i.e., the LFCSP prescription is used as a replacement of the CM expression. Consequently, previously derived corrections that account for radiation-reaction (Draine 1988) or propagation effects (Draine & Goodman 1993) can be applied to the LFCSP.

Rahmani et al. (2002) illustrated the relevance of the LFCSP by computing the field inside and outside a slab. Note that the slab was actually treated as a three-dimensional problem using a generalization of the DDA to periodic systems (Chaumet et al. 2003). This made it possible to use the conventional, three-dimensional expressions for the field susceptibility and the polarizability. Using the example of a slab, we showed that accounting for the influence of the local environment of the dipoles on their electromagnetic response led to a more accurate estimate of the macroscopic field inside the slab as well as a more accurate calculation of reflected and transmitted fields.

However, it is of interest to test the prescription of equations (6) and (7) on a fully three-dimensional scatterer. In the next section, we consider the case of a spherical scatterer.

2.2. *Example: Light Scattering by a Homogeneous Spherical Particle*

The case of a homogeneous spherical scatterer is of particular interest because an analytic solution is known in the form of a Mie series. We shall use the Mie result as our reference in the computation of the scattering properties of spheres. The Mie scattering numerical code we use is the Bohren-Huffman Mie scattering subroutine modified by Draine. Our DDA light-scattering code is derived from our DDA spontaneous emission code (Rahmani et al. 2001; Rahmani & Bryant 2002) by solving for the electric field instead of the field susceptibility. The local field at each lattice site is found by solving a linear system using the QMR iterative solver developed by Freund & Nachtigal (1991). For free-space computations, we perform matrix-vector multiplications using the Temperton fast Fourier transform routine (FFT; Temperton 1992) as implemented in the DDSCAT code of Draine and Flatau.[1]

For a homogeneous sphere with permittivity ϵ, the depolarization tensor $\mathbf{L}$ is constant within the volume of the sphere and equal to $4\pi/3$ (note that our definition of $\mathbf{L}$ and that of Yaghjian 1980 differ by a factor 4π). Following equation (7), the local-field tensor becomes

$$\mathbf{\Lambda}_i = \frac{\epsilon + 2}{3} + \frac{\epsilon - 1}{4\pi} d^3 \sum_{j \neq i} \mathbf{F}_{ij}, \tag{8}$$

where the sum involves the static limit of the free space field susceptibility. It is of interest to note that d^3 times the sum is a finite lattice sum that depends only on the relative position of the dipoles on the lattice. Therefore, the sum pertaining to a homogeneous sphere with a given number N of dipoles need not be computed again if the wavelength of the incident light, the permittivity of the sphere, the lattice spacing or any other parameter is changed.

We plot in Figures 1, 2, and 3 the relative error (using Mie as a reference) for the extinction, absorption, and scattering efficiencies, as a function of $|n|kd$ where n is the complex refractive index of the sphere, k the magnitude of the wave

[1] DDSCAT is a software package developed by Draine and Flatau that applies the DDA to calculate scattering and absorption of electromagnetic waves by targets with arbitrary geometries and complex refractive index. DDSCAT is available at http://www.astro.princeton.edu/~draine/DDSCAT.6.0.html. Note that the routines we use come from ver. 5.10 of DDSCAT.

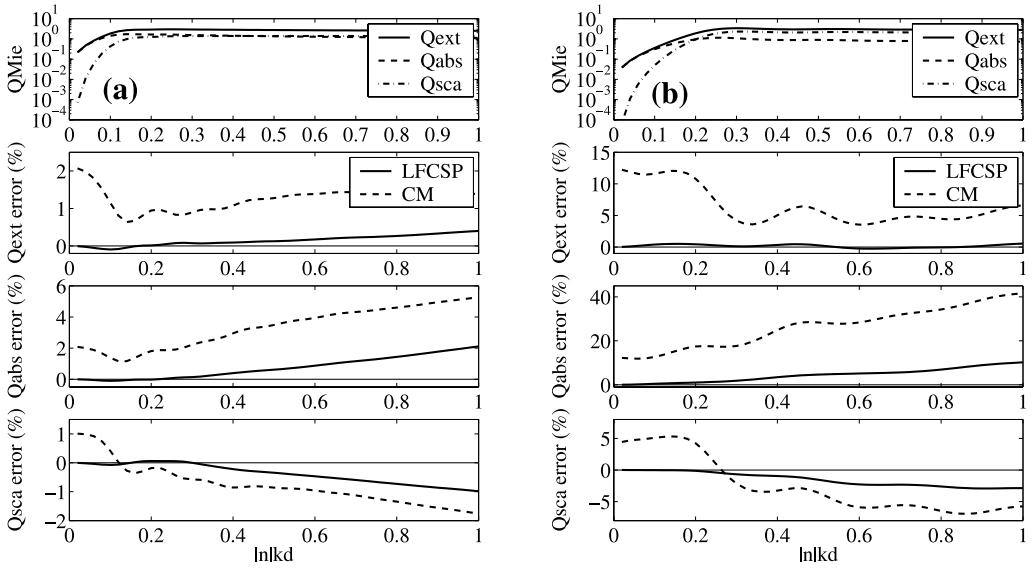

FIG. 2.—Same as Fig. 1, but for (*a*) silicate at 20 μm ($\epsilon = n^2 = 2.3 + 4i$) and (*b*) silicon carbide at 12 μm ($\epsilon = n^2 = -9 + 20i$). The radiation-reaction correction is used in both cases.

vector in vacuum of the incident light, and d the DDA lattice spacing. The scatterer is a pseudosphere composed of $N = 17,904$ dipoles. The plots in all the figures are for an incident field with a wave vector parallel to direction $[1\,1\,1]$ of the lattice and polarized along direction $[2\,\bar{1}\,\bar{1}]$. Other combinations of propagation direction and polarization lead to similar results for the effectiveness of the LFCSP prescription. The extinction and absorption efficiencies are calculated from the respective cross sections (Draine 1988, eqs. [3.02] and [3.06]). The scattering efficiency is computed as the difference of the two other efficiencies after we check that it yields a value in agreement with what can be found by a direct computation (Draine 1988, eq. [3.07]).

A good assessment of the relevance of the LFCSP prescription can be made by considering a scatterer with $|\epsilon^2 - 1| > 1$. We consider in Figures 1*a* and 1*b* a sphere with permittivity $\epsilon = 5 + 5i$. The two figures differ by the nature of the radiative correction. On Figure 1*a*, the LDR prescription is used (in addition to the "static prescription"; either CM or LFCSP), whereas the radiation-reaction corrective term is used in Figure 1*b*. We consider two dynamic correction terms merely to illustrate the fact that the LFCSP leads to an improvement of the accuracy of the DDA irrespective of the specifics of the additional correction procedure used to account for finite frequency effects. The overall effect of the LFCSP is to bring the DDA computation closer to the Mie result. In

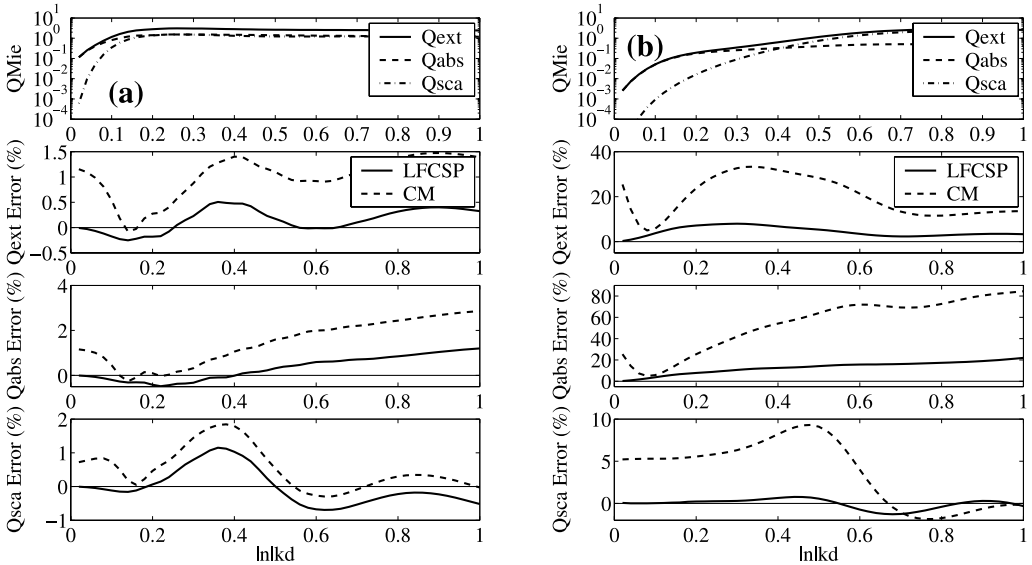

FIG. 3.—Same as Fig. 1, but for graphite at 20 μm. (*a*) Electric field parallel to c-axis, $\epsilon = n^2 = 3 + 1.4i$; (*b*) electric field perpendicular to c-axis, $\epsilon = n^2 = -34 + 140i$. The radiation-reaction correction is used.

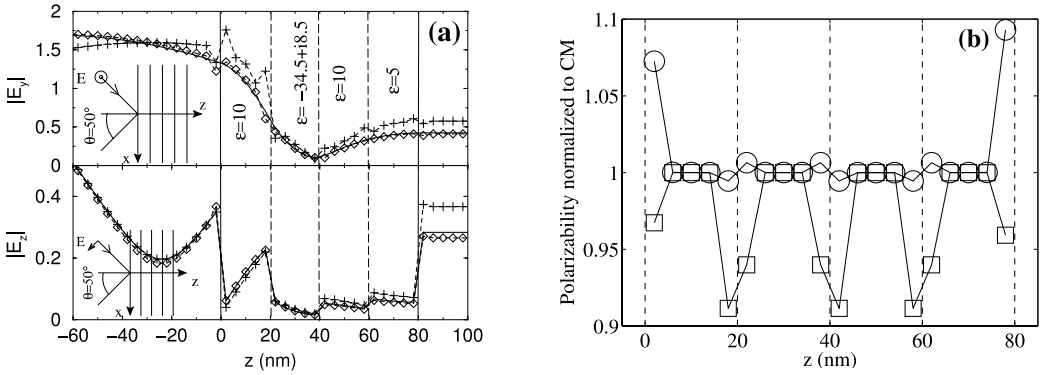

FIG. 4.—(*a*): Reflected, internal, and transmitted electric field for a multilayered slab. The polarization of the incident light is shown on the figures. *Solid line*: exact result; *dashed line with crosses*: DDA using CM; *dashed line with diamonds*: DDA with LFCSP. The radiation-reaction prescription is applied to both forms of the static polarizability. (*b*): Plot of the *xx* (*squares*) and the *zz* (*circles*) components of the LFCSP normalized to the CM result for the structure of Fig. 3*a*. The dashed vertical lines mark the interfaces.

particular, the tendency of the DDA to overestimate the absorption is noticeably moderated by the use of the LFCSP. Another striking feature is that the local-field corrected DDA converges toward the exact result, whereas the conventional DDA (using the CM polarizability) converges toward a result with a relative error of a few percent in the long-wavelength limit ($|n|kd \rightarrow 0$). We emphasize that this does not depend on the permittivity of the sphere; the local-field correction of equation (8) was designed precisely to yield the exact result in the static limit. This point is illustrated further in the next figures. As we mentioned previously, the DDA might have great difficulties at describing accurately scattering processes in the infrared region of the spectrum. Figures 2*a* and 2*b* pertain to a spherical particle with permittivities $\epsilon = n^2 = 2.3 + 4i$ and $\epsilon = n^2 = -9 + 20i$, respectively. These rounded-off values are close to the permittivity of silicate around 20 μm and that of silicon carbide around 12 μm (Laor & Draine 1993). Figures 3*a* and 3*b* pertain to a spherical particle with permittivities $\epsilon = n^2 = 3 + 1.4i$ and $\epsilon = n^2 = -34 + 140i$, respectively, which corresponds to graphite around 20 μm with the electric field parallel (Fig. 3*a*) or perpendicular (Fig. 3*b*) to the *c*-axis (Laor & Draine 1993).

One can see that, irrespective of the permittivity, the LFCSP prescription leads to a higher accuracy of the DDA. Most striking is the fact that the DDA using our new prescription *always* converges toward the exact result in the long-wavelength limit. Moreover, we see again that the LFCSP lessens the tendency of the DDA to overestimates absorption. This is most noticeable in Figure 3*b*, where the imaginary part of the permittivity is large.

These examples demonstrate the dramatic effect that the local-field correction has on the computation of the electromagnetic properties of a sphere with the DDA, despite the fact that the correction is significant only for the dipoles at the surface of the sphere. In the next section, we discuss the possibility of a generalization of this approach to arbitrary scatterers.

3. SCATTERERS WITH ARBITRARY SHAPE

3.1. *Class A: Objects with Uniform Depolarization*

For this class of objects, the LFCSP is readily found using equation (7) with the appropriate value of **L** in place of the $4\pi/3$ value for a sphere. For objects from this class, or sometimes a collection of objects as illustrated in Figure 4*a*, the use of the LFCSP prescription will make the DDA converge toward the exact result in the long-wavelength limit and should improve significantly the performances of the DDA at finite frequencies, not only for far-field computations but for internal fields as well. We emphasize again that the LFCSP will differ from the CM polarizability only near interfaces. To illustrate this point, we plot in Figure 4*b* the *xx* (*squares*) and *zz* (*circles*) components of the LFCSP, normalized to the CM result, for the multilayered structure of Figure 4*a*. Figure 4*b* shows that only the dipoles at the interfaces have optical responses that depart notably from the CM prescription.

3.2. *Class B: Objects with Nonuniform Depolarization*

This class comprises objects that would exhibit a nonuniform polarization when placed in a uniform static field. One of the simplest examples of such an object is a dielectric cube. For this class of objects, the derivation described above or in Rahmani et al. (2002) is not valid.[2]

While investigating the possibility of extending the LFCSP to class B objects, we found that Karam (1997) derived the general expression for the macroscopic field at position $\boldsymbol{r}$ inside an arbitrary object placed in a static field $\boldsymbol{E}^0$. The macroscopic field reads

$$\boldsymbol{E}^m(\boldsymbol{r}) = \boldsymbol{E}^0(\boldsymbol{r}) - \frac{(\epsilon - 1)}{4\pi} \int_S \frac{\hat{R}\, d\boldsymbol{s}'}{|\boldsymbol{r} - \boldsymbol{r}'|^2} \boldsymbol{E}^m(\boldsymbol{r}'), \qquad (9)$$

where ϵ is the permittivity of the object, $\hat{R} = (\boldsymbol{r} - \boldsymbol{r}')/|\boldsymbol{r} - \boldsymbol{r}'|$, and the integration is performed over the surface S enclosing the object. Note that when the macroscopic field is uniform, equation (9) reduces to equation (2), with the depolarization tensor given by

$$\boldsymbol{L} = \int_S \frac{\hat{R}\, d\boldsymbol{s}'}{|\boldsymbol{r} - \boldsymbol{r}'|^2}. \qquad (10)$$

[2] Note that because the necessity of a uniform depolarization was not explicit, eq. (8) in Rahmani et al. (2002) is misleading as it does not include the simplifications that result from the depolarization tensor being uniform. However, it is clear that eq. (8) is not valid for a class B object since it would yield a nonsymmetric static polarizability; a physical impossibility.

Therefore, the obstacle in deriving the LFCSP for a class B objects lies in the fact that a simple term of proportionality between the incident and the macroscopic field cannot be found. However, it will be of great interest to investigate the possibility of estimating numerically the surface effect of equation (9) in order to derive a more appropriate expression of the static polarizability when the DDA is used to represent class B objects. We are currently working to extend the LFCSP to this class of objects.

4. CONCLUSION

We have considered an electric dipole on a lattice and we have shown that its electrostatic response (static polarizability) depends on its local environment (local-field effect). From this observation, we have derived a new prescription for the static polarizability to be used in the DDA in place of the Clausius-Mossotti expression. Our general derivation is valid for any value of the refractive index and always converging to the exact result in the long-wavelength limit. We also showed that, at finite frequencies, the usual radiative corrections to the polarizability can still be used. As a result, when the DDA is used to model light scattering by a spherical scatterer, the accuracy of the computation is globally enhanced and the long-wavelength problem pointed out by Draine (1988) is resolved. Moreover, our prescription improves significantly the description of strongly absorbing material. The derivation of the static polarizability presented in this work is valid for any scatterer whose depolarization tensor, and by extension macroscopic field, is uniform. For other shapes, there is no simple factor of proportionality between the macroscopic field and the incident field, which hinders the derivation of a static polarizability that account for local-field effects. However, as we have shown, the local-field correction can lead to significant improvements in the modeling of scattering and internal properties of scatterers, particularly in the infrared region. Therefore, even an approximate solution of the local-field problem is worth investigating.

REFERENCES

Chaumet, P. C., & Nieto-Vesperinas, M. 2000, Opt. Lett., 25, 1065
Chaumet, P. C., Rahmani, A., & Bryant, G. W. 2003, Phys. Rev. B, 67, 165404
Chaumet, P. C., Rahmani, A., & Nieto-Vesperinas, M. 2002, Phys. Rev. Lett., 88, 126601
Draine, B. T. 1988, ApJ, 333, 848
———. 2003, ARA&A, 41, 241
Draine, B. T., & Flatau, P. J. 1994, J. Opt. Soc. Am. A, 11, 1491
Draine, B. T., & Goodman, J. 1993, ApJ, 405, 685
Draine, B. T., & Weingartner, J. C. 1996, ApJ, 470, 551
Dungey, C. E., & Bohren, C. F. 1991, J. Opt. Soc. Am. A, 8, 81
Freund, R. W., & Nachtigal, N. M. 1991, Numer. Math., 60 315
Kahnert, F. M. 2003, J. Quant. Spectrosc. Radiat. Tranfer, 79, 775
Karam, M. A. 1997, Appl. Opt., 36, 5238
Lakhtakia, A. 1992, Int. J. Mod. Phys. C, 34, 583
Laor, A., & Draine, B. T. 1993, ApJ, 402, 441
Mishchenko, M. I., Hovenier, J. W., & Travis, L. D. 2000, Light Scattering by Nonspherical Particles (San Diego: Academic Press)
Purcell, E. M., & Pennypacker, C. R. 1973, ApJ, 186, 705
Rahmani, A., & Bryant, G. W. 2002, Phys. Rev. A, 65, 033817
Rahmani, A., Chaumet, P. C., & Bryant, G. W. 2002, Opt. Lett., 27, 2118
Rahmani, A., Chaumet, P. C., & de Fornel, F. 2001, Phys. Rev. A, 63, 023819
Temperton, C. 1992, SIAM J. Sci. Stat. Comput., 13, 676
Yaghjian, A. D. 1980, Proc. IEEE, 68, 248

2118 OPTICS LETTERS / Vol. 27, No. 23 / December 1, 2002

Coupled dipole method with an exact long-wavelength limit and improved accuracy at finite frequencies

Adel Rahmani

Atomic Physics Division, National Institute of Standards and Technology, Gaithersburg, Maryland 20899-8423

Patrick C. Chaumet

Institut Fresnel (Unité Mixte de Recherche 6133), Faculté des Sciences et Techniques de St. Jérôme, Avenue Escadrille Normandie-Niemen, F-13397 Marseille Cedex 20, France

Garnett W. Bryant

Atomic Physics Division, National Institute of Standards and Technology, Gaithersburg, Maryland 20899-8423

Received September 6, 2002

We present a new formulation of the coupled dipole method that accounts for local-field effects and is exact in the long-wavelength limit. This formulation also leads to improved accuracy of the description of light-scattering processes at finite frequencies. © 2002 Optical Society of America

OCIS codes: 260.2110, 290.0290.

Since its introduction in the early seventies[1] the discrete dipole approximation, also called the coupled dipole method (CDM), has been used extensively to study many problems, such as light scattering by arbitrary objects,[2–4] near-field molecular probes,[5] optical forces,[6] and nanosources in microcavities.[7] The versatility of the method resides in the simplicity of its formalism. An arbitrary scatterer can always be viewed as a collection of polarizable subunits. Provided that the sizes of the subunits are small enough compared with the local spatial variations of the field, the dipole approximation applies, and each subunit can be represented by a polarizability α. Several formulations of the CDM exist. They differ by the polarizabilities used to describe the optical response of the subunits. Nevertheless, the polarizabilities always reduce to the Clausius–Mossotti (CM) expression in the long-wavelength limit. As it is often pointed out, for a uniform excitation the CM expression for the polarizability of a small particle is exact in the long-wavelength limit. However, as demonstrated by Draine,[2] when the CM polarizability is used within the CDM to describe a small particle as a collection of dipoles, one does not get the exact result in the long-wavelength limit. The reason for this is that the common assumption that all dipoles must have the same optical response, irrespective of their environment, is flawed. Indeed, near interfaces, one must account for the particular local environment of each dipole.

In this Letter we present a form of the CDM that is exact in the long-wavelength regime. This form is achieved by derivation of a self-consistent local-field correction that accounts for the particular environment of each subunit. Accordingly, the performance of the CDM at finite frequencies is improved as well. We start with a general derivation of the self-consistent local-field correction and of the corresponding polarizability. Consider an arbitrary scatterer discretized over a cubic lattice with spacing d. The self-consistent local field at subunit i is given by

$$\mathbf{E}_i^{\mathrm{loc}} = \mathbf{E}_i^{0} + \sum_{j \neq i} \mathsf{F}_{ij} \alpha_j \mathbf{E}_j^{\mathrm{loc}}, \tag{1}$$

where $\mathbf{E}_i^{0}$ is the incident field at subunit i and F is the free-space field susceptibility,[8] i.e., $F_{ij}\alpha_j\mathbf{E}_j^{\mathrm{loc}}$, gives the electric field at location i produced by subunit j. The sum over j runs over all the subunits ($j \neq i$) that form the scatterer. Our aim is to find the exact local-field factor in the long-wavelength limit (electrostatic approximation) from which we will infer the polarizability. After making the electrostatic approximation and introducing macroscopic field $\mathbf{E}^m$, which is related to the incident field by $\mathbf{E}^m[1 + \mathsf{L}_i(\epsilon_i - 1)/(4\pi)] = \mathbf{E}_i^{0}$, with depolarization tensor L_i, we find that Eq. (1) becomes

$$\mathbf{E}_i^{\mathrm{loc}} = \left(1 + \mathsf{L}_i \frac{\epsilon_i - 1}{4\pi}\right)\mathbf{E}_i^{m} + \sum_{j \neq i} \mathsf{F}_{ij} \alpha_j \mathbf{E}_j^{\mathrm{loc}}, \tag{2}$$

where 1 is the identity tensor and ϵ_i, assumed to be scalar for simplicity, is the permittivity of subunit i. By definition, local-field tensor Λ_i satisfies

$$\mathbf{E}_i^{\mathrm{loc}} = \Lambda_i \mathbf{E}_i^{m}. \tag{3}$$

Using the fact that the polarization can be written as

$$\mathbf{P}_i = \frac{\alpha_i}{d^3}\,\mathbf{E}_i^{\mathrm{loc}}, \tag{4}$$

$$= \frac{\epsilon_i - 1}{4\pi}\,\mathbf{E}_i^{m}, \tag{5}$$

$$= \frac{\epsilon_i - 1}{4\pi}\,\Lambda_i^{-1}\mathbf{E}_i^{\mathrm{loc}}, \tag{6}$$

0146-9592/02/232118-03$15.00/0

we can express the polarizability in terms of the local-field tensor:

$$\alpha_i = \frac{\epsilon_i - 1}{4\pi} \Lambda_i^{-1} d^3. \tag{7}$$

We derive the local-field tensor by use of Eqs. (3)–(7) to express the local field in terms of the macroscopic field in Eq. (2), leading to

$$\Lambda_i = \mathsf{C}_i + \sum_{j \neq i} \mathsf{F}_{ij} \frac{\epsilon_j - 1}{4\pi} d^3 \mathsf{C}_j^{-1} \mathsf{C}_i \,, \tag{8}$$

where the tensors C_i are defined as

$$\mathsf{C}_i = 1 + \frac{\epsilon_i - 1}{4\pi} \mathsf{L}_i \,. \tag{9}$$

The depolarization tensor, L_i, is essentially a geometrical factor whose value is determined by the shape of the object.[9] Note that to arrive at Eq. (8) we assumed that the initial, static field $\mathbf{E}^0$ was uniform (static limit of a plane wave, for instance). If this were not the case, there would simply be an additional term in the sum on the right-hand side of Eq. (8) to account for the variation of $\mathbf{E}^0$ from one subunit to another.

The polarizability of Eq. (7) reduces to the CM expression only for a single, isolated dipolar scatterer or a subunit lying away from any interface. In the general case the polarizability accounts for the environment of the subunit via the local-field tensor [Eq. (8)]. Note that because of its dependence on the environment the polarizability can be anisotropic even for an isotropic material (scalar ϵ). We emphasize that Eq. (7) replaces the CM expression. This means that the usual radiation reaction correction[2] can now be applied to Eq. (7). All the results presented below include the radiation-reaction correction.

To illustrate the method presented above, we consider a slab (infinite along directions x and y) of material with permittivity ϵ and thickness t along direction z. This configuration has an analytic solution that will be our reference. Note that for a slab (as well as for ellipsoids and infinite cylinders[10]) L_i is uniform over the slab. For more-complex geometries L_i is not constant and can easily be calculated numerically.[9]) We emphasize that although the geometry of a slab allows a two-dimensional treatment we describe the slab as a three-dimensional object, using an extension of the CDM to periodic structures.[11] This approach allows us to use three-dimensional expressions for the polarizabilities and will make it easier to apply the present approach to more-complex scatterers. The case of a slab makes the physical content of Eq. (7) obvious. A subunit near the surface of the slab will respond (be polarized) differently depending on the polarization of the incident field, because of the subunit's particular environment near the interface. However, a subunit that lies within the bulk of the slab will be have an isotropic response.

We focus on the behavior of the new formulation of the CDM at finite frequencies. Indeed, in the long-wavelength limit, Eq. (7) is exact by design. We first consider a dielectric slab ($\epsilon = 20$, $t = 50$ nm) illuminated by a plane wave, with wavelength $\lambda = 400$ nm and angle of incidence $\theta = 50°$, polarized in the xz plane. The slab occupies the region $0 \leq z \leq 50$ nm and is discretized into 20 layers. We choose a large value of ϵ to emphasize the effects of the new formulation of the CDM. We compare in Fig. 1 the x component of the macroscopic field outside and inside the slab, for the old (conventional) and new forms of the CDM, with the exact result. The old CDM predicts strong, nonphysical oscillations of the field inside the slab. These oscillations have been pointed out before, although they have not been explained.[12–14] They result from the erroneous assumption that the bulk local-field correction can be used for every subunit. Indeed, the assumption that each subunit of the CDM is well described by the CM polarizability and experiences a local-field correction $(\epsilon + 2)/3$ is incorrect near interfaces. However, the new form of the CDM reduces drastically the oscillations of the macroscopic field inside the slab. As a result, the reflected and the transmitted fields are improved as well. We emphasize that the new local-field correction is most important at interfaces. In general, the new polarizability differs significantly from the CM value only for the first two or three layers near an interface.

To illustrate further the influence of the local-field correction on the calculation of the scattered field, we present in Figs. 2 and 3 the relative error (in percent) of the transmitted field as a function of the number of layers used to discretize the slab. The incident light is polarized in the xz plane or along y, and we represent the x or the y components of the field. The z component has a behavior similar to the x component. The inclusion of local-field corrections [Eq. (7)] improves significantly the convergence of the CDM for dielectric (Fig. 2), metals (Fig. 3), and strongly absorbing media (not shown). Because the optical response of each subunit accounts for its local environment, the induced dipole moment at each subunit is calculated more precisely,

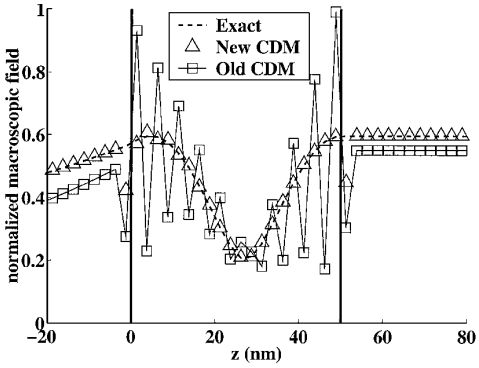

Fig. 1. Macroscopic field outside and inside a dielectric slab. The slab occupies the region $0 \leq z \leq 50$ nm delimited by the vertical lines. The plane wave ($\lambda = 400$ nm) is incident from the left of the figure. Angle $\theta = 50°$, permittivity of the slab $\epsilon = 20$ (see text for details).

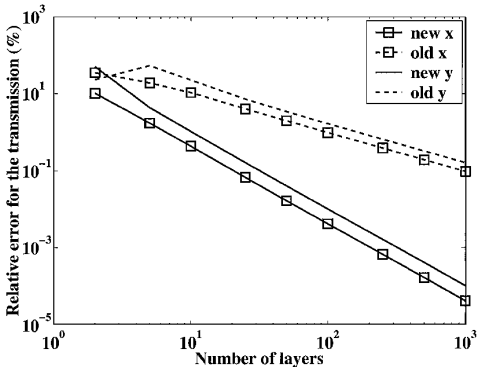

Fig. 2. Relative error of the field transmitted through a slab. Results for the x and the y components are plotted as a function of the number of discretization layers. The parameters of the calculation are $\epsilon = 20$, $t = 50$ nm, $\theta = 50°$, and $\lambda = 600$ nm.

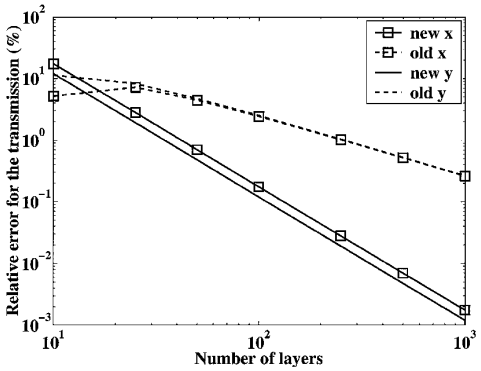

Fig. 3. Same as Fig. 2 but for an aluminum slab and parameters $\epsilon = -34.5 + 8.5i$, $t = 50$ nm, $\theta = 50°$, and $\lambda = 488$ nm.

and therefore the error on the scattered field is reduced.

In summary, we have presented a new form of the CDM in which the local field is derived so that the CDM is exact in the long-wavelength limit. The polarizability of the subunits is expressed in terms of a local-field tensor that is derived self-consistently and accounts for the local environment of each subunit. Accordingly, the convergence of the CDM at finite frequencies is drastically improved, and fewer subunits are needed for a given accuracy. In this Letter we explicitly considered a slab to make the physical basis for the new form of the CDM clear. It will be interesting to consider more-complex geometries. Indeed, calculations for spherical scatterers show that the performance of the CDM for three-dimensional scatterers can be significantly improved.

A. Rahmani's e-mail address is adel.rahmani@ec-lyon.fr.

References

1. E. M. Purcell and C. R. Pennypacker, Astrophys. J. **186,** 705 (1973).
2. B. T. Draine, Astrophys. J. **333,** 848 (1988).
3. B. T. Draine and J. Goodman, Astrophys. J. **405,** 685 (1993).
4. B. T. Draine and P. J. Flatau, J. Opt. Soc. Am. A **11,** 1491 (1994), and references therein.
5. A. Rahmani, P. C. Chaumet, and F. de Fornel, Phys. Rev. A **63,** 023819 (2001).
6. P. C. Chaumet, A. Rahmani, and M. Nieto-Vesperinas, Phys. Rev. Lett. **88,** 123601 (2002).
7. A. Rahmani and G. W. Bryant, Phys. Rev. A **65,** 033817 (2002).
8. J. D. Jackson, *Classical Electrodynamics*, 2nd ed. (Wiley, New York, 1980).
9. A. D. Yaghjian, Proc. IEEE **68,** 248 (1980).
10. J. A. Stratton, *Electromagnetic Theory* (McGraw-Hill, New York, 1941).
11. P. C. Chaumet, A. Rahmani, and G. W. Bryant have prepared a manuscript called "Generalization of the coupled dipole method to periodic structures."
12. N. Kar and A. Bagchi, Solid State Commun. **31,** 645 (1980).
13. W. L. Mochán and R. G. Barrera, Phys. Rev. Lett. **55,** 1192 (1985).
14. G. P. M. Poppe and C. M. J. Wijers, Physica B **167,** 221 (1990).

August 1, 2000 / Vol. 25, No. 15 / OPTICS LETTERS 1065

Time-averaged total force on a dipolar sphere in an electromagnetic field

P. C. Chaumet and M. Nieto-Vesperinas

Instituto de Ciencia de Materiales de Madrid, Consejo Superior de Investigaciones Cientificas, Campus de Cantoblanco, Madrid 28049, Spain

Received February 11, 2000

We establish the time-averaged total force on a subwavelength-sized particle in a time-harmonic-varying field. Our analysis is not restricted to the spatial dependence of the incident field. We discuss the addition of the radiative reaction term to the polarizability to deal correctly with the scattering force. As an illustration, we assess the degree of accuracy of several previously established polarizability models. © 2000 Optical Society of America

OCIS codes: 260.2110, 260.0260.

In the past few years there has been an increase of interest in the manipulation of small particles by means of the Lorentz force. For the subwavelength radius of a sphere the total force that is due to a light wave is usually split into two parts from the use of the dipole approximation (cf. Ref. 1): a gradient force $(\mathbf{p}\cdot\boldsymbol{\nabla})\mathbf{E}$, which is essentially due to interaction of the particle-induced dipole moment $\mathbf{p}$ with the electric field $\mathbf{E}$ and scattering and absorbing forces $^1/_c\,\dot{\mathbf{p}}\times\mathbf{B}$, where $\mathbf{B}$ is the magnetic vector, $\dot{\mathbf{p}} = \partial\mathbf{p}/\partial t$, and c is the speed of light in vacuum. It has been customary, after Ref. 1, to express the gradient force $\mathbf{F}_{\text{grad}}$ as (see, e.g., Ref. 2)

$$\mathbf{F}_{\text{grad}} = (1/2)\alpha_0\boldsymbol{\nabla}\mathbf{E}^2, \tag{1}$$

where α_0 is the particle polarizability that satisfies the Clausius–Mossotti equation

$$\alpha_0 = a^3\,\frac{\epsilon - 1}{\epsilon + 2}, \tag{2}$$

where a is the particle radius and ϵ denotes the dielectric permittivity. On the other hand, the absorbing and scattering forces are written in the approximation of small spheres through the absorbing (C_{abs}) and scattering (C_{scat}) cross sections as

$$\mathbf{F} = \frac{|E|^2}{(8\pi)}\,(C_{\text{abs}} + C_{\text{scat}})\,\frac{\mathbf{k}}{k}, \tag{3}$$

where $\mathbf{k}$ represents the light vector ($k = |\mathbf{k}|$). When one is using the expression of these cross sections in the dipole approximation, only the first term of their Taylor expansion versus the size parameter, $x = 2\pi a/\lambda$, is usually considered.[3]

At the optical frequencies involved in many experiments, however, only the time average of the electromagnetic force is observed. In this Letter we establish the form of the time-averaged total force on a particle without restriction on the spatial dependence of the electromagnetic field. Further, we discuss some of the consequences of this new relation. For time-harmonic electromagnetic waves,[4] we write $\mathbf{E}(\mathbf{r}, t) = \text{Re}[\mathbf{E}_0\exp(-i\omega t)]$, $\mathbf{B}(\mathbf{r}, t) = \text{Re}[\mathbf{B}_0\exp(-i\omega t)]$, and $\mathbf{p}(\mathbf{r}, t) = \text{Re}[\mathbf{p}_0\exp(-i\omega t)]$; $\mathbf{E}_0$, $\mathbf{B}_0$, and $\mathbf{p}_0$ are complex functions of position in space, and Re denotes the real part. Then the time average of the total force is

$$\langle\mathbf{F}\rangle = \frac{1}{4T}\int_{-T/2}^{T/2}\Big[(\mathbf{p} + \mathbf{p}^*)\cdot\boldsymbol{\nabla}(\mathbf{E} + \mathbf{E}^*) + \frac{1}{c}\,(\dot{\mathbf{p}} + \dot{\mathbf{p}}^*)\times(\mathbf{B} + \mathbf{B}^*)\Big]\mathrm{d}t, \tag{4}$$

where * denotes the complex conjugate. On performing the integral and using $\mathbf{E}_0$, $\mathbf{B}_0$, and $\mathbf{p}_0$, we find that Eq. (4) yields, for each ith Cartesian component of the averaged total force,

$$\langle F^i\rangle = (1/2)\text{Re}\Big[\,p_{0j}\partial^j(E_0^i)^* + \frac{1}{c}\,\epsilon^{ijk}\dot{p}_{0j}(B_{0k})^*\,\Big] \tag{5}$$

for $i = 1, 2, 3$, where ϵ_{ijk} is the Levi–Civita tensor. Using the relations $\mathbf{B}_0 = {}^c/_{i\omega}\,\boldsymbol{\nabla}\times\mathbf{E}_0$, $\mathbf{p}_0 = \alpha\mathbf{E}_0$, and $\dot{\mathbf{p}}_0 = -i\omega\mathbf{p}_0$, one gets for Eq. (5)

$$\langle F^i\rangle = (1/2)\text{Re}\{\alpha[E_{0j}\partial^j(E_0^i)^* + \epsilon^{ijk}\epsilon_{klm}E_{0j}\partial^l(E_0^m)^*]\}. \tag{6}$$

On taking into account that $\epsilon^{ijk}\epsilon_{klm} = \delta_l^i\delta_m^j - \delta_m^i\delta_l^j$ one can finally express $\langle F^i\rangle$ as

$$\langle F^i\rangle = (1/2)\text{Re}[\alpha E_{0j}\partial^i(E_0^j)^*]. \tag{7}$$

Equation (7) is the main result of this Letter. It represents the total averaged force exerted by an arbitrary time-harmonic electromagnetic field on a small particle.

In this connection, Ref. 5 establishes the average force on an object represented by a set of dipoles when the electromagnetic field is a plane wave. We note that in this case Eq. (7) reduces to just Eq. (3), in agreement with the results reported in Ref. 5. However, as we illustrate next, Eq. (7) allows one to apply the coupled-dipole method (CDM) to more-complex configurations such as that of a small particle in front of a dielectric surface, under arbitrary illumination (see Ref. 6 for a discussion of the coupled-dipole method for large particles). Also, the

0146-9592/00/151065-03$15.00/0

absence of the magnetic field $\mathbf{B}_0$ in Eq. (7) eases the computations.

Conversely, when Eq. (2) for the polarizability is introduced into Eq. (7), one obtains for the ith component of the time-averaged optical force

$$\langle F^i \rangle = (1/2)\alpha_0 \,\mathrm{Re}[E_{0j}\partial^i (E_0^j)^*] = (1/4)\alpha_0 \,\mathrm{Re}(\partial^i |\mathbf{E}_0|^2) = (1/4)\alpha_0 (\partial^i |\mathbf{E}_0|^2), \quad (8)$$

which is just the gradient force. Notice the factor (1/4) (see, e.g., Ref. 7) instead of (1/2), which often appears for nonaveraged fields in the literature (see, for example, Refs. 2, 8, and 9). In agreement with the remarks in Ref. 10, the scattering force, Eq. (3), vanishes, and thus $\langle \mathbf{F} \rangle$ reduces to the gradient force. Therefore, the static expression of α_0 from Eq. (2) must be replaced with an added damping term. This was done by Draine,[10] who, with the help of the optical theorem, obtained

$$\alpha = \alpha_0 / [1 - (2/3) i k^3 \alpha_0]. \quad (9)$$

The existence of the imaginary term for α in Eq. (9) is essential for deriving the correct value for the averaged total force that is due to a time-varying field.

As an illustration, let the field that illuminates the particle be the beam whose electric vector is

$$E_x = \exp(-x^2/2)\exp[i(kz - \omega t)], \qquad E_y = 0, E_z = 0. \quad (10)$$

Using Eqs. (2) and (10) in Eq. (7), we find

$$\langle F_x \rangle = -(\alpha_0/2) x \exp(-x^2), \quad (11a)$$

$$\langle F_z \rangle = 0. \quad (11b)$$

On the other hand, if the correct polarizability, Eq. (9), is introduced with Eqs. (10) into Eq. (7), the total force is then expressed as

$$\langle F_x \rangle = (1/2)\mathrm{Re}[-\alpha x \exp(-x^2)] = \frac{-(\alpha_0/2) x \exp(-x^2)}{1 + (4/9) k^6 \alpha_0^2}, \quad (12a)$$

$$\langle F_z \rangle = (1/2) k \exp(-x^2)\mathrm{Re}(-i\alpha) = \frac{\exp(-x^2) k^4 \alpha_0^2 / 3}{1 + (4/9) k^6 \alpha_0^2}. \quad (12b)$$

For a particle with a radius $a \ll \lambda$, e.g., $a = 10$ nm, at wavelength $\lambda = 632.8$ nm and $\epsilon = 2.25$, the factor $[1 + (4/9) k^6 \alpha_0^2]$ is very close to 1 (notice in passing that the expression used for α in Ref. 11 makes this factor unity). Thus we can see that, in contrast with Eqs. (11), the correct form for the polarizability, Eq. (9), leads to a total force given by Eqs. (12a) and (12b), which can be associated with the gradient and scattering components, namely, with the time average of Eq. (1) and Eq. (3) with $C_{\mathrm{abs}} = 0$, respectively.

In the case of an absorbing sphere, the dielectric constant becomes complex, and so is α_0. Then, Eqs. (12) with $a \ll \lambda$ become

$$\langle F_x \rangle = -(1/2)\mathrm{Re}(\alpha_0) x \exp(-x^2), \quad (13a)$$

$$\langle F_z \rangle = \frac{\exp(-x^2) k^4 |\alpha_0|^2}{3} + \frac{k \exp(-x^2)}{2} \mathrm{Im}(\alpha_0). \quad (13b)$$

The imaginary part of α_0 does not contribute to the component $\langle F_x \rangle$, that is, to the gradient force, Eq. (13a). On the other hand, the absorbing and scattering force, Eq. (13b), exactly coincides with the expression obtained from Eq. (3).

We next illustrate the above arguments with numerical calculations that permit us to assess the degree of accuracy of several previously established polarizability models. We first compare the relative difference between the force obtained from the exact Mie calculation and the most-typical polarizability models, namely, those of Lakhtakia[12] (LAK) and Dungey and Bohren[13] (DB) and the Clausius–Mossotti relation with the radiative reaction term[10] (CM-RR), versus the radius a of a sphere illuminated by a propagating plane wave in free space (Fig. 1). Next, when this sphere is illuminated by an evanescent wave created by total internal reflection on a dielectric surface, the component of the force perpendicular to the incident wave vector (Fig. 2) is compared with the result derived from the CDM.[6] All curves are represented up to $\alpha = \lambda/10$. The percent relative difference in Fig. 2 is defined as $100 \times (F_{\mathrm{ref}} - F_{\mathrm{pol}})/F_{\mathrm{ref}}$, where pol denotes the force obtained from the corresponding method used for the polarizability (LAK, DB, or CM-RR) and ref stands for

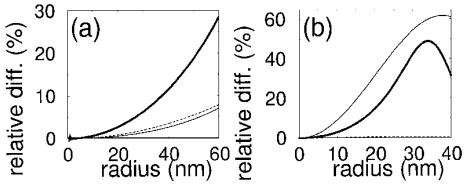

Fig. 1. (a) Relative difference between the force computed by the exact Mie calculation and by the dipole approximation: thin curve, CM-RR; thick curve, LAK; dashed curve, DB. The sphere is glass ($\epsilon = 2.25$) illuminated by an incident propagating plane wave ($\lambda = 600$ nm). (b) Same as (a) but for a silver sphere ($\lambda = 400$ nm, $\epsilon = -4 + i0.7$).

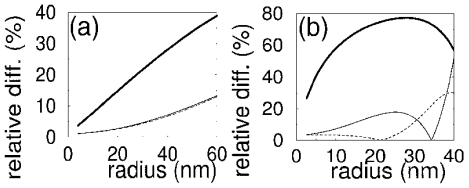

Fig. 2. (a) Relative difference between the component of the force perpendicular to the incident wave vector obtained by the CDM and by the dipole approximation: thin curve, CM-RR; thick curve, LAK; dashed curve, DB. The sphere is glass ($\epsilon = 2.25$) illuminated by an incident evanescent wave ($\lambda = 600$ nm). (b) Same as (a) but for a silver sphere ($\lambda = 400$ nm, $\epsilon = -4 + i0.7$).

the force derived from the Mie calculation when the incident wave is propagating and from the CDM when the incident wave is evanescent.

We first consider a dielectric sphere (glass, $\epsilon = 2.25$) illuminated at $\lambda = 600$ nm [Figs. 1(a) and 2(a)]. We observe that, for an incident propagating wave [Fig. 1(a)], the result from the CM-RR relation is better than that of DB, and this, in turn, is better than the result from LAK. The force over a dielectric particle given by the exact Mie calculation is $F = C_{\text{scat}}(1 - \overline{\cos\theta})|E|^2/(8\pi)$, and that obtained from the dipole approximation is $F = (1/2)|E|^2\ \text{Re}(-i\alpha)$. When the DB model is used, $\alpha = (3/2)ia_1/k^3$, where a_1 is the first Mie coefficient, and hence, $4\pi\ \text{Re}(-i\alpha)$ is the scattering cross section for an electric dipole. However, when Eq. (9) for the CM-RR is employed, $4\pi\ \text{Re}(-i\alpha)$ constitutes only the first term of the Taylor expansion of the scattering cross section versus the size parameter x. This is why C_{scat} is underestimated when it is calculated from the CM-RR model. Therefore the DB model should be better. However, in both cases the factor $\overline{\cos\theta}$ has not been taken into account in the dipole approximation, and thus both results overestimate the force. Hence, this factor $\overline{\cos\theta}$ produces a balance, making the CM-RR result closer to the Mie solution. In the case of an incident evanescent wave [Fig. 2(a)], the DB and CM-RR results are very close together; this is due to the fact that the real parts of both polarizabilities are very close to each other. One can see that the LAK result, as with a propagating wave, is far from the correct solution.

As a second example, we consider a metallic sphere (silver) illuminated at $\lambda = 400$ nm ($\epsilon = -4 + i0.7$). We now observe that for an incident propagating wave [Fig. 1(b)] the DB model yields the best result. The force can be exactly written as $F = (C_{\text{ext}} + C_{\text{scat}}\overline{\cos\theta})|E|^2/(8\pi)$. Notice that now $C_{\text{scat}}\overline{\cos\theta}$ is of the sixth order in x in comparison with C_{ext}. Since $C_{\text{ext}} \propto \text{Re}(a_1)$ in the electric dipole limit, the DB formulation appears to be the best. Also, for incident evanescent waves [Fig. 2(b)], the DB formulation gives the most accurate solution. However, for a metallic sphere, the relative permittivity greatly depends on the wavelength used. Hence, it is difficult to establish a generalization of these results. We checked and found that, for a gold or silver sphere in free space in the visible, the DB formulation is often the best.

In summary, we have established the average total force on a small particle in a time-harmonic-varying field of arbitrary form and thus clarified the use of this finding in the interpretation of experiments as well as of previous theoretical works. For instance, we showed that Eq. (7) is not just the gradient force as stated previously (see, e.g., Ref. 14). Also, this general expression shows the importance of the radiative reaction term in the polarizability of the sphere as put forward by other authors. In the derivation of Eq. (7) we make no assumptions about the surrounding environment. It is necessary only to know both the electric field and its derivative at the position of the sphere, and thus Eq. (7) permits easy handling of illuminating evanescent fields. An immediate important consequence is that it allows one to assess the adequacy of several polarizability models.

This work was supported by Dirección General de Investigacíon Científica y Técnica, grant PB 98-0464, and the European Union. M. Nieto-Vesperinas's e-mail address is mnieto@.icmm.csic.es.

References

1. J. P. Gordon, Phys. Rev. A **8,** 14 (1973).
2. A. Ashkin, J. M. Dziedzic, J. E. Bjorkholm, and S. Chu, Opt. Lett. **11,** 288 (1981).
3. H. C. van de Hulst, *Light Scattering by Small Particles* (Dover, New York, 1981).
4. M. Born and E. Wolf, *Principles of Optics* (Pergamon, Oxford, 1975), Sec. 1.4.3.
5. B. T. Draine and J. C. Weingartner, Astrophys. J. **470,** 551 (1996).
6. P. C. Chaumet and M. Nieto-Vesperinas, Phys. Rev. B **61,** 14119 (2000).
7. Y. Harada and T. Asakura, Opt. Commun. **124,** 529 (1996).
8. P. W. Smith, A. A. Ashkin, and W. J. Tomlison, Opt. Lett. **6,** 284 (1986).
9. P. W. Smith, P. J. Maloney, and A. Ashkin, Opt. Lett. **7,** 347 (1982).
10. B. T. Draine, Astrophys. J. **333,** 848 (1988).
11. K. Klumme and J. Rahola, Astrophys. J. **425,** 653 (1994).
12. A. Lakhtakia, Int. J. Mod. Phys. C **34,** 583 (1992).
13. C. E. Dungey and C. F. Bohren, J. Opt. Soc. Am. A **8,** 81 (1991).
14. K. Visscher and G. J. Brakenhoff, Optik **89,** 174 (1992).

PHYSICAL REVIEW B VOLUME 61, NUMBER 20 15 MAY 2000-II

Coupled dipole method determination of the electromagnetic force on a particle over a flat dielectric substrate

P. C. Chaumet and M. Nieto-Vesperinas
Instituto de Ciencia de Materiales de Madrid, Consejo Superior de investigaciones Cientificas, Campus de Cantoblanco, Madrid 28049, Spain

(Received 13 October 1999; revised manuscript received 13 December 1999)

We present a theory to compute the force due to light upon a particle on a dielectric plane by the coupled dipole method. We show that, with this procedure, two equivalent ways of analysis are possible, both based on Maxwell's stress tensor. The interest in using this method is that the nature and size or shape of the object can be arbitrary. Even more, the presence of a substrate can be incorporated. To validate our theory, we present an analytical expression of the force due to the light acting on a particle either in presence, or not, of a surface. The plane wave illuminating the sphere can be either propagating or evanescent. Both two- and three-dimensional calculations are studied.

I. INTRODUCTION

The demonstration of mechanically acting upon small particles with radiation pressure was done by Ashkin.[1,2] A consequence of these works was the invention of the optical tweezer for nondestructive manipulation of suspended particles[3] or molecules and other biological objects.[4–6] Recently, these studies have been extended to the nanometer scale,[7–12] and multiple particle configurations based on optical binding have been studied.[13–17] Also, the effect of evanescent waves created by total internal reflection on a dielectric surface on which particles are deposited was studied in Ref. 18. However, the only theoretical interpretation of such a system is given in Refs. 19 and 20. In Ref. 19 no multiple interaction of the light between the particles and the dielectric surface was taken into account. On the other hand, in Ref. 20 a multiple scattering numerical method was put forward limited to a two-dimensional (2D) configuration.

It is worth remarking here that several previous theoretical works on optical forces usually employ approximations depending on the radius of the particle; if the particle is electrically small it has been usual to split the force into three parts: the gradient, scattering, and absorbing forces.[21] However, a rigorous and exact calculation requires the use of Maxwell's stress tensor. We shall use it in this paper. Some work has been done in free space,[7,22] or for a spherical particle over a dielectric surface illuminated by a Gaussian beam.[23]

We shall present, therefore, a detailed theoretical analysis in three dimensions of how the optical force is built on the multiple interaction of light with the particle and the dielectric surface. This will be done whatever its size, shape, or permittivity. To this end, we shall make use of the coupled dipole method (CDM), whose validity was studied in detail in Ref. 25.

In Sec. II we present the CDM, and two possibilities that arise with this method to compute the force by means of Maxwell's stress tensor. Concerning the first possibility, in Sec. II A we use Maxwell's stress tensor directly and perform the surface integrations. As regards the second possibility, we present in Sec. II B the dipole approximation on each subunit of discretization for the numerical calculations. Since, however, these methods are somewhat cumbersome from a numerical point of view, we have introduced in Sec. III an analytical calculation for the force due to the light on a electrically small particle in the presence of the surface. Results are illustrated in three dimensions in Sec. III A (a little sphere) and in two dimensions in Sec. III B (a small cylinder). In Sec. IV we compute the force with the CDM and validate these calculations on electrically small particles by means of the analytical solution presented in Sec. III. After this validation of the CDM on little particles, we present in Sec. IV C calculations on larger particles.

II. ELECTROMAGNETIC FORCE COMPUTED WITH THE COUPLED DIPOLE METHOD

The CDM was introduced by Purcell and Pennypacker in 1973 for studying the scattering of light by nonspherical dielectric grains in free space.[26] This system is represented by a cubic array of N polarizable subunits. The electric field $\mathbf{E}(\mathbf{r}_i,\omega)$ at each subunit position $\mathbf{r}_i$ can be expressed as

$$\mathbf{E}(\mathbf{r}_i,\omega)=\mathbf{E}_0(\mathbf{r}_i,\omega)+\sum_{j=1}^{N}[\mathbf{S}(\mathbf{r}_i,\mathbf{r}_j,\omega)+\mathbf{T}(\mathbf{r}_i,\mathbf{r}_j,\omega)]\alpha_j(\omega)\mathbf{E}(\mathbf{r}_j,\omega), \quad (1)$$

where $\mathbf{E}_0(\mathbf{r}_i,\omega)$ is the field at the position $\mathbf{r}_i$ in the absence of the scattering object, $\mathbf{T}$ is the linear response to a dipole in free space,[27] and $\mathbf{S}$ represents the linear response of a dipole in the presence of a surface in front of which the particle is placed (see Fig. 1). We take the weak form of the CDM, as in our configuration the strong form does not adapt.[28] However, in fact for very small discretization subunits, the difference of results derived from the strong and weak forms is not significant. The derivation of $\mathbf{S}$ is extensively developed in Refs. 29 and 30. $\alpha_j(\omega)$, the polarizability of the subunit j, is expressed as:

$$\alpha_j(\omega)=\alpha_j^0(\omega)/[1-(2/3)ik_0^3\alpha_j^0(\omega)], \quad (2)$$

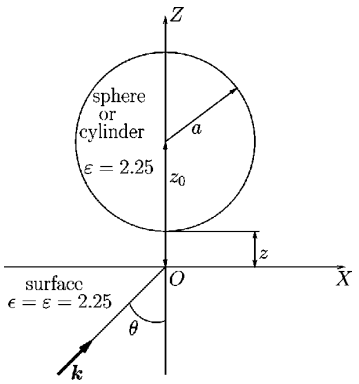

FIG. 1. Geometry of the configuration considered in this paper: sphere, or cylinder, of radius a on a dielectric flat surface. The relative permittivity is $\varepsilon=2.25$ both for the sphere (or the cylinder) and the surface. The wavelength used is $\lambda=632.8$ nm in vacuum and the incident wave vector $\mathbf{k}$ is in the XZ plane.

where $k_0=|\mathbf{k}_0|=\omega/c$ ($\mathbf{k}_0$ being the incident wave vector of the electromagnetic field in vacuum) and $\alpha_j^0(\omega)$ is given by the Clausius-Mossotti relation:

$$\alpha_j^0(\omega)=\frac{3d^3}{4\pi}\,\frac{\varepsilon(\omega)-1}{\varepsilon(\omega)+2}. \tag{3}$$

In Eq. (3) d is the spacing of lattice discretization and $\varepsilon(\omega)$ stands for the relative permittivity of the object. Let us remark that the polarizability is expressed according to Eq. (2) as defined by Draine.[31] The term $(2/3)ik_0^3\alpha_j^0(\omega)$ is the radiative reaction term, necessary for the optical theorem to be satisfied and for a correct calculation of forces via the CDM.[32]

Once the values of $\mathbf{E}(\mathbf{r}_i,\omega)$ are obtained by solving the linear system, Eq. (1) (whose size is $3N\times 3N$), it is easy to compute the field at an arbitrary position $\mathbf{r}$:

$$\mathbf{E}(\mathbf{r},\omega)=\mathbf{E}_0(\mathbf{r},\omega)+\sum_{j=1}^{N}[\mathbf{S}(\mathbf{r},\mathbf{r}_j,\omega)+\mathbf{T}(\mathbf{r},\mathbf{r}_j,\omega)]\alpha_j(\omega)\mathbf{E}(\mathbf{r}_j,\omega). \tag{4}$$

The computation of the force also requires the magnetic field radiated by the scattering object. We obtain it through Faraday's equation, $\mathbf{H}(\mathbf{r},\omega)=c/(i\omega)\boldsymbol{\nabla}\times\mathbf{E}(\mathbf{r},\omega)$.

A. Force computed with Maxwell's stress tensor

The force $\mathbf{F}$ on an object due to the electromagnetic field[33] is computed from Maxwell's stress tensor:[34]

$$\mathbf{F}=1/(8\pi)\mathrm{Re}\left[\int_S\{[\mathbf{E}(\mathbf{r},\omega)\cdot\mathbf{n}]\mathbf{E}^*(\mathbf{r},\omega)+[\mathbf{H}(\mathbf{r},\omega)\cdot\mathbf{n}]\mathbf{H}^*(\mathbf{r},\omega)-1/2[|\mathbf{E}(\mathbf{r},\omega)|^2+|\mathbf{H}(\mathbf{r},\omega)|^2]\mathbf{n}\}d\mathbf{r}\right], \tag{5}$$

where S is a surface enclosing the object, $\mathbf{n}$ is the local outward unit normal, the asterisk denotes the complex conjugate, and Re represents the real part of a complex number. Let us notice that Eq. (5) is written in CGS units for an object in vacuum, and so will be given all forces presented in Sec. IV. To apply Eq. (5) with the CDM, we must first solve Eq. (1) to obtain $\mathbf{E}(\mathbf{r}_i,\omega)$ at each dipole position, and then, through Eq. (4) and the Faraday equation, the electromagnetic field is computed at any position $\mathbf{r}$ of S. This enables us to numerically perform the two-dimensional quadrature involved in Eq. (5).

B. Force determined via the dipolar approximation

Let us consider a small spherical particle with a radius smaller than the wavelength. Then the u component of the force can be written in the dipole approximation:[35,32]

$$F_u(\mathbf{r}_0)=(1/2)\mathrm{Re}\sum_{v=1}^{3}\left(p_v(\mathbf{r}_0,\omega)\frac{\partial E_v^*(\mathbf{r}_0,\omega)}{\partial u}\right),\quad u=1,2,3 \tag{6}$$

where $\mathbf{r}_0$ is the position of the center of the sphere and u and v stand for the components along x, y, or z. We discretize the object into N small dipoles $\mathbf{p}(\mathbf{r}_i,\omega)$ ($i=1,\ldots,N$) so that it is possible to compute the force on each dipole from Eq. (6). Hence, to obtain the total force on the particle it suffices to sum the contributions $\mathbf{F}(\mathbf{r}_i)$ from all of the dipoles. To use this method it is necessary to know $\partial E_v(\mathbf{r}_i,\omega)/\partial u$ at each discretization subunit. On performing the derivative of Eq. (1) we obtain

$$\left(\frac{\partial\mathbf{E}(\mathbf{r},\omega)}{\partial\mathbf{r}}\right)_{\mathbf{r}=\mathbf{r}_i}=\left(\frac{\partial\mathbf{E}_0(\mathbf{r},\omega)}{\partial\mathbf{r}}\right)_{\mathbf{r}=\mathbf{r}_i}+\sum_{j=1}^{N}\left(\frac{\partial}{\partial\mathbf{r}}[\mathbf{S}(\mathbf{r},\mathbf{r}_j,\omega)+\mathbf{T}(\mathbf{r},\mathbf{r}_j,\omega)]\right)_{\mathbf{r}=\mathbf{r}_i}\alpha_j(\omega)\mathbf{E}(\mathbf{r}_j,\omega). \tag{7}$$

Thus, the derivative of the field at $\mathbf{r}_i$ requires that of $\mathbf{E}_0(\mathbf{r}_i,\omega)$ and that of $\mathbf{T}$ and $\mathbf{S}$ for all pairs $(\mathbf{r}_i,\mathbf{r}_j)$. Hence we now have two tensors with 27 components each. It is important to notice that the derivative of the field at $\mathbf{r}_i$ has been directly computed from just the field at this position $\mathbf{r}_i$, so it is not computed in a self-consistent manner. To have the required self-consistence for the derivative, it is necessary to perform in Eq. (1) a multipole expansion up to second order. Then, this equation must be written up to the quadrupole order after taking its derivative. As a result, we obtain a linear system whose unknowns are both the electric field and its derivative. The disadvantage of this method is that the size of the linear system increases up to $12N\times 12N$ and requires the computation of the second derivative of $\mathbf{T}$ and $\mathbf{S}$ (81 components). More information about the CDM by using the multipole expansion can be found in Ref. 25.

In what follows, we shall denote CDM-A the force computed directly from Maxwell's stress tensor Eq. (5) and CDM-B the force obtained on using the field derivative Eq. (6). The advantages of these two methods is that they are not restricted to a particular shape of the object to be discretized. Furthermore, this object can be inhomogeneous, metallic, or in a complex system whenever it is possible to compute its linear response to a dipole.

III. FORCE ON A DIPOLAR PARTICLE

A. The three-dimensional case: A sphere

Equation (1) with $N=1$, taking the surface into account, gives for the field at the position $\mathbf{r}_0=(x_0,y_0,z_0)$ of the sphere of a radius a:

$$\mathbf{E}(\mathbf{r}_0,\omega)=[\mathbf{I}-\alpha(\omega)\mathbf{S}(\mathbf{r}_0,\mathbf{r}_0,\omega)]^{-1}\mathbf{E}_0(\mathbf{r}_0,\omega), \tag{8}$$

where $\mathbf{I}$ is the unit tensor and $\alpha(\omega)$ the polarizability of the sphere according to Eq. (2) with $\alpha_0(\omega)=a^3[\varepsilon(\omega)-1]/[\varepsilon(\omega)+2]$. We notice that $\mathbf{S}$ is purely diagonal and depends only on the distance z_0 between the center of the sphere and the surface (see Fig. 1). We also assume that the sphere is near the surface, and hence $\mathbf{S}$ can be used in the static approximation ($k_0=0$, we shall discuss the validity of this approximation in Sec. IV). Therefore, the components of this tensor become $S_{xx}=S_{yy}=-\Delta/(8z_0^3)$ and $S_{zz}=-\Delta/(4z_0^3)$, with $\Delta=(1-\epsilon)/(1+\epsilon)$ representing the Fresnel coefficient of the surface. Since we consider the object in the presence of a surface with a real relative permittivity, Δ is real. As shown by Fig. 1, the light incident wave vector $\mathbf{k}_0$ lies in the XZ plane. Therefore, there is no force in the Y direction. On using Eqs. (6) and (8), and assuming the incident field $\mathbf{E}_0$ above the surface to be a plane wave either propagating or evanescent, depending on the illumination angle θ, the components of the force on the sphere can be written as

$$F_x=\frac{\mathrm{Re}}{2}\left[4\alpha z_0^3(ik_x)^*\left(\frac{2|E_{0x}|^2}{8z_0^3+\alpha\Delta}+\frac{|E_{0z}|^2}{4z_0^3+\alpha\Delta}\right)\right], \tag{9}$$

$$F_z=|E_{0x}|^2\frac{\mathrm{Re}}{2}\left(\frac{8z_0^3\alpha(ik_z)^*}{8z_0^3+\alpha\Delta}+\frac{12z_0^2|\alpha|^2\Delta}{|8z_0^3+\alpha\Delta|^2}\right)+|E_{0z}|^2\frac{\mathrm{Re}}{2}\left(\frac{4z_0^3\alpha(ik_z)^*}{4z_0^3+\alpha\Delta}+\frac{6z_0^2|\alpha|^2\Delta}{|4z_0^3+\alpha\Delta|^2}\right) \tag{10}$$

for p polarization and

$$F_x=|E_{0y}|^2\frac{\mathrm{Re}}{2}\left[\frac{8z_0^3\alpha(ik_x)^*}{8z_0^3+\alpha\Delta}\right], \tag{11}$$

$$F_z=|E_{0y}|^2\frac{\mathrm{Re}}{2}\left(\frac{8z_0^3\alpha(ik_z)^*}{8z_0^3+\alpha\Delta}+\frac{12z_0^2|\alpha|^2\Delta}{|8z_0^3+\alpha\Delta|^2}\right) \tag{12}$$

for s polarization. We see that the advantage of working with the static approximation is that an analytic form of the force is obtained. To see the effect of the incident field only (i.e., without interaction with the surface), we can put $z_0\to\infty$ or $\Delta=0$ in Eqs. (9)–(12). The forces are then expressed as

$$F_x=|E_0|^2\frac{\mathrm{Re}}{2}[\alpha(ik_x)^*], \tag{13}$$

$$F_z=|E_0|^2\frac{\mathrm{Re}}{2}[\alpha(ik_z)^*], \tag{14}$$

with $|E_0|^2=|E_{0y}|^2$ for s polarization and $|E_0|^2=|E_{0x}|^2+|E_{0z}|^2$ for p polarization. Equations (13) and (14) show a spherical symmetry, and hence the results both in p and s polarization are the same.

If we look at Fig. 1, we see that the incident field above the surface always has k_x real, but k_z can be either real (propagating wave) or imaginary (evanescent wave when $\theta>\theta_c$, where θ_c is the critical angle defined as $\sqrt{\epsilon}\sin\theta_c=1$). Hence, all forces in the X direction have the form $A\,\mathrm{Re}[\alpha(ik_x)^*]$, where A is always a positive number. In using Eq. (2) we find that $\mathrm{Re}[\alpha(ik_x)^*]\simeq(2/3)\alpha_0^2k_0^3k_x$ [we have assumed that $(4/9)k_0^6\alpha_0^2\ll1$; in fact, this expression is about 6.6×10^{-7} for $a=10$ nm, $\lambda=632.8$ nm, and $\varepsilon=2.25$; thus this approximation is perfectly valid]. Hence, whatever the field, either propagating or evanescent, and whether the system is in the presence of a surface or in free space, the force in the X direction is always along the incident field.

From Eq. (14) and from the discussion above, it is easy to see that in the absence of interfaces the force is positive for a propagating incident wave (k_z real). In the case of an evanescent incident wave, $k_z=i\gamma$ with $\gamma>0$, and hence the force becomes $F_z=-\gamma\alpha_0|E_0|^2/2$; namely, the sphere is attracted towards the higher intensity field. Concerning the force along the Z direction, its sign will depend on the nature of the field and the interaction of the sphere with the surface. We shall discuss this in Sec. IV A.

B. The two-dimensional case: A cylinder

For a cylinder with its axis at (x_0,z_0), parallel to the Y axis (Fig. 1), the electric field at its center is obtained by an equation similar to Eq. (8), but with a different polarizability. With the help of Refs. 36 and 37 we write this polarizability:

$$\alpha_1(\omega)=\frac{\alpha_1^0(\omega)}{1-ik_0^2\pi\alpha_1^0(\omega)/2}\quad\text{with}\quad\alpha_1^0(\omega)=\frac{\varepsilon(\omega)-1}{\varepsilon(\omega)+1}\frac{a^2}{2}, \tag{15}$$

$$\alpha_2(\omega)=\frac{\alpha_2^0(\omega)}{1-ik_0^2\pi\alpha_2^0(\omega)}\quad\text{with}\quad\alpha_2^0(\omega)=[\varepsilon(\omega)-1]\frac{a^2}{4}. \tag{16}$$

The subscripts $i=1$ and 2 correspond to the field perpendicular and parallel to the axis of the cylinder, respectively. The linear response in the presence of a surface in the two dimensional case is given in Ref. 38 for s-polarization and in Ref. 39 for p polarization. Since we address a cylinder with a small radius a and near the surface, we use the static approximation, and then $S_{xx}=S_{zz}=-\Delta/(2z_0^2)$ and $S_{yy}=0$. In the same way as seen before, the force is written as

$$F_x=|E_0|^2\frac{\mathrm{Re}}{2}[\alpha_2(ik_x)^*], \tag{17}$$

$$F_z=|E_0|^2\frac{\mathrm{Re}}{2}[\alpha_2(ik_z)^*] \tag{18}$$

for s polarization and

TABLE I. Force on a sphere of radius $a=10$ nm in free space. Numerical results for different number of subunits N in the CDM-A, CDM-B. Comparison of calculation with the dipolar approximation and Mie's calculation. % (Mie) is the relative difference (in percent) between the exact Mie calculation and the method used.

CDM-A			CDM-B			Dipole approx.		Mie
Force	N	% (Mie)	Force	N	% (Mie)	Force	% (Mie)	Force
2.8119×10^{-22}	81	0.46	2.8338×10^{-22}	81	1.24	2.8027×10^{-22}	0.13	2.7991×10^{-22}
2.8181×10^{-22}	912	0.68	2.8243×10^{-22}	912	0.91			
2.8151×10^{-22}	1791	0.57	2.8194×10^{-22}	1791	0.73			
2.8151×10^{-22}	2553	0.57	2.8186×10^{-22}	2553	0.70			

$$F_x=|E_0|^2\frac{\mathrm{Re}}{2}\left(\frac{2z_0^2\alpha_1(ik_x)^*}{2z_0^2+\alpha_1\Delta}\right), \tag{19}$$

$$F_z=|E_0|^2\frac{\mathrm{Re}}{2}\left(\frac{2z_0^2\alpha_1(ik_z)^*}{2z_0^2+\alpha_1\Delta}+\frac{2z_0|\alpha_1|^2\Delta}{|2z_0^2+\alpha_1\Delta|^2}\right) \tag{20}$$

for p polarization. $|E_0|^2=|E_{0y}|^2$ for s polarization and $|E_0|^2=|E_{0x}|^2+|E_{0z}|^2$ for p polarization. If, again, $z_0\to\infty$ or $\Delta=0$ and there is no interaction between the cylinder and the surface, then we find the same equations as those established for the sphere with only a replacement of α by α_1 or α_2, depending on the polarization. Concerning the force along the X direction, we have the same effect as for the sphere, namely, F_x has the sign of k_x.

IV. NUMERICAL RESULTS AND DISCUSSION

In this section we present numerical results on forces acting on either an electrically small sphere or a small cylinder. Theses forces are normalized in the form $F_u/|E_0|^2$, where F_u is the u component of the force and $|E_0|$ stands for the modulus of the incident field at the center of either the sphere or the cylinder. All calculations are done for a body in glass ($\varepsilon=2.25$), at a wavelength of 632.8 nm, in front of a flat surface ($\epsilon=\varepsilon=2.25$) illuminated from the glass side by internal reflection (Fig. 1).

A. Results for an electrically small sphere

We have first checked our CDM calculation by comparing it with the well known Mie scattering results for a sphere in free space illuminated by a plane wave.[40] The force is

$$\mathbf{F}_{Mie}=\frac{1}{8\pi}|E_0|^2(C_{ext}-\overline{\cos\theta}C_{sca})\frac{\mathbf{k}_0}{k_0}, \tag{21}$$

where C_{ext} denotes the extinction cross section, C_{sca} the scattering cross section, and $\overline{\cos\theta}$ the average of the cosine of the scattering angle. Calculations are done for a sphere of radius $a=10$ nm.

Table I compares the force obtained from the CDM on using, without any approximation, either the method developed in Sec. II A (CDM-A) or that from Sec. II B (CDM-B), and from the dipolar approximation presented in Sec. III A, with the Mie calculation [% (Mie) is the relative difference in percent between the Mie result and the other corresponding method]. For an incident field with $|E_0|=94825$ V/m, which corresponds to a power of 1.19 mW distributed on a surface of 10 μm^2, the force on the sphere in MKSA units is 2.7991×10^{-22} N. One can see that for both CDM-A and CDM-B the convergence is reached even for a coarse discretization, and hence either one of the two CDM approaches can be used. As regards the dipolar approximation, we conclude that it is perfectly valid to use it for a sphere of radius a=10 nm ($a/\lambda<0.016$). Notice that in this article we prefer the Clausius-Mossotti relation with the radiative reaction term to the polarizability defined by Dungey and Bohren[24] as the force obtained in free space for an electrically small sphere is less accurate than the one obtained from the Clausius-Mossotti relation.

Now that we have validated our methods (both analytic and CDM) we proceed to take the surface into account. It should be remarked that with the CDM-A it is not possible to compute the force when the sphere is on the surface. This is because for an observation point very close to the sphere, the electromagnetic field values are affected by the discretization of the sphere, and so the field is not correctly computed. An empirical criterion that we have found[25] is that the electric field must be computed at least at a distance d from the sphere, but this criterion depends on the relative permittivity. For more precision about the dependence of the criterion and the relative permittivity one can look to Ref. 31. With the CDM-B this problem does not occur because with this approach it is not necessary to obtain the field outside the sphere.

In all figures shown next, we plot the force versus the distance z between the sphere (or the cylinder, see Sec. IV B)

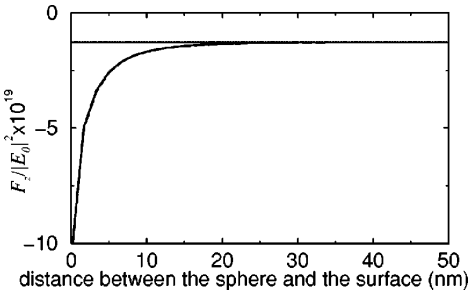

FIG. 2. Normalized force in the Z direction on the sphere of $a=10$ nm versus distance Z. The angle of incidence of illumination is $\theta=42°$ in p polarization. The full line represents the exact calculation with CDM-B, the dashed line corresponds to the static approximation with CDM-B, and the dotted line is the calculation without interaction between the sphere and the surface.

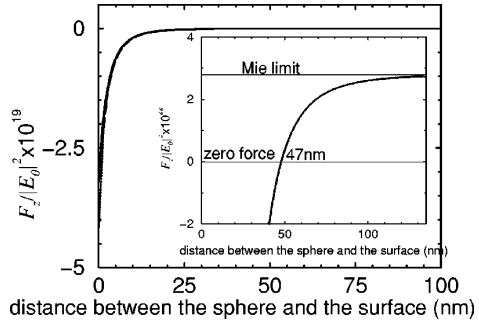

FIG. 3. Normalized force in the Z direction on a sphere of radius $a=10$ nm. The full line corresponds to the dipole approximation, the dashed line to the CDM-A, and the dotted line to the CDM-B. The angle of incidence is $\theta=0°$. The inset shows the force near $z=50$ nm. We show the zero force and the force computed from Mie's limit with Eq. (21).

and the plane (notice that we represent by z_0 the distance between the center of the sphere, or cylinder, and the plane). The calculation using the dipole approximation, as well as the CDM (A or B), has been done with the static approximation for the linear response of a dipole in the presence of a surface (SALRS). However, the distance between the sphere and the surface goes generally up to 100 nm. In order to justify the study of the force at distances about 100 nm between the sphere and the plane through a calculation done in the static approximation, we plot in Fig. 2 the normalized force F_z for p polarization, with a sphere of radius $a=10$ nm, at an angle of incidence $\theta=42°$, without any approximation with the CDM-A (namely, taking into account all retardation effects) with the SALRS, and with the approximation in which no interaction between the sphere and the surface is considered. The difference between SALRS and the exact calculation is less than 1.5%. This is in fact logical. Near the surface, the SALRS is correct, far from the surface. However, **S** in the exact calculation is significantly different from **S** derived from a static approximation. Nevertheless, for distances larger than $z=30$ nm the curves overlap because the sphere does not ''feel'' the substrate at this distance. This is manifested by a difference of only 2% between the exact calculation result and that computed without addressing the surface (horizontal line).

Figure 3 shows the normalized force for light at an angle of incidence $\theta=0°$. The curves corresponding to CDM-A and CDM-B are similar, and the dipole approximation appears slightly above when the sphere is close to the surface. This may seem strange at first sight in view of the good results presented in Table I (we will discuss it later). We can see that although the illuminating wave is propagating, if the sphere is near the surface, it is attracted towards it, opposite to the propagation direction. To understand this, we look at Eq. (12), established with the dipole approximation with the values $k_x=0$, $k_z=k_0$, and $E_{0z}=0$, which corresponds to $\theta=0°$. After some approximations [namely $(4/9)k_0^6\alpha_0^2\ll 1$, which implies $|\alpha|^2\simeq\alpha_0^2$], the force can be written:

$$F_z=\frac{|E_0|^2 64 z_0^6}{|8z_0^3+\alpha\Delta|^2}\left(\alpha_0^2 k_0^4/3+\frac{3\alpha_0^2\Delta}{32 z_0^4}\right). \tag{22}$$

The factor before the parentheses of Eq. (22) corresponds to the intensity of the field at the position of the sphere. The first term in the parentheses of this equation is due to the light scattering on the particle (as in free space) and is always positive. The second term in the parentheses is always negative as $\Delta<0$. Therefore, the relative weight of the two terms in Eq. (22) determines the direction of F_z. F_z given by Eq. (22), becomes zero for

$$z_0^4=\frac{9(\varepsilon-1)}{32k_0^4(\varepsilon+1)}. \tag{23}$$

Hence, in our example we find $z_0=57$ nm. Below the value of Eq. (23) the force is attractive towards the surface, and above this value the sphere is pushed away. This is seen in the inset of Fig. 3 which enlarges those details. We find $F_z=0$ at $z=47$ nm namely at $z_0=(47+10)$ nm$=57$ nm, which is exactly the same value previously found. Physically, the attraction of the sphere is due to the second term of Eq. (22), which corresponds to the interaction of the dipole with its own evanescent field reflected by the surface. Now we can explain the discrepancy between the dipole approximation and the CDM as regards the good results obtained in free space. In fact, when the computation is done in free space the field can be considered uniform over a range of 20 nm. However, in an evanescent field, the applied field is not uniform inside the sphere and the Clausius-Mossotti relation is less adequate. Hence the dipole approximation departs more from the exact calculation. However, when the sphere is out from the near field zone, the three methods match well (see the inset of Fig. 3). We can also see in the

TABLE II. Force on a finite cylinder of radius $a=10$ nm in free space. The discretization interval is $d=4$ nm. Numerical results are presented for different lengths L of the cylinder for both CDM-A and CDM-B. Comparison is made with both the dipolar approximation and Mie's calculation. % (Mie) is the relative difference between the exact Mie calculation for an infinite cylinder and the method used. Calculations are done for the field perpendicular to the axis of the cylinder.

CDM-A			CDM-B			Dipole approx.		Mie
Force	L (nm)	% (Mie)	Force	L (nm)	% (Mie)	Force	% (Mie)	Force
2.1540×10^{-13}	197	24	2.1625×10^{-13}	197	24	2.8433×10^{-13}	0.27	2.8354×10^{-13}
2.9906×10^{-13}	391	5.47	3.0013×10^{-13}	391	5.85			
2.7907×10^{-13}	777	1.58	2.8000×10^{-13}	777	1.25			
2.8661×10^{-13}	1164	1.08	2.8756×10^{-13}	1164	1.42			
2.8347×10^{-13}	1551	0.03	2.8439×10^{-13}	1551	0.30			

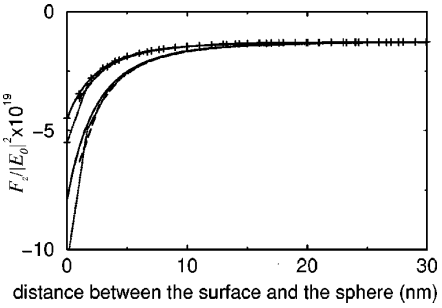

FIG. 4. Normalized force in the Z direction acting on the sphere with $a=10$ nm. The angle of incidence $\theta=42°$ is larger than the critical angle $\theta_c=41.8°$. The full line corresponds to the dipole approximation, the dashed line to the CDM-A, and the dotted line to the CDM-B. Curves without symbols are for p polarization, and those with symbol + are for s polarization.

inset of Fig. 3 that these three curves tend towards the Mie limit because at large distance there is no interaction with the surface.

Figure 4 shows the z component of the normalized force when the incident wave illuminated at $\theta=42°>41.8°=\theta_c$. Then, for s polarization we can write Eq. (12) as

$$F_z=\frac{|E_{0y}|^2}{|8z_0^3+\alpha\Delta|^2}[-4z_0^3\gamma\alpha_0(\alpha_0\Delta+8z_0^3)+6z_0^2\alpha_0^2\Delta]. \tag{24}$$

It is easy to see that for a dielectric sphere both the first and second terms within the brackets of Eq. (24) are always negative. Hence, the sphere is always attracted towards the surface (the same reasoning can be done for p polarization). Near the surface the force becomes larger because of the interaction of the sphere with its own evanescent field. We notice that the normalized force becomes constant at larger z. This constant reflects the fact that the force decreases as $e^{-2\gamma z}$ from the surface.

B. Results for a small cylinder

Let us now address an infinite cylinder. Since the CDM method used here works in three dimensions, we have computed the force on a finite length cylinder. In order to verify this approximation, we once again compare the force, obtained in free space from the CDM with different cylinders lengths, with that from a calculation done with the dipole approximation established in Sec. III B, and that from an exact calculation for an infinite cylinder[40] (i.e., the well known 2D version for cylinders of the Mie calculation for spheres). We consider a radius of the cylinder, $a=10$ nm, with the same spacing lattice as for the case of the sphere, namely 81 subunits. We have seen that this value of $d=4$ nm gives consistent results. In all cases we compute the force per unit length of the cylinder.

The first case addressed is with the electric field perpendicular to the axis of the cylinder (p polarization). The results are given in the Table II. The second case considered is with the electric field parallel to the axis of the cylinder (s polarization) in Table III.

We notice that the dipole approximation gives the correct results for p polarization, but it is worse for s polarization. If we compare CDM-A and CDM-B, we see that they both give the same results. But we also see that the length of the cylinder has a great influence, although up to a different extent according to whether we deal with p or s polarization. For p polarization, the simulation of an infinite cylinder becomes correct at $L\simeq\lambda/2$ and for s polarization only it is so at $L\simeq 2\lambda$. This can be understood by the fact that in p polarization the electric field is continuous at the end of the cylinder; thus the end does not have a large influence on the field computed around the cylinder. However, in s polarization the field is discontinuous at the end of the cylinder and then the field will strongly vary around this end and so will do the force. This is why in s polarization it is necessary to consider cylinders with large lengths in order to avoid edge effects. Now let us address the presence of the plane surface to compute the force. We consider the cylinder length $L=1551$ nm. Like for the sphere, we address both $\theta=0°$ (Fig. 5), and 42° (Fig. 6). The curves from CDM-B stop at $z=10$ nm due to the disadvantage previously noted.

Concerning Fig. 5, if we focus on F_z for p polarization, we can write this force approximated from Eq. (20) by

$$F_z=\frac{4z_0^4|E_0|^2}{|2z_0^2+\alpha_1\Delta|^2}\left((\alpha_1^0)^2k_0^3\pi/4+\frac{(\alpha_1^0)^2\Delta}{4z_0^3}\right). \tag{25}$$

Equation (25) is of the same form as Eq. (22). Hence, the same consequence is derived: near the surface the cylinder is attracted towards the plane surface. But far from the plane the cylinder is pushed away because at this distance the cylinder cannot interact with itself. As with the sphere, we can compute the distance z_0 at which the force is null,

$$z_0^3=\frac{(\varepsilon-1)}{\pi k_0^3(\varepsilon+1)}, \tag{26}$$

which in our illustration leads to $z_0=50$ nm. Although we do not present now an enlargement with details of Fig. 5, we

TABLE III. The same as in Table II but for the electric field parallel to the axis of the cylinder.

CDM-A			CDM-B			Dipole. approx.		Mie
Force	L (nm)	% (Mie)	Force	L (nm)	% (Mie)	Force	% (Mie)	Force
0.5649×10^{-12}	197	63	0.2163×10^{-12}	197	86	1.5015×10^{-12}	2.31	1.5370×10^{-12}
0.9986×10^{-12}	391	35	1.0021×10^{-12}	391	35			
1.3059×10^{-12}	777	15.0	1.3103×10^{-12}	777	14.7			
1.3971×10^{-12}	1164	9.10	1.4018×10^{-12}	1164	8.80			
1.4430×10^{-12}	1551	6.12	1.4479×10^{-12}	1551	5.80			

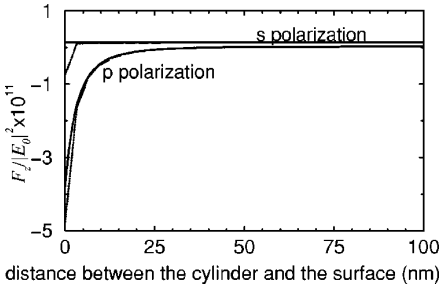

FIG. 5. Normalized force in the Z direction on a cylinder with radius $a=10$ nm, $\lambda=632.8$ nm, and $\varepsilon=2.25$. The light angle of incidence is $\theta=0°$. The full line corresponds to the dipole approximation, the dashed line to the CDM-A, and the dotted line to the CDM-B.

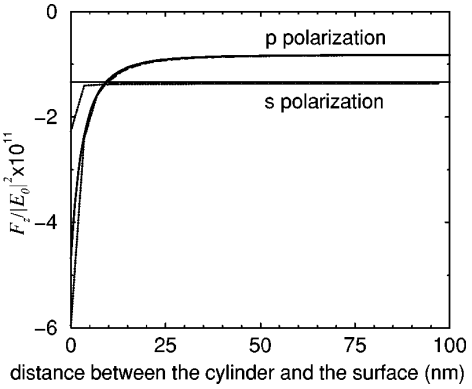

FIG. 6. Normalized force in the Z direction on the same cylinder as described in Fig. 5 but with an angle of incidence $\theta=42°$ larger than the critical angle $\theta_c=41.8°$. The full line corresponds to the dipole approximation, the dashed line to the CDM-A, and the dotted line to the CDM-B.

have found the value $z_0=(40+10)$ nm$=50$ nm. The cylinder in p polarization has the same behavior as the sphere. However, in s polarization there is a difference. Then the force obtained from the dipolar approximation is always constant because there is no interaction with the surface. This is clear from Eq. (19), and it is due to the fact that in the electrostatic limit S_{yy} tends to zero, and then there is no influence of the surface on the cylinder. This is a consequence of the continuity of both the field and its derivative of both the plane and the cylinder.[38] Therefore, the cylinder does not feel the presence of the plane. As the wave is propagating, the force is positive, thus pushing the cylinder away from the plane with magnitude values given by Table III. Notice that the force obtained from CDM-B, when the cylinder is in contact with the surface, becomes negative in s polarization. This is due to the diffraction of the field at the end of the cylinder, which induces a component perpendicular to the plane, and therefore an attractive force.

In the case represented in Fig. 6, as for the sphere, we observe a force always attractive ($F_z<0$) whatever the polarization. For p polarization we have exactly the same behavior as for the sphere. However, for s polarization the normalized force is always constant whatever the distance between the cylinder and the surface, due to the same reason as before, namely, $S_{yy}=0$. Only when the cylinder is on the surface can we see from the CDM-B calculation that the force is slightly more attractive for the same reason previously quoted.

C. Results for a sphere beyond the Rayleigh regime

Let us now consider a sphere of radius $a=100$ nm. This size is far from the Rayleigh scattering regime ($\approx\lambda/3$). As in previous cases, we first validate our method with the aid of Mie's calculation in free space. Table IV shows the results. As before, as d decreases, the CDM results tend to the Mie calculation, the error never exceeding 1.7%. Now, we address the presence of a flat dielectric surface. The forces, to be shown next, are computed with CDM-B only since the particle can be in contact with the surface.

In Fig. 7 we present the case for $\theta=0°$. We have plotted two curves: the exact calculation and the SALRS done with $N=1791$. In the inset of Fig. 7, we see that even near the surface SALRS is not good. This is due to the large radius of the sphere; then the discretization subunits on the top of the sphere are at 100 nm from the surface, and thus the effects of retardation are now important. The SALRS calculation also shows that at a distance of 200 nm (which corresponds to the size of the sphere: $2a=200$ nm) the sphere does not ''feel'' the surface, as manifested by the fact that then the curve obtained from this computation reaches the Mie scattering limit previously obtained in Table IV (cf. the full horizontal line in the inset). Hence, we conclude that evanescent waves are absent from the interaction process at distances beyond this limit. From the exact calculation we obtain a very low force near the surface, due to the interaction of the sphere with itself. This effect vanishes beyond $z\approx 50$ nm where oscillations of the force F_z take place with period $\lambda/2$. As these oscillations do not occur in the SALRS, this means that they are due to interferences from multiple reflections between the surface and the sphere. As expected, they decrease as the sphere goes far from the surface.

TABLE IV. Force on a sphere of radius $a=100$ nm in free space. Numerical results are for different number of subunits N in CDM-A and CDM-B. Comparison with Mie's calculation also given.

CDM-A			CDM-B			Mie
Force	N (d in nm)	% (Mie)	Force	N (d in nm)	% (Mie)	Force
2.1355×10^{-16}	280 (25)	1.31	2.1439×10^{-16}	280 (25)	1.71	2.1080×10^{-16}
2.1353×10^{-16}	912 (17)	1.30	2.1402×10^{-16}	912 (17)	1.53	
2.1332×10^{-16}	1791 (13)	1.20	2.1367×10^{-16}	1791 (13)	1.37	
2.1312×10^{-16}	4164 (10)	1.11	2.1333×10^{-16}	4224 (10)	1.21	

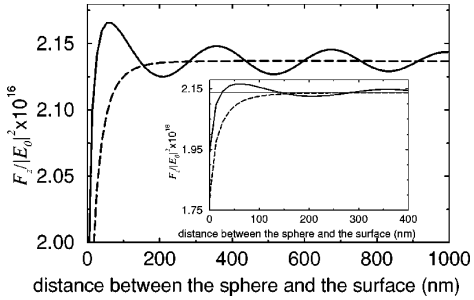

FIG. 7. Normalized force in the Z direction on a sphere with radius $a=100$ nm, $\lambda=632.8$ nm, and $\varepsilon=2.25$. The light angle of incidence is $\theta=0°$. The full line corresponds to the exact calculation with CDM-B, and the dashed line represents the static approximation.

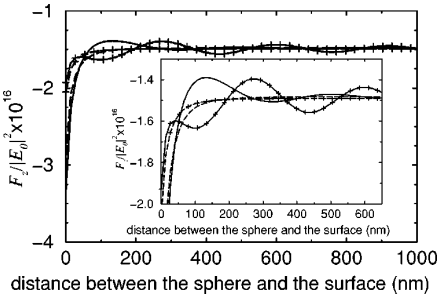

FIG. 8. Normalized force in the Z direction on a sphere with radius $a=100$ nm, $\lambda=632.8$ nm, and $\varepsilon=2.25$. The light angle of incidence is $\theta=42°>\theta_c$. The full line corresponds to the exact calculation with CDM-B, and the dashed line to the static approximation. The curves without symbol are in p polarization, and those with the + symbol in s polarization.

Figure 8 shows the force computed with an angle of incidence $\theta=42°$. We plot the exact calculation (full line) and the SALRS (dashed line) both for p polarization (no symbol) and s polarization (+ symbol). Once again, we see that the SALRS is not adequate even near the surface. On the other hand, in the exact calculation, the two polarizations show oscillations of the force F_z with period $\lambda/2$. However, there is a large difference of magnitude of these oscillations between the two polarizations (see inset of Fig. 8). To understand this difference, we must recall that the sphere is a set of dipoles. When a dipole is along the Z direction there is no propagating wave in this direction. But if the dipole is oriented in the X (or Y) direction, its radiation is maximum in the Z direction. However, in s polarization all dipoles are, approximately, parallel to the surface, so there is an important radiation from the dipole in the Z direction and consequently between the sphere and the surface.

V. CONCLUSIONS

In this paper we have presented exact three-dimensional calculations based on the coupled dipole method and an analytical expression for the force on either a sphere or an infinite cylinder, both in front of a flat dielectric surface. The results for electrically small bodies show that, whatever the polarization, in the case of a sphere, and in p polarization for the cylinder, the force always has the same behavior: namely, in the case of illumination under total internal reflection, the particle is always attracted towards the surface. A surprising result in the case when the illuminating beam is perpendicular to the surface and the object remains stuck to the surface is that the force is attractive due the interaction of the particle with itself, and therefore this object keeps stuck to the surface. However, when the object is far from the surface, the force becomes repulsive, as one would have expected.

For s polarization, the cylinder does not ''feel'' the presence of the substrate. This is more noticeable for a propagating wave, namely, at angles of incidence lower than the critical angle. However, when an evanescent wave is created by total internal reflection, the force is attractive under s polarization.

The scope of the static calculation for this configuration has been validated. We have also shown the advantage of having an analytical form that shows the contribution of the incident field on the particle, as well as that of the force induced by the sphere (or cylinder) on itself, thus yielding a better understanding of the physical process involved.

For bigger spheres, we have observed somewhat different effects of the forces. Under the action of evanescent waves, the force is always attractive, but it always becomes repulsive when it is due to propagating waves. Unlike the case of the small sphere, there is no point of zero force.

ACKNOWLEDGMENTS

This work has been supported by the European Union, Grant No. ERBFMRXCT 98-0242 and by the DGICYT, Grant No. PB 98-0464. The authors would like to thank J.-J Greffet and R. Carminati for helpful and valuable discussions. One of us, P. C., is particularly grateful to A. Rahmani for many constructive discussions.

[1] A. Ashkin, Phys. Rev. Lett. **24**, 56 (1970).
[2] A. Ashkin, Phys. Rev. Lett. **25**, 1321 (1970).
[3] A. Ashkin, J.M. Dziedzic, J.E. Bjorkholm, and S. Chu, Opt. Lett. **11**, 288 (1986).
[4] A. Ashkin, J.M. Dziedzic, and T. Yamane, Nature (London) **330**, 769 (1987).
[5] S.M. Block, D.F. Blair, and H.C. Berg, Nature (London) **338**, 514 (1989).
[6] A. Ashkin, Proc. Natl. Acad. Sci. USA **94**, 4853 (1997).
[7] L. Novotny, R.X. Bian, and X. Sunney Xie, Phys. Rev. Lett. **79**, 645 (1997).
[8] M. Tanaka, and K. Tanaka, J. Opt. Soc. Am. A **15**, 101 (1998).
[9] M. Renn, and R. Pastel, J. Vac. Sci. Technol. B **16**, 3859 (1998).
[10] K. Svoboda and S. Block, Opt. Lett. **19**, 930 (1994).
[11] T. Sugiura, T. Okada, Y. Inouye, O. Nakamura, and S. Kawata, Opt. Lett. **22**, 1663 (1997).
[12] R. Omori, T. Kobayashi, and A. Suzuki, Opt. Lett. **22**, 816 (1997).

[13] M. Burns, J.-M. Fournier, and J. Golovchenko, Phys. Rev. Lett. **63**, 1233 (1989).
[14] M. Gu and P. Ke, Appl. Phys. Lett. **75**, 175 (1999).
[15] M.I. Antonoyiannakis and J.B. Pendry, Phys. Rev. B **60**, 2363 (1999).
[16] M.I. Antonoyiannakis, and J.B. Pendry, Europhys. Lett. **40**, 613 (1997).
[17] M. Bayer, T. Gutbrod, A. Forchel, T.L. Reinecke, P.A. Knipp, A.A. Dremin, V.D. Kulakovskii, and J.P. Reithmaier, Phys. Rev. Lett. **81**, 2582 (1997).
[18] S. Kawata and T. Sugiura, Opt. Lett. **17**, 772 (1992).
[19] E. Almaas and I. Brevik, J. Opt. Soc. Am. B **12**, 2429 (1995).
[20] M. Lester and M. Nieto-Vesperinas, Opt. Lett. **24**, 936 (1999).
[21] K. Visscher and G.J. Brakenhoff, Optik (Stuttgart) **89**, 174 (1992).
[22] J.P. Barton, D.R. Alexander, and S.A. Scaub, J. Appl. Phys. **66**, 4594 (1989).
[23] S. Chang, J.H. Jo, and S.S. Lee, Opt. Commun. **108**, 133 (1994).
[24] C.E. Dungey and C.F. Bohren, J. Opt. Soc. Am. A **8**, 81 (1991).
[25] P.C. Chaumet, A. Rahmani, F. de Fornel, and J.-P. Dufour, Phys. Rev. B **58**, 2310 (1998).
[26] E.M. Purcell and C.R. Pennypacker, Astrophys. J. **186**, 705 (1973).
[27] J.D. Jackson, *Classical Electrodynamics*, 2nd ed. (Wiley, New York, 1975), p. 395.
[28] A. Rahmani (private communication).
[29] G.S. Agarwal, Phys. Rev. A **11**, 230 (1975); **12**, 1475 (1975).
[30] A. Rahmani, P.C. Chaumet, F. de Fornel, and C. Girard, Phys. Rev. A **56**, 3245 (1997).
[31] B.T. Draine, Astrophys. J. **333**, 848 (1988).
[32] P.C. Chaumet and M. Nieto-Vesperinas (unpublished).
[33] In fact **F** is the time averaged force on the particle.
[34] J.A. Stratton, *Electromagnetic Theory* (McGraw-Hill, New York, 1941).
[35] J.P. Gordon, Phys. Rev. A **8**, 14 (1973).
[36] A. Lakhtakia, Int. J. Mod. Phys. C **34**, 583 (1992).
[37] A.D. Yaghjian, Proc. IEEE **68**, 248 (1980).
[38] F. Pincemin, A. Sentannac, and J.-J. Greffet, J. Opt. Soc. Am. A **11**, 1117 (1994).
[39] J.-J. Greffet, Opt. Commun. **72**, 274 (1989).
[40] H.C. van de Hulst, *Light Scattering by Small Particles* (Dover, New York, 1981).

PHYSICAL REVIEW B VOLUME 62, NUMBER 16 15 OCTOBER 2000-II

Electromagnetic force on a metallic particle in the presence of a dielectric surface

P. C. Chaumet and M. Nieto-Vesperinas
Instituto de Ciencia de Materiales de Madrid, Consejo Superior de Investigaciones Científicas, Campus de Cantoblanco, Madrid 28049, Spain
(Received 5 April 2000)

By using a method, previously established, to calculate electromagnetic fields, we compute the force of light upon a metallic particle. This procedure is based on both Maxwell's stress tensor and the couple dipole method. With these tools, we study the force when the particle is over a flat dielectric surface. The multiple interaction of light between the particle and the surface is fully taken into account. The wave illuminating the particle is either evanescent or propagating depending an whether or not total internal reflection takes place. We analyze the behavior of this force on either a small or a large particle in terms of the wavelength. A remarkable result obtained for evanescent field illumination is that the force on a small silver particle can be either attractive or repulsive depending on the wavelength. This behavior also varies as the particle becomes larger.

I. INTRODUCTION

Since the first demonstration of particle manipulation by the action of optical forces,[1,2] optical tweezers[3] and other configurations of light beams have been established to hold suspended particles like molecules, [4] or more recently, dielectric spheres.[5–7] Also, the possibilities of creating microstructures by optical binding and resonance effects have been discussed[8–12] as well as the control of particles by evanescent waves.[13,14] Only a few works exist on the interpretation, prediction, and control of the optical force acting on a small particle on a plane surface. To our knowledge, the only theoretical works dealing with this subject are those of Refs. 15–17. In Ref. 15 no multiple interaction of the light between the particle and the dielectric surface is considered. On the other hand, Ref. 16 deals with a two-dimensional (2D) situation. Only recently in Ref. 17 the full 3D case with multiple scattering was addressed for dielectric particles.

This paper, extends the study of Ref. 17 to metallic particles and, as such, this is the first theoretical study of light action on a metallic particle. We shall therefore present a rigorous procedure to evaluate the electromagnetic force in three dimensions. Further, we shall analyze how this force depends on the wavelength, distance between the particle and the surface, angle of incidence (whether the excitation is a plane propagating or an evanescent wave), and on the excitation of plasmons on the sphere. We shall make use of the couple dipole method previously employed, whose validity was analyzed in detail in Ref. 17.

In Sec. II we introduce a brief outline on the method used to compute the optical force on a particle. We also write its expression from the dipole approximation for a metallic sphere in the presence of a surface. Then, in Sec. III A we present the results and discussion obtained in the limit of a small sphere, and in Sec. III B we analyze the case of larger spheres compared to the wavelength.

II. COMPUTATION OF THE OPTICAL FORCES

The coupled dipole method (CDM) was introduced by Purcell and Pennypacker in 1973.[18] In this paper we use this procedure together with Maxwell's stress tensor[19] in order to compute the optical forces on a metallic object in the presence of a surface. Since we developed this method in a previous paper,[17] we shall now outline only its main features. It should be remarked that all calculations next will be written in cgs units for an object in vacuum.

The system under study is a sphere, represented by a cubic array of N polarizable subunits, above a dielectric flat surface. The field at each subunit can be written:

$$\mathbf{E}(\mathbf{r}_i,\omega)=\mathbf{E}_0(\mathbf{r}_i,\omega)+\sum_{j=1}^{N}[\mathbf{S}(\mathbf{r}_i,\mathbf{r}_j,\omega)+\mathbf{T}(\mathbf{r}_i,\mathbf{r}_j,\omega)]\alpha_j(\omega)\mathbf{E}(\mathbf{r}_j,\omega) \quad (1)$$

where $\mathbf{E}_0(\mathbf{r}_i,\omega)$ is the field at the position $\mathbf{r}_i$ in the absence of the scattering object, and $\mathbf{T}$ and $\mathbf{S}$ are the field susceptibilities associated to the free space[20] and the surface,[21,22] respectively. $\alpha_i(\omega)$ is the polarizability of the ith subunit. Like in Ref. 17 we use the polarizability of the Clausius-Mossotti relation with the radiative reaction term given by Draine:[23]

$$\alpha=\frac{\alpha_0}{1-(2/3)ik_0^3\alpha_0}, \quad (2)$$

where α_0 holds the usual Clausius-Mossotti relation $\alpha_0=a^3(\varepsilon-1)/(\varepsilon+2)$.[17,24] In a recent paper,[25] we have shown the importance to compute the optical forces taking into account the radiative reaction term in the equation for the polarizability of a sphere. For a metallic sphere, the polarizability is written as $\alpha=\alpha_0[1+(2/3)ik_0^3\alpha_0^*]/D$ with $D=1+(4/3)k_0^3\,\mathrm{Im}(\alpha_0)+(4/9)k_0^6|\alpha_0|^2$, where the asterisk stands for the complex conjugate and $\Im m$ denotes the imaginary part.

The force[26] at each subunit is[25]

$$F_k(\mathbf{r}_i)=(1/2)\mathrm{Re}\left[\alpha_i E_{il}(\mathbf{r}_i,\omega)\left(\frac{\partial}{\partial k}E^l(\mathbf{r},\omega)\right)^*_{\mathbf{r}=\mathbf{r}_i}\right], \quad (3)$$

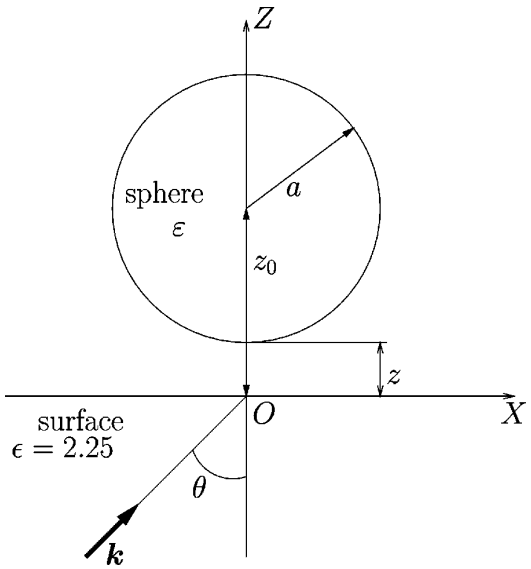

FIG. 1. Geometry of the configuration considered. Sphere of radius a on a dielectric flat surface ($\epsilon=2.25$). The incident wave vector $\mathbf{k}$ is in the XZ plane.

where k and l stand for the components along either x, y or z, and Re denotes the real part. The object is a set of N small dipoles so that it is possible to compute the force on each one from Eq. (3). Hence, to obtain the total force on the particle, it suffices to sum the contributions $\mathbf{F}(\mathbf{r}_i)$ on each dipole.

Being the object under study a small sphere located at $\mathbf{r}_0=(0,0,z_0)$ (see Fig. 1), we can employ the dipole approximation, and hence use directly Eq. (3) with $N=1$. Within the static approximation for the field susceptibility associated to the surface (SAFSAS) (that is to say $k_0=0$), we have found an analytical expression for $\mathbf{E}(\mathbf{r}_0,\omega)$ that yields the force components:[17]

$$F_x=\frac{\mathrm{Re}}{2}\left[4\alpha z_0^3(ik_x)^*\left(\frac{2|E_{0x}|^2}{8z_0^3+\alpha\Delta}+\frac{|E_{0z}|^2}{4z_0^3+\alpha\Delta}\right)\right], \quad (4)$$

$$F_z=|E_{0x}|^2\frac{\mathrm{Re}}{2}\left(\frac{8z_0^3\alpha(ik_z)^*}{8z_0^3+\alpha\Delta}+\frac{12z_0^2|\alpha|^2\Delta}{|8z_0^3+\alpha\Delta|^2}\right)+|E_{0z}|^2\frac{\mathrm{Re}}{2}\left(\frac{4z_0^3\alpha(ik_z)^*}{4z_0^3+\alpha\Delta}+\frac{6z_0^2|\alpha|^2\Delta}{|4z_0^3+\alpha\Delta|^2}\right). \quad (5)$$

for p-polarization, and

$$F_x=|E_{0y}|^2\frac{\mathrm{Re}}{2}\left[\frac{8z_0^3\alpha(ik_x)^*}{8z_0^3+\alpha\Delta}\right], \quad (6)$$

$$F_z=|E_{0y}|^2\frac{\mathrm{Re}}{2}\left(\frac{8z_0^3\alpha(ik_z)^*}{8z_0^3+\alpha\Delta}+\frac{12z_0^2|\alpha|^2\Delta}{|8z_0^3+\alpha\Delta|^2}\right). \quad (7)$$

for s-polarization, with $\Delta=(1-\epsilon)/(1+\epsilon)$ being the Fresnel coefficient of the surface. We have assumed a dielectric surface, hence Δ is real.

From Fig. 1 is easy to see that k_x is always real whatever the angle θ, hence we can write Eqs. (4) and (6) for metallic particles as

$$F_x=\left(\frac{|E_{0x}|^2 64z_0^6}{|8z_0^3+\alpha\Delta|^2}+\frac{|E_{0z}|^2 16z_0^6}{|4z_0^3+\alpha\Delta|^2}\right)[k_x\ \mathrm{Im}(\alpha_0)/(2D)+k_xk_0^3|\alpha_0|^2/(3D)] \quad (8)$$

for p polarization, and

$$F_x=\frac{|E_{0y}|^2 64z_0^6}{|8z_0^3+\alpha\Delta|^2}[k_x\ \mathrm{Im}(\alpha_0)/(2D)+k_xk_0^3|\alpha_0|^2/(3D)] \quad (9)$$

for s polarization. In Eq. (8) the factor in front of $[k_x\ \mathrm{Im}(\alpha_0)/(2D)+k_xk_0^3|\alpha_0|^2/(3D)]$ for the two polarizations constitutes the field intensity at z_0. The first term within these square brackets corresponds to the absorbing force whereas the second represents the scattering force on the sphere. We see from Eqs. (8) and (9) that F_x always has the sign of k_x. Notice that it is not possible to write a general equation for the force along the Z direction, as k_z will be either real or imaginary, according to the angle of incidence.

III. RESULTS AND DISCUSSION

All forces calculated in this section are in cgs units with the modulus of the incident field normalized to unity.

A. Small particles

We first address a small isolated silver particle with radius $a=10$ nm. In this case we can use the dipole approximation, hence we consider Eqs. (4)–(7) with $\Delta=0$. Figure 2(a) presents the polarizability modulus ($|\alpha_0|$) of the sphere. The maximum of the curve corresponds to the plasmon resonance, i.e., when the dielectric constant is equal to -2 in Drude's model. Notice that in this model the dielectric constant is real, on using experimental values,[27] the dielectric constant is complex and the resonance is not exactly at $\mathrm{Re}(\varepsilon)=-2$ but slightly shifted. In Fig. 2(b) we plot the real part of the polarizability [$\mathrm{Re}(\alpha_0)$], and Fig. 2(c) shows its imaginary part [$\mathrm{Im}(\alpha_0)$]. Figure 2(d) represents the force in free space computed from an exact Mie calculation (full line) and by the dipole approximation from Eqs. (4)–(7) with $\Delta=0$ (dashed line) and Eq. (2) for α. In this case, the dipole approximation slightly departs from Mie's calculation between 350 nm and 375 nm. We can compute the polarizability α from the first Mie coefficient a_1 given by Dungey and Bohren (DB).[28] Therefore, the electric-dipole polarizability is $\alpha=3ia_1/(2k_0^3)$.[29] The symbol + in Fig. 2(d) corresponds to the DB polarizability and it is exactly coincident with the Mie calculation. When the optical constant of the metallic sphere is close to the plasmon resonance, the calculation from the Clausius-Mossotti relation with the radiative reaction term, departs from the exact calculation, even for a small radius. We shall next use the polarizability of DB. Analytical calculations will always be done with Eq. (2) to get simple expressions, and thus a better understanding of the physics involved. The curve of the force obtained by

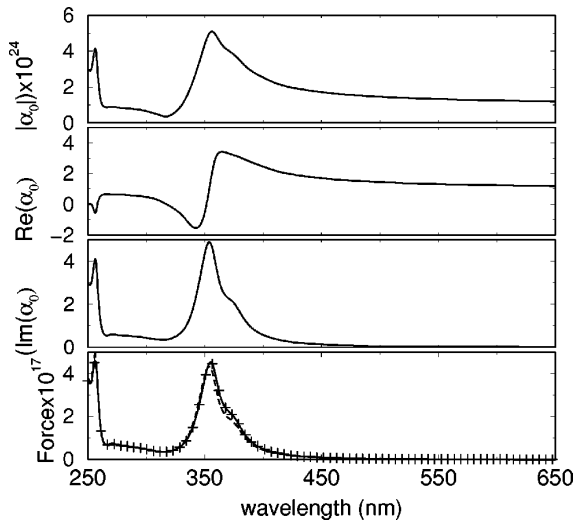

FIG. 2. From top to bottom: the first three curves represent the modulus, the real part, and the imaginary part of the polarizability of a silver sphere with radius $a=10$ nm versus the wavelength. The fourth curve is the force on this particle in free space. Plain line: Mie calculation, dashed line: polarizability of Clausius-Mossotti relation with the radiative reaction term, symbol +: DB polarizability.

Mie's calculation has exactly the same shape as the imaginary part of the polarizability, this is due to the fact that for a small metallic sphere the absorbing force is larger than the scattering force.

Next, we consider the small sphere on a dielectric plane surface as shown by Fig. 1. Illumination takes place from the dielectric side with $\theta=0°$, hence in vacuum $k_z=k_0$ and $k_x=0$. Figure 3 represents the force in the Z direction from Eq. (7) versus z for different wavelengths. Far from the surface the force tends to the Mie limit. Near the surface the force decreases, and, depending on the wavelength, it can become negative. For a better understanding of this force we write Eq. (7) as

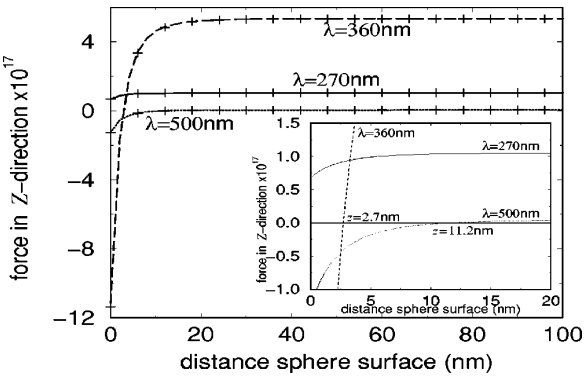

FIG. 3. Force along the Z direction on a silver sphere with $a=10$ nm versus distance z in the dipole approximation. The angle of incidence is $\theta=0°$. With the static approximation (no symbol) and in an exact calculation (+) for **k**. Dashed line $\lambda=360$ nm, plain line $\lambda=270$ nm, and dotted line $\lambda=500$ nm. The inset shows details of the zero force.

$$F_z=\frac{64z_0^6|E_0|^2}{|8z_0^3+\alpha\Delta|^2}\left[\frac{k_0}{2}\mathrm{Im}(\alpha_0)+\frac{k_0^4}{3}|\alpha_0|^2+\frac{3|\alpha_0|^2\Delta}{32z_0^4}\right], \tag{10}$$

having made the approximation $|\alpha|\approx|\alpha_0|$, and $D\approx1$ since we have a small sphere compared to the wavelength ($k_0a\ll1$). The factor in front of the bracket corresponds to the intensity of the field at z_0. The first and the second terms within brackets represent the interaction between the dipole moment associated to the sphere and the incident field: the first term is the absorbing force whereas the second one corresponds to the scattering force, hence these forces are always positive. The third term is due to the interaction between the dipole and the field radiated by the dipole and reflected by the surface. We can consider this term as a gradient force exerted on the sphere due to itself via the surface. Hence, this force is always negative whatever the relative permittivity ε. Since this term is proportional to $1/z_0^4$, it becomes more dominant as the sphere approaches the surface, hence the force decreases. To derive the point z_0 at which the force vanishes, if such a point exists, let us assume the scattering force smaller than the absorbing force, then from Eq. (10) the zero force is

$$z_0^4=\frac{3|\alpha_0|^2}{16k_0\ \mathrm{Im}(\alpha_0)}\,\frac{\epsilon-1}{\epsilon+2}. \tag{11}$$

This equation always has a solution. We find z_0 for the three wavelengths used to be: $\lambda=270$ nm, $z_0=7.9$ nm, $\lambda=360$ nm, $z_0=12.8$ nm, $\lambda=500$ nm, and $z_0=21.6$ nm. Now, z_0 (the location of the center of the sphere) must be larger than the radius a, or else, the sphere would be buried in the surface. Therefore the first of those values of z_0 is not possible. Hence, the force is always positive. Thus, the distance between the sphere and the surface is $z=2.8$ nm and 11.6 nm for $\lambda=360$ nm and 500 nm, respectively. These values are very close to those shown in the inset of Fig. 2. Notice that near the plasmon resonance for the sphere ($\lambda\approx360$ nm) both $|\alpha_0|$ and $\mathrm{Im}(\alpha_0)$ are maxima, hence the force is very large when the sphere is far from the surface and, due to the third term of Eq. (10), which depends of $|\alpha_0|^2$, the decay of this force is very fast. We have used the SAFSAS at large distance. We plot in Fig. 2 with crosses the force obtained from an exact calculation for **S** with the dipole approximation. As we see, these crosses coincide with those curves obtained with the SAFSAS whatever the distance z. Yet, we obtain for dielectric spheres the following: near the surface the SAFSAS is valid, whereas far from the surface the sphere does not feel its presence, and, thus, whether using the tensor susceptibility associated to the surface in its exact form, or within the static approximation, has no influence.

We next consider the surface illuminated at angle of incidence θ larger than the critical angle: $\theta=50°>41.8°=\theta_c$. Now the transmitted electromagnetic wave above the surface is evanescent. We plot in Fig. 4 from Eqs. (4)–(7) the force on the sphere for the two polarizations in the Z direction versus the wavelength, and in the X direction in Fig. 5, when the sphere is located at $z_0=30$ nm. In Fig. 4 we see that the force in the Z direction is also either positive or negative. In a previous work,[17] we have observed that the force on a

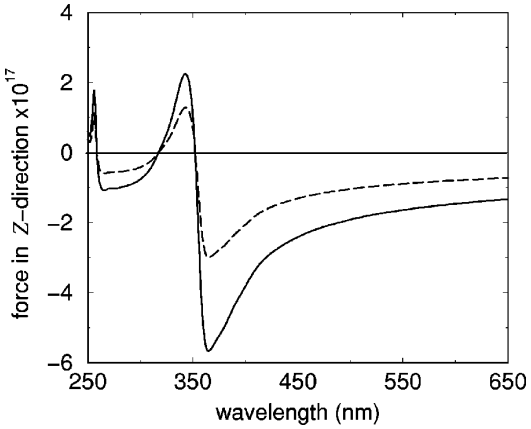

FIG. 4. Force along the Z direction on a silver sphere with $a=10$ nm versus the wavelength λ in the dipole approximation. The angle of incidence is $\theta=50°$. Plain line: p polarization and dashed line: s polarization.

small dielectric sphere is always attractive when the sphere is located in an evanescent wave. This is no longer the case for a metallic sphere. To understand this difference, and as the two polarizations have the same behavior, we take the analytical solution for F_z with $k_z=i\gamma$ ($\gamma>0$) for s polarization. Then Eq. (7) can be written:

$$F_z=\frac{|E_{0y}|^2}{|8z_0^3+\alpha\Delta|^2}\frac{\mathrm{Re}}{2}[-\gamma 8z_0^3\alpha(8z_0^3+\alpha^*\Delta)+12z_0^2|\alpha|^2\Delta] \tag{12}$$

On using the approximation $D\approx 1$ and $|\alpha|\approx|\alpha_0|$ we obtain

$$F_z=\frac{64z_0^6|E_{0y}|^2}{|8z_0^3+\alpha\Delta|^2}\left(-\frac{\gamma\,\mathrm{Re}(\alpha_0)}{2}-\frac{\gamma|\alpha_0|^2\Delta}{16z_0^3}+\frac{3|\alpha_0|^2\Delta}{32z_0^4}\right) \tag{13}$$

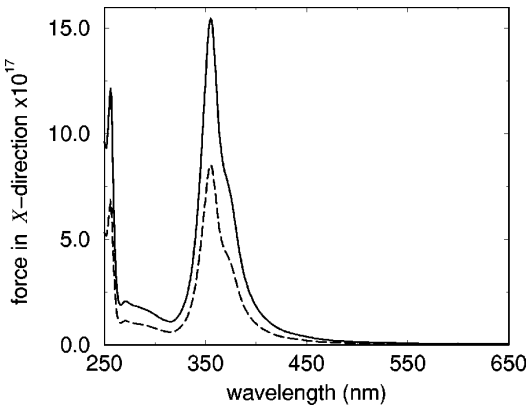

FIG. 5. Force along the X direction on a silver sphere with $a=10$ nm versus the wavelenght λ in the dipole approximation. The angle of incidence is $\theta=50°$. Plain line: p polarization and dashed line: s polarization.

As shown by Fig. 3, when the sphere is located at $z_0=30$ nm, the influence of the surface becomes negligible, thus we can use Eq. (13) with the hypothesis that z_0 is large. Hence, $F_z\approx-|E_{0y}|^2\gamma\,\mathrm{Re}(\alpha_0)/2$. This is the gradient force due to the incident field, and therefore due to the interaction between the dipole associated to the sphere and the applied field. This force exactly follows the behavior of $\mathrm{Re}(\alpha_0)$ (cf. Fig. 2). When $\mathrm{Re}(\alpha_0)$ is negative, the dipole moment of the sphere oscillates in opposition to the applied field and so the sphere is attracted towards the weaker field. Notice that the same phenomenon is used to build an atomic mirror: for frequencies of oscillation higher than the atomic frequency of resonance, the induced dipole oscillates in phase opposition with respect to the field. The atom then undergoes a force directed towards the region of weaker field.[30] For p polarization, the force can be written $F_z\approx-(|E_{0x}|^2+|E_{0z}|^2)\gamma\,\mathrm{Re}(\alpha_0)/2$. As the modulus of the field becomes more predominant in p polarization, the magnitude of the force becomes more important. We now search more carefully the change of sign in the force. Writing $\varepsilon=\varepsilon'+i\varepsilon''$ for the relative permittivity, we get

$$\mathrm{Re}(\alpha_0)=a^3\frac{(\varepsilon'-1)(\varepsilon'+2)+\varepsilon''^2}{(\varepsilon'+2)^2+\varepsilon''^2}, \tag{14}$$

$$\mathrm{Im}(\alpha_0)=a^3\frac{3\varepsilon''}{(\varepsilon'+2)^2+\varepsilon''^2} \tag{15}$$

If the damping is weak, then the change of sign of F_z happens both for $\varepsilon'\approx 1$ and at the plasmon resonance for the sphere, i.e., $\varepsilon'\approx-2$. Between these two values, the gradient force is positive. In fact, the limiting values of the positive gradient force are always strictly in the interval $[-2,1]$ due to damping. For example, the force vanishes at $\lambda=352$ nm with $\varepsilon=-1.91+0.6i$ and $\lambda=317$ nm with $\varepsilon=0.66+0.95i$. We notice that the change of sign happens steeply at the plasmon resonance since then the denominator of the real part of the polarizability becomes very weak [see Eq. (14)], hence the zero force is surrounded by the two maxima of the force (one positive and the other negative). At $\lambda=317$ nm the change of sign is smoother, as in that case, the denominator is far from zero. The third case, $\lambda=259$ nm, lies between those two previous cases as the damping of the relative permittivity is important: $\varepsilon=-1.65+1.12i$. We have also investigated the cases of gold and copper spheres, where a plasmon easily takes place, but we found a change of sign not possible for F_z for these two materials as the damping is then too important: if $\varepsilon''>3/2$, then $\mathrm{Re}(\alpha_0)$ is always positive whatever ε'. However, if the particle is embedded in a liquid with a relative permittivity 2, then it is possible to get $\mathrm{Re}(\alpha)<0$ for gold. Notice that if θ is close to θ_c, then $\gamma\approx 0$ and so we only have the third term of Eq. (13), then the force is always negative whatever the wavelength. In Fig. 5 we see, as previously, that the force in the X direction has the sign of k_x and, as the absorbing force is the most predominant one, the curve has the same shape as the imaginary part of the polarizability (cf. Fig. 2). In that case, the maximum of the force F_x is at the plasmon resonance [see Eq. (15)] namely, at $\lambda=354$ nm.

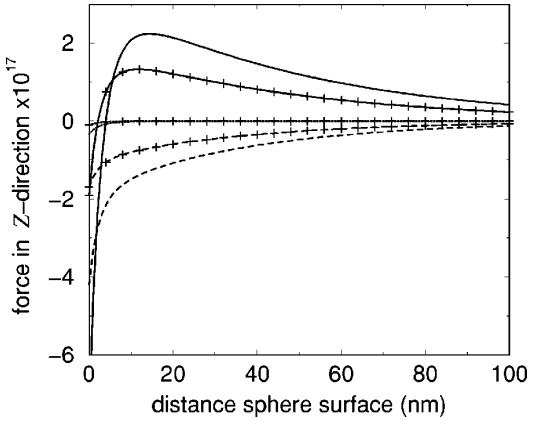

FIG. 6. Force along the Z direction on a silver sphere with $a=10$ nm versus distance z in the dipole approximation. The angle of incidence is $\theta=50°$. Without symbol: p polarization, with cross (+): s polarization. Plain line: $\lambda=340$ nm, dashed line: $\lambda=260$ nm, and dotted line: $\lambda=317.5$ nm.

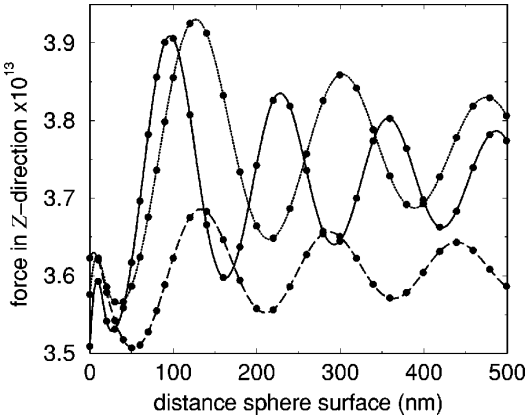

FIG. 7. Force along the Z direction on a silver sphere versus distance z with $\theta=0$ and $a=100$ nm for the following wavelengths: Plain line: $\lambda=255$ nm, dashed line: $\lambda=300$ nm, and dotted line: $\lambda=340$ nm. Dots correspond to computed points.

Figure 6 shows the force in the Z direction versus z for both s (symbol +) and p polarization (without any symbol) at three different wavelengths ($\lambda=265,340,317.5$ nm) for $\theta=50°$. The behavior is the same for both polarizations, only appearing as a difference of magnitude, this is due to the component of the field perpendicular to the surface in p polarization. All curves manifest that near the surface the force is attractive, this is due, as seen before, with a propagating wave, to the term of Δ/z_0^4 in Eqs. (10) and (13) which is always negative, irrespective of the kind of wave above the surface. At $\lambda=317.5$ nm (dotted line), we have $\mathrm{Re}(\alpha)=0$ which is why the force very quickly goes to zero when z grows. The two other cases correspond to $\mathrm{Re}(\alpha)>0$ ($\lambda=260$ nm) and $\mathrm{Re}(\alpha)<0$ ($\lambda=340$ nm) and far from the surface the force tends to zero. As the force is proportional to $|\mathbf{E}_0|^2$, we have $F_z \propto e^{(-2\gamma z)}$.

Notice, that when the sphere is close to the surface, the Casimir-Polder force[31] may be not negligible. In fact, as the light force depends on the intensity of the incident beam, in practice, a comparison of the two forces must be done for each specific configuration under study. In the case of a small sphere, either dielectric or metallic, in front of a dielectric plane surface, one can look at the discussion of Ref. 32.

B. Large particles

It is difficult to obtain convergence of the CDM calculations when the relative permittivity of the medium to be discretized is large. This imposes a very fine sampling. In this section, we use the range 250-355 nm for the wavelength, the real part of the relative permittivity being small. In that case, the difference between the force upon a sphere of radius $a=100$ nm, in free space, calculated from the CDM and that obtained from the exact calculation[33] is less than 7% at the plasmon resonance, and outside this range it is less than 4%. In this range of wavelengths, we have a good convergence of the CDM, and in addition, this is the most interesting case as $\mathrm{Re}(\alpha)$ crosses three times the axis $\mathrm{Re}(\alpha)=0$ in this interval of wavelengths. We do not take into account the Casimir-Polder force yet, but it can be computed in first approximation from Ref. 34.

In Fig. 7 we plot the force in the Z direction for an incident propagating wave ($\theta=0°$) versus the distance between the sphere and the surface at three different wavelengths: $\lambda=255$ nm, 300 nm, and 340 nm. The calculations are done without any approximation. The curves have a similar magnitude and behavior at the three wavelengths. The forces present oscillations due to the multiple reflection of the radiative waves between the sphere and the surface, hence the period of these oscillations is $\lambda/2$. The magnitude of these oscillations depends on the reflectivity of the sphere, so the higher the Fresnel coefficient is, the longer these oscillations are. As expected, they are less remarkable when the sphere goes far from the surface. We notice that the decay of the force when the metallic sphere gets close to the surface is not comparable to that on a dielectric sphere (see Ref. 17). This is due to strong absorbing and scattering forces on the metallic sphere in comparison to the gradient force induced by the presence of the dielectric plane.

In Fig. 8 we plot for $\theta=50°$ the normalized force in the Z direction, i.e., $F_z/|\mathbf{E}_0|^2$, $\mathbf{E}_0$ being the field at z_0 in the absence of the sphere. We relate two important facts at this angle of incidence. First, the decay of the force when the sphere is near the surface is more important in p polarization. Notice that with the CDM it is not possible to numerically split the scattering, absorbing, and gradient forces. Therefore, when the sphere is large we shall argue on the set of dipoles forming it. In p polarization, due to the z component of the incident field, the dipoles also have a component perpendicular to the surface, and this is larger than in s polarization. Hence, in agreement with Fig. 6, due to this z component, the attraction of the sphere towards the surface is larger for p polarization. Second, all forces are positive when the sphere is far from the surface except for $\lambda=300$ nm in p polarization. At this wavelength, for a small sphere, the force is negative for both s and p polarization, hence we can assume an effect due to the size of the sphere. Just to see this effect, we present in Fig. 9, the force in the Z direction versus the radius a, on a sphere located at $z_0=100$ nm for an angle of incidence $\theta=50°$ but without taking into account

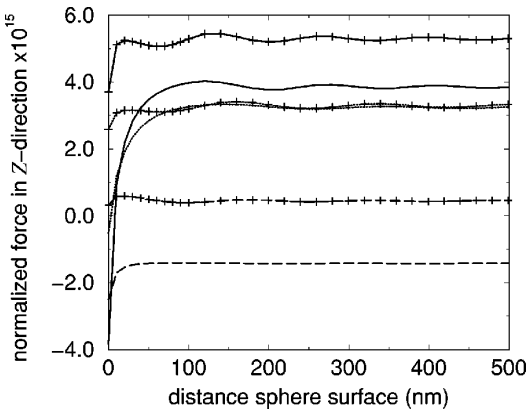

FIG. 8. Force along the Z direction on a silver sphere with $a=100$ nm versus distance z with $\theta=50°$ for the following wavelengths: Plain line: $\lambda=255$ nm, dashed line: $\lambda=300$ nm, and dotted line: $\lambda=340$ nm. symbol $+$: s-polarization and without symbol: p-polarization.

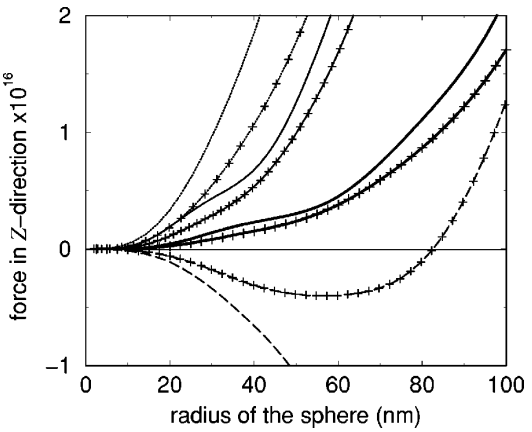

FIG. 9. Force along the Z direction on a silver sphere located at $z_0=100$ nm, with $\theta=50°$, versus the radius a for plain line: $\lambda=255$ nm, dashed line: $\lambda=300$ nm, dotted line: $\lambda=340$ nm, and thick line: $\lambda=351.5$ nm. Symbol $+$: s-polarization and without symbol: p-polarization. The interaction between the sphere and the surface is not taken into account.

the multiple interaction with the surface (i.e., $\mathbf{S}=0$). We take the previous wavelength of Fig. 8 ($\lambda=255$ nm, 300 nm, and 340 nm) more the wavelength at the plasmon resonance, $\lambda=351.5$ nm, where $\mathrm{Re}(\alpha_0)=0$. For small radius, we observe the same behavior as in the previous section for an incident evanescent wave. These curves show a dependence proportional to the cube of the radius as $\mathrm{Re}(\alpha_0)\propto a^3$. At the plasmon resonance, the force is slightly positive as there is no gradient force, but only weak absorbing and scattering forces. But as shown by Fig. 9, when the radius grows, in s polarization at $\lambda=300$ nm, the force sign changes and it becomes positive around 82 nm as p polarization keep the same behavior. This confirms the fact that the positive force obtained in Fig. 8 for $\lambda=300$ nm is only a size effect. For the cases $\lambda=255$ nm, and 340 nm, the gradient force is positive in the Z direction, like the scattering and absorbing forces. Hence, the force, is always positive whatever the radius. Nevertheless, for $\lambda=300$ nm, there is a negative gradient force, the two other forces being positive. As previously said, it is not possible to know the relative contribution of the different forces, but since the dipoles are mainly oriented along the direction of the incident electric field, namely, parallel to the surface for s polarization, and in the plane of incidence for p polarization, we can assume that due to the field radiative part in the normal direction, which is larger in s polarization, the absorbing and scattering forces acting on each subunit in the sphere, become relevant when its radius increases, thus counterbalancing the negative gradient force. At the plasmon resonance $\lambda=351.5$ nm, when the radius grows, the absorbing and scattering forces become larger, but then as no gradient force exists, the force is lower than those obtained at $\lambda=255$ nm and 340 nm. In fact, the curve shown at $\lambda=340$ nm is the one showing the largest force contribution, due to the onset of the plasmon resonance, thus $|\alpha_0|$ and $\mathrm{Im}(\alpha_0)$ are near their maximum, and $\mathrm{Re}(\alpha_0)$ is close to its minimum. In this case, the gradient force is maximum and positive.

IV. CONCLUSIONS

We have presented a theoretical study of the optical forces acting upon a metallic particle on a dielectric plane surface either illuminated at normal incidence or under total internal reflection. This paper is done both with the coupled dipole method and Maxwell's stress tensor. We observe that when the incident wave is propagating, the difference between the force acting on a dielectric sphere and that on a metallic sphere stems from the absorbing force. Due to this contribution, the force upon a small silver sphere close to the dielectric surface can be positive in spite of the gradient force. The opposite happens with a dielectric sphere. The main difference between the two cases (dielectric and metallic) arises however on illumination under total internal reflection. In that case, the effect on a small silver sphere is completely different to that observed on a dielectric sphere. Depending on the wavelength, the gradient force due to the incident field can be either repulsive or attractive. The change of sign happens both at the plasmon resonance and when ε becomes close to one. In the interval between these two values the gradient force is positive. The explanation is very similar to that on the effect used to build an atomic mirror. At a wavelength where the gradient force on a small sphere is negative, we see that when the sphere radius grows, the force along the Z direction stays negative for p polarization, and it becomes positive for s polarization due to the size effect. Nevertheless, at any arbitrary wavelength and angle of incidence, as the sphere approaches close to the surface, the attraction of the surface on the sphere increases, repulsive forces diminish and even can change sign, eventually becoming attractive at certain wavelengths. Attractive forces, on the other hand, increase their magnitude.

ACKNOWLEDGMENTS

This work was supported by the European Union and Dirección General de Investigación Científica y Técnica. P. C. acknowledges financial support from a TMR contract of the European Union.

[1] A. Ashkin, Phys. Rev. Lett. **24**, 156 (1970).
[2] A. Ashkin, Phys. Rev. Lett. **25**, 1321 (1970).
[3] A. Ashkin, J. M. Dziedzic, J. E. Bjorkholm, and S. Chu, Opt. Lett. **11**, 288 (1986).
[4] A. Ashkin and J. M. Dziedzic, Science **235**, 1517 (1987).
[5] S. D. Collins, R. J. Baskin, and D. G. Howitt, Appl. Opt. **38**, 6068 (1999).
[6] R. C. Gauthier and A. Frangioudakis, Appl. Opt. **39**, 26 (2000).
[7] K. Taguchi, K. Atsuta, T. Nakata, and M. Ikeda, Opt. Commun. **176**, 43 (2000).
[8] M. Burns, J.-M. Fournier, and J. Golovchenko, Phys. Rev. Lett. **63**, 1233 (1989).
[9] M. I. Antonoyiannakis, and J. B. Pendry, Phys. Rev. B **60**, 2363 (1999).
[10] M. I. Antonoyiannakis and J. B. Pendry, Europhys. Lett. **40**, 613 (1997).
[11] M. Bayer, T. Gutbrod, A. Forchel, T. L. Reinecke, P. A. Knipp, A. A. Dremin, V. D. Kulakovskii, and J. P. Reithmaier, Phys. Rev. Lett. **81**, 2582 (1998).
[12] L. Novotny, R. X. Bian, and X. Sunney Xie, Phys. Rev. Lett. **79**, 645 (1997).
[13] S. Kawata and T. Sugiura, Opt. Lett. **17**, 772 (1992).
[14] T. Sugiura, T. Okada, Y. Inouye, O. Nakamura, and S. Kawata, Opt. Lett. **22**, 1663 (1997).
[15] E. Almaas and I. Brevik, J. Opt. Soc. Am. B **12**, 2429 (1995).
[16] M. Lester and M. Nieto-Vesperinas, Opt. Lett. **24**, 936 (1999).
[17] P. C. Chaumet and M. Nieto-Vesperinas, Phys. Rev. B **61**, 14 119 (2000).
[18] E. M. Purcell and C. R. Pennypacker, Astrophys. J. **186**, 705 (1973).
[19] J. A. Stratton, *Electromagnetic Theory* (McGraw-Hill, New-York, 1941).
[20] J. D. Jackson, *Classical Electrodynamics*, 2nd ed. (Wiley, New York, 1975), p. 395.
[21] G. S. Agarwal, Phys. Rev. A **11**, 230 (1975); **12**, 1475 (1975).
[22] A. Rahmani, P. C. Chaumet, F. de Fornel, and C. Girard, Phys. Rev. A **56**, 3245 (1997).
[23] B. T. Draine, Astrophys. J. **333**, 848 (1988).
[24] $a^3 = 3d^3/(4\pi)$ where d is the spacing of lattice discretization. In the case of the dipole approximation a is the radius of the sphere.
[25] P. C. Chaumet and M. Nieto-Vesperinas, Opt. Lett. (to be published).
[26] In fact **F** is not exactly the force but moreever the time-averaged force.
[27] *Handbook of Optical Constants of Solids*, edited by E. D. Palik (Academic Press, New York, 1985).
[28] C. E. Dungey and C. F. Bohren, J. Opt. Soc. Am. A **8**, 81 (1991).
[29] W. T. Doyle, Phys. Rev. B **39**, 9852 (1989).
[30] L. Cognet, V. Savalli, G. Zs. K. Horvath, D. Holleville, R. Marani, C. I. Westbrook, N. Westbrook, and A. Aspect, Phys. Rev. Lett. **81**, 5044 (1998); A. Landragin, J.-Y. Courtois, G. Labeyrie, N. Vansteenkiste, C. I. Westbrook, and A. Aspect, *ibid.* **77**, 1464 (1996).
[31] H. B. G. Casmir and D. Polder, Phys. Rev. **73**, 360 (1948).
[32] L. H. Ford, Phys. Rev. A **58**, 4279 (1998).
[33] H. C. van de Hulst, *Light Scattering by Small Particles* (Dover, New York, 1981).
[34] S. K. Lamoreaux, Phys. Rev. Lett. **78**, 5 (1997); **81**, 5475 (1998).

PHYSICAL REVIEW B, VOLUME 64, 035422

Optical binding of particles with or without the presence of a flat dielectric surface

P. C. Chaumet and M. Nieto-Vesperinas
Instituto de Ciencia de Materiales de Madrid, Consejo Superior de Investigaciones Cientificas, Campus de Cantoblanco Madrid 28049, Spain
(Received 29 November 2000; published 28 June 2001)

Optical fields can induce forces between microscopic objects, thus giving rise to different structures of matter. We study theoretically these optical forces between two spheres, either isolated in water, or in the presence of a flat dielectric surface. We observe different behavior in the binding force between particles at large and at small distances (in comparison with the wavelength) from each other. This is due to the great contribution of evanescent waves at short distances. We analyze how the optical binding depends on the size of the particles, the material composing them, the wavelength, and, above all, the polarization of the incident beam. We also show that depending on the polarization the force between small particles at small distances changes its sign. Finally, the presence of a substrate surface is analyzed, showing that it only slightly changes the magnitudes of the forces, but not their qualitative nature, except when one employs total internal reflection, in which case the particles are induced to move together along the surface.

DOI: 10.1103/PhysRevB.64.035422 PACS number(s): 78.70.−g, 03.50.De, 42.50.Vk

I. INTRODUCTION

Some time ago, it was demonstrated that optical fields can produce forces on neutral particles;[1,2] since then this mechanical action has been used in optical tweezers[3] and more recently in optical force microscopy,[4,5] as well as in manipulating molecules[6] and dielectric spheres.[7–9] In addition, the possibility of binding objects[10] through optical forces and thus creating microstructures, in on- or off-resonant conditions,[11–13] was pointed out.

In this paper we wish to undertake a detailed study of optical forces on neutral particles, based on a rigorous analysis that we have carried out[14–16] in a full three-dimensional configuration by using the coupled dipole method of Purcell and Pennypacker[17] via the Maxwell stress tensor.[18] Specifically, we study the forces induced by light between two spheres, either isolated in solution, or in the presence of a flat dielectric surface. We shall monitor the nature, either attractive or repulsive, of the light induced force between the spheres, according to the wavelength, polarization of the incident wave, and size and composition of the spheres.

In Sec. II we outline the calculation method employed to determine the optical binding forces; then, in Sec. III we present results for spheres either isolated in water (Sec. III A) or suspended in this liquid in the presence of a flat dielectric interface (Sec. III B).

II. METHOD USED FOR COMPUTING THE OPTICAL BINDING

In a previous article[14] we showed the possibility of computing the optical forces on a sphere with the coupled dipole method.[17] For the computation of the optical binding between particles, we now use the same procedure; thus we shall only outline the main equations and the changes introduced in them to address the presence of multiple objects.

Let K objects be above a flat dielectric surface. Each object is discretized into N_k subunits, with $k=1,\ldots,K$. Following the procedure of Ref. 17, the field at the (i,k)th subunit, namely, the ith subunit of the kth object, can be written as

$$\mathbf{E}(\mathbf{r}_i^k,\omega)=\mathbf{E}_0(\mathbf{r}_i^k,\omega)+\sum_{l=1}^{K}\sum_{j=1}^{N_l}[\mathbf{S}(\mathbf{r}_i^k,\mathbf{r}_j^l,\omega)+\mathbf{T}(\mathbf{r}_i^k,\mathbf{r}_j^l,\omega)]\alpha_j^l\mathbf{E}(\mathbf{r}_j^l,\omega), \quad (1)$$

where α_j^l is the polarizability of the (j,l) subunit, $\mathbf{T}$ is the linear response to a dipole in free space,[19] and $\mathbf{S}$ represents the linear response of a dipole in the presence of a surface.[20,21] The value of the electric field at each subunit position is obtained by solving the linear system Eq. (1) written for all subunits, so that the size of the system to solve is $\Pi_{k=1}^{K}N_k$. Once the electric field is obtained, the component of the total averaged force on the (i,k)th subunit can be deduced from both the field and its derivative at its position $\mathbf{r}_i^k$:[15]

$$F_u(\mathbf{r}_i^k)=(1/2)\mathrm{Re}\sum_{v=1}^{3}\left(p_v(\mathbf{r}_i^k,\omega)\frac{\partial E_v^*(\mathbf{r}_i^k,\omega)}{\partial u}\right) \quad (u=1,2,3), \quad (2)$$

where u,v stand for x,y,z, and $\mathbf{p}(\mathbf{r}_i^k,\omega)$ is the electric dipole of the (i,k)th subunit due to the incident field and all the other subunits. Note that the derivative of the field can be obtained from the derivative of Eq. (1).[14] Then the following relation can be written:

$$\mathbf{F}^k=\sum_{i=1}^{N_k}\mathbf{F}(\mathbf{r}_i^k), \quad (3)$$

where $\mathbf{F}^k$ is the total force on the kth object due to both the incident field and the multiple interaction with the surface and the other $K-1$ objects. If the kth object is a sphere small compared to the wavelength, the dipole approximation can be made; hence $N_k=1$. We also remark that, in what follows, when we represent the normalized force, this means $\mathbf{F}/(4\pi\varepsilon_0|\mathbf{E}_i|^2)$, where ε_0 is the permittivity of vacuum and $|\mathbf{E}_i|^2$ denotes the intensity of the incident beam.

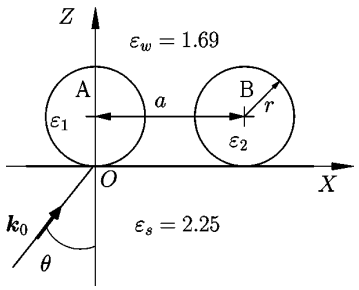

FIG. 1. The most complex geometry considered in this paper: two spheres of radius r on a dielectric flat surface. The spheres are embedded in water with $\varepsilon_w = 1.69$, and the relative permittivity of the surface is $\varepsilon_s = 2.25$. The incident wave vector $\mathbf{k}_0$ is in the XZ plane, and θ is the angle of incidence.

III. RESULTS AND DISCUSSION

In Fig. 1 we represent the more complex geometry that we shall consider in this work. Two spheres (either dielectric or metallic) are embedded in water ($\varepsilon_w = 1.69$). Illumination with an incident plane wave takes place in the XZ plane at an angle of incidence θ. When a dielectric flat surface at $z=0$ is used, we consider it separating glass ($\varepsilon_s = 2.25$) at $z<0$ from water ($z>0$).

A. Particles in water

In this section we do not address yet the presence of the surface ($\varepsilon_s = \varepsilon_w = 1.69$), i.e., $\mathbf{S}(\mathbf{r}_i^k, \mathbf{r}_j^l, \omega) = 0$ in Eq. (1), and the angle of incidence is $\theta = 0°$. Even in the absence of a surface, we make reference to the polarization and thus we shall always use the terms *p* polarization and *s* polarization when the electric field vector is in the XZ plane and along the Y axis, respectively.

We begin with the simplest case, i.e., the radius r of the two particles is small compared to the wavelength employed. As previously said, we then use the dipole approximation. We study, first, the case of two identical spheres with $\varepsilon_1 = \varepsilon_2 = 2.25$ and radius $r = 10$ nm at a wavelength $\lambda = 632.8$ nm in vacuum. Figure 2 represents the force along the X direction on the sphere B at different positions of this sphere on the X axis. The sphere A remains fixed. We have plotted only the force exerted on sphere B, since by symmetry the force along the X axis on sphere A is opposite to that on B. We observe two facts: first, the oscillation of the force when the spheres are far from each other, and, second, the strong force, either attractive or repulsive, when the spheres are very close to each other, depending on the polarization. For a better understanding of the physical process, using Eq. (1) and its derivative for two dipolar objects, we can analytically determine, through Eq. (2), the force on the spheres. Then, on using the fact that there is a plane wave in the Z direction (the incident wave is $E_{0_i} e^{ik_0 z}$, where $i = x$ or y depending on the polarization of the incident field) the force on the second sphere can be written as

$$F_x(\mathbf{r}_2) = \tfrac{1}{2}\mathrm{Re}\left(\alpha_2 E_i(\mathbf{r}_2, \omega) \alpha_1^* E_i^*(\mathbf{r}_1, \omega) \frac{\partial}{\partial x} T_{ii}^*(\mathbf{r}_2, \mathbf{r}_1, \omega) \right), \tag{4}$$

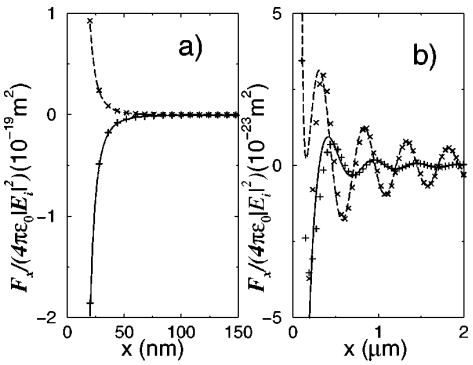

FIG. 2. Normalized force in the X direction on sphere B versus distance x between the centers of the spheres. Both spheres are of glass ($\varepsilon_1 = \varepsilon_2 = 2.25$), with $r = 10$ nm. The angle of incidence of the illuminating plane wave is $\theta = 0°$ and the wavelength $\lambda = 632.8$ nm in vacuum. The full line corresponds to *p* polarization, and the dashed line represents *s* polarization. (a) Force for short distances between the spheres; the symbols + (×) correspond to the values from the nonretarded approximation for *p* polarization (*s* polarization). (b) Force in far field; the symbols + (×) represent the values from the nonretarded approximation in far field for *p* polarization (*s* polarization).

where $i = x$ for *p* polarization and $i = y$ for *s* polarization of the incident field. Notice that to obtain the force on sphere A the indices 1 and 2 must be permuted. But, even in this simple case, the exact analytical solution of Eq. (4) is not easy to interpret. Hence, we make in Eq. (1) the approximation that the term $\mathbf{T}(\mathbf{r}_i^k, \mathbf{r}_j^l, \omega)\alpha_j^l$ is smaller than 1 (we will discuss this approximation further). Now, if we use the hypothesis that the two spheres are identical ($\alpha_1 = \alpha_2$), Eq. (4) becomes

$$F_x(\mathbf{r}_2) = \tfrac{1}{2}|\alpha_1 E_{0_i}|^2 \,\mathrm{Re}\left(\frac{\partial}{\partial x} T_{ii}(\mathbf{r}_2, \mathbf{r}_1, \omega) \right). \tag{5}$$

At short distances we can make the nonretarded approximation ($k_0 = 0$) and, as shown in the Appendix, we have that $F_x(\mathbf{r}_2) = -3|\alpha_1 E_{0_x}|^2/a^4$ in *p* polarization and $F_x(\mathbf{r}_2) = (3/2)|\alpha_1 E_{0_y}|^2/a^4$ in *s* polarization. The points (with the symbols + and ×) obtained with this approximation are shown in Fig. 2(a) and fit the curves obtained correctly without any approximation, as seen in this figure. Thus, they validate the approximation $\mathbf{T}(\mathbf{r}_i^k, \mathbf{r}_j^l, \omega)\alpha_j^l \ll 1$ previously made. Only when the spheres are very close to each other does this approximation slightly depart from the exact calculation due to the increase of the free space susceptibility. In fact, this approximation assumes the dipole associated with the spheres to be due only to the incident field, which is a good assumption when the polarizabilities are small, as for glass spheres. It is now easy to physically understand from Eq. (5) the reason for this either attractive or repulsive force. As the spheres are small, the scattering force is negligible[22] and thus only the gradient force remains, due to the interaction between the dipole associated with sphere B, and to the variation of the field created by sphere A at the position of

sphere *B*. In *p* polarization, the field due to sphere *A* at the position of sphere *B* and the dipole of sphere *B* are in phase; hence sphere *B* is pushed to the higher intensity region, namely, toward sphere *A*. In *s* polarization, as the field due to sphere *A* at the position of sphere *B* and the dipole of sphere *B* are in opposite phase, sphere *B* is pushed to the lower intensity region, namely, far from sphere *A*. One can observe a similar effect in an atom mirror,[23] or on a small silver particle in an evanescent field.[16]

On the other hand, in the far field we obtain, from the Appendix, the force upon sphere *B* as $F_x(\mathbf{r}_2) = |\alpha_1 E_{0_x}|^2 k_0^2 \cos(k_0 a)/a^2$ in *p* polarization and $F_x(\mathbf{r}_2) = -|\alpha_1 E_{0_y}|^2 k_0^3 \sin(k_0 a)/(2a)$ in *s* polarization, with $k_0 = 2\pi\sqrt{\varepsilon_w}/\lambda$. The same explanation as before can be used for the sign of the force: following the phase relationship between the dipole and the field due to sphere *A*, the force is either positive or negative; hence, the oscillations of the force F_x take place with period $\lambda/\sqrt{\varepsilon_w}$. The phase difference $\lambda/(4\sqrt{\varepsilon_w})$ that appears in the far field between the oscillations of *s* and *p* polarization comes from the difference between the derivatives of the components *xx* and *yy* of the free space susceptibility. We observe that the force in *p* polarization decreases faster than in *s* polarization; this is due to the absence of a propagating field along the *X* axis in the far field. The magnitude of the force differs by a factor of 10^4 between far field and near field. This is due to the strong interaction between the spheres through the evanescent waves.

We can make an analogy in the near field with molecular physics. If we look at the dipole moments of the two spheres, we compare our system of forces with the interaction between two molecules. In *p* polarization, as the dipole moments are aligned and antisymmetric, they produce an attractive force analogous to that between two orbitals p_z, giving rise to a bonding state σ_u. In *s* polarization, the dipole moments are parallel and symmetric, so we have antibonding states π_g^*, where * means that the two spheres cannot be bound.

We represent in Fig. 3 the force along the *Z* direction. In this case the scattering force is predominant. The interaction between the spheres is now directly responsible for the oscillation of the force. Notice that when the spheres are far from each other, as the interaction between the spheres becomes weak when the distance increases, the force tends toward the scattering force upon one sphere due to the incident field. As this force is not responsible for optical binding, we are not going to discuss it further.

More interesting is the case of two different small spheres, one (*B*) being dielectric and the other (*A*) being metallic (silver). The first fact easily observed from Eq. (4) pertains to the nonretarded case; as the derivative of the free space susceptibility is real, the forces on spheres *A* and *B* are equal but of opposite sign to each other (this is no longer the case in the far field). In Fig. 4 we represent the force on sphere *B* at short distances from sphere *A* (in comparison with the wavelength), for $\lambda = 365$ nm, 388.5 nm, and 600 nm. For *p* polarization, we observe that the force at the wavelength $\lambda = 365$ nm has a rather strange behavior as it is

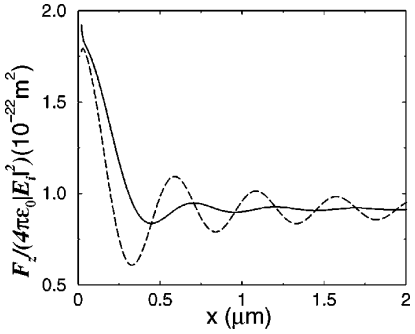

FIG. 3. Normalized force in the *Z* direction on sphere *B* versus distance *x* between the centers of the spheres. Both spheres are of glass with $r = 10$ nm, $\theta = 0°$, and $\lambda = 632.8$ nm in vacuum. The full line corresponds to *p* polarization, whereas the dashed line represents *s* polarization.

positive, and only when the spheres are almost in contact does this force change and become similar to those at the other wavelengths. With the approximation $\mathbf{T}(\mathbf{r}_i^k, \mathbf{r}_j^l, \omega)\alpha_j^l \ll 1$, the force in the nonretarded approximation can be written

$$F_x(\mathbf{r}_2) = 1/2 \frac{\partial T_{ii}(\mathbf{r}_2, \mathbf{r}_1, \omega)}{\partial x} |E_{0_i}|^2 \alpha_2 \ \mathrm{Re}(\alpha_1). \qquad (6)$$

We observe that the sign of the force depends on $\mathrm{Re}(\alpha_1)$. When $\mathrm{Re}(\alpha_1) > 0$ ($\lambda = 600$ nm), which is the common case, the dipole associated with the silver sphere is in phase with the applied field, so everything happens as for the dielectric sphere. Conversely, when $\mathrm{Re}(\alpha_1) < 0$ ($\lambda = 365$ nm) the dipole is in opposite phase to the applied field, and hence the force becomes positive. But when the spheres are almost in contact the approximation $\mathbf{T}(\mathbf{r}_i^k, \mathbf{r}_j^l, \omega)\alpha_j^l \ll 1$ is no longer valid as shown when $\mathrm{Re}(\alpha_1) = 0$ ($\lambda = 388.5$ nm), in which case the force is not null but negative. This is due to the fact that the polarizability of the silver sphere is large and hence the approximation is no longer valid for short distances. Physically, this represents the contribution of the metallic

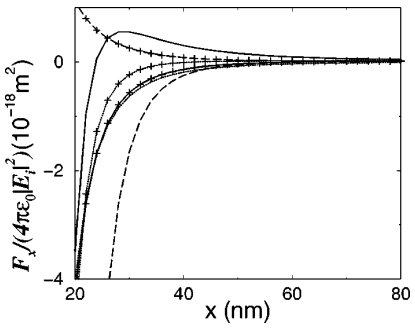

FIG. 4. Nonretarded approximation normalized force in the *X* direction on sphere *B* versus distance *x* between the centers of the spheres. The sphere *A* is of silver and the sphere *B* is of glass with $r = 10$ nm. $\lambda = 365$ nm (full line), 388.5 nm (dotted line), and 600 nm (dashed line). Without symbols, *p* polarization; with symbol +, *s* polarization.

sphere to the electric field acting on the dielectric sphere, which is larger than that of the incident field; hence the dipoles associated with the two spheres are in phase and the force is attractive. Notice that the change of sign occurs both at the plasmon resonance $[\mathrm{Re}(\varepsilon_1)\approx -2\varepsilon_w]$ and when $\mathrm{Re}(\varepsilon_1)\approx\varepsilon_w$. When ε_1 is between these two values, the real part of the polarizability is negative. For a more complete discussion of this, one can see Ref. 16. Similar reasoning applies for *s* polarization. If we now make the analogy previously done with the molecular orbitals, then depending on the wavelength in *s* polarization we shall obtain either antibonding states π_g^* or bonding states π_u.

In the far field, for *p* polarization, on using Eq. (4) and the approximation $\mathbf{T}(\mathbf{r}_i^k,\mathbf{r}_j^l,\omega)\alpha_j^l \ll 1$, we can write the force on the sphere *B* as

$$F_x(\mathbf{r}_2)=[\mathrm{Re}(\alpha_1^*\alpha_2)\cos(k_0a) - \mathrm{Im}(\alpha_1^*\alpha 2)\sin(k_0a)]k_0^2|E_{0_x}|^2/a^2 \qquad (7)$$

and the force on sphere *A* as

$$F_x(\mathbf{r}_1)=[-\mathrm{Re}(\alpha_1^*\alpha_2)\cos(k_0a) - \mathrm{Im}(\alpha_1^*\alpha_2)\sin(k_0a)]k_0^2|E_{0_x}|^2/a^2. \qquad (8)$$

As the spheres are small, we can take only the gradient force as this is now the predominant one; then α_2 is real.[15] Therefore, the forces on spheres *A* and *B* for the wavelength $\lambda=600$ nm, where $\mathrm{Im}(\alpha_1)$ is weak, are opposite to each other as for two identical spheres. But at $\lambda=388.5$ nm, where $\mathrm{Re}(\alpha_1)=0$, the forces on the two spheres are completely identical.

It should be remarked that, if the laser intensity of the incident light is assumed to be 0.2 W/μm^2,[24] the optical forces for these small spheres are not strong enough to create optical binding, since then the Brownian motion remains the dominant force. In this respect, the interest of the case of these small spheres is mainly the interpretative value it yields for the underlying physics. However, for larger radius in comparison to the wavelength, the forces become larger and so does the trapping potential. In Figs. 5(b) and 6(b) we plot the force along the *X* axis for two dielectric spheres (glass) with radius $r=100$ nm and 200 nm, respectively. We observe that with the intensity used previously (0.2 W/μm^2) the magnitude of the force is now enough to optically bind both spheres. We compute the potential energy of the optical trap by integration of the force (we take the potential energy as null when the second sphere is at infinity). As the two spheres are identical, the potential energy is the same for both. The efficiency of the trapping force requires it to be larger than the force due to the Brownian motion; hence the depth of the potential wells of the trap should be larger than k_bT, T being the temperature of water and k_b the Boltzmann constant. Considering $T=290$ K, then $k_bT=4\times10^{-21}$ J. We plot in Figs. 5(a) and 6(a) the potential normalized to the value k_bT. We adopt the criterion that the trap is efficient when the potential well is larger that $3k_bT$. Hence the bars plotted at the bottom of the wells in Figs. 5(a) and 6(a) correspond to the value 3. We see from Fig. 5 that for *p* polarization the trap is not feasible except when the spheres are in contact. For *s* polarization, we have three equilibrium positions spaced out by one wavelength. This behavior is explained by the previous results on small spheres, and in agreement with experiments.[10] When the size of the sphere is close to one wavelength, we see from Fig. 6 that the depth of the potential well is larger than in the previous case. In *p* polarization there is no possibility of sticking the spheres together, but now we have one potential minimum of stable position. Thus, we observe that it is easier to trap particles when their radii are large, in agreement with the experiments of Burns *et al.*[10]

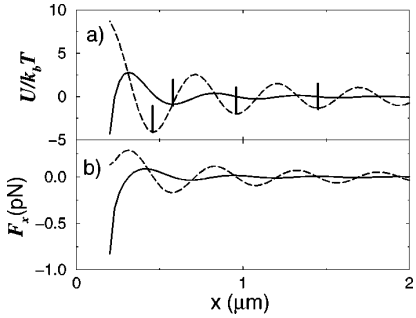

FIG. 5. Two glass spheres of radius $r=100$ nm, $\theta=0°$, and $\lambda=632.8$ nm in vacuum. The laser intensity of the incident light is 0.2 W/μm^2. Full line curves are for *p* polarization. Dashed line curves correspond to *s*-polarization. (a) Potential of sphere *B* normalized to k_bT versus distance between the centers of the spheres. The height of the bars corresponds to a normalized potential equal to 3. (b) Force in the *X* direction versus the distance between the spheres.

Notice that the gravity force is 6.16×10^{-5} pN and 4.93×10^{-4} pN for the spheres of radii $r=100$ nm and 200 nm, respectively. Another force that exists between the spheres is the Casimir-Polder force F_c. To our knowledge, F_c has often been studied either between two plates or between a sphere and a plate,[25] but it has never been established between two spheres. In the nonretarded approximation and the dipole approximation for the spheres, F_c is reduced to the dispersion force (London's force) which is inversely proportional to the seventh power of the distance between the dipoles (see, for example, Ref. 26). Hence, only when the spheres are in contact, or at distances smaller than

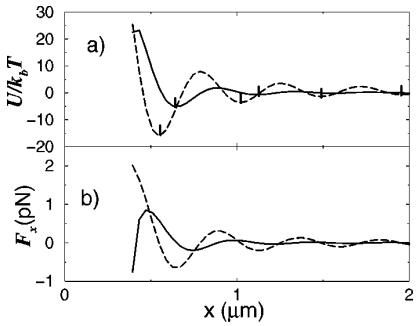

FIG. 6. Same as Fig. 5 but with a radius $r=200$ nm.

TABLE I. Minimum radius in nm to get one minimum position of the potential for two identical spheres. The following cases are addressed: glass sphere and silver sphere (both off and on plasmon resonance). The criterion of stability used is that the potential well depth must be larger that $3k_bT$.

Spheres	Glass ($\lambda=632.8$ nm)	Silver ($\lambda=394$ nm)	Silver ($\lambda=314$ nm)
Limiting radius in nm (*p* pol.)	123	33	180
Limiting radius in nm (*s* pol.)	85	21	50

the wavelength from each other, might this force be of the same magnitude as the optical forces. However, the fast decay of this force at distances larger than the wavelength prevents it from perturbing the optical trap.

In Table I we give some examples of the limiting radius to get optical trapping for two identical spheres embedded in water (notice that for *p* polarization we do not mean optical trapping when the spheres are stuck in contact), i.e., the minimum radius to obtain one potential minimum or stable position for the two spheres using the same criterion as before (namely, $U>3k_bT$). We should remark that this is the limiting radius only to obtain the first stable position; if we want to get more stable positions, as in Ref. 10, the radius must be larger. As mentioned before, the table shows that the optical trapping is easier for *s* polarization. For the silver sphere, the value $\lambda=394$ nm corresponds to the plasmon resonance, and that of $\lambda=314$ nm is for a wavelength out of resonance. At the plasmon resonance the polarizability is largest, so it is easier to perform optical binding at this wavelength.

As a last instance, we now consider two spheres in free space, with radii $r=100$ nm, one being of glass and the other of silver, illuminated by a plane wave at $\lambda=388.5$ nm. We plot in Fig. 7 the potential energy for the two polarizations and the two spheres, since now this magnitude depends on the sphere material. We then observe that it is not possible to obtain a stable equilibrium since the potentials of the two spheres are now different. This result is explainable from the previous calculation on small spheres (of silver and glass), since then the forces were always opposed to each other at this wavelength. In fact, as the spheres are now large, the forces at this wavelength are not exactly in opposition, due to the larger scattering and absorbing force. Hence it is possible to obtain points where the potential of the two spheres is minimum. This happens when the forces on each sphere are the same and positive. In that case, the two spheres move in the direction of the positive *X* axis while keeping constant the distance between them.

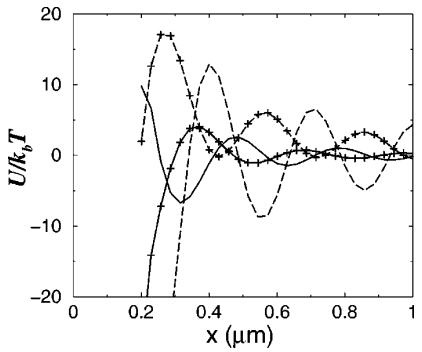

FIG. 7. The sphere *A* is of glass and the sphere *B* of silver with $r=100$ nm, $\lambda=388.5$ nm. The laser intensity of the incident light is 0.2 W/μm^2. Plot of the potential normalized to k_bT for the two spheres versus the distance between them. The full line is for *p* polarization and dashed line corresponds to *s* polarization. The potential of sphere *A* is without symbols, and the potential of sphere *B* is with symbol +.

B. Particles in water on a dielectric flat surface

In this section we consider a flat dielectric surface upon which the spheres are suspended in water, as shown by Fig. 1. We compute the force along the *X* axis on sphere *B* when both spheres are dielectric (glass), with $\theta=0°$ (Fig. 8). We now observe that for both large and small spheres the force has a behavior similar to that acting on dielectric spheres isolated in water. When the spheres are in contact, the force on sphere *B* is the same as in the absence of the interface, whereas when the spheres are far from each other this force is slightly smaller than that without the interface. This means that optical binding is more difficult to perform when the spheres are on a surface than when they are far from interfaces. Also, there is a change in the period of oscillation due to interaction between the spheres via the light reflected by the surface. However, in the case when one of the spheres is metallic (silver), we observe the same behavior of the forces when the surface is present as without it. Thus, as previously observed for dielectric spheres, there appears only a shift in the oscillation and magnitude of the forces.

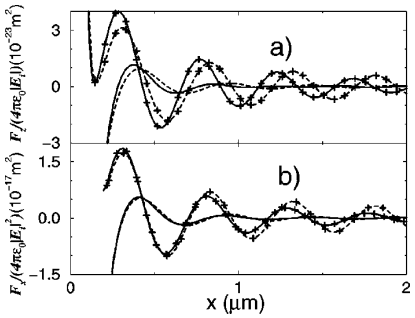

FIG. 8. Force in the *X* direction upon sphere *B* when the spheres are placed on a flat dielectric surface. $\theta=0°$, $\lambda=632.8$ nm. The full line represents the force in the presence of the surface, and the dashed line corresponds to the force computed without the interface. The curves with symbols + denote *s* polarization, and those without symbols correspond to *p* polarization. (a) Spheres of glass with $r=10$ nm. (b) Spheres of glass with $r=100$ nm.

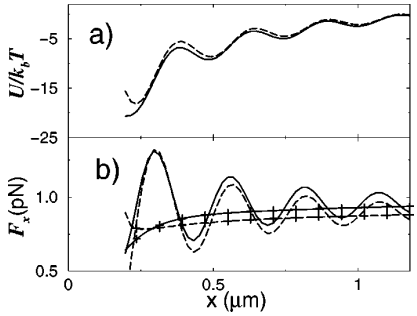

FIG. 9. Two glass spheres of radius $r=100$ nm in vacuum, in front of a flat dielectric surface. $\theta=50°$, $\lambda=632.8$ nm. The laser intensity of the incident light is 0.2 W/μm^2. Full line curves are for *p* polarization. Dashed line curves correspond to *s* polarization. (a) Potential of interaction between the two spheres, normalized to k_bT, versus distance between the centers of the spheres. (b) Force in the *X* direction against distance between the spheres. The curve of force on sphere *A* is without symbols, and the force on sphere *B* is marked with symbol $+$.

In Fig. 9 we investigate the potential and optical force on two glass spheres in front of a dielectric surface, illuminated by total internal reflection ($\theta=50°$). Figure 9(b) shows that the force component along the *X* axis always pushes the spheres in the direction of the wave vector component parallel to the surface. Hence, it is not possible to obtain a stable equilibrium with the two spheres remaining fixed. But if we compute the potential of the two spheres together [Fig. 9(a)], we observe some minima, indicating that the system can acquire internal equilibrium, namely, the relative positions of the spheres can be kept fixed. Hence, when both spheres move impelled by the evanescent wave propagating along the surface, their velocity remains parallel to this surface, while the distance between them keeps some particular values given by the positions of the potential minima [cf. Fig. 9(a)]. Notice that the force on the second sphere (in both polarizations) has no oscillation; a very similar behavior was observed by Okamoto and Kawata.[24] The computational prediction of similar collective movements in systems of more than two spheres will involve long computing times of their relative positions by potential energy minimization.

IV. CONCLUSION

We have studied the optical binding between two spheres embedded in water, in either the presence or absence of a flat dielectric interface. We have presented results for different sizes and illumination conditions. Some of them agree with previous experiments[10] for two identical spheres; however, when they are composed of different materials, the force between them may have quite different behavior, depending on the wavelength of the light employed. In future work, it would be interesting to investigate the effect of light on several spheres in water in order to build up particle arrays. However, the vertical force that pushes the spheres away from the substrate constitutes a hindrance to this aim. This work shows, however, that this problem can be avoided by illuminating the system under total internal reflection at the substrate interface. Then the spheres will be stuck to the surface by the gradient force due to the transmitted evanescent wave. The horizontal force of this surface wave on the sphere, which pushes them along the interface, can be compensated by means of a second counterpropagating evanescent wave, created by an additional beam. Notice, in addition, that if both surface waves are mutually coherent, the resulting standing wave pattern can introduce further structure in the resulting potential wells seen by the spheres.

ACKNOWLEDGMENTS

This work was supported by the European Union and the Direccion General de Investigacion Cientifica y Tecnica, Grant No. PB98 0464.

APPENDIX: DERIVATIVE OF THE FREE SPACE SUSCEPTIBILITY

The derivative of the free space susceptibility used in this paper is

$$\frac{\partial}{\partial x}T_{xx}(x,x_0)=-\frac{6\mathbf{a}}{a^5}, \tag{A1}$$

$$\frac{\partial}{\partial x}T_{yy}(x,x_0)=\frac{\partial}{\partial x}T_{zz}(x,x_0)=\frac{3\mathbf{a}}{a^5} \tag{A2}$$

in the nonretarded case, and

$$\frac{\partial}{\partial x}T_{xx}(x,x_0,\omega)=\frac{2\mathbf{a}k_0^2}{a^3}e^{ik_0a}, \tag{A3}$$

$$\frac{\partial}{\partial x}T_{yy}(x,x_0,\omega)=\frac{\partial}{\partial x}T_{zz}(x,x_0,\omega)=\frac{i\mathbf{a}k_0^3}{a^2}e^{ik_0a} \tag{A4}$$

in the far field, where $\mathbf{a}=(x-x_0)$ and $a=|\mathbf{a}|$. x is the abscissa of the observation point and x_0 that of the dipole position.

[1] A. Ashkin, Phys. Rev. Lett. **24**, 156 (1970).
[2] A. Ashkin, Phys. Rev. Lett. **25**, 1321 (1970).
[3] A. Ashkin, J. M. Dziedzic, J. E. Bjorkholm, and S. Chu, Opt. Lett. **11**, 288 (1986).
[4] A. R. Clapp, A. G. Ruta, and R. B. Dickinson, Rev. Sci. Instrum. **70**, 2627 (1999).
[5] A. C. Dogarin and R. Rajagopalan, Langmuir **16**, 2770 (2000).
[6] A. Ashkin and J. M. Dziedzic, Science **235**, 1517 (1987).
[7] S. D. Collins, R. J. Baskin, and D. G. Howitt, Appl. Opt. **38**, 6068 (1999).

[8] R. C. Gauthier and A. Frangioudakis, Appl. Opt. **39**, 26 (2000).
[9] K. Taguchi, K. Atsuta, T. Nakata, and M. Ikeda, Opt. Commun. **176**, 43 (2000).
[10] M. Burns, J.-M. Fournier, and J. Golovchenko, Phys. Rev. Lett. **63**, 1233 (1989).
[11] M. I. Antonoyiannakis and J. B. Pendry, Phys. Rev. B **60**, 2363 (1999).
[12] M. I. Antonoyiannakis and J. B. Pendry, Europhys. Lett. **40**, 613 (1997).
[13] M. Bayer, T. Gutbrod, A. Forchel, T. L. Reinecke, P. A. Knipp, A. A. Dremin, V. D. Kulakovskii, and J. P. Reithmaier, Phys. Rev. Lett. **81**, 2582 (1997).
[14] P. C. Chaumet and M. Nieto-Vesperinas, Phys. Rev. B **61**, 14 119 (2000).
[15] P. C. Chaumet and M. Nieto-Vesperinas, Opt. Lett. **25**, 1065 (2000).
[16] P. C. Chaumet and M. Nieto-Vesperinas, Phys. Rev. B **62**, 11 185 (2000).
[17] E. M. Purcell and C. R. Pennypacker, Astrophys. J. **186**, 705 (1973).
[18] J. A. Stratton, *Electromagnetic Theory* (McGraw-Hill, New York, 1941).
[19] J. D. Jackson, *Classical Electrodynamics*, 2nd ed. (John Wiley, New York, 1975), p. 395.
[20] G. S. Agarwal, Phys. Rev. A **11**, 230 (1975); **12**, 1475 (1975).
[21] A. Rahmani, P. C. Chaumet, and F. de Fornel, Phys. Rev. A, **63,** 023819 (2001); A. Rahmani, P. C. Chaumet, F. de Fornel, and C. Girard, Phys. Rev. A **56**, 3245 (1997).
[22] For a small sphere, the gradient and scattering forces are proportional to a^3 and a^6, respectively.
[23] L. Cognet, V. Savalli, G. Zs. K. Horvath, D. Holleville, R. Marani, C. I. Westbrook, N. Westbrook, and A. Aspect, Phys. Rev. Lett. **81**, 5044 (1998); A. Landragin, J.-Y. Courtois, G. Labeyrie, N. Vansteenkiste, C. I. Westbrook, and A. Aspect, *ibid.* **77**, 1464 (1996).
[24] K. Okamoto and S. Kawata, Phys. Rev. Lett. **83**, 4534 (1999).
[25] G. L. Klimchitskaya, U. Mohideen, and V. M. Mostepanko, Phys. Rev. A **61,** 062107 (2000).
[26] P. W. Milonni, Phys. Rev. A **53**, 3484 (1996).

Optical Trapping and Manipulation of Nano-objects with an Apertureless Probe

Patrick C. Chaumet,[1] Adel Rahmani,[2] and Manuel Nieto-Vesperinas[3]

[1]*Institut Fresnel (UMR 6133), Faculté des Sciences et Techniques de St Jérôme, F-13397 Marseille Cedex 20, France*
[2]*Atomic Physics Division, National Institute of Standards and Technology, Gaithersburg, Maryland 20899-8423*
[3]*Instituto de Ciencia de Materiales de Madrid, CSIC, Campus de Cantoblanco, Madrid 28049, Spain*

(Received 10 July 2001; published 8 March 2002)

We propose a novel way to trap and manipulate nano-objects above a dielectric substrate using an apertureless near-field probe. A combination of evanescent illumination and light scattering at the probe apex is used to shape the optical field into a localized, three-dimensional optical trap. We use the coupled-dipole method and the Maxwell stress tensor to provide a self-consistent description of the optical force, including retardation and the influence of the substrate. We show that small objects can be selectively captured and manipulated under realistic conditions.

DOI: 10.1103/PhysRevLett.88.123601 PACS numbers: 42.50.Vk, 03.50.De, 68.65.–k, 78.70.–g

Since the seminal work of Ashkin [1] on radiation pressure, the possibility to exploit the mechanical action of optical fields to trap and manipulate neutral particles has spawned a wide range of applications. From atomic and nonlinear physics to biology, optical forces have provided a convenient way to control the dynamics of small particles (see Ref. [1] for a review). Optical tweezers, for example, have proved useful not only for trapping particles but also for assembling objects ranging from microspheres to biological cells [2]. However, most of these manipulations involve particles whose size is between one and several micrometers. While for much smaller particles, such as atoms or molecules, the scanning tunneling microscope provides a powerful tool for manipulation and engineering [3]; dealing with neutral particles of a few nanometers requires new experimental approaches.

The idea of using a metallic probe to trap small particles was reported by Novotny *et al.* [4]. Their calculations showed that strong field enhancement from light scattering at a gold tip could generate a trapping potential deep enough to overcome Brownian motion and capture a nanometric particle in water (a related work by Okamoto and Kawata demonstrates theoretically the trapping of a nanometric sphere in water near an aperture probe [5]). This technique should be delicate to implement in practice for three reasons. First, before the particle can be captured, Brownian fluctuations will have a disruptive effect. Second, radiation pressure from the illuminating laser will impart momentum to the particle. Therefore, one would have to capture a moving object. Third, it will be rather difficult to use a near-field probe to find in water a particle a few nanometers in size. One might wait for a particle to wander in the trapping region, but such an operating mode does not allow for selective capture.

In this Letter, we propose an experimental scheme to selectively capture and manipulate nanoparticles in vacuum or air above a substrate, using the tungsten probe of an apertureless near-field microscope. The particles are not in a liquid environment, hence there is no Brownian motion and the apertureless probe can be used as a near-field optical probe to localize and select the particles [6,7]. This is an important asset when different particles have to be placed according to a specific pattern or when interactions between particles are investigated.

We first consider a spherical particle with radius 10 nm placed in air on a substrate (Fig. 1). Unless it is stated otherwise the permittivity of both the particle and the substrate is $\epsilon = 2.25$. The particle is illuminated (wavelength 500 nm) by two counterpropagating evanescent waves created by the total internal reflection of plane waves at the substrate/air interface (angle $\theta > \theta_c = 41.8°$ with $\sqrt{\epsilon}\sin\theta_c = 1$). These two waves have the same polarization and a random phase relation [8]. This symmetric illumination ensures that the lateral force vanishes when

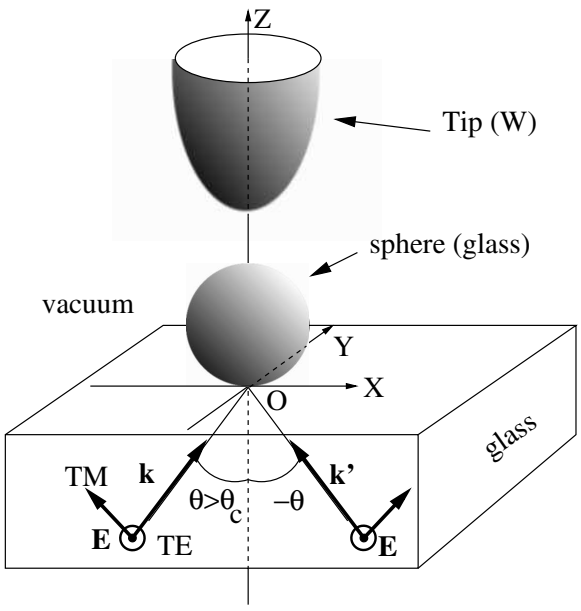

FIG. 1. Scheme of the configuration. A dielectric sphere (radius 10 nm) on a flat dielectric surface is illuminated under total internal reflection. A tungsten probe is used to create an optical trap.

 0031-9007/02/88(12)/123601(4)$20.00

the sphere is just below the tip, thus avoiding that the sphere be pushed away from the tip.

We study the interactions between the particle and a tungsten probe (commonly used in apertureless microscopy) with a radius at the apex of 10 nm. The theory used to compute the optical forces has been presented in detail elsewhere [9]. Here we give a succinct summary. We use the coupled-dipole method [10,11] to model the light scattering and find the electromagnetic field inside the tip and the particle. Note that this procedure takes into account the multiple scattering between the sphere, the tungsten tip, and the substrate. We then use the Maxwell stress tensor technique to derive the optical forces [12]. We emphasize that the stress tensor approach is exact and does not rely on any assumption regarding the nature of the field (whether evanescent or propagating) or of the objects.

All forces are computed for an irradiance of 0.05 $W/\mu m^2$ (this corresponds, for example, to a 5 W laser beam focused over an area of 100 μm^2). Figure 2 shows the z component of the force experienced by the sphere versus the vertical position of the tip above the sphere, for both TE and TM polarizations and for two angles of illumination ($\theta = 43°$ and $\theta = 50°$). As the tip moves closer to the sphere, the evolution of the force for the two polarizations is radically different. For TM illumination there is a large enhancement of the field near the apex of the probe because of the discontinuity of the z component of the electric field across the air/tungsten boundary [4]. This enhancement is responsible for the force being positive at short distances. Note that, for the sphere, the force of gravity is on the order of 10^{-7} pN. The z component of the force experienced by the sphere (when the tip is in contact with the sphere) is about 3 pN which is 10^8 times its weight. Hence, gravity can be neglected. Figure 2a shows that for TM polarization the force is larger for $\theta = 43°$ than for $\theta = 50°$. This is related to the slower decay of the evanescent wave for the smaller angle, which results in a weaker coupling between the sphere and the substrate. Moreover, the slower the decay of the evanescent field, the larger the field that reaches the tip, and the larger the (positive) gradient force caused by the field enhancement at the apex of the probe. As a consequence, when the tip approaches the sphere, the sign reversal (negative to positive) of the z component of the force occurs at a larger distance for $\theta = 43°$ ($z = 21$ nm) than for $\theta = 50°$ ($z = 13$ nm). This is shown in the inset of Fig. 2a. On the other hand, for TE polarization (Fig. 2b), the magnitude of the z component of the force increases while the force remains negative (directed toward the substrate and away from the tip) as the tip gets closer to the particle. This prevents any trapping. Our calculations show that this behavior is caused by the decrease of the field inside the upper part of the sphere which, in turn, causes a decrease of the gradient force. Another way of explaining this is to note that, because the apex of the tip and the sphere are small compared to the wavelength, they can be approximated by two dipoles. For TE polarization these dipoles are essentially parallel to the substrate and, as shown in Ref. [13], two parallel dipoles tend to repel each other. Since the magnitude of the dipole is stronger for $\theta = 43°$ (due to the larger intensity of the field), the repulsive force is also stronger. Note that, for a silver tip at the plasmon resonance frequency, the force acting on the sphere is positive for both polarizations. At the frequency considered here, tungsten behaves like an absorbing dielectric and the force is positive only for TM polarization.

To fully assess the probe-particle coupling we study the evolution of the force experienced by the particle as the probe is moved laterally, the sphere remaining fixed. The components of the force acting on the sphere are plotted in Figs. 3 and 4 for two distances between the tip and the substrate (20 and 31 nm), and for two angles of illumination (43° and 50°). For TM polarization (Fig. 3a), the z component of the force is negative when the tip is far from the particle. When the tip gets closer, the particle starts experiencing a positive force along z. The change of sign occurs between $|x| = 30$ nm for $\theta = 43°$ and $z = 20$ nm, and $|x| = 7$ nm for $\theta = 50°$ and $z = 31$ nm.

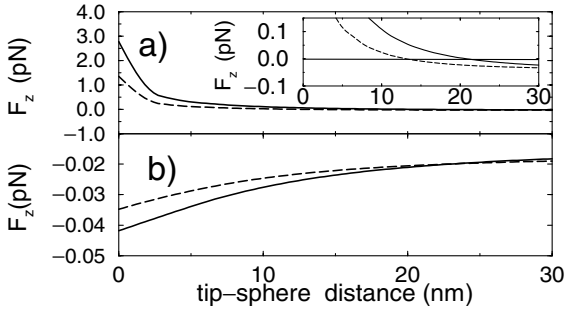

FIG. 2. z component of the force experienced by the sphere versus the distance between the tip and the sphere. Solid lines: $\theta = 43°$; dashed lines: $\theta = 50°$. (a) TM polarization; (b) TE polarization. [See text for explanation of inset in (a)].

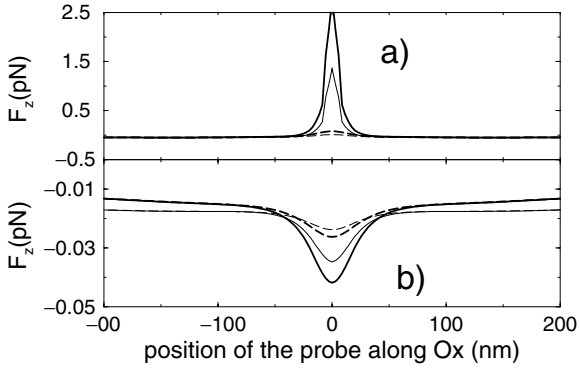

FIG. 3. Force along z experienced by the sphere as a function of the lateral position of the probe. The sphere is at the origin. (a) TM polarization; (b) TE polarization. Thick lines: $\theta = 43°$; thin lines: $\theta = 50°$. The tip is either 20 nm (solid lines) or 31 nm (dashed lines) above the substrate.

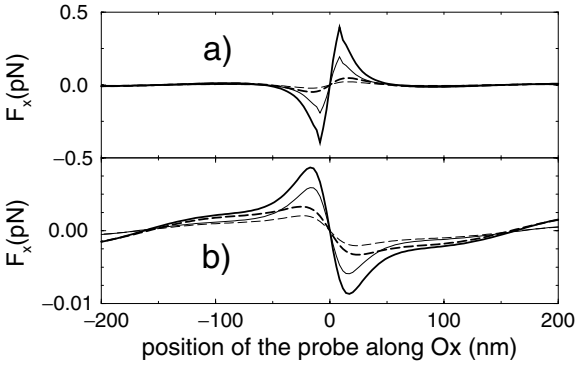

FIG. 4. Same as Fig. 3 for the force along x.

For TE polarization the force is negative (Fig. 3b). Similarly, we plot in Fig. 4 the lateral force. The symmetry of the force plot is a consequence of the symmetric illumination. For TM polarization (Fig. 4a) this force tends to push the particle toward the tip. For example, if the tip is located at $x = 10$ nm, we can see in Fig. 4a that the x component of the force experienced by the sphere is positive, hence the lateral force pushes the sphere toward the tip. If the tip is located at $x = -10$ nm, the x component of the force is negative and, again, it pushes the sphere toward the tip. Therefore, when the tip and the particle are close enough for the z component of the force to be positive and to lift the particle off the surface, the lateral force actually helps bring the particle into the trap. Again TE polarization gives a different result. The lateral force always pushes the particle away from the tip. However, since the magnitude of the (downward) z component of the force is larger than the x component by a factor of 5, we expect that the sphere is not displaced when the tip is scanned over it under TE illumination. Note that apertureless probes are often used in tapping mode when imaging a surface. This mode minimizes the lateral motion imparted to the object by the optical force.

We have shown that a tungsten probe can be used to trap efficiently a nanometric object above a surface using TM illumination. For nanomanipulation it is important to assess the stability of the trap as the probe lifts the particle off the substrate. Figure 5 shows the z component of the force when the sphere is fixed at the apex of the tip and the tip is moved vertically (solid and dashed curves). The optical force remains larger than the weight of the particle over a range of several tens of nanometers. The particle can therefore be manipulated vertically as well as horizontally. Note that the evolution of the force with the distance to the substrate is linear rather than exponential. The particle experiences a negative gradient force due the exponential decay of the intensity of the illumination. At the same time, the particle suffers a positive gradient force due to the field enhancement at the tip apex, which also decreases exponentially with z because this enhancement depends on the intensity of the evanescent illuminating light. The competition between these two contributions results in a

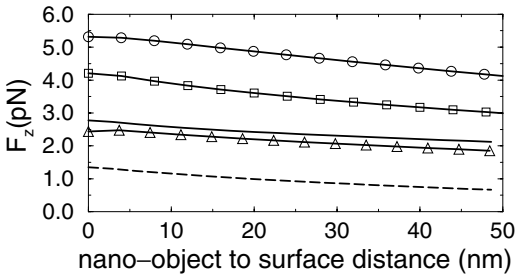

FIG. 5. z component of the force experienced by a particle as a function of the distance between the particle and the substrate under TM illumination. The particle is placed at the apex of the probe. Solid line: sphere ($\epsilon = 2.25$, radius: 10 nm, $\theta = 43°$). Dashed line: sphere ($\epsilon = 2.25$, radius: 10 nm, $\theta = 50°$). Circles: sphere ($\epsilon = 2.25$, radius: 30 nm, $\theta = 50°$). Triangles (force $\times 0.1$): sphere of gold ($\epsilon = -2.81 + 3.18i$, radius: 10 nm, $\theta = 50°$). Squares: cube ($\epsilon = 2.25$, size: 20 nm, $\theta = 50°$).

weak decrease of the trapping force as the particle is moved away from the substrate. If we change the nature, size, or shape of the object the magnitude of the force changes but the conclusions are qualitatively the same (Fig. 5, curves with symbols).

It is fundamental to know whether our procedure also works if several particles are clustered together. We consider a set of three spheres (radius 10 nm, permittivity 2.25) aligned along x. The probe is placed above the middle sphere. We account for the multiple scattering between the three spheres, the substrate, and the tip; therefore the optical binding experienced by the spheres [13] is included in our description. For this configuration, TE illumination again does not lead to trapping. For TM illumination, we plot in Fig. 6 the z component of the force experienced by the middle sphere and by those on the sides as a function of the vertical distance between the probe and the middle sphere. For an angle of incidence $\theta = 43°$, the z component of the force, although largest for the middle

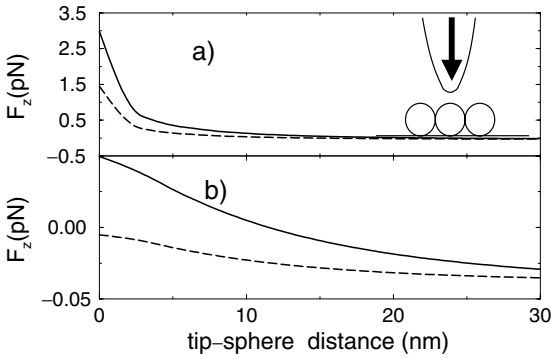

FIG. 6. Force along z versus the vertical position of the probe for three spheres aligned along x. The probe is centered over the middle sphere. Solid lines: $\theta = 43°$. Dashed lines: $\theta = 50°$. (a) Force on the middle sphere; (b) force experienced by the spheres on the sides.

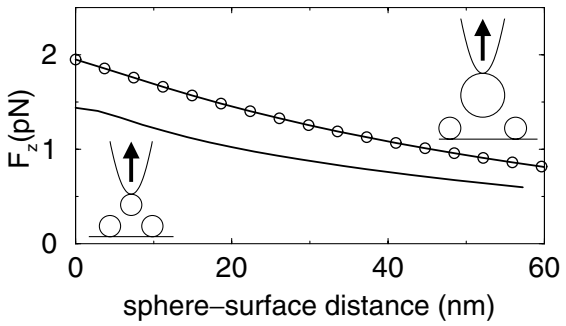

FIG. 7. Force along z as experienced by the middle sphere (solid line) versus vertical position of the middle sphere trapped at the apex probe ($\theta = 50°$). Solid line: sphere with a 10 nm radius; circles: sphere with a 20 nm radius.

sphere, is positive for all the spheres. This could be a problem if one wanted to manipulate only one particle. The central particle can be selectively trapped by increasing the angle of incidence of the illuminating beams to tighten the trap in the x direction (Fig. 4). In Fig. 6 we see that for $\theta = 50°$ the optical force induced by the probe is positive only for the middle sphere. This remains true for three spheres aligned along y. Figure 7 shows the extraction of the middle sphere by the tip. Our calculation shows that the vertical force experienced by the two side spheres remains negative when the probe moves away from the substrate. Therefore, the spheres on the sides do not hinder the capture of the middle sphere.

In Fig. 7, the curve with circles shows that the selective trapping works as well when the middle sphere is twice as big as the others. Once the chosen particle has been trapped, it can be moved above the substrate. Our calculations show that the presence of other particles on the substrate does not destroy the trap, provided that during the manipulation the trapped sphere is kept at least 5 nm above the spheres that are on the substrate. We have checked that, if the optical binding causes the side spheres to move laterally toward the middle sphere, increasing the angle of illumination still creates a negative (downward) force on the two side spheres, and the selective capture of the middle sphere is not hampered.

The procedure to trap a small object with a tungsten tip is therefore the following: TE illumination is used while the tip scans the surface in tapping mode or in constant-height mode if the area under investigation is small enough. Such modes avoid the displacement of the particle by the tip. Once an object has been selected, the probe is placed above the object and the polarization of the illumination is rotated to TM. The probe is then brought down over the particle and captures it. The probe can then move the particle above the substrate, both horizontally and vertically, to a new position where it can be released by switching back to TE polarization (note that if, for some reason, one wishes to move the particle over distances larger than the size of the illumination spot, one could move *the sample* with the piezoelectric device once the sphere is trapped at the apex of the tip). The lack of trapping under TE illumination is actually an important advantage during the imaging (selection) and release phases of the manipulation. Indeed, under TE illumination, when the tip is above a particle it actually increases the downward optical force, which contributes to prevent the tip from sweeping the particle away.

In conclusion, we propose a new method to trap and manipulate nanometric particles in air above a substrate, using an apertureless tungsten probe. The probe is used to scatter two counterpropagating evanescent waves, generating an optical trap at the apex. We showed that an object of a few nanometers can be selectively trapped and manipulated. An interesting extension of this work will be a study of the influence of different illuminations (e.g., focused beam) and a systematic study of the influence of the nature of the particle and the tip on the trapping mechanism. For example, the strong spectral dependence of the electromagnetic response of metal particles (or resonance excitation of both dielectric and metallic particles) could lead to a material selective trapping.

P. C. C. and A. R. thank Stéphanie Emonin for many fruitful discussions.

[1] A. Ashkin, Proc. Natl. Acad. Sci. U.S.A. **94**, 4853 (1997).
[2] R. Holmlin *et al.,* Angew. Chem., Int. Ed. Engl. **39**, 3503 (2000); E. R. Dufresne *et al.,* Rev. Sci. Instrum. **72**, 1810 (2001).
[3] S. Hla *et al.,* Phys. Rev. Lett. **85**, 2777 (2000); T. W. Fishlock *et al.,* Nature (London) **404**, 743 (2000); H. C. Manoharan *et al.,* Nature (London) **403**, 512 (2000).
[4] L. Novotny *et al.,* Phys. Rev. Lett. **79**, 645 (1997).
[5] K. Okamoto and S. Kawata, Phys. Rev. Lett. **83**, 4534 (1999).
[6] F. Zenhausern *et al.,* Science **269**, 1083 (1995); R. Bachelot *et al.,* Opt. Lett. **20**, 1924 (1995).
[7] F. de Fornel, *Evanescent Waves,* Springer series in Optical Sciences Vol. 73 (Springer-Verlag, Berlin, 2001).
[8] Because typical laser coherence times are small (e.g., 200 ps for an argon laser), a simple calculation shows that a glass sphere with a radius of 10 nm, trapped by an optical force of about 4 pN, will see spatial fluctuations in the 30 pm range, due to the laser phase fluctuation. Therefore, in real cases the trapped particule will only feel the time-averaged trapping potential, without actually being perturbed by the laser fluctuations.
[9] P. C. Chaumet and M. Nieto-Vesperinas, Phys. Rev. B **61**, 14 119 (2000); **62**, 11 185 (2000); Opt. Lett. **25**, 1065 (2000).
[10] E. M. Purcell and C. R. Pennypacker, Astrophys. J. **186**, 705 (1973); B. T. Draine, Astrophys. J. **333**, 848 (1988).
[11] P. C. Chaumet *et al.,* Phys. Rev. B **58**, 2310 (1998); A. Rahmani *et al.,* Phys. Rev. A **63**, 023819 (2001).
[12] J. A. Stratton, *Electromagnetic Theory* (McGraw-Hill, New York, 1941).
[13] P. C. Chaumet and M. Nieto-Vesperinas, Phys. Rev. B **64**, 035422 (2001).

PHYSICAL REVIEW B **66**, 195405 (2002)

Selective nanomanipulation using optical forces

Patrick C. Chaumet
Institut Fresnel (UMR 6133), Faculté des Sciences et Techniques de St Jérôme, Av. Escadrille Normandie-Niemen, F-13397 Marseille cedex 20, France

Adel Rahmani
Laboratoire d'Electronique, Optoélectronique et Microsystèmes-UMR CNRS 5512-Ecole Centrale de Lyon, 36 avenue Guy de Collongue, BP 163, F-69131 Ecully Cedex, France

Manuel Nieto-Vesperinas
Instituto de Ciencia de Materiales de Madrid, Consejo Superior de Investigaciones Cientificas, Campus de Cantoblanco Madrid 28049, Spain
(Received 27 June 2002; published 13 November 2002)

We present a detailed theoretical study of the recent proposal for selective nanomanipulation of nanometric particles above a substrate using near-field optical forces [P.C. Chaumet *et al.*, Phys. Rev. Lett. **88**, 123601 (2002)]. Evanescent light scattering at the apex of an apertureless near-field probe is used to create an optical trap. The position of the trap is controlled on a nanometric scale via the probe, and small objects can be selectively trapped and manipulated. We discuss the influence of the geometry of the particles and the probe on the efficiency of the trap. We also consider the influence of multiple scattering among the particles on the substrate and its effect on the robustness of the trap.

DOI: 10.1103/PhysRevB.66.195405 PACS number(s): 03.50.De, 78.70.−g, 42.50.Vk

I. INTRODUCTION

Thirty years ago, it was demonstrated by Ashkin that optical fields produce a net force on neutral particles.[1,2] Since then, it has been shown that it was possible to exploit the mechanical action of optical fields in a wide range of applications. From atomic and nonlinear physics to biology, optical forces have provided a convenient way to manipulate, nondestructively, small particles in a liquid environment.[3–6] These optical forces can also be used to create microstructures by optical binding[7] or measure the van der Waals force between a dielectric wall and an atom.[8] But one of the most interesting applications of optical forces is optical tweezers. They have proved useful not only for trapping particles, but also for assembling objects ranging from microspheres to biological cells[9,10] (notice that in Ref. 10 the trapped spheres are 50 times larger than the wavelength used in the experiment). More recently, optical tweezers have been used to transport Bose-Einstein condensates over a large distance.[11] However, most of these manipulations involve objects whose size is of the order of one to several micrometers. While for much smaller objects, such as atoms or molecules, the scanning tunneling microscope provides a powerful tool for manipulation and engineering,[12] dealing with neutral particles of a few nanometers requires new experimental approaches.

A novel approach was presented recently, where an apertureless near-field probe is used to create localized optical traps and allow for the selectively capture and manipulation of nanoparticles in vacuum or air above a substrate.[13] In this paper we analyze in detail the scheme presented in Ref. 13 and we discuss the interplay of the different physical processes that contribute to the force experienced by the particles (including van der Waals forces). The particles are not in a liquid environment; hence there is no Brownian motion (which would otherwise induce a disruptive force for small particles) and the apertureless probe can be used as a near-field optical probe to localize and select the particles.[14,15]

In Sec. II we describe briefly the method used to compute the optical forces. In Sec. III A we study the optical force experienced by a sphere in presence of a tungsten tip. First we explain the principle of the manipulation of a nano-object with the apertureless probe and then we look at the influence of the different parameters of the system (geometry of the tip, size of the nanoparticle, illumination) on the trapping. In Sec. III B the presence of many particles on the substrate is investigated to study the influence of neighbors on the manipulation of a particle. Finally in Sec. IV we present our conclusions. In Appendix A we underline the importance of using total internal reflection to get an efficient optical trap at the tip apex, and in Appendix B we compare the optical force with the other forces present in this system (gravitational force, van der Waals force, electrostatic force, and capillary force).

II. COMPUTATION OF THE OPTICAL FORCES

The theory used to compute the optical forces has been presented previously.[16] We use the couple dipole method (CDM). Here we only recall the main steps. First, the coupled dipole method[17,18] is used to derive the field inside the different objects (probe and particles). Each object is discretized into dipolar subunits and the field at each subunit satisfies the following self-consistent equation:

$$\mathbf{E}(\mathbf{r}_i,\omega)=\mathbf{E}_0(\mathbf{r}_i,\omega)+\sum_{j=1}^{N}\left[\mathbf{S}(\mathbf{r}_i,\mathbf{r}_j,\omega)+\mathbf{T}(\mathbf{r}_i,\mathbf{r}_j,\omega)\right]\alpha_j(\omega)\mathbf{E}(\mathbf{r}_j,\omega). \quad (1)$$

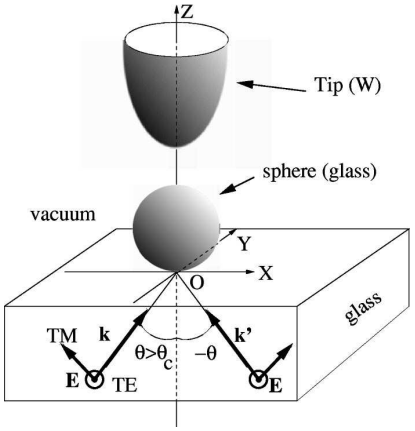

FIG. 1. Scheme of the configuration. A dielectric sphere (radius 10 nm) on a flat dielectric surface is illuminated under total internal reflection. A tungsten probe is used to create an optical trap.

$\alpha_j(\omega)$ is the dynamic polarizability of subunit j,[19] **T** is the field linear response to a dipole in free space,[20,21] and **S** the field linear response to a dipole in the presence of a substrate.[22,23] Note that the field obtained in Eq. (1) takes into account all the multiple interactions between the particles, the substrate, and the tip. The second step is to derive the optical forces experienced by each subunit. Once the electric field is known, the component of the total force[24] on the ith subunit is given by

$$F_u(\mathbf{r}_i) = (1/2)\mathrm{Re}\left(\sum_{v=1}^{3} p_v(\mathbf{r}_i,\omega) \frac{\partial [E^v(\mathbf{r}_i,\omega)]^*}{\partial u} \right), \quad (2)$$

where u or v stand for either x, y, or z, and $\mathbf{p}(\mathbf{r}_i,\omega)$ is the electric dipole moment of the ith subunit.[25] Notice that the derivative of the field is obtained by differentiating Eq. (1). To compute the force exerted by the light on any given object, one has to sum the force experienced by each dipole forming the object. The main advantage of using the CDM to compute the optical force is that retardation and multiple scattering between the objects, the tip, and the substrate are accounted for.

III. RESULTS

We consider a particle in glass, placed either in air or vacuum, with relative permittivity $\varepsilon = 2.25$ and a radius a, above a dielectric substrate. The particle is illuminated by two evanescent waves created by total internal reflection at the substrate/air interface (angle of incidence $\theta > \theta_c = 41.8°$ with $\sqrt{\epsilon}\sin\theta_c = 1$ where $\epsilon = 2.25$ is the relative permittivity of the substrate). The importance of illuminating the particle on the substrate with evanescent waves is explained in Appendix A. The two evanescent waves are counterpropagating, i.e., $\mathbf{k}_\parallel = -\mathbf{k}'_\parallel$, with the same polarization and a random phase relation (Fig. 1). As discussed later, this is to ensure a symmetric lateral force. The optical trap is created by the interaction of the incident waves with a tungsten probe with a radius of curvature at the apex r.

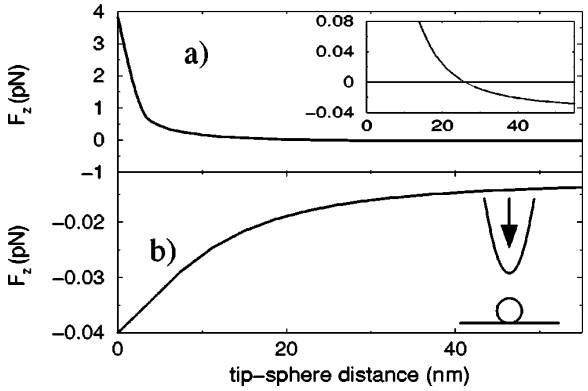

FIG. 2. z component of the force experienced by the sphere vs the distance between the tip and the sphere. (a) TM polarization. The inset is an enhancement of (a) near the sign reversal. (b) TE polarization. The arrow indicates the direction along which the tip is moved.

Notice that all forces are computed for an irradiance of 0.05 W/μm^2, which corresponds, for a laser with a power of 5 W, to a beam focused over an area of 100 μm^2.

A. Isolated particle

1. Principle of the manipulation

In order to foster understanding of the selective trapping scheme, we start by studying the interaction between a single sphere with radius $a = 10$ nm and a tungsten tip (a tip often used in apertureless microscopy as they are not expensive and easy to prepare) with a radius at the apex $r = 10$ nm, which is a typical size for tips used in experiments. The illumination wavelength is $\lambda = 514.5$ nm. Figure 2 shows the z component of the force experienced by the sphere versus the vertical position of the tip above the sphere, for both TE and TM polarizations. The illumination angle is close to the critical angle, $\theta = 43°$. As the tip gets closer to the sphere, the evolution of the force is radically different for the two polarizations. The sphere experiences mainly three gradient forces (because the sphere is small, the scattering force is negligible, and since the relative permittivity is real, absorption does not contribute to the force). The three forces are, first, the negative gradient force due to the evanescent incident field (notice that for a dielectric sphere, the gradient force always pushes the sphere toward the region of high field intensity; as the evanescent field decays in the direction of z positive, the gradient force is negative); second, the negative gradient force due to the interaction of the sphere with itself via the substrate (this force can be understood as the interaction between the dipole associated with the sphere and the field at the dipole location, radiated by this dipole and reflected by the surface; this force is always negative whatever the dielectric constant of the sphere[16]); and third, the gradient force resulting from the interaction between the probe and sphere. This last gradient force can be either positive or negative. For TM illumination, there is a large enhancement of the field near the apex of the probe due to the

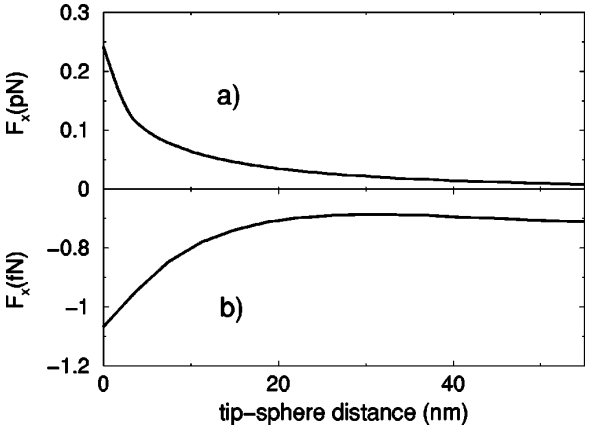

FIG. 3. *x* component of the force if the symmetric illumination is not used. (a) TM polarization. (b) TE polarization.

discontinuity across the air/tungsten boundary.[26] This enhancement generates a positive gradient force which, at short distances, counterbalances the two negative contributions (due to the interaction of the particle with itself via the substrate and the incident evanescent waves). The inset in Fig. 2(a) shows that the force experienced by the sphere changes sign when the tip is 25 nm away from the sphere. On the other hand, for TE polarization [Fig. 2(b)], as the tip gets closer to the particle, the magnitude of the *z* component of the force increases while the force remains negative (directed toward the substrate and away from the tip), hence preventing any trapping. This due to a decrease of the field at the tip apex for this polarization (one can see the electromagnetic field around a gold tip apex in Ref. 26), thus giving a third negative contribution to the gradient force. Because the apex of the tip and the sphere are small compared to the wavelength, the nature of the interaction between the tip and sphere can be understood by considering the tip and sphere as two dipoles. In TM polarization, these two dipoles have two components, parallel and perpendicular to the substrate. As shown in Ref. 27 two aligned dipoles tend to attract each other and two parallel dipoles tend to repel each other. For the same magnitude of the two components (parallel and perpendicular) the attractive force due to the component perpendicular to the substrate is twice that of the repulsive force due to the parallel component. Hence in TM polarization the sphere is attracted by the tip. For the TE polarization, however, the two dipoles are essentially parallel to the substrate and the sphere experiences a negative gradient force. Notice that if we only use a single laser beam, a lateral force would appear as shown in Fig. 3. For TE polarization, the lateral force is very small (in the fN range) and negative, showing that it is mainly due to the gradient force arising from the presence of the tip (the radiation pressure from the incident field always gives a force in the direction of the wave vector, hence in this case a positive force). When the sphere is in contact with the substrate, the lateral force (*x* component) is weaker than the *z* component of the force by a factor of 40. As the static friction coefficient is 1 (glass on glass), the sphere cannot slide along the surface. Indeed, as shown by Kawata and Sugiura,[28] for the sphere to slide on the substrate, its radius has to be large enough for radiation pressure to overcome the gradient force. For TM polarization the lateral force may have a disruptive effect as it tends to push the sphere away from the tip, particularly when F_z becomes positive. In order to avoid this problem, we introduce a second, counterpropagating, evanescent wave with a random phase relation with respect to the first wave. In this way, the sphere experiences no lateral force when it is right underneath the tip. Note that due to the coherence time of the laser (e.g., 200 ps for an argon laser), one can suspect that the sphere experiences spatial fluctuations. We compute these spatial fluctuations for a glass sphere with a radius $a = 10$ nm, trapped by an optical force $|\mathbf{F}| = 4$ pN. From the second law of Newton the distance covered by the sphere, during the time of coherence, is equal to $|\mathbf{F}|t^2/2m = 8$ pm. Therefore, in any realistic configuration, the trapped particle will only be sensitive to the time-averaged trapping potential, without actually being perturbed by the laser fluctuations. If the sphere is larger, its sensitivity to the spatial fluctuation becomes even smaller due to its larger weight.

To assess fully the probe-particle coupling we need to study the evolution of the force experienced by the particle, as the probe is moved laterally. The coordinates (x,y) represent the lateral position of the sphere. The tip is at (0,0) [see Fig. 4(a)]. Figure 4 shows the *z* component of the force when the tip is 25 nm above the substrate for TE and TM polarizations and for an angle of incidence $\theta = 43°$. For TM polarization, Fig. 4(b) represents the magnitude of the *z* component of the force. We see that when the tip is far from the particle the force is negative: the sphere does not feel the tip. As the tip gets closer, the particle starts to experience a positive force along *z*. The change of sign of the *z* component of the force occurs when the sphere is about 30 nm away laterally from the tip. Below this distance the sphere is in the area of the enhancement of the field at the tip apex and the gradient force changes sign; hence the sphere is attracted toward the tip. The region where $F_z = 0$ is represented by a solid closed curve in Fig. 4(b). If the tip is farther away from the substrate, the zero-force curve becomes smaller because of the dependence of the force on the tip-surface distance (Fig. 2). If we approximate the zero-force curve by a circle, the radius of the circle is about 7 nm when the tip is 31 nm above the substrate (and as shown by Fig. 2 it vanishes when the tip is 45 nm above the substrate). Figure 4(c), which pertains to TE polarization, shows that the *z* component of the force is always negative and smaller in magnitude by a factor of 100 than the force associated with the TM polarization. Note that the force becomes stronger (more negative) when the sphere gets closer the tip. Figure 5 represents the lateral force ($\mathbf{F}_\parallel$) experienced by the sphere when the tip scans the surface (the arrows represent the direction of the force experienced by the sphere at the origin of the arrow, and the length of the arrows shows the magnitude of this force). We only consider an area of 40 nm around the origin as the lateral force decreases very quickly away from the tip. In Fig. 5(a), the vectors show that the sphere is attracted by the tip; hence the lateral force pushes the sphere toward the tip. Therefore, when the tip and particle are close enough to

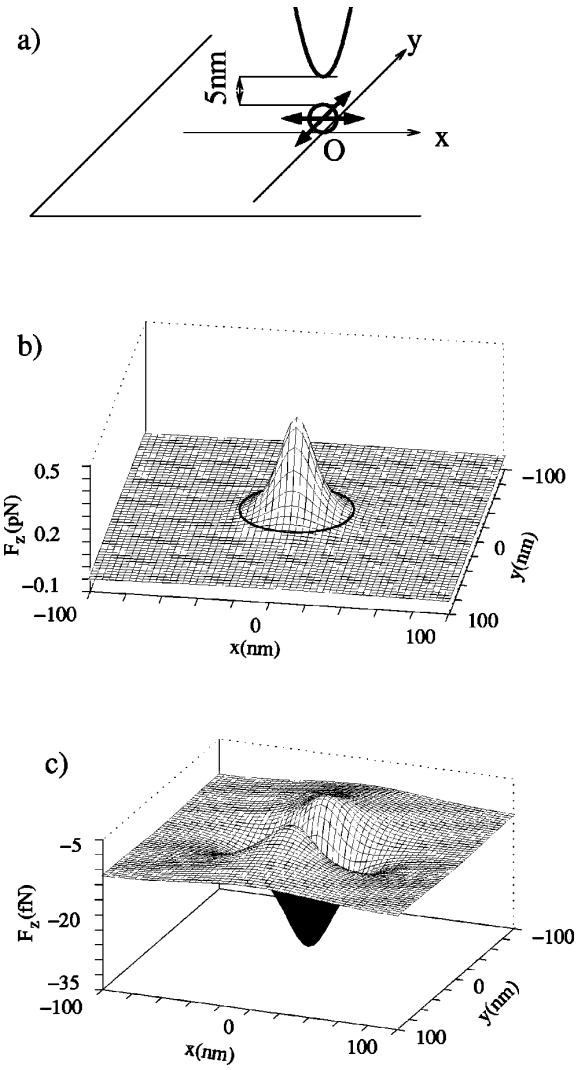

FIG. 4. z component of the force vs the position of the sphere ($a=10$ nm) when the tip is located at the origin. (a) Sketch of the configuration. (b) TM polarization. The thick line represents the case $F_z=0$. (c) TE polarization.

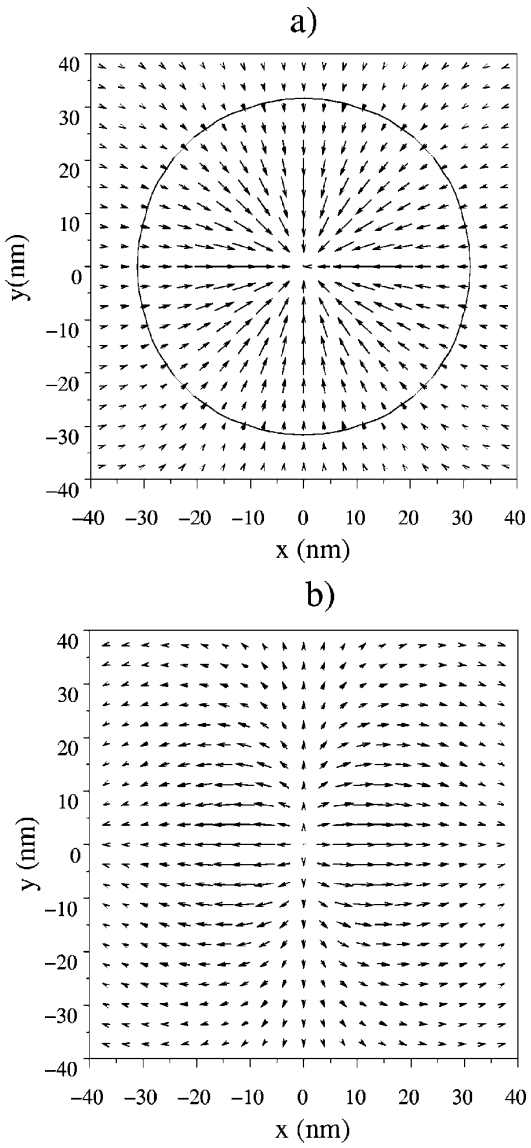

FIG. 5. Parallel component of the force vs the position of the sphere when the tip is located at the origin. (a) TM polarization. The thick line represents the case $F_z=0$. (b) TE polarization.

each other for the z component of the force to be positive (the zero force $F_z=0$ is always represented by the black circle) and large enough to lift the particle off the surface, the lateral force actually helps bringing the particle in the trap. This effect is due to the symmetric illumination. Again TE polarization gives a different result. Figure 5(b) shows that the lateral force pushes the particle away from the tip. However, since the magnitude of the (downward) z component of the force is larger than the x component by a factor of 5, we expect that the sphere is not displaced when the tip is scanned over it under TE illumination. Note that apertureless probes are often used in the tapping mode when imaging a surface. This mode minimizes the lateral motion imparted to the object by the optical force.

We have shown that a tungsten probe can be used to trap efficiently a nanometric object above a surface using TM illumination. For nanomanipulation purposes it is important to assess the stability of the trap as the probe lifts the particle off the substrate. Figure 6 shows the z component of the force when the sphere is located at the apex of the tip and the tip is moved vertically. For the TM polarization [Fig. 6(a)] the optical force remains positive over a large distance, at least 200 nm. The particle can therefore be manipulated vertically as well as horizontally. The stability of the trap when the tip-particle pair is away from the substrate prevents any disruptive interaction with the surface roughness as shown in the next section. Note that the evolution of the force versus the distance to the substrate is linear rather than exponential. The particle experiences a negative gradient force due the

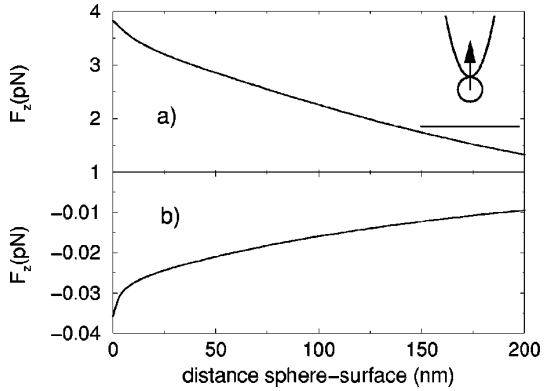

FIG. 6. *z* component of the force experienced by the sphere as a function of the distance between the sphere and substrate. The sphere is placed at the apex of the probe. $\theta = 43°$. (a) TM polarization. (b) TE polarization.

exponential decay of the intensity of the illumination. At the same time, the particle experiences a positive gradient force due to the field enhancement at the tip apex, which also decreases exponentially with *z* because this enhancement depends on the intensity of the evanescent illuminating light. The competition between these two contributions results in a weak decrease of the trapping force as the particle is moved away from the substrate.

As described in Ref. 13, the procedure to trap a small object with a tungsten tip is the following: first TE illumination is used while the tip scans the surface in tapping mode or in constant-height mode if the area under investigation is small enough. Such modes avoid the displacement of the particle by the tip. Once an object has been selected, the probe is placed above the object and the polarization of the illumination is rotated to TM. The probe is then brought down over the particle and captures it. The probe can then move the particle above the substrate, both horizontally and vertically, to a new position (note that if, for some reason, one wishes to move the particle over distances larger than the size of the illumination spot, one could move *the sample* with a piezoelectric device once the sphere is trapped at the apex of the tip). As shown by Fig. 6(b), as the *z* component of the force in TE polarization is always negative, the nanoparticle can be released by switching back to TE polarization. The lack of trapping under TE illumination is actually an important advantage during both the imaging (selection) and release phases of the manipulation. Indeed, under TE illumination, when the tip is above a particle, it actually increases the downward optical force, which contributes to prevent the tip from sweeping the particle away.

2. Efficiency of the manipulation scheme

In the previous section we have established the possibility to manipulate selectively a nanoparticle above a flat dielectric substrate. Now we study the influence of the different parameters of the system (tip radius at the apex, angle of incidence, etc.) on the efficiency of the trap.

a. Influence of the illumination. So far we have considered an angle of incidence 43°, which corresponds to a slow decay of the evanescent field above the substrate. Figures 7 and 8 show the influence of the angle of incidence on the capability of the tip to manipulate the nano-object. Figure 7 shows the evolution of the *z* component of the force as the tip gets closer the surface versus the angle of incidence for both polarizations. In Fig. 7(a) (TM polarization) one can see that for a fixed distance between the tip and substrate, the larger the angle of incidence, the smaller the magnitude of the force experienced by the trapped object. Note that as the angle of incidence increases, the initial (evanescent) field decays faster. Accordingly, a weaker field reaches the tip and

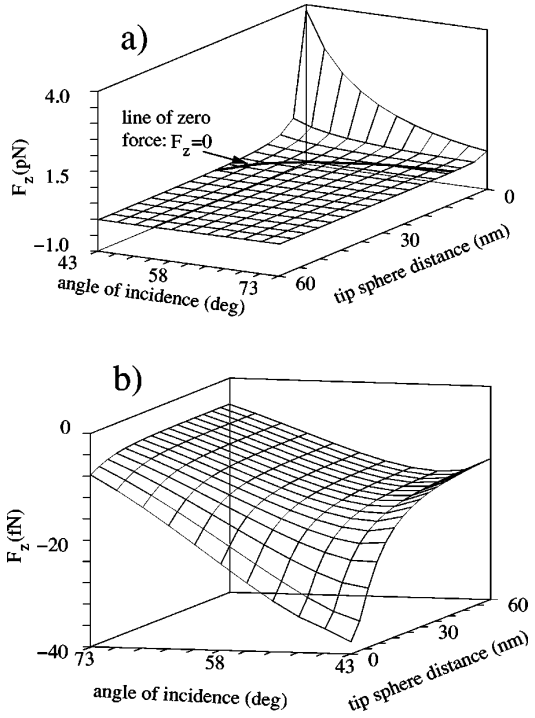

FIG. 7. *z* component of the force experienced by the sphere as a function of the distance between the tip and sphere and the substrate and angle of incidence. (a) TM polarization. (b) TE polarization.

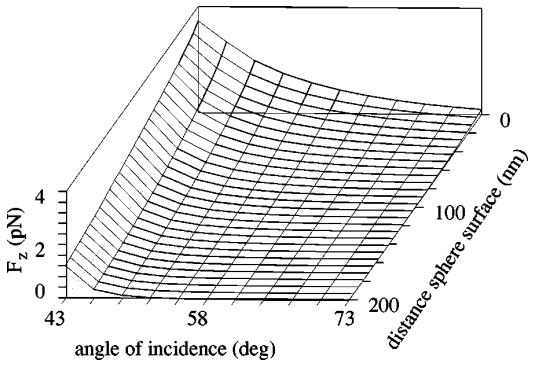

FIG. 8. *z* component of the force experienced by the sphere as a function of the distance between the sphere and substrate with $\theta = 43°$ for TM polarization.

the enhancement of the field at the tip apex is less important, leading to a smaller positive gradient force. As a consequence, when the tip approaches the sphere, the change of sign for the z component of the force occurs for smaller tip-sphere distances at larger angles of incidence [cf. the thick line in Fig. 7(a) which represents the level curve $F_z=0$]. For example, for $\theta=43°$, $z=25$ nm, and for $\theta=73°$, $z=8$ nm. This means that it is easier to manipulate the sphere when the angle of incidence is close to the critical angle. Notice that for TE polarization [Fig. 7(b)], when the angle of incidence increases, the magnitude of the negative z force decreases. The explanation for this evolution is similar to that of the TM polarization case: the incident field that reaches the apex of the tip is weaker for large angles of incidence. Accordingly, the interaction between the tip and particle becomes weaker as the angle increases, and the magnitude of the repulsive force decreases. Figure 8 represents the z force experienced by the sphere when it is located at the apex of the tip versus the angle of incidence and distance between the trapped sphere and substrate. The force along z decays more rapidly for larger angles of incidence. The exponential decay of the incident field is stronger when the angle of incidence is far from the critical angle. As the positive force along z is due to the enhancement of the field at the apex of the tip and it depends on the value of the incident evanescent field at the tip apex, the z component of the force follows the same behavior as the incident field. Note that the influence of the wavelength is easy to infer. The initial field decays as $e^{-\gamma z}$ with $\gamma=\sqrt{2\pi(\varepsilon\sin^2\theta-1)/\lambda}$, where λ is the wavelength in vacuum. When λ increases, γ decreases; hence the exponential decay is slower and the manipulation is easier to perform.

b. Influence of the geometry. In the previous section, both the radius of the tip, r, and the radius of the sphere, a, were 10 nm. In this paragraph we study the influence of these two geometrical parameters. Figure 9 shows the evolution of the force along z versus a for both polarizations and two angles of incidence. The tip ($r=10$ nm) is in contact with the sphere. One might expect a force proportional to a^3 as the gradient force is proportional to the real part of the polarizability, hence to the volume of the sphere. Actually, this behavior is only observed for the TE polarization [Fig. 9(b)]. For the TM polarization, when a increases, so does the distance between the tip and substrate. Thus we have competition between the increase of the gradient force due to a larger a and the decrease of the field enhancement at the tip apex due to a larger distance between the tip and substrate. For the smallest angle ($\theta=43°$), because the decrease of the field is slow, the force starts by increasing linearly for small values of a. When a increases, the enhancement of the field at the tip decreases and the positive gradient force due to this enhancement vanishes. The competition between these two effects leads to a maximum of the force for $a=40$ nm. For the largest angle ($\theta=60°$) the incident field decays rapidly in that case, and for a larger than 40 nm the z force experienced by the sphere becomes negative. Thus it would not be possible to manipulate a larger particle. For TE polarization the z component of the force varies roughly as a^3. This implies that the main contribution to the force is due to the incident field: the tip has a very weak influence on the force experienced by the sphere. To check this argument we plot the force along z without the presence of the tip [line with the "+" symbol in Fig. 9(b)]. These curves show that for the largest angle ($\theta=60°$) the above argument is true; only when the radius is small can we see a slight shift of the force due to the presence of the tip [see inset in Fig. 9(b)]. For the smallest angle ($\theta=43°$) the presence of the tip shifts the force curves toward negative values, as explained in the previous section. This holds even for a very large radius of the sphere because of the slow evanescence of the incident field.

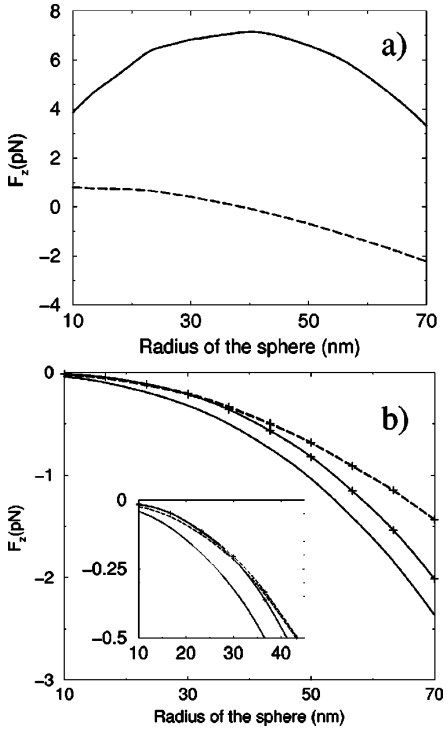

FIG. 9. z component of the force experienced by the sphere as a function of its radius. Plain line $\theta=43°$, and dashed line $\theta=60°$. (a) TM polarization. (b) TE polarization. The symbol + pertains to results for when the tip is not taken into account in the computation.

We must now check that for large radii it is always possible to manipulate the sphere above the substrate. Figure 10 shows the z component of the force at two different angles of incidence for two different radii: $a=30$ nm and 50 nm. One can see that it is possible to lift the spheres up to 200 nm above the surface without any problem, even for the case $\theta=60°$ with $a=30$ nm which corresponds to a radius close to the limiting case [Fig. 9(a) shows $F_z=0$ for $a=40$ nm if $\theta=60°$]. In that case, the force is small and the trap is less robust than for smaller angles of illumination. Therefore, the trapping scheme presented here works over a wide range of particle sizes. Notice that although we could not compute the largest radius that we could manipulate at $\theta=43°$ because it would require too many subunits, we can estimate that spheres with a radius up to around 90 nm can be trapped and manipulated.

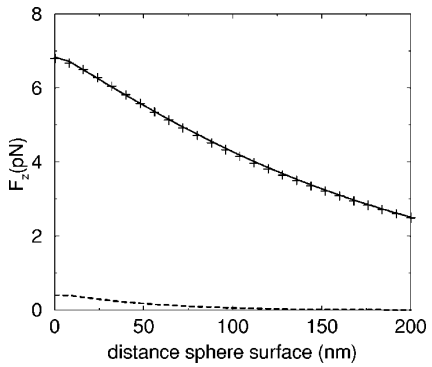

FIG. 10. z component of the force experienced by the sphere in TM polarization. Solid line: $a=30$ nm, $\theta=43°$. Dashed line: $a=30$ nm, $\theta=60°$. Crosses: $a=50$ nm, $\theta=43°$.

Another relevant geometric parameter is the radius of curvature at the apex of the tip. It is easy to see the importance of this parameter for our optical trap because the enhancement of the field at the tip apex depends directly on this radius. Figure 11 shows the z component of the force versus r for a particle with radius $a=10$ nm for two different angles of incidence. One can see that the z component of the force depends strongly on the radius of the tip apex. For $\theta=43°$ the squares are the CDM results and show a decay of the force for larger radii. The solid line is a fit of the form $a_0/r+a_1$ where a_0 and a_1 are the parameters of the fit. This form is associated to the $1/r$ dependence of the z force, which is found irrespective of the angle of incidence (see circles in Fig. 11).

B. Many particles on the surface

In the preceding section we studied the case of an isolated sphere to illustrate how to select and manipulate a nanoobject above a surface. It is nevertheless important to know whether the proposed manipulation scheme would still work if several particles are clustered together. We consider a set

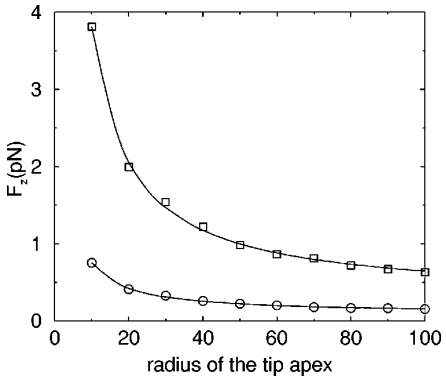

FIG. 11. z component of the force experienced by the sphere for TM polarization vs the radius of the tip apex. $a=10$ nm. Solid line (fit of the form $a_0/r+a_1$) and squares (CDM results) for $\theta=43°$ and circles (CDM results) for $\theta=60°$.

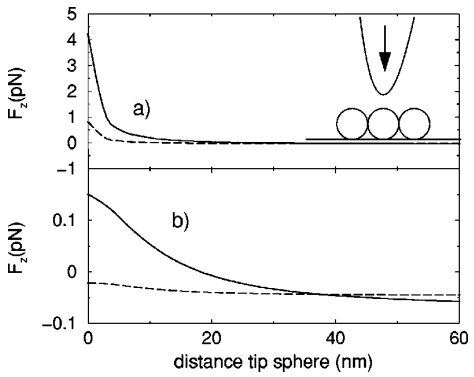

FIG. 12. z component of the force experienced by the sphere in TM polarization. Solid line $\theta=43°$, dashed line $\theta=60°$. (a) Force experienced by the middle sphere. (b) Force experienced by the side spheres.

of three spheres (radius 10 nm, permittivity 2.25) aligned along the x axis. The probe is placed above the middle sphere. We account for the multiple scattering between the three spheres, the substrate, and the tip. The optical binding induced among the spheres[27] is also included in our description. For this configuration again, TE illumination does not permit trapping. For TM illumination, we plot in Fig. 12 the z component of the force experienced by the middle sphere and by those on the sides as a function of the vertical distance between the probe and middle sphere. For an angle of incidence $\theta=43°$, as the tip gets closer to the middle sphere, the z component of the force, although the strongest for the middle sphere, remains positive for the two side spheres. This could be a problem if one wanted to manipulate only one particle among several. The central particle can be selectively trapped by increasing the angle of incidence of the illuminating beams to tighten the trap in the x direction. In Fig. 12 we see that for $\theta=60°$ the optical force induced by the probe is positive only for the middle sphere. This remains true for three spheres aligned along y. Figure 13 shows the extraction of the middle sphere by the tip. Our calculation

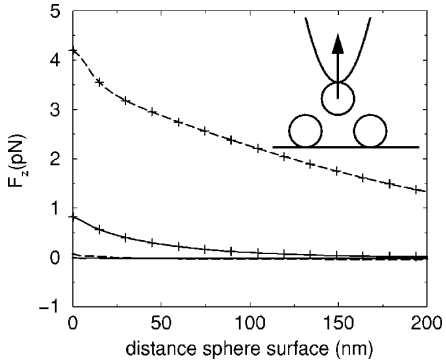

FIG. 13. z component of the force experienced by the sphere in TM polarization. Solid line $\theta=43°$, dashed line $\theta=60°$. With symbol "+": force experienced by the middle sphere. With no symbol: force experienced by the side spheres.

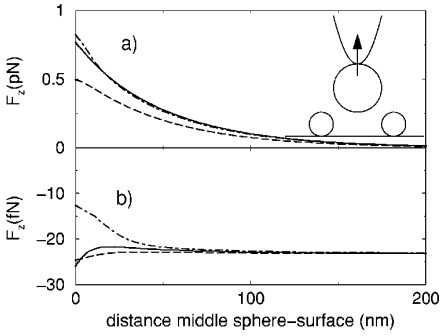

FIG. 14. z component of the force experienced by the sphere in TM polarization with $\theta=60°$. The radius of the side spheres is 10 nm. The radius of the middle sphere is $a=10$ nm (dot-dashed line), $a=17$ nm (solid line), and $a=28$ nm (dashed line). (a) Force experienced by the middle sphere. (b) Force experienced by the side spheres.

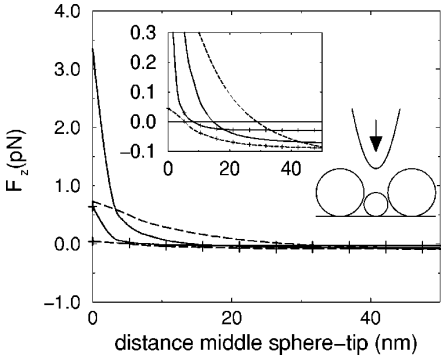

FIG. 15. z component of the force experienced by the sphere in TM polarization. The radius of the middle sphere is 10 nm. The radius of the side sphere is $a=17$ nm. Solid line: force experienced by the middle sphere. Dashed line: force experienced by the side spheres. Curve with no symbol: $\theta=43°$. Curve with symbol "+": $\theta=60°$. The inset is a magnification of what happens close to the sign reversal for the force along z.

shows that the vertical force experienced by the two side spheres remains negative when the probe moves away from the substrate for an angle of incidence $\theta=60°$. Therefore, the spheres on the sides do not hinder the capture of the middle sphere if the angle of incidence is adequately chosen.

Notice that this computation is done for three identical spheres. We show in Fig. 14 that if the middle sphere is larger than the other two, it is still possible to trap the middle sphere without disturbing the side spheres. Figure 14(a) shows the z component of the force experienced by the middle sphere for three different radii: $a=10$, 17, and 28 nm. The side spheres have a fixed radius: $a=10$ nm. When the middle sphere is lifted off the surface by the tip (angle of incidence $\theta=60°$) the force along z is always positive; hence the manipulation of the middle sphere is not disturbed by the side spheres. Figure 14(b) shows the evolution of the z force experienced by the sides spheres during the extraction of the middle sphere. This force is always negative; therefore the side spheres are not attracted by the tip. Moreover, as the radius of the middle sphere increases, the z component of the force becomes larger while being negative, thus excluding the possibility of having the side spheres captured by the tip. This reflects the fact that as the radius of the middle sphere increases, so does the distance between the side spheres and the apex of the tip. Hence as the tip is farther from the sides sphere its influence is weaker.

In Fig. 15 we present the case where the middle sphere is smaller than the side spheres. First for an angle of incidence close to the critical angle ($\theta=43°$) the three spheres experience a positive force when the tip approaches the substrate. If we look carefully (see the inset), we see that the z component of the force becomes positive for the side spheres before the middle sphere experiences a positive force. Hence it is impossible to only manipulate the middle sphere. If the angle of incidence is increased to the value $\theta=60°$ to make the trap smaller, we show that the z component of the force becomes positive for the middle sphere first. However, when the tip is in contact with the middle sphere the z force is positive for all three spheres. Notice that to get a smaller trap one can increase the angle of incidence but in that case the force would be very small compare to the other force in the system (see Appendixes A and B). Therefore, in this case it is impossible to capture selectively the middle sphere. The solution would be to first move the side spheres aways to isolate the smaller middle sphere, and only after would it be possible to trap it. Notice that when the tip is far from the surface the negative force is stronger for the largest spheres. This is due to the gradient force proportional to a^3.

In the previous section we showed that a tungsten probe can be used to trap efficiently a nanometric object above a surface using TM illumination. By moving the tip laterally, it is possible to transport the selected particle in a precise manner. However, we must check that the electromagnetic field scattered by another particle on the substrate would not disturb the trap during the transport. Figure 16 shows the evolution of the force experienced by the sphere trapped by the tip when a second sphere is on the surface as shown by Fig. 16(a) (both spheres have a radius of 10 nm). Figure 16(b) shows that the z component of the force on the trapped sphere is not altered by the presence of the other sphere. When the two spheres are 30 nm apart ($h=50$ nm), the force along z does not depend on the position of the tip. Figure 16(c) shows that the lateral force is more sensitive and we can see some oscillations when the two spheres are close to each other. However, this is not really a problem since even if the two spheres are only 30 nm apart, the lateral force is 1000 times smaller than the force along z, and therefore, would not hinder the optical trapping. We have studied the case where the tip and trapped sphere scan the surface at $h=20$ nm. When the tip is located at the origin, the two spheres are in contact (the trapped sphere and the sphere on the substrate) and the z component of the force becomes negative, of the order of -5 pN, and the lateral force when the spheres are close to each other is about 1 pN. In this configuration the trapped sphere can escape and thus be lost by the tip. In summary, if the distance between the two spheres is larger than 3 times the radius of the sphere on the surface, then the trapped sphere is not disturbed.

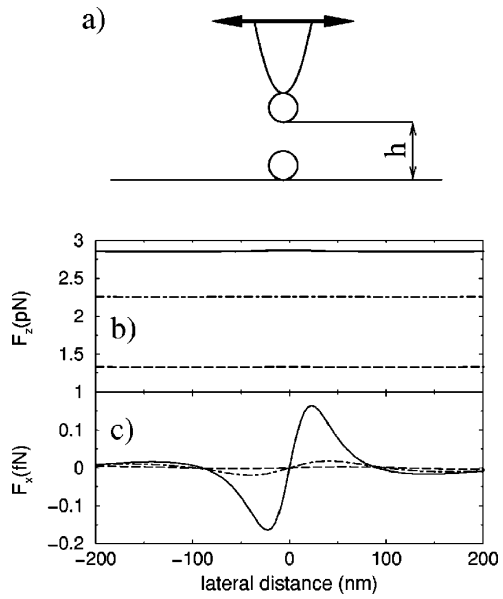

FIG. 16. Force experienced by a sphere ($a=10$ nm) trapped at the apex of the tungsten tip, when the tip scans the substrate at different height h, with another particle ($a=10$ nm) on the surface localized at the origin. Solid line: $h=50$ nm. Dot-dashed line: $h=100$ nm. Dashed line: $h=200$ nm. (a) sketch of the configuration. (b) z component of the force. (c) x component of the force.

IV. CONCLUSION

We have presented a detailed study of a trapping scheme that allows one to trap and nanomanipulate, in a selective manner, nanometric particles in air above a substrate. The substrate is illuminated under total internal reflection by two laser beams which create two counterpropagating evanescent waves. An apertureless tungsten probe is used to scatter these two waves and generate a localized optical trap. An object of a few nanometers can be selectively brought into the trap and manipulated with the probe. An important advantage of this scheme is the possibility to use the probe to localize the particles upon the surface. Using TE polarization the tip can scan the surface in tapping mode or constant-height mode, and it allows one to acquire an optical near-field image of the surface. Because in TE polarization the z component of the optical force is directed toward the substrate, there is no risk of displacing the particles during the imaging phase. Then, just by switching to TM polarization, we can manipulate the particles. As we showed, even if many particles are clustered, varying the angle of incidence still makes it possible to manipulate selectively only one particle.

An interesting extension of this work will be a study of the influence of different illuminations (e.g., focused beam) and a study when the particle is either absorbing or metallic. In that case the optical force has two contributions: the gradient force and the momentum transfer from the laser to the particle due to absorption. For metallic particles, the strong spectral dependence of the electromagnetic response (or the resonances in the response of dielectric and metallic particles) could lead to new effects. For example, at some wavelength the gradient force on a silver particle vanishes, and only the absorbing force remains. Such phenomena could lead to a material-selective trapping. It will also be interesting to explore the possibility of trapping a small gold particle, a few nanometers in size, and use it as a highly localized probe for topographic or spectroscopic studies.[29,30]

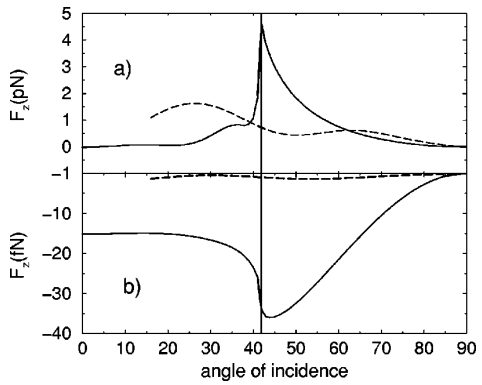

FIG. 17. z component of the force experienced by the sphere vs the angle of incidence. The vertical line is plotted for $\theta=\theta_c$ in the case of total internal reflection. The solid line pertains to the substrate illuminated from below the surface, and the dashed line pertains to an illumination from above the surface. (a) TM polarization. (b) TE polarization.

APPENDIX A: IMPORTANCE OF THE EVANESCENT ILLUMINATION

In this Appendix we show that the choice of total internal reflection illumination is the most adequate to get a strong optical force. Figure 17 shows the z component of the force when the angle of incidence is varied between 0 and 90° for an illumination either from above or from below the surface. For an illumination from below the surface (internal reflection) and for TM polarization, the largest force is obtained for $\theta=\theta_c$. The magnitude of the force decreases exponentially when θ increases. For θ smaller than the critical angle, the force is small and even negligible for θ smaller than 20°. For TE polarization the minimum of the z component of the force is obtained for $\theta=43°>\theta_c$. This negative force is important as it prevents the tip from displacing the particle during scans. If the surface is illuminated from above, for TM polarization the z components of the force remain weaker than the force obtained with an evanescent wave, and for TE polarization the negative force is very weak compared to those obtained with an evanescent wave above the surface. Hence to trap and manipulate a nano-object it is best to choose an angle of incidence close to but larger than the critical angle.

APPENDIX B: DISCUSSION ON THE ROLE OF FORCES OTHER THAN THE OPTICAL FORCE

In an actual experiment, there would be other forces attracting the sphere toward the substrate. These forces are mainly four: van der Waals, electrostatic, capillary, and

gravitational forces. One must therefore compare their effect with that of the optical forces in order to assess the robustness of the scheme.

1. van der Waals force

The van der Waals force[31] between two particles (which is the Casimir force in the nonretarded case[32]) can be described as a short-range force, derived from the Lennard-Jones 6-12 potential, in the form

$$F_w = \frac{AS}{6h^2}\left(\frac{z^6}{4h^6} - 1\right), \tag{B1}$$

h being the distance between the two particles, A the Hamaker constant ($A = 60$ zJ for glass, and about 200 zJ for tungsten), z corresponds to the separation of lowest energy between two particles (i.e., the position of the minimum of the Lennard-Jones potential), which we have estimated at 0.5 nm, and S is the Derjaguin geometrical factor related to the mutual curvature of the two particles. Notice that the van der Waals force is maximum when $z = h$.

If we compute the van der Waals force between the glass sphere and glass surface, we have $S = a$ (a radius of the sphere); hence the force is $F_w = 0.3$ pN. This force is not a problem as the optical force when the tip is in contact with the sphere is larger than 1 pN. In addition we have to consider the van der Waals force between the apex of the tip and the sphere when they are in contact. We have estimated it for the case where the radius of the sphere and the curvature of the tip apex are equal to 10 nm, with $S = a/2 = 5$ nm, $A = \sqrt{60 \times 200}$ zJ, for which we obtain $F_w = 0.27$ pN. Hence the two van der Waals forces are of comparable magnitude and cancel each other when the particle is in contact with both the substrate and tip. Therefore the van der Waals force does not hamper the manipulation of the particle. A problem can arise when we want to release the sphere from the trap, as switching back to TE polarization may not create a strong enough repulsive force. There are many ways to avoid this problem. One is to approach the tip-sphere system to the surface to benefit from the van der Waals force between the substrate and the sphere. Another solution is to choose an angle of incidence close to the critical angle to increase the magnitude of the repulsive force. Of course, one could also increase the intensity of the incident field.

Notice that the van der Waals force is computed here for perfectly smooth bodies. In reality this force should be weaker. Indeed, for a surface roughness about 2 nm, the van der Waals force is reduced by a factor of 10.[33]

2. Electrostatic force

The electrostatic force (Coulomb force) between an electrically charged sphere and an uncharged plane can be expressed as[33]

$$F_e = \frac{\pi}{\varepsilon_0}\frac{\varepsilon - 1}{\varepsilon + 1} a^2 \sigma^2, \tag{B2}$$

σ being the charge surface density (10^{-3} C m^{-2} in very dry conditions), $\varepsilon_0 = 8.85 \times 10^{-12}$ F m^{-1} the permittivity of vacuum, and ε the relative permittivity of the dielectric substrate. For $a = 10$ nm and $\varepsilon = 2.25$, we get $F_e = 0.013$ pN. This force is clearly negligible compared to the optical force. And moreover this force will be weaker for a conductor.[33]

3. Capillary force

If there is water on the surface, there will be a capillary force which can be expressed as[33]

$$F_c = 2\pi a \gamma, \tag{B3}$$

γ being the surface tension of water, with $\gamma = 72 \times 10^{-3}$ N m^{-1}. For a radius of the sphere $a = 10$ nm we get $F_c = 4.5$ pN. This force is of the same order as the optical force; hence it is necessary to work in a dry environment in order to reduce this capillary force.

4. Gravitational force

The force of gravity is

$$F_g = mg = \frac{4}{3}\pi a^3 \rho g, \tag{B4}$$

where $g = 10$ m s^{-2} is the gravitational acceleration and $\rho = 2500$ kg m^{-3} is the density of glass. If the radius is equal to 10 nm, we find $F_g = 0.1$ aN, and the z component of the optical force experienced by the sphere is larger (by a factor of 10^7) than the gravitational force. Hence gravity can be neglected.

5. Conclusion

In conclusion, in a dry environment (no capillary force) only the van der Waals force could perturb the release of the particle, but as we mentioned previously, this force becomes weaker when roughness is taken into account. Note, however, that these four forces do not depend on the illumination whereas the optical forces depends on the intensity of the incident field. Therefore, one solution to avoid any disruptive contribution from the van der Waals force is to increase the power of the laser beam. For example, with the power used by Okamoto and Kawata,[34] which corresponds to an irradiance of 0.2 W/μm^2, the optical force is multiplied by a factor of 4 compared to the computation presented in this paper. Another way of increasing the optical force is to choose another material for the probe. For example, at a wavelength of 450 nm, a silver tip when in contact with the sphere generates an optical force 6 times stronger than that created by a tungsten tip at $\lambda = 514.5$ nm.

[1] A. Ashkin, Phys. Rev. Lett. **24**, 156 (1970).
[2] A. Ashkin, Phys. Rev. Lett. **25**, 1321 (1970).
[3] A. Ashkin, J. M. Dziedzic, J. E. Bjorkholm, and S. Chu, Opt. Lett. **11**, 288 (1986).
[4] A. Ashkin, J. M. Dziedzic, and T. Yamane, Nature (London) **330**, 769 (1987).
[5] S. M. Block, D. F. Blair, and H. C. Berg, Nature (London) **338**, 514 (1989).
[6] A. Ashkin, Proc. Natl. Acad. Sci. U.S.A. **94**, 4853 (1997).
[7] M. Burns, J.-M. Fournier, and J. Golovchenko, Phys. Rev. Lett. **63**, 1233 (1989).
[8] A. Landragin, J.-Y. Courtois, G. Labeyrie, N. Vansteenkiste, C. I. Westbrook, and A. Aspect, Phys. Rev. Lett. **77**, 1464 (1996).
[9] R. Holmlin, M. Schiavoni, C. Chen, S. Smith, M. Prentiss, and G. Whitesides, Angew. Chem. Int. Ed. Engl. **39**, 3503 (2000); E. R. Dufresne, G. C. Spalding, M. T. Dearing, S. A. Sheets, and D. G. Grier, Rev. Sci. Instrum. **72**, 1810 (2001); E. R. Dufresne and David G. Grier, *ibid.* **69**, 1974 (1998).
[10] M. P. Macdonald, L. Paterson, K. Volke-Sepulveda, J. Arlt, W. Sibbet, and K. Dholakia, Science **296**, 1101 (2002).
[11] T. L. Gustavson, A. P. Chikkatur, A. E. Leanhardt, A. Görlitz, S. Gupta, D. E. Pritchard, and W. Ketterle, Phys. Rev. Lett. **88**, 020401 (2002).
[12] S. Hla, L. Bartels, G. Meyer, and K. Rieder, Phys. Rev. Lett. **85**, 2777 (2000); T. W. Fishlock, A. Oral, R. G. Edgell, and J. B. Pethica, Nature (London) **404**, 743 (2000); H. C. Manoharan, C. P. Lutz, and D. M. Eigler, *ibid.* **403**, 512 (2000).
[13] P. C. Chaumet, A. Rahmani, and M. Nieto-Vesperinas, Phys. Rev. Lett. **88**, 123601 (2002).
[14] F. Zenhausern, Y. Martin, and H. K. Wickramasinghe, Science **269**, 1083 (1995); R. Bachelot, P. Gleyzes, and A. C. Boccara, Opt. Lett. **20**, 1924 (1995).
[15] F. de Fornel, *Evanescent Waves*, Springer Series in Optical Sciences, Vol. 73 (Springer-Verlag, Berlin, 2001).
[16] P. C. Chaumet and M. Nieto-Vesperinas, Phys. Rev. B **61**, 14 119 (2000); **62**, 11 185 (2000).
[17] E. M. Purcell and C. R. Pennypacker, Astrophys. J. **186**, 705 (1973).
[18] P. C. Chaumet, A. Rahmani, F. de Fornel, and J.-P. Dufour, Phys. Rev. B **58**, 2310 (1998).
[19] B. T. Draine, Astrophys. J. **333**, 848 (1988).
[20] J. D. Jackson, *Classical Electrodynamics*, 2nd ed. (John Wiley, New York, 1975), p. 395.
[21] A. Rahmani and G. W. Bryant, Opt. Lett. **25**, 433 (2000).
[22] G. S. Agarwal, Phys. Rev. A **11**, 230 (1975); **12**, 1475 (1975).
[23] A. Rahmani, P. C. Chaumet, and F. de Fornel, Phys. Rev. A **63**, 023819 (2001).
[24] In fact the optical force is the time-averaged force as shown in Ref. 25.
[25] P. C. Chaumet and M. Nieto-Vesperinas, Opt. Lett. **25**, 1065 (2000).
[26] L. Novotny, R. X. Bian, and X. Sunney Xie, Phys. Rev. Lett. **79**, 645 (1997).
[27] P. C. Chaumet and M. Nieto-Vesperinas, Phys. Rev. B **64**, 035422 (2001).
[28] S. Kawata and T. Sugiura, Opt. Lett. **17**, 772 (1992).
[29] O. Sqalli, M. P. Bernal, P. Hoffmann, and F. Marquis-Weible, Appl. Phys. Lett. **76**, 2134 (2000).
[30] T. Kalkbrenner, M. Ramstein, J. Mlynek, and V. Sandoghdar, J. Microsc. **202**, 72 (2001).
[31] A. Feiler, I. Larson, P. Jenkins, and P. Attard, Langmuir **16**, 10 269 (2000).
[32] H. B. G. Casimir and D. Polder, Phys. Rev. **73**, 360 (1948).
[33] F. Arai (unpublished).
[34] K. Okamoto and S. Kawata, Phys. Rev. Lett. **83**, 4534 (1999).

PHYSICAL REVIEW B **71**, 045425 (2005)

Photonic force spectroscopy on metallic and absorbing nanoparticles

Patrick C. Chaumet
Institut Fresnel (UMR 6133), Université d'Aix-Marseille III, Avenue Escadrille Normandie-Niemen, F-13397 Marseille Cedex 20, France

Adel Rahmani
Laboratoire d'Electronique, Optoélectronique et Microsystèmes, UMR CNRS, 5512 Ecole Centrale de Lyon 36, avenue Guy de Collongue, F-69134 Ecully Cedex, France

Manuel Nieto-Vesperinas
Instituto de Ciencia de Materiales de Madrid, Consejo Superior de Investigaciones Cientificas, Campus de Cantoblanco, Madrid 28049, Spain

(Received 18 March 2004; revised manuscript received 9 July 2004; published 26 January 2005)

We present a detailed study of the optical trapping and manipulation of nanoparticles with complex permittivity using an apertureless near-field probe. We use a three-dimensional, self-consistent description of the electromagnetic scattering processes that accounts for retardation and the intricate many-body interaction between the substrate, the particle, and the probe. We analyze the influence of absorption on the optical force. For metals we describe how the optical force spectrum is influenced by the optical response of the metal, and in particular by plasmon resonances. We find that the optical force spectrum can provide an intrinsic signature of the particle composition which can be used to achieve a material-selective trapping and nanomanipulation.

DOI: 10.1103/PhysRevB.71.045425 PACS number(s): 78.70.−g, 03.50.De, 42.50.Vk

I. INTRODUCTION

Since the pioneering work of Ashkin,[1,2] the use of optical forces has led to the development of optical tweezers techniques which use light to manipulate dielectric particles larger than the wavelength.[3–5] On the other hand, schemes to trap and manipulate nanometric objects in a controlled and selective manner are still scarce. In a previous article,[6] we proposed a scheme to *selectively manipulate* dielectric nanoobjects on a flat dielectric substrate in air or vacuum. This manipulation was achieved using the scattering of evanescent waves at the apex of an apertureless near-field probe. However, that study was restricted to lossless dielectric particles.

The case of metallic particles is more complex due to the imaginary part of the relative permittivity and the existence of plasmon resonances. For large particles (compared to the wavelength of illumination), a two-dimensional optical trap can be created under special conditions, i.e., using TEM_{00} and TEM_{01}^{*} laser modes.[7,8] But it is only very recently that large metallic particle have been trapped in three dimension.[9,10] In the case of small particles, i.e., particles smaller than the wavelength (Rayleigh particles), the optical trapping can be achieved in three dimensions.[11–13] The large interest of small metallic particles is their plasmon resonance which produces an enhancement of the optical force experienced by the particle. This can be used in photonic force microscopy[14] or to trap single molecules to study surface-enhanced Raman scattering.[15]

In this article, using the selective trapping scheme proposed in Refs. 6 and 16, we extend the analysis of our optical trap to the selective manipulation of absorbing and metallic particles. The optical trapping of dielectric particles is the result of the gradient force only, as the scattering force is negligible, compared to this gradient force, for small particles. However, absorbing and metallic particles, due to the nonzero imaginary part of their relative permittivity, experience an absorbing force of the same order of magnitude as the gradient force. We shall investigate the consequences of this force on the stability of the optical trap. Moreover, we shall address the effect of the plasmon resonance of small particles on the optical forces.

Since the details of the computation of optical forces have been described previously,[17–19] only a brief account of the theory is given in Sec. II. Section III A presents the results for absorbing dielectric particles (e.g., quantum dots). Section III B addresses the case of metallic particles. The influence of plasmon resonances on the optical trapping is discussed, with a particular emphasis on the case of silver particles which exhibit an intricate behavior. In Sec. III C we study the possibility of scanning the surface in tapping mode with a metallic particle trapped at the tip apex. Finally, we present our conclusions in Sec. IV.

II. CALCULATION OF THE OPTICAL FORCES

We use the coupled dipole method (CDM) to compute the optical forces. The method consists in discretizing the object under study as a set of polarizable subunits arranged on a cubic lattice. As the incident field ($\mathbf{E}_0$) is time-harmonic-dependent, we shall omit the frequency dependence. The field at each subunit is obtained by the following self-consistent relation:

$$\mathbf{E}(\mathbf{r}_i) = \mathbf{E}_0(\mathbf{r}_i) + \sum_{j=1}^{N} [\mathbf{T}(\mathbf{r}_i,\mathbf{r}_j) + \mathbf{S}(\mathbf{r}_i,\mathbf{r}_j)]\alpha(\mathbf{r}_j)\mathbf{E}(\mathbf{r}_j), \quad (1)$$

where $\alpha(\mathbf{r}_j)$ is the polarizability of subunit j, $\mathbf{T}$ is the electric field linear susceptibility in free space,[20] and $\mathbf{S}$ denotes the

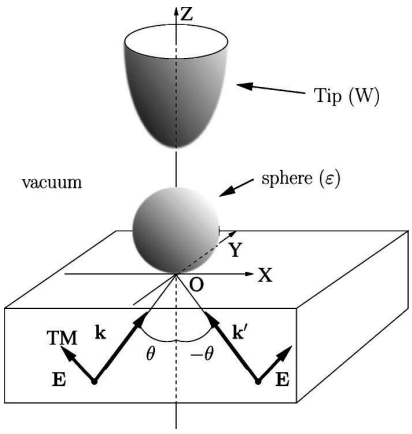

FIG. 1. Schematic of the configuration. A sphere on a flat dielectric surface is illuminated under total internal reflection, i.e., $\theta > \theta_c$ with $\sqrt{\epsilon}\sin(\theta_c)=1$. A tungsten probe is used to create an optical trap. The illumination can be done either in TM polarization (as drawn in the figure) or in TE polarization.

field linear susceptibility in the presence of a substrate.[21] The polarizability contains the radiative reaction term which ensures that the optical theorem is satisfied.[22,23] Since we are dealing with optical frequencies, we need to compute the time-averaged force. This net force on one subunit is[23]

$$F_u(\mathbf{r}_i) = (1/2)\mathrm{Re}\left(\sum_v p_v(\mathbf{r}_i)\frac{\partial[E^v(\mathbf{r}_i)]^*}{\partial u}\right), \tag{2}$$

where u or v stands for either x, y, or z, $\mathbf{p}(\mathbf{r}_i)$ is the electric dipole moment of the ith subunit, and $*$ denotes the complex conjugate. Notice that the derivative of the electromagnetic field is obtained by differentiation of Eq. (1) with respect to the vector $\mathbf{r}_i$. Hence, the net optical force on the object is obtained as

$$\mathbf{F} = \sum_{i=1}^{N} \mathbf{F}(\mathbf{r}_i). \tag{3}$$

III. RESULTS

Consider a particle with complex relative permittivity $\varepsilon = \varepsilon_r + i\varepsilon_i$ placed in air above a flat dielectric substrate (relative permittivity $\epsilon = 2.25$). The particle is illuminated by two evanescent waves created by the total internal reflection of plane waves at the substrate/air interface ($\theta > \theta_c = 41.8°$ with $\sqrt{\epsilon}\sin\theta_c = 1$). These two waves are counterpropagating evanescent waves, i.e., $\mathbf{k}_\parallel = -\mathbf{k}'_\parallel$, with the same polarization and a random-phase relation (Fig. 1, see Ref. 16 for the more details). The irradiance due to the laser illuminating the surface is taken to be 0.05 $\mathrm{W}/\mu\mathrm{m}^2$.[16]

A. Absorbing particles

In this section we consider an absorbing particle with radius $a = 10$ nm and $\mathrm{Re}(\varepsilon) = 2.25$. We shall study the influence of the complex relative permittivity on the trapping and nanomanipulation process. The trapping is performed with a tungsten tip of radius at the apex $r = 10$ nm. The wavelength is $\lambda = 514$ nm. The angle of incidence for the illumination is chosen to be $\theta = 43°$; this is the angle at which the optical potential is deepest.[16] We recall briefly here the procedure used to manipulate a particle; the procedure has been described in detail for dielectric particles in Refs. 6 and 16 and it remains the same in the case of absorbing or metallic particles. In TE polarization, the probe scans the surface to localize the particles. In that case the optical force is always negative. Then the polarization is switched to TM and the optical force becomes positive when the tip is close (a few nanometers) to the particle. Once the particle is trapped at the apex of the tip, it can be manipulated and subsequently released by switching back to TE polarization.

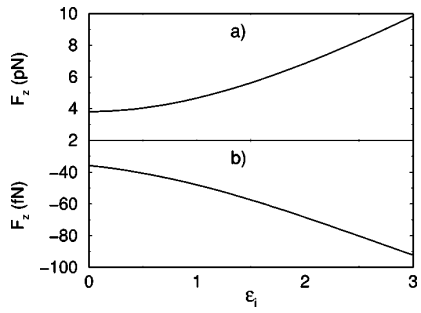

FIG. 2. z component of the force experienced by an absorbing sphere [$\mathrm{Re}(\varepsilon) = 2.25$] vs the imaginary part of the relative permittivity. The tungsten tip is in contact with the sphere and the angle of incidence is $\theta = 43°$. (a) TM polarization. (b) TE polarization.

Figure 2 shows the z component of the force experienced by the sphere, for the two polarizations, when the imaginary part of the relative permittivity increases [Fig. 2(a), transverse magnetic (TM) polarization, and Fig. 2(b), transverse electric (TE) polarization] and the tip is in contact with the sphere. For both polarizations, the magnitude of the force is enhanced when the imaginary part of the relative permittivity increases. For a better understanding of this effect, let us decompose the polarizability α of a small sphere (compared to the wavelength of illumination) into its real and imaginary parts,[24]

$$\mathrm{Re}(\alpha) = a^3\frac{(\varepsilon_r - 1)(\varepsilon_r + 2) + \varepsilon_i^2}{(\varepsilon_r + 2)^2 + \varepsilon_i^2}, \tag{4}$$

$$\mathrm{Im}(\alpha) = a^3\frac{3\varepsilon_i}{(\varepsilon_r + 2)^2 + \varepsilon_i^2}, \tag{5}$$

where a is the radius of the sphere. For our geometry the z component of the optical force on the small sphere is mainly due to the gradient force[25] which is proportional to the real part of the polarizability of the sphere. From Eq. (4) it is obvious that when ε_i increases, the real part of the polarizability increases and so does the gradient force, hence the force becomes more positive for TM polarization, and more negative for TE polarization. Note that as ε_i becomes very large, $\mathrm{Re}(\alpha)$ tends toward a finite limit.

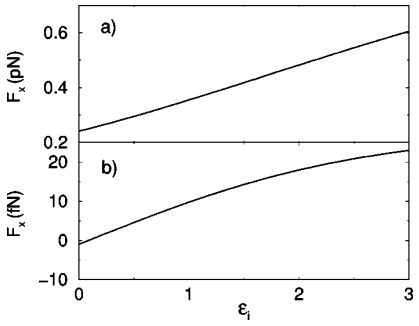

FIG. 3. Lateral (x) component of the force experienced by an absorbing sphere [$\mathrm{Re}(\varepsilon)=2.25$] vs the imaginary part of the relative permittivity if the symmetric illumination is not used. The tungsten tip is in contact with the sphere, $\theta=43°$. (a) TM polarization. (b) TE polarization.

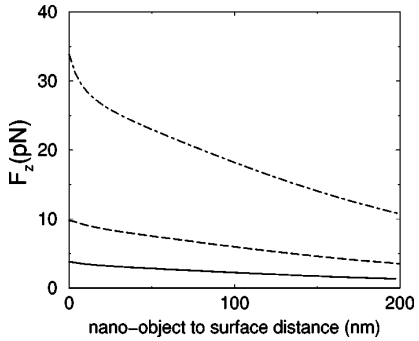

FIG. 4. z component of the force experienced by the sphere as a function of the distance between the sphere and the substrate for TM polarization. The sphere is placed at the apex of the probe. $\theta=43°$. Solid line $\varepsilon=2.25$, dashed line $\varepsilon=2.25+3i$, dot-dashed line $\varepsilon=12.5+i$.

Figure 3 shows the lateral force experienced by the sphere for both polarizations if only one laser beam is used for the illumination. The force is plotted for the case $\mathbf{k}_{\parallel}>\mathbf{0}$ (illumination from the left side of Fig. 1). We note that for both polarizations, the lateral optical force is never zero and therefore it should be difficult to trap a particle with a single beam illumination. The symmetric illumination prevents the sphere from escaping from the optical trap.[19] For TM polarization, the increase of the absorption only gives an enhancement of the lateral force as the two forces—the gradient force and the absorbing force—are both positive (the gradient force is positive because the maximum of the intensity of the electromagnetic field is obtained slightly to the right of the tip apex due to the nonsymmetric illumination). But for TE polarization the behavior is different because the sign of the lateral force changes. When the absorbing part of the relative permittivity vanishes, only the (negative) gradient force remain (the scattering force is negligible due to the small size of the particle compared to the wavelength of illumination). Conversely to the TM polarization, for TE polarization the minimum of the intensity of the electromagnetic field is obtained slightly to the left of the tip apex which produces a negative gradient force. But when the imaginary part of the polarizability increases, there appears an absorbing force. This absorbing force comes from the incident evanescent wave which propagates parallel to the substrate. Due to the choice of illumination, this force is positive. Because the lateral gradient force is weak, it is easily outweighed by the absorbing force which yields the main contribution. This is why a large, positive lateral force exists in this case.

Since we have shown (Fig. 3) the importance of using a symmetric illumination, all the following computations will be done in that case. Figure 4 shows the z component of the force when the sphere is lifted by the probe (the sphere is placed at the tip apex). We have plotted the results for three values of the relative permittivity: a lossless dielectric sphere with $\varepsilon=2.25$ (which is our reference), and two absorbing spheres with $\varepsilon=2.25+3i$ and $\varepsilon=12.5+i$, respectively. A comparison of the lossless sphere case (solid line) and the absorbing case (dashed line) shows that a nonzero imaginary part of the relative permittivity increases the force experienced by the sphere, and hence it helps trap and manipulate the particle. In the case of $\varepsilon=12.5+i$, due to the large real part of the polarizability, the z component of the force is clearly stronger than in the two previous cases. But a closer look at the curves shows that the z component of the force is not directly proportional to $\mathrm{Re}(\alpha)$. We have for $\varepsilon=2.25$, $\mathrm{Re}(\alpha)=0.3a^3$; for $\varepsilon=2.25+3i$, $\mathrm{Re}(\alpha)=0.5a^3$; and for $\varepsilon=12.5+i$, $\mathrm{Re}(\alpha)=0.8a^3$. Between the lossless dielectric sphere and the sphere with $\varepsilon=12.5+i$, the real part of the polarizability is multiplied by 2.6 and the force by a factor 8. The proportionality relation only applies for a sphere in free space. However, due to the strong interaction between the sphere and the tungsten tip, there is a strong enhancement of the field around the tip apex when the relative permittivity of the particle increases. This effect improves the efficiency of the trapping and, therefore, the larger the real part of the polarizability, the easier the manipulation. Notice that although the radius of the trapped sphere is about 10 nm, we have checked that the trapping is achieved up to a radius of 85 nm for the absorbing sphere ($\varepsilon=3+i$). Hence the approach presented here could, for instance, allow one to manipulate quantum-dot nanocrystals and place them into a specific configuration to study dot-dot interactions, or one nanocrystal could be isolated to study single-dot properties.[26]

We have not plotted the force experienced by the sphere versus the distance between the sphere and the tip, nor did we plot the evolution of the optical force as the tip scans the surface above the substrate, because these results are similar to those obtained for dielectric particles.[16] However, we emphasize that it is particularly important to use a symmetric illumination with absorbing particles to avoid the disruptive effect of the lateral force.

B. Metallic particles

In this section, we consider metallic particles which exhibit plasmon resonances, i.e., gold, silver, and copper particles. We shall start by illustrating the convergence of the CDM calculation for a sphere in free space. This problem can be solved exactly in the form of a Mie series which we

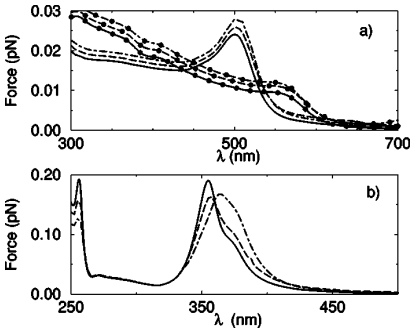

FIG. 5. Force experienced by a sphere with radius $a=10$ nm in free space vs the wavelength of illumination. Solid line: Mie calculation. Dotted line: CDM with $d=4$ nm. Dashed line: CDM with $d=0.95$ nm. (a) Without symbol: gold sphere; circles: copper sphere. (b) Silver sphere.

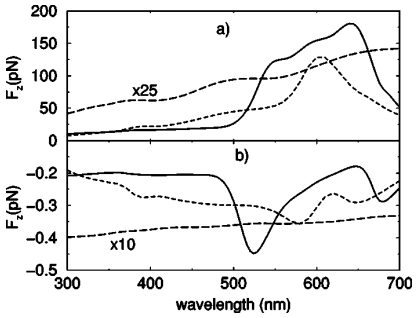

FIG. 6. z component of the force experienced by a sphere of radius $a=10$ nm vs the wavelength of illumination. The tungsten tip is in contact with the sphere. The solid line pertains to a gold sphere, the dotted line a copper sphere, and the dashed line a dielectric sphere. (a) TM polarization. (b) TE polarization.

shall use as a reference. The comparison to the Mie result is done for the three metals studied in this work; the sphere has a radius $a=10$ nm. We plot in Fig. 5(a) the optical force for the gold and copper spheres. The Mie results are plotted with a solid line. The other curves pertain to the CDM. With a dotted line we plot the result computed with $d=4$ nm, and with a dashed line the force computed with $d=0.95$ nm. It is obvious that when d decreases, the force computed with the CDM converges toward the Mie result. With $d=4$ nm, the error in the magnitude of the force is small (we slightly overestimate the optical force), hence a lattice spacing of $d=4$ nm is sufficient for our purpose of studying the general physical process of optical trapping and manipulation of metallic particles. For a silver sphere, as shown in Fig. 5(b), again the CDM converge towards the Mie result when d decreases. However, the convergence is slower than for gold or copper. To get a quantitatively accurate representation of the resonance, one should take the smaller discretization, but for the sake of computation time and memory, we shall take $d=4$ nm for the silver as well. Notice that the comparison with Mie is for a sphere in free space. In a more complex geometry, such as ours, the variation of the field is most likely stronger. However, because the sphere is very small and it is discretized, we are taking into account the variation of the field inside the sphere, and we can assume that the degree of convergence of the CDM remains the same in our complex configuration.

Notice that beside the dipole mode, a metallic sphere can support quadrupole or higher electromagnetic modes. Because the sphere is discretized in small subunits, we actually take into account all the multipolar modes of the sphere as described in Ref. 27, hence our force calculation takes into account the multipolar response of the sphere. However, for a small metallic sphere, as in our case, the effect of modes higher than the dipole mode is negligible. One can see in Ref. 28 that for a small metallic sphere (in an evanescent incident field), the plasmon resonance computed with the dipole approximation or with the CDM gives an accurate result. The multipole expansion only changes the magnitude of the scattered field, and therefore no important physics is overlooked by treating the sphere as a dipole.

Figure 6 shows the z component of the force experienced by a sphere versus the wavelength of illumination for both polarizations when the tip is in contact with the sphere and the sphere is lying on the glass substrate (see Fig. 1). The solid line pertains to a gold sphere, while the dotted line is related to a copper sphere. In both cases the sphere has a radius $a=10$ nm. Since the relative permittivity of the tungsten tip depends on the wavelength, the dashed line corresponds to the case of a dielectric sphere with constant permittivity, and shows the influence of the tungsten tip only. We see that in TM polarization, the z component of the force experienced by the dielectric sphere increases with the wavelength λ. This is due to the fact that the imaginary part of the relative permittivity of tungsten increases slowly with λ. For TE polarization, as we have no enhancement of the field at the tip apex, the force is less sensitive to the slow variation of the relative permittivity of tungsten. For the gold sphere, and for TM polarization, we find a very strong enhancement of the z component of the force for $\lambda=643$ nm ($F_z=180$ pN). Notice that the plasmon resonance for a small gold sphere is about $\lambda=520$ nm. This difference is due to the strong coupling between the tungsten tip and the sphere. In fact, we do not have the plasmon resonance of one sphere but a plasmon mode of the cavity formed by the sphere and the apex of the tip, which redshifts the resonance of the sphere.[29] Outside the resonance of the plasmon mode, the force is 20 times weaker, but stays stronger than in the case of a dielectric sphere. For TE polarization, the z component of the force is always negative. We can point out that the force varies little with the wavelength of illumination. Only around $\lambda=520$ nm do we observe a decrease of the force by a factor of 2. This minimum corresponds to the plasmon resonance of the sphere alone. This is due to the lack of field enhancement at the tip apex for TE polarization, which produces a weak coupling between the tip and the sphere. For the copper sphere we have the same behavior; for TM polarization the maximum is at $\lambda=605$ nm, hence the plasmon resonance of the copper sphere is redshifted by the presence of the tip. As for TE polarization, the minimum of the force is found again at the plasmon resonance of a single sphere, i.e., $\lambda=585$ nm.

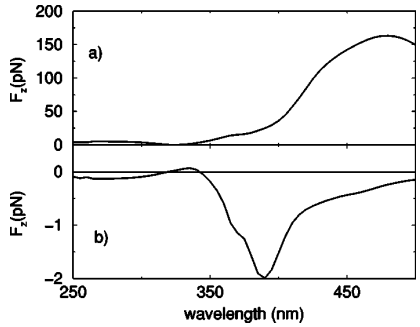

FIG. 7. Same as Fig. 6 but for a silver sphere. (a) TM polarization. (b) TE polarization.

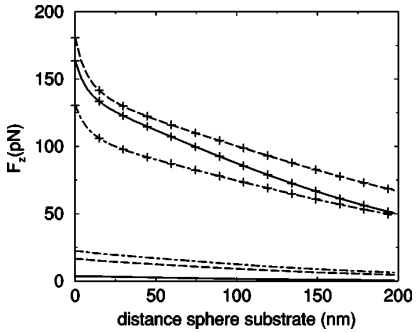

FIG. 8. z component of the force when the sphere is manipulated with the tip. The particle is made of silver (solid line), gold (dashed line), and copper (dot-dashed line). Curves with the "+" marker pertain to forces computed at the plasmon resonance wavelength ($\lambda_{Au}=640$ nm, $\lambda_{Cu}=605$ nm, $\lambda_{Ag}=480$ nm). Curves without a marker are computed away from the plasmon resonance ($\lambda_{Au}=400$ nm, $\lambda_{Cu}=400$ nm, $\lambda_{Ag}=300$ nm).

Figure 7 pertains to a silver sphere ($a=10$ nm). At first the results for the force spectrum are intriguing. For TM polarization, a maximum of the z component of the force is found at $\lambda=480$ nm (the plasmon resonance of a silver sphere is around $\lambda=360$ nm) while the force is close to zero at $\lambda=324$ nm. For TE polarization, we get a range of wavelengths over which a weak positive force along z is obtained, unlike anything we found for gold, copper, or absorbing dielectric particles. To explain the behavior of the silver sphere, let us recall that the gradient force experienced by a small particle in the z direction can be written as

$$F_z = \mathrm{Re}(\alpha)\partial_z|\mathbf{E}|^2/2. \tag{6}$$

Therefore, the sign of F_z depends on the sign of $\mathrm{Re}(\alpha)$. In the case of a dielectric, gold, or copper particle, we have $\mathrm{Re}(\alpha)>0$, which produces, for an incident field evanescent along the z direction, a negative gradient force. For the silver sphere, we have $\mathrm{Re}(\alpha)<0$ in the 316–351 nm spectral range. Therefore, within that range, the sphere experiences from the incident evanescent field a force directed toward regions of lower intensity of the field, that is, away from the substrate (note that at $\lambda=316$ and $\lambda=351$ nm the gradient force on the sphere vanishes as the dipole associated to the sphere is in quadrature with the phase of the incident field). Hence, for silver, the incident evanescent field produces a positive optical force. On the other hand, the interaction between the sphere and the substrate always leads to a negative optical force, irrespective of the dielectric constant of the sphere.[17,18] This force can be understood as the interaction between the dipole associated to the sphere and the reflected field at the dipole location. For a dipole close to a lossless dielectric substrate, the reflected field at the location of the dipole is always in phase with the dipole. This is why the force due to the reflected field is always negative. This is easy to understand as the scattered field at the location of the dipole can be written as

$$\mathbf{E}(\mathbf{r}_i) = \mathbf{S}(\mathbf{r}_i,\mathbf{r}_i)\mathbf{p}(\mathbf{r}_i), \tag{7}$$

where $\mathbf{p}(\mathbf{r}_i)$ is the dipole moment associated with the sphere. Since the dipole is close to the substrate, we can use the static approximation wherein $\mathbf{S}\propto b/z^3$ with z the distance from the dipole to the substrate and b a real positive constant.[17–19] Hence $\mathbf{E}(\mathbf{r}_i)$ is in phase with $\mathbf{p}(\mathbf{r}_i)$ and therefore the gradient force is always negative irrespective of the dipole moment (i.e., the nature of the sphere). Notice that this force is strongest when the dipole moment associated to the sphere is largest, as is the case near the plasmon resonance. As a result, for the silver sphere with a TE polarized incident field, the interaction between the tip and the sphere is weak and the only significant contribution to the optical force experienced by the sphere comes from the interaction with the substrate. Accordingly, a strong negative force is found at $\lambda=385$ nm, which is close to the plasmon resonance of the sphere alone. On the other hand, around $\lambda=320$ nm we have $\mathrm{Re}(\alpha)>0$ and the sphere is attracted toward low-intensity regions, yielding a positive gradient force. However, the modulus of the polarizability is small, which entails a small negative force due to the interaction of the sphere with itself via the substrate. The net force in that case is close to zero. For TM polarization, the explanation is more complex. Due to the field enhancement at the apex of the tip there is a positive contribution to the optical force, but the force remains weak at $\lambda=320$ nm as $\mathrm{Re}(\alpha)\approx 0$ at this wavelength, hence the sum of all the contributions to the gradient force vanishes. We observe a redshift of the maximum of the curve which is now at $\lambda=480$ nm as the plasmon resonance is now a plasmon mode of the cavity shaped by the tip and the sphere. We mentioned previously that when $\mathrm{Re}(\alpha)<0$ (for example, at $\lambda=340$ nm), the sphere is pushed toward low-intensity regions. Therefore, the enhancement of the field at the tip apex in TM polarization should create, in that case, a negative optical force on the sphere, however this is not the case. This is due to the fact that strong evanescent components of the field exist near the tip. As shown in Ref. 18 [see, for instance, Eq. (13)], in the presence of an evanescent field, a sphere close to a dielectric surface (tungsten at the wavelengths we consider in this paper behaves as an absorbing dielectric) will experience a gradient force that will pull it towards the surface irrespective of the nature of the sphere.

In Fig. 8, we present the z component of the force experienced by a gold, silver, or copper sphere at different wave-

lengths (in and out of plasmon resonance) as the sphere is trapped and manipulated by the tip. The behaviors of the three spheres are similar and show that it is easier to manipulate the particle at the plasmon resonance. Notice that the resonance for the three metallic spheres occurs at different wavelengths, and more generally, the behavior of the force versus the wavelength is different. By using the dependence of the force on the spectral response of the sphere, it would be possible to perform a material-selective trapping. For example, at $\lambda = 325$ nm the z component of the force on a silver sphere is close to zero and for this same wavelength the force on the gold sphere is around 12 pN. Hence only the gold sphere would be trapped and manipulated at this wavelength. Finally, we can mention that the decay of the z component of the force with the sphere-substrate distance is different for each curve. This is due to the use of a different wavelength in each case, thus the decay of the evanescent field is different.

When we have many spheres clustered together, for example three identical spheres in contact and aligned following the x axis, we have shown in a previous article that, in the case of dielectric spheres, it is possible to adapt the angle of incidence so as to capture, say, the middle sphere.[16] In the case of metallic spheres it is more complex, as the behavior depends on the wavelength. For three gold spheres, our calculations show that depending on the wavelength, it may or may not be possible only to capture the middle sphere.

C. Apertureless probe with a metallic sphere at the tip apex

We have seen in the previous section that a metallic sphere can be trapped and manipulated at the apex of a tungsten tip. By keeping the same polarization (TM), it should be possible to scan the surface in taping mode, i.e., the tip vibrating perpendicularly to the substrate, in the so-called apertureless scanning near-field optical microscopy mode.[30] Typically, the frequency used in this mode is $f = 4$ kHz with a magnitude for the oscillations $h = 10 - 200$ nm.[30] We take $h = 100$ nm. Assuming a sinusoidal oscillation, $z(t) = h \sin(\omega t)/2$ with $\omega = 2\pi f$, we can compute the z component of the inertial force experienced by the sphere during this oscillation: $F(t) = m d^2 z(t)/dt^2 = -mh\omega^2 \sin(\omega t)/2$. Hence the maximum force experienced by the sphere is $mh\omega^2/2 = 25$ aN for a gold sphere and 14 aN for a silver sphere. This maximum is always smaller than the optical forces over the distance h (see Fig. 8), even when the particle is manipulated with a wavelength of illumination out of the plasmon resonance, hence it would be possible to scan the surface while keeping the sphere at the tip apex, in spite of the oscillations of the tip. The advantage of scanning the surface with a small metallic sphere as a nanoprobe is to improve the quality of the imaging owing to the increase of the scattered field, as shown in Refs. 31 and 32. Accordingly, at a given operating wavelength, one can choose the nature of the particle trapped at the tip apex such that it yields the largest enhancement of the scattered field. This enhancement yields a better resolution of the near-field microscope. Also, following the resolution wanted one can change also the size of the particle trapped, as the smaller the probe is, the better would be the resolution.

IV. CONCLUSION

In conclusion, we have presented a detailed study of the nanomanipulation of particles with a complex relative permittivity, using an apertureless near-field probe. We considered both absorbing dielectric and metallic particles. In the case of absorbing dielectric particles, such as quantum dots, the presence of an imaginary part in the relative permittivity increases the efficiency (depth) of the optical trap and helps manipulate the particle. In the case of metallic particles, the manipulation is improved if the wavelength of illumination corresponds to the plasmon resonance of the cavity formed by the tip and the particle. We showed that depending on the nature of the metallic sphere, the characteristics of the optical force spectrum are very different. This suggests the possibility of achieving a material selective manipulation. Similarly, the present approach can be applied to the optical manipulation of semiconductor nanoparticles (radius smaller than 100 nm), under an excitonic resonance condition which can increase the optical force as much as four orders of magnitude more than in the absence of excitation.[33]

ACKNOWLEDGMENTS

P.C.C. thanks Kamal Belkebir for many fruitful discussions. A.R. thanks the Ecole Centrale de Lyon BQR program for funding. M.N-V acknowledges grants from the Spanish MCYT and from the EU.

[1] A. Ashkin, Phys. Rev. Lett. **24**, 156 (1970).
[2] A. Ashkin, Phys. Rev. Lett. **25**, 1321 (1970).
[3] R. Holmlin, M. Schiavoni, C. Chen, S. Smith, M. Prentiss, and G. Whitesides, Angew. Chem., Int. Ed. **39**, 3503 (2000); E. R. Dufresne, G. C. Spalding, M. T. Dearing, S. A. Sheets, and D. G. Grier, Rev. Sci. Instrum. **72**, 1810 (2001); E. R. Dufresne and David G. Grier, *ibid.* **69**, 1974 (1998); R. L. Eriksen, V. R. Darias, and J. Glückstad, Opt. Express **10**, 597 (2002); J. Leach, G. Sinclair, P. Jordan, J. Courtal, M. J. Padgett, J. Cooper, and Z. J. Laczik, *ibid.* **12**, 220 (2004).
[4] M. P. Macdonald, L. Paterson, K. Volke-Sepulveda, J. Arlt, W. Sibbet, and K. Dholakia, Science **296**, 1101 (2002).
[5] M. J. Lang and S. M. Block, Am. J. Phys. **71**, 201 (2003).
[6] P. C. Chaumet, A. Rahmani, and M. Nieto-Vesperinas, Phys. Rev. Lett. **88**, 123601 (2002).
[7] S. Sato, Y. Harada, and Y. Waseda, Opt. Lett. **19**, 1807 (1994).
[8] H. Furukawa and I. Yamaguchi, Opt. Lett. **23**, 216 (1998).
[9] M. Gu and D. Morrisk, J. Appl. Phys. **91**, 1606 (2002).
[10] S. A. Tatarkova, A. E. Carruthers, and K. Dholakia, Phys. Rev. Lett. **89**, 283901 (2002).
[11] K. Svoboda and S. M. Block, Opt. Lett. **19**, 930 (1994).
[12] L. Novotny, R. X. Bian, and X. Sunney Xie, Phys. Rev. Lett. **79**,

645 (1997).
[13] A. Rohrbach, H. Kress, and E. H. K. Stelzer, Opt. Lett. **28**, 411 (2003).
[14] J. R. Arias-Gonzàlez, M. Nieto-Vesperinas, and M. Lester, Phys. Rev. B **65**, 115402 (2002).
[15] H. Xu and M. Käll, Phys. Rev. Lett. **89**, 246802 (2002).
[16] P. C. Chaumet, A. Rahmani, and M. Nieto-Vesperinas, Phys. Rev. B **66**, 195405 (2002).
[17] P. C. Chaumet and M. Nieto-Vesperinas, Phys. Rev. B **61**, 14119 (2000).
[18] P. C. Chaumet and M. Nieto-Vesperinas, Phys. Rev. B **62**, 11185 (2000).
[19] P. C. Chaumet and M. Nieto-Vesperinas, Phys. Rev. B **64**, 035422 (2001).
[20] J. D. Jackson, *Classical Electrodynamics*, 2nd ed. (John Wiley, New York, 1975), p. 395.
[21] A. Rahmani, P. C. Chaumet, and F. de Fornel, Phys. Rev. A **63**, 023819 (2001).
[22] P. C. Chaumet, Appl. Opt. **43**, 1825 (2004).
[23] P. C. Chaumet and M. Nieto-Vesperinas, Opt. Lett. **25**, 1065 (2000).
[24] For the sake of simplicity, the radiation-reaction term is omitted.
[25] For a sphere above a surface in an evanescent field, the *z* component of the force is the result of the gradient force only; see Refs. 17 and 18.
[26] P. Michler, A. Imamoğlu, M. D. Mason, P. J. Carson, G. F. Strouse, and S. K. Buratto, Nature (London) **406**, 968 (2000).
[27] C. Bourrely, P. Chiappetta, T. Lemaire, and B. Torresani, J. Opt. Soc. Am. A **9**, 1336 (1992).
[28] P. C. Chaumet, A. Rahmani, F. de Fornel, and J.-P Dufour, Phys. Rev. B **58**, 2310 (1998).
[29] P. C. Chaumet, Ph.D. thesis, Université de Bourgogne, France (1998).
[30] G. Wurtz, R. Bachelot, and P. Royer, Eur. Phys. J.: Appl. Phys. **5**, 269 (1999).
[31] M. Gu and P. C. Ke, Opt. Lett. **24**, 74 (1999).
[32] T. Kalkbrenner, M. Ramstein, J. Mlynek, and V. Sandoghdar, J. Microsc. **202**, 72 (2001).
[33] T. Iida and H. Ishihara, Phys. Rev. Lett. **90**, 057403 (2003).

PHYSICAL REVIEW B **69**, 245405 (2004)

Three-dimensional subwavelength optical imaging using the coupled dipole method

P. C. Chaumet, K. Belkebir, and A. Sentenac
Institut Fresnel (UMR 6133), Université d'Aix-Marseille, Av. Escadrille Normandie-Niemen, F-13397 Marseille Cedex 20, France

(Received 6 November 2003; revised manuscript received 4 March 2004; published 18 June 2004)

We simulate a three-dimensional optical diffraction tomography experiment in which the scattered field from an unknown object is measured for various observation and incident angles. We propose a fast inversion scheme based on the coupled dipole method that enables us to reconstruct the three-dimensional map of permittivity of the object from the far-field data. We show that a power of resolution of $\lambda/4$ can be expected and that the method is robust to noise.

DOI: 10.1103/PhysRevB.69.245405 PACS number(s): 42.30.Wb, 42.25.Fx

I. INTRODUCTION

There has been considerable interest in the development of methods which extend the spatial resolution of optical microscopy beyond the classical diffraction limit and provide information on the three-dimensional structure of the sample. Among their potential applications, one quotes *in-vivo* cell imaging or the optical control of wafers in semiconductor industries.

The existing imaging systems with a resolution smaller than several tens of nanometers, such as atomic force microscopes or optical near-field microscopy,[1] are plagued by the need of approaching a probe in the vicinity (a few nanometers) of the object. Moreover, they are generally limited to surface imaging although, recently, an inversion procedure has been proposed to extract, from the near-field data, the three-dimensional map of permittivity of the sample.[2]

Optical far-field microscopes, on the other hand, permit one to obtain three-dimensional images in a convenient, noninvasive way. Their transverse resolution is limited by the Rayleigh criterion, $\lambda/(2NA)$, where $NA=n\sin\theta$ is the numerical aperture of the objective, with n the index of refraction of the medium surrounding the sample and θ the half-angle of the collection cone of the lenses.[3,4] Enlarging the numerical aperture can be done by immersing the objective in a liquid with a high refractive index or by using a hemispherical prism to collect the scattered light, as in subsurface microscopy.[5] However, the distance of separation of the best microscopes working with visible light and immersed objectives does not exceed 200 nm in the transverse plane and 500 nm in the axial direction.

Optical diffraction tomography (ODT) is another far-field imaging technique that permits one to retrieve the internal structure of semitransparent objects. Although its principles have been established more than 30 years ago,[6] it is only recently that ODT has addressed with success the issue of three-dimensional imaging with subwavelength resolution.[7] It consists of successively illuminating the sample under different directions and collecting the diffracted field for many scattered angles. Then, a numerical inversion procedure is developed to reconstruct the three-dimensional map of permittivity of the sample from the measured data. ODT differs from classic microscopy in that many different illumination configurations are used and that both the phase and amplitude of the scattered field are detected. This last point is the main problem of ODT from an experimental point of view. Indeed, it is very difficult to control the phase of the incident field in an optical experiment, even more so when many different incident directions are required. Yet, under the assumption that the sample does not alter much the transmitted specular beam, it is possible to compensate the noncontrolled incident phase-shift and thus to obtain the absolute phase of the scattered field for all illuminations.[7]

Several elaborate nonlinear inversion schemes have been proposed, mainly in the acoustic and microwave domains, in the simplified case of two-dimensional geometries. These techniques, that account for multiple scattering and incorporate some *a priori* information on the scatterer, may possess a power of resolution smaller than $\lambda/(7NA)$.[8] Yet, their numerical cost is high and their extension to the three-dimensional vectorial problem remains problematic. In this latter case, the few proposed inversion schemes are usually based on Born approximation and they often neglect the vectorial nature of the field.[7,9–11]

In this paper, we simulate an ODT experiment and investigate the power of resolution of the inversion technique. In Sec. II A, we describe briefly the coupled dipole method (CDM) that enables one to calculate the field scattered by a three-dimensional object. In Sec. II B, we propose a fast linear inversion scheme based on the CDM. In Sec. III, we present reconstructions of various objects and study the robustness of the inversion scheme to uncorrelated and correlated noise. Finally, in Sec. IV we conclude on the advantages and drawbacks of our method.

II. THEORY

A. Formulation of the forward scattering problem

The coupled dipole method (CDM) was introduced by Purcell and Pennypacker in 1973 for studying the scattering of light by nonspherical dielectric grains in free space.[12] The object under study is represented by a cubic array of N polarizable subunits. The electromagnetic field at each subunit can be expressed with the following self-consistent equation:

$$\mathbf{E}(\mathbf{r}_i,\omega) = \mathbf{E}^{\mathrm{inc}}(\mathbf{r}_i,\omega) + \sum_{j=1, j\neq i}^{N} \mathbf{T}(\mathbf{r}_i,\mathbf{r}_j,\omega)\alpha(\mathbf{r}_j,\omega)\mathbf{E}(\mathbf{r}_j,\omega), \quad (1)$$

where $\mathbf{E}^{\mathrm{inc}}(\mathbf{r}_i,\omega)$ is the incident field at the position $\mathbf{r}_i$ in the absence of the scattering object, $\mathbf{T}$ is the linear response to a dipole in free space,[13] and $\alpha(\mathbf{r}_j,\omega)$ is the polarizability of the subunit j. As the electromagnetic wave is time harmonic dependent we can omit ω in the expressions. The polarizability is written as

$$\alpha(\mathbf{r}_j) = \frac{\alpha^0(\mathbf{r}_j)}{1 - (2/3)ik^3\alpha^0(\mathbf{r}_j)}, \quad (2)$$

with

$$\alpha^0(\mathbf{r}_j) = \frac{3d^3}{4\pi}\frac{\varepsilon_1(\mathbf{r}_j) - \varepsilon_0}{\varepsilon_1(\mathbf{r}_j) + 2\varepsilon_0}, \quad (3)$$

where d is the spacing of lattice discretization, $\varepsilon_1(\mathbf{r}_j)$ the relative permittivity of the object, and ε_0 and k the relative permittivity and the wave number of the homogeneous medium which contains the object, respectively. The material is isotropic so that $\varepsilon_1(\mathbf{r}_j)$ and the polarizability are scalar. The radiative reaction term in the polarizability, Eq. (2), is important if one wants to compute the optical forces[14–16] or the extinction cross section of an object.[17] But the correction brought by the radiative reaction term, if we are interested only by the scattered field, is small and can be neglected in our study. Hence the polarizability reduces to the Clausius-Mossotti expression, Eq. (3).[18] In that case, for a nonabsorbing object, the polarizability is real.

Once Eq. (1) is solved, the total field scattered by the object at an arbitrary position $\mathbf{r}$ is given by

$$\mathbf{E}(\mathbf{r}) = \mathbf{E}^{\mathrm{inc}}(\mathbf{r}) + \sum_{j=1}^{N} \mathbf{T}(\mathbf{r},\mathbf{r}_j)\alpha(\mathbf{r}_j)\mathbf{E}(\mathbf{r}_j). \quad (4)$$

We can write Eq. (1) in the condensed form

$$\overline{\mathbf{E}} = \overline{\mathbf{E}}^{\mathrm{inc}} + \overline{\overline{\mathbf{A}}}\,\overline{\mathbf{p}}, \quad (5)$$

where the overline on $\overline{\mathbf{E}}$ indicates a vector $3N$ which gathers the electric field at each subunit of the object: $\overline{\mathbf{E}} = [E_x(\mathbf{r}_1), E_y(\mathbf{r}_1), E_z(\mathbf{r}_1), \ldots, E_x(\mathbf{r}_N), E_y(\mathbf{r}_N), E_z(\mathbf{r}_N)]$. $\mathbf{p}(\mathbf{r}_i) = \alpha^0(\mathbf{r}_i)\mathbf{E}(\mathbf{r}_i)$ is the dipole moment of the subunit i and $\overline{\overline{\mathbf{A}}}$ is a square matrix (whose size is $3N \times 3N$) which contains the field tensors susceptibilities $\mathbf{T}(\mathbf{r}_i,\mathbf{r}_j)$.

In an ODT experiment, the scattered field is detected at M observation points for L successive illuminations. Denoting by $\bar{\mathbf{f}}_l$ the vector of the scattered field at each observation points for the lth illumination, we can write the far-field equation, Eq. (4), in the following condensed form:

$$\bar{\mathbf{f}}_l = \overline{\overline{\mathbf{B}}}\,\overline{\mathbf{p}}_l, \quad (6)$$

where $l = 1, \cdots, L$, and $\overline{\overline{\mathbf{B}}}$ is a matrix whose size is $3M \times 3N$. $\overline{\overline{\mathbf{B}}}$ contains the tensors field susceptibilities, $\mathbf{T}(\mathbf{r}_k,\mathbf{r}_j)$ where $\mathbf{r}_j$ denotes a point in the discretized object, $j = 1, \ldots, N$, while $\mathbf{r}_k$ is an observation point, $k = 1, \ldots, M$. Note that $\overline{\overline{\mathbf{B}}}$ does not depend on the angle of incidence.

B. Formulation of the inverse scattering problem

We assume that an unknown object is confined in a bounded box Ω (test domain or an investigating domain) and illuminated successively by $l = 1, \ldots, L$ electromagnetic excitation $\overline{\mathbf{E}}^{\mathrm{inc}}_{l=1,\ldots,L}$. For each excitation l, the scattered field $\bar{\mathbf{f}}_l$ is measured on a surface Γ at M points. The inverse scattering problem is now stated as finding the permittivity distribution ε_1 inside the investigating area Ω such that the associated scattered field matches the measured field $\bar{\mathbf{f}}_{l=1,\ldots,L}$. Many accurate iterative techniques have been developed to solve this inverse problem. In these methods, starting from an initial guess, one adjusts the parameter of interest gradually by minimizing a cost functional involving the measured scattered-field data. Two main approaches can be found in the literature. In the first one,[19–22] the linearized methods, the field in the test domain is considered fixed. This field is the solution of the forward problem, Eq. (5), for the best available estimation of the permittivity at each iteration step, or it is the reference field if the Born approximation is assumed. In the second approach,[23,24] typically the modified gradient method, the field inside the test domain Ω is an unknown that is obtained, together with the permittivity, by the minimization procedure. A hybrid method[25,26] that combines the ideas from the two approaches has also been developed. All these methods deal with two-dimensional inverse scattering problems. In three-dimensions, most techniques use a linear inversion based on Born approximation[9,11] and are restricted to the scalar case. Recently, a more advanced method, namely the contrast source inversion (CSI) method,[27] has been introduced for solving the full vectorial three-dimensional problem.[28,29] In the CSI method the induced dipoles are reconstructed iteratively by minimizing at each iteration step a cost functional involving both the far-field equation, Eq. (6), and the domain-field equation, Eq. (5).

Inspired by the CSI method, we propose in the present paper a simpler iterative scheme. The dipoles are reconstructed using a reduced cost functional involving only the far-field equation. We build up a sequence $\overline{\mathbf{p}}_{l,n}$ according to the following recursive relation:

$$\overline{\mathbf{p}}_{l,n} = \overline{\mathbf{p}}_{l,n-1} + \beta_{l,n}\overline{\mathbf{d}}_{l,n}, \quad (7)$$

where $\overline{\mathbf{d}}_{l,n}$ is an updating direction and will be specified later in the paper. The weighting scalar number $\beta_{l,n}$ is determined at each iteration step by minimizing the cost functional $\mathcal{F}_n$ that represents the discrepancy between the data (measurements) and the scattered field corresponding to the best available estimate of the object $\overline{\mathbf{p}}_{l,n}$. The cost functional $\mathcal{F}_n$ is defined as

$$\mathcal{F}_n(\overline{\mathbf{p}}_{l,n}) = W_\Gamma \sum_{l=1}^{L} \|\bar{\mathbf{f}}_l - \overline{\overline{\mathbf{B}}}\,\overline{\mathbf{p}}_{l,n}\|_\Gamma^2, \quad (8)$$

where W_Γ is a normalizing coefficient,

$$W_\Gamma = \frac{1}{\sum_{l=1}^{L} \|\bar{\mathbf{f}}_l\|_\Gamma^2} \quad (9)$$

and $\|\bar{\mathbf{Q}}\|_\Gamma$ is the deduced norm from the inner product of two vectors $\langle \bar{\mathbf{R}}, \bar{\mathbf{Q}} \rangle_\Gamma$ defined on Γ. This inner product reads as

$$\langle \bar{\mathbf{R}}, \bar{\mathbf{Q}} \rangle_\Gamma = \sum_{\mathbf{r}_k \in \Gamma} \mathbf{R}^*(\mathbf{r}_k) \cdot \mathbf{Q}(\mathbf{r}_k), \tag{10}$$

where $\mathbf{R}^*$ denotes the complex conjugate of $\mathbf{R}$.

Substituting $\bar{\mathbf{p}}_{l,n}$ from Eq. (7) in Eq. (8) leads to a polynomial expression of the weighting coefficients $\beta_{l,n}$. The cost functional $\mathcal{F}_n(\bar{\mathbf{p}}_{l,n})$ is then reduced to a simple cost function $\mathcal{F}_n(\beta_{l,n})$ with respect to L scalar coefficients $\beta_{l,n}$. The minimization is accomplished according to a Polak-Ribière conjugate gradient procedure.[30]

As updating direction $\bar{\mathbf{d}}_{l,n}$ the authors took the Polak-Ribière conjugate gradient direction

$$\bar{\mathbf{d}}_{l,n} = \bar{\mathbf{g}}_{l,n;\mathbf{p}} + \gamma_{l,n} \bar{\mathbf{d}}_{l,n-1}, \tag{11}$$

with

$$\gamma_{l,n} = \frac{\langle \bar{\mathbf{g}}_{l,n;\bar{\mathbf{p}}}, \bar{\mathbf{g}}_{l,n;\bar{\mathbf{p}}} - \bar{\mathbf{g}}_{l,n-1;\bar{\mathbf{p}}} \rangle_\Omega}{\|\bar{\mathbf{g}}_{l,n-1;\bar{\mathbf{p}}}\|_\Omega^2}, \tag{12}$$

where $\langle \cdot, \cdot \rangle_\Omega$ is the same inner product as Eq. (10) but acting on vectors defined on Ω.

The vector function $\bar{\mathbf{g}}_{l;\bar{\mathbf{p}}}$ is the gradient of the cost functional $\mathcal{F}$ with respect to $\bar{\mathbf{p}}_l$ evaluated for the $(n-1)$th quantities. This gradient reads as

$$\bar{\mathbf{g}}_{l,n;\bar{\mathbf{p}}} = W_\Gamma \bar{\bar{\mathbf{B}}}^\dagger [\bar{\mathbf{f}}_l - \bar{\bar{\mathbf{B}}} \bar{\mathbf{p}}_{l,n-1}], \tag{13}$$

where $\bar{\bar{\mathbf{B}}}^\dagger$ is the transpose complex conjugate matrix of the matrix $\bar{\bar{\mathbf{B}}}$.

Once the sources $\bar{\mathbf{p}}_l$ are reconstructed, one can determine the fields $\bar{\mathbf{E}}_l$ inside Ω using Eq. (5). The polarizability α^0 at the position $\mathbf{r}_j$ is then given by

$$\alpha^0(\mathbf{r}_j) = \frac{\sum_{l=1}^{L} \mathbf{E}_l^\star(\mathbf{r}_j) \cdot \mathbf{p}_l(\mathbf{r}_j)}{\sum_{l=1}^{L} |\mathbf{E}_l(\mathbf{r}_j)|^2}. \tag{14}$$

Notice that, if the material under the test is assumed to be without losses, ε_1 is real, the polarizability may be rewritten as

$$\alpha^0(\mathbf{r}_j) = \mathrm{Re}\left\{ \frac{\sum_{l=1}^{L} \mathbf{E}_l^\star(\mathbf{r}_j) \cdot \mathbf{p}_l(\mathbf{r}_j)}{\sum_{l=1}^{L} |\mathbf{E}_l(\mathbf{r}_j)|^2} \right\}. \tag{15}$$

The permittivity ε_1 distribution is determined easily using Eq. (3).

As initial estimate for $\bar{\mathbf{p}}_l$ the authors took the estimate obtained by the back-propagation procedure. This technique is described for the two-dimensional problem in Refs. 26, 31, and 32. The extension to the three-dimensional problem is straightforward and therefore does not need to be presented herein.

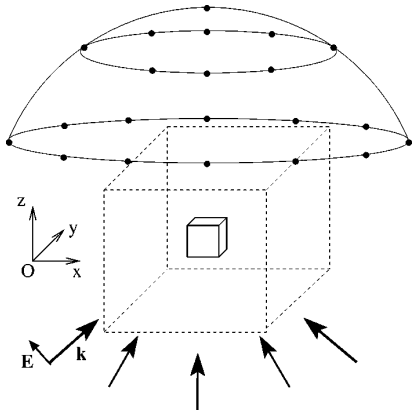

FIG. 1. Sketch of the illumination and detection configuration of the ODT experiment. The points regularly placed on the half sphere are the observation points in far-field.

III. RESULTS

In this section, we simulate an ODT experiment and we present reconstructed maps of permittivity for various objects.

A. Isolated object

We first consider a unique homogeneous object, with relative permittivity ε_1, embedded in a homogeneous medium with relative permittivity ε_0. We define $\varepsilon = \varepsilon_1/\varepsilon_0$ and λ the wavelength in the homogeneous medium.

Figure 1 is a sketch of the experimental configuration. The unknown object is drawn in a plain line while the box in dashed line indicates the domain of investigation taken in the reconstruction procedure. We take $L=31$ incident angles, and $M=65$ observation points. The latter are regularly placed on a half sphere with radius 400 λ, above the (x,y) plane so that one can consider that the scattered field is detected in far-field along 65 directions in a cone of half-angle 80°. Each electromagnetic excitation is a plane wave with wave vector $\mathbf{k}$ belonging to the (x,z) plane with $k_z > 0$. The incident angle with respect to the z-axis θ_i varies from −80° to 80°. In this example, the polarization of the incident electric field lies in the (x,z) plane as shown in Fig. 1. We have done the same study with an incident polarization parallel to the (x,y) plane and obtained very similar results.

The object under study is a cube whose size is $a \times a \times a$ with $a = \lambda/4$, and $\varepsilon = 2.25$. The scattered field at each observation point and for each incident angle is calculated with the CDM [Eqs. (5) and (6)]. The direct problem is solved with a discretization in $N=125$ subunits with width $d = \lambda/20$. Notice that we avoid using the same discretization in the forward and the inverse problems, hence the reconstruction procedure is applied to a test domain discretized into subunits of width $d=\lambda/10$.

Figure 2 shows the maps of the relative permittivity obtained after inversion. In Figs. 2(a), 2(c), and 2(e) the size of the test domain is $1.8\lambda \times 1.8\lambda \times 1.8\lambda$ (6859 subunits) while in Figs. 2(b), 2(d), and 2(f) the size of the test domain is

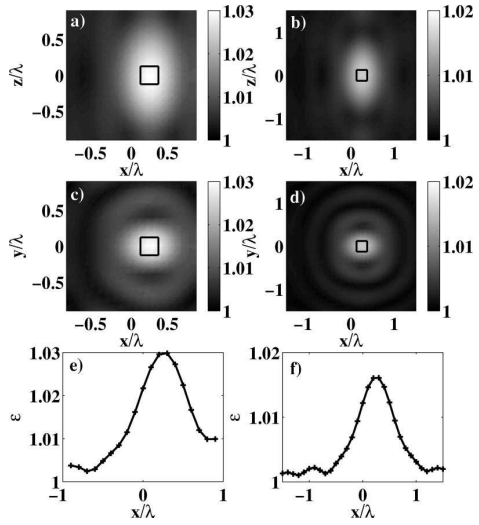

FIG. 2. Reconstructed map of permittivities for two sizes of the test domain. The left side is computed when the size is $1.8\lambda \times 1.8\lambda \times 1.8\lambda$ and the right side when the size is $3\lambda \times 3\lambda \times 3\lambda$. (a) and (b) are the maps of the relative permittivity in the plane (x,z) for $y=0$. (c) and (d) are the maps of the relative permittivity in the plane (x,y) for $z=0$. (e) and (f) are the relative permittivity vs x for $y=z=0$. The bold square indicates the position of the cube.

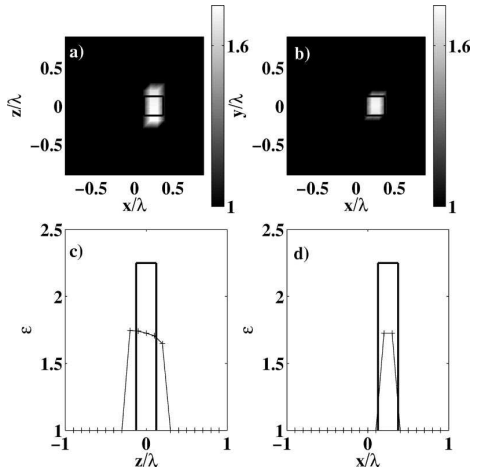

FIG. 3. (a) Map of the relative permittivity in the (x,y) plane $(z=0)$. (b) Map of the relative permittivity in the (x,z) plane $(x=0)$. (c) Relative permittivity vs z for $y=0$, $x=\lambda/8$. (d) Relative permittivity vs x for $y=z=0$.

$3\lambda \times 3\lambda \times 3\lambda$ (29 791 subunits). The center of the cube [indicated by the bold square in Figs. 2(a)–2(d)] is located at $(\lambda/8,0,0)$. The time of computation for the inversion of the smallest problem ($N=6859$ subunits) is less than 7 min on a modern computer (Opteron at 2 GHz). Most of the calculation time (80%) is taken by the resolution of Eq. (5) which permits one to obtain the electromagnetic field from the dipoles in the test domain. This step could be avoided by assuming that the field is close to the incident field, thus resorting to the Born approximation. In this case, the method is close to the singular value decomposition technique presented in Ref. 9. We note that, whatever the size of the box used for the reconstruction, we always localize the position of the object. Yet, the value of the relative permittivity is greatly underestimated and this effect is stronger when the size of the test domain is increased. Indeed, we note that with our simple inversion scheme, the dipoles in the test domain are never equal to zero. Hence we get a kind of "dilution" of the object which reduces the value found for the relative permittivity of the object. To get a physical insight into this phenomenon, we define the "optical volume" of the cube, in analogy with the optical path, as $a^3(\varepsilon-1)$, and we call V the volume of the test domain and $\overline{\varepsilon}$ the average of the relative reconstructed permittivity obtained inside V. When the algorithm's convergence is obtained we find that $V(\overline{\varepsilon}-1) \approx a^3(\varepsilon-1)$. When the volume V increases, $\overline{\varepsilon}$ diminishes and the relative permittivity at the location of the object is lower. This systematic behavior suggests a possible posttreatment to improve the quality of the reconstruction.

If one knows the value of the relative permittivity of the object under study, which is often the case, one can put the values of the weaker dipoles at zero and iterate the process until the known relative permittivity is reached. In fact this posttreatment amounts to reducing the size of the test domain and permits one to avoid the dilution effect. As the mesh of the test box does not fit exactly the volume of the unknown object, we stop the iterative process when the average of the relative reconstructed permittivity is equal to 0.7ε. Figure 3 shows the images obtained after the posttreatment. We see that in the (x,y) plane [Figs. 3(b) and 3(d)] the object is perfectly localized and the reconstructed shape is close to the real one. On the other hand, the reconstruction of the object deteriorates in the (x,z) or (y,z) plane. This lack of accuracy in the z direction is due to the illumination and collection configuration of our experiment. In transmission diffraction tomography, the incident field comes from below the sample while the detectors are placed above the sample. In this case, the portion of the Ewald sphere that is covered with the far-field data is two times smaller in the axial direction than in the transverse plane.[7] Hence the resolution is twice as large along the z axis than in the (x,y) plane. The same phenomenon is observed with classic optical transmission microscopes. To improve the axial resolution, it is necessary to illuminate and collect the diffracted light from both sides of the sample. This has been done in the 4π microscope[33] and the same resolution is obtained in the transverse and axial directions in that case.

We now study the robustness of our algorithm with respect to noise. We corrupt the scattered far-field data, $\mathbf{f}_{l=1,\ldots,L}$, by an additive uncorrelated noise on each component of the electric field at each position of observation,

$$\tilde{f}_l^v(\mathbf{r}_k) = f_l^v(\mathbf{r}_k) + uAe^{i\phi}, \tag{16}$$

where v stands for the components along x, y, or z, $A = \max(|\bar{\mathbf{f}}_{l=1,\ldots,L}|)$, and $k=1,\ldots,M$. ϕ is a random number taken for each component of the positions of observation and angles of incidence with uniform probability density in

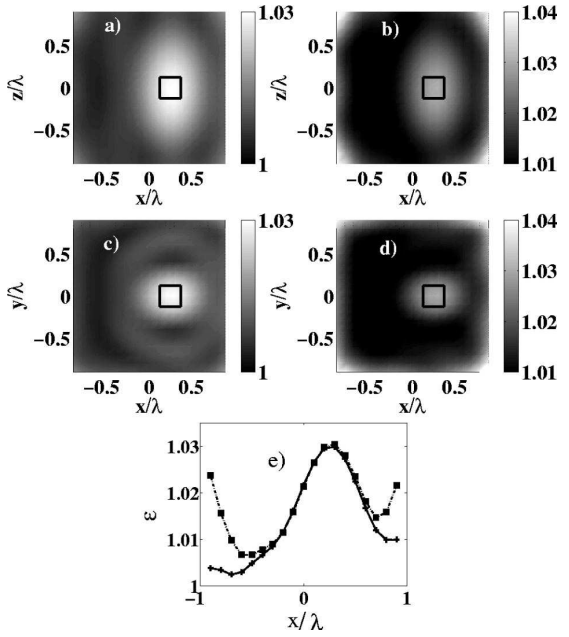

FIG. 4. (a) and (b) map of the relative permittivity in the (x,y) plane at $z=0$. (c) and (d) Map of the relative permittivity in the (x,z) plane at $x=0$. (a) and (c) correspond to $u=0.1$ and (b) and (d) to $u=0.3$. (e) Relative permittivity vs x at $y=z=0$: plain line $u=0$, dashed line with crosses $u=0.1$, and point-dashed line with squares $u=0.3$.

$[0,2\pi]$, and u is a real number smaller than unity that monitors the noise level. We take the same object and the same experimental conditions as those of Figs. 2(a) and 2(c). In Fig. 4 we present the reconstructed map of permittivity in the (x,y) and (x,z) planes for $u=10\%$ and 30%, and in Fig. 4(e) the relative permittivity along the x axis for the three different values of $u=0$ (no noise), 0.1, and 0.3. We note that in Fig. 4(e) the two curves $u=0$ and $u=0.1$ are confounded, and the curves obtained for $u=0.3$ depart from the others only at both extremities of the investigation line. If we look carefully at the map of the relative permittivity, Figs. 4(b) and 4(d), we see that the perturbation due to the noise appears essentially at the edge of the test domain and more particularly at the corner of the box. This behavior is found whatever the size of the investigation box. The perturbation induced by the noise is thus easily eliminated with the posttreatment proposed in Fig. 3 albeit with some precautions. We introduce a second test domain, smaller than the original one, and we apply the regularization only within this second zone. Thus the dipoles located at the edges of the first test domain are never forced to zero. Their role is to absorb the noise so that it does not perturb the second test domain. We finally obtain an image very close to that of Fig. 3. The observed robustness of the inversion scheme must, however, be qualified. Indeed, the noise we have chosen is uncorrelated and can be regarded as a high frequency function added to the scattered amplitudes. Since the far-field data are basically linked to the induced dipoles through a Fourier transform, the noise perturbation will be interpreted as the interference pattern of dipoles as far as possible, i.e., at the extremity of the test domain. Thus the reconstruction of small centered objects is not affected.

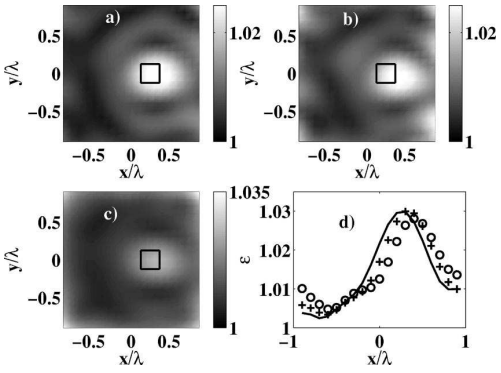

FIG. 5. (a)–(c) Map of the relative permittivity in the (x,y) plane $(z=0)$. (a) $\sigma=0$, $\gamma=\pi/3$. (b) $\sigma=0$, $\gamma=2\pi/3$. (c) $\sigma=\pi/3$, $\gamma=\pi/3$. (d) Relative permittivity vs x for $y=z=0$. Solid line is without noise, crosses correspond to $\gamma=\pi/3$ (a), and circles to $\gamma=2\pi/3$ (b).

Unfortunately, it is most likely that the experimental noise will be correlated. Indeed, due to the envisaged experimental setup, one can expect systematic cumulative errors on the phase measurements as one moves away from the specular direction. We have investigated the behavior of the inversion technique in the presence of correlated noise on the phase, in the form,

$$\tilde{f}_l^{\upsilon}(\mathbf{r}_k) = f_l^{\upsilon}(\mathbf{r}_k)e^{i\psi} \quad \text{with} \quad \psi = \psi_g + \psi_a, \tag{17}$$

where $\upsilon=x$, y, or z, $l=1,\ldots,L$, and $k=1,\ldots,M$. ψ_g is a Gaussian noise with mean 0 and standard deviation σ while ψ_a is a correlated noise defined as $\psi_a=(\gamma/2)|\mathbf{k}_d-\mathbf{k}|/|\mathbf{k}|$ where $\mathbf{k}_d$ is the wave vector of the scattered field. In our experimental configuration, Fig. 1, the most important error on the phase, $\max(\psi_a)\approx\gamma$, occurs when $k_{d_x}=-k_x$ and $\theta_i=\pm 80°$.

We observe in Fig. 5(b) that this kind of noise has a small effect on the map of the permittivity, even when the value of the phase error reaches $2\pi/3$ for the furthest directions of observation. In fact, its main effect is to move the location of the object in the x direction, Fig. 5(d). This phenomenon is directly linked to the fact that the object is not at the center of the test box. The second effect is to decrease the value of ε and create some object ghosts. If we add an uncorrelated Gaussian noise, σ, to the correlated noise, we observe in Fig. 5(c) the same behavior as for the white noise previously studied: in addition to the lateral shift, a perturbation at the edge of the test domain appears. Clearly, a correlated noise cannot be eliminated with a simple post-treatment. However, as it stands, the reconstruction scheme is able to provide a rather accurate map of permittivity even with phase errors reaching $2\pi/3$ in certain directions.

B. Many objects

We have also checked the efficiency of the inverse technique when many objects are embedded in the homogeneous

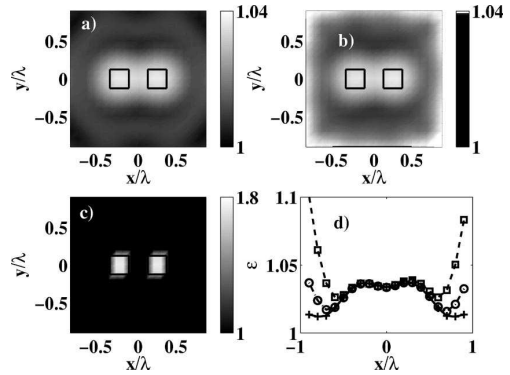

FIG. 6. Two identical cubes ($\varepsilon=2.25$) with $a=\lambda/4$ separated by $\lambda/4$ along the x direction: the center of the first cube is located at $(-\lambda/4,0,0)$ and of second cube at $(\lambda/4,0,0)$. (a)–(c) Map of the relative permittivity in the plane (x,y) with $z=0$. The bold square represents the position of the cubes. (a) Reconstruction with no noise. (b) Reconstruction with 30% of noise. (c) Reconstruction with the regularization used in Fig. 3. (d) Relative permittivity vs x at $y=z=0$: plain line with crosses for $u=0$, dashed line with circles for $u=0.1$, and point-dashed line with squares for $u=0.3$.

medium. If the objects are far from each other, we first take a large test domain with a loose mesh (for example, $d=\lambda/2$) in order to localize the objects. Then, we reduce the domain of investigation to small boxes surrounding every detected site (we can take many separated test domains) and we diminish the spacing of the mesh in each box. This technique is a simple extension of the posttreatment described in the previous section and it can be applied indifferently to objects far apart or close to each other.

To investigate the power of resolution of our imaging system, we take two small cubes of width $a=\lambda/4$ and separated by $\lambda/4$ along the x direction. The conditions of illumination and discretization are the same as those used in Figs. 3–5.

Figures 6(a)–6(c) show the map of the relative reconstructed permittivity in the (x,y) plane at $z=0$ with or without noise and with posttreatment. All the conclusions drawn for an isolated object apply in the case of several objects. First, the perturbation due to the white noise, Eq. (16), appears only at the edge of the investigation box and does not alter the reconstruction of the permittivity. Then, in Figs. 6(a) and 6(b), the two objects are localized, yet the separation between the two cubes is not frankly marked [see Fig. 6(d) plain line with crosses]. Last, if we use the posttreatment, Fig. 6(c), the map of the reconstructed relative permittivity perfectly fits the real shape of the objects in the (x,y) plane. The reconstruction in the (x,y) plane, not shown, displays the same lack of accuracy as that observed in Fig. 3(a). More precisely, we have checked that the resolution is twice as large along the z axis than that along the x axis, by studying the image of two cubes separated by $\lambda/4$ and $\lambda/2$ along the z axis. As expected, we were not able to distinguish the two objects in the first case whereas the separation was clearly visible in the second one.

It is worth noting that the reconstructed image depends on the illumination configuration. In our case the incident beam is varied in the (x,z) plane and the centers of the cubes belong to the x axis. A simple analysis of the portion of the Ewald sphere covered with these illuminations shows that this configuration is the best for obtaining details along the x axis. Indeed, if the plane of incidence is changed to the (y,z) plane, the inversion procedure does not allow one to distinguish the two objects. Now, in general, the orientation of the objects is unknown. Thus the solution consists of illuminating the sample with at least two orthogonal planes of incidence, i.e., the (x,z) and the (y,z) planes. In this case, the separation between the two cubes is less pronounced than that presented in Fig. 6(d) but the posttreatment gives the same maps of permittivity as those presented in Fig. 6(c).

Finally, to investigate further the power of resolution of our technique, we have taken two cubes separated by $\lambda/7$ along the x axis. The inversion procedure, even with the posttreatment, failed to reconstruct the two objects. In this case, it is necessary to implement more sophisticated inversion procedures (such as those developed in 2D[8]).

IV. CONCLUSION

We have simulated a three-dimensional transmission diffraction tomography experiment applied to the optical domain. The inversion algorithm, based on the coupled dipole method, gives the map of permittivity of the object from the far-field amplitudes. This technique does not possess all the refinements of nonlinear inversion procedures but it is simple to implement and its numerical cost is reasonable inasmuch as it does not require one to inverse any matrix. Moreover, it appears quite robust to white noise or phase errors. Taking into account the weakness of the algorithm, we have proposed a posttreatment that significantly improves the images. We show that it is possible to distinguish two objects separated by $\lambda/4$ with relatively few illumination and collection angles. The main interest of this simple inversion technique is its versatility. We intend to extend it to configurations in which the object is placed in the vicinity of a substrate. This can be achieved by adding to the tensor of the free-space susceptibility the tensor of the surface susceptibility.[34] In a more general way if the object is in an environment where we can compute the tensor susceptibility (for example, a multilayer system[35] or a grating[36]) the method presented here can be applied.

ACKNOWLEDGMENTS

This work was supported by a grant of the Ministère de la Recherche, ACI 02 2 0225, and the Conseil Général des Bouches du Rhône and the Conseil Régional PACA. The authors would like to thank Frédéric Forestier for the computer science support.

[1] F. de Fornel, in *Evanescent Waves*, Vol. 73 of Springer Series in Optical Sciences (Springer-Verlag, Berlin, 2001).
[2] P. S. Carney and J. C. Schotland, Appl. Phys. Lett. **77**, 2798 (2000).
[3] O. Haeberlé, C. Xu, A. Dieterlen, and S. Jacquey, Opt. Lett. **26**, 1684 (2001).
[4] J. Enderlein, Opt. Lett. **25**, 634 (2000).
[5] S. B. Ippolito, B. B. Goldberg, and M. S. Ünlü, Appl. Phys. Lett. **78**, 4071 (2001).
[6] E. Wolf, Opt. Commun. **1**, 153 (1969).
[7] V. Lauer, J. Microsc. **205**, 165 (2002).
[8] K. Belkebir and A. Sentenac, J. Opt. Soc. Am. A **20**, 1223 (2003).
[9] P. S. Carney, V. A. Markel, and J. C. Schotland, Phys. Rev. Lett. **86**, 5874 (2001).
[10] E. Wolf, Opt. Commun. **1**, 153 (1969).
[11] S. Kawata, O. Nakamura, and S. Minami, J. Opt. Soc. Am. A **4**, 292 (1987).
[12] A. M. Purcell and C. R. Pennypacker, Astrophys. J. **186**, 705 (1973).
[13] J. D. Jackson, *Classical Electrodynamics*, 2nd ed. (Wiley, New York, 1975).
[14] P. C. Chaumet and M. Nieto-Vesperinas, Phys. Rev. B **61**, 14 119 (2000).
[15] P. C. Chaumet and M. Nieto-Vesperinas, Phys. Rev. B **62**, 11 185 (2000).
[16] P. C. Chaumet and M. Nieto-Vesperinas, Opt. Lett. **25**, 1065 (2000).
[17] B. T. Draine, Astrophys. J. **333**, 848 (1988).
[18] A. Lakhtakia, Int. J. Mod. Phys. C **3**, 583 (1992).
[19] W. C. Chew and Y. M. Wang, IEEE Trans. Med. Imaging **9**, 218 (1990).
[20] N. Joachimowicz, C. Pichot, and J.-P. Hugonin, IEEE Trans. Antennas Propag. **39**, 1742 (1991).
[21] A. G. Tijhuis, Wave Motion **11**, 151 (1989).
[22] A. G. Tijhuis, K. Belkebir, A. C. S. Litman, and B. P. de Hon, IEEE Trans. Geosci. Remote Sens. **39**, 1316 (2001).
[23] R. E. Kleinman and P. M. van den Berg, J. Comput. Appl. Math. **42**, 17 (1992).
[24] R. E. Kleinman and P. M. van den Berg, Radio Sci. **28**, 877 (1993).
[25] K. Belkebir and A. G. Tijhuis, Inverse Probl. **17**, 1671 (2001).
[26] K. Belkebir, S. Bonnard, F. Pezin, P. Sabouroux, and M. Saillard, J. Electromagn. Waves Appl. **14**, 1637 (2000).
[27] P. M. van den Berg and R. E. Kleinman, Inverse Probl. **13**, 1607 (1997).
[28] A. Abubakar, P. M. van den Berg, and B. J. Kooij, IEICE Trans. Electron. **E83-C**, 1864 (2000).
[29] A. Abubakar and P. M. van den Berg, Inverse Probl. **18**, 495 (2002).
[30] W. H. Press, B. P. Flannery, S. A. Teukolski, and W. T. Vetterling, *Numerical Recipes: The Art of Scientific Computing* (Cambridge University Press, Cambridge, England, 1986).
[31] L. Souriau, B. Duchêne, D. Lesselier, and R. E. Kleinman, Inverse Probl. **12**, 463 (1996).
[32] R. E. Kleinman and P. M. van den Berg, Radio Sci. **29**, 1157 (1994).
[33] M. Schrader and S. Hell, J. Appl. Phys. **84**, 4033 (1998).
[34] P. C. Chaumet, A. Rahmani, F. de Fornel, and J.-P. Dufour, Phys. Rev. B **58**, 2310 (1998).
[35] A. Rahmani, P. C. Chaumet, and F. de Fornel, Phys. Rev. A **63**, 023819 (2001).
[36] P. C. Chaumet, A. Rahmani, and G. W. Bryant, Phys. Rev. B **67**, 165404 (2003).

2740 OPTICS LETTERS / Vol. 29, No. 23 / December 1, 2004

Superresolution of three-dimensional optical imaging by use of evanescent waves

Patrick C. Chaumet, Kamal Belkebir, and Anne Sentenac

Institut Fresnel, Centre National de la Recherche Scientifique, Unité Mixte de Recherche (UMR 6133), Campus de Saint Jérôme, Case 162, Université d'Aix-Marseille I & III, 13397 Marseille Cedex, France

Received July 8, 2004

We simulate a three-dimensional optical diffraction tomography experiment in which superresolution is achieved by illuminating the object with evanescent waves generated by a prism. We show that accounting for multiple scattering between the object and the prism interface is mandatory to obtain superresolved images. Because the Born approximation leads to poor results, we propose a nonlinear inversion method for retrieving the map of permittivity of the object from the scattered far field. We analyze the sensitivity to noise of our algorithm and point out the importance of using incident propagative waves together with evanescent waves to improve the robustness of the reconstruction without losing the superresolution. © 2004 Optical Society of America

OCIS codes: 180.6900, 110.6960, 290.3200.

There has been considerable interest in the development of optical microscopes with lateral resolution below the usual Rayleigh criterion, $\lambda/(2\mathrm{NA})$, where λ is the wavelength of the illumination and NA is the numerical aperture of the imaging system. The resolution has been improved well below the classical limit in optical near-field microscopy[1] by bringing a probe within a few nanometers of the sample. In far-field fluorescence microscopy an important amelioration has been obtained by taking advantage of nonlinear effects[2] or by use of numerical postprocessing with strong prior information on the fluorescent sources. In classical far-field microscopes the NA has been increased with immersed lenses, hemispherical prisms,[3] or the placement of several objectives on opposite sides of the sample.[4,5] It has also been proposed to illuminate the sample with many structured illuminations and to mix the different images through simple arithmetics.[6] This last technique is, in principle, close to optical diffraction tomography (ODT), in which the sample is illuminated under various angles of incidence, the phase and intensity of the diffracted far-field is detected along several directions of observation,[7] and a numerical procedure is used to retrieve the map of permittivity of the object from the far-field data.[8] In general, the inversion methods are based on the Born approximation, so that there is a linear relationship between the scattered field and the permittivity of the object.[9] Experimental and theoretical studies have shown that using several illuminations permits one to exceed the classical diffraction limit by a factor of 2.[6,8] To ameliorate further the resolution of the system, it has been proposed to illuminate the sample with evanescent waves through a prism in total internal reflection.[10] Actually, superresolution is obtained if the objects are close to the surface of the prism or even deposited onto it.[11] In this case the influence of the interface cannot be neglected, as was done in the pioneering work on this technique.[10] In this Letter we simulate accurately a full-vectorial three-dimensional ODT experiment in total internal reflection configuration. We point out that multiple scattering between the object and the interface is not negligible. Hence, contrary to what happens for configurations without an interface, the Born approximation leads to nonsatisfactory results even for objects that are small with respect to the wavelength. We thus propose a full-vectorial nonlinear inversion method and investigate its power of resolution. Last, we show that the robustness of the reconstruction with respect to noise can be significantly increased by use of both propagative- and evanescent-wave illumination beams.

The geometry of the problem is depicted in Fig. 1. Assume that an unknown three-dimensional object is entirely confined in a bounded box $\Omega \subset \mathbb{R}^3$ (investigation domain) and illuminated successively by $l = 1, \ldots, L$ electromagnetic waves $\mathbf{E}^{\mathrm{inc}}_{l=1,\ldots,L}$. For each excitation l the scattered field $\mathbf{f}_l$ is measured at M points on a surface Γ located outside the investigation domain Ω. We use the coupled dipole method

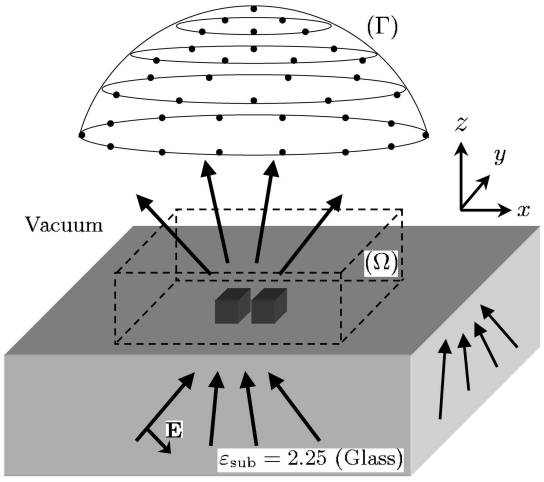

Fig. 1. Sketch of the ODT experiment.

0146-9592/04/232740-03$15.00/0

(CDM) to model the scattered field by an arbitrary three-dimensional object deposited on a semi-infinite medium.[12] In this method the scatterer is discretized into a cubic lattice of N subunits with spacing d that are considered radiating dipoles. The self-consistent local field at a subunit i inside Ω can be written as

$$\mathbf{E}_l(\mathbf{r}_i \in \Omega) = \mathbf{E}_l^{\mathrm{inc}}(\mathbf{r}_i) + \sum_{j=1}^{N} \overleftrightarrow{\mathbf{G}}(\mathbf{r}_i, \mathbf{r}_j)\alpha(\mathbf{r}_j)\mathbf{E}_l(\mathbf{r}_j)\,, \quad (1)$$

where $\overleftrightarrow{\mathbf{G}}$ is the field susceptibility tensor that takes into account the substrate[12] and $i = 1, \ldots, N$. $\alpha(\mathbf{r}_j)$ denotes the polarizability of subunit j depending on d through the Clausius–Mossotti relation.[12] The scattered field on Γ reads as

$$\mathbf{E}_l^d(\mathbf{r}_m \in \Gamma) = \sum_{j=1}^{N} \overleftrightarrow{\mathbf{G}}(\mathbf{r}_m, \mathbf{r}_j)\alpha(\mathbf{r}_j)\mathbf{E}_l(\mathbf{r}_j)\,. \quad (2)$$

For each illumination the forward scattering problem, Eqs. (1) and (2), can be reformulated symbolically as

$$\mathbf{E}_l^d = \overline{\overline{\mathbf{G}}}_{\mathrm{far}}\alpha\mathbf{E}_l\,, \quad (3)$$

$$\mathbf{E}_l = \mathbf{E}_l^{\mathrm{inc}} + \overline{\overline{\mathbf{G}}}_{\mathrm{near}}\alpha\mathbf{E}_l\,, \quad (4)$$

where $\overline{\overline{\mathbf{G}}}_{\mathrm{far}}$ and $\overline{\overline{\mathbf{G}}}_{\mathrm{near}}$ are matrices that contain the field susceptibility tensor and are $(3N \times 3M)$ and $(3N \times 3N)$, respectively. The inverse scattering problem consists of finding the permittivity distribution ε inside investigation area Ω such that the associated scattered field matches measured field $\mathbf{f}_{l=1,\ldots,L}$. To solve this nonlinear and ill-posed inverse scattering problem, we propose an iterative approach as described for the two-dimensional case in Ref. 13. In this approach, starting from an initial guess, the parameter of interest (the polarizability distribution and subsequently the permittivity) is adjusted gradually by minimizing a cost functional $\mathcal{F}(\alpha)$ involving the discrepancy between the data $\mathbf{f}_l$ and the scattered field that is predicted by the model through Eqs. (3) and (4). In fact, the inverse problem is stated as an optimization problem in which for each iteration step n the cost functional

$$\mathcal{F}_n(\alpha_n) = \sum_{l=1}^{L} \|\mathbf{f}_l - \overline{\overline{\mathbf{G}}}_{\mathrm{far}}\alpha_n\mathbf{E}_{l,n}\|_{\Gamma}^2 \Big/ \sum_{l=1}^{L} \|\mathbf{f}_l\|_{\Gamma}^2 \quad (5)$$

is minimized by the Polak–Ribière conjugate gradient procedure as in Ref. 13. When the extended Born approximation[14] is assumed, local field $\mathbf{E}_l$ is approximated by incident field $\mathbf{E}_l^{\mathrm{inc}}$. When multiple scattering is taken into account, local field $\mathbf{E}$ is the solution of Eq. (4) for the best available estimation of the polarizability distribution, i.e.,

$$\mathbf{E}_{n,l} = \left[\overline{\overline{\mathbf{I}}} - \overline{\overline{\mathbf{G}}}_{\mathrm{near}}\alpha_{n-1}\right]^{-1}\mathbf{E}_l^{\mathrm{inc}}, \quad (6)$$

with $\overline{\overline{\mathbf{I}}}$ being the identity matrix.

We check the performance of the inverse procedure on synthetic data by simulating an ODT experiment with the CDM. Consider two cubes of side $\lambda/4$ and of relative permittivity 2.25 separated by $\lambda/10$, deposited on a semi-infinite medium with a relative permittivity of $\varepsilon_{\mathrm{sub}} = 2.25$ (as depicted in Fig. 1). The superstrate is a vacuum, whereas the substrate is made of glass. The object is illuminated by 16 plane waves coming from the substrate, whose wave vectors and electric field are either in the (x, z) plane or in the (y, z) plane. Let θ_l^{inc} be the angle of incidence with respect to the z axis corresponding to the lth illumination. For the total internal reflection experiment, all the incident plane waves are totally reflected at the interface; hence $\theta_l^{\mathrm{inc}} \in [-80, -43] \bigcup [80, 43]$ deg. The amplitude and phase of the scattered fields are detected at 65 points regularly distributed on a half-sphere Γ (see Fig. 1). The radius of the sphere is 400λ so that only data from far-field components are considered. Azimuthal angle of observation θ, defined as the angle between the diffracted wave vector and the z axis, ranges from $-80°$ to $80°$. In all the examples the synthetic data are computed with a mesh size of $\lambda/40$, which differs from that used in the inversion, $\lambda/20$. In all the reported results we display the map of the reconstructed relative permittivity distribution after enough iterations for the cost function to reach a plateau. During the minimization process the value of the relative permittivity was enforced not to exceed 2.25; thus the convergence was obtained within 100 iterations. We first investigate the efficiency of the extended Born approximation[14] (worse results were obtained with the standard Born approximation). In Figs. 2(a) and 2(b) we plot the top and side views of the reconstructed relative permittivity in the (x, y) and (x, z) planes with the linear inversion method. We observe that the two cubes are not resolved and that the relative permittivity quickly saturates at 2.25, especially in the vicinity of the interface. This result can be explained easily by studying the behavior of the local field inside a small dielectric sphere placed above a substrate and illuminated under normal incidence in transmission. When the distance between the object and the interface tends to zero, the amplitude of the local field increases and departs from the transmitted incident field. Thus, although the extended Born approximation underestimates the local

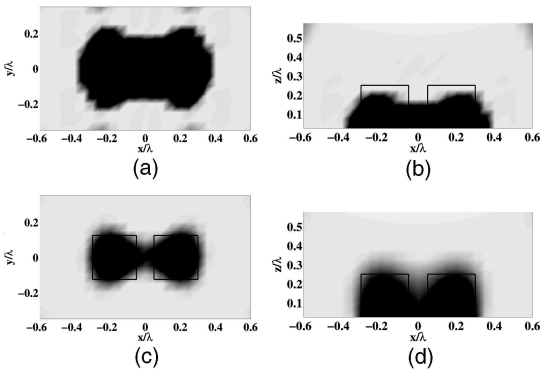

Fig. 2. Reconstructed relative permittivity distribution with only evanescent-wave illumination: (a), (b) with the extended Born approximation; (c), (d) with the nonlinear inverse scheme.

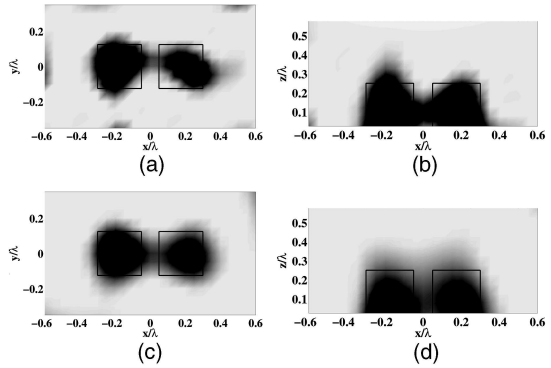

Fig. 3. Reconstructed relative permittivity distribution with the nonlinear inverse algorithm from corrupted data with noise: (a), (b) with evanescent waves; (c), (d) with evanescent and propagative waves.

field, the inversion method compensates this error by overestimating the polarizability of the dipoles close to the interface. The failure of the linear inversion method is clearly due to the presence of the interface. Indeed, we checked the linear inversion method with the same two cubes separated by $\lambda/7$ and illuminated by propagative plane waves only. When objects are deposited on the interface, the reconstructed map of the permittivity is similar to that obtained in Figs. 2(a) and 2(b), whereas, when the objects are in vacuum, they are correctly resolved. Hence it is mandatory to account for the multiple scattering between the objects and the interface in the inverse problem. In Figs. 2(c) and 2(d) we plot the maps of the relative permittivity obtained by taking into account the multiple scattering effect, i.e., the self-consistent Eq. (4) for the local field is solved at each iteration step. The improvement in the resolution and accuracy is manifest. The ability to resolve two cubes separated by $\lambda/10$ is due to both the nonlinear inversion method that accounts for the multiple scattering and the set of incident evanescent plane waves that maximizes the radius of the Ewald sphere that can be covered in such a configuration.[11] When only propagative waves are used, i.e., $\theta_l^{\mathrm{inc}} \in [-43, 43]$ deg, the two cubes are not resolved.

In Fig. 3 we checked the robustness of the inverse method by adding an uncorrelated noise to the scattered far-field data. The noise amplitude is 20% of the maximum of the scattered field for all the illuminations. We note, by comparing Figs. 3(a) and 3(b) with Figs. 2(c) and 2(d), that the reconstructed map of the permittivity is strongly affected by the noise. The same algorithm, used in a homogeneous configuration, shows a better robustness to noise. In our opinion this is because the incident waves that illuminate the objects are evanescent. Indeed, the convergence of iterative inverse schemes deteriorates when the frequency of the illumination is increased.[15] Now, one can consider evanescent waves as high-frequency illumination. It is possible to circumvent the sensitivity of the reconstruction to noise by using both evanescent and propagative waves as illumination. Indeed, it has been shown that low-frequency illumination, although yielding poorly resolved images, ameliorates the convergence of iterative inversion schemes.[15] In Figs. 3(c) and 3(d) we plot the reconstructed map of the permittivity obtained when $\theta_l^{\mathrm{inc}} \in [-80, 80]$ deg is used to build the set of data. This result has to be compared with Figs. 3(a) and 3(b), in which only evanescent waves are used. The robustness of the inversion algorithm is clearly improved. Note that the resolution is not deteriorated by the use of propagative waves together with evanescent waves.

In conclusion, we have presented a realistic optical diffraction tomography experiment that can image three-dimensional objects with a resolution much higher than the one reached with classical microscopes. The superresolution is attained by illuminating the sample with evanescent waves and taking into account the multiple scattering between the objects and the interface in the inversion procedure. We stress that the Born approximation leads to poor results in this configuration and that adding incident propagative waves to the evanescent waves permits one to improve the robustness with respect to noise of the reconstruction.

The authors acknowledge a project grant from the Ministère de la Recherche Français, ACI jeune chercheur 2115, and support from the Conseil Régional Provence-Alpes-Côte d'Azur and Conseil général CG13. K. Belkebir's e-mail address is kamal.belkebir@fresnel.fr.

References

1. J.-J. Greffet and R. Carminati, Prog. Surf. Sci. **56,** 133 (1997).
2. M. Dyba and S. Hell, Phys. Rev. Lett. **88,** 163901 (2002).
3. S. B. Ippolito, B. B. Goldberg, and M. S. Ünlü, Appl. Phys. Lett. **78,** 4071 (2001).
4. O. Haeberlé, A. Dieterlen, and S. Jacquey, Opt. Lett. **26,** 1684 (2001).
5. J. Enderlein, Opt. Lett. **25,** 634 (2000).
6. M. Gustafsson, J. Microsc. **198,** 82 (2000).
7. N. Destouches, C. A. Guérin, M. Lequime, and H. Giovannini, Opt. Commun. **198,** 233 (2001).
8. V. Lauer, J. Microsc. **205,** 165 (2002).
9. E. Wolf, Opt. Commun. **1,** 153 (1969).
10. P. S. Carney and J. C. Schotland, Opt. Lett. **26,** 1072 (2001).
11. K. Belkebir and A. Sentenac, J. Opt. Soc. Am. A **20,** 1223 (2003).
12. P. C. Chaumet, A. Rahmani, F. de Fornel, and J.-P. Dufour, Phys. Rev. B **58,** 2310 (1998).
13. K. Belkebir and A. G. Tijhuis, Inverse Probl. **17,** 1617 (2001).
14. T. M. Habashy, R. W. Groom, and B. R. Spies, J. Appl. Phys. **98,** 1759 (1993).
15. A. G. Tijhuis, K. Belkebir, A. Litman, and B. de Hon, IEEE Trans. Geosci. Remote Sens. **39,** 1316 (2001).

Superresolution in total internal reflection tomography

Kamal Belkebir, Patrick C. Chaumet, and Anne Sentenac

Institut Fresnel, UMR-CNRS 6133, Campus de Saint Jérôme, case 162, Université d'Aix-Marseille I & III, 13397 Marseille Cedex 20, France

Received October 28, 2004; revised manuscript received March 3, 2005; accepted March 15, 2005

We simulate a total internal reflection tomography experiment in which an unknown object is illuminated by evanescent waves and the scattered field is detected along several directions. We propose a full-vectorial three-dimensional nonlinear inversion scheme to retrieve the map of the permittivity of the object from the scattered far-field data. We study the role of the solid angle of illumination, the incident polarization, and the position of the prism interface on the resolution of the images. We compare our algorithm with a linear inversion scheme based on the renormalized Born approximation and stress the importance of multiple scattering in this particular configuration. We analyze the sensitivity to noise and point out that using incident propagative waves together with evanescent waves improves the robustness of the reconstruction. © 2005 Optical Society of America

OCIS codes: 180.6900, 110.6960, 290.3200.

1. INTRODUCTION

There is considerable interest in developing optical microscopes presenting a lateral resolution below the usual Rayleigh criterion $\lambda/(2\mathrm{NA})$, where λ is the wavelength of the illumination and NA is the numerical aperture of the imaging system, while retaining the convenience of far-field illumination and collection. Among the various ways to ameliorate the resolution, it has been proposed to illuminate the sample with many structured illuminations, namely standing waves, and to mix the different images through simple arithmetic.[1] This technique is very close to optical diffraction tomography, in which the sample is illuminated under various angles of incidence, the phase and intensity of the diffracted far field is detected along several directions of observation,[2–4] and a numerical procedure is used to retrieve the map of the permittivity distribution of the object from the far-field data.[3] Experimental and theoretical studies have shown that using several illuminations permits one to exceed the classical diffraction limit by a factor of 2.[1,3]

Recently, the diffraction tomography approach has been applied to total internal reflection microscopy.[5,6] In total internal reflection tomography (TIRT), the sample is illuminated with different evanescent waves through a prism in total internal reflection. The use of incident evanescent waves permits circumvention of the diffraction limit, as in near-field microscopy, without the inconvenience of bringing a probe close to the sample.[7] A resolution of $\lambda/7$ has been observed in standing-wave total internal reflection fluorescent microscopy.[8] Note that superresolution in the TIRT is obtained only if the objects under test are close to the surface of the prism or even deposited on it.[9]

In all microscopy techniques using several successive illuminations, one needs a numerical procedure to combine the different images and extract the map of the relative permittivity distribution of the object from the scattered far field. In general, one assumes that the object is a weak scatterer so that there is a linear relationship between the scattered field and the relative permittivity of the object, that is, one assumes that the Born approximation is valid.[5,10] In this case, the transverse resolution limit can be inferred from simple considerations on the portion of the Ewald sphere that is covered by the experiment.[3] It is limited by $\lambda/2(n_i+n_d)$ for configurations in which the incident waves propagate in a medium of refractive index n_i while the diffracted waves propagate in a medium of refractive index n_d.[3]

However, the Born approximation restricts the field of application of these imaging techniques to weakly scattering objects whose dielectric contrast with the surrounding medium does not exceed 0.1, typically immersed biological samples. In particular, it cannot be used for imaging manufactured nanostructures or integrated circuits, where the dielectric contrast can reach several unities. Developing reconstruction procedures that account for multiple scattering, in the framework of TIRT, is thus mandatory for a wide domain of applications. It is all the more interesting in that it has been shown recently, in a classical optical tomography configuration, that the presence of multiple scattering permits one to improve the resolution limit beyond that classically foreseen with the study of the Ewald sphere.[11,12]

In this paper, we simulate accurately a TIRT experiment, and we stress the role of the interface and of the multiple scattering. We propose a full-vectorial nonlinear inversion method, and we investigate its power of resolution with respect to the nature—propagative, evanescent, *s*-polarized (TE polarization), *p*-polarized (TM polarization)—of the illuminations. We compare our reconstruction procedure with a linear inversion technique based on the renormalized Born approximation. Last, we

1084-7529/05/091889-9/$15.00

show that the robustness of the reconstruction with respect to noise can be significantly increased by using both propagative and evanescent wave illumination beams.

2. FORMULATION OF THE FORWARD SCATTERING PROBLEM

The coupled dipole method (CDM) was introduced by Purcell and Pennypacker in 1973 to study the scattering of light by nonspherical dielectric grains in free space.[13] In the configuration presented in this article, the objects are deposited on a flat dielectric substrate, but the principle stays the same. The objects under study are represented by a cubic array of N polarizable subunits, and the local field at each subunit of discretization is expressed with the following self-consistent equation:

$$\mathbf{E}(\mathbf{r}_i) = \mathbf{E}^{\mathrm{inc}}(\mathbf{r}_i) + \sum_{j=1, j\neq i}^{N} \ddot{\mathbf{T}}(\mathbf{r}_i, \mathbf{r}_j)\alpha(\mathbf{r}_j)\mathbf{E}(\mathbf{r}_j) + \sum_{j=1}^{N} \ddot{\mathbf{S}}(\mathbf{r}_i, \mathbf{r}_j)\alpha(\mathbf{r}_j)\mathbf{E}(\mathbf{r}_j), \quad (1)$$

where $\mathbf{E}^{\mathrm{inc}}(\mathbf{r}_i)$ denotes the incident field at the position $\mathbf{r}_i$. The quantity $\alpha(\mathbf{r}_j)$ represents the polarizability of the subunit j. According to the Clausius–Mossotti expression, the polarizability distribution α can be written as

$$\alpha(\mathbf{r}_j) = \frac{3d^3}{4\pi}\frac{\varepsilon(\mathbf{r}_j) - 1}{\varepsilon(\mathbf{r}_j) + 2}, \quad (2)$$

where d is the spacing of the lattice discretization and $\varepsilon(\mathbf{r}_j)$ is the relative permittivity of the object. In Eq. (2), the radiative reaction term is not taken into account in the expression of the polarizability,[14] the weak form of the CDM being accurate enough for the present study.[15] $\ddot{\mathbf{T}}$ is the field linear response to a dipole in free space, also called the free-space field susceptibility (see Appendix A). $\ddot{\mathbf{S}}$ is the field linear response to a dipole in the presence of a substrate, also called the surface field susceptibility.[16] The elements of this tensor are reported in Appendix B. Once the linear system represented by Eq. (1) is solved, the scattered field in the far-field zone, $\mathbf{E}^{\mathrm{d}}(\mathbf{r})$, can be computed at an arbitrary position $\mathbf{r}$ with

$$\mathbf{E}^{\mathrm{d}}(\mathbf{r}) = \sum_{j=1}^{N} [\ddot{\mathbf{T}}^{\mathrm{d}}(\mathbf{r}, \mathbf{r}_j) + \ddot{\mathbf{S}}^{\mathrm{d}}(\mathbf{r}, \mathbf{r}_j)]\alpha(\mathbf{r}_j)\mathbf{E}(\mathbf{r}_j). \quad (3)$$

$\ddot{\mathbf{T}}^{\mathrm{d}}$ is the field linear response of a dipole in the far field, and hence it corresponds to the term that decays as $1/|\mathbf{r} - \mathbf{r}_j|$ in the expression of $\ddot{\mathbf{T}}$. The surface field susceptibility $\ddot{\mathbf{S}}^{\mathrm{d}}$ is the field linear response to a dipole in the presence of a substrate when the observation is in the far field zone. In that case, the tensor can be written in a simple analytical form that can be computed rapidly. The expression of $\ddot{\mathbf{S}}^{\mathrm{d}}$ is given in Appendix C.

The self-consistent equation (1) can be rewritten in a more condensed form as

$$\mathbf{E} = \mathbf{E}^{\mathrm{inc}} + \bar{\bar{\mathbf{A}}}\mathbf{p}, \quad (4)$$

where $\bar{\bar{\mathbf{A}}}$ is a square matrix of size $3N \times 3N$ and contains all the tensors $\ddot{\mathbf{G}}(\mathbf{r}_i, \mathbf{r}_j) = \ddot{\mathbf{S}}(\mathbf{r}_i, \mathbf{r}_j) + \ddot{\mathbf{T}}(\mathbf{r}_i, \mathbf{r}_j)$. We have

$$\mathbf{E} = [E_x(\mathbf{r}_1), E_y(\mathbf{r}_1), E_z(\mathbf{r}_1), \ldots, E_z(\mathbf{r}_N)],$$

$$\mathbf{E}^{\mathrm{inc}} = [E_x^{\mathrm{inc}}(\mathbf{r}_1), E_y^{\mathrm{inc}}(\mathbf{r}_1), E_z^{\mathrm{inc}}(\mathbf{r}_1), \ldots, E_z^{\mathrm{inc}}(\mathbf{r}_N)],$$

$$\mathbf{p} = [p_x(\mathbf{r}_1), p_y(\mathbf{r}_1), p_z(\mathbf{r}_1), \ldots, p_z(\mathbf{r}_N)],$$

where $\mathbf{E}$ and $\mathbf{E}^{\mathrm{inc}}$ denote the local field and the incident field, respectively. The dipole moment $\mathbf{p}$ is related to the local electric field through $\mathbf{p}(\mathbf{r}_i) = \alpha(\mathbf{r}_i)\mathbf{E}(\mathbf{r}_i)$. Calculating rigorously the local field (4) is time-consuming, especially for a large number of subunits. Hence it is advantageous to first check the validity of the renormalized Born approximation

$$\mathbf{E} \approx \mathbf{E}^{\mathrm{inc}}. \quad (5)$$

In a TIRT experiment, the scattered field is collected at M observation points for L successive illuminations. Let $\mathbf{E}_l^{\mathrm{d}}$ be the scattered field corresponding to the lth illumination; then we can rewrite the far-field equation (3) in the following condensed form:

$$\mathbf{E}_l^{\mathrm{d}} = \bar{\bar{\mathbf{B}}}\mathbf{p}_l, \quad (6)$$

where $l = 1, \ldots, L$ and $\bar{\bar{\mathbf{B}}}$ is a matrix of size $3M \times 3N$. The matrix $\bar{\bar{\mathbf{B}}}$ contains the tensors $\ddot{\mathbf{G}}^{\mathrm{d}}(\mathbf{r}_k, \mathbf{r}_j) = \ddot{\mathbf{T}}^{\mathrm{d}}(\mathbf{r}_k, \mathbf{r}_j) + \ddot{\mathbf{S}}^{\mathrm{d}}(\mathbf{r}_k, \mathbf{r}_j)$, where $\mathbf{r}_j$, $j = 1, \ldots, N$, denotes a point in the discretized object and $\mathbf{r}_k$, $k = 1, \ldots, M$, is an observation point. Note that $\bar{\bar{\mathbf{B}}}$ does not depend on the angle of incidence.

3. FORMULATION OF THE INVERSE SCATTERING PROBLEM

Most reconstruction procedures proposed in the framework of three-dimensional optical tomography have been developed under the Rytov or the Born approximation. In this case, the amplitude of the plane wave with wave vector $\mathbf{k}_{\mathrm{d}}$, diffracted by an object illuminated by a plane wave with wave vector $\mathbf{k}_{\mathrm{inc}}$, is proportional to the Fourier transform of the dielectric contrast $\varepsilon(\mathbf{r}) - 1$ taken at $\mathbf{k}_{\mathrm{d}} - \mathbf{k}_{\mathrm{inc}}$. Thus, if the Fourier space is accurately described by taking a sufficient number of incident and observation angles, it is possible to obtain the map of permittivity of the object by performing a three-dimensional inverse Fourier transform of the diffracted field.[3,10] However, in general, the set of measurements and illuminations is discrete and limited, and there are missing cones in the Fourier space representation. When the Born approximation is assumed, Eq. (6) is linear with respect to the polarizability distribution α. In this case, the incomplete linear system linking the permittivity to the measured far field can be solved in the least-mean-squares sense by using backpropagation algorithms,[4] conjugate gradient techniques,[17] or singular value decomposition.[5,9,18] Note that these techniques require the assumption that the unknown object is entirely confined in a bounded box (test

domain or domain of investigation). This *a priori* information can be used to increase the resolution of the inversion.

To avoid the Born approximation, several nonlinear reconstruction procedures such as the conjugate gradient, modified gradient, and hybrid methods[19–21] have been developed, especially in the microwave domain. In these iterative methods, the field in the scattering domain Ω is no longer assumed to be the incident field. The modified gradient method consists in updating simultaneously the contrast of permittivity as well as the total field inside the investigating domain Ω by minimizing a cost functional involving the residual errors of both Eqs. (4) and (6). In the conjugate gradient method, the total field inside Ω is considered at each iteration step as a fixed solution of Eq. (4) for the best available estimation of the contrast permittivity, and the contrast permittivity is determined by minimizing a cost functional involving the sole residual error of Eq. (6). The hybrid method combines ideas of the two approaches mentioned above. Due to their computational cost, very few have been extended to the vectorial three-dimensional case. Recently, it has been proposed to reconstruct the induced dipoles, $\mathbf{p}(\mathbf{r})=\alpha(\mathbf{r})\mathbf{E}(\mathbf{r})$ in the test domain, by minimizing a cost functional involving the linear far-field equation (6), then calculating the field inside the box with Eq. (4), and deducing the permittivity through the polarizability. With adequate postprocessing, this technique led to satisfactory results for objects with a moderate dielectric constant.[22] In a more advanced method, namely the contrast source inversion method,[23,24] the induced dipoles are reconstructed iteratively by minimizing at each iteration step a cost functional involving both the far-field equation (6) and the near-field equation (4). In the present algorithm, the polarizability in the test domain, $\alpha(\mathbf{r})$, is modified so as to minimize a cost functional involving Eq. (6). At each step of the iterative procedure, the local field is obtained by solving Eq. (4) for the available estimation of the polarizability. In the present section, we briefly present this nonlinear reconstruction procedure, extended to the stratified case.

The geometry of the problem is depicted in Fig. 1. The object under test is assumed to be confined in an investigating domain $\Omega\subset\mathbb{R}^3$ and illuminated successively by $l=1,\ldots,L$ electromagnetic excitations $\mathbf{E}^{\text{inc}}_{l=1,\ldots,L}$. For each excitation l, the scattered field $\mathbf{f}_l$ is measured on a surface Γ at M points and located outside the investigating domain Ω. The inverse scattering problem is stated as finding the permittivity distribution ε inside the investigating area Ω such that the associated scattered field matches the measured field $\mathbf{f}_{l=1,\ldots,L}$.

The sequence $\{\alpha_n\}$ is built up according to the following recursive relation:

$$\alpha_n=\alpha_{n-1}+a_n d_n, \tag{7}$$

where the updated polarizability α_n is deduced from the previous one, α_{n-1}, by adding a correction $a_n d_n$. This correction is composed of two terms: a scalar weight a_n and an updating direction d_n. Once the updating direction d_n is found (this step will be specified later in the paper), the scalar weight a_n is determined by minimizing the cost functional $\mathcal{F}_n(\alpha_n)$ involving the residual error $\mathbf{h}_{l,n}$ on the scattered field computed from observation equation (6):

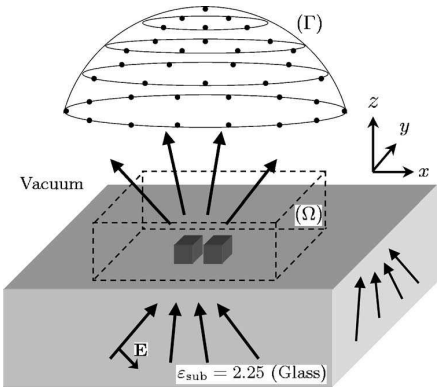

Fig. 1. Illumination and detection configuration of the TIRT experiment. The observation points are regularly placed on the half-sphere Γ (with a radius of 400λ). The illumination is as represented by the arrows, corresponding to a plane wave propagating toward the positive values of z. For the TIRT experiments, the authors took as illumination 16 plane waves in both the planes (x,z) and (y,z), either in p or s polarization. The angle between the incident wave vector and the z axis ranges over -80 to 80 deg.

$$\mathbf{h}_{l,n}=\mathbf{f}_l-\bar{\bar{\mathbf{B}}}\alpha_n\mathbf{E}_{l,n}, \tag{8}$$

with $\mathbf{E}_{l,n}$ being the total electric field that would be present in Ω if the polarizability distribution were α_{n-1}, i.e., solution of the forward problem with α_{n-1}. This field can be written symbolically from Eq. (4) as

$$\mathbf{E}_{n,l}=[\bar{\bar{\mathbf{I}}}-\bar{\bar{\mathbf{A}}}\alpha_{n-1}]^{-1}\mathbf{E}^{\text{inc}}_l, \tag{9}$$

with $\bar{\bar{\mathbf{I}}}$ being the identity matrix.

The cost functional $\mathcal{F}_n(\alpha_n)$ mentioned above that is minimized at each iteration step reads as

$$\mathcal{F}_n(\alpha_n)=\frac{\sum_{l=1}^{L}\|\mathbf{h}_{l,n}\|^2_\Gamma}{\sum_{l=1}^{L}\|\mathbf{f}_l\|^2_\Gamma}=W_\Gamma\sum_{l=1}^{L}\|\mathbf{h}_{l,n}\|^2_\Gamma, \tag{10}$$

where the subscript Γ is included in the norm $\|\cdot\|$ and later the inner product $\langle\cdot|\cdot\rangle$ in L^2 to indicate the domain of integration.

Note that substituting the expression of the polarizability α_n derived from Eq. (7) into Eq. (10) leads to a polynomial expression with respect to the scalar coefficient a_n. Thus the minimization of the cost functional $\mathcal{F}_n(\alpha_n)$ is reduced to the minimization of a simple cost function $\mathcal{F}_n(\alpha_n)$. Moreover, for the particular case of a dielectric material, i.e., the polarizability α is real, the cost function $\mathcal{F}_n(a_n)$ takes the following form:

$$\mathcal{F}_n(a_n)=W_\Gamma\sum_{l=1}^{L}(\|\mathbf{h}_{l,n-1}\|^2_\Gamma+a_n^2\|\bar{\bar{\mathbf{B}}}d_n\mathbf{E}_{l,n}\|^2_\Gamma - 2a_n\,\text{Re}\langle\mathbf{h}_{l,n-1}|\bar{\bar{\mathbf{B}}}d_n\mathbf{E}_{l,n}\rangle_\Gamma). \tag{11}$$

In this case, the unique minimum of $\mathcal{F}_n(a_n)$ is reached for

$$a_n = \frac{\sum_{l=1}^{L} \mathrm{Re}\langle \mathbf{h}_{l,n-1} | \bar{\bar{\mathbf{B}}} d_n \mathbf{E}_{l,n} \rangle_\Gamma}{\sum_{l=1}^{L} \| \bar{\bar{\mathbf{B}}} d_n \mathbf{E}_{l,n} \|_\Gamma^2}. \quad (12)$$

As updating direction d_n, the authors take the Polak–Ribière conjugate gradient direction

$$d_n = g_{n;\alpha} + \gamma_n d_{n-1}, \quad (13)$$

where g_n is the gradient of the cost functional $\mathcal{F}_n$ with respect to the polarizability assuming that the total fields $\mathbf{E}_l$ do not change.

$$g_{n;\alpha} = -W_\Gamma \sum_{l=1}^{L} \mathbf{E}_{l,n}^* \cdot \bar{\bar{\mathbf{B}}}^\dagger \mathbf{h}_{l,n-1}, \quad (14)$$

in which $\mathbf{u}^*$ denotes the complex conjugate of $\mathbf{u}$ and $\bar{\bar{\mathbf{B}}}^\dagger$ represents the transpose complex conjugate matrix of the matrix $\bar{\bar{\mathbf{B}}}$.

The scalar coefficient γ_n is defined as in the Polak–Ribière conjugate gradient method[25]:

$$\gamma_n = \frac{\langle g_{n;\alpha} | g_{n;\alpha} - g_{n-1;\alpha} \rangle_\Gamma}{\| g_{n-1;\alpha} \|_\Gamma^2}. \quad (15)$$

To complete the inverse scheme, we need to specify the initial guess. As initial estimate for α_0, the authors take the estimate obtained by the backpropagation procedure. This technique is described in detail for the two-dimensional problem in Refs. 26–28. The extension to the three-dimensional problem is described in Appendix D.

4. NUMERICAL EXPERIMENTS

We check the performance of the inverse procedure on synthetic data by simulating a TIRT experiment with the CDM. We consider two cubes of side $a=\lambda/4$, of relative permittivity 2.25, separated by a distance $c=\lambda/10$, deposited on a semi-infinite medium of relative permittivity $\varepsilon_s=2.25$ (as depicted in Fig. 1). The superstrate is vacuum, while the substrate is made of glass. The object is illuminated by 16 plane waves coming from the substrate: eight plane waves in the (x,z) plane and eight plane waves in the (y,z) plane. The plane waves can be p or s polarized. Let θ_l^{inc} be the angle of incidence with respect to the z axis corresponding to the lth illumination. The amplitude and phase of the scattered fields are detected at $M=65$ points regularly distributed on a half-sphere Γ (see Fig. 1). The radius of the sphere is 400λ, so that only far-field component data are considered. The azimuthal angle of observation, θ, defined as the angle between the diffracted wave vector and the z axis, ranges from -80 to 80 deg. In all examples, the synthetic data are computed with a mesh size of $d=\lambda/40$, which differs from the one used in the inversion, $d=\lambda/20$. In all reported results, the investigation domain is a box of size $1.25\lambda \times 0.75\lambda \times 0.6\lambda$ surrounding the cubes, except in Fig. 5, where the size of the box is $1.25\lambda \times 0.75\lambda \times 1.2\lambda$. We display the map of the reconstructed relative permittivity distribution after enough iterations for the cost function to reach a plateau. During the minimization process, the value of the relative permittivity was enforced not to exceed 2.25; thus the convergence was obtained within 100 iterations.

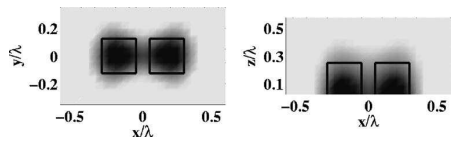

Fig. 2. Left side: map of the relative permittivity in the plane (x,y) just above the substrate, i.e., $z=\lambda/40$. Right side: map of the relative permittivity in the plane (x,z) for $y=0$. We have $a=\lambda/4$, $c=\lambda/10$, $\varepsilon_s=2.25$, $\theta^{\mathrm{inc}} \in [-80,80]$ deg, and p-polarized incident waves.

In Fig. 2, we plot the map of relative permittivity obtained with the nonlinear inversion procedure scheme. The left side corresponds to the map of the relative permittivity in the plane (x,y) just above the substrate, i.e., at $z=\lambda/40$, and the right side corresponds to the map of the relative permittivity in the plane (x,z) for $y=0$. The incident field is p polarized, and the objects are illuminated with both propagative and evanescent waves: $\theta^{\mathrm{inc}} \in [-80,-80]$ deg. Note that, except for Fig. 6, we consider only p-polarized illuminations. One can see that the two objects are perfectly resolved and that the permittivity level saturates at 2.25 inside the cubes. The map of permittivity displayed in Fig. 2, obtained with the nonlinear algorithm, without any noise on the synthetic data and in a "complete" configuration, with evanescent and propagative illuminations, can be considered a reference for all the following reconstructions.

A. Influence of the Substrate

In many numerical simulations of TIRT,[5,9] the object is assumed to be immersed in a homogeneous medium and illuminated by evanescent waves. Yet, the generation of an evanescent wave necessitates the presence of an interface close to the object. Hence this approach amounts to neglecting the influence of the interface on the field scattered by the object. The main advantage of this assumption is that, the free-space susceptibility tensor being a convolution operator with a simple analytical formulation in the direct space, the calculations are greatly simplified in the inversion procedure. Thus it is worth comparing the reconstructed maps of permittivity obtained by first neglecting and then taking into account the interface in the inversion procedure. In Fig. 3(a), we neglect the interface in both the near- and far-field equations (4) and (6), respectively, that are solved at each iteration of the reconstruction algorithm. This is done by suppressing the susceptibility tensor of the interface, i.e., $\vec{\vec{\mathbf{S}}}^{\mathrm{d}}=\vec{\vec{\mathbf{S}}}=0$. We observe that the image is strongly deteriorated as compared with Fig. 2, and the two cubes are not resolved anymore. In Fig. 3(b), we neglect the susceptibility tensor of the interface in the near-field calculations only ($\vec{\vec{\mathbf{S}}}=0$). The reconstruction appears better than that in Fig. 3(a) but still less accurate than that obtained in Fig. 2. These numerical simulations show that accounting for the interface is mandatory, especially for the far-field calculations. This can be explained rather easily by comparing the field radiated by a dipole in free space with that radiated by a

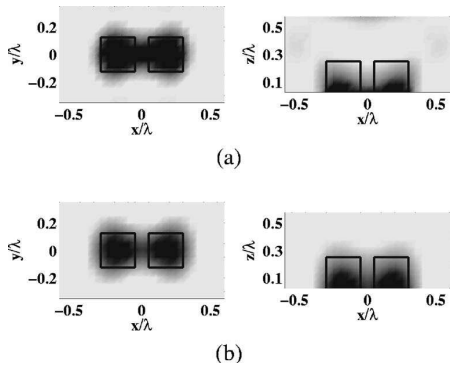

Fig. 3. Influence of the interface in the inverse scattering problem: (a) map of the relative permittivity when the interaction between the objects and the substrate is not taken into account ($\vec{\mathbf{S}}^{d}=\vec{\mathbf{S}}=0$), (b) map of the relative permittivity when the substrate is taken into account only in the far-field zone ($\vec{\mathbf{S}}=0$).

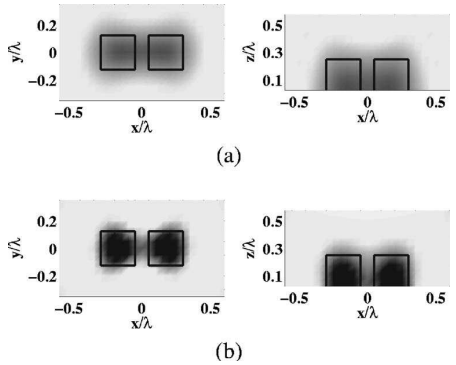

Fig. 4. Influence of the illuminations: (a) map of the relative permittivity with only propagative wave illuminations ($\theta^{inc}\in[-40,40]$ deg), (b) same as (a) but with evanescent wave illuminations ($\theta_i^{inc}\in[-80,-43]\cup[80,43]$ deg).

dipole placed in the vicinity of a plane interface. In the first case, the scattered far field radiated in the plane normal to the polarization of the dipole is constant whatever the direction of observation. In the second case, it tends to zero at grazing angles. Thus, accounting for the interface is most important for accurate modeling of the scattered far field. On the other hand, the error caused by neglecting the multiple scattering between the object and the interface in the evaluation of the field inside the object can be overlooked, in a first approximation, when both the diopter and the sample are dielectric with moderate permittivities. The advantage of this approximation is that solving the near-field equation (4) with the free-space susceptibility tensor yields an important time gain due to the convolution properties of the operator.[29]

B. Influence of Evanescent Illumination

We show in Figs. 4(a) and 4(b) the reconstructed maps of permittivity obtained when the incident angles belong to $[-40,40]$ and $[-80,43]\cup[43,80]$ deg, respectively. When the objects are illuminated by propagative waves only, it is impossible to distinguish the two cubes. On the contrary, if evanescent waves are used, one obtains an accurate reconstruction of the target, with sharp edges. Indeed, the transverse resolution is better the higher the spatial frequencies in the (x,y) plane of the incident plane waves.[9] When propagative waves are solely used, the horizontal components of the incident wave vectors are bounded by k_0, while they reach nk_0, where n is the refractive index of the prism, in the evanescent illumination configuration.

Figure 5 checks the influence of the position of the objects with respect to the interface in a complete illumination configuration $\theta_{inc}\in[-80,80]$ deg. The cube centers are placed 0.6λ above the prism. We observe that the reconstructed map of permittivity is close to that obtained when only propagative waves are used. Indeed, due to the exponential decay of the incident evanescent waves along the z axis, the far field scattered by the object when it is illuminated by an evanescent wave is negligible as compared with that scattered by the object when it is illuminated by a propagative wave. As a result, the weight of the evanescent illuminations in the cost functional is insufficient to elicit new information as compared with that given by propagative waves alone.

C. Influence of the Polarization

In Fig. 6, we plot the map of permittivity obtained under the complete illumination configuration but with s-polarized plane waves. The reconstructed image is close to that obtained with p-polarized waves (Fig. 2), although we observe that the edges are less accurately defined and the permittivity levels inside the cubes do not saturate in the same way. The p-polarized illuminations yield more accurate reconstructions than the s-polarized ones. This conclusion is not surprising inasmuch as the modulus of the incident evanescent waves at the surface of the prism is greater in p polarization than in s polarization. The weight of the evanescent illuminations in the cost functional being smaller in s polarization than in p polarization, the high-frequency features of the object are less defined.

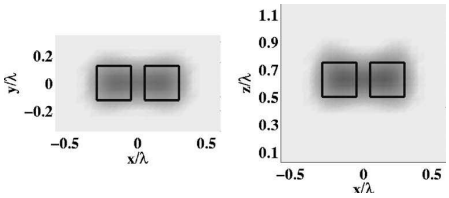

Fig. 5. Influence of the position of the sample with respect to the interface. This figure is the same as Fig. 2, except that the centers of the cubes are located at $z\approx 0.6\lambda$ from the interface.

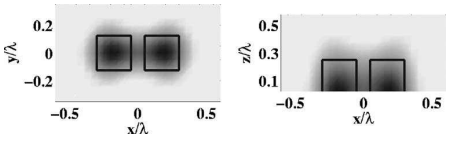

Fig. 6. Reconstruction of the permittivity using s-polarized wave illumination. The parameters are the same as those for Fig. 2.

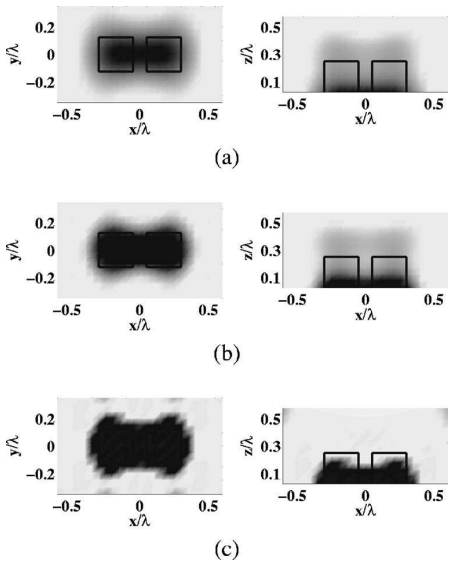

Fig. 7. Map of the relative permittivity in using the renormalized Born approximation: (a) with only propagative waves ($\theta^{\mathrm{inc}} \in [-40, 40]$ deg), (b) with both propagative and evanescent waves ($\theta^{\mathrm{inc}} \in [-80, 80]$ deg), (c) with only evanescent waves ($\theta_l^{\mathrm{inc}} \in [-80, -43] \cup [80, 43]$ deg).

It is worth noting that one could enhance the high-frequency information by increasing artificially the weight of the far-field data stemming from the evanescent illuminations in the cost function. This remark holds also for the experiment depicted in Fig. 5. However, this technique can be applied only if the signal-to-noise ratio is high enough for the data obtained with evanescent illuminations to be meaningful.

D. Using the Renormalized Born Approximation

In this subsection, we present reconstructions obtained with a linear inversion technique based on the renormalized Born approximation. The latter consists in replacing the local near field given by Eq. (4) by the incident one. It is more accurate than the classical Born approximation, since it accounts for the static depolarization that occurs inside any dielectric, as shown in Appendix A. Under this approximation, one does not need to solve Eq. (4), and the computation time is greatly reduced. Note that, bearing in mind the remarks made in Subsection 4.A, the far-field equation (3) is calculated with the tensor of susceptibility that accounts for the interface. We observe in Fig. 7 that, whatever the incident illuminations (propagative, evanescent, or both), the reconstructed maps of permittivity do not permit the resolution of the two cubes, and the permittivity is overestimated close to the interface. This last point can be explained by noting that the local field inside a small sphere increases when the distance between the sphere and the interface decreases.[30] The renormalized Born approximation thus underestimates the field inside the objects, especially close to the interface. The inversion procedure compensates this error by overestimating the polarizability of the dipoles close to the interface.

E. Robustness with Respect to Noise

In this subsection, we analyze the robustness of our inversion scheme when an uncorrelated noise is added to the scattered field. This noise can be related to the detector background noise or to uncontrolled dust scattering. We corrupt each component of the scattered field as

$$\mathrm{Re}[\tilde{f}_{l;v}(\mathbf{r}_k)] = \mathrm{Re}[f_{l;v}(\mathbf{r}_k)] + uA_r\xi_{l;v}, \tag{16}$$

$$\mathrm{Im}[\tilde{f}_{l;v}(\mathbf{r}_k)] = \mathrm{Im}[f_{l;v}(\mathbf{r}_k)] + uA_i\eta_{l;v}, \tag{17}$$

where v stands for the component along x, y, or z. $\xi_{l;v}$ and $\eta_{l;v}$ are random numbers with uniform probability density in $[-1, 1]$, and u is a real number smaller than unity that monitors the noise level. $A_r = \max[\mathrm{Re}(f_{l;v})] - \min[\mathrm{Re}(f_{l;v})]$, and $A_i = \max[\mathrm{Im}(f_{l;v})] - \min[\mathrm{Im}(f_{l;v})]$. Figure 8 shows the effect of the noise on the reconstructed maps of relative permittivity when the noise level u is equal to 20% for different configurations of illumination. Figure 8(a) shows the reconstruction when only evanescent waves are used, i.e., $\theta_l^{\mathrm{inc}} \in [-80, -43] \cup [80, 43]$ deg. We observe that the reconstruction is relatively deteriorated by the presence of noise. This can be due to the fact that, in this configuration, the scattered far field obtained for the most evanescent incident waves, $\theta_{\mathrm{inc}} = 80$ deg, is totally blurred by the noise, whose level is related to the most important far-field intensity, i.e., that obtained for $\theta_{\mathrm{inc}} = 43$ deg. Thus, although these data do not reveal any information, their intensity becomes comparable with that obtained with moderate evanescent incident waves and they strongly perturb the reconstruction. In Fig. 8(b), we plot the map of permittivity obtained from noisy data in a complete configuration, containing both evanescent and propagative waves. Through the propagative waves, we have added low-spatial-frequency data that are less deteriorated by the noise and have suppressed several incident evanescent waves. We observe that the reconstruction becomes less sensitive to the noise and that, most important, the superresolution stemming from the use of evanescent illumination is still present. Hence it seems that using propagative together with evanescent wave illuminations permits one to increase the robustness to noise of

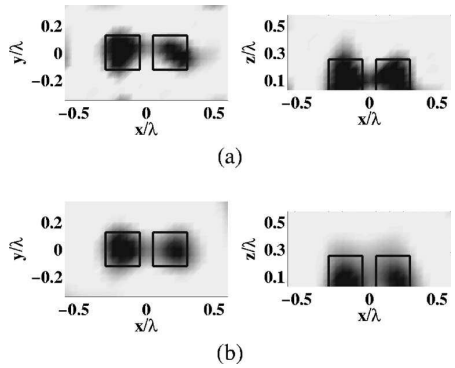

Fig. 8. Robustness of the inverse scattering algorithm with respect to uncorrelated noise: (a) map of the relative permittivity using only evanescent wave illuminations ($\theta_l^{\mathrm{inc}} \in [-80, -43] \cup [80, 43]$ deg), (b) same as (a) but with both evanescent and propagative wave illuminations ($\theta^{\mathrm{inc}} \in [-80, 80]$ deg).

the inversion procedure while retaining the superresolution.

5. CONCLUSION

We have simulated a realistic total internal reflection tomography (TIRT) experiment. We have proposed a full-vectorial nonlinear inversion scheme to retrieve the map of permittivity of the objects from the scattered far field. We have shown that it is possible to resolve two cubes of width $\lambda/4$ separated by $\lambda/10$ deposited on a prism made of glass ($\varepsilon=2.25$). We have investigated the power of resolution of our reconstructions with respect to the incident solid angle, the polarization, and the distance between the objects and the interface. We have presented a linear inversion method based on the renormalized Born approximation and pointed out that the presence of the interface restricts considerably the field of application of such a technique. Last, we have checked the influence of noise on the reconstructions. We have shown that adding propagative incident waves, together with evanescent ones, increases the robustness of our inversion procedure. To ameliorate the spatial resolution of the TIRT, it is necessary to generate evanescent waves with a large tangential wave vector. Unfortunately, in optics, the highest refractive index of the prism is about 2. Thus the resolution of the TIRT will be two times better than that of a standard tomography technique. To go further, one can modify the substrate so as to support high-frequency evanescent waves such as thin-film surface plasmons. Work in this direction is in progress.

APPENDIX A: BORN APPROXIMATION AND RENORMALIZED BORN APPROXIMATION

For the sake of simplicity, we explain the difference between the Born approximation and the renormalized Born approximation for an object in free space. Adding an interface does not change the explanation. The self-consistent electric field inside the object can be obtained from the following integral equation:

$$\mathbf{E}^{\mathrm{m}}(\mathbf{r}) = \mathbf{E}^{\mathrm{inc}}(\mathbf{r}) + \int_V \overleftrightarrow{\mathbf{T}}(\mathbf{r},\mathbf{r}')\chi(\mathbf{r}')\mathbf{E}^{\mathrm{m}}(\mathbf{r}')\mathrm{d}\mathbf{r}', \qquad \text{(A1)}$$

where $\mathbf{E}^{\mathrm{m}}(\mathbf{r})$ denotes the macroscopic field inside the object and $\chi(\mathbf{r}')=[\varepsilon(\mathbf{r}')-1]/(4\pi)$ is the linear susceptibility of the object. $\overleftrightarrow{\mathbf{T}}$ is the free-space susceptibility tensor,[31] given by

$$\overleftrightarrow{\mathbf{T}}(\mathbf{r},\mathbf{r}') = \exp(ik_0R)\left[\left(3\frac{\mathbf{R}\otimes\mathbf{R}}{R^2}-\overleftrightarrow{\mathbf{I}}\right)\left(\frac{1}{R^3}-\frac{ik_0}{R^2}\right) + \left(\overleftrightarrow{\mathbf{I}}-\frac{\mathbf{R}\otimes\mathbf{R}}{R^2}\right)\frac{k_0^2}{R}\right] - \frac{4\pi}{3}\overleftrightarrow{\mathbf{I}}\delta(\mathbf{R}), \qquad \text{(A2)}$$

where $\mathbf{R}=\mathbf{r}-\mathbf{r}'$, $R=|\mathbf{R}|$, k_0 is the free-space wave number, and $\overleftrightarrow{\mathbf{I}}$ is the unit tensor. To solve Eq. (A1), we discretize the object into N subunits, arranged on a cubic lattice. The size d of the elementary cell is small enough that the macroscopic field can be considered constant over it (typically, the cell side is one tenth of the wavelength in the object). The discretized Eq. (A1) reads as

$$\mathbf{E}^{\mathrm{m}}(\mathbf{r}_i) = \mathbf{E}^{\mathrm{inc}}(\mathbf{r}_i) + \sum_{j=1,j\neq i}^{N} \overleftrightarrow{\mathbf{T}}(\mathbf{r}_i,\mathbf{r}_j)\chi(\mathbf{r}_j)d^3\mathbf{E}^{\mathrm{m}}(\mathbf{r}_j) - \frac{\varepsilon(\mathbf{r}_i)-1}{3}\mathbf{E}^{\mathrm{m}}(\mathbf{r}_i). \qquad \text{(A3)}$$

If we factorize the terms corresponding to index i, we get an equation for the local field,

$$\mathbf{E}(\mathbf{r}_i) = \mathbf{E}^{\mathrm{inc}}(\mathbf{r}_i) + \sum_{j=1,j\neq i}^{N} \overleftrightarrow{\mathbf{T}}(\mathbf{r}_i,\mathbf{r}_j)\alpha(\mathbf{r}_j)\mathbf{E}(\mathbf{r}_j), \qquad \text{(A4)}$$

where the macroscopic field and the local field are linked by the relation

$$\frac{\varepsilon+2}{3}\mathbf{E}^{\mathrm{m}}(\mathbf{r}_i) = \mathbf{E}(\mathbf{r}_i). \qquad \text{(A5)}$$

Equation (A4) is the usual form of the CDM introduced by Purcell and Pennypacker.[13]

The so-called Born approximation consists in the hypothesis that the macroscopic field inside the object is close to the incident field, i.e., Eq. (A1) is reduced to $\mathbf{E}^{\mathrm{m}}(\mathbf{r}_i)=\mathbf{E}^{\mathrm{inc}}(\mathbf{r}_i)$. The renormalized Born approximation amounts to assimilating the local field inside the object to the incident field; hence Eq. (A4) is reduced to $\mathbf{E}(\mathbf{r}_i) \approx \mathbf{E}^{\mathrm{inc}}(\mathbf{r}_i)$. In this case, the relation between the macroscopic field and the incident field reads as

$$\mathbf{E}^{\mathrm{m}}(\mathbf{r}_i) \approx \frac{3}{\varepsilon+2}\mathbf{E}^{\mathrm{inc}}(\mathbf{r}_i). \qquad \text{(A6)}$$

This approximation is thus different from the classical Born approximation. It is more accurate than the latter, especially when the dielectric contrast between the object and the surrounding medium is high.[32]

APPENDIX B: EXPRESSION OF THE SURFACE FIELD SUSCEPTIBILITY

In this appendix, we express the elements of the tensor of the surface field susceptibility $\overleftrightarrow{\mathbf{S}}$. In general, the tensor in the presence of an interface normal to the z axis is given, in Cartesian coordinates, under the Weyl development.[18] It requires the numerical calculation of a two-dimensional Fourier transform over the conjugate variables of x and y. Here we propose an alternative expression of the surface field susceptibility, in cylindrical coordinates, that necessitates a single numerical integration.

The dyadic tensor has nine components, but the symmetry of the surface suggests some relations between the elements of the tensor. Hence only four integrals are needed to derive all the elements. Let the angle φ be defined by

$$a=[(x-x_0)^2+(y-y_0)^2]^{1/2},$$

$$\sin\varphi=(x-x_0)/a,$$

$$\cos\varphi=(y-y_0)/a, \tag{B1}$$

where (x,y,z) is the position of the observation point and (x_0,y_0,z_0) the location of the dipole. Let us also define the Fresnel reflection coefficients Δ_s and Δ_p for s- and p-polarized plane or evanescent waves:

$$\Delta_p=\frac{w_1-\varepsilon_s w_0}{w_1+\varepsilon_s w_0},\qquad \Delta_s=\frac{w_1-w_0}{w_1+w_0}, \tag{B2}$$

with $w_1^2=\varepsilon_s k_0^2-u^2$ and $w_0^2=k_0^2-u^2$. u is the modulus of the wave vector parallel to the surface. $\ddot{\mathbf{S}}$ can be written as[33]

$$\ddot{\mathbf{S}}(\mathbf{r},\mathbf{r}_0)=\begin{bmatrix} I_1+\cos(2\varphi)I_2 & -\sin(2\varphi)I_2 & \sin\varphi I_3 \\ -\sin(2\varphi)I_2 & I_1-\cos(2\varphi)I_2 & \cos\varphi I_3 \\ -\sin\varphi I_3 & -\cos\varphi I_3 & I_4 \end{bmatrix}, \tag{B3}$$

with

$$I_1=\frac{i}{2}\left(-\int_0^{k_0}+\int_0^{i\infty}\right)\mathrm{d}w_0 J_0(au)\exp[iw_0(z+z_0)] \times(k_0^2\Delta_s-w_0^2\Delta_p), \tag{B4}$$

$$I_2=\frac{i}{2}\left(-\int_0^{k_0}+\int_0^{i\infty}\right)\mathrm{d}w_0 J_0(au)\exp[iw_0(z+z_0)] \times(-k_0^2\Delta_s-w_0^2\Delta_p), \tag{B5}$$

$$I_3=\left(-\int_0^{k_0}+\int_0^{i\infty}\right)\mathrm{d}w_0 J_1(au)\exp[iw_0(z+z_0)]\Delta_p w_0 u, \tag{B6}$$

$$I_4=i\left(-\int_0^{k_0}+\int_0^{i\infty}\right)\mathrm{d}w_0 J_0(au)\exp[iw_0(z+z_0)]\Delta_p u^2. \tag{B7}$$

The functions J_0, J_1, and J_2 are Bessel functions of the first kind and are zero, first, and second order, respectively. Equations (B4)–(B7) correspond to the sum of two integrals: One is evaluated over the propagative waves, and the second over the evanescent waves. When $a=0$, $\ddot{\mathbf{S}}$ becomes diagonal.

APPENDIX C: EXPRESSION IN THE FAR-FIELD ZONE OF THE SURFACE FIELD SUSCEPTIBILITY

When the observation point is in the far field, one can use the method of stationary phase[34] for computing the surface field susceptibility tensor $\ddot{\mathbf{S}}^{\mathrm{d}}$:

$$\ddot{\mathbf{S}}^{\mathrm{d}}(\mathbf{r},\mathbf{r}_0)=\frac{k_0^2}{r}\exp\{ik_0[x(x-x_0)+y(y-y_0)+z(z+z_0)]/r\} \times\begin{bmatrix} \left(\frac{xz}{r\rho}\right)^2\Delta_p'-\frac{y^2}{\rho^2}\Delta_s' & \frac{xy}{\rho^2}\left(\frac{z^2}{r^2}\Delta_p'+\Delta_s'\right) & \frac{xz}{r^2}\Delta_p' \\ \frac{xy}{\rho^2}\left(\frac{z^2}{r^2}\Delta_p'+\Delta_s'\right) & \left(\frac{yz}{r\rho}\right)^2\Delta_p'-\frac{x^2}{\rho^2}\Delta_s' & \frac{yz}{r^2}\Delta_p' \\ -\frac{xz}{r^2}\Delta_p' & -\frac{yz}{r^2}\Delta_p' & -\frac{\rho^2}{r^2}\Delta_p' \end{bmatrix}, \tag{C1}$$

with $r=(x^2+y^2+z^2)^{1/2}$ and $\rho=(x^2+y^2)^{1/2}$. The Fresnel reflection coefficients are given by

$$\Delta_p'=\frac{(\varepsilon_s r^2-\rho^2)^{1/2}-\varepsilon_s z}{(\varepsilon_s r^2-\rho^2)^{1/2}+\varepsilon_s z},\quad \Delta_s'=\frac{(\varepsilon_s r^2-\rho^2)^{1/2}-z}{(\varepsilon_s r^2-\rho^2)^{1/2}+z}. \tag{C2}$$

If $x=y=0$, then

$$\ddot{\mathbf{S}}^{\mathrm{d}}(z,z_0)=\frac{k_0^2}{z}\exp[ik_0(z+z_0)]\begin{bmatrix}\Delta_p' & 0 & 0\\ 0 & \Delta_p' & 0\\ 0 & 0 & 0\end{bmatrix}. \tag{C3}$$

The analytical form of $\ddot{\mathbf{S}}^{\mathrm{d}}$ permits a quick computation of the matrix $\bar{\bar{\mathbf{B}}}$.

APPENDIX D: BACKPROPAGATION PROCEDURE TO GENERATE AN INITIAL GUESS TO THE ITERATIVE INVERSE SCATTERING ALGORITHM

We present here the derivation of an initial guess that is used to start the iterative scheme described in Section 3. First, we determine, for each illumination l, an estimation of the dipole distribution $\mathbf{p}_l^{\mathrm{init}}$ lying in the investigating domain Ω by backpropagating the measured fields $\mathbf{f}_l$ into Ω:

$$\mathbf{p}_l^{\mathrm{init}}=\gamma_l\bar{\bar{\mathbf{B}}}^{\dagger}\mathbf{f}_l, \tag{D1}$$

where $\bar{\bar{\mathbf{B}}}^{\dagger}$ denotes the transpose complex conjugate matrix of the matrix $\bar{\bar{\mathbf{B}}}$. The scalar weight γ_l is determined by minimizing the cost function $\mathcal{M}(\gamma_l)$ describing the discrepancy between the data $\mathbf{f}_l$ and those that would be obtained with $\mathbf{p}_l^{\mathrm{init}}$:

$$\mathcal{M}(\gamma_l)=\|\mathbf{f}_l-\bar{\bar{\mathbf{B}}}\mathbf{p}_l^{\mathrm{init}}\|_{\Gamma}^2=\|\mathbf{f}_l-\gamma_l\bar{\bar{\mathbf{B}}}\bar{\bar{\mathbf{B}}}^{\dagger}\mathbf{f}_l\|_{\Gamma}^2. \tag{D2}$$

Writing down the necessary condition $\partial\mathcal{M}/\partial\gamma_l=0$ for $\mathcal{M}$ to be a minimum leads to an analytical expression of γ_l:

$$\gamma_l=\frac{\langle\bar{\bar{\mathbf{B}}}\bar{\bar{\mathbf{B}}}^{\dagger}\mathbf{f}_l|\mathbf{f}_l\rangle_{\Gamma}}{\|\bar{\bar{\mathbf{B}}}\bar{\bar{\mathbf{B}}}^{\dagger}\mathbf{f}_l\|_{\Gamma}^2}. \tag{D3}$$

Once the estimation of the dipoles is determined, an estimation of the total field $\mathbf{E}_l^{\mathrm{init}}$ in the investigating domain Ω can be derived either by assuming the Born approximation or by applying Eq. (4):

$$\mathbf{E}_l^{\text{init}} = \mathbf{E}_l^{\text{inc}} + \bar{\bar{\mathbf{A}}}\mathbf{p}_l^{\text{init}}. \tag{D4}$$

Finally, the initial guess for the polarizability distribution α^{init} at a position $\mathbf{r}$ inside Ω is deduced from $\mathbf{p}_l^{\text{init}}$ and $\mathbf{E}_l^{\text{init}}$ as follows:

$$\alpha^{\text{init}}(\mathbf{r}) = \text{Re}\left[\frac{\sum_{l=1}^{L} \mathbf{p}_l^{\text{init}}(\mathbf{r}) \cdot \mathbf{E}_l^{\text{init}^*}(\mathbf{r})}{\sum_{l=1}^{L} \|\mathbf{E}_l^{\text{init}}(\mathbf{r})\|^2}\right]. \tag{D5}$$

K. Belkebir's e-mail address is kamal.belkebir @fresnel.fr.

REFERENCES

1. M. Gustafsson, "Surpassing the lateral resolution limit by a factor of two using structured illumination microscopy," J. Microsc. **198**, 82–87 (2000).
2. N. Destouches, C. A. Guérin, M. Lequime, and H. Giovannini, "Determination of the phase of the diffracted field in the optical domain. Application to the reconstruction of surface profiles," Opt. Commun. **198**, 233–239 (2001).
3. V. Lauer, "New approach to optical diffraction tomography yielding a vector equation of diffraction tomography and a novel tomographic microscope," J. Microsc. **205**, 165–176 (2002).
4. T. Wedberg and J. Stammes, "Experimental examination of the quantitative imaging properties of optical diffraction tomography," J. Opt. Soc. Am. A **12**, 493–500 (1995).
5. D. Fischer, "Subwavelength depth resolution in near-field microscopy," Opt. Lett. **25**, 1529–1531 (2000).
6. P. So, H. Kwon, and C. Dong, "Resolution enhancement in standing-wave total-internal reflection microscopy: a point spread function engineering approach," J. Opt. Soc. Am. A **18**, 2833–2845 (2001).
7. F. de Fornel, *Evanescent Waves*, Vol. 73 of Springer Series in Optical Sciences (Springer Verlag, 2001).
8. G. Cragg and P. So, "Standing wave total-internal reflection microscopy," Opt. Lett. **25**, 46–48 (2000).
9. P. S. Carney and J. C. Schotland, "Three-dimensional total-internal reflection microscopy," Opt. Lett. **26**, 1072–1074 (2001).
10. E. Wolf, "Three-dimensional structure determination of semi-transparent objects from holographic data," Opt. Commun. **1**, 153–156 (1969).
11. K. Belkebir and A. Sentenac, "High resolution optical diffraction microscopy," J. Opt. Soc. Am. A **20**, 1223–1229 (2003).
12. P. C. Chaumet, K. Belkebir, and A. Sentenac, "Superresolution of three-dimensional optical imaging by use of evanescent waves," Opt. Lett. **29**, 2740–2742 (2004).
13. E. M. Purcell and C. R. Pennypacker, "Scattering and absorption of light by nonspherical dielectric grains," Astrophys. J. **186**, 705–714 (1973).
14. P. C. Chaumet and M. Nieto-Vesperinas, "Time-averaged total force on a dipolar sphere in an electromagnetic field," Opt. Lett. **25**, 1065–1067 (2000).
15. A. Lakhtakia, "Strong and weak forms of the method of moments and the coupled dipole method for scattering of time-harmonic electromagnetics fields," Int. J. Mod. Phys. C **3**, 583–603 (1992).
16. P. C. Chaumet, A. Sentenac, and A. Rahmani, "Coupled dipole method for scatterers with large permittivity," Phys. Rev. E **70**, 036606 (2004).
17. S. Kawata, O. Nakamura, and S. Minami, "Optical microscope tomography. I. Support constraint," J. Opt. Soc. Am. A **4**, 292–297 (1987).
18. P. S. Carney and J. C. Schotland, "Theory of total-internal-reflection tomography," J. Opt. Soc. Am. A **20**, 542–547 (2003).
19. A. G. Tijhuis, K. Belkebir, A. C. S. Litman, and B. P. de Hon, "Theoretical and computational aspects of 2-D inverse profiling," IEEE Trans. Geosci. Remote Sens. **39**, 1316–1330 (2001).
20. R. E. Kleinman and P. M. van den Berg, "A modified gradient method for two-dimensional problems in tomography," J. Comput. Appl. Math. **42**, 17–35 (1992).
21. K. Belkebir and A. G. Tijhuis, "Modified^2 gradient method and modified Born method for solving a two-dimensional inverse scattering problem," Inverse Probl. **17**, 1671–1688 (2001).
22. P. C. Chaumet, K. Belkebir, and A. Sentenac, "Three-dimensional subwavelength optical imaging using the coupled dipole method," Phys. Rev. B **69**, 245405 (2004).
23. A. Abubakar, P. M. van den Berg, and B. J. Kooij, "A conjugate gradient contrast source technique for 3D profile inversion," IEICE Trans. Electron. **E83-C**, 1864–1874 (2000).
24. A. Abubakar and P. M. van den Berg, "The contrast source inversion method for location and shape reconstructions," Inverse Probl. **18**, 495–510 (2002).
25. W. H. Press, B. P. Flannery, S. A. Teukolski, and W. T. Vetterling, *Numerical Recipes: The Art of Scientific Computing* (Cambridge U. Press, 1986).
26. K. Belkebir, S. Bonnard, F. Pezin, P. Sabouroux, and M. Saillard, "Validation of 2D inverse scattering algorithms from multi-frequency experimental data," J. Electromagn. Waves Appl. **14**, 1637–1667 (2000).
27. K. Belkebir, R. E. Kleinman, and C. Pichot, "Microwave imaging—location and shape reconstruction from multifrequency scattering data," IEEE Trans. Microwave Theory Tech. **45**, 469–476 (1997).
28. R. E. Kleinman and P. M. van den Berg, "Two-dimensional location and shape reconstruction," Radio Sci. **29**, 1157–1169 (1994).
29. J. J. Goodman, B. T. Draine, and P. J. Flatau, "Application of fast-Fourier-transform techniques to the discrete-dipole approximation," Opt. Lett. **16**, 1198–1200 (1991).
30. F. Pincemin, A. Sentenac, and J.-J. Greffet, "Near-field scattered by a dielectric rod below a metallic surface," J. Opt. Soc. Am. A **11**, 1117–1127 (1994).
31. J. D. Jackson, *Classical Electrodynamics*, 2nd ed. (Wiley, 1975).
32. T. M. Habashy, R. W. Groom, and B. R. Spies, "Beyond the Born and Rytov approximations—a nonlinear approach to electromagnetic scattering," J. Geophys. Res. [Solid Earth] **98**, 1759–1775 (1993).
33. A. Rahmani, P. C. Chaumet, F. de Fornel, and C. Girard, "Field propagator of a dressed junction: fluorescence lifetime calculations in a confined geometry," Phys. Rev. A **56**, 3245–3254 (1997).
34. M. Born and E. Wolf, *Principles of Optics* (Pergamon, 1959).

586 J. Opt. Soc. Am. A/Vol. 23, No. 3/March 2006 Belkebir *et al.*

Influence of multiple scattering on three-dimensional imaging with optical diffraction tomography

Kamal Belkebir, Patrick C. Chaumet, and Anne Sentenac

Institut Fresnel (UMR 6133), Université d'Aix-Marseille I & III, Avenue Escadrille Normandie–Niemen, F-13397 Marseille cedex 20, France

Received May 3, 2005; revised July 8, 2005; accepted August 23, 2005

Optical diffraction tomography is an imaging technique that permits retrieval of the map of permittivity of an object from its scattered far field. Most reconstruction procedures assume that single scattering is dominant so that the scattered far field is linearly linked to the permittivity. In this work, we present a nonlinear inversion method and apply it to complex three-dimensional samples. We show that multiple scattering permits one to obtain a power of resolution beyond the classical limit imposed by the use of propagative incident and diffracted waves. Moreover, we stress that our imaging method is robust with respect to correlated and uncorrelated noise. © 2006 Optical Society of America

OCIS codes: 180.6900, 110.6960, 290.3200.

1. INTRODUCTION

In an optical diffraction tomography (ODT) experiment, the unknown object is illuminated under several angles of incidence and the diffracted field is collected along many directions of observation. In contrast to optical microscopy, in which lenses are used to image the object, ODT relies entirely on a numerical procedure to retrieve the three-dimensional map of permittivity of the sample. For a long time, this technique has been limited to the study of absorbing objects whose typical length scale is much larger than the wavelength. In the short-wavelength limit, the reconstruction algorithms are based on a geometrical model of propagation similar to techniques developed in x-ray tomography, and sole intensity measurements are necessary for retrieving the three-dimensional (3D) variations of the absorption in the sample. When the features of the object of interest are of the same order as the wavelength, the physical optics approximation is no longer valid and a more precise model of the electromagnetic scattering is necessary. In this case, most inverse procedures require amplitude and phase measurements. The latter can be obtained with a phase-shifting interferometry setup, as proposed by Lauer[1] or Destouches *et al.*[2]

The inversion procedures used in ODT experiments are usually based on the Rytov or the Born approximation under which the 3D Fourier components of the 3D scatterer are obtained from the two-dimensional (2D) Fourier components of the scattered field[3] by varying the angle of the incident plane wave. The reconstruction of the map of permittivity is then performed with a simple Fourier transform. To compensate for the missing cones in the Fourier space due to the limited solid angle of collection and illumination and the discrete number of measures, reconstruction procedures using interpolation techniques, backpropagation algorithms, and least-squares minimizations have been developed.[4,5] These methods are justified when there is a linear relationship between the scattered field and the Fourier components of the permittivity, i.e., under the weak-scattering approximation.

Recently, a 3D linear inversion procedure based on the reconstruction of the induced currents in the object has been proposed to address imaging of objects with moderate dielectric contrast and size.[6] Combined with an appropriate posttreatment, it leads to the resolution of two cubes of permittivity $\varepsilon=2.25$ and of side $\lambda/4$ separated by $\lambda/4$ in the transverse plane, or $\lambda/2$ in the axial direction, with relatively few illumination and observation directions.

In this work, we consider the same experimental configuration, and we propose a nonlinear inversion scheme that takes into account the multiple-scattering effect. Although the presented inverse scheme does not use any regularization technique nor postprocessing procedure including prior information on the sample, it yields a higher resolution than that reached in the previous work of the authors.[6] In Subsection 2.A, we sketch the coupled-dipole method that is used to simulate the experiment and in Subsection 2.B we describe the inversion procedure. In Section 3, we present several reconstructions from synthetic data and investigate the axial and transverse resolution and the role of multiple scattering. We analyze the sensitivity of the reconstruction to correlated and uncorrelated noise, and we point out the ability of our technique to image complex 3D objects. In Section 4 we present our conclusions.

2. THEORY

A. Formulation of the Forward-Scattering Problem

The coupled-dipole method (CDM) was introduced by Purcell and Pennypacker in 1973 for studying the scattering of light by nonspherical, dielectric grains in free space.[7] The object under study is represented by a cubic array of N polarizable subunits. The monochromatic electromag-

1084-7529/06/030586-10/$15.00

netic field at each subunit can be expressed with the following self-consistent equation:

$$\mathbf{E}(\mathbf{r}_i) = \mathbf{E}^{\mathrm{inc}}(\mathbf{r}_i) + \sum_{j=1, j\neq i}^{N} \overleftrightarrow{\mathbf{T}}(\mathbf{r}_i, \mathbf{r}_j)\alpha(\mathbf{r}_j)\mathbf{E}(\mathbf{r}_j), \tag{1}$$

where $\mathbf{E}^{\mathrm{inc}}(\mathbf{r}_i)$ denotes the incident field at the position $\mathbf{r}_i$, i.e., the total electric field that would be observed in the absence of the scattering object. $\overleftrightarrow{\mathbf{T}}$ describes the linear response of a dipole in free space[8] and $\alpha(\mathbf{r}_j)$ is the polarizability of the subunit j. According to the Clausius–Mossotti expression,[9] the polarizability distribution α may be written as

$$\alpha(\mathbf{r}_j) = \frac{3d^3}{4\pi}\frac{\varepsilon(\mathbf{r}_j) - \varepsilon_0}{\varepsilon(\mathbf{r}_j) + 2\varepsilon_0}, \tag{2}$$

where d is the spacing of lattice discretization and $\varepsilon(\mathbf{r}_j)$ the relative permittivity of the object. The relative permittivity of the homogeneous background medium is denoted by ε_0. This expression of the polarizability corresponds to the weak form of the CDM and is accurate enough for the present study. However, in a different topic, such as optical force analysis[10–12] or extinction-cross-section modeling,[13] one needs to take into account the radiative reaction term. The material under test is assumed to be isotropic. Hence, the relative permittivity $\varepsilon(\mathbf{r}_j)$ and subsequently the polarizability are both scalars.

Once Eq. (1) is solved, the scattered field $\mathbf{E}^{\mathrm{d}}(\mathbf{r})$ at an arbitrary position $\mathbf{r}$ exterior to the object is given by

$$\mathbf{E}^{\mathrm{d}}(\mathbf{r}) = \sum_{j=1}^{N} \overleftrightarrow{\mathbf{T}}(\mathbf{r}, \mathbf{r}_j)\alpha(\mathbf{r}_j)\mathbf{E}(\mathbf{r}_j). \tag{3}$$

For the sake of simplicity Eq. (1) is rewritten in a more condensed form as

$$\mathbf{E} = \mathbf{E}^{\mathrm{inc}} + \bar{\bar{\mathbf{A}}}\mathbf{p}, \tag{4}$$

where $\bar{\bar{\mathbf{A}}}$ is a square matrix of size $3N \times 3N$ and contains all the field susceptibilities $\overleftrightarrow{\mathbf{T}}(\mathbf{r}_i, \mathbf{r}_j)$. Further

$$\mathbf{E} = [E_x(\mathbf{r}_1), E_y(\mathbf{r}_1), E_z(\mathbf{r}_1), \ldots, E_z(\mathbf{r}_N)],$$

$$\mathbf{E}^{\mathrm{inc}} = [E_x^{\mathrm{inc}}(\mathbf{r}_1), E_y^{\mathrm{inc}}(\mathbf{r}_1), E_z^{\mathrm{inc}}(\mathbf{r}_1), \ldots, E_z^{\mathrm{inc}}(\mathbf{r}_N)],$$

$$\mathbf{p} = [p_x(\mathbf{r}_1), p_y(\mathbf{r}_1), p_z(\mathbf{r}_1), \ldots, p_z(\mathbf{r}_N)],$$

where $\mathbf{E}$ and $\mathbf{E}^{\mathrm{inc}}$ denote the total and the incident electric field, respectively. The dipole moment $\mathbf{p}$ is related to the electric field as $\mathbf{p}(\mathbf{r}_i) = \alpha(\mathbf{r}_i)\mathbf{E}(\mathbf{r}_i)$.

In an ODT experiment, the scattered field is collected at M observation points for L successive illuminations. Let $\mathbf{E}_l^{\mathrm{d}}$ be the scattered field corresponding to the lth illumination. We can then rewrite the far-field Eq. (3) in the condensed form

$$\mathbf{E}_l^{\mathrm{d}} = \bar{\bar{\mathbf{B}}}\mathbf{p}_l, \tag{5}$$

where $l = 1, \ldots, L$, and $\bar{\bar{\mathbf{B}}}$ is a matrix of size $3M \times 3N$. The matrix $\bar{\bar{\mathbf{B}}}$ contains the field susceptibilities $\overleftrightarrow{\mathbf{T}}(\mathbf{r}_k, \mathbf{r}_j)$, where $\mathbf{r}_j$ denotes a point in the discretized object with $j = 1, \ldots, N$, while $\mathbf{r}_k$ is an observation point with $k = 1, \ldots, M$. Note that $\bar{\bar{\mathbf{B}}}$ does not depend on the angle of incidence.

B. Formulation of the Inverse-Scattering Problem

The geometry of the problem investigated in this paper is illustrated in Fig. 1. We assume that an unknown 3D object is entirely confined in a bounded box $\Omega \subset \mathbb{R}^3$ (test domain or an investigating domain) and illuminated successively by $l = 1, \ldots, L$ electromagnetic excitations $\mathbf{E}^{\mathrm{inc}}_{l=1,\ldots,L}$. For each excitation l, the scattered field $\mathbf{f}_l$ is measured at M points on a surface Γ that is located outside the investigating domain Ω.

The inverse-scattering problem is stated as finding the permittivity distribution ϵ inside the investigation domain Ω such that the associated scattered field matches the measured field $\mathbf{f}_{l=1,\ldots,L}$. Many accurate iterative techniques have been developed to solve this inverse problem. In these methods, starting from an initial guess, one adjusts the parameter of interest gradually by minimizing a cost functional involving the measured scattered-field data. Two main approaches can be found in the literature. In the first one,[14–17] the linearized method, the field in the test domain Ω is considered fixed. This field is the solution of the forward problem—the solution of Eq. (4)—for the best available estimation of the permittivity at each iteration step, or it is the reference field if the Born approximation is assumed.

In the second approach,[18,19] typically the modified gradient method, the field inside the test domain Ω is an un-

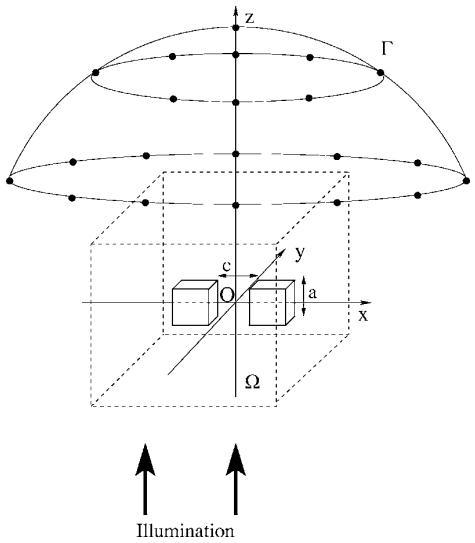

Fig. 1. Sketch of the illumination and detection configuration of the ODT experiment. The observation points are regularly placed on the half-sphere Γ (with a radius of 400 λ). The illumination is as represented by the arrows, which denote a plane wave propagating toward positive z. For the ODT experiments, the authors took as illumination 16 plane waves in both planes (x,z) and (y,z). The angle between the incident wave vector and the z axis ranges over −80° to 80°. See text for more detail.

known that is obtained, together with the permittivity, by the minimization procedure. A hybrid method[20–22] that combines the ideas from the two approaches has also been developed. All these methods deal with 2D inverse-scattering problems. In three dimensions, most techniques use a linear inversion based on the Born approximation[4,23] and are restricted to the scalar case.

Recently, a more advanced method, namely the contrast-source-inversion (CSI) method,[24] has been introduced for solving the full vectorial 3D problem.[25,26] In the CSI method the induced dipoles are reconstructed iteratively by minimizing at each iteration step a cost functional involving both far-field Eq. (5) and domain-field Eq. (4). Here, we also present an iterative approach to solving this nonlinear and ill-posed inverse-scattering problem in which at each iteration step the forward problem, Eq. (4), is solved for the available estimation of the polarizability α. Thus, the field inside the test domain Ω is considered fixed at each iteration step. The sequence $\{\alpha_n\}$ is built up according to the recursive relation

$$\alpha_n = \alpha_{n-1} + a_n d_n, \tag{6}$$

where the updated polarizability α_n is deduced from the previous one α_{n-1} by adding a correction. This correction is composed of two terms: a scalar weight a_n and a search direction d_n. Once the updating direction d_n is found (this will be specified below), the scalar weight a_n is determined by minimizing the cost functional $\mathcal{F}_n(\alpha_n)$ involving the residual error $\mathbf{h}_{l,n}$ on the scattered field computed from observation Eq. (5),

$$\mathbf{h}_{l,n} = \mathbf{f}_l - \bar{\bar{\mathbf{B}}}\alpha_n \mathbf{E}_l, \tag{7}$$

with $\mathbf{E}_l$ being the total electric field that would be present in Ω if the polarizability distribution were α. This field can be written symbolically from Eq. (4) as

$$\mathbf{E}_l = [\bar{\bar{\mathbf{I}}} - \bar{\bar{\mathbf{A}}}\alpha]^{-1}\mathbf{E}_l^{\text{inc}}, \tag{8}$$

with $\bar{\bar{\mathbf{I}}}$ being the identity matrix.

The cost functional $\mathcal{F}_n(\alpha_n)$ mentioned above reads as

$$\mathcal{F}_n(\alpha_n) = \frac{\sum_{l=1}^{L} \|\mathbf{h}_{l,n}\|_\Gamma^2}{\sum_{l=1}^{L} \|\mathbf{f}_l\|_\Gamma^2} = W_\Gamma \sum_{l=1}^{L} \|\mathbf{h}_{l,n}\|_\Gamma^2, \tag{9}$$

where the subscript Γ is included in the norm $\|\cdot\|$ and later the inner product $\langle\cdot|\cdot\rangle$ in L^2 to indicate the domain of integration.

Note that substituting the expression of the polarizability α_n derived from Eq. (6) in Eq. (9) and approximating the actual field $\mathbf{E}_l$ by the field that would be present in the investigating domain Ω for the best available estimate of the polarizability α, i.e.,

$$\mathbf{E}_l \approx \mathbf{E}_{l,n-1} = [\bar{\bar{\mathbf{I}}} - \bar{\bar{\mathbf{A}}}\alpha_{n-1}]^{-1}\mathbf{E}_l^{\text{inc}},$$

leads to a polynomial expression with respect to the scalar coefficient a_n. Thus the minimization of the cost functional $\mathcal{F}_n(\alpha_n)$ is reduced to a minimization of a simple cost function $\mathcal{F}_n(\alpha_n)$. Moreover, for the particular case of dielectric material, i.e., the polarizability α is real, the cost function $\mathcal{F}_n(\alpha_n)$ takes the form

$$\mathcal{F}_n(a_n) = W_\Gamma \sum_{l=1}^{L} (\|\mathbf{h}_{l,n-1}\|_\Gamma^2 + a_n^2 \|\bar{\bar{\mathbf{B}}} d_n \mathbf{E}_{l,n-1}\|_\Gamma^2 - 2a_n \,\text{Re}\langle \mathbf{h}_{l,n-1} | \bar{\bar{\mathbf{B}}} d_n \mathbf{E}_{l,n-1}\rangle_\Gamma). \tag{10}$$

In this case, the unique minimum of $\mathcal{F}_n(\alpha_n)$ is reached for

$$a_n = \frac{\sum_{l=1}^{L} \text{Re}\langle \mathbf{h}_{l,n-1} | \bar{\bar{\mathbf{B}}} d_n \mathbf{E}_{l,n-1}\rangle_\Gamma}{\sum_{l=1}^{L} \|\bar{\bar{\mathbf{B}}} d_n \mathbf{E}_{l,n-1}\|_\Gamma^2}. \tag{11}$$

As updating direction d_n, the authors take

$$d_n = g_{n;\alpha} + \gamma_n d_{n-1}, \tag{12}$$

where g_n is the gradient of the cost functional $\mathcal{F}_n$ with respect to the polarizability assuming that the total fields $\mathbf{E}_l$ do not change:

$$g_{n;\alpha} = -W_\Gamma \sum_{l=1}^{L} \mathbf{E}_{l,n-1}^* \cdot \bar{\bar{\mathbf{B}}}^\dagger \mathbf{h}_{l,n-1}, \tag{13}$$

in which $\mathbf{u}^*$ denotes the complex conjugate of $\mathbf{u}$ and $\bar{\bar{\mathbf{B}}}^\dagger$ represents the transposed complex conjugate matrix of the matrix $\bar{\bar{\mathbf{B}}}$.

The scalar coefficient γ_n is defined as in the Polak–Ribière conjugate-gradient method[27] by

$$\gamma_n = \frac{\langle g_{n;\alpha} | g_{n;\alpha} - g_{n-1;\alpha}\rangle_\Gamma}{\|g_{n-1;\alpha}\|_\Gamma^2}. \tag{14}$$

To complete the inverse scheme, we need to specify the initial guess. As initial estimate for α_0 the authors take the estimate obtained by the back-propagation procedure. This technique is described in detail for the 2D problem in Refs. 21 and 28–30. The extension to the 3D problem is straightforward and therefore does not need to be presented here.

3. NUMERICAL RESULTS

In this section we report some examples of reconstruction of targets from synthetic data for different configurations simulating ODT experiments. In all examples, the synthetic data were computed using the CDM in which the mesh size $\lambda/20$ of the scattering domain Ω is different from that used in the inversion $\lambda/10$, where λ stands for the wavelength of the incident field in the background medium. The scattered fields are evaluated at 65 points regularly distributed on half-sphere Γ (see Fig. 1). The radius of the sphere is $400\,\lambda$ so that only far-field component data are considered and the diffracted field at the observation point can be considered a plane wave with wave vector $\mathbf{k}_d$. The azimuthal angle of observation, defined as the angle between the diffracted wave vector and the z axis, ranges from $\theta = -80°$ to $80°$. The incident fields con-

sist of 16 plane waves. Eight plane waves have their wave vector $\mathbf{k}$ and their electric field in the (x,z) plane (which corresponds to the p polarization), while the others have their wave vector and field in the (y,z) plane. The angle of incidence, defined as the angle between the incident wave vector and the z axis, varies from $\theta^{\mathrm{inc}}=-80°$ to 80°. In all the reconstructions, the investigation domain is a box of side 1.6λ surrounding the object, except in Figs. 9 and 10 below where the side of Ω is 2λ. The reconstructed permittivity is plotted after enough iterations for the cost function to reach a plateau.

A. Image of a Single Scatterer; Role of Multiple Scattering

In most imaging techniques in optics, such as far-field or near-field microscopes, the resolution is obtained by studying the "impulsional response" of the system, i.e., the image of a dipole (namely, a sphere or cube small enough that the electromagnetic field can be assumed to be constant over its volume). The latter is a function of the three variables of space, called the point-spread function (PSF). It presents a peak at the dipole position whose width at midheight along the x,y,z axis is commonly used to determine the transverse and axial power of resolution of the imaging technique. In a standard optical microscope in transmission, the width of the PSF is roughly $0.6\lambda/\mathrm{NA}$ transversally and $2n\lambda/(\mathrm{NA})^2$ axially, where $\mathrm{NA}=n\sin\varphi$ is the numerical aperture of the system, n being the index of the propagation medium and φ being the half-aperture of the imaging optics–objective.

Defining the resolution of an imaging system from its response to a point source is relevant if one can assume that the image of a collection of dipoles is the convolution of the PSF with the dipole distribution. While this assumption is clearly justified in fluorescence microscopy, in which the sources radiate incoherently, it can be questioned in coherent microscopy or tomography, especially when multiple scattering is present.

To point out this difficulty, we have studied the image of a cube of width $\lambda/20$ and permittivity $\varepsilon=2.25$ as obtained with the nonlinear inversion scheme. Because of its small width and moderate permittivity, the object can

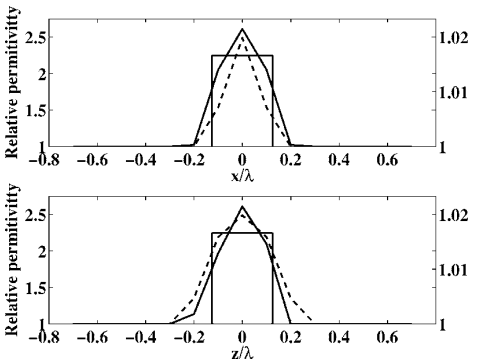

Fig. 2. Reconstructed permittivity of a single cube of permittivity $\varepsilon=2.25$ of widths $\lambda/20$ (dashed curve) and $\lambda/4$ (solid curve). Upper figure, plot of the relative permittivity along the x axis; lower figure, plot along the z axis. The legend on the left is for the solid curve (large cube), on the right for the dashed curve (small cube).

be assimilated to a radiating dipole and its image can be considered as the PSF of our system. In Fig. 2 we compare the reconstructed permittivity of the dipole along the x and z axis to that of a cube of width $\lambda/4$ and same permittivity. The most important feature of Fig. 2 is that the width of the permittivity peak of the larger cube along the z axis is smaller than that of the dipole.

To confirm this surprising result, we have applied our nonlinear inversion scheme to two dipoles whose centers are separated by 0.6λ, and we compare the reconstructed map of permittivity to that of two cubes of width $\lambda/4$ whose centers are separated by the same distance. In Fig. 3(a) we display a map of the reconstructed permittivity of the dipoles while in Fig. 3(b) we plot the normalized reconstructed permittivity contrast $(\varepsilon-1)/\max(\varepsilon-1)$ along the z axis for the two dipoles and the two cubes. We observe that the two dipoles are not resolved while the cubes are easily distinguished. In our opinion, the presence of multiple scattering and the use of a nonlinear inversion scheme is responsible for the better resolution of the image of the two cubes. This observation calls in question the notion of resolution as usually defined by the PSF and it points up the difficulty of defining it in a nonlinear imaging system.

One can get a physical insight into the role of multiple scattering with the following arguments. Consider an object defined by its permittivity contrast with the background medium (vacuum), $\Delta\varepsilon(\mathbf{r})=\varepsilon(\mathbf{r})-1$. The object is illuminated by a plane wave with wave vector $\mathbf{k}$. The far field diffracted along the direction defined by the wavevector $\mathbf{k}_{\mathrm{d}}$ can be assimilated to a plane wave with amplitude $\mathbf{E}(\mathbf{k}_{\mathrm{d}},\mathbf{k})$. Assuming the Born approximation, the latter is proportional to $\widetilde{\Delta\varepsilon}(\mathbf{k}_{\mathrm{d}}-\mathbf{k})$ where $\widetilde{\Delta\varepsilon}$ is the 3D Fourier transform of $\Delta\varepsilon$.[31] Hence, under the single-scattering approximation, the far-field amplitudes are directly linked to the Fourier transform of the permittivity contrast. By studying the spatial frequency domain, or the portion of the Ewald sphere that is covered by the experiment, one can estimate the limit of the resolution of the imaging system. In our configuration, the boundaries of the accessible spatial frequencies are roughly $[-2k_0,2k_0]$ in the (x,y) plane and $[-k_0,k_0]$ along the z axis. Consequently, the expected widths at midheight of the dipole image are about $\lambda/4$ along the x axis and $\lambda/2$ along the z axis. The better result observed in Fig. 2 is due to the *a priori* information of the location of the dipole in a relatively small investigation box.[6] Note that the PSF of a tomography experiment is naturally smaller than that of a microscope with the same NA[1] because of the use of multiple illuminations.

When multiple scattering is present, the classical Fourier analysis no longer holds. Indeed, in this case, the amplitude of the far field diffracted in the $\mathbf{k}_{\mathrm{d}}$ direction carries information on the Fourier transform of the permittivity for all spatial frequencies. More precisely, by iterating the Born series, it is shown that the second order of $\mathbf{E}(\mathbf{k}_{\mathrm{d}},\mathbf{k})$ can be cast in the form $\int\mathbf{B}(\mathbf{k}_{\mathrm{d}},\mathbf{k},\mathbf{k}')\widetilde{\Delta\varepsilon}(\mathbf{k}_{\mathrm{d}}-\mathbf{k}')\widetilde{\Delta\varepsilon}(\mathbf{k}'-\mathbf{k})\mathrm{d}\mathbf{k}'$.[32] Thus, it should be possible to obtain a better resolution than that classically expected from considerations of the single-scattering approximation. Note that the presence of multiple scatter-

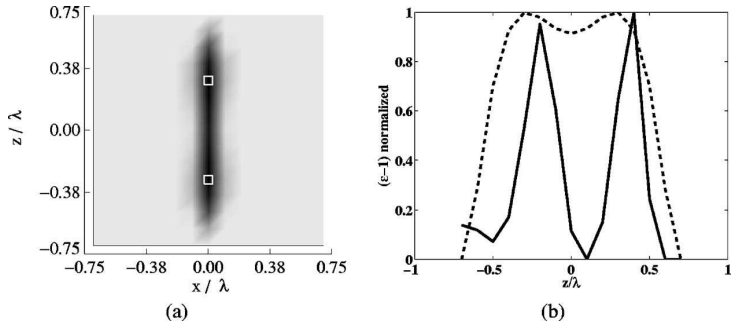

Fig. 3. (a) Map in the $y=0$ plane of the reconstructed permittivity of two dipoles (cubes of width $\lambda/20$, $\varepsilon=2.25$) separated by 0.6λ along the z axis. (b) Normalized reconstructed permittivity contrast $[(\varepsilon-1)/\max(\varepsilon-1)]$ versus z/λ for $x=y=0$: dashed curve, two dipoles separated by 0.6λ along the z axis; solid curve, two cubes of width $\lambda/4$, $\varepsilon=2.25$, whose centers are separated by the same distance as the dipoles, 0.6λ, along the z axis.

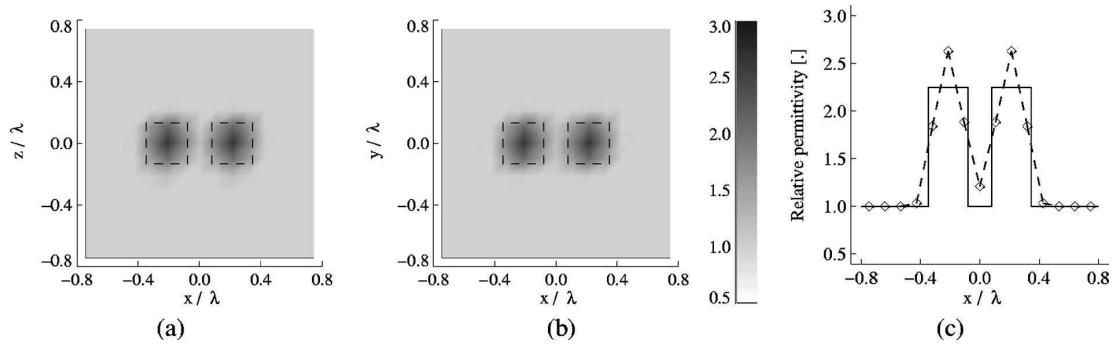

Fig. 4. Two cubes of side $a=\lambda/4$ separated by a distance $c=\lambda/7$ along the x axis. (a) and (b) show reconstructed maps of permittivities with a test domain of size $(1.6\times1.6\times1.6)\ \lambda^3$; the square in dashed line indicates the position of the actual cubes: (a) map of the relative permittivity in the plane (x,z) for $y=0$; (b) map of the relative permittivity in the plane (x,y) for $z=0$. (c) Relative permittivity versus x for $y=z=0$ (dashed curve) and the actual profile (solid curve).

ing is linked to the size of the objects and to their dielectric contrast. Thus, it is to be expected that the power of resolution of a nonlinear imaging system depends on these two parameters. This will be confirmed in Subsection 3.B.

B. Spatial Separation of Two Scatterers

To check the resolution along the x axis or z axis, we have taken two cubes of side $a=\lambda/4$ and permittivity $\varepsilon=2.25$ that are placed either along the x axis and separated by a distance $c=\lambda/7$ or along the z axis and separated by a distance $c=\lambda/3$ (the centers of the cubes are separated by $c+\lambda/4$).

We have first tried the linear inversion scheme presented in Ref. 6, which is based on the reconstruction of the induced dipoles inside the test domain. Even with a posttreatment, the method failed to distinguish the two cubes, either in the x or z directions. We have also checked an inversion procedure based on the extended Born approximation. This approximation yields a better estimation of the internal electric field than the standard Born approximation, Ref. 33, and it permits one to skip the resolution of Eq. (8) during the iterative process. This method allowed us to resolve the two objects placed along the x axis, though with an estimation of the relative permittivity significantly smaller than the actual one, but failed in resolving the two cubes placed along the z axis.

On the other hand, the full nonlinear scheme was successful in retrieving accurately the location, permittivity, and size of the cubes in both configurations, as can be seen in the views of the reconstructed permittivity maps in the (x,y) and (x,z) planes, Figs. 4 and 5. Not surprising, when multiple scattering is present a nonlinear inversion scheme is more efficient than a linear one. The slight shift of the positions of the cubes in Fig. 5 along the positive z axis can possibly be explained by the nonsymmetric configuration of the illumination and collection and the shadowing effect between the cubes. This shift vanishes when the illumination is symmetric with respect to the (x,y) plane, or when the separation of the cubes is increased.

We now check the influence of the permittivity of the objects on the reconstruction. In Figs. 6(a)–6(c) we plot the reconstructed permittivity versus z/λ for $x=y=0$ of two cubes of width $\lambda/4$ separated by $c=\lambda/3$ along the z axis, with permittivities $\varepsilon=1.01$, 2.25, and 4, respectively. We first observe that the retrieved value of the permittivity is correct in the three cases. This shows that our imaging system permits the characterization of the sample. Second, we find, as expected, that the greater the permittivity, the better the resolution of the two cubes. In par-

ticular, when $\varepsilon=1.01$, the Born approximation is valid and the inversion scheme fails to resolve the two cubes. In our opinion, this example emphasizes the role of multiple scattering in the resolution.

C. Robustness against Noise

In this section we analyze the robustness of our inversion algorithm with respect to different kinds of noise. First, the scattered far-field data, $\mathbf{f}_{l=1,\ldots,L}$, are corrupted with uncorrelated noise on each component of the electric field, and for each observation point

$$\mathrm{Re}[\tilde{f}_{l;v}(\mathbf{r}_k)] = \mathrm{Re}[f_{l;v}(\mathbf{r}_k)] + uA_r\xi_{l;v}, \tag{15}$$

$$\mathrm{Im}[\tilde{f}_{l;v}(\mathbf{r}_k)] = \mathrm{Im}[f_{l;v}(\mathbf{r}_k)] + uA_i\eta_{l;v}, \tag{16}$$

where v stands for the component along x, y, or z. $\xi_{l;v}$ and $\eta_{l;v}$ are random numbers with uniform probability density in $[-1,1]$, and u is a real number smaller than unity that monitors the noise level:

$$A_r = \max\{[\mathrm{Re}(f_{l;v})] - \min[\mathrm{Re}(f_{l;v})]\}_{l=1,\ldots,L;v},$$

$$A_i = \max\{[\mathrm{Im}(f_{l;v})] - \min[\mathrm{Im}(f_{l;v})]\}_{l=1,\ldots,L;v}.$$

Figure 7 shows the effect of noise on the reconstructed maps of relative permittivity versus the noise level u. The reconstructed objects are always perfectly localized in both planes (x,z) and (x,y) whatever the value of u [5% or 15%; see Figs. 7(a), 7(b), 7(d), and 7(e)]. The separation between the two cubes is still visible, the only effect of the uncorrelated noise being an increase of the relative permittivity. As shown in Figs. 7(c) and 7(f), when u increases, the maximum of the relative permittivity increases. In fact, in the case presented A_r and A_i are both positive, hence the intensity of the noisy scattered field, averaged over the observation domain Γ, is larger than the intensity of the uncorrupted field. In our opinion the consequence is a larger relative permittivity in the reconstruction to counterbalance the increase in this intensity.

The previous noise was uncorrelated but it is most likely that experimental noise will be correlated. Indeed, because of the envisaged experimental setup, we have suspected cumulative errors on the phase measurements as one moves away from the specular direction. Hence, to be faithful to the experimental setup, we have chosen a correlated noise of the form

$$\tilde{f}_{l;v}(\mathbf{r}_k) = f_{l;v}(\mathbf{r}_k)e^{i\psi_{l;v}}, \qquad \psi_{l;v} = \psi^g_{l;v} + \psi^a_l, \tag{17}$$

where v denotes the component x, y, or z; $l=1,\ldots,L$; and $k=1,\ldots,M$. $\psi^g_{l;v}$ is a Gaussian noise with mean 0 and standard deviation σ while ψ^a_l is a correlated noise defined as $\psi^a_l=|\mathbf{k}_d-\mathbf{k}|/|\mathbf{k}|\gamma/2$. In the experimental configu-

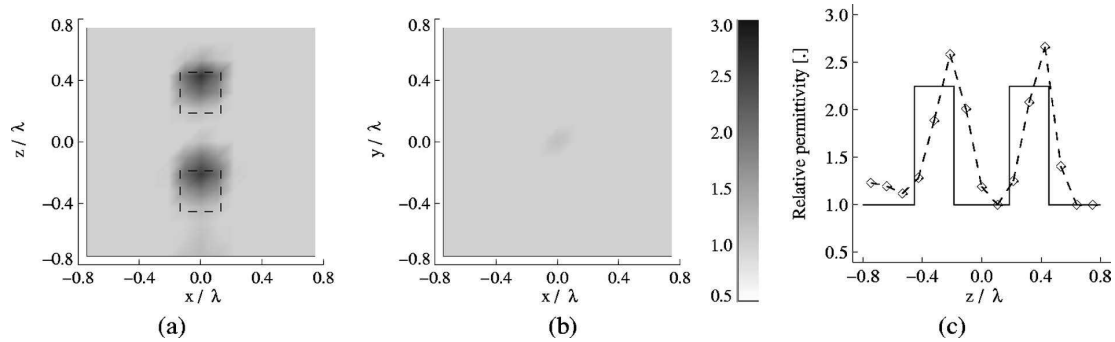

Fig. 5. Two cubes of size $a=\lambda/4$ separated by a distance $c=\lambda/3$ along the z axis. (a) and (b) show reconstructed maps of permittivities for a test domain Ω sized $(1.6\times1.6\times1.6)\ \lambda^3$; the square in dashed line indicates the position of the actual cubes: (a) map of the relative permittivity in the plane (x,z) for $y=0$; (b) map of the relative permittivity in the plane (x,y) for $z=0$. (c) Comparison between the reconstructed relative permittivity (dashed curve) and the actual profile (solid curve) versus z for $x=y=0$.

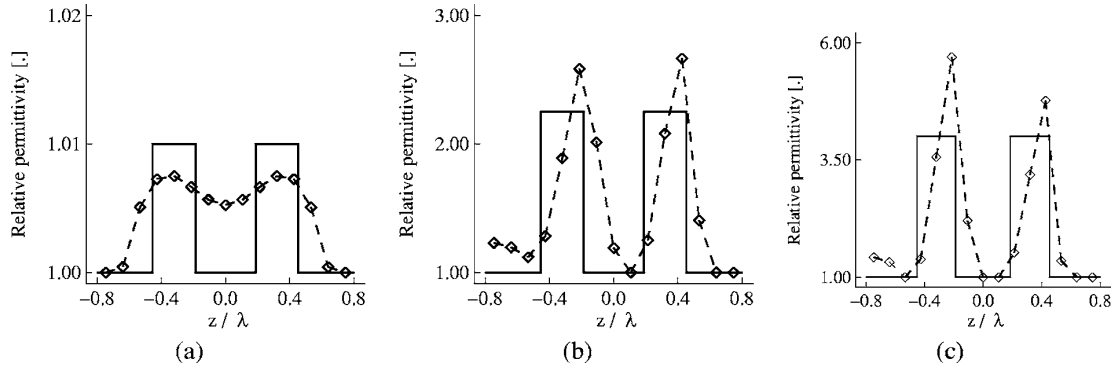

Fig. 6. Two cubes of side $a=\lambda/4$ separated by a distance $c=\lambda/3$ along the z axis for different permittivities. We display the permittivity versus z/λ for $x=y=0$. In solid is the actual profile, in dashed curve with diamond symbols, the reconstruction obtained with the nonlinear inversion scheme. The actual permittivity of the two cubes is ε (a) 1.01, (b) 2.25, (c) 4.0.

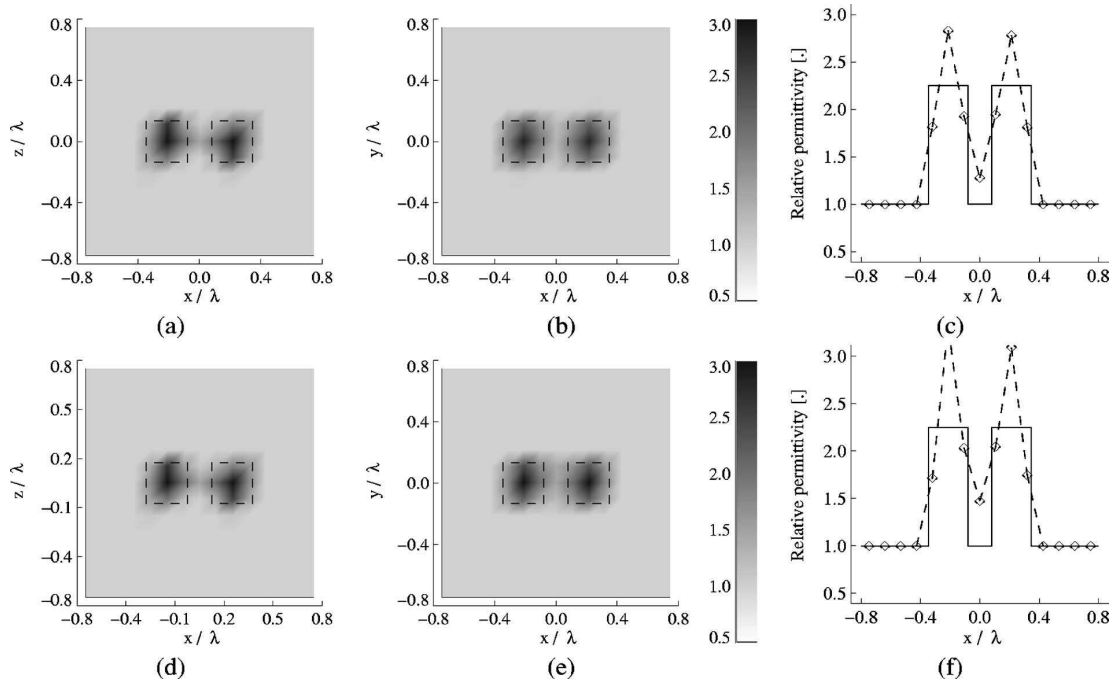

Fig. 7. The objects are the same as those in Fig. 4, and we have kept the same representation, but with uncorrelated noise on the scattered field. The upper figures (a), (b), (c) are obtained for a level of noise $u=5\%$, the lower figures (d), (e), (f) for a stronger noise $u=15\%$.

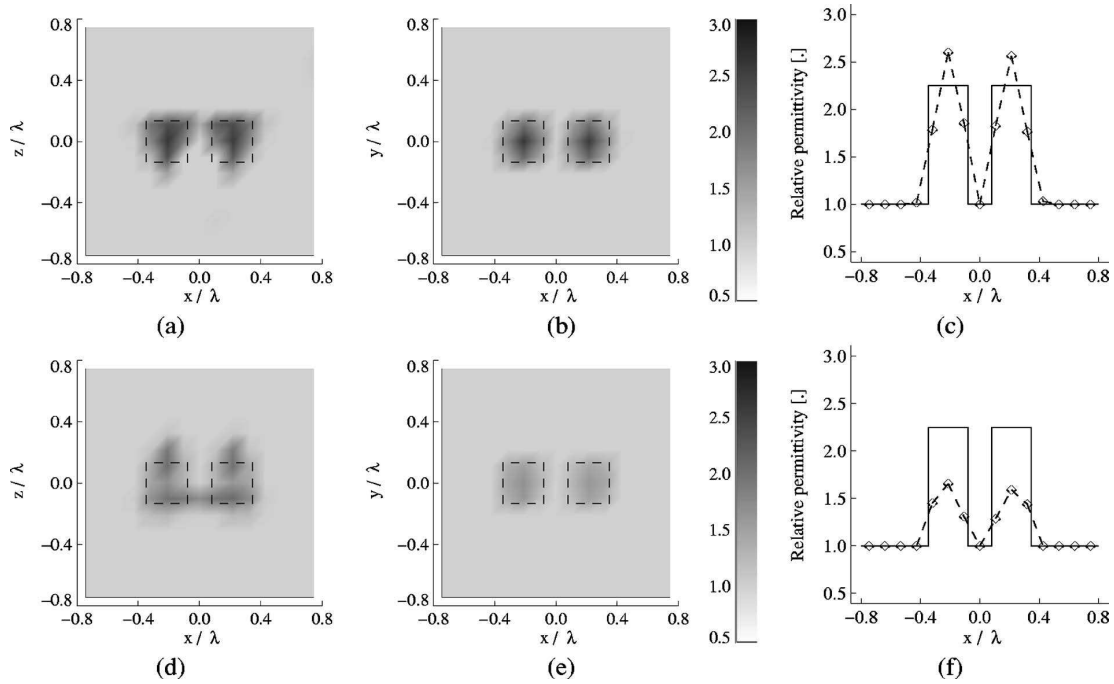

Fig. 8. Same as Fig. 7 but the noise consists now of multiplying the scattered field by a phase factor of the form $e^{i\psi}$ as specified in Eq. (17). The term of Gaussian noise is of a standard deviation $\sigma=5°$, and for the correlated phase ψ^a we have chosen $|\gamma|=10°$. For the upper figures $\gamma=10°$, for the lower figures, $\gamma=-10°$.

ration, Fig. 1, the most important error on the phase, $\max(\psi^a) \approx \gamma$, occurs when $k_{d;x}=-k_x$, or $k_{d;y}=-k_y$, and the maximum angle of incidence is $\theta^{\text{inc}}=\pm 80°$.

We note that the correlated noise, Fig. 8, has more impact than the uncorrelated one on the reconstructed map of permittivity. In the (x,y) plane, the localization, size, and value of permittivity are still accurate [Figs. 8(b) and 8(e)]. The two cubes are resolved without any doubt since the reconstructed relative permittivity vanishes between them as shown in Figs. 8(c) and 8(f). The main changes appear in the (x,z) plane where we observe a shift of the center of the cubes along the z axis. We note that the shift is different, following the sign of γ. If γ is positive (negative) the reconstructed cubes are shifted in the direction of negative (positive) z. In fact, when γ is positive the phase factor ψ^a is also positive.

With our model, the maximum error on the phase occurs for the scattered fields far from the specular direction, i.e., for the data richest in information on the position of the objects. For the scattered field far from the specular direction, the added phase ψ^a can be interpreted as an increase of the optical path. Since the points of observation are above the plane (x,y) the phase error yields a shift of the objects in the direction of negative z. Conversely, when γ is negative the error on the phase translates the two cubes in the direction of positive z. One notes that whereas for $\gamma>0$ the value of the relative permittivity is close to the actual one, this is not the case for $\gamma<0$: The reconstructed relative permittivity is weaker. Unfortunately, we did not find a complete explanation of the underestimation of the permittivity when $\gamma<0$. However, it is obvious that the two values of γ cannot lead to the same result. This is due to the nonsymmetrical measurement configuration: The illumination and the observation points are located on opposite sides of the (x,y) plane.

D. Multiple Scatterers

In the previous cases, we considered a simple target made of only two cubes. The number of data was $65\times 16 = 1040$ (this number should be multiplied by a factor of 2 since we are considering the complex amplitude of the

Table 1. Coordinates of the Center of the Nine Cubes ($a=\lambda/4$) Embedded in an Investigation Domain Ω of Volume $8\lambda^3$[a]

	Coordinates			Relative Permittivity	
Scatterer	x/λ	y/λ	z/λ	Fig. 9	Fig. 10
1	−0.575	−0.375	−0.675	2.25	1.5
2	0.675	−0.375	−0.675	2.25	1.5
3	−0.325	−0.375	−0.425	2.25	2.25
4	0.675	−0.375	−0.075	2.25	1.5
5	−0.575	−0.375	0.575	2.25	2.25
6	−0.175	−0.375	0.575	2.25	2.25
7	0.575	−0.375	0.575	2.25	2.25
8	−0.325	0.575	−0.425	2.25	1.5
9	0.675	0.575	−0.075	2.25	2.25

[a]Maps of the reconstructed relative permittivity by our nonlinear inversion algorithm are presented in Figs. 9 and 10.

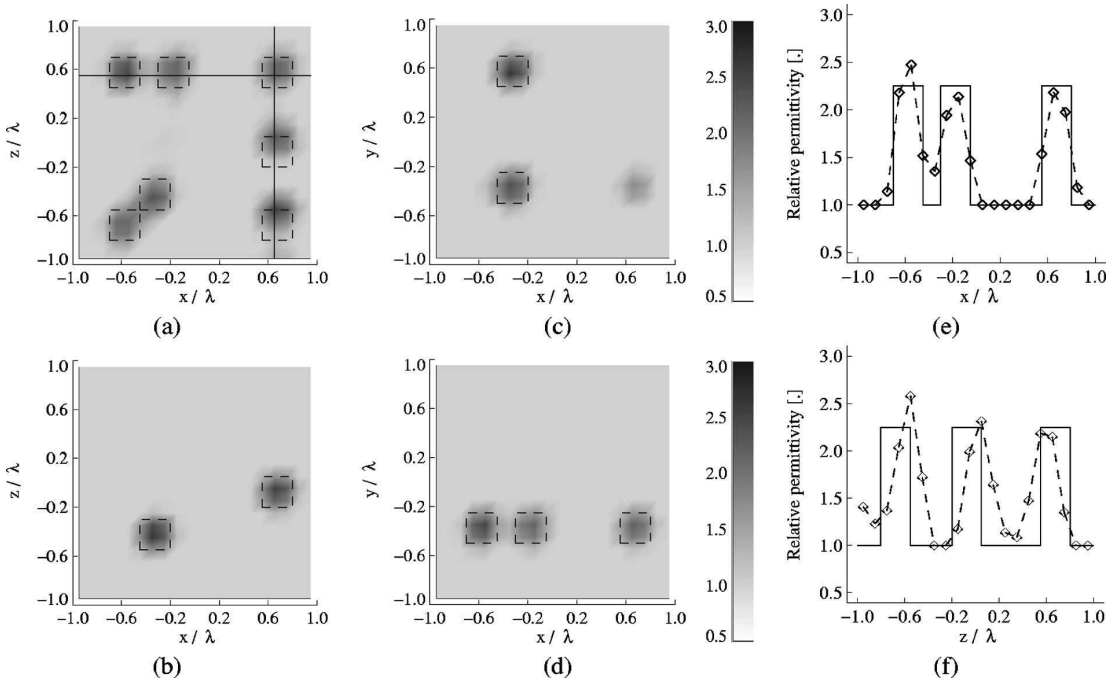

Fig. 9. Nine cubes of side $a=\lambda/4$ distributed in a test domain of volume $8\lambda^3$ (see Table 1 for their positions). (a), (b), (c), (d) are the reconstructed maps of the relative permittivities: (a) map in the (x,z) plane for $y/\lambda=-0.375$, (b) map in the (x,z) plane for $y/\lambda=0.575$, (c) map in the (x,y) plane for $z/\lambda=-0.675$, (d) map in the (x,y) plane for $z/\lambda=0.575$. (e) Relative permittivity versus x/λ along the horizontal line plotted in (a). (f) Relative permittivity versus z/λ along the vertical line plotted in (a).

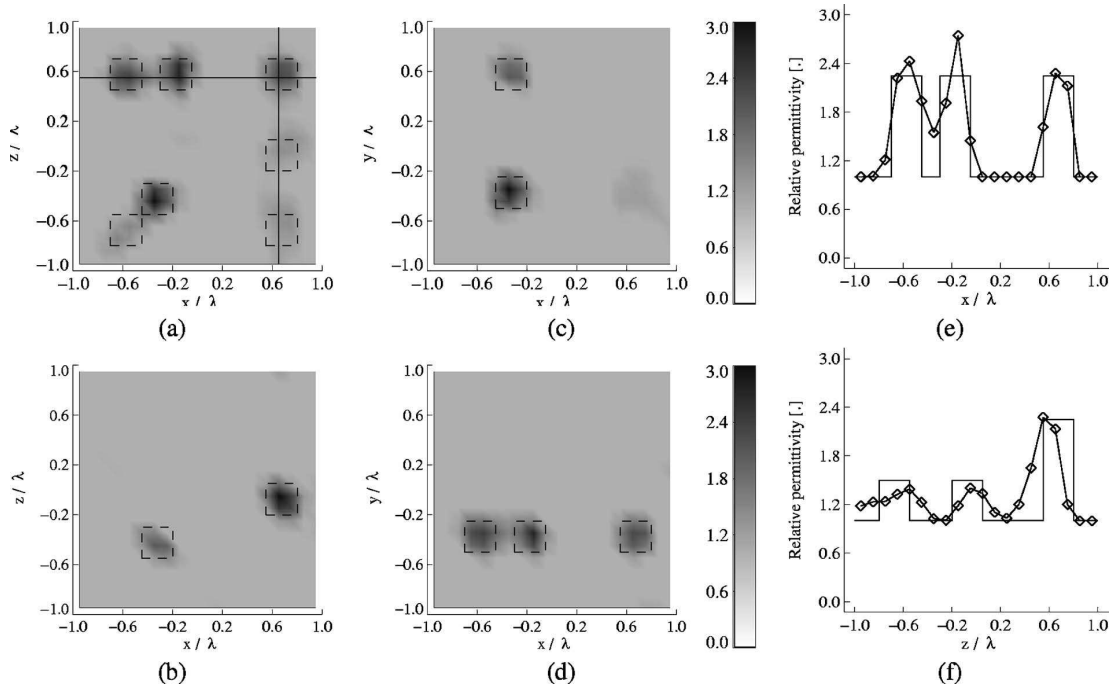

Fig. 10. Same as Fig. 9 but the cubes have different relative permittivities as detailed in Table 1.

electric field) while that of the unknowns, i.e., the polarizability of each cell, was about 3375. Hence, the number of measurements and unknowns were close to each other and, finally, only few polarizabilities departed from that of the background medium. One can wonder what would happen if the test domain were larger, with several objects, and the number of unknowns larger than that of the measurements. Hence, in the last example, we consider an investigation domain Ω of side 2λ ($V=8\lambda^3$) which yields 8000 unknowns (note that if the relative permittivity were complex the number of unknowns would be multiplied by a factor of 2) while the number of data remains equal to 1040. The sample consists of nine cubes of side $a=\lambda/4$, distributed in the box Ω as specified in Table 1.

Figure 9 shows, in different planes, comparisons between the reconstructed relative permittivities and the actual ones. One can note that, even with many objects and a number of unknowns larger than the number of measurements, the reconstructed maps localize without any doubt the positions of the objects [see Figs. 9(a)–9(d)]. Satisfactory reconstructed profiles have been obtained. These profiles are plotted in dashed curves in Figs. 9(e) and 9(f), which show also that the presence of many objects does not alter the power of resolution along the x or z axis. The two cubes that are separated by a distance of $\lambda/7$ along the x axis (cubes 5 and 6 of Table 1) and the two cubes separated by $\lambda/3$ along the z axis (cubes 2 and 4) are accurately resolved. In Fig. 9(f) one can notice the same shift along the z axis as that observed in Fig. 5.

The nonlinear scheme is also able to characterize unknown objects by giving a correct estimation of their permittivity. In Fig. 10 we plot the map of permittivity of a target made of several cubes placed at the same positions as in Fig. 9 but presenting different permittivities (see Table 1). The scattered far-field data are corrupted with the uncorrelated noise described in Eqs. (15) and (16) with $u=5\%$. We observe that the location, size, and permittivity of each cube are accurately retrieved. We have also checked the robustness of the reconstruction to correlated noise, Eq. (17), and obtained satisfactory results.

4. CONCLUSION

We have proposed a three-dimensional nonlinear inversion scheme that permits one to retrieve the map of permittivity of unknown objects from their scattered far field in an optical diffraction tomography experiment in transmission. The efficiency of the algorithm, based on the coupled-dipole method, has been checked successfully on complex targets made of many cubes positioned on various planes of a box. We have shown that, for objects small compared to the wavelength and with moderate dielectric constant, accounting for multiple scattering in the reconstruction procedure improves the image significantly. Moreover, we have pointed out that the presence of multiple scattering permits one to obtain a power of resolution beyond that classically expected. Moreover, our algorithm is robust to both correlated and uncorrelated noise. Last, our method can be extended without conceptual difficulties to configurations that are closer to realistic experiments, for example, objects deposited on a known substrate or buried inside a semi-infinite medium. This can be done by adding to the tensor of the free-space field susceptibility the tensor of the environment.[34–36]

ACKNOWLEDGMENTS

This work was supported by a grant of the Ministère de la Recherche, ACI 02 2 0225, and the Conseil Général des

Bouches du Rhône and the Conseil Régional PACA. The authors thank Frédéric Forestier for the computer science support. Kamal Belkebir's e-mail address is kamal.belkebir@fresnel.fr.

REFERENCES

1. V. Lauer, "New approach to optical diffraction tomography yielding a vector equation of diffraction tomography and a novel tomographic microscope," J. Microsc. **205**, 165–176 (2002).
2. N. Destouches, C. A. Guérin, M. Lequime, and H. Giovannini, "Determination of the phase of the diffracted field in the optical domain. Application to the reconstruction of surface profiles," Opt. Commun. **198**, 233–239 (2001).
3. E. Wolf, "Three-dimensional structure determination of semi-transparent objects from holographic data," Opt. Commun. **1**, 153–156 (1969).
4. S. Kawata, O. Nakamura, and S. Minami, "Optical microscope tomography. I. Support constraint," J. Opt. Soc. Am. A **4**, 292–297 (1987).
5. P. S. Carney and J. C. Schotland, "Three-dimensional total-internal reflection microscopy," Opt. Lett. **26**, 1072–1074 (2001).
6. P. Chaumet, K. Belkebir, and A. Sentenac, "Three-dimensional subwavelength optical imaging using the coupled dipole method," Phys. Rev. B **69**, 245405 (2004).
7. E. M. Purcell and C. R. Pennypacker, "Scattering and absorption of light by nonspherical dielectric grains," Astrophys. J. **186**, 705–714 (1973).
8. J. D. Jackson, *Classical Electrodynamics*, 2nd ed. (Wiley, 1975).
9. A. Lakhtakia, "Strong and weak forms of the method of moments and the coupled dipole method for scattering of time-harmonic electromagnetics fields," Int. J. Mod. Phys. C **3**, 583–603 (1992).
10. P. C. Chaumet and M. Nieto-Vesperinas, "Coupled dipole method determination of the electromagnetic force on a particle over a flat dielectric substrate," Phys. Rev. B **61**, 14119–14127 (2000).
11. P. C. Chaumet and M. Nieto-Vesperinas, "Electromagnetic force on a metallic particle in the presence of a dielectric surface," Phys. Rev. B **62**, 11185–11191 (2000).
12. P. C. Chaumet and M. Nieto-Vesperinas, "Time-averaged total force on a dipolar sphere in an electromagnetic field," Opt. Lett. **25**, 1065–1067 (2000).
13. B. T. Draine, "The discrete dipole approximation and its application to interstellar graphite grains," Astrophys. J. **333**, 848–872 (1988).
14. W. C. Chew and Y. M. Wang, "Reconstruction of two-dimensional permittivity distribution using the distorted wave Born iterative method," IEEE Trans. Med. Imaging **9**, 218–235 (1990).
15. N. Joachimowicz, C. Pichot, and J.-P. Hugonin, "Inverse scattering: An iterative numerical method for electromagnetic imaging," IEEE Trans. Antennas Propag. **39**, 1742–1751 (1991).
16. A. G. Tijhuis, "Born-type reconstruction of material parameters of an inhomogeneous, lossy dielectric slab from reflected-field data," Wave Motion **11**, 151–173 (1989).
17. A. G. Tijhuis, K. Belkebir, A. C. S. Litman, and B. P. de Hon, "Theoretical and computational aspects of 2-D inverse profiling," IEEE Trans. Geosci. Remote Sens. **GE–39**, 1316–1330 (2001).
18. R. E. Kleinman and P. M. van den Berg, "A modified gradient method for two-dimensional problems in tomography," J. Comput. Appl. Math. **42**, 17–35 (1992).
19. R. E. Kleinman and P. M. van den Berg, "An extended range-modified gradient technique for profile inversion," Radio Sci. **28**, 877–884 (1993).
20. K. Belkebir and A. G. Tijhuis, "Modified^2 gradient method and modified Born method for solving a two-dimensional inverse scattering problem," Inverse Probl. **17**, 1671–1688 (2001).
21. K. Belkebir, S. Bonnard, F. Pezin, P. Sabouroux, and M. Saillard, "Validation of 2D inverse scattering algorithms from multi-frequency experimental data," J. Electromagn. Waves Appl. **14**, 1637–1667 (2000).
22. K. Belkebir and A. Sentenac, "High resolution optical diffraction microscopy," J. Opt. Soc. Am. A **20**, 1223–1229 (2003).
23. P. S. Carney, V. A. Markel, and J. C. Schotland, "Near-field tomography without phase retrieval," Phys. Rev. Lett. **86**, 5874–5877 (2001).
24. P. M. van den Berg and R. E. Kleinman, "A contrast source inversion method," Inverse Probl. **13**, 1607–1620 (1997).
25. A. Abubakar, P. M. van den Berg, and B. J. Kooij, "A conjugate gradient contrast source technique for 3D profile inversion," IEICE Trans. Electron. **E83-C**, 1864–1874 (2000).
26. A. Abubakar and P. M. van den Berg, "The contrast source inversion method for location and shape reconstructions," Inverse Probl. **18**, 495–510 (2002).
27. W. H. Press, B. P. Flannery, S. A. Teukolski, and W. T. Vetterling, *Numerical Recipes: The Art of Scientific Computing* (Cambridge U. Press, 1986).
28. K. Belkebir, R. E. Kleinman, and C. Pichot, "Microwave imaging—Location and shape reconstruction from multifrequency scattering data," IEEE Trans. Microwave Theory Tech. **45**, 469–476 (1997).
29. L. Souriau, B. Duchêne, D. Lesselier, and R. E. Kleinman, "Modified gradient approach to inverse scattering for binary objects in stratified media," Inverse Probl. **12**, 463–481 (1996).
30. R. E. Kleinman and P. M. van den Berg, "Two-dimensional location and shape reconstruction," Radio Sci. **29**, 1157–1169 (1994).
31. J. Daillant and A. Gibaud, *X-Ray and Neutron Reflectivity* Lecture Notes in Physics (Springer-Verlag, 1999), p. 130.
32. C.-A. Guérin and A. Sentenac, "Second-order perturbation theory for scattering from heterogeneous rough surfaces," J. Opt. Soc. Am. A **21**, 1251–1260 (2004).
33. T. M. Habashy, R. W. Groom, and B. R. Spies, "Beyond the Born and Rytov approximations–A nonlinear approach to electromagnetic scattering," J. Geophys. Res., [Solid Earth] **98**, 1759–1775 (1993).
34. P. C. Chaumet, A. Rahmani, F. de Fornel, and J.-P. Dufour, "Evanescent light scattering: The validity of the dipole approximation," Phys. Rev. B **58**, 2310–2315 (1998).
35. A. Rahmani, P. C. Chaumet, and F. de Fornel, "Environment-induced modification of spontaneous emission: Single-molecule near-field probe," Phys. Rev. A **63**, 023819 (2001).
36. P. C. Chaumet, A. Rahmani, and G. W. Bryant, "Generalization of the coupled dipole method to periodic structure," Phys. Rev. B **67**, 165404 (2003).

PRL 97, 243901 (2006) PHYSICAL REVIEW LETTERS week ending 15 DECEMBER 2006

Beyond the Rayleigh Criterion: Grating Assisted Far-Field Optical Diffraction Tomography

Anne Sentenac, Patrick C. Chaumet, and Kamal Belkebir

Institut Fresnel (UMR 6133), Université Paul Cézanne and Université de Provence, F-13397 Marseille Cedex 20, France

(Received 5 July 2006; published 11 December 2006)

We propose an optical imaging system, in which both illumination and collection are done in far field, that presents a power of resolution better than one-tenth of the wavelength. This is achieved by depositing the sample on a periodically nanostructured substrate illuminated under various angles of incidence. The superresolution is due to the high spatial frequencies of the field illuminating the sample and to the use of an inversion algorithm for reconstructing the map of relative permittivity from the diffracted far field. Thus, we are able to obtain wide-field images with near-field resolution without scanning a probe in the vicinity of the sample.

DOI: 10.1103/PhysRevLett.97.243901 PACS numbers: 42.30.Wb, 42.25.Fx

Developing optical imaging systems with sub-100 nm resolution stirs a considerable interest especially in the nanotechnology and biology domains. The barrier to be broken is the well-known Rayleigh criterion that states that two radiating dipoles are distinguishable on the image of their far-field intensity if their interdistance is greater than 0.6λ where λ is the wavelength of radiation. This intrinsic limitation, caused by light diffraction, applies, in particular, to classic optical microscopes [1]. Shortening the wavelength of radiation with immersion techniques [2], the use of hemispherical prisms [3,4] or the excitation of surface plasmons [5,6] has permitted the increase of the power of resolution of these systems. Yet, due to the narrow range of available transparent material in optics, the power of resolution remains close to 150 nm for a free-space wavelength of 500 nm. A similar result has been obtained with the so-called silver superlens imaging technique [7]. The breakthroughs in high resolution optical imaging have been obtained in near-field optical microscopy by scanning a probe in subwavelength proximity to the sample [8], and more recently, in far-field fluorescence microscopy by taking advantage of nonlinear effects [9] and the use of structured illumination [10,11]. Yet, these spectacular ameliorations of the resolution are achieved at the expense of a certain readiness or versatility of utilization, probe scanning, or need for fluorescent objects.

In this Letter, we propose an optical imaging system dedicated to nonfluorescent objects that presents a nanometer-scale resolution without resorting to probe scanning or nonlinear phenomena. Our approach relies on diffraction tomography principles, a relatively new imaging technique in optics which is closely related to that developed in the microwave or acoustic domains. In an optical diffraction tomography (ODT) experiment, the sample is illuminated by a laser beam along different successive directions of incidence and the amplitude and phase of the far field is detected for many angles of observations. Note that the problem of measuring the phase of the diffracted field in this configuration has been solved experimentally with an astute interferometric setup by [12]. The image, or map of relative permittivity of the sample, is then numerically synthesized from the diffracted far-field data. The inversion algorithm uses the fact that, under single scattering approximation, when a sample is illuminated by a monochromatic plane wave with wave vector $\mathbf{k}^{\mathrm{inc}}$, its diffracted far field in the direction given by the wave vector $\mathbf{k}^{\mathrm{diff}}$ yields the spatial Fourier transform of the sample permittivity, $\hat{\varepsilon}(\mathbf{k}^{\mathrm{inc}} - \mathbf{k}^{\mathrm{diff}})$. Hence, in an ideal optical diffraction tomography system with all possible angles of incidence and detection, the resolution is about 0.3λ, already half that obtained with a classical microscope [12]. From these considerations, it is easily seen that the power of resolution of ODT is all the better than the spatial frequency of the field incident on the sample is high. Hence, it has been proposed to deposit the objects on a prism and to illuminate them under total internal reflection [13]. In total internal reflection tomography (TIRT), the highest spatial frequency of the incident field in the plane of the substrate is n/λ, where n is the index of refraction of the prism. Recent numerical simulations have shown that, in this case, a resolution of $0.6\lambda/(n+1)$ can be expected [14]. Thus, to reach a power of resolution comparable to that of near-field optical microscopes or saturated fluorescent microscopes, it is necessary to overcome the bounds imposed by the available refraction indices in the optical domain to generate high-spatial-frequency incident fields. For example, this can be obtained with a combination of ODT and near-field microscopy by scanning a diffractive element in the near zone of the sample [15]. Yet, this technique is still hampered by the need of moving an object close to the sample. To the contrary, our approach does not borrow any features to near-field microscopy inasmuch as the near-field resolution is reached with a classical far-field ODT setup [12,14] by depositing the sample on a periodically nanostructured substrate, see Fig. 1.

We consider a biperiodic grating that is illuminated from below by a plane wave with wave vector $\mathbf{k}^{\mathrm{inc}} = (\mathbf{k}_{\parallel}^{\mathrm{inc}}, k_z^{\mathrm{inc}})$ where, the subscript $\parallel$ indicates the projection onto the plane of the substrate while the subscript z indicates the projection onto the normal of the substrate plane. The field above the grating, for $z > 0$, can be written as a Rayleigh series,

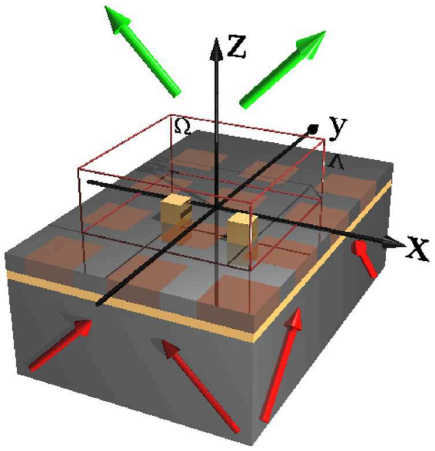

FIG. 1 (color online). Geometry of the imaging system. the objects are deposited on a nanostructured substrate and successively illuminated from below by eight plane waves. The incident angle with respect to Oz is always 80° while the incident angle with respect to Ox varies with a step of 45°. The far field is detected above the substrate along 64 directions equally spaced within a cone of half-angle 80°. The sample is made of two cubes with side $\lambda/20$ and centers interdistance $\lambda/10$.

$$\mathbf{E}_{\mathrm{ref}}(\mathbf{k}_{\parallel}^{\mathrm{inc}}, \mathbf{r}_{\parallel}, z) = \sum_{\mathbf{K}\in W} \mathbf{E}_{\mathbf{K}}(\mathbf{k}_{\parallel}^{\mathrm{inc}}) e^{i[(\mathbf{K}+\mathbf{k}_{\parallel}^{\mathrm{inc}})\cdot\mathbf{r}_{\parallel}+ik_z z]}, \quad (1)$$

where W denotes the reciprocal space of the periodic structure, $k_z = [k_0^2 - |\mathbf{K} + \mathbf{k}_{\parallel}^{\mathrm{inc}}|^2]^{1/2}$ with imaginary part of k_z positive, and the dependence in $\exp(-i\omega t)$ with $k_0 = 2\pi/\lambda = \omega/c$ is omitted. From Eq. (1) it is easily seen that provided that $\mathbf{E}_{\mathbf{K}}$ does not decay too quickly with increasing $\mathbf{K}$, the field incident on the sample will present high spatial frequencies. Now, to use the simple relationship between the diffracted far field and the Fourier coefficient of the sample permittivity, it is preferable that one order, denoted by $\mathbf{E}_{\mathbf{K}_c}$, be predominant in Eq. (1). One solution consists in using the periodic nanostructuration as a grating coupler for high-frequency surface modes such as those supported by metallic films. Indeed, it is well known that metallic layers support surface plasmons whose wave vectors $\mathbf{k}_p$ are all the larger than their thickness is small [16]. These plasmons can be coupled, via the grating, to a free-space incident plane wave if there exists one vector of the reciprocal space $\mathbf{K}_c$ such that

$$\mathbf{k}_p \approx \mathbf{k}_{\parallel}^{\mathrm{inc}} + \mathbf{K}_c. \quad (2)$$

Unfortunately, contrary to long-range plasmons, plasmons whose wave vector modulus is much larger than the free-space wave number k_0 present high losses. Hence, they are difficult to excite even with an optimized periodic perturbation. In all the structures we have studied, the field amplitude $\mathbf{E}_{\mathbf{K}_c}$, which bears the signature of the plasmon excitation, turned out to be comparable to the specular transmitted amplitude $\mathbf{E}_{\mathbf{0}}$. Hence, the relationship between the far-field data and the permittivity is not as simple as in the usual ODT, since the object is illuminated simultaneously by several plane waves. Moreover, due to the interferences, the field intensity at the surface of the grating is strongly inhomogeneous. To avoid the formation of blind and bright spots, it is necessary to check that the average of the illumination over all the incidences is roughly homogeneous within one period of the grating. This can be obtained with a weak periodic modulation. Bearing these requirements in mind, we designed a substrate consisting in a 7 nm silver film, deposited on a glass prism, and surmounted by a 7 nm layer of SiO_2. This last layer is etched periodically with square holes that are filled with Ta_2O_5. Hence, the nanostructure is a phase grating with relatively small contrast $n_{\mathrm{SiO_2}} = 1.5$, $n_{\mathrm{Ta_2O_5}} = 2.1$ and presents flat interfaces. The square period d of the bidimensional grating is 100 nm while the side of the holes is 67 nm and the free-space wavelength of illumination $\lambda = 500$ nm. The short-range plasmon that can be excited with this structure, taking $n_{\mathrm{silver}} = 0.12 + 2.91i$ has a wave number close to $6k_0$, much larger than that obtained with usual plasmon-assisted sensors. The incident wave vector is taken in the Oxz plane with an angle of incidence of 80° that roughly satisfies Eq. (2) with $\mathbf{K}_c = \frac{2\pi}{d}\hat{\mathbf{x}}$. To excite the plasmon, the incident polarization is also in the Oxz plane. We have used eight different illuminations by rotating the incident plane of 45° about the z axis. In Fig. 2 we plot the modulus of the field just above the grating for various angles of incidence and we verify that, eventually, the grating surface is illuminated rather homogeneously.

We have simulated a grating-assisted diffraction tomography experiment with a rigorous numerical method based on the coupled dipole technique. This tool permits one to calculate the field diffracted by an aperiodic object depos-

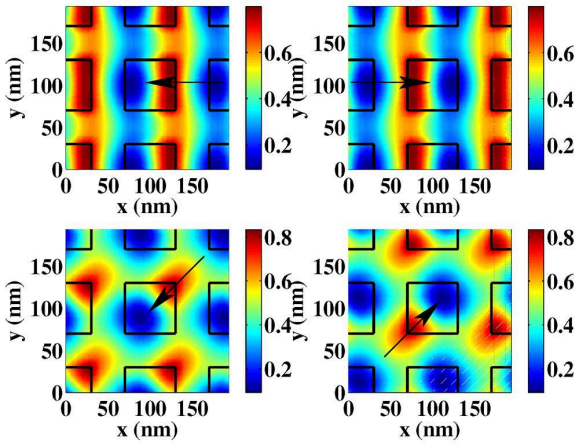

FIG. 2 (color online). Modulus of the field above the grating at the altitude $z = 10$ nm for various incident angles. The projection of the incident wave vector onto the Oxy plane is represented by an arrow. One observes that the bright and dark spots vary with the incident direction.

ited on a periodically structured substrate [17]. The diffracted field is evaluated (both in amplitude and phase) for 64 directions of observation homogeneously spaced in a cone of half-angle 80° above the substrate for each eight illuminations. The unavoidable experimental noise is taken into account by corrupting the simulated data with an additive complex uniform noise with an amplitude equal to 10% of the diffracted field modulus. Then, the permittivity distribution ε of the sample is determined by minimizing the cost functional [14],

$$\mathcal{F}(\varepsilon) = \sum_{\mathbf{k}^{\mathrm{inc}},\mathbf{k}^{\mathrm{diff}}} \| \mathbf{F}(\mathbf{k}^{\mathrm{inc}},\mathbf{k}^{\mathrm{diff}}) - \mathbf{E}(\mathbf{k}^{\mathrm{inc}},\mathbf{k}^{\mathrm{diff}},\varepsilon) \|^2, \quad (3)$$

where $\mathbf{F}$ is the "experimental" data and $\mathbf{E}$ is the simulated field radiated by the best available estimated permittivity ε. More precisely, we assume that the sample is included in a bounded domain Ω above the grating (see Fig. 1) and ε is deduced iteratively at the nodes of a regular meshing of Ω with a conjugate gradient algorithm. To speed up the inversion procedure, $\mathbf{E}$ is evaluated under the extended Born approximation [14] or by replacing the nanostructured top layer by a homogeneous film.

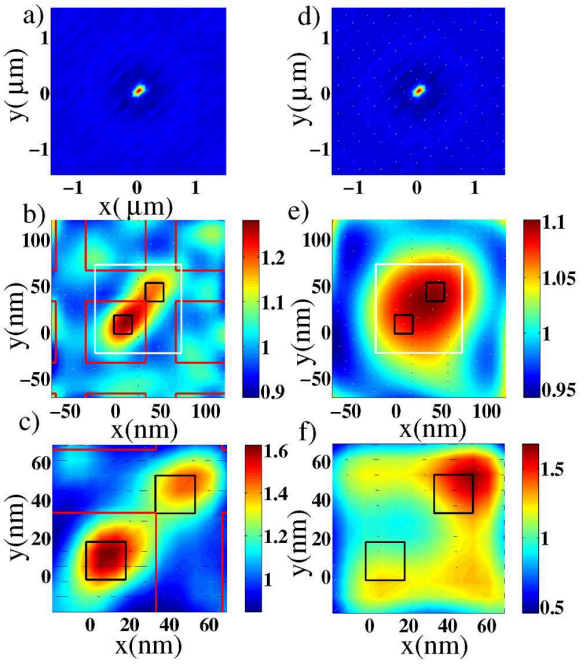

FIG. 3 (color online). Map in the (x, y) plane at altitude $z = 12$ nm of the real part of the permittivity for various investigation domains Ω obtained with the inversion procedure from the diffracted far-field data. (a)–(c) The objects are deposited on the nanostructured substrate. (e)–(g) The objects are deposited on the same substrate with the nanostructured top layer replaced by an homogeneous film with same thickness and permittivity 2.25. When present, the positions of the high index motif of the grating are indicated with squares. The investigation domain volume is $6\lambda \times 6\lambda \times \lambda/2$ in (a) and (e), $\lambda/2 \times \lambda/2 \times \lambda/5$ in (b) and (f), and $\lambda/5 \times \lambda/5 \times \lambda/10$ in (c) and (g).

In a first example, we study the image of two dipolelike objects, namely, two cubes of glass with side $\lambda/20$. The interdistance between the cube centers is taken equal to $\lambda/10$, thus much smaller than the Rayleigh criterion. To assess the role of the grating in the enhanced resolution, we compare the reconstructed permittivity obtained when the objects are deposited on the nanostructured substrate to that obtained when the nanostructured top layer is replaced by a homogeneous film with the same thickness and permittivity 2.25. The inversion procedures in these two configurations differ solely by the use of different Green tensors for calculating the illumination and the far field [14,17]. In Fig. 3, we present the map of permittivity obtained with the inversion algorithms for different domains Ω of investigation. In Figs. 3(a) and 3(d) the domain Ω covers $6\lambda \times 6\lambda \times \lambda/2$ with a mesh side about $\lambda/2$. The reconstructed relative permittivity points out the ability of our technique to localize the objects whatever the substrate. Then, we diminish the size of the investigation domain Ω to $\lambda/2 \times \lambda/2 \times \lambda/5$ and we reconstruct the permittivity over a meshing of side $\lambda/60$, see Figs. 3(b) and 3(e). We observe already that the reconstructed permittivity is more accurate when the objects are deposited on the grating than when they are deposited on the homogeneous metallic multilayer. To ameliorate further the resolution, we focus in the zone of interest, indicated by the white lines in Figs. 3(b) and 3(e), while keeping the same mesh size. Indeed, decreasing the data-to-unknown ratio generally allows one to improve the reconstruction. With the nanostructured substrate, Fig. 3(c), the two cubes are now clearly distinguishable while, with the layered substrate, Fig. 3(f) the image is a nonsense that depends

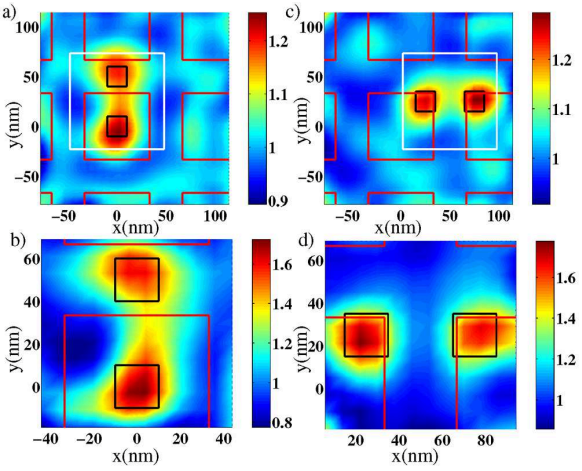

FIG. 4 (color online). (a),(c) Map in the (x, y) plane at altitude $z = 12$ nm of the real part of the permittivity for different positions of the objects with respect to the grating. (b),(d) idem (a),(c) but with a smaller investigation domain indicated with white lines in (a),(c). Ten different positions and orientations of the objects have been studied. Sole the worst and best reconstructions are presented.

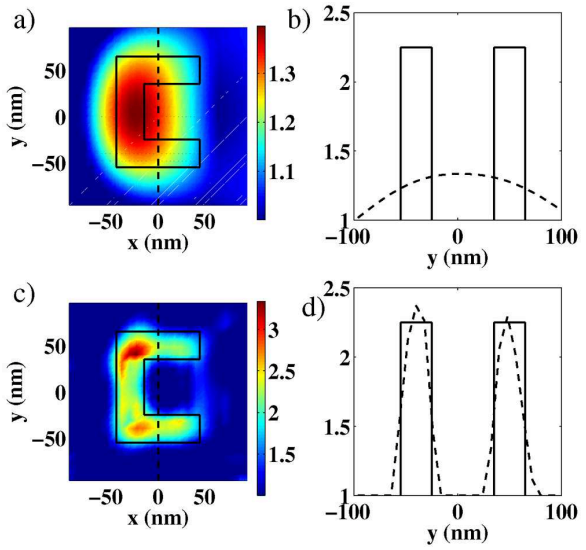

FIG. 5 (color online). Plain lines in (a),(b) [(c),(d)] indicate the real shape (permittivity profile) of the object. (a),(b) The C-shaped object is deposited on the homogeneous layered substrate. Map in the Oxy plane at altitude $z = 4$ nm of the real part of the reconstructed permittivity for a C-shaped object deposited on an homogeneous layered substrate, (b) plot of the estimated permittivity along the dash line in (a). (c) and (d) same as (a) and (b) but the nanostructured layer is replaced by an homogeneous film as in Fig. 3.

strongly on the noise. This focusing technique can be used to obtain wide-field images of more complex samples. First, the objects scattered on the substrate are localized with a coarse meshing, then, several disjoined investigation domains with smaller meshes are generated about their location to improve the resolution.

Since the nanostructured substrate is not invariant by translation, it is necessary to check the influence of the relative position of the objects with respect to the grating on the resolution. In Fig. 4, we present the worst and the best images that we have obtained for ten different positions of the cubes. It is always possible to distinguish precisely the two cubes. The width at midheight of the peaks is about $\lambda/12$. This resolution is in agreement with the criterion obtained in the TIRT configuration $0.6\lambda/(n_p + 1)$, where n_p is the effective index of the plasmon, $k_p = n_p k_0 \approx 6k_0$.

In a second example, Fig. 5, we present the reconstructed permittivity of a C-shaped object with a relative permittivity of 2.25. In Figs. 5(a) and 5(b) the object is deposited on the homogeneous multilayer. One observes that the shape of the object is not retrieved and that the value of the permittivity is badly estimated. On the contrary, when the object is deposited on the nanostructured substrate, Figs. 5(c) and 5(d), the topography of the object is well described and the permittivity is accurately estimated. The role of the grating is again clearly demonstrated.

We have shown the interest and the feasibility of a grating-assisted optical diffraction tomography experiment for obtaining wide-field, highly resolved images. In our imaging system, the grating is used as a delocalized probe in order to generate evanescent waves with high spatial frequencies at each point of the substrate. The reconstruction algorithm is simple and fast since linear inversion using the extended Born approximation is sufficient in most cases. The image resolution is not limited by the wavelength of illumination but depends on the ability of the grating to generate electromagnetic field with high spatial frequencies. Hence, it is linked essentially to the period of the grating. The proposed nanostructured substrate can be realized with present nanolithography techniques but gratings with period smaller than 100 nm yielding better resolution could be envisaged in the future. Last, our system can easily be adapted to fluorescent imaging with structured illumination without saturation. [11,18].

This work was supported by a grant of the Ministère de la Recherche, No. ACI 02 2 0225, and the Conseil Général des Bouches du Rhône and the Conseil Régional PACA. The authors would like to thank Frédéric Forestier for the computer science support.

[1] N. Streibl, J. Opt. Soc. Am. A **2**, 121 (1985).
[2] D. Courjon, K. Sarayeddine, and M. Spajer, Opt. Commun. **71**, 23 (1989).
[3] S. B. Ippolito, B. B. Goldberg, and M. S. Unlu, Appl. Phys. Lett. **78**, 4071 (2001).
[4] G. E. Cragg and P. T. C. So, Biophys. J. **78**, 248a (2000).
[5] B. Rothenhäusler and W. Knoll, Nature (London) **332**, 615 (1988).
[6] I. I. Smolyaninov, J. Elliott, A. V. Zayats, and C. Davis, Phys. Rev. Lett. **94**, 057401 (2005).
[7] N. Fang, H. Lee, C. Sun, and X. Zhang, Science **308**, 534 (2005).
[8] J.-J. Greffet and R. Carminati, Prog. Surf. Sci. **56**, 133 (1997).
[9] M. Dyba and S. Hell, Phys. Rev. Lett. **88**, 163901 (2002).
[10] M. Gustafsson, Proc. Natl. Acad. Sci. U.S.A. **102**, 13 081 (2005).
[11] R. Heintzmann, T. Jovin, and C. Cremer, J. Opt. Soc. Am. A **19**, 1599 (2002).
[12] V. Lauer, J. Microsc. **205**, 165 (2002).
[13] P. S. Carney and J. C. Schotland, J. Opt. Soc. Am. A **20**, 542 (2003).
[14] K. Belkebir, P. C. Chaumet, and A. Sentenac, J. Opt. Soc. Am. A **22**, 1889 (2005).
[15] D. Marks and P. S. Carney, Opt. Lett. **30**, 1870 (2005).
[16] E. N. Economou, Phys. Rev. **182**, 539 (1969).
[17] P. C. Chaumet and A. Sentenac, Phys. Rev. B **72**, 205437 (2005).
[18] M. Gustafsson, J. Microsc. **198**, 82 (2000).

PHYSICAL REVIEW A, VOLUME 63, 023819

Environment-induced modification of spontaneous emission: Single-molecule near-field probe

Adel Rahmani
Atomic Physics Division, National Institute of Standards and Technology, Gaithersburg, Maryland 20899-8423

Patrick C. Chaumet
Instituto de Ciencia de Materiales de Madrid, Consejo Superior de Investigaciones Cientificas, Campus de Cantoblanco, Madrid 28049 Spain

Frédérique de Fornel
Groupe d'Optique de Champ Proche, LPUB, CNRS UMR 5027, Faculté des Sciences Mirande, Boîte Postale 47870, F-21078 Dijon Cedex, France

(Received 20 June 2000; published 18 January 2001)

The modification of lifetime experienced by a fluorescent molecule placed in an arbitrary environment is investigated theoretically within the framework of linear response theory. We present a complete description of the interaction of the particle with arbitrary structures on a plane substrate or inside a cavity. The theory is based on a self-consistent scattering procedure in which retardation effects and contributions from both homogeneous and evanescent modes of the electromagnetic field are included. The decay rate variations are computed and the concept of single-molecule near-field probe is discussed.

DOI: 10.1103/PhysRevA.63.023819 PACS number(s): 42.50.Ct, 32.70.Cs, 32.70.Jz, 07.79.Fc

I. INTRODUCTION

Since the pioneering work of Drexhage [1], the study of fluorescence emission in finite geometries has emphasized the influence of the environment on the dynamics of the fluorescent particle [2–4]. In finite geometries, the fluorescence lifetime, or the spontaneous emission rate, differs from the free-space value because the presence of matter near the decaying particle modifies the boundary conditions imposed on the electromagnetic field [5]. If, for a fluorescent molecule, we adopt the picture of a dipole interacting with its surroundings through its field, it is the reflected field which conveys back to the molecule information concerning its environment. While this interpretation has a classical flavor, it nevertheless remains consistent with the quantum-mechanical aspects of the source-field interactions as both vacuum and radiation modes conform to the same laws and, hence, are modified in a same way when particular boundary conditions are imposed [6,7]. While exact treatments have been proposed for simple geometries [3,8], the influence of complex structures on the molecular lifetime is usually dealt with by resorting to a perturbative approach for the electromagnetic field, and/or by neglecting retardation effects, as it is the case, for instance, for a substrate with shallow roughness [9–15]. In the two-dimensional case, Bian *et al.* presented a nonperturbative treatment using the method of finite difference in time domain [16]. They computed the lifetime and the (classical) frequency shift for a dipole on a substrate as a function of its position relative to the tip of a scanning near-field optical microscope. Their calculation showed a great sensitivity of the dynamics of the dipole with respect to its position beneath the tip consistent with experimental observations [17–19]. Another numerical study of lifetime modification was presented by Girard *et al.* [20], however, these authors based their work on a misconception of the coupling of a two level atom with radiation, as they ignored the fundamental relation between the free-space decay rate of spontaneous emission and the atom polarizability, leading to an unsound model. The three-dimensional problem was addressed by Novotny who studied the influence of a scanning near-field optical microscope tip, represented by an aluminum disk-shaped object, on the fluorescence lifetime of a dipole lying on a substrate [21]. His calculation, using a semianalytical method derived from the multiple multipole method [22], showed that the orientation of the dipole was critical, especially when the dipole was located close to the rim of the object.

The great sensitivity of a fluorescent molecule to its environment, makes it an interesting candidate for an elementary near-field probe [23–27]. In order to assess the potential of such a single-molecule probe, it is crucial to describe properly the coupling of the molecule to its environment. The purpose of this work is thus to study, in three dimensions, the modification of the fluorescence decay rate of a molecule by arbitrary structures, including ones too large to be used in a Born-type perturbative approach. The formalism presented here is based on a knowledge of the dynamical electromagnetic response of a plane surface or cavity to both homogeneous and evanescent modes of the field. The dressed, retarded field susceptibility pertaining to the environment is derived through a self-consistent procedure. The decay rate of the molecule is then computed according to linear response theory. Our paper is organized as follows. Using linear response theory, we relate in Sec. II the spontaneous emission rate to the field susceptibility. Using the theory of Agarwal [28,29], we then derive the exact retarded field susceptibility tensor associated with a surface (interface between two media). The relevant quantity in the problem of spontaneous emission is the field correlation function. Since this correlation function can be related to the field linear susceptibility through the fluctuation-dissipation theorem [28], this approach, while rigorously quantal, avoids an explicit quantization of the field. In Sec. III, we insert this tensor into the self-consistent procedure of the coupled di-

pole method (CDM) and compute the dressed field-susceptibility accounting for many-body interactions between the fluorescent particle, a plane surface, and an arbitrary object deposited on it, and we compute the decay rate for a transition dipole moment with arbitrary orientation. Since our calculation includes retardation effects, we are able to treat the case of extended structures. Both lossless dielectric and absorbing materials (dielectric or metallic) are considered. Section IV is devoted to the application of the CDM to the study of decay rate modification near microstructures placed on a plane substrate. Several examples are considered (dielectrics and metals) to foster understanding of the interactions between the molecular source and the environment. Particularly, we illustrate the different coupling mechanisms involved in the alteration of the dynamics of the molecular source. The molecular dynamics is studied further in Sec. V, where the possibility of a single-molecule near-field probe is demonstrated. Finally, our conclusions are presented in Sec. VI.

II. EXACT RETARDED FIELD SUSCEPTIBILITY OF A FLAT SURFACE

Since Purcell's prediction [5], the study of the influence of finite geometries on spontaneous emission gave rise to a large body of work, where both the viewpoint of classical [1,3,4] and quantum [26–32] electrodynamics were adopted (see the recent reviews by Haroche [6] and Barnes [33]). For our purpose, the choice of the formalism (classical versus quantum-mechanical) to describe the particle has little consequence on the final conclusion, at least as far as the decay rate, or its inverse the lifetime, is concerned (level shifts are discussed in the Appendix). Note that this is true because we consider a weak coupling regime (irreversible decay). We might either consider an excited two-level atom and compute its electric-dipole transition rate from the excited to the ground state (separated by an energy $\hbar\omega$) according to Fermi's golden rule, or a classical oscillating dipole whose oscillations (at frequency ω) are damped or enhanced by the field reflected by the environment. Both approaches lead to the same result [26]. We will use the shorthand ''dipole'' to identify the decaying particle, and whenever it will be appropriate, we shall exploit the intuitive character of the classical interpretation. In linear-response theory, the (linear) field susceptibility is the response of the electromagnetic field to an elementary excitation [28,34–36]. Let the dipole $\boldsymbol{\mu}(\mathbf{r}_0,\omega)$ be located at $\mathbf{r}_0=(x_0,y_0,z_0)$, $z_0>0$ in vacuum (permittivity $\epsilon_0=1$) above a substrate [permittivity $\epsilon_s(\omega)$ for $z<0$]. The electric field at position $\mathbf{r}=(x,y,z)$ above the interface is given by

$$\mathbf{E}(\mathbf{r},\omega)=\mathbf{T}(\mathbf{r},\mathbf{r}_0,\omega)\boldsymbol{\mu}(\mathbf{r}_0,\omega), \tag{1}$$

where $\mathbf{T}$, the total field-susceptibility tensor, consists of $\mathbf{F}$, the free-space [37] and $\mathbf{S}$, the surface field susceptibilities:

$$\mathbf{T}(\mathbf{r},\mathbf{r}_0,\omega)=\mathbf{F}(\mathbf{r},\mathbf{r}_0,\omega)+\mathbf{S}(\mathbf{r},\mathbf{r}_0,\omega). \tag{2}$$

To derive the damping rates, we need to find the *dissipative* part of the force acting upon the dipole. This damping force consists of the part of the electric field which is $\pi/2$ out-of-phase with respect to the dipole's oscillations. From linear-response theory we can write the normalized damping (decay) rate as

$$\left(\frac{\Gamma}{\Gamma_0}\right)_l=1+\frac{3q}{2k_0^3}\mathrm{Im}[S_{ll}(\mathbf{r}_0,\mathbf{r}_0,\omega)], \tag{3}$$

where $\mathrm{Im}(X)$ is the imaginary part of X, $k_0=2\pi/\lambda$ (λ is the wavelength, in vacuum, of the electric dipole transition), and q denotes the intrinsic quantum yield of the molecule. For simplicity we will take $q=1$. The subscript l stands for one of the three Cartesian coordinates x,y,z. The quantity Γ_0 is the free-space decay rate, it includes the contribution from $\mathbf{F}$ so that only the surface contribution remains in the expression of the *normalized* decay rate [Eq. (3)]. The next step consists in deriving the surface field susceptibility $\mathbf{S}$ through a rigorous treatment of the boundary-value problem at the interface. Starting from the field emitted by a dipole in free space, one must perform a plane wave expansion of the field and consider the interaction of each mode (either homogeneous or evanescent) with the surface [28]. At the end one can write the components of the surface field susceptibility as [26]

$$\begin{aligned}S_{xx}(\mathbf{r},\mathbf{r}_0,\omega)=\frac{i}{2}\left(\int_0^{k_0}-\int_0^{i\infty}\right)dw_0\{&[\Delta_p w_0^2-\Delta_s k_0^2]\\&\times e^{iw_0(z+z_0)}J_0(R\sqrt{k_0^2-w_0^2})-\cos(2\phi)\\&\times[\Delta_p w_0^2+\Delta_s k_0^2]e^{iw_0(z+z_0)}J_2(R\sqrt{k_0^2-w_0^2})\},\end{aligned} \tag{4}$$

$$\begin{aligned}S_{xy}(\mathbf{r},\mathbf{r}_0,\omega)=-\frac{i}{2}\sin(2\phi)\left(\int_0^{k_0}-\int_0^{i\infty}\right)dw_0[&\Delta_p w_0^2+\Delta_s k_0^2]\\&\times e^{iw_0(z+z_0)}J_2(R\sqrt{k_0^2-w_0^2}),\end{aligned} \tag{5}$$

$$\begin{aligned}S_{xz}(\mathbf{r},\mathbf{r}_0,\omega)=-i\cos\phi\left(\int_0^{k_0}-\int_0^{i\infty}\right)dw_0\sqrt{k_0^2-w_0^2}\\\times J_0(R\sqrt{k_0^2-w_0^2})e^{iw_0(z+z_0)}w_0\Delta_p,\end{aligned} \tag{6}$$

$$\begin{aligned}S_{zz}(\mathbf{r},\mathbf{r}_0,\omega)=-i\left(\int_0^{k_0}-\int_0^{i\infty}\right)dw_0(k_0^2-w_0^2)\\\times J_0(R\sqrt{k_0^2-w_0^2})e^{iw_0(z+z_0)}\Delta_p,\end{aligned} \tag{7}$$

where Δ_p and Δ_s are the Fresnel coefficients for p-polarized (transverse magnetic) and s-polarized (transverse electric) homogeneous or evanescent waves falling onto the interface. The distance $R=\sqrt{(x-x_0)^2+(y-y_0)^2}$, ϕ is the angle defined by $\cos\phi=(x-x_0)/R$, and $w_0^2=k_0^2-k_x^2-k_y^2$. The functions J_0 and J_2 are Bessel functions of the first kind [38]. The other components of this tensor can be deduced by symmetry. The respective contributions from homogeneous and evanescent modes of the field are readily identified by looking at the domains of integration of the two integrals. The

decay rates can then be computed by inserting the expression of $\mathbf{S}$ in Eq. (3). Here both homogeneous and evanescent parts of the surface field susceptibility are likely to contribute to the decay rate, unlike the free-space case where evanescent modes of the field are absent from the dissipative process [39].

III. MANY-BODY INTERACTIONS AND SELF-CONSISTENT FIELD SUSCEPTIBILITY

In the preceding section we considered the case of a dipole above a bare surface. Let us now consider the situation where an object is present near or on the surface. In such a case, the response of the environment to the dipole is not given by $\mathbf{S}$ anymore. One possible way to describe the influence of the object on the scattering process is to use the coupled dipole method [40] where the object is described as a collection of N polarizable subunits with dynamical polarizabilities $\boldsymbol{\alpha}_i(\omega)$ located at positions $\mathbf{r}_i$ $(i=1,N)$ on a cubic lattice. Let the molecule be located at $\mathbf{r}_0$, the self-consistent field susceptibility associated with the dressed surface is thus given by a set of N linear equations

$$\mathbf{S}_D(\mathbf{r}_i,\mathbf{r}_0,\omega)=\mathbf{F}(\mathbf{r}_i,\mathbf{r}_0,\omega)+\mathbf{S}(\mathbf{r}_i,\mathbf{r}_0,\omega)+\sum_{j=1}^{N}[\mathbf{F}(\mathbf{r}_i,\mathbf{r}_j,\omega)+\mathbf{S}(\mathbf{r}_i,\mathbf{r}_j,\omega)]\boldsymbol{\alpha}_j(\omega)\mathbf{S}_D(\mathbf{r}_j,\mathbf{r}_0,\omega), \tag{8}$$

for $i=1,N$. We shall assume that the optical properties of the object is isotropic so that the polarizability is scalar. The dynamical polarizability of each unit of discretization is given by [41–43]

$$\alpha_i(\omega)=\frac{\alpha^{\mathrm{CM}}(\omega)}{1-(2/3)ik_0^3\alpha^{\mathrm{CM}}(\omega)}, \tag{9}$$

where $\alpha^{\mathrm{CM}}(\omega)$ is the expression for the polarizability derived from the Clausius-Mossotti relation

$$\alpha^{\mathrm{CM}}(\omega)=\frac{3d^3}{4\pi}\frac{\epsilon(\omega)-1}{\epsilon(\omega)+2}, \tag{10}$$

with $\epsilon(\omega)$ the permittivity of the object and d the lattice spacing of the discretization.

Since the decay rate of the dipole is related to the dissipative part of the field susceptibility tensor at the position of the dipole, we seek to find $\mathbf{S}_D(\mathbf{r}_0,\mathbf{r}_0,\omega)$. After solving the self-consistent equation (8) for $\mathbf{S}_D(\mathbf{r}_i,\mathbf{r}_0,\omega)$ $(i=1,N)$, we can write [26,27]

$$\mathbf{S}_D(\mathbf{r}_0,\mathbf{r}_0,\omega)=\mathbf{S}(\mathbf{r}_0,\mathbf{r}_0,\omega)+\sum_{i=1}^{N}[\mathbf{F}(\mathbf{r}_0,\mathbf{r}_i,\omega)+\mathbf{S}(\mathbf{r}_0,\mathbf{r}_i,\omega)]\alpha_i(\omega)\mathbf{S}_D(\mathbf{r}_i,\mathbf{r}_0,\omega), \tag{11}$$

where the free-space term $\mathbf{F}(\mathbf{r}_0,\mathbf{r}_0,\omega)$ has been discarded because the contribution of this self-term is included in the free-space decay rate.

A convenient way to understand the physical content of Eq. (11) is to think in terms of electric field [44]. To do so we introduce the dipole moment and cast Eq. (11) in the form

$$\begin{aligned}\mathbf{S}_D(\mathbf{r}_0,\mathbf{r}_0,\omega)\boldsymbol{\mu}(\mathbf{r}_0,\omega)&=\mathbf{S}(\mathbf{r}_0,\mathbf{r}_0,\omega)\boldsymbol{\mu}(\mathbf{r}_0,\omega)\\&+\sum_{i=1}^{N}[\mathbf{F}(\mathbf{r}_0,\mathbf{r}_i,\omega)+\mathbf{S}(\mathbf{r}_0,\mathbf{r}_i,\omega)]\alpha_i(\omega)\\&\times\mathbf{S}_D(\mathbf{r}_i,\mathbf{r}_0,\omega)\boldsymbol{\mu}(\mathbf{r}_0,\omega).\end{aligned} \tag{12}$$

The right-hand side of Eq. (12) can be decomposed as follows.

The term $\mathbf{S}(\mathbf{r}_0,\mathbf{r}_0,\omega)\boldsymbol{\mu}(\mathbf{r}_0,\omega)$ represents the radiation reaction effect caused by the interaction of the molecule with its own field reflected by the substrate.

The term $\mathbf{S}_D(\mathbf{r}_i,\mathbf{r}_0,\omega)\boldsymbol{\mu}(\mathbf{r}_0,\omega)$ represents the self-consistent field induced by the molecule at the position of the ith polarizable element of the object (this element being coupled to the $N-1$ others).

Finally, as a whole, the sum in Eq. (12) represents the reaction of all the elements of the object, self-consistently coupled to the substrate, on the molecule.

The spontaneous emission rates are still given by Eq. (3) except that the field susceptibility of the bare surface ($\mathbf{S}$) is now to be replaced by the field susceptibility of the dressed surface ($\mathbf{S}_D$).

IV. SPONTANEOUS-EMISSION RATES

We shall now use the theory described in the preceding sections to compute the decay rate of a fluorescent molecule. The configuration is the following. The molecule is located in vacuum at a distance z_0 from a surface [(x,y) plane]. The structures considered are parallelepipeds with square base $b\times b$ and height h. Other shapes can be considered (see, for instance, Refs. [43–47]) but because of the cubic symmetry of the CDM discretization procedure, for an equal volume, they would require a larger number of elements to be described properly. Moreover this choice will allow us to study the effect of sharp edges and corners on the molecular fluorescence lifetime. In the following we will always plot the normalized decay rate (inverse of the normalized lifetime, the normalization being performed with respect to the molecule in vacuum) as a function of the molecule position in the plane $z=z_0$. Except for Fig. 2 the parallel dipole is chosen to be oriented along x. The values of the permittivity for metals are taken from Ref. [48].

A. Dielectrics

We first consider the case of a dielectric substrate ($\epsilon_s=2.25$), the wavelength of the transition is 612 nm. Deposited on the substrate are three dielectric parallelepipeds ($\epsilon=2.25$) with dimensions $h=50$ nm and $b=100$, 200, and 250 nm, respectively (Fig. 1). This example will serve to illustrate an important feature which stems from the near-

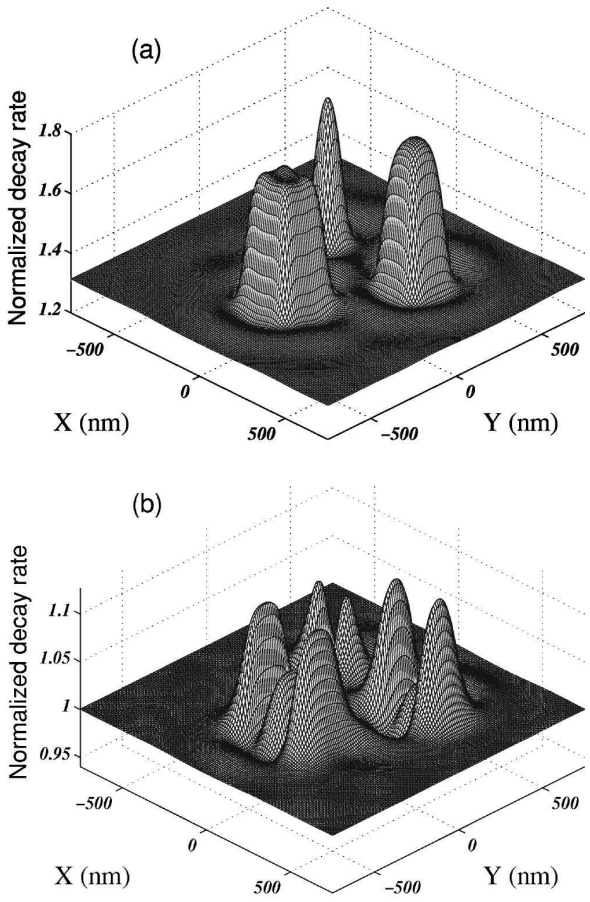

FIG. 1. Normalized decay rate above three dielectric objects (see text) placed on a dielectric substrate ($\epsilon=\epsilon_s=2.25$, $\lambda=612$ nm, $d=25$ nm, $z_0=90$ nm). (a) Dipole moment along z. (b) Dipole moment along x.

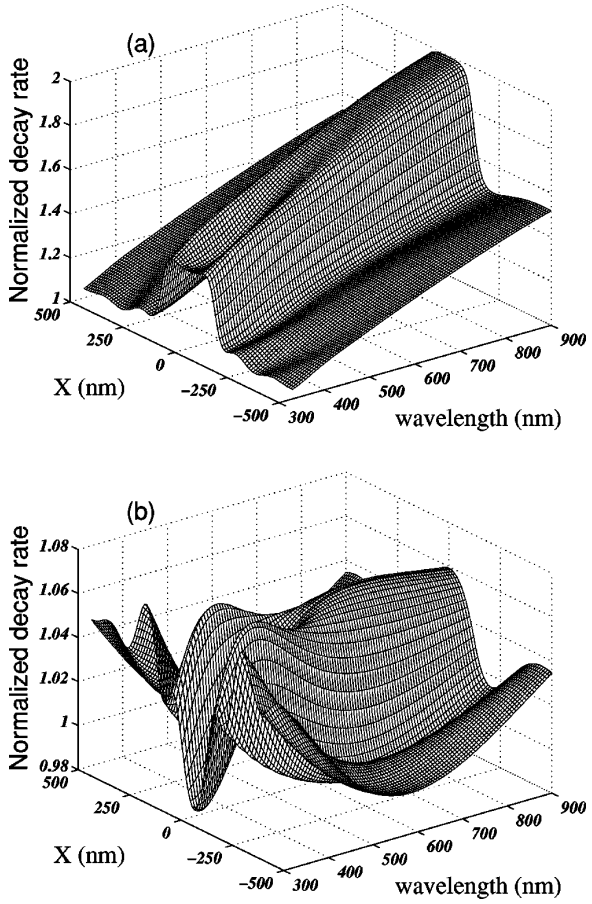

FIG. 2. Normalized decay rate above a dielectric object ($h=50$ nm, $b=250$ nm, $d=25$ nm, $\epsilon=2.25$, $z_0=90$ nm), on a dielectric substrate ($\epsilon_s=2.25$) as a function of the position along the x axis ($y=0$) and of the wavelength of emission. The dipole moment is along z (a) or y (b).

field nature of the interaction between the molecule and its environment. In this regime the role of evanescent modes of the field is essential [49]. Indeed, it is through these modes that the molecule couples to the high spatial frequencies (edges, corners) of the objects. On the other hand, the fast damping associated with these modes entails that the larger the distance between the molecule and the object, the softer the spatial variations of the lifetime, because the highly evanescent modes of the field that would interact with the sharpest features of the object decay so fast that they vanish before they could be scattered (or absorbed in the material in the case of a lossy material). Moreover, the orientation of the molecule dipole moment influences strongly the decay rate. The variations observed on Fig. 1(a), for the perpendicular (with respect to the substrate) orientation of the dipole moment of the molecule, reflects more closely the actual shape of the adsorbed structure as the object gets larger. The case of a parallel dipole (along x) is different as the rotational symmetry around the z axis is broken and boundary effects prevail [Fig. 1(b)]. The strong edge effect is a consequence of the normal component of the electric field being discontinuous (see Ref. [26]). Particularly, this effect is responsible for an inhibition ($\Gamma/\Gamma_0<1$) of spontaneous emission above the smallest pad. As the pad gets larger, the edges recede away from each other and the decay rate above the center of the pad tends towards that of a molecule located z_0-h away from a bare surface. The sensitivity of the decay rate on the emission wavelength is illustrated further on Fig. 2. Note that this is a purely ''geometrical'' effect as we assume that the permittivity of the object is constant over the whole spectrum ($\epsilon=2.25$). Figure 2(a) shows the variation of the perpendicular decay rate along direction x, as a function of the wavelength of the light emitted by the dipole, for an object with $h=50$ nm and $b=250$ nm, and a distance dipole substrate of $z_0=90$ nm. As we mentioned, for any given distance, the ability of the dipole to ''see'' the spatial variation of the object depends on the wavelength of the emission; the larger the wavelength and the more uniform the decay rate over the object. One can also note that the substrate contribution to the decay rate increases with the wavelength. This is a reflection of the growing importance of frustration of

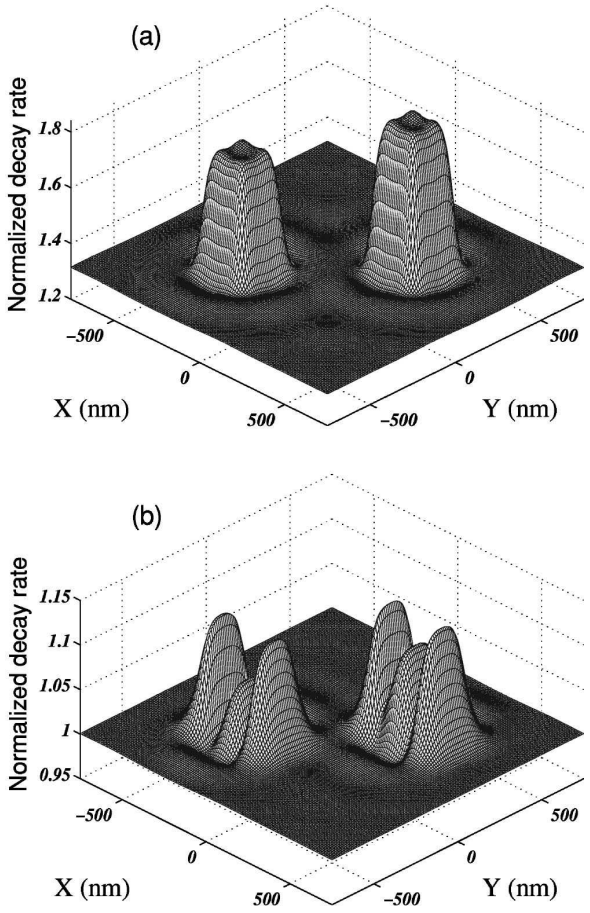

FIG. 3. Normalized decay rate above two dielectric objects (left: $\epsilon=2.25$ and right: $\epsilon=2.25+0.1i$) placed on a dielectric substrate ($\epsilon_s=2.25$, $\lambda=612$ nm, $d=25$ nm, $z_0=90$ nm). (a) Dipole moment along z. (b) Dipole moment along x.

evanescent waves as z_0/λ decreases. This near-field effect is somewhat more difficult to observe in the case of a parallel dipole [Fig. 2(b)] because, for this orientation, it is concealed by the reflection of the propagating ($\sim 1/r$) component of the field.

We shall now consider an absorbing dielectric. The consequence of absorption is illustrated on Fig. 3. The two objects are identical except for the imaginary part of the permittivity. Note how retardation makes the decay rate oscillates away from the parallelepipeds. Aside from orientational features, the effect of absorption is to increase the decay rates. Indeed, recall that the normalized decay rate represents the losses of the molecule; absorption in the material provides the molecule with an additional decay channel. Unlike the mechanism of frustration, absorption affects all the evanescent modes of the field emitted by the decaying particle; as a result this decay channel dominates the molecular losses at very short distances. As the dipole gets closer to a lossless medium, its lifetime tends towards a finite value because the mechanism of frustration affects only those evanescent modes whose component of the wave vector parallel to the interface is between k_0 and $k_0\sqrt{\epsilon}$. The case of an absorbing medium is different. The closer the dipole to the absorbing surface and the more evanescent modes reach the material and are absorbed which makes the lifetime go to zero (of course, the lifetime does not become zero because the present description in terms of dipole and flat surface would actually become invalid for distances smaller than a few Å).

B. Metals

If at first we disregard the object, the influence of a metallic surface on the decay rate of the dipole will significantly depend on the wavelength of the transition, and since we are in a near-field regime, on the distance between the molecule and the surface. The interaction of a dipole with a flat metallic surface is addressed in detail in Refs. [3,4,9,27], and references therein, and we will here merely underline the major features. First, an important contribution to the decay rate arises from the excitation of surface plasmon on the metallic surface. It can be shown that this contribution might prevail over any other process even at fairly large (a few hundreds nm) distances from the surface [50]. For small separations, absorption dominates; the coupling to surface modes is, however, more efficient when the wavelength of the dipole transition is close to the surface plasmon wavelength. One can also note that when the dipole is close to the surface, retardation becomes negligible and the perpendicular decay rate is twice the parallel decay rate as expected [limit $k_0=0$ in Eqs. (4) and (7)]. In summary, the case of a metallic substrate is a combination of reflection, frustration, absorption, and surface mode excitation [27].

Thus, when metals are involved, the decay rate variations will strongly depend on the wavelength of the dipole transition. Since the purpose of this work is to give a general picture of the near-field coupling of a decaying particle to its environment, in the following, we shall restrict ourselves to a few situations that will help us illustrate the various physical processes involved. Let us now consider the same objects as on Fig. 3, but located on a gold substrate. The decay rate maps are shown on Fig. 4. The differences in the influence of the two objects on the molecule are attenuated by the presence of the gold substrate. While the overall variation of the decay rate for a perpendicular dipole [Fig. 4(a)] strongly resembles the one observed for a dielectric substrate, the situation is quite different for the parallel dipole [Fig. 4(b)]. The presence of the metallic substrate leads, for the emission wavelength considered, to a strong damping when the molecule is above one of the objects.

Actually, when the molecule is above one of the objects, the coupling mechanism can be understood with a simple model. The width of the objects is large enough to allow the decay rate to get fairly close to the limit value it would have, had the molecule been placed above a multilayered structure composed of a gold substrate and a dielectric layer of thickness h. To compute the decay rate in such an environment, we replace the Fresnel coefficients appearing in Eqs. (4)–(7) by those of a multiple interface system [51]. We can then study the evolution of the decay rates for a molecule located

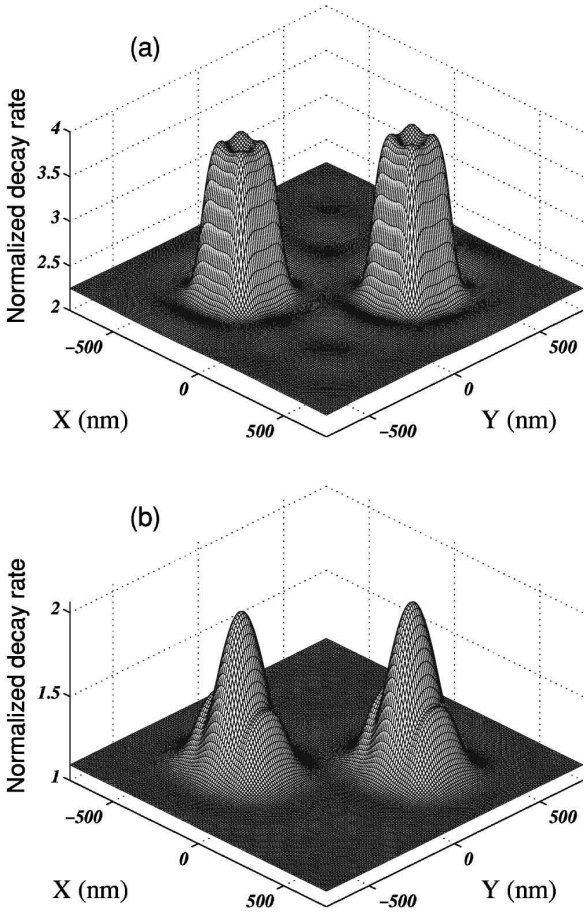

FIG. 4. Same as Fig. 3 but with a substrate of gold.

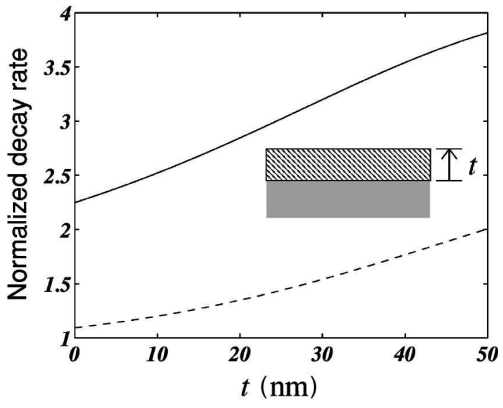

FIG. 5. Rate evolution for a multilayer system as a function of the thickness (t) of a dielectric layer ($\epsilon=2.25, \lambda=612$ nm) deposited on top of a gold substrate. The distance between the dipole and the substrate is 90 nm. Solid line, dipole moment perpendicular to the surface, dashed line, dipole moment parallel.

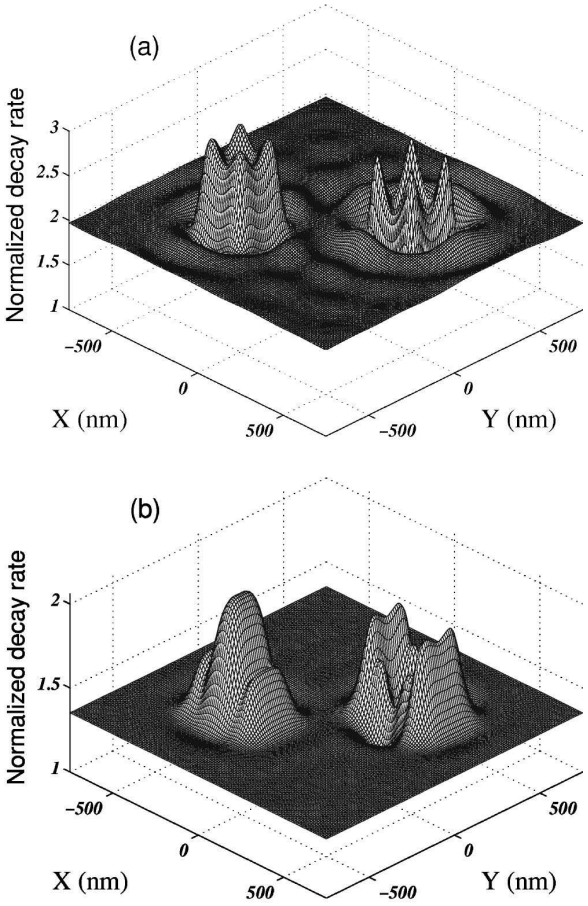

FIG. 6. Normalized decay rate above two dielectric objects (left: $\epsilon=2.25$ and right: $\epsilon=5$) placed on a gold substrate ($\lambda=520$ nm, $d=25$ nm, $z_0=90$ nm). (a) Dipole moment along z. (b) Dipole moment along x.

at distance z_0 from the gold substrate, as a dielectric layer ($\epsilon=2.25$) is grown on top of it (Fig. 5). It becomes clear that the strong damping experienced by the molecule over the parallelepipeds comes from this multilayer effect. Note that, as we shall see on the next example, the enhancement of the decay rate, as the dielectric layer is grown, does not translate a mere effect of frustration of the near field of the dipole as the thickness of the dielectric increases.

The previous example shows that a small difference between the imaginary parts of the permittivities of the two structures has little consequence on the decay rate of the molecule; at least for the distances we just considered. In order to have a better insight let us consider a case where the difference between the permittivities of two nonabsorbing objects is larger (2.25 and 5). The substrate is still gold, and the wavelength of the transition is chosen to be 520 nm. The variations of the decay rates for this case are shown on Fig. 6. The decay rate variations are now significantly different for the two structures. Particularly, one can see that the interaction of the molecule with the objects does not amount to a mere mechanism of frustration of the near-field of the mol-

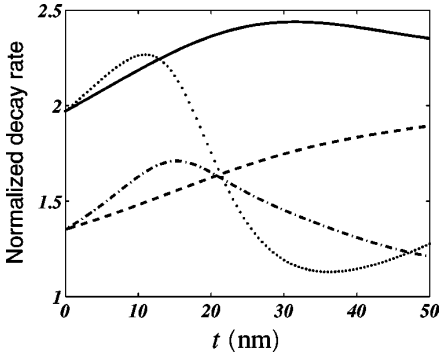

FIG. 7. Same as Fig. 5 but with $\lambda = 520$ nm. Solid line: $\epsilon = 2.25$, dipole along z. Dot-dashed line: $\epsilon = 2.25$, dipole along x. Dotted line: $\epsilon = 5$, dipole along z. Dashed line: $\epsilon = 5$, dipole along x.

ecule. The decay rate is more enhanced over the parallelepiped with the *lowest* permittivity. Once again, this feature can be explained by considering a multilayer configuration (Fig. 7). Despite its simplicity, this simple model is extremely valuable in that it provides us with an easy way to understand the behavior of the molecule above the objects. However, one should bear in mind that the good agreement between the value of the decay rates when the molecule is centered above one object, and the one given by a simple (infinite) multilayer model will hold as long as the lateral dimensions of the object are large enough.

The next two cases will allow us to illustrate further the sensitivity to the environment of the molecular response. For a transition wavelength of 520 nm, we consider the silver/gold pair. In the first case an object made of gold is placed on a silver substrate (Fig. 8). In the second case, the roles of the two metals are exchanged (Fig. 9). From this single example, it is obvious that not only the magnitude, but also the qualitative variations of the decay rates depend drastically on the nature of the materials forming the environment of the

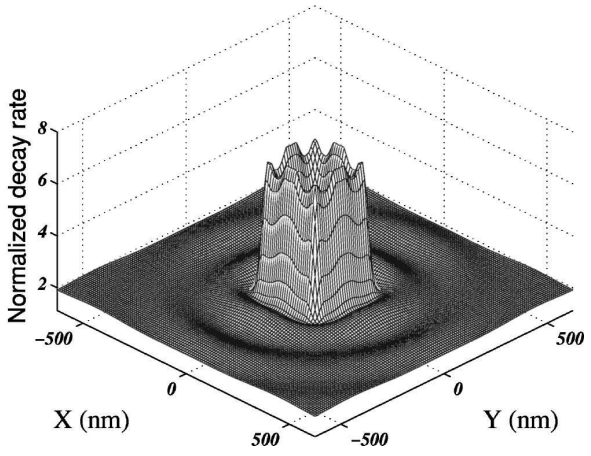

FIG. 8. Normalized decay rate above a gold structure ($\lambda = 520$ nm, $d = 12.5$ nm, $z_0 = 90$ nm) placed on a silver substrate. Dipole moment along z.

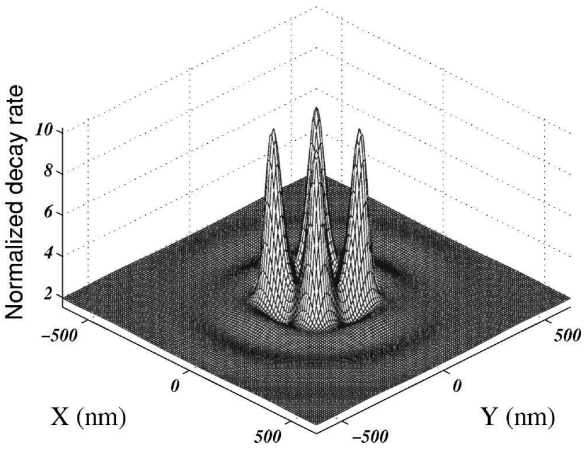

FIG. 9. Normalized decay rate above a silver structure ($\lambda = 520$ nm, $d = 12.5$ nm, $z_0 = 90$ nm) placed on a gold substrate. Dipole moment along z.

molecule (see also Ref. [27]). Nevertheless, a general conclusion may be drawn. Spatially localized perturbations of the environment of the molecule can couple to the evanescent modes pervading the near field of the molecule. Hence, although these evanescent modes do not contribute to the dissipation of energy for a molecule in free space [39], their scattering by the environment provides the molecule with an additional decay channel (in addition to frustration, absorption, and reflection).

V. SINGLE-MOLECULE NEAR-FIELD PROBE

In the preceding section we saw the great diversity of the molecular response; the way the molecule couples to its environment depends on the geometry as well as on the nature of the environment. On the one hand, such diversity might be construed as a hindrance for an easy correspondence between the environment and the molecular response; a correspondence crucial if the molecule were to be used as a near-field probe. On the other hand, the fact that different objects yield radically different molecular responses can be viewed as an asset for two different material could, at least in principle, be unambiguously distinguished. To assess the potential for imaging of a single-molecule probe in a somewhat more transparent way, let us consider a structure of no particular symmetry. We are interested in the ability for the molecular decay rate to reflect the symmetry of the structure. For simplicity we model the structure by a single layer of 410 coupled dipoles. The height of the structure is 20 nm and its permittivity is 2.25 (same as the permittivity of the substrate). The probe molecule is scanned over the structure at constant height 40 nm. If the scanning distance were to be shortened, the size of the dipoles forming the structure would simply have to be reduced. Moreover, we suppose that the molecule is attached to a dielectric material with permittivity 2.25, which consists of a semi-infinite medium occupying the half space $z \geqslant 40.5$ nm. This geometry corresponds to a worst case scenario since for any material of finite lateral extend, multiple scattering would be less important. The de-

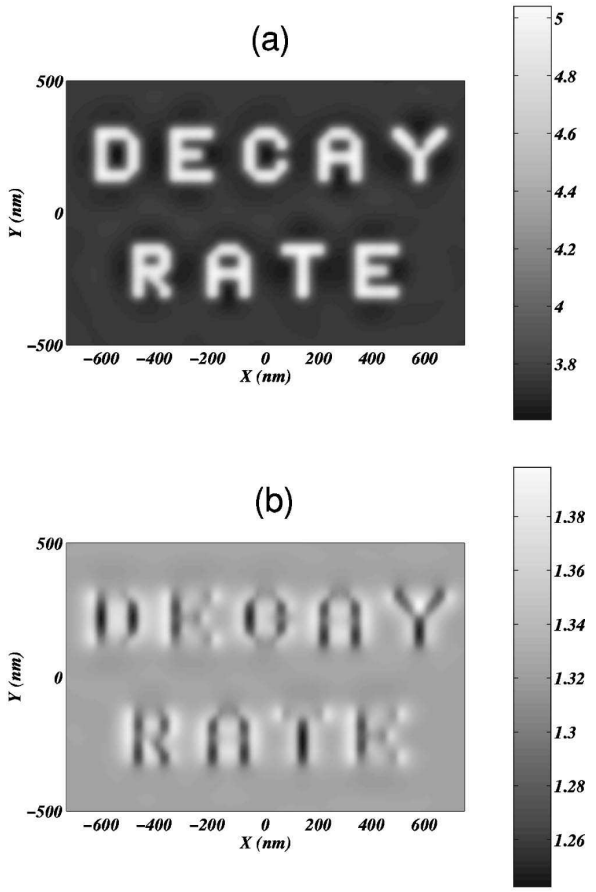

FIG. 10. Single-molecule near-field image ($\lambda = 488$ nm) in a cavity configuration (see text) for a dielectric substrate ($z_0 = 40$ nm). The dipole moment is along z (a) or x (b).

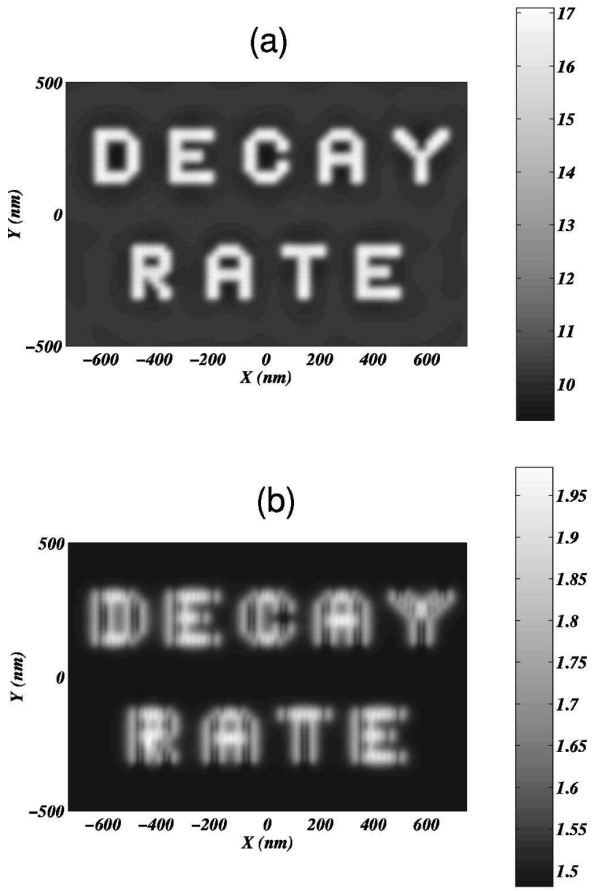

FIG. 11. Same as Fig. 10 but for a gold substrate.

cay rate is computed by deriving the self-consistent field susceptibility of a dressed cavity [26,27] in a fashion similar to the one described in Sec. II, but with the surface now replaced by a three-media junction. The results presented on Fig. 10 show that the decay rate variations are strongly correlated to the actual shape of the sample only in the case of a molecule transition moment oriented along the z axis. This is a logical result as, for the perpendicular (z) case the molecular probe response is symmetric in the scanning plane, while in the parallel (x) case, the true features of the sample are concealed by strong edge effects which are a reflection of the fact that the normal component of the electric field is discontinuous across an interface. Hence, in the case of a perpendicular dipole moment, there exists a rather obvious correspondence between the decay rate variations and the actual shape of the sample. The same applies in the case of a metallic substrate (Fig. 11). This correspondence holds for more extended structures [27]. Hence, provided that the dipole moment of the probe is oriented perpendicular to the substrate, a single molecule could in principle act as a localized near-field probe. On the other hand, for parallel orientation, one obtains a probe sensitive to the frontiers between domains with different permittivities. One should also note that since the dynamics of the molecular probe depends on the optical properties of the environment, the decay rate would also be affected if the molecule were scanned over a flat sample (no topographic features) exhibiting a strong optical contrast.

VI. CONCLUSION

We have presented a theoretical model for the study of near-field modification of spontaneous emission. The coupled dipole method (CDM), allied with a rigorous derivation of the self-consistent electric field linear susceptibility which includes retardation effects, allowed us to address the electromagnetic coupling between an elementary source (molecule or atom) and its environment. Our approach is not restricted to a perturbative scattering regime or to a particular type of environment. Once the electromagnetic response (susceptibility) of a simple environment is determined, in our case a substrate or a cavity, the flexibility of the CDM allows one to consider general structures.

Using this approach, we have computed the decay rates for a single molecule represented by an oscillating dipole, as a function of its position above various structures deposited

on a substrate. We have considered both the dielectric and the metallic case. While the details of the molecular response depend on the very nature of its environment, we have shown that the orientation of the dipole moment of the probe is crucial as in the parallel case (dipole in the scanning plane) the near-field decay rate map is dominated by features stemming from the discontinuity of the normal component of the electric field across interfaces [26]. Also, the scattering of the evanescent modes by sharp features of the sample provides the molecule with an additional decay channel. Accordingly, the decay rates are enhanced around corners or sharp features in general. This result is consistent with previous experimental and theoretical investigations [16–19,21]. For a better assessment of the potential of a single molecule for use as a near-field probe, we placed the molecule in a cavity, thus maximizing multiple scattering, and we considered a geometrically complex sample. This example demonstrated that, provided that the probe's dipole moment is conveniently oriented (in the cases considered in this paper this corresponds to a moment perpendicular to the scanning plane), the decay rate near-field map, is indeed strongly correlated to the actual geometry of the sample. Of course, in the case of a sample composed of several materials whose optical responses are radically different, especially in the case of metals, such a simple correspondence between decay rate variations and sample geometry is likely to be lost. As in any near-field interaction, the distance between the probe and the sample will also influence the decay rate variations. As the distance decreases (increases), the identification of the sample through its near-field signature on the decay rate of the probe becomes easier (more difficult). More detailed studies are presented in Ref. [27].

To conclude, let us state that the theoretical validation of the concept of a single-molecule near-field probe should not occult the difficulties encumbering the road to an experimental realization of such a single-molecule near-field probe (some of these aspects are discussed in Refs. [27,15]). However, the main idea behind an efficient near-field probe is localization and while using a single-molecule might prove to be difficult, if one could gather several of these molecules in a small volume, coherent coupling between these molecules could well permit the realization of a multimolecular probe without compromising the near-field sensitivity. Yet another possibility might be to isolate spectrally a molecule embedded in a host crystal by taking advantage of the inhomogeneous spectral broadening as was done recently to create a single molecule near-field source [52]. Also, let us mention that as pointed out by Agarwal [53], the effect of the environment on the field can be viewed as the breaking of the isotropy of the mode distribution of the vacuum state of the field. This is another way of explaining the dependence of the decay rate on the orientation of the transition moment of the molecule. However, as Agarwal demonstrated, this anisotropy of the vacuum also has the interesting property that it can lead to interferences in the decay from two close lying states to a common state, even if the dipole moments of the two states are orthogonal. Such interference effects could, in principle, also be studied with a single-molecule near-field probe.

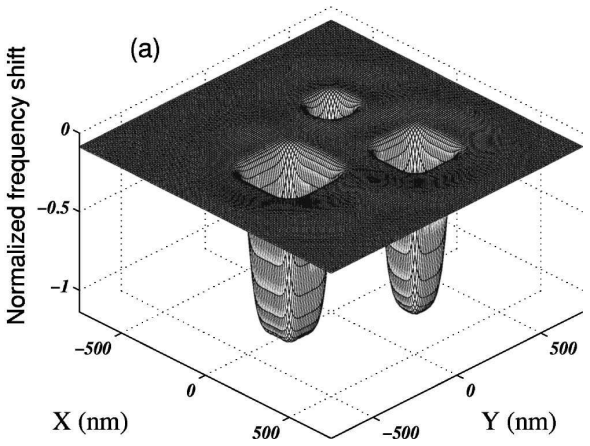

FIG. 12. Same as Fig. 1(a) but for the normalized frequency shift $\Delta\omega/\Gamma_0$.

APPENDIX: FREQUENCY SHIFTS AND MULTILEVEL ATOM

In this paper we use a classical treatment of the interaction between the molecule and the field. As we mentioned, owing to the classical nature of the field linear susceptibility, this classical approach is, for the decay rate, equivalent to a quantum-electrodynamics calculation where the molecule would be represented as a two-level system [54]. Indeed, the normalized decay rates computed in this way are identical to those that would stem from a quantum-mechanical description, only their derivation in a classical framework is simpler for complex geometries. For a multilevel system, the principle of the calculation is the same, one merely needs to add the contributions from all the allowed transitions to the decay rate. The case of the frequency shifts is different, however. The difference lies in the fact that part of the level shift is purely quantum mechanical. Let us assume that the molecular polarizability for a level a has the form

$$\alpha^a_{\alpha\beta}(\omega)=\frac{2}{\hbar}\sum_n \frac{\omega_{na}\mu^{an}_\alpha \mu^{na}_\beta}{\omega^2_{na}-(\omega+i\eta)^2}. \tag{A1}$$

It can then be shown [30] that the shift for level a consists of the two contributions

$$\delta E^{\mathrm{vdW}}_a=-\frac{\hbar}{2\pi}\int_0^\infty S_{\alpha\beta}(\mathbf{r}_0,\mathbf{r}_0,i\xi)\alpha^a_{\alpha\beta}(i\xi)d\xi, \tag{A2}$$

$$\delta E^{RR}_a=-\sum_n \mu^{an}_\alpha \mu^{na}_\beta \,\mathrm{Re}[S_{\alpha\beta}(\mathbf{r}_0,\mathbf{r}_0,\omega_{an})]\theta(\omega_{an}), \tag{A3}$$

where θ is the usual Heaviside step function. The first term (van der Waals or Casimir-Polder according to whether or not retardation is included), pertains to the polarization of the

molecule by vacuum fluctuations (in the presence of the environment). This term has no classical analog. The second term, on the other hand, has an obvious classical interpretation. It corresponds to the shift induced by radiation reaction, i.e., the dispersive effect of the component of the field reflected back by the environment and in phase with the dipole (source) oscillations. Also, unlike the preceding contribution, the derivation of this term does not require an explicit form of the polarizability. In the case of a transition from an excited state a to the (stable) ground state b, the classical frequency shift is given by $\delta E_a^{RR}/\hbar$. Actually, to get a classical expression, this shift should be normalized to the free space decay rate Γ_0 to yield, in the case of a two-level atom, the classical result (see Ref. [55])

$$\frac{\Delta\omega}{\Gamma_0} = -\frac{3}{4k_0^3}\mathrm{Re}[S_{zz}(\mathbf{r}_0,\mathbf{r}_0,\omega)], \tag{A4}$$

where a term $-\Gamma_0/(8\omega)$ negligible compared to 1 has been dropped out. Therefore, the classical shift can be calculated by simply computing the real part of the field susceptibility in the self-consistent procedure described in Sec. III. An example is provided in Fig. 12.

[1] K.H. Drexhage, J. Lumin. **1**,**2**, 693 (1970); K.H. Drexhage, *Progress in Optics XII*, edited by E. Wolf (North-Holland, Amsterdam, 1974), p. 163.

[2] C.K. Carniglia, L. Mandel, and K.H. Drexhage, J. Opt. Soc. Am. **62**, 479 (1972).

[3] R.R. Chance, A. Prock, and R. Silbey, J. Chem. Phys. **60**, 2184 (1974); **60**, 2744 (1974); Adv. Chem. Phys. **37**, 1 (1978).

[4] R.E. Kunz and W. Lukosz, J. Opt. Soc. Am. **67**, 1607 (1977); **67**, 1615 (1977); R.E. Kunz and W. Lukosz, Opt. Commun. **20**, 195 (1977); W. Lukosz, Phys. Rev. B **21**, 4814 (1980); **22**, 3030 (1980); J. Opt. Soc. Am. **71**, 744 (1981); W. Lukosz and M. Meier, Opt. Lett. **6**, 251 (1981); Ch. Fattinger and W. Lukosz, J. Lumin. **31**,**32**, 933 (1984); M. Lieberherr, Ch. Fattinger, and W. Lukosz, Surf. Sci. **189**,**190**, 954 (1987).

[5] E.M. Purcell, Phys. Rev. **69**, 681 (1946).

[6] S. Haroche, in *Fundamental Systems in Quantum Optics*, edited by J. Dalibard, J. M. Raimond, and J. Zinn-Justin (North-Holland, Amsterdam, 1992), pp. 767–940.

[7] P.W. Milonni, *The Quantum Vacuum* (Academic, San Diego, 1994).

[8] H. Chew, Phys. Rev. A **38**, 3410 (1988).

[9] H. Metiu, Prog. Surf. Sci. **17**, 153 (1984).

[10] P.T. Leung and T.F. George, Phys. Rev. B **36**, 4664 (1987).

[11] D. Barchiesi, T. Pagnot, C. Pieralli, and D. Van Labeke, Proc. SPIE **2384**, 90 (1995).

[12] W.L. Blacke and P.T. Leung, Phys. Rev. B **56**, 12 625 (1997).

[13] D. Pastré, P. Grossel, and M. Troyon, J. Phys. D **31**, 2718 (1998); Opt. Commun. **156**, 92 (1998).

[14] C. Henkel and V. Sandoghdar, Opt. Commun. **158**, 250 (1998).

[15] G. Parent, D. Van Labeke, and D. Barchiesi, J. Opt. Soc. Am. A **16**, 896 (1999).

[16] R.X. Bian, R.C. Dunn, X.S. Xie, and P.T. Leung, Phys. Rev. Lett. **75**, 4772 (1995).

[17] X.S. Xie and R.C. Dunn, Science **265**, 361 (1994).

[18] W.P. Ambrose, P.M. Goodwin, J.C. Martin, and R.A. Keller, Science **265**, 364 (1994).

[19] J.K. Trautman and J.J. Macklin, Chem. Phys. **205**, 221 (1996).

[20] C. Girard, O.J.F. Martin, and A. Dereux, Phys. Rev. Lett. **75**, 3098 (1995).

[21] L. Novotny, Appl. Phys. Lett. **69**, 3806 (1996).

[22] C. Hafner, *The Generalized Multipole Technique for Computational Electromagnetics* (Artech, Boston, 1990).

[23] R. Kopelman, K. Lieberman, A. Lewis, and W. Tan, J. Lumin. **48-49**, 871 (1991).

[24] E. Betzig and R.J. Chichester, Science **262**, 1422 (1993).

[25] S.K. Sekatskii and V.S. Letokhov, Appl. Phys. B: Lasers Opt. **63**, 525 (1996).

[26] A. Rahmani, P.C. Chaumet, F. de Fornel, and C. Girard, Phys. Rev. A **56**, 3245 (1997).

[27] A. Rahmani, Ph.D. thesis, Université de Bourgogne, France, 1998; A. Rahmani and F. de Fornel, *Emission Photonique en Espace Confiné* (Eyrolles, Paris, 2000).

[28] G.S. Agarwal, Phys. Rev. A **11**, 230 (1975).

[29] G.S. Agarwal, Phys. Rev. A **12**, 1475 (1975).

[30] J.M. Wylie and J.E. Sipe, Phys. Rev. A **30**, 1185 (1984); **32**, 2030 (1985).

[31] H. Nha and W. Jhe, Phys. Rev. A **54**, 3505 (1996).

[32] M.S. Yeung and T.K. Gustafson, Phys. Rev. A **54**, 5227 (1996).

[33] W.L. Barnes, J. Mod. Opt. **45**, 661 (1998).

[34] J. Dalibard, J. Dupont-Roc, and C. Cohen-Tannoudji, J. Phys. (Paris) **43**, 1617 (1982).

[35] C. Cohen-Tannoudji, J. Dupont-Roc, and G. Grynberg, *Introduction à l'Électrodynamique Quantique* (InterEdition, Paris, 1987), pp. 223, 354–358; English translation: *Photons and Atoms: Introduction to Quantum Electrodynamics* (Wiley-Interscience, New York, 1989).

[36] C. Cohen-Tannoudji, J. Dupont-Roc, and G. Grynberg, *Processus d'Interaction Entre Photons et Atomes* (InterEdition, Paris, 1988), complément A_{IV}; English translation: *Atom-Photon Interactions: Basic Processes and Applications* (Wiley-Interscience, New York, 1992).

[37] J.D. Jackson, *Classical Electrodynamics*, 2nd ed. (Wiley, New York, 1975), p. 395.

[38] I.S. Gradshteyn and I.M. Ryzhik, *Table of Integrals, Series and Products, Corrected and Enlarged Edition* (Academic, New York, 1980).

[39] A. Rahmani and Garnett W. Bryant, Opt. Lett. **25**, 433 (2000).

[40] E.M. Purcell and C.R. Pennypacker, Astrophys. J. **186**, 705 (1973).

[41] F. Hynne and R.K. Bullough, J. Phys. A **5**, 1272 (1972).

[42] A. Wokaun, J.P. Gordon, and P.F. Liao, Phys. Rev. Lett. **48**, 957 (1982).

[43] B.T. Draine, Astrophys. J. **333**, 848 (1988); B.T. Draine and P.J. Flatau, J. Opt. Soc. Am. A **11**, 1491 (1994).

[44] P.C. Chaumet, A. Rahmani, F. de Fornel, and J.P. Dufour, Phys. Rev. B **58**, 2310 (1998).
[45] R. Schmehl, B.M. Nebeker, and E.D. Hirleman, J. Opt. Soc. Am. A **14**, 3026 (1997).
[46] P.C. Chaumet and M. Nieto-Vesperinas, Phys. Rev. B **61**, 14 119 (2000).
[47] P. C. Chaumet and M. Nieto-Vesperinas, Opt. Lett. **25**, 1065 (2000).
[48] *Handbook of Optical Constants of Solids*, edited by E. D. Palik (Academic Press, New York, 1985).
[49] F. de Fornel, *Evanescent Waves*, Vol. 73 of *Springer Series in Optical Sciences* (Springer Verlag, Berlin, 2000).
[50] W.H. Weber and C.F. Eagen, Opt. Lett. **4**, 236 (1979).
[51] M. Born and E. Wolf, *Principles of Optics*, 6th ed. (Cambridge University Press, Cambridge, 1980).
[52] J. Michaelis, C. Hettich, J. Mlynek, and V. Sandoghdar, Nature (London) **405**, 325 (2000).
[53] G.S. Agarwal, Phys. Rev. Lett. **84**, 5500 (2000).
[54] For a discussion of level shifts for a two-level atom see G. Barton, J. Phys. B **7**, 2134 (1974), and Ref. [29].
[55] R.R. Chance, A. Prock, and R. Silbey, Phys. Rev. A **12**, 1448 (1975).

430 OPTICS LETTERS / Vol. 27, No. 6 / March 15, 2002

Local-field correction for an interstitial impurity in a crystal

Adel Rahmani, Patrick C. Chaumet,* and Garnett W. Bryant

Atomic Physics Division, National Institute of Standards and Technology, Gaithersburg, Maryland 20899-8423

Received December 13, 2001

The local-field correction experienced by an interstitial impurity in a crystal with cubic symmetry is derived by use of a rigorous, self-consistent, semimicroscopic description of spontaneous emission in a microcavity. We compute the local-field factor for various positions of the impurity inside the crystal. Furthermore, we demonstrate that the local-field factor can be computed from a simple electrostatic model as a rapidly converging lattice sum. We show that the agreement between the predictions of this simple model and the rigorous calculations is remarkable, opening the way to a simple, general theory of a local-field effect for an impurity in a crystal with arbitrary symmetry.

OCIS codes: 260.2510, 270.5580.

The influence of the local environment on the electromagnetic properties of a nanosource is of crucial importance in modern optics and optoelectronics. As optical devices become smaller, the nature of the local-field correction experienced by a nanosource (atom, molecule, quantum dot) becomes a central issue. In this Letter we present a self-consistent calculation of the local-field correction experienced by an interstitial impurity source in a crystal with cubic symmetry. The local-field correction is obtained from a rigorous description of spontaneous emission[1] that includes the Purcell effect and the dipole–dipole coupling between the source and the host.

Consider a two-level atom that is located at $\mathbf{r}_0$ in a microcavity and has an electric dipole transition moment along direction $\sigma = x, y, z$. The normalized decay rate is given by[2,3]

$$\frac{\Gamma_\sigma}{\Gamma_0} = 1 + \frac{2}{2k_0^3}\,\mathrm{Im}[\overleftrightarrow{F}_{\sigma\sigma}(\mathbf{r}_0, \mathbf{r}_0; \omega)], \tag{1}$$

where Γ_0 and $k_0 = \omega/c$ are the decay rate and the wave vector in free space, respectively, and $\overleftrightarrow{F}$ is the electric-field susceptibility that represents the electromagnetic response of the cavity. Finding the field susceptibility related to the expressions for the decay rate amounts to finding the electric field reflected back to the source by the cavity. To do so we use the coupled dipole method (CDM), which was developed for study of the scattering of light by particles with arbitrary shapes.[4–12] In the CDM the scatterer is discretized over a cubic lattice. Details of the theory are given elsewhere.[1,13,14] Local-field correction L is defined as[13,14]

$$\Gamma = L^2\Gamma_{\mathrm{cav}} + \delta\Gamma, \tag{2}$$

where Γ_{cav} represents the effect of the cavity geometry (reflection at the boundaries of the cavity). The term $\delta\Gamma$ represents the dissipative part of the dipole–dipole interaction between the source and the polarizable elements of the host medium (for a lossless medium, $\delta\Gamma = 0$). When we consider a spherical cavity, we can use the theory of Chew[15] to compute Γ_{cav}. By comparing this result and the CDM result, we can find $|L|$ from Eq. (2).[13,14] Therefore the CDM allows us to compute rigorously the retarded, self-consistent local-field correction.

To gain a better insight into the rigorous scattering theory of the local-field correction it is useful to have a simple model to describe the local-field correction experienced by an impurity source in a crystal. Here we show how the local-field factor can be derived as a rapidly converging sum. In what follows, we consider an infinite crystal. However, it is implicit that all derivations are to be performed for a slab with finite thickness in the z direction. The limit of an infinite crystal is taken once all the relevant lattice sums have been transformed into an absolutely convergent series by the planewise summation technique.[17]

Consider an infinite cubic lattice of point dipoles (polarizability α) with lattice spacing d. We neglect retardation (electrostatic approximation) and assume that a uniform external field $\mathbf{E}^{\mathrm{ext}}$ creates a uniform polarization $\mathbf{P}$ in the lattice. At any interstitial location in the lattice the local field is the sum of the external (applied) field and the field that is due to all the dipoles of the lattice (the case of a substitutional impurity is discussed in Refs. 13 and 14):

$$\mathbf{E}^{\mathrm{loc}} = \mathbf{E}^{\mathrm{ext}} + \mathbf{E}^{\mathrm{dip}}. \tag{3}$$

Let (a, b, c) be the coordinates, normalized by d, of the field point where we evaluate the local field inside a unit cell. We have $-1/2 < x \leq 1/2$, where $x = a, b, c$ and $(a, b, c) \neq (0, 0, 0)$.

The total field created at an interstitial location $\mathbf{r}$ by the dipoles of the lattice is

$$\mathbf{E}^{\mathrm{dip}}(\mathbf{r}) = \sum_i \overleftrightarrow{F}_0(\mathbf{r}, \mathbf{r}_i; 0)\,\frac{\alpha}{d^3}\,\mathbf{E}^{\mathrm{loc}}_{\mathrm{dip}}(\mathbf{r}_i), \tag{4}$$

where the sum runs over the infinite lattice. $\overleftrightarrow{F}_0/d^3$ is the vacuum field susceptibility.[18] Because all dipoles experience the same local field, $\mathbf{E}^{\mathrm{loc}}_{\mathrm{dip}}$, we can write (the dependence on $\mathbf{r}$ is omitted henceforth)

$$\mathbf{E}^{\mathrm{dip}} = \frac{\alpha}{d^3}\,\overleftrightarrow{A}\,\mathbf{E}^{\mathrm{loc}}_{\mathrm{dip}}. \tag{5}$$

Tensor $\overleftrightarrow{A}$ contains all the lattice sums (sums over the lattice of the vacuum field susceptibility) for all dipole

0146-9592/02/060430-03$15.00/0

components. For instance, element (i, j) of the tensor gives the lattice sum along direction i that is due to a lattice of dipoles oriented along direction j. All the elements of $\overleftrightarrow{A}$ can be converted to rapidly converging sums that are readily computed by the general approach of De Wette and Schacher.[19] Polarization $\mathbf{P}$ can be expressed as

$$\mathbf{P} = \frac{\alpha}{d^3}\,\mathbf{E}_{\mathrm{dip}}^{\mathrm{loc}} = \frac{\epsilon - 1}{4\pi}\,\mathbf{E}^{\mathrm{macro}}, \tag{6}$$

where $\mathbf{E}^{\mathrm{macro}}$ is the macroscopic field. Using the continuity relations at an interface for the electric field and the electric induction, we also have

$$\overleftrightarrow{\eta}\,\mathbf{E}^{\mathrm{macro}} = \mathbf{E}^{\mathrm{ext}}, \tag{7}$$

with

$$\overleftrightarrow{\eta} = \begin{bmatrix} 1 & 0 & 0 \\ 0 & 1 & 0 \\ 0 & 0 & \epsilon \end{bmatrix}, \tag{8}$$

where ϵ is the permittivity. This expression for $\overleftrightarrow{\eta}$ relates to our definition of the infinite crystal as the limit for infinite thickness of a slab normal to direction z. Equation (3) becomes

$$\mathbf{E}^{\mathrm{loc}} = \overleftrightarrow{\eta}\,\mathbf{E}^{\mathrm{macro}} + \frac{\epsilon - 1}{4\pi}\,\overleftrightarrow{A}\,\mathbf{E}^{\mathrm{macro}}. \tag{9}$$

By definition, local-field factor $\overleftrightarrow{\Lambda}$ satisfies

$$\mathbf{E}^{\mathrm{loc}} = \overleftrightarrow{\Lambda}\,\mathbf{E}^{\mathrm{macro}}. \tag{10}$$

Using Eqs. (9) and (10), we obtain

$$\overleftrightarrow{\Lambda} = \frac{\epsilon - 1}{4\pi}\,\overleftrightarrow{A} + \overleftrightarrow{\eta}\,. \tag{11}$$

The local-field factor is obtained at once from Eq. (11). For example, the local field factor in direction i is

$$|L_i| = \left(\sum_{j=1}^{3} |\Lambda_{ij}|^2\right)^{1/2}. \tag{12}$$

To foster understanding we first consider special high-symmetry cases. At certain locations of the lattice there is no mixing of polarization in the contribution of the dipoles to the local field, and the tensors $\overleftrightarrow{A}$ and $\overleftrightarrow{\Lambda}$ are diagonal. For example, an impurity source with a transition moment along z and located at $(a, b, 0)$ or $(0, 0, c)$ will experience a local-field correction

$$L \equiv L_z = \frac{\epsilon - 1}{4\pi}\,A_{zz} + \epsilon\,, \tag{13}$$

with

$$A_{zz} = \sum_{m=-\infty}^{\infty} [3(m + c)^2 S_{5/2} - S_{3/2}], \tag{14}$$

$$S_n = \sum_{k,l=-\infty}^{\infty} [(k + a)^2 + (l + b)^2 + (m + c)^2]^{-n}. \tag{15}$$

Note that A_{zz} is a geometrical factor that is independent of ϵ. In Table 1 we list the values of dipole sum A_{zz} and local-field factor L_z at various locations inside the unit cell. The dipole sum satisfies[17] $A_{zz}(a, b, c) + A_{zz}(c, a, b) + A_{zz}(b, c, a) = -8\pi$.

Because the local-field factor in our CDM treatment of spontaneous emission is obtained from the decay rate (power losses) and not from the field, the CDM approach actually yields $|L|$. We plot in Figs. 1 and 2 the local-field factor found with the CDM (the direction of the transition moment of the source defines direction z). The dashed lines are the results computed from Table 1. The agreement is remarkable. Note that when $c = 0$ (source in a lattice plane and oriented normally to it) $L = 0$ for certain values of ϵ, which would correspond to an inhibition of spontaneous emission by local-field effects. The reason for the excellent agreement between the rigorous CDM scattering theory and the simple quasi-static model is that the CDM calculation of the local field in a crystal is

Table 1. Dipole Sum and Local-Field Factor at Various Locations in the Lattice

Location				
a	b	c	Dipole Sum A_{zz}	Local-Field Factor L_z
1/2	0	0	−23.4186008171	$-0.864\epsilon + 1.864$
1/2	1/2	0	−17.0453117498	$-0.356\epsilon + 1.356$
0	0	1/2	21.7044604055	$2.727\epsilon - 1.727$
0	1/2	1/2	−4.04371473946	$0.678\epsilon + 0.322$
1/4	0	0	−73.5999217727	$-4.857\epsilon + 5.857$
0	0	1/4	122.067102317	$10.71\epsilon - 9.710$
1/2	1/2	1/2	−8.37758040957	$(\epsilon + 2)/3$

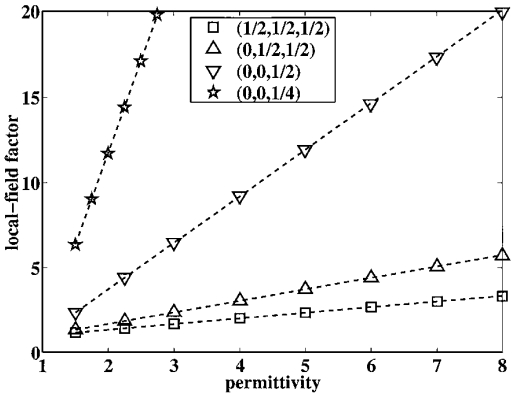

Fig. 1. Absolute value of the local-field factor versus permittivity ϵ for an interstitial source: symbols, self-consistent CDM calculation; dashed curves, results from Table 1 [Eq. (13)]. The numbers in parentheses give the (a, b, c) coordinates of the source in the lattice. The transition moment of the source defines the z direction.

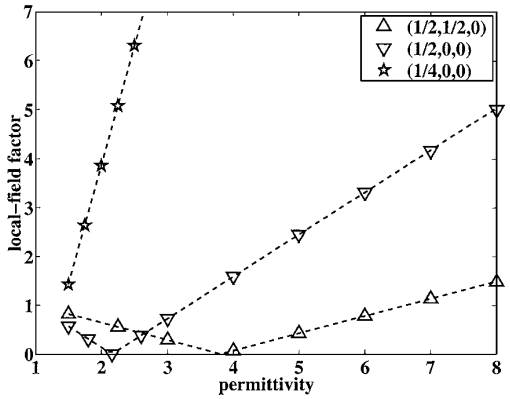

Fig. 2. Same as Fig. 1 but at different locations in the lattice.

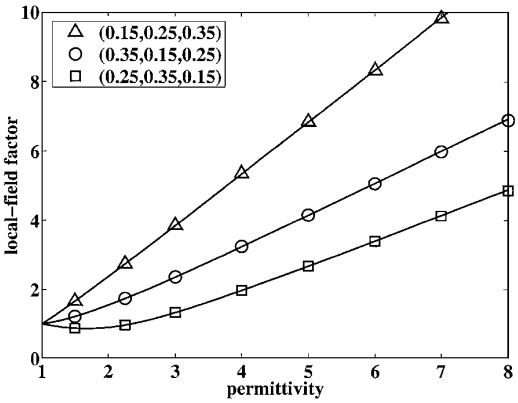

Fig. 3. Same as Fig. 1 but here we have computed the solid curves by using the generalized local-field factor [Eq. (12)].

meaningful only if $k_0 d \ll 1$. When this condition is satisfied, because only the dipoles closest to the source make a significant contribution to the local-field,[13,14] the phase associated with retardation remains small and has a negligible effect on the local-field correction.

Whereas in the special cases of Table 1 the local-field factor depends linearly on the permittivity, we emphasize that in the general case the linearity of the local-field factor with respect to the permittivity is only asymptotic (for large ϵ). This condition is illustrated in Fig. 3, in which we compare Eq. (12) and our rigorous, self-consistent calculation for sources at some arbitrary location in the lattice. Again, the agreement is excellent.

In conclusion, we have used a rigorous, self-consistent scattering theory of spontaneous emission in microcavities to derive the local-field correction experienced by an interstitial impurity source in a crystal. We also presented a simple but general theory of local-field correction based on rapidly converging sums, whose validity we have demonstrated. Although we explicitly considered a cubic lattice here, this simple model of a local-field effect can be extended to crystals with lower symmetry by use of the appropriate lattice sums.[19]

Correspondence should be addressed to G. W. Bryant at garnett.bryant@nist.gov.

*Permanent address, Institut Fresnel (Unité Mixte de Recherche 6133), Faculté des Sciences et Techniques de St. Jérôme, F-13397 Marseille Cedex 20, France.

References

1. A. Rahmani, P. C. Chaumet, and F. de Fornel, Phys. Rev. A **63,** 0238-19 (2001).
2. G. S. Agarwal, Phys. Rev. A **11,** 230 (1975).
3. G. S. Agarwal, Phys. Rev. A **12,** 1475 (1975).
4. E. M. Purcell and C. R. Pennypacker, Astrophys. J. **186,** 705 (1973).
5. B. T. Draine, Astrophys. J. **333,** 848 (1988).
6. B. T. Draine and P. J. Flatau, J. Opt. Soc. Am. A **11,** 1491 (1994), and references therein.
7. P. C. Chaumet, A. Rahmani, F. de Fornel, and J.-P. Dufour, Phys. Rev. B **58,** 2310 (1998).
8. P. C. Chaumet and M. Nieto-Vesperinas, Phys. Rev. B **61,** 141-19 (2000).
9. P. C. Chaumet and M. Nieto-Vesperinas, Phys. Rev. B **62,** 111-85 (2000).
10. P. C. Chaumet and M. Nieto-Vesperinas, Opt. Lett. **25,** 1065 (2000).
11. P. C. Chaumet and M. Nieto-Vesperinas, Phys. Rev. B **64,** 0354-22 (2001).
12. A. Liu, A. Rahmani, G. W. Bryant, L. Richter, and S. Stranick, J. Opt. Soc. Am. A **18,** 704 (2001).
13. A. Rahmani and G. W. Bryant, "Spontaneous emission in microcavity electrodynamics," Phys. Rev. A (to be published).
14. A. Rahmani and G. W. Bryant, Phys. Status Solidi B **224,** 807 (2001).
15. H. Chew, J. Chem. Phys. **87,** 1355 (1987).
16. H. Chew, Phys. Rev. A **38,** 3410 (1988).
17. B. R. A. Nijboer and F. W. De Wette, Physica **24,** 422 (1958).
18. A. Rahmani and G. W. Bryant, Opt. Lett. **25,** 433 (2000).
19. F. W. De Wette and G. E. Schacher, Phys. Rev. **137,** A78 (1965).

Résumé

Le travail présenté dans ce tapuscript correspond à mon travail en tant que post-doc, durant 18 mois au sein de l'Instituto de Ciencia de Materiales de Madrid, et maître de conférence à l'université d'Aix-Marseille III durant ces 7 dernières années. Mes domaines de recherche portent sur :

- les forces optiques. Depuis l'observation de la queue des comètes, il est connu que les objets peuvent être mis en mouvement par la lumière. Nous avons étudié ces forces optiques pour des objets (de taille mésoscopique ou nanoscopique) déposés ou proche d'un substrat plan. Nous avons notamment montré qu'il était possible dans la configuration d'un microscope de champ proche optique sans ouverture, éclairé en réflexion totale interne, de manipuler sélectivement des nano-particules diélectriques ou métalliques.
- le sondage électromagnétique. Des objets inconnus sont éclairés successivement avec différents faisceaux incidents et à partir du champ électromagnétique diffracté par ces objets en champ lointain, à l'aide d'algorithmes d'inversion, nous pouvons en déduire leurs positions et leurs permittivités relatives. Nous avons notamment montré qu'en mettant des nano-objets sur un réseau nanostructuré, alors une résolution inférieure à $\lambda/10$ était possible, battant ainsi largement le critère de Rayleigh.
- la fluorescence : Nous avons étudié comment la dynamique d'une source fluorescente était modifiée par son environnement. Nous avons alors appliqué cette étude pour montrer qu'une molécule fluorescente pouvait être utilisée comme une sonde de champ proche révélant ainsi la géométrie de l'échantillon avec une résolution latérale de 20 nm.

Tous ces sujets de recherche ont bien sûr en commun d'être de l'optique, mais surtout un domaine où les ondes évanescentes ont toute leur importance.

Mots clés : Forces optiques ; sondage électromagnétique ; fluorescence.